Karlsruhe Institute of Technology

Surface Displacements from Fusion of Geodetic Measurement Techniques Applied to the Upper Rhine Graben Area

Inaugural dissertation

for the fulfilment of the requirements
for the academic degree of

Doctor of Engineering (Dr.-Ing.)

Accepted by
the Department of Civil Engineering,
Geo and Environmental Sciences of the
Karlsruhe Institute of Technology

Submitted by

Dipl.-Ing. Thomas Fuhrmann

from Oberderdingen, Baden-Württemberg, Germany

Day of examination:	12.04.2016
Main referee:	Prof. Dr.-Ing. Dr. h.c. Bernhard Heck, Karlsruhe Institute of Technology, Karlsruhe, Germany
Co-referees:	Prof. Dr.-Ing. Stefan Hinz, Karlsruhe Institute of Technology Karlsruhe, Germany
	Prof. Dr. ir. Ramon Hanssen, Delft University of Technology, Delft, The Netherlands

Karlsruhe 2016

Further members of the doctoral committee:

Prof. Dr. Philipp Blum,
Karlsruhe Institute of Technology
Karlsruhe, Germany

Prof. Dr. rer. nat. Martin Breunig,
Karlsruhe Institute of Technology
Karlsruhe, Germany

Prof. Dr. rer. nat. Nico Goldscheider,
Karlsruhe Institute of Technology
Karlsruhe, Germany

Prof. Dr.-Ing. Maria Hennes,
Karlsruhe Institute of Technology
Karlsruhe, Germany

PD Dr.-Ing. Boris Jutzi,
Karlsruhe Institute of Technology
Karlsruhe, Germany

Prof. Dr. rer. nat. Frank Schilling,
Karlsruhe Institute of Technology
Karlsruhe, Germany

Fuhrmann, Thomas

Surface Displacements from Fusion of Geodetic Measurement Techniques Applied to the Upper Rhine Graben Area

Department of Civil Engineering, Geo and Environmental Sciences,
Karlsruhe Institute of Technology (KIT)

Keywords: Upper Rhine Graben, surface displacement, levelling, GNSS, InSAR, data fusion, Kriging interpolation, least-squares adjustment

Typeset by the author using the LaTeX Documentation System.
Some figures have been generated using the Generic Mapping Tools (GMT, Wessel et al., 2013).

This work is simultaneously published in:
German Geodetic Commission, series C, No. 773
Bavarian Academy of Sciences and Humanities, Munich, 2016
ISBN 978-3-7696-5185-0

“Zwischen all den Sternen schaut ein Satellit auf mich,
ich kann ihn zwar nicht sehn, doch sieht er alles, glaube ich.”

(“Between all those stars, a satellite looks down on me,
I cannot see it, but it sees everything, I guess.”)

from “Satellitenbild *(satellite image)*”,
The Wohlstandskinder, German rock band (1995–2005)

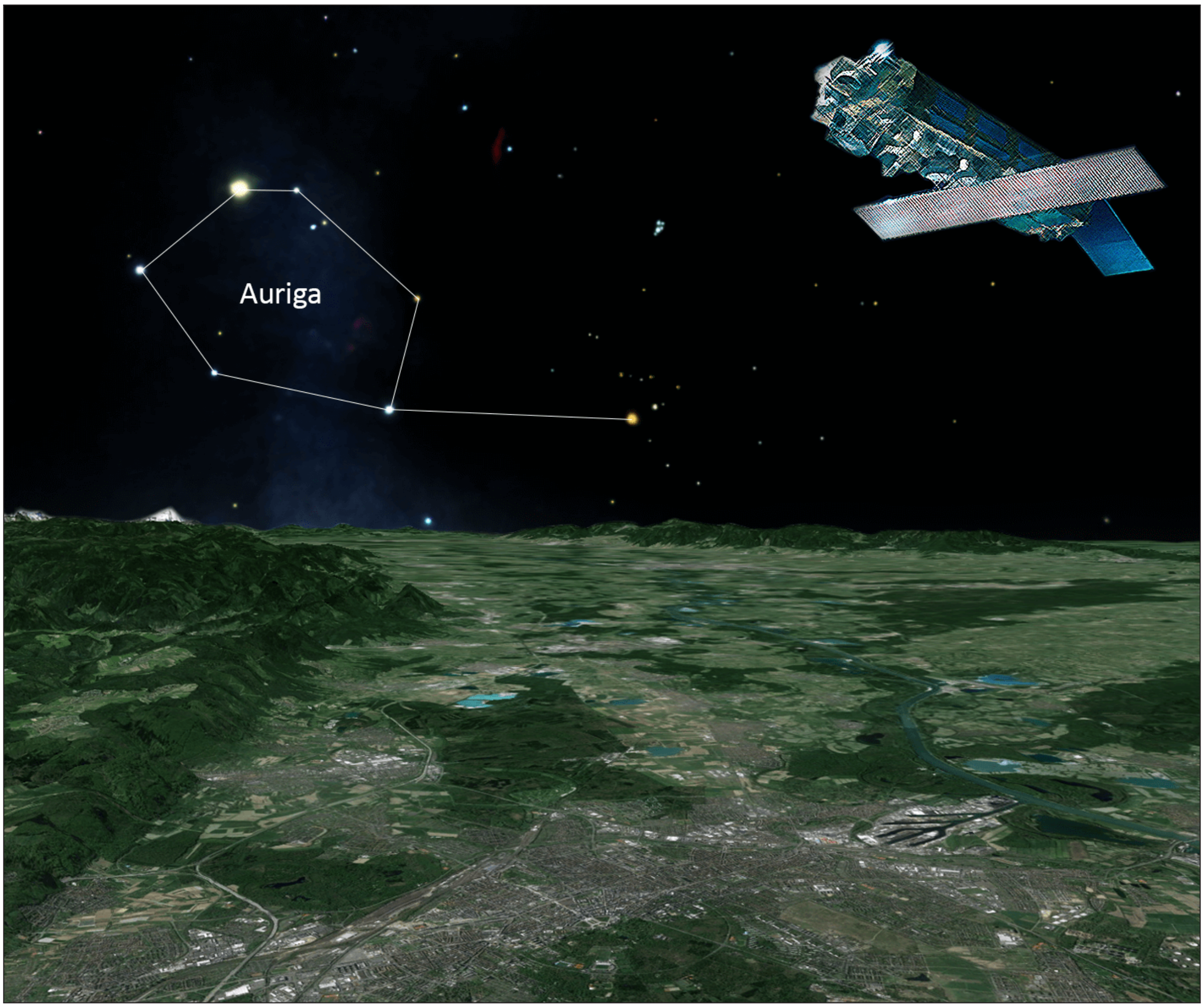

Artist view on Karlsruhe and the Upper Rhine Graben, assembled by C. Fuhrmann, image source: Google Earth, ESA

Abstract

Detailed information on the present-day intraplate deformation of the Upper Rhine Graben (URG) is of interest for both researchers and decision makers. The URG is part of the European Cenozoic Rift System and carrying a significant probability for strong earthquakes. Furthermore, anthropogenic activities such as mining, groundwater usage and geothermal energy production may affect the deformation of the complex fault system. Within this work, surface displacements in the URG area bounded by the Rhenish Massif in the north and the Alps in the south are detected with geodetic measurement techniques. The three considered techniques use (i) terrestrial measurements from precise levelling, (ii) satellite signals received at ground-based GNSS[1] antennas and (iii) spaceborne radar data acquired by SAR[2] satellites.

Levelling data measured in several campaigns between 1867 and 2012 provides detailed insight into the vertical displacements of the investigation area. A least-squares adjustment of a large database of levelling measurements from Germany, France and Switzerland yields vertical displacement rates at 14,098 levelling benchmarks with a mean standard deviation (1σ) of 0.18 mm/a. GNSS signals observed by a network of permanently operating sites are analysed to estimate 3D coordinates. Horizontal and vertical displacement rates are derived from the coordinate time series between 2002 and 2011 at 85 GNSS sites in the URG area. Resulting standard deviations (2σ) of horizontal and vertical site velocities are 0.4 mm/a and 1.3 mm/a, respectively. SAR data acquired by the ERS[3] and Envisat[4] missions provide surface displacements along the slant line of sight towards the satellites in two time intervals, 1992–2000 and 2002–2010, respectively. A combination of displacement time series of both time intervals results in mean standard deviations (2σ) of displacement rates of 0.6 mm/a. The SAR data available at one descending and two ascending tracks covering the whole URG area are analysed, resulting in slant displacement components with different looking directions.

The results of the single-technique analyses provide useful information on the current deformation behaviour of the investigation area. The levelling results reveal uplift tendencies in the Black Forest and in parts of the Vosges Mountains and the Palatinate Forest w.r.t. subsidence in most parts of the URG. Horizontal velocities at GNSS sites evidence a relative southward motion of the Rhenish massif w.r.t. a northward motion of the Alps resulting in sinistral shearing at the URG. InSAR[5] is most suitable to investigate the temporal and spatial behaviour of surface displacements related to anthropogenic activities in the URG area. In order to exploit the advantages of the three techniques w.r.t. accuracy, sensitivity to different displacement components and spatial as well as temporal resolution, a new approach for the fusion of displacements from levelling, GNSS and InSAR is presented. The resulting map of 3D surface displacement rates resolves the neotectonic movements in the URG area with unprecedented spatial resolution and accuracy. With mean standard deviations of 0.4 and 0.2 mm/a for the horizontal and vertical velocities, respectively, the combined velocity solution is particularly able to resolve the relative movements of the graben interior. The 3D velocity field contributes to an improved understanding of intraplate deformation processes and strain accumulation

---

[1] GNSS: Global Navigation Satellite Systems such as the Global Positioning System (GPS)

[2] SAR: Synthetic Aperture Radar

[3] ERS: European Remote Sensing Satellites

[4] Envisat: Environmental Satellite

[5] InSAR: Interferometric SAR

in the URG. In addition, the temporal and spatial behaviour of surface displacements related to anthropogenic activities is resolved at several places, providing a fundamental basis for interpretation and discussion, for researchers as well as for decision makers.

Zusammenfassung

Detaillierte Informationen zum heutigen Deformationszustand des Oberrheingrabens (ORG) und seiner Umgebung sind von großem Interesse für Wissenschaftler und Entscheidungsträger. Der ORG ist der prominenteste Teil eines mitteleuropäischen Riftsystems, das Europa vom Mittelmeer bis zur Nordsee durchquert. Die tektonisch interessante Grabenstruktur ist in den letzten Jahrzehnten von moderater seismischer Aktivität geprägt. Allerdings gibt es eine signifikante Wahrscheinlichkeit für starke Erdbeben bis zur Magnitude $M_W = 7$. Außerdem kommt es durch die intensive Nutzung des Untergrunds im Oberrheingrabengebiet in den letzten Jahrzehnten verstärkt zu größeren, anthropogenen Deformationen, die im Zusammenhang mit Erdölförderung, Bergbau, Grundwasserentnahme oder Geothermie stehen. In der vorliegenden Arbeit werden Oberflächenbewegungen im Gebiet des ORG zwischen dem Rheinischen Schiefergebirge im Norden und den Alpen im Süden aus drei geodätischen Verfahren abgeleitet. Die drei Verfahren verwenden (1) terrestrische Messungen mittels Präzisionsnivellement, (2) Satellitensignale, die an GNSS[1]-Antennen auf der Erde empfangen werden und (3) satellitengestützte Radardaten, die von SAR[2]-Satelliten aufgezeichnet werden.

Die Nivellementdaten im Bereich der trinationalen Oberrheingrabenregion wurden von den zuständigen Landesvermessungsbehörden aus Deutschland, Frankreich und der Schweiz in mehreren Kampagnen gemessen. Als Datenbasis stehen Nivellementmessungen aus den Jahren 1867 bis 2012 zur Verfügung. Aus Messdaten an mehrfach beobachteten Nivellementpunkten können vertikale Verschiebungen der Erdoberfläche berechnet werden. Dazu werden die gemessenen Höhenunterschiede an den Nivellementpunkten mit einem kinematischen Modell nach der Methode der kleinsten Quadrate ausgeglichen. Aus mehr als 40.000 Beobachtungen können vertikale Verschiebungsraten an mehr als 14.000 Nivellementpunkten im gesamten Oberrheingrabengebiet abgeleitet werden. Mit einer mittleren Standardabweichung von unter 0,2 mm/a (1σ) lassen sich aus den Verschiebungsraten Rückschlüsse über die rezente Geodynamik des ORG ziehen. Die Nivellementsergebnisse zeigen unter anderem eine relative Absenkung des Grabeninneren bezüglich der Grabenschultern (Schwarzwald, Teile der Vogesen und des Pfälzer Walds) von 0,5–0,8 mm/a. Zusätzlich zu mittleren, linearen Verschiebungsraten kann das zeitliche Bewegungsverhalten entlang einzelner Nivellementlinien untersucht werden, beispielsweise an den Hauptrandverwerfungen des Grabens oder in Gebieten mit anthropogenen Aktivitäten.

Aus GNSS-Daten können 3D-Koordinaten mit einer Genauigkeit von wenigen mm bis cm abgeleitet werden. Im Gebiet des ORG kann auf ein Netz aus permanenten GNSS-Stationen zurückgegriffen werden, die von unterschiedlichen öffentlichen oder privaten Institutionen aus Deutschland, Frankreich und der Schweiz betrieben werden. Die Datenbasis umfasst GNSS-Beobachtungen von mehr als 80 Stationen und startet im Jahr 2002. In einer differenziellen Auswertung der zur Verfügung stehenden Daten werden zunächst tägliche Koordinatenlösungen für Ost-, Nord- und Vertikalkomponente berechnet. Die Koordinatenzeitreihen über den kompletten ausgewerteten Zeitraum zwischen 2002 und 2011 liefern schließlich Verschiebungsraten für jede Komponente. Die 2σ-Standardabweichungen der resultierenden Raten an 85 permanenten Stationen liegen im Mittel bei 0,4 mm/a für die horizontalen Komponenten und bei 1,3 mm/a für die vertikale Komponente. An einigen Stationen (10 %) reicht

---

[1] GNSS: Global Navigation Satellite Systems wie z. B. das Global Positioning System (GPS)

[2] SAR: Synthetic Aperture Radar

die Länge der ausgewerteten Zeitreihe derzeit nicht aus, um die kleinen tektonischen Bewegungen des ORG signifikant nachzuweisen. Die horizontalen Geschwindigkeiten an 76 Stationen zeigen jedoch ein plausibles Bewegungsmuster und machen die großräumige tektonische Deformation des ORG sichtbar. Der ORG ist eingespannt zwischen SSO-gerichteten Bewegungen des Rheinischen Schiefergebirges und NNO-gerichteten Bewegungen im Alpenvorland, was zu erhöhten Strainraten insbesondere im südlichen Bereich des Grabens führt.

Mittels SAR-Interferometrie (InSAR) lassen sich Oberflächenbewegungen entlang der Sichtlinie zu einem SAR-Satelliten in der Größenordnung weniger mm nachweisen. Im Bereich des ORG wurden SAR-Daten der ESA[1]-Satelliten ERS[2] und Envisat[3] ausgewertet. Die Daten decken einen Zeitraum von 1992–2000 beziehungsweise 2002–2010 ab und sind entlang von ca. 300 km langen und 100 km breiten Streifen in aufsteigenden und absteigenden Satellitenbahnen verfügbar. Im Rahmen dieser Arbeit werden Daten aus zwei aufsteigenden und einer absteigenden Bahn mit der Persistent-Scatterer-Methode ausgewertet. Das Ergebnis der Auswertungen eines SAR-Streifens sind eindimensionale Verschiebungen entlang der Sichtlinie zum Satelliten an Punkten mit gleichbleibenden Rückstreueigenschaften (Persistent Scatterer). In den Städten und Dörfern des Untersuchungsgebietes sind die Reflexionseigenschaften der nutzbaren Punktstreuer über die ausgewerteten Zeiträume stabil. Hier wird eine hohe räumliche Auflösung für die Verschiebungen erzielt. Um die Genauigkeit der Ergebnisse zu steigern, werden die Verschiebungszeitreihen der beiden Datenzeiträume mathematisch kombiniert. Die mittleren 2σ-Standardabweichungen der resultierenden Verschiebungsraten liegen bei 0,6 mm/a. Insbesondere in Gebieten mit größeren (anthropogenen) Deformationen lässt sich die räumliche und zeitliche Entwicklung der Oberflächenbewegungen mit InSAR nachverfolgen. Für die großräumige Tektonik des ORG ist die erzielbare Genauigkeit nicht ausreichend, um Bewegungen im sub-mm/a-Bereich signifikant nachzuweisen. Insbesondere in Datenstapeln, die nur wenige SAR-Szenen enthalten, lassen sich atmosphärische Effekte dann nicht vollständig vom Deformationssignal trennen. Eine Fusion von InSAR mit Nivellement und GNSS auf Basis der Verschiebungsraten soll es ermöglichen sowohl die langwelligen als auch die kurzwelligen Anteile des Deformationssignals aufzulösen.

Die Ergebnisse aus den Einzelauswertungen der drei Techniken liefern bereits ein bemerkenswertes Gesamtbild der aktuellen Oberflächenbewegungen im Untersuchungsgebiet. Um die Vorteile der drei komplementären Messverfahren hinsichtlich ihrer Sensitivität für horizontale und vertikale Bewegungskomponenten, der räumlichen und zeitlichen Auflösung der Messungen sowie ihrer Genauigkeit optimal auszunutzen, wird ein neuer Ansatz vorgestellt, der die Ergebnisse der Techniken gewinnbringend zu einem 3D-Geschwindigkeitsfeld fusioniert. Dazu werden die resultierenden Verschiebungsraten der drei Techniken zunächst mittels Kriging auf ein gemeinsames Gitter interpoliert. In diesem Schritt werden die Verschiebungen der InSAR-Auswertungen von ERS- und Envisat-Daten auf Basis der Zeitreihen zu einer mittleren Verschiebungsrate über den Gesamtzeitraum kombiniert. Zur Datenfusion werden aus linearen Verschiebungsraten von Nivellement (vertikal), GNSS (horizontal) und InSAR (aufsteigende und absteigende Bahnen) 3D-Verschiebungsraten berechnet. Im Rahmen der Datenfusion werden auch die unterschiedlichen Referenzrahmen der drei Techniken berücksichtigt. Das resultierende 3D-Geschwindigkeitsfeld visualisiert die rezente Geodynamik des ORG in bisher unerreichter räumlicher Auflösung und Genauigkeit und trägt zu einem besseren Verständnis der vorherrschenden Deformationsprozesse bei. Unter anderem zeigen die Ergebnisse, dass das Grabeninnere Bereiche mit unterschiedlichen Bewegungsmustern aufweist

---

[1] ESA: European Space Agency

[2] ERS: European Remote Sensing Satellites

[3] Envisat: Environmental Satellite

wie z. B. eine relative Senkung im Bereich des *Heidelberger Lochs* gegenüber der Gegend um Karlsruhe in Verbindung mit einer linksdrehenden Rotationsbewegung in den horizontalen Bewegungskomponenten. Die Standardabweichungen von 0,38, 0,45 und 0,18 mm/a für Ost-, Nord-, bzw. Vertikalkomponente belegen die hohe Qualität des Kombinationsansatzes und der ausgewerteten Daten.

Oberflächenbewegungen im Zusammenhang mit anthropogenen Aktivitäten konnten an verschiedenen Stellen im Untersuchungsgebiet nachgewiesen werden, insbesondere im Bereich des ehemaligen Kohleabbaus im Saarland und in Lothringen, im ehemaligen Kalisalzabbaugebiet Wittelsheim bei Mulhouse und im Bereich der Erdölfelder Landau. Letzteres liefert die Möglichkeit, die drei Verfahren gegenseitig zu validieren, da Messdaten aller drei Techniken in hoher zeitlicher Auflösung vorliegen und sowohl Senkungen als auch Hebungen im Bereich von bis zu 7 mm/a signifikant nachweisbar sind. Die durchgeführten Untersuchungen zu Oberflächenbewegungen im gesamten Oberrheingrabengebiet bilden eine gute Basis, um die künftige Nutzung des Untergrunds wissenschaftlich und strategisch zu diskutieren. Die kontinuierliche Erfassung von GNSS-Daten an den permanenten Stationen im ORG und angrenzenden Gebieten sowie die Fortführung der SAR-Datenbasis mit den Starts der beiden Sentinel-1-Satelliten ermöglichen zukünftige Untersuchungen zu Oberflächenbewegungen im ORG unter Verwendung einer zeitlich längeren Datenbasis. Die in dieser Arbeit entwickelten Auswerte- und Kombinationsansätze können dabei direkt auf künftige Studien und andere Untersuchungsgebiete übertragen werden.

Contents

Appendix

Chapter 1

Introduction

The first chapter of the thesis is dedicated to introduce the background of the performed investigations and put the work into a broader context (Sect. 1.1). Sect. 1.2 presents the research objectives and addresses some major questions to be handled within the thesis. The outline of the thesis is given in Sect. 1.3, considering different groups of readers.

1.1 Motivation and Background

Every two years, the organisation Naturefriends International elects a transnational and ecologically valuable European region as *Landscape of the year* (NFI, 2015). It is a happy coincidence that at present the Upper Rhine Valley is the latest designated landscape of the year (for the years 2013/2014), right at the moment while the major results of this work have been achieved. Nonetheless, from a scientific point of view, the widely used term *Upper Rhine Valley* is not correct as valleys are washed out by a river by definition (Röhr, 2014). However, the river Rhine developed about 15 Ma ago (Böhme et al., 2012) and thus may not be responsible for the subsidence of the Earth's crust at the Upper Rhine Graben (URG), which already started about 45 Ma ago (Rouchy, 1997, p. 82). By definition, a *graben* is a piece of crust which is sunk w.r.t. its surroundings along parallel striking faults (Murawski & Meyer, 2010, p. 65 f.). A graben may exist on the cm- as well as on the km-scale, with the URG standing out as a rather large specimen. The highly interesting URG system has been studied by many scientists, but is not yet fully understood in various respects.

If one would ask people living in or close to the URG whether they have ever felt an earthquake, many of them would deny it, at least most of the younger people. However, strong earthquakes happen with a certain frequency in the URG area. The strongest and most devastating event known today is constrained to a moment magnitude M_W of 6.7 to 7.1 and happened in 1356 close to the city of Basel (Fäh et al., 2009). In 1728 a $M_W = 5.3$ event was registered close to Mahlberg, between Freiburg and Strasbourg (Meidow, 1998). The largest earthquakes in recent years occurred 2003 close to Rambervillers in the Vosges Mountains with $M_W = 4.8$ (Grünthal & Wahlström, 2012) and 2004 close to Waldkirch, northeast of Freiburg, with $M_W = 4.6$ (Häge & Joswig, 2009). Events with smaller magnitudes occur much more frequently. It is worth having a look at the daily updated catalogue of the Seismological Service conducted by the Federal State Office for Geology, Natural Resources and Mining of Baden-Württemberg (LGRB, 2015). Epicentres of instrumentally measurable earthquakes located in the URG area appear every few days in the catalogue. Despite all the progress that has been made, the scientific community cannot unambiguously assess how frequently strong earthquakes may occur in the URG area and how likely the occurrence of an earthquake like the Basel 1356 event is. Hence, it is important to better understand the current tectonic setting of the URG – not least, because the region is highly populated and economically important.

The aim of this work is to contribute to the knowledge of the present-day tectonics of the URG area by quantifying the deformation from a geodetic point of view. In addition, anthropogenic activities in the subsurface are supposed to affect the deformation behaviour of the region. The URG has been intensively exploited in the past decades by coal, potash and oil mining, groundwater usage and for geothermal energy production. The influence of these activities on the surface are unknown in most cases. For scientific monitoring and public acceptance of future subsurface activities in the URG area, detailed knowledge of the spatial and temporal behaviour of surface displacements is essential for both geoengineers and decision makers.

Within this work, all available geodetic data suitable for the measurement of surface displacements in the URG area is collected, evaluated and analysed. Fortunately, there is a lot of data available in the region, measured with levelling, GNSS[1] and SAR[2] satellites. On the other hand, it is lengthy and hard work to analyse the large amount of data, along with the development of new strategies in order to achieve the best possible results. The thesis will also provide insights into the characteristics of the three techniques *levelling*, *GNSS* and *SAR interferometry (InSAR)*. Focussing on the estimation of surface displacements, the major challenges concerning a suitable and up-to-date analysis of the available database will be given for each technique.

It is an honourable task to analyse data which was measured more than 100 years ago. Geodesists used to wear a suit and top hat for the field work at that time. Except for the clothing, the execution of levelling measurements has not significantly changed, since the first levelling line used within this work was measured in 1867. Furthermore, it is amazing that the accuracy of the old measurements is almost at the same level as it is today. In general, deep respect is due to the hundreds of surveyors who organised and carried out the measurements resulting in the database available for the geodynamic studies presented within this work – a real treasury of data. Thereby, the discrepancies of measured height differences along close levelling loops over hundreds of km are on a scale of several mm only. This corresponds to observing from one goal line of a football pitch to the other, whether a fine dust particle ($< 10\ \mu$m) lies on a football or not.

One of the most crucial advances of modern geodesy is the availability of GNSS, enabling world-wide 3D positioning at the mm- to cm-scale. Furthermore, positioning and navigation with low-cost GNSS receivers has rapidly become part of our everyday life in the last years. For geodetic tasks, high-tech antennas are used to receive and process the GNSS signals, emitted from satellites at about 20,000 km distance. Analysing the GNSS signals of several satellites over some hours along with a sophisticated consideration of error sources, such as the atmospheric delay, the position on Earth may be determined with an accuracy of a few mm. This is like distinguishing the location of two adjacent fine dust particles at Strasbourg Cathedral from the tower of the Karlsruhe Castle.

"Between all those stars, a satellite looks down on me" (a line of the song "satellite image") sounds like a poetic description of a SAR satellite. In fact, the SAR satellites carry sensors which actively "look" down on Earth and receive the reflected signal. However, their "eyes" are exceptionally sharp, taking into account that only a small fraction of the transmitted signal is received back at the satellite. It is even more astonishing that surface displacements in the range of several mm can be observed with SAR satellites orbiting our planet at an altitude of 500 to 800 km with a speed of approximately 25,000 km/h. This is like observing the movement of a football at the fine-dust-particle-scale from the goal line of the opposite side of the football pitch – while continuously moving.

---

[1] GNSS: Global Navigation Satellite Systems

[2] SAR: Synthetic Aperture Radar

1.2 Problem statement

The research objective of this work is to provide a complete picture of recent surface displacements in the whole URG area at a spatial extent of about 300 km × 200 km in N–S and E–W direction, respectively. Thereby, both large-scale tectonic deformation and local displacements at faults or related to man-made activities are of interest. The following questions shall be addressed within the thesis:

- Is it possible to measure the small tectonic deformation in the URG area with the available geodetic data sets?

  From geological estimates, e. g. from thickness distribution of Quaternary deposits or from outcrops at faults, the tectonic deformation of the URG is supposed to be well below 1 mm/a. Hence the question arises, whether it is possible to measure these small displacements with significance at all. The determination of a displacement is strongly related to the length of the total period covered by the data. It is thus important to cover the largest possible period with each of the techniques. Furthermore, a focus should be set on the best analysis strategies for each technique.

- How can the single-technique analyses of levelling, GNSS and InSAR be enhanced in order to derive the best possible accuracy for the displacement estimates?

  For each technique, the resulting displacements shall be at the best possible accuracy level. Therefore, (i) the database of each technique is evaluated w.r.t. quality and usability and (ii) the processing strategy is evaluated and adapted w.r.t. the technique-specific error sources. Note that the displacements resulting from all three techniques are relative quantities and hence also the resulting precision estimates depend on the introduced reference frame. Separated for each technique the following issues have to be considered.

  Levelling:

    - assessment of the usability of levelling data from the 19th century,
    - calculation of loop misclosures and detection of strong systematic effects,
    - application of gravity corrections,
    - appropriate weighting of the observations using variance component estimation.

  GNSS:

    - coordinate time series analysis incorporating the consideration of periodic effects and jumps,
    - selection of usable GNSS sites w.r.t. the length of the time series and the noise level,
    - proper subtraction of the major trend of the Eurasian plate.

  InSAR:

    - selection of appropriate master and slave images for the InSAR stack processing,
    - reduction of atmospheric effects by filtering methods or additional meteorological data,
    - selection of high quality pixels using appropriate quality measures,
    - combination of displacement data from different SAR sensors at the level of time series.

- Is it possible to combine surface displacements from levelling, GNSS and InSAR in a reasonable and gainful way?

  The properties of the three techniques are different in many aspects, such as temporal and spatial resolution, location and distribution of the measurement points, accuracy and datum definition. A major difference is that levelling can only provide information on vertical displacements, GNSS on horizontal as well as vertical displacements and InSAR on displacements along a slant line of sight towards the side-looking SAR satellite. One may ask in particular whether a combined displacement field benefits from the advantages of each technique and thus provides useful information on the present-day deformation of the URG area or not. Furthermore, it would be desirable if the developed combination approach was also applicable to other regions and for new satellite missions, such as Sentinel-1.

- How do the results affect the current knowledge of the complex graben system?

  Both the single-technique results and a combined 3D displacement solution shall be discussed w.r.t. the current knowledge of the tectonics of the URG and its surroundings. Hence, the findings of previously published geoscientific investigations on the URG have to be summarised and discussed, including previous geodetic studies. It will be interesting to see whether the geodetically derived surface displacements are in accordance or discordance with general concepts of tectonic deformation of the URG from geology and geophysics. In this context, the reader should keep in mind that the displacements observed at the surface with geodetic techniques are a superposition of all effects acting in the subsurface such as tectonic deformation, sedimentation and anthropogenic effects.

- At which locations may the observed surface displacements be related to anthropogenic activities?

  The natural resources of the URG area are exploited at several locations in the investigation area. A compilation of all past and current man-made subsurface activities with best knowledge and conscience will give an overview of the areas potentially affected by anthropogenic deformation. Areas with conspicuous surface displacements w.r.t. the magnitude of displacements and the temporal and spatial behaviour can be investigated in detail by one or more techniques. Especially InSAR is well suited to trace the spatio-temporal behaviour of surface displacements related to local anthropogenic activities. However, the combined surface displacement solution is dedicated to tectonic deformation, and hence should suppress non-tectonic features at the best possible rate.

1.3 Outline

This work is supposed to be of interest for readers with different backgrounds like geodesy, radar remote sensing, geology, geophysics or geodynamics. Within this section, the outline of the thesis is presented, designating the group of readers for whom the corresponding chapters are of special interest.

Chap. 2 is intended to give a comprehensive overview of the investigation area. The evolution of the URG as well as the current knowledge of the tectonic setting of the region are presented including previous geodetic studies. The chapter enlightens the URG from different perspectives and is hence dedicated to incorporate the whole geoscientific community.

Sect. 2.4 gives an overview on known anthropogenic activities in the tri-national URG area and may furthermore be of some value for decision makers.

Chap. 3 could as well be denoted *Material and Methods* as it introduces the reader to the general concepts for the analysis of the geodetic databases of levelling, GNSS and SAR data. It has a repeating structure for the three techniques and subsequently presents: (i) the general methodology of each technique, (ii) the available database in the URG area and (iii) the strategies to derive surface displacements from the techniques. Without going into too much detail, this chapter may be particularly useful for non-geodesists in order to understand the principal features of each technique.

Chap. 4–6 describe in detail the single-technique analyses of levelling, GNSS and SAR data in the URG area. People with a background in classical geodesy are probably more interested in the specific mathematical and statistical investigations performed with the levelling and GNSS database (Chap. 4 and 5). Radar scientists may find useful information on the processing and evaluation of ERS and Envisat data in Chap. 6. However, the resulting surface displacements obtained with the three techniques are highly valuable for the whole geoscientific community dealing with the URG area. Major results are found in Sect. 4.5.4 and 4.6 for the levelling part, Sect. 5.3.1 and 5.3.3 for the GNSS part, and in Sect. 6.5.4 and 6.5.5 for InSAR.

Chap. 7 presents the developed approach to combine surface displacements from levelling, GNSS and InSAR to a high-resolution 3D velocity field. The chapter also contains theoretical and practical aspects on spatial interpolation using the geostatistical Kriging technique. The presented approach for the fusion of different SAR sensors based on displacement time series is particularly relevant for the InSAR community. The finally resulting combined 3D displacement rates for the URG area are presented and discussed in Sect. 7.5.

Chap. 2–7 are terminated by a brief summary section, which lists the key points of the content discussed within the whole chapter. Finally, Chap. 8 gives an overall conclusion of the whole thesis. Furthermore, open questions and future works are briefly discussed.

Chapter 2

The Upper Rhine Graben (URG)

The study area of all investigations performed in this thesis is the URG area located in the tri-national region of Germany, France and Switzerland. More than six million people live at the Upper Rhine area consisting of the national regions Südpfalz, Baden, Alsace and North-western Switzerland. For the year 2010, the German-French-Swiss conference of the Upper Rhine (GFSC, 2012) calculated a population density of 279 inhabitants per km^2, which is higher than the mean population densities of Germany, France, Switzerland or whole Europe, although also the mountain regions surrounding the URG have been included in the statistical assessment. The URG comprises large cities and industrial areas listed in Tab. 2.1 mainly contributing to the economic development of the region.

Table 2.1: Population of large cities in the URG area listed from north to south.

City	Inhabitants	Inhabitants per km^2	Inhab. of the agglomeration
Mannheim	296,690 [a]	2,047 [a]	1,148,497 [d]
Karlsruhe	299,103 [a]	1,724 [a]	509,452 [d]
Strasbourg	272,222 [b]	3,478 [b]	488,552 [d]
Freiburg	220,286 [a]	1,439 [a]	364,283 [d]
Basel	174,974 [c]	7,333 [c]	739,228 [d]

[a] Source: Statistisches Bundesamt (2014), status: 2013-12-31
[b] Source: Insee (2015), status: 2011-12-31
[c] Source: Statistisches Amt (2015), status: 2015-05-31
[d] Source: Brinkhoff (2015)

Besides the methodological items concerning the analysis and combination of geodetic data w.r.t. the determination of surface displacements, the main goal of the thesis is to provide significant displacement results for the geoscientific community working on topics relevant to the URG. The quantification and qualification of surface displacements is an important factor for decision makers dealing with current and future projects in the URG area such as earthquake-resistant construction standards, groundwater usage, oil extraction or geothermal power generation. This chapter aims to introduce the URG area to the reader. Sect. 2.1 integrates the region into the geological context of Europe, whereas Sect. 2.2 focusses on the evolution of the graben structure itself. Sect. 2.3 gives an overview of the recent tectonics of the URG from previous geological, geophysical and geodetic studies. As the natural resources of the URG area are increasingly exploited in the last decades revealing clearly visible deformation features in the analysed geodetic data, this topic is discussed in an extra section at the end of this chapter (Sect. 2.4).

2.1 Geological overview of Europe

The URG is the most prominent segment of a continental Cenozoic rift system in Central Europe (Ziegler, 1992). In a topographic view of Central Europe, the graben structure bounded by the Vosges Mountains (VG) in the west and the Black Forest (BF) in the east is clearly visible, see Fig. 2.1. The term *Cenozoic* is used for the era 66 Ma ago until present (Cohen et al., 2013) and therefore covers a quite young period in geological time scales. If the age of the Earth of 4.54 billion years corresponds to one day, the Cenozoic era would only cover the last 21 minutes. In order to integrate the evolution of the URG into a broader context, a geological overview of Europe is given within this section.

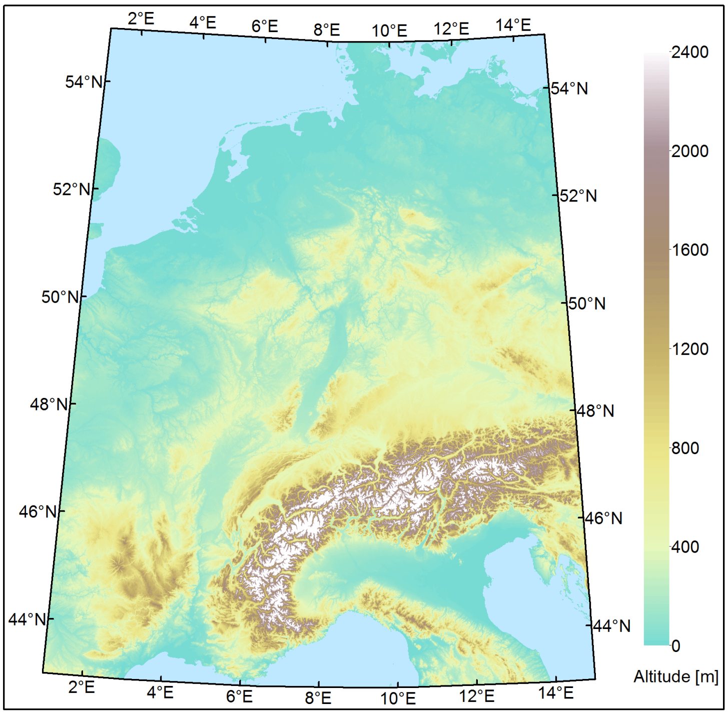

Figure 2.1: Topographic map of Central Europe generated from elevation data of the Shuttle Radar Topography Mission (SRTM). The URG is located north of the Alps at approximately 8°E and between 47°30′ and 50°N. Spatial reference: Universal Transverse Mercator (UTM) coordinate system, zone 32N.

The evolution of our planet Earth as we know it today is largely influenced by the phenomenon of plate tectonics. At the beginning of the 20th century, A. Wegener tried to prove a concept of rigid continental plates which are slowly drifting away from each other (Wegener, 1929). He supported the concept of continental drift by geological, paleontological, biological and climatological observations. T. J. Wilson expanded the theory of sliding plates which destruct and create crustal material, when he discovered transform faults and established what is known today as the Wilson cycle (Wilson, 1963, 1965). He postulated a multiple tectonic cycle of about 300 Ma length describing aggregation and dispersal of continental crust (Murawski & Meyer, 2010, p. 188):

1. Continental rifting	Divergent boundary
2. Ocean-floor-spreading	
3. Subduction	Convergent boundary
4. Collision-type orogeny	

In this way, the Earth's continents and oceans evolved to what we have today. The earliest continental crust existing in Europe are Precambrian[1] terranes in Fennoscandia and the Ukraine which can be traced back to 3.5–3.2 Ga (Bogdanova et al., 2008). Further Precambrian rocks are present on the British Isles, on the Iberian Peninsula and in Southern Italy. The crystalline basement rocks of Central and Western Europe were mainly built in the Cadomian orogen (650–550 Ma ago, Plant et al., 2005). A presently prominent mountain building in Northern Europe, i. e. Scotland, Ireland, Scandinavia, is part of the Caledonian orogen, occuring between Late Cambrian and Earliest Devonian (490–390 Ma ago, Plant et al., 2005; Frisch et al., 2011, p. 161 f.). The crystalline basements of the VG and the BF were built in the Variscan orogen (370–280 Ma ago, also called Hercynian orogen, Eisbacher & Fielitz, 2010, p. 16 ff.). The Variscan mountains cross Central Europe in E–W direction and are subdivided into different zones (von Raumer et al., 2003), most parts of the Upper Rhine massifs (VG, BF) belonging to the Moldanubian zone (Frisch et al., 2011, p. 163 ff.). The terranes of Europe are summarised in a map by Oczlon (2006) providing a view on the growth of the Earth over billions of years. Fig. 2.2(a) displays a crop of the terrane map for Central Europe including a description for terranes relevant to the URG area. Fig. 2.2(b) shows the distribution of the Variscan basement in Central Europe. The granitic and metamorphic rocks of the Moldanubian zone can be traced from Spain over the Massif Central, VG and BF to the Bohemian Massif.

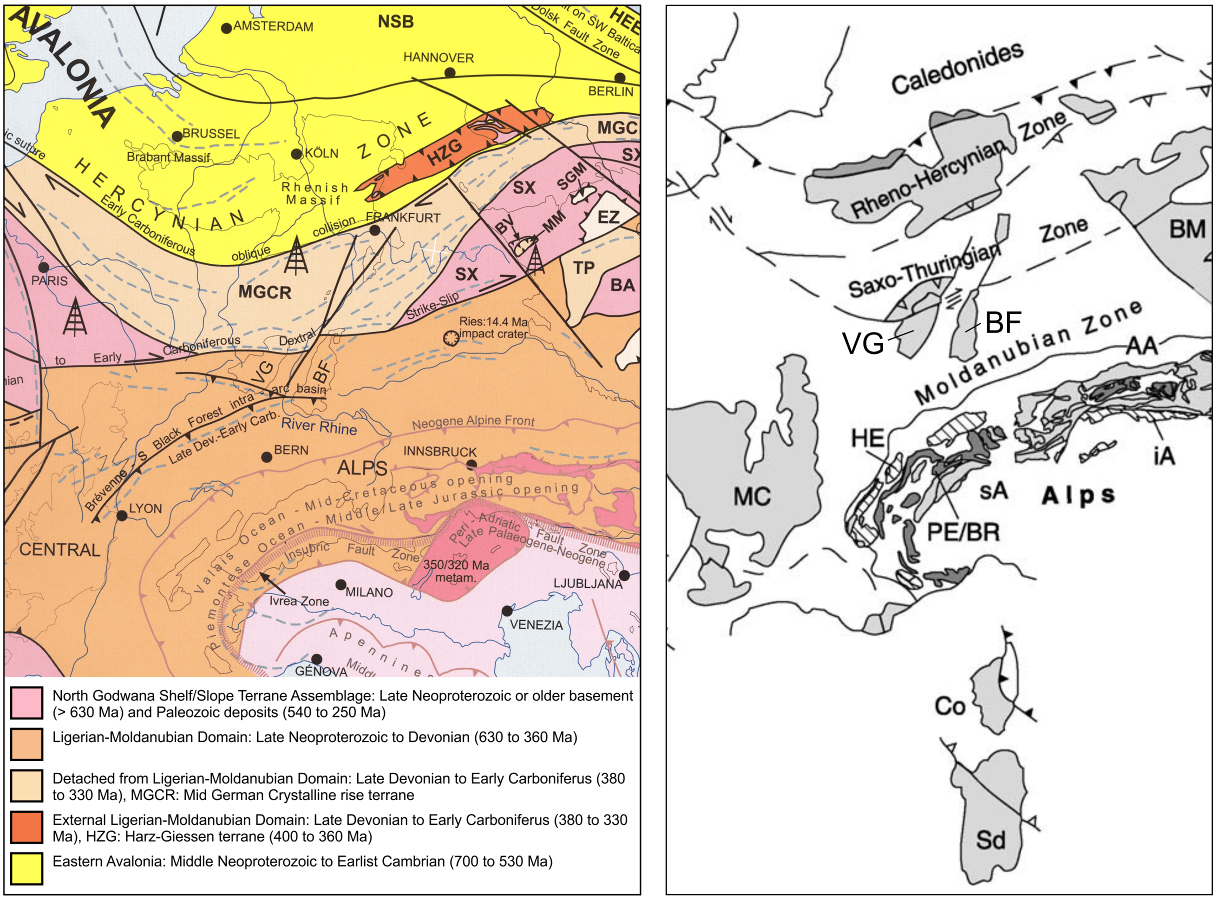

(a) Growth of Europe's lithosphere documented in the *Terrane Map of Europe*, modified from Oczlon (2006).

(b) Geological map of Variscan basement areas, modified from von Raumer et al. (2003).

Figure 2.2: Crops of geological maps for Central Europe, VG: Vosges mountains, BF: Black Forest, MC: Massif Central, BM: Bohemian Massif.

---

[1] see stratigraphy table published by Cohen et al. (2013) for chronology and age of geological eras

The evolution of the Alps started in Cretaceous and mainly affects the present tectonics of Central Europe. Bonnet et al. (2007) subdivides the Alpine mountain building into three main orogenic phases: Eoalpine (140–60 Ma), Mesoalpine (60–30 Ma) and Neoalpine (30–0 Ma) events, while the main mountain building processes took place during the younger phases. As typical for an Alpine style orogeny, the foreland of the mountain front is filled up with the debris of the ascending mountains building a Molasse basin (Frisch et al., 2011, p. 149 ff.). Since the Paleocene (60 Ma ago), the axis of maximum compressive stress north of the alps has changed from NNE–SSW to NW–SE (Ahorner, 1975) pushing the Molasse basin and the Jura Mountains towards NW and still affecting the present-day horizontal deformation of the URG. During late Eocene (35 Ma ago), the N directed compressional stresses originating in the Alpine and Pyrenean collision zones created the European Cenozoic rift system (Dèzes et al., 2004). Fig. 2.3 displays the locations of the individual grabens belonging to the European rift system w.r.t. the Alps. The URG is the most prominent segment of the rift system and is discussed in the following section.

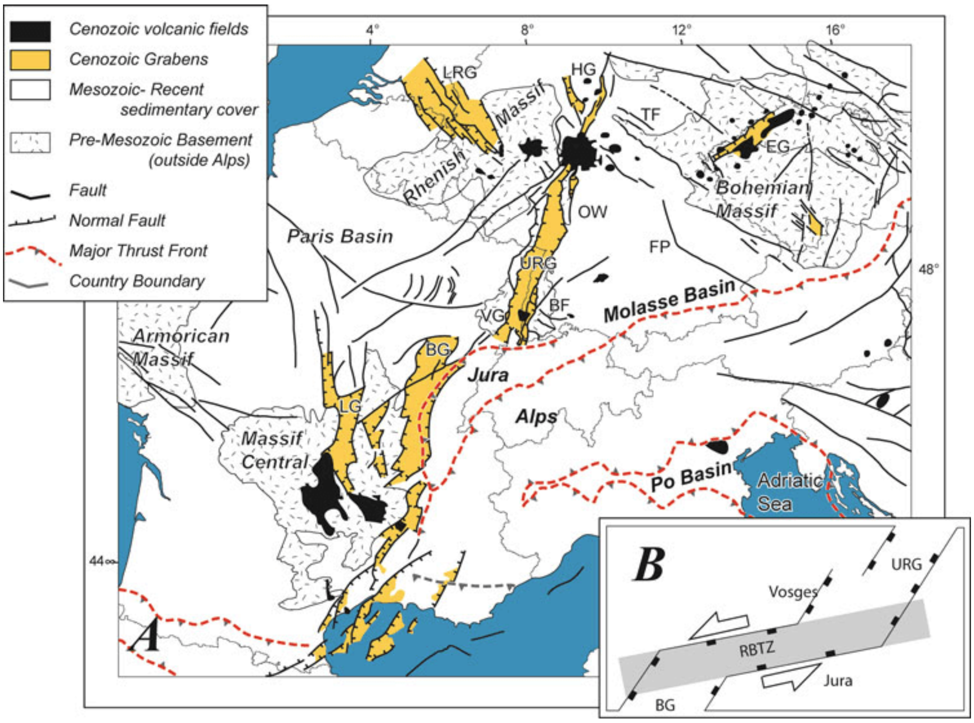

Figure 2.3: Location of the European Cenozoic rift system and oblique opening of Rhine and Bresse graben from Schlunegger & Mosar (2011). In addition to the URG, the Lower Rhine Graben (LRG) and the Bresse Graben (BG) are shown in Fig. 2.1.

2.2 Evolution of the URG

The URG is part of an intracontintental rift zone. According to Milanovsky (1972), rift zones may be classified into three categories:

(a) oceanic rift zones: axial graben bordered by oceanic crust on both sides, e. g. mid ocean ridges,

(b) intracontinental rift zones: rift floor and shoulders are of continental crust, e. g. URG,

(c) intercontinental rift zones: oceancic rift floor bordered by continental crust on both sides, e. g. Red Sea.

The formation of the URG started in Eocene and is visualised in Fig. 2.4. At the end of Eocene, a vertical displacement between the graben basin and its shoulders of more than 1000 m existed. During Oligocene (30 Ma ago), the graben surface was situated below sea level allowing for marine ingression. The Upper Rhine developed into a channel connecting the Alpine Molasse zone with the North Sea Basin (Schumacher, 2002), and might have looked similar to the Red Sea today. In Early Miocene (20 Ma ago), the Kaiserstuhl volcano was formed in the southern part of the URG where the crust is thinnest and large faults exist (Frisch et al., 2011, p. 34). Being interrupted between Late Miocene and Early Pliocene (5 Ma ago), sedimentation restarted resulting in a total thickness of sediments in the graben of more than 3 km in the northern part (Doebl & Olbrecht, 1974).

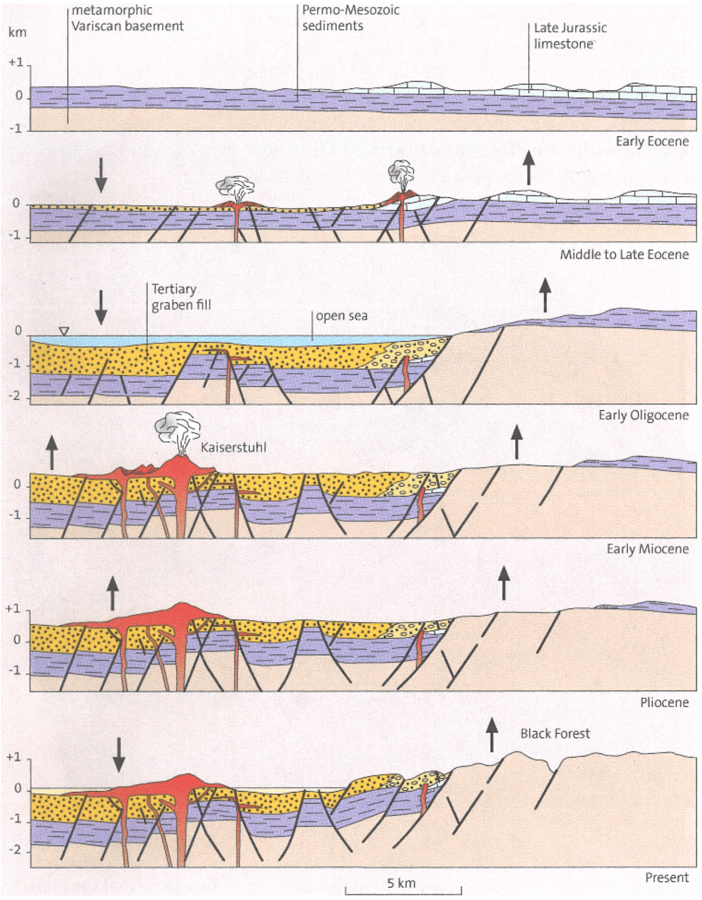

Figure 2.4: Cross sections showing the evolution of the URG, from Frisch et al. (2011, p. 32).

Quaternary deposits are concentrated at the so called *Heidelberger Loch* (northern URG, 350 m thick) and at the *Geiswasser basin* (southern URG, 200 m thick), see Buchmann & Connolly (2007). For the *Heidelberger Loch*, Pflug (1982, p. 42 f.) derives an average subsidence rate of 0.1–0.2 mm/a from the thickness of Quaternary deposits. Peters & van Balen (2007a) investigate Pleistocene terraces in the northern URG in order to better constrain the recent tectonic activity. From dating of terraces, they derive vertical displacement rates between 0.01 and 0.08 mm/a, which is well below the rates in the adjacent Rhenish Massif (0.1–0.3 mm/a uplift, van Balen et al., 2000) and in the *Heidelberger Loch* (Pflug, 1982).

2.3 Recent Tectonics of the URG area

This section describes the recent tectonics of the URG area from different points of view. It presents the currently available findings and conclusions related to geomorphology, geology, the faulting mechanism, seismicity and surface displacements of the URG. The evolution and neotectonics of the URG have been intensively studied within the EUCOR[1]-URGENT[2] project, see Behrmann et al. (2005). This multi-disciplinary research and training programme lasting from 1999 to 2009 aimed at a better understanding of the seismic hazard, neotectonics and evolution of the URG and surrounding areas. Some of the cited publications in this section are based on the investigations carried out within the EUCOR-URGENT framework.

2.3.1 Geomorphology

As the most prominent segment of the European Cenozoic rift system, see Fig. 2.3, the shape of the URG is nicely visible in the landscape. The graben has a length of more than 300 km, a fairly constant width of approximately 36 km (Frisch et al., 2011, p. 31) and appears as vast lowland plain in the landscape. It is bounded by the VG in the west, by the BF in the east, by the Jura Mountains and the Alps in the southeast and by the Rhenish Massif in the northwest. The average height above sea level in the graben interior varies between 85 m in the northern part (river Rhine at Mainz) and 250 m in the southern part (river Rhine at Basel), with an anomaly at the Kaiserstuhl volcano which has a maximum height of 557 m above sea level. The graben shoulders reach maximum heights of 1424 m (Grand Ballon, VG) and 1493 m (Feldberg, BF) in the west and east, respectively. In the northern part, the graben is bounded by the Palatinate Forest (Pfälzer Wald) in the west and the Kraichgau and the Odenwald in the east, but with significantly lower heights of the graben shoulders (below 673 m).

2.3.2 Geology

The geological layers existing in the URG are strongly correlated with the evolution of the graben system as presented in Sect. 2.2. Fig. 2.5 shows the major geological units present at the surface. The oldest rocks are found in the BF and the VG, mainly granites and gneisses, belonging to the Variscan basement, see Sect. 2.1 and Fig. 2.2(b). The geological layers on both sides of the URG are found in symmetrical sequence forming the Southwest German and the Lorraine cuesta landscape (Lower Triassic, Middle Triassic, Upper Triassic, Jurassic). In the east, the Swabian Jura forms the backbone of the Southwest German cuesta landscape and is of special interest from a tectonic and seismic point of view (Geyer et al., 2011, p. 19 and p. 446). In the northwest, Paleozoic rocks of the Rhenish Massif bound the URG as discussed by Murawski et al. (1983). South of the Rhenish Massif, Permian rocks of the Saar-Nahe Basin and the Tertiary Mainz Basin form the boundary of the URG.

The graben itself is filled with sediments of different thickness and distribution, particularly along the NNW–SSE axis of the graben. Subsidence and sedimentation started in the southern URG and developed further north within Tertiary (Pflug, 1982, p. 7). Sedimentation was interrupted in late Miocene in the whole URG, but restarted in Pliocene and is still going on. The thickness of Quaternary sediments in the graben reaches up to 350 m at the *Heidelberger Loch*. The spatial distribution of Quaternary deposits is shown in a map by Bartz (1974), also given in Buchmann & Connolly (2007). Vertical profiles of the different deposit layers and their distribution within the graben are shown in several publications (Roll, 1979; Pflug,

---

[1] EUCOR: EUropean COnfederation of Upper Rhine universities

[2] URGENT: Upper Rhine Graben: Evolution and NeoTectonics

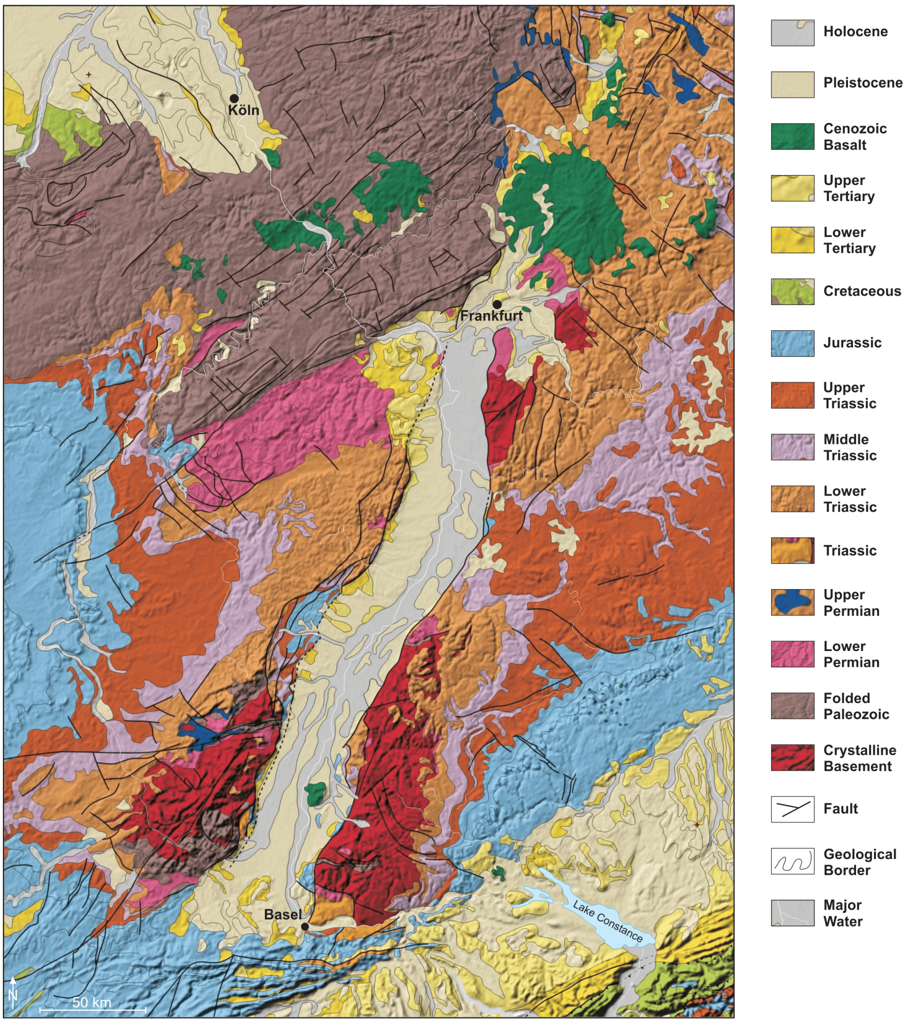

Figure 2.5: Geological map of the URG area, modified from Röhr (2014).

1982; Geyer et al., 2011; Frisch et al., 2011). Doebl & Olbrecht (1974) present a map of the Tertiary base in the graben and observe a maximum thickness of 3,335 m close to Frankenthal (northern URG, Germany). Roll (1979, p. 72) estimates the deposit volume of the graben shoulders to more than 27,000 km^3 and the total volume of sediments within the graben to nearly 19,000 km^3. This is about 400 times the volume of water in the Lake Constance (48 km^3, IKGB (2013)). It is important to keep in mind that the total subsidence measured at the surface is caused by a superposition of tectonic subsidence and sedimentary load, see Eisbacher (1996, p. 249 ff.). Following Eisbacher & Fielitz (2010, p. 74), the mass of the sediments in the graben is responsible for more than half of the total subsidence of the graben interior.

Regarding the deeper subsurface, Ziegler & Dèzes (2006) presented a map showing the depth of the Moho discontinuity for Western and Central Europe and adjacent oceanic domains derived from a compilation of already published regional Moho maps. It becomes obvious that the URG area is located in a zone with relatively low Moho depths. In the southern URG, the Moho depth is found at only 24 km, see also Illies (1977), whereas it increases to 58 km below the Alps. The regional uplift of the crust-mantle boundary extends up to 75 km east and west of the graben boundaries (Prodehl et al., 1992). According to Eisbacher & Fielitz (2010, p. 15), the crust in the URG area is exposed to expansion and thinning since approximately 40 Ma.

2.3.3 Faulting mechanisms

The URG comprises many faults, capable of both strike-slip and normal faulting. Schumacher (2002) characterises the contemporary URG as a strike-slip system with two pull-apart basins in the northern and southern part, separated by a restraining bend in the central part. Illies (1977) observes local grabens and horsts in the southern URG segment, compression and thus uplift and erosion in the central segment, and active normal faulting and thus subsidence in the northern segment. This setting has partly been confirmed by analyses of levelling data carried out by Zippelt & Mälzer (1987). In general, the URG is stuck between southward movements of the Rhenish Massif and northward movements of the Alps resulting in a sinistral shear at the main border faults along with extension.

Insights into the current fault setting are based on the interpretation of seismic sections, collected on behalf of hydrocarbon exploration in the 1960s and 1970s and on geological mapping of the surface, particularly at the URG shoulder areas (Lemeille et al., 1999; Peters & van Balen, 2007b). The orientation of intra-graben faults and faults at the shoulder areas is mainly NNE, see Fig. 2.6. Some faults, particularly in the northern URG, strike in NW directions matching Variscan fault trends (Peters, 2007, p. 13, 17). As one can see in Fig. 2.6, many of the big cities in the URG are close to active faults potentially capable of strong earthquakes.

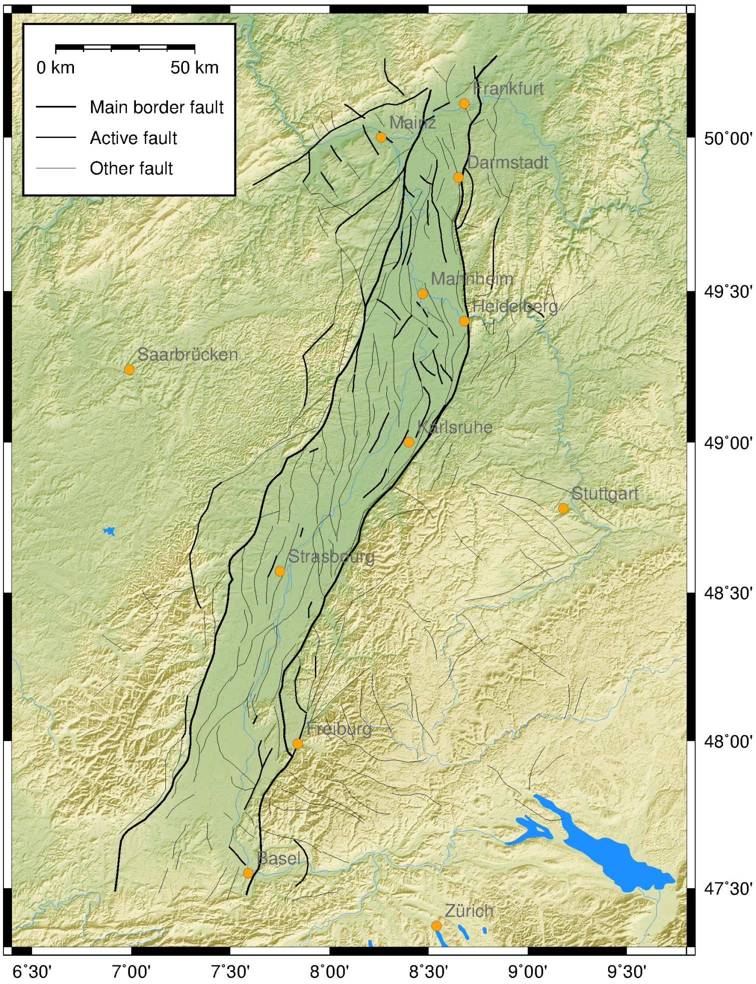

Figure 2.6: Relevant faults in the URG area. Fault data from Peters (2007, p. 166), background: shaded DEM using SRTM-3 data.

2.3.4 Stress field

Schumacher (2002) gives an overview of the stress field in the URG area within different geological epochs. The ambient stress field largely changed during different epochs of the graben evolution. He distinguishes between six consecutive intervals of basin subsidence that are related to changes in the stress field and displays isopach maps including the inherent stress field for Priabonian, Lower Rupelian, Upper Rupelian, Chattian, Early Miocene and Quaternary. The stress field was derived by paleostress analyses (Villemin & Bergerat, 1987) for the early periods and by in-situ measurements (Baumann, 1981) and focal plane solutions (Ahorner et al., 1983) for the Quaternary period. Most stress axes given for the Quaternary period in the URG area are NW–SE orientated, predominantly along with a strike-slip regime, see also Fig. 2.7. In principle, the stress orientation of present-day tectonics can be derived from (i) focal mechanisms of earthquakes, (ii) well bore breakouts and drilling-induced fractures, (iii) in-situ stress measurements (overcoring and hydraulic fracturing) and (iv) geologic indicators (young geologic data from fault-slip analysis and volcanic vent alignments), see Heidbach et al. (2008); Eisbacher (1996, p. 91 ff.).

Fig. 2.7 shows the recent maximum horizontal stress directions in the URG and adjacent areas. Most of the information on the stress field is derived from focal mechanisms of earthquakes. A general NW–SE trend of the maximum horizontal compressional stress is observed in the area. However, the information on the present-day stress field of the URG area is sparsely distributed, particularly in the central and northern part of the graben. Ritter et al. (2009) analyse seismic waveforms of three minor earthquake events ($M_L = 2.4$, 1.5 and 2.8) close to Speyer and Heidelberg (central/northern URG) and conclude that normal faulting across the whole crustal depth dominates in this part of the URG. However, efforts to determine fault plane solutions from small earthquakes have to be extended in order to better constrain the regional stress field.

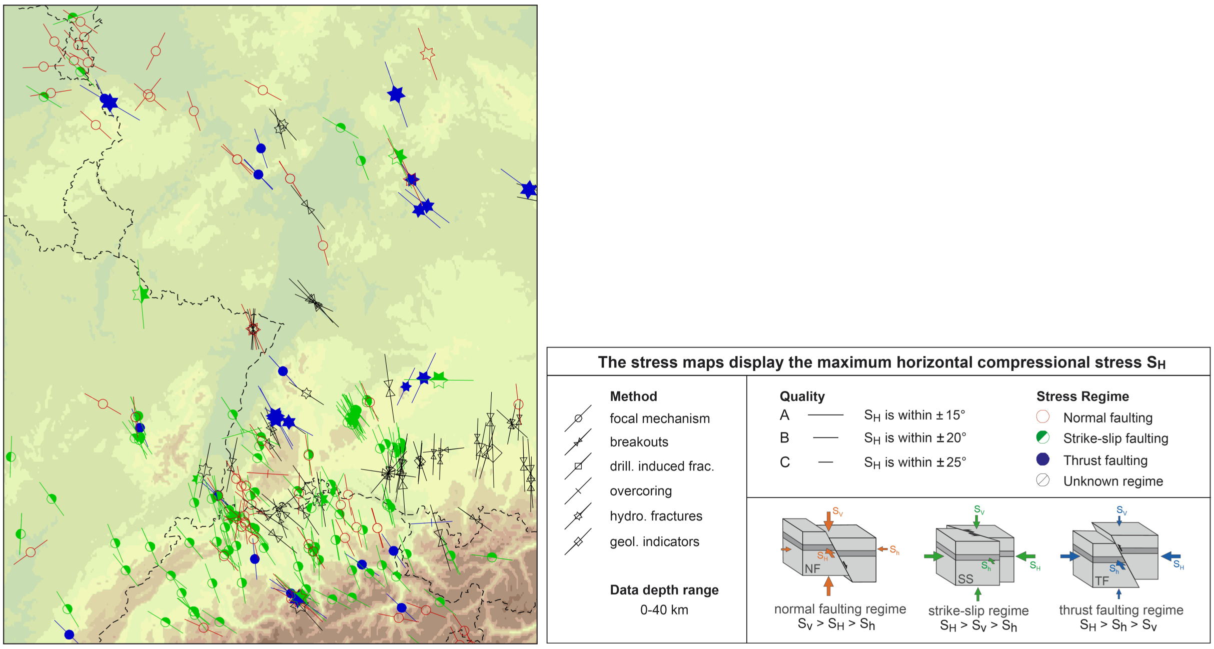

Figure 2.7: Crop of the world stress map 2008 (Heidbach et al., 2008) for the URG area. Maximum horizontal compressional stress derived from different methods.

2.3.5 Seismicity

The Cenozoic rift system is a seismically active region within Central Europe (Ziegler, 1992). The URG as the most prominent part of the rift system is characterised by low to moderate earthquake activity, documented e. g. by Ahorner et al. (1983); Bonjer (1997). Together with the Lower Rhine Graben, the URG area is among the most seismically active regions in Western Europe, north of the Alps (Grünthal et al., 2009a,b; Leydecker, 2011). Fig. 2.8 shows the distribution and magnitude of earthquakes in the URG area since 1000 AD. The historical catalogue of earthquake events given in Grünthal et al. (2009b) is visualised for events until 1970 mainly based on macroseismic estimations of epicentre locations and intensity. In addition, Barth et al. (2015) compiled the data of different catalogues after 1970 for the URG area, see Fig. 2.8(b). It becomes obvious that large earthquakes are concentrated in the URG and its shoulder areas and in the Alpine foreland. Only few seismic events have been recorded in the northern URG in the last decades, whereas the southern URG is exposed to a large number of small events (Barth & Ritter, 2010; Barth et al., 2015). Within the graben, focal depths vary typically between 5 and 15 km, increasing in the BF to values between 15 and 23 km (Plenefisch & Bonjer, 1997). Significantly less seismic activity is found in the shoulder areas north of the BF and the VG.

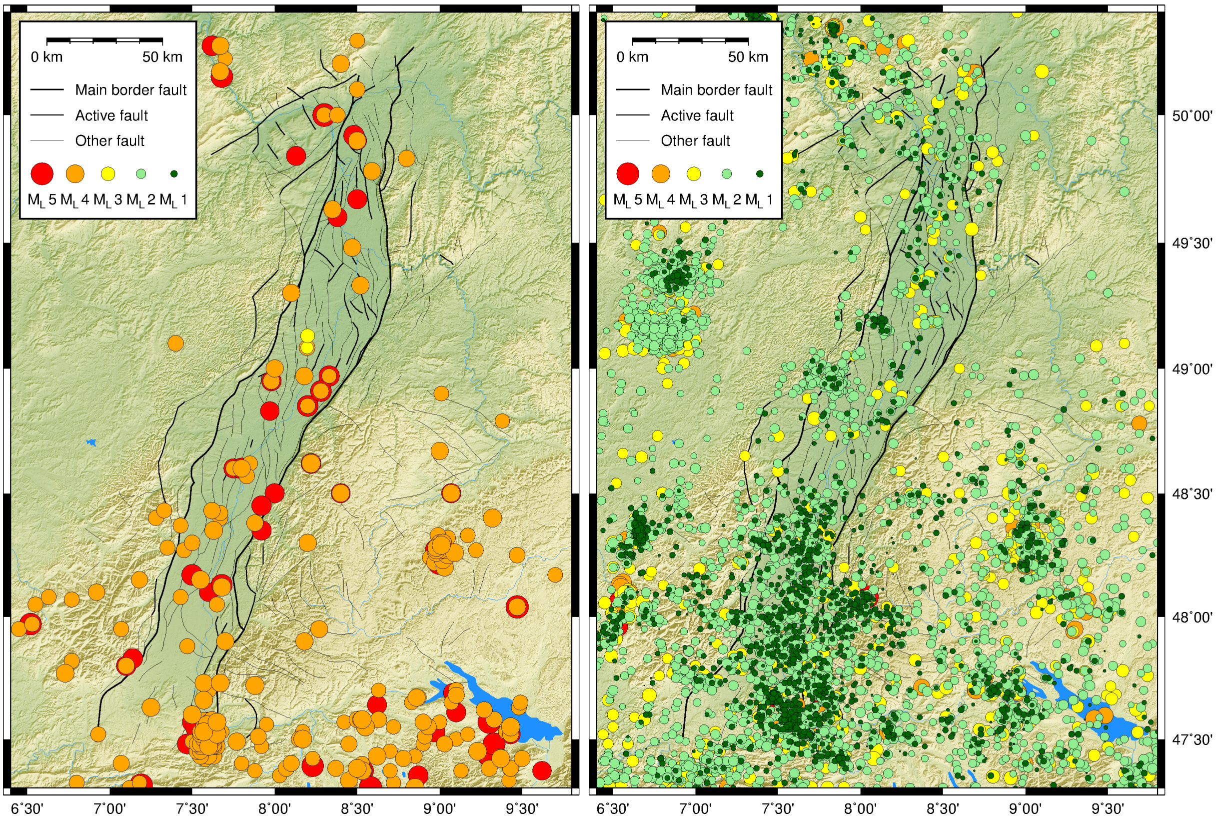

(a) CENEC catalogue (Grünthal et al., 2009a,b) from 1000 AD to 1970, mainly from macroseismic estimations.

(b) Compilation of different catalogues from 1971 to 2012 published by Barth et al. (2015), mainly from instrumental records.

Figure 2.8: Seismicity in the URG area: earthquake epicentre registrations from different catalogues.

The largest reported earthquake in the URG was the Basel event in 1356 with a moment magnitude M_W between 6.7 and 7.1 (Fäh et al., 2009). With intensities up to VIII on EMS[1] within a 30 km radius around the epicentre at 47.47°N, 6.70°E, it is the most destructive earthquake known in Central Europe. Mayer-Rosa & Cadiot (1979) estimate the maximum intensity equal or greater IX on MSK[2] and deduce a focal depth between 10 and 20 km. Meghraoui et al. (2001) investigate an active normal fault in the epicentral area close to Basel, which might be responsible for the Basel event in 1356. From paleoseimic records (trench measurements), they identify two additional earthquake events within the last 8500 years and estimate a mean uplift rate of 0.21 mm/a at the fault. The most recent earthquake related to the URG with a local magnitude M_L above 5.0 was recorded in Waldkirch (close to Freiburg) in 2004. The event is located at 48.08°N, 8.04°E (Brüstle & Stange, 2005), east of the eastern border fault, and showing predominantly strike-slip character (Häge & Joswig, 2009).

2.3.6 Surface displacements from previous geodetic studies

Major results from previous geodetic studies in the URG area are discussed within this section. Levelling data has been systematically analysed w.r.t. geodynamics in the URG area since the 1960s until today. Several investigations have been performed within the past decades on a regional and local scale, particularly using levelling data from the German and Swiss parts of the URG. Between 1967 and the 1980s, electronic distance measurements (EDM) have been used to get insights into the horizontal motion across the URG, later also in combination with GPS data. In the southern URG, old French triangulation data has also been used together with GPS campaign measurements in order to evaluate the horizontal deformation of the URG. Recently, the focus is put on GNSS data acquired at permanent sites or from campaigns.

Regarding vertical displacements, Mälzer (1967) and Mälzer et al. (1983, 1988) published maps of height changes in the URG area and the Rhenish Massif. They used repeated precise levelling data on first-order lines of the German and Swiss surveying authorities and found several indications for active tectonic deformation, but presented also examples for man-induced subsidence related to the extraction of oil and groundwater. Kuntz et al. (1975) presented measurements from several geodetic techniques, among others, levelling profiles in the Offenburg and Freiburg region. Zippelt & Mälzer (1987) published maps of height changes from available levelling data in the German part of the URG area using the kinematic adjustment model provided by Zippelt (1988) and described in Sect. 3.1.3. Most of the detected vertical rates are within ±1 mm/a, along with uplift of up to 0.7 mm/a in the Palatinate Forest, west of the graben, and subsidence of 0.7 mm/a in the northern part of the graben and east of it. They conclude that the principal deformation feature within the URG (subsidence in the northern part, uplift in the central segment, subsidence in the southern part) is in accordance with the present-day graben mechanism as published by Illies (1979). In the French part of the URG, Ermery (1960) compared the heights of levellings carried out on behalf of the Prussian kingdom at the end of the 19th century (Prussia, 1883, 1894) with the French principal levelling in Alsace-Lorraine, mainly measured between 1920 and 1924. The resulting map of height changes between these two measurement epochs already confirms that vertical displacement rates in the URG are small (< 1 mm/a), except from some movements up to 2 mm/a close to the mining area of Lorraine, see Sect. 2.4. A comparison of height changes between different measurement epochs at levelling lines in the southern URG was carried out by Schweizer (1992). The author concludes that there is mostly subsidence within the graben w.r.t. a slight uplift of the levelling benchmarks in the BF. Demoulin et al. (1998) performed a local study of

---

[1] EMS: European Macroseismic Scale

[2] MSK: Medvedev-Sponheuer-Karnik scale

fault movements in the southern BF and concluded that the faults in this region are creeping aseismically at rates varying between 0.2 and 1.1 mm/a. A similar investigation was carried out by Rózsa et al. (2005a) at several faults close to Freiburg resulting in displacement rates between 0.2 and 0.7 mm/a. Schlatter et al. (2005) presented a map of vertical displacement rates for Switzerland, which clearly proves the alpine uplift of up to 1.5 mm/a w.r.t. a reference point in the southern Jura Mountains. Only small movements are seen between levelling benchmarks within the southern URG and at the eastern graben shoulder. Furthermore, the study contains local comparisons of height changes along levelling lines close to Basel. From data of the last 30 years, no significant height changes are visible at levelling lines crossing the eastern border fault close to Basel. Zippelt & Dierks (2007) continued the work of Mälzer et al. (1988) performed on behalf of the Swiss National Cooperative for the Disposal of Radioactive Waste (Nationale Genossenschaft für die Lagerung radioaktiver Abfälle, Nagra). They analysed data of up to five levelling campaigns between 1922 and 2004 in southern Baden-Württemberg and northern Switzerland, including also second-order lines. It could be proved that the second-order lines contribute useful information about vertical movements in the interior of the wide first-order loops, albeit the quality standards and repetition rates of second-order measurements are below those of first-order measurements. However, no analysis has been carried out covering the whole URG area (including the French part) in previous geodetic studies.

Since 1967, EDM have been carried out across the URG primarily to investigate external influences on the measurements, such as atmospheric perturbations (Bozorgzadeh & Kuntz, 1974). The measurements have been repeated several times in order to derive horizontal movements between the eight measurement sites located on both sides of the graben (the number of sites increased to 11 in 1975). Kuntz et al. (1975) conclude that the precision of EDM with relative distance errors on the order of $3 \cdot 10^{-7}$ could be sufficient for geodynamic investigations. On the other hand, a sensitivity analysis of the EDM network, performed by Heck (1986), proved that a relative horizontal movement of the graben shoulders of 0.5 mm/a could only be measured with significance at a repeat time of 50 to 60 years. Heck et al. (1995) use the EDM data in the URG area along with simultaneous mutual zenith angle measurements and astronomically observed longitudes and latitudes at the measurement sites. Additionally, GPS measurements have been carried out at nine of the measurement sites since 1988 and were analysed in a joint deformation analysis. The authors conclude that visible deformation trends are not yet significant and have to be confirmed by subsequent GPS campaigns. Triangulation measurements have not been used largely to detect crustal motion in the URG area, mainly because the measurement accuracy of cm to dm over large measurement distances is not high enough. Aufranc (2000) calculated the maximum compressive strain in the southern URG and the Jura Mountains from old triangulation measurements and one GPS campaign resulting in N–S directed compression of the order of 0.1 μrad/a. This work is currently extended by additional GNSS campaigns (Ferhat et al., 2015).

Early GPS measurements in the URG suffered from a small number of occupied sites and a low data volume. Nocquet & Calais (2003, 2004) combined 64 permanent GPS sites in western Europe and the western Mediterranean to a geodetic velocity field including two sites in the URG, i. e. KARL (Karlsruhe, Germany) and STJ9 (Strasbourg, France; identical with STRA). They did not find significant motion of sites located west of the URG with respect to a stable reference frame located east of the graben and placed an upper bound for horizontal motion across the graben of 0.5 mm/a. The upper bound has been reduced to 0.3 mm/a by a state-of-the-art compilation of European geodetic data for the Mediterranean region and the Alpine belt, presented by Nocquet (2012). Similar analyses have been carried out by Tesauro et al. (2005, 2006) also including the two sites located in Karlsruhe and Strasbourg. The resulting standard deviations given in Tesauro et al. (2006) are 0.6 mm/a and 0.5 mm/a for KARL and STRA, respectively. With a maximum time span of four years, the GPS time series were not long enough to recover the small tectonic motions in the URG with significance. As only a few permanent stations were available in the URG area at the end of the 1990s, three campaign measurements were performed within the EUCOR-URGENT project in 1999, 2002 and 2003, each covering a period of a few days. Average root mean square values of the derived coordinates are 1.9 mm for the horizontal and 4.2 mm for the vertical component, respectively, which is an order of magnitude larger than the expected tectonic displacements accumulated within a few years (Rózsa et al., 2005a,b). At that time, the geodetic efforts were not able to resolve active deformation in the URG area unambiguously as the available networks and datasets were not dense enough, neither in space nor in time. In addition, many data sets were restricted to national use only and therefore most studies are based on a limited amount of data. Early GPS measurements have been carried out in campaigns and suffer from additional error sources, such as centering inaccuracies and seasonal effects.

2.4 Natural resources and their exploitation

This section aims at giving an overview of anthropogenic activities in the URG area, which may affect the local deformation behaviour. Fig. 2.9 shows the location of sites at which anthropogenic activities took place within the last decades (periods of the activities are given in Tab. 2.2). Even if this map might not be complete, it gives an impressive overview of the geopotentials of the URG region. The following paragraphs concisely summarise the activities in the URG w.r.t. coal and potash mining, hydrocarbon production, groundwater usage and geothermal energy.

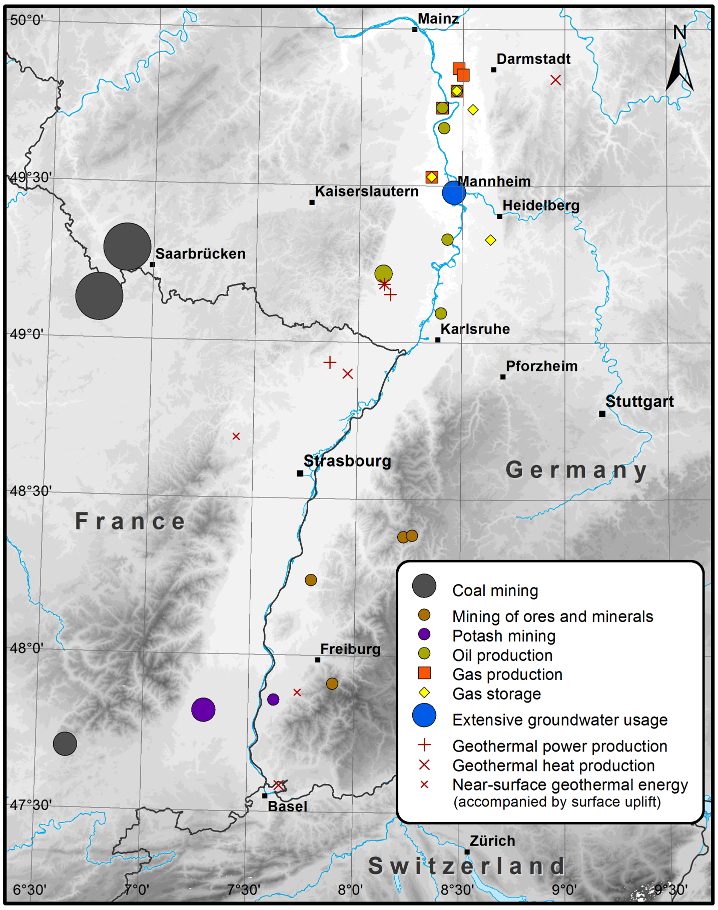

Figure 2.9: Compilation of subsurface anthropogenic activities in the past 100 years possibly inducing surface movements in the URG area. The scale of the markers gives an impression of the spatial extent of the activity. Information on location and period of the activities is given in Tab. 2.2.

First mining activities in the URG and surrounding areas were performed in Celtic and Roman times and are evidenced, e. g. by funeral supplements. Silver was extracted in Val d'Argent (Silver Valley, Alsace, France) since the 10th century with a major mining epoch between the 15th and 18th century (Benoît & Bailly-Maître, 1997, p. 31). The system of pits and underground tunnels still exists at some places and might even affect the recent surface deformation behaviour in the VG. In the BF, the extraction of iron ore started 2,600 years ago and is evidenced close to Neuenbürg (northern BF, Germany), see Eisbacher & Fielitz (2010, p. 116). In the middle ages, several main epochs of mining activities existed in the BF. Between the 14th and 16th century mainly silver, in the 18th and 19th century mainly ore was extracted, and within the last 150 years mining activities focussed on barite and fluorite (Eisbacher & Fielitz,

Table 2.2: Subsurface anthropogenic activities in the past 100 years possibly inducing surface movements in the URG area. Compiled from various sources mentioned within the text.

Site	Longitude	Latitude	Activity	Period
Saarland	6.87°	49.29°	Coal mining	1821–2012
Lorraine	6.74°	49.13°	Coal mining	1818–2004
Ronchamp	6.64°	47.7°	Coal mining	1810–1956
Oberwolfach	8.229°	48.380°	Mining of ores and minerals	since 1898
Wildschapbach	8.270°	48.385°	Mining of ores and minerals	1850-1955
Schauinsland	7.899°	47.910°	Mining of ores and minerals	1876-1954
Ringsheim	7.79°	48.24°	Mining of ores and minerals	1937-1969
Wittelsheim	7.29°	47.82°	Potash mining	1910–2002
Buggingen	7.621°	47.856°	Potash mining	1926–1973
Landau	8.12°	49.22°	Oil production	since 1955
Leopoldshafen	8.4°	49.095°	Oil production	1957–1986
Speyer	8.43°	49.33°	Oil production	since 2008
Stockstadt	8.470°	49.805°	Oil production	1952–1994
Wattenheim	8.410°	49.685°	Oil production	1954–1976
Eich	8.4°	49.75°	Gas production	since 1959
Stockstadt	8.47°	49.805°	Gas production	1955–1979
Wolfskehlen	8.5°	49.855°	Gas production	1957–1991
Eich	8.4°	49.75°	Gas production	1955–1972
Dornheim	8.48°	49.875°	Gas production	1957–1980
Frankenthal	8.35°	49.53°	Gas production	1959–1961
Stockstadt	8.470°	49.805°	Gas storage	since 1994?
Hähnlein	8.55°	49.745°	Gas storage	before 1972
Frankenthal	8.35°	49.53°	Gas storage	before 1980?
Sandhausen	8.64°	49.33°	Gas storage	before 1980?
Mannheim/Ludw.	8.46°	49.48°	Extensive groundwater usage	mainly 1970s
Landau	8.123°	49.186°	Geothermal power/heat production	since 2007
Insheim	8.153°	49.154°	Geothermal power production	since 2012
Soultz-sous-Forêts	7.865°	48.935°	Geothermal power production	since 2008
Rittershoffen	7.95°	48.9°	Geothermal heat production	start in 2016
Heubach	8.955°	49.841°	Geothermal heat production	since 2013
Basel-Riehen	7.651°	47.584°	Geothermal heat production	since 1994
Staufen	7.732°	47.882°	Near-surface geothermal energy	since 2007
Lochwiller	7.418°	48.695°	Near-surface geothermal energy	since 2008

2010, p. 117; Geyer et al., 2011, p. 465), whereas one mine in the central BF, *Grube Clara* at Oberwolfach, is still active today (Eisbacher & Fielitz, 2010, p. 150; Geyer et al., 2011, p. 467). Coal mining was extensively performed in Lorraine and southern Saarland. The 58 French mines have been in use between 1818 and 2004 (Urek & Jegentowicz, 2003). The systematic coal extraction in southern Saarland started in 1751 (first mining pit was sunk in 1821) and lasted with short interruptions until 2012 (Heinz, 2012). Currently, the former mines are flooded with water. Coal deposits close to Ronchamp (southern Alsace, France) were discovered in 1750 and have been exploited with pits between 1810 and 1956 (Banach, 2009).

Within the URG, potash mining was performed in the so-called Wittelsheim formation (Geyer et al., 2011, p. 354 f.), which is found west of the river Rhine in Wittelsheim (northwest of Mulhouse, France) and east of the river Rhine in Buggingen (southwest of Freiburg, Germany).

In Wittelsheim 24 pits have been operated between 1910 and 2002 (Ringenbach, 2013), in Buggingen, three pits between 1926 and 1973 (Hamm, 2012).

The use of hydrocarbons in the URG is firstly documented in 1498 at Pechelbronn (northern Alsace, France), where bitumen was found in spring water and used for medical purposes (Eisbacher & Fielitz, 2010, p. 119; Geyer et al., 2011, p. 473). However, mining activities were not started until the middle of the 18th century, firstly using 100 to 400 m deep pits and since the end of 19th century using geophysical exploration methods and drillings. The major epoch of oil production was between 1920 and 1970, while some of the sites are still operative, particularly the oil fields close to Landau (Rheinland-Pfalz, Germany) discovered in 1955 (Eisbacher & Fielitz, 2010, p. 119 f.). Efforts on the exploration of hydrocarbons have been restarted within the last years in the URG, not least because a deep geothermal drilling close to Speyer (Baden-Württemberg, Germany) surprisingly stroke an unknown oil deposit in 2003. Natural gases have been extracted in the northern URG, in the area between Mannheim and Darmstadt (Germany), between 1955 and 1980 (Weinberger, 2015). Two of the former gas fields, i. e. Stockstadt and Frankenthal, are used as underground gas storages today. Furthermore, two gas storages in the URG are operated in Hähnlein and Sandhausen (Sedlacek, 2002).

The URG is a very rich groundwater area. The Quaternary unconsolidated rocks build a large aquifer system, which almost fully covers the groundwater demand of population, industry and irrigation in the URG and peripheral areas (Wirsing & Luz, 2007). Surface deformations close to groundwater wells were investigated by Schweizer (1992, p. 13 ff.) using a local levelling network at the waterworks Hausen (southern URG, Germany). The author concludes that the resulting subsidence of a maximum of 1.2 mm within four years is caused by consolidation as well as erosion of the ground. In the industrial area of Mannheim/Ludwigshafen, a low groundwater level is observed in the 1970s, which has been correlated with subsidence estimates from levelling by Wolf (2014, p. 29 ff.). The influence of local groundwater changes, anthropogenic as well as natural, may also affect the surface deformation in other parts of the investigation area.

Within the transnational project GeORG[1], institutions from Germany, France and Switzerland investigated the potential of the URG for geothermal heat and power production and for gas storage. Due to its thin lithosphere and large scale geothermal temperature anomalies, see Baillieux et al. (2013), the URG is highly appropriate for geothermal applications (GeORG, 2013, p. 60 ff.). Deep geothermal heat and power production is already used in several parts of the URG as shown in Fig. 2.9. Unfortunately, induced seismicity at deep geothermal sites in Basel (Häring et al., 2008) and Landau (Groos et al., 2013; Gaßner et al., 2014; Frietsch et al., 2015) and large surface uplift at near-surface geothermal sites in Staufen (Engesser et al., 2010; Lubitz et al., 2013; Schenk, 2015) and Lochwiller (Louis et al., 2014) are reducing the public acceptance of the technique in the last years. In contrast to deep geothermal projects, near-surface geothermal sites make use of the subsurface heat above 400 m depth and are mainly used to heat buildings. In Baden-Württemberg about 14,000 geothermal probes were in use by 2010 (Geyer et al., 2011, p. 499). The Federal State Office for Geology, Natural Resources and Mining of Baden-Württemberg (LGRB), recently launched a web service that provides information on the geothermal efficiency and possible limitations w.r.t. groundwater protection, subsurface cavities or sulphate rocks for every location in Baden-Württemberg, see ISONG (2015), including the locations of already existing geothermal probes and groundwater heat pumps.

---

[1] GeORG: Geopotenziale des tieferen Untergrundes im Oberrheingraben (geological potential of the deep URG)

2.5 Summary

- The URG is the most prominent part of a rift system crossing entire Central Europe.
- The graben is bounded by two main border faults with NNE–SSW direction.
- The graben interior is filled with sediments of up to 3,335 m thickness.
- Sinistral shearing mainly dominates the current faulting mechanism.
- The complex system of faults within the graben is capable of both strike-slip and normal faulting.
- More seismic activity is observed in the southern URG. The largest known earthquake happened in 1356 close to Basel with M_W between 6.7 and 7.1.
- Previous geodetic studies in the URG area set the upper bound for tectonic motion to about 0.5–1.0 mm/a in horizontal and vertical directions.
- Natural resources have been largely exploited in the URG area within the last 100 years and may affect the surface displacements measured by geodetic techniques.

Chapter 3

Geodetic Measurement Techniques

This chapter aims at describing the three geodetic techniques used within this work in order to estimate surface displacements: levelling, GNSS and InSAR. Besides the principal methodology of each technique, the focus is put on the application of levelling, GNSS and InSAR measurements w.r.t. the derivation of surface displacements.

The first geodetic study on horizontal surface displacements inferred by an earthquake was published by Hayford & Baldwin (1908) using triangulation measurements acquired before and after the large 1906 San Francisco earthquake ($M_W = 7.8$). Triangulation measurements in the URG area are currently under investigation by G. Ferhat at Université de Strasbourg, also in combination with GNSS campaign measurements of formerly used triangulation benchmarks. Regarding vertical motions of the Earth's surface, Parkin (1948) published maps displaying changes in elevation at levelling benchmarks for the Los Angeles region. In the 1970s, geoscientists started to systematically analyse geodetic levelling networks for an accurate estimation of vertical displacements caused by active tectonics. Wernthaler (1939) already proposed geodetic analyses of the tectonics of Europe using the measurements of the European levelling network REUN (Réseau Européen Unifié de Nivellement), which was expanded and renamed to UELN (United European Levelling Network) in the 1990s. First large-scale investigations using levelling data have been performed at the San Andreas Fault, Southern California (Holdahl & Hardy, 1979; Holdahl, 1983), at Chesapeake Bay, Virginia (Vanìček & Christodulidis, 1974), or at the Rhenish Massif, Western Germany (Mälzer et al., 1983). Heck & Mälzer (1983a,b) investigated the influence of temporal changes of the gravity field on crustal movements derived from repeated levelling data in a region with large vertical displacements (eastern Hokkaido, Japan). In the late 1980s, GPS campaign measurements were used to gain a more detailed insight into horizontal tectonic deformations (Billiris et al., 1991). Later on, it became possible to measure the motions of continental plates using a network of globally distributed and permanently operating GNSS sites (Boucher et al., 1993). At the end of the 1980s, differential radar interferometry was successfully applied to measure surface deformations by Gabriel et al. (1989) using Seasat data over Imperial Valley, California. With the Persistent Scatterer (PS) approach developed by Ferretti et al. (2001), it is possible to monitor surface displacement rates over several years at the mm/a-level.

Aiming at a map of the recent 3D displacement field, it is desirable to combine velocity estimates in a multi-technique approach exploiting the advantages of each technique. Therefore, single-technique displacement estimates are calculated in a first step. The following three sub-chapters describe the principal methodology of the three measurement techniques, the corresponding database available in the URG area and the basic analysis strategies w.r.t. the estimation of surface displacements.

Parts of this chapter have already been published by the author in the following papers: Fuhrmann et al. (2013a), Fuhrmann et al. (2014a), Fuhrmann et al. (2014b), Fuhrmann et al. (2015b), Fuhrmann et al. (2015c). These publications are not explicitly cited within the text.

3.1 Levelling

This section describes the methodology of levelling measurements including the historical evolution of the measurement technique (Sect. 3.1.1), the available levelling data in the URG countries Germany, France and Switzerland (Sect. 3.1.2) and the analysis strategies for the derivation of displacements from the data sets (Sect. 3.1.3).

3.1.1 Methodology

The principle of levelling is simple and has not changed since its development. In the third millennium BC, first levels were used by the ancient Egyptians and Chinese in order to construct buildings. Deumlich & Staiger (2002, p. 19) estimate the accuracy of ancient Egyptian levellings to 8 cm per 200 m. In Greek and Roman times, levelling instruments enabling a horizontal sighting to a rod were used, called Dioptra and Chorobates, see Deumlich & Staiger (2002, p. 20). Levelling instruments with a telescope and a bubble tube are first reported in France at the end of the 17th century (Deumlich & Staiger, 2002, p. 23). The introduction of large-scale levelling networks in Europe with the intention to provide national height systems started at the end of the 19th century (Heck, 2003, p. 297 ff.).

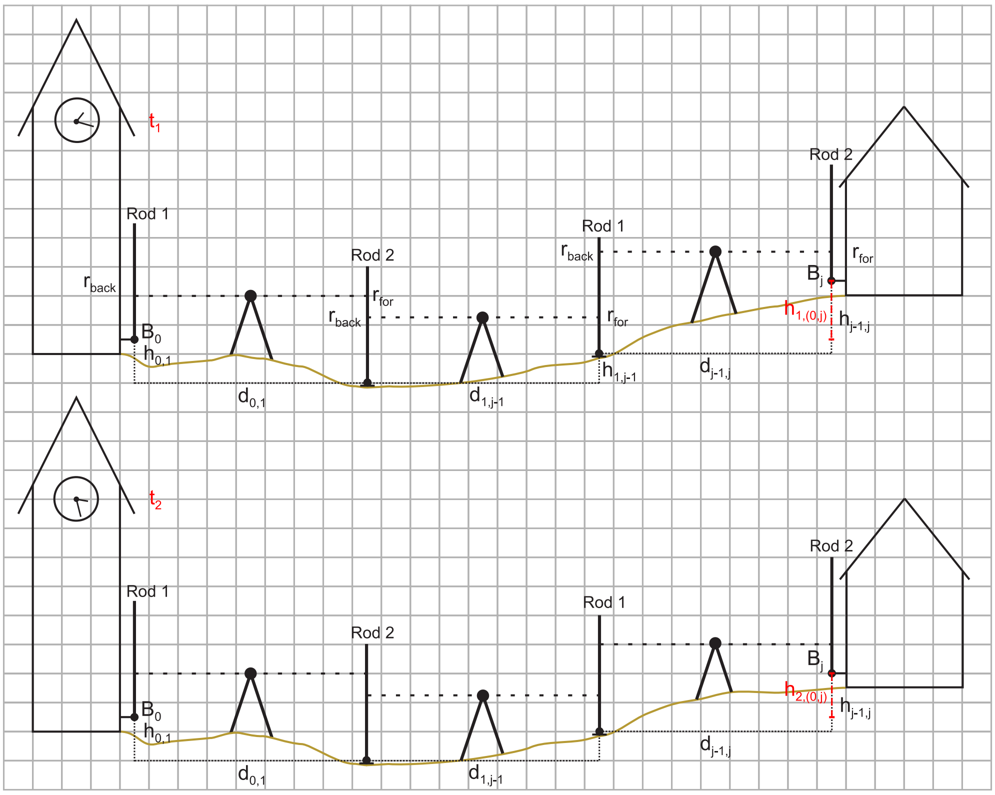

Figure 3.1: Principle of levelling: Measurement of height differences h from rod readings r_{back} and r_{for} at rods placed on fixed benchmarks B at distances d. A displacement at a benchmark B_j between two measurement epochs t_1 and t_2 results in a different height difference.

The basic observations of levelling are height differences between two points. As shown in Fig. 3.1, the levelling instrument is placed in the middle between two points (fixed benchmarks and/or intermediate points) and is horizontally aligned. A reading of the horizontal sighting is performed at each point using a rod placed vertically over the point. The difference between the backward reading r_{back} and the forward reading r_{for} is the measured height difference h between the two points. Starting at a benchmark with a well-known absolute (conventionally fixed) height H_0, e. g. a tide gauge, heights of other benchmarks can be estimated by consecutively adding the measured height differences to the height of the starting point B_0. The physical heights of points on the surface are related to the gravity field of the Earth and the corresponding gravitational potential. Equipotential surfaces are generally not parallel due to inhomogeneous mass distributions of the Earth's interior. Hence, the height differences observed with levelling depend on the path taken (Torge & Müller, 2012, p. 63 f. and p. 217). A detailed investigation on the influence of gravity is given in Sect. 4.3.

Geodetic levelling networks are created by subsequently summing height differences along levelling lines using closed loops of levelling measurements for an internal check of the observations. These networks were constructed about 100 years ago by the national surveying authorities and have been remeasured several times allowing for the calculation of vertical displacements. A vertical shift of a levelling benchmark between two measurement epochs results in a difference of the relative heights obtained in the measurement epochs t_1 and t_2 w.r.t. the height of an adjacent benchmark, see Fig. 3.1. Analysis strategies for the determination of vertical displacements from levelling data of several measurement epochs are discussed in Sect. 3.1.3.

Albeit the principle of levelling has not changed since the creation of national levelling networks, the instrumentation did. The evolution of levelling instruments can be nicely traced throughout the levelling campaigns of the German main height network (Deutsches Haupthöhennetz, DHHN). First campaigns have been carried out in Germany since 1865 (Weber, 1993b, p. 8) using optical instruments and wooden rods, see e. g. Baden (1885, p. 4 ff.) and Fig. 3.2(a). The measurements in the German states Saxony, Bavaria, Prussia, Württemberg and Baden were finished in 1894. The geodetic datum of this primary height system for all German states refers to a height benchmark located at the astronomical observatory in Berlin, which in turn refers to the tide gauge in Amsterdam. The non-parallism of equipotential surfaces was not considered within the calculation of height, except in Bavaria, where a normal-orthometric correction was applied to the measurements.

The second measurement epoch was interrupted by World War I and II and therefore lasted from 1912 until 1956. It is known as DHHN12 (Weber, 1993b, p. 9 f.). A noticeable improvement of the optical instruments was the vertical screw which was established in 1898 (Berndt, 1930, p. 37 f.). Another improvement in that period was the use of temperature-stable materials for the graduation of the rods, instead of a purely wooden rod. It was already recognised in the levelling measurements at the end of the 19th century that the influence of thermal expansion on the length of the rods is not negligible. Rod comparisons have been performed, e. g. by Seibt (1882, p. 5 ff.); Hirsch & Plantamour (1883, p. 557 ff.); Hirsch & Plantamour (1891, p. 578 ff.). It could be observed that the wooden rods increase in length from spring to autumn and decrease during the winter months (Berndt, 1930, p. 41). Temperature-stable rods made of Invar (nickel-iron alloy) have been used since 1913 in Switzerland (Schlatter, 2007, p. 142), but only since 1936 in Germany (Heller & Wernthaler, 1955, p. 9 f.). A normal-orthometric correction was applied in order to account for the influence of gravity using a normal gravity field, see Sect. 4.3. The influence of the non-parallelism of equipotential surfaces was investigated using the levelling measurements along a loop in the southern BF, concluding that gravity anomalies have to be considered in mountainous areas in order to reduce loop errors (HVA, 1952, p. 6 f.). It is worth mentioning that the relevance of the levelling networks for tectonic investigations was already realised resulting in geological essays within the publication of the DHHN12 by Wagner (1952); Kutscher (1952); Schottler (1959).

(a) Kern precise levelling instrument, since 1864, image source: Stadtmuseum Aarau (2015)

(b) Zeiss precise levelling instrument Ni A, around 1940, image source: Popp (2009)

(c) Zeiss precise levelling instrument Ni 2, since 1951, image source: Egelkraut (2014)

(d) Leica precise levelling instrument DNA03, since 2001, image source: SCCS Survey (2013)

Figure 3.2: Levelling instruments used for the surveying of German levelling lines.

In Baden-Württemberg almost all levelling lines of the DHHN12 have been remeasured between 1956 and 1970 (Schulze, 1976, p. 11). The instruments used (Zeiss Ni A, see Fig. 3.2(b)) were equipped with a parallel-plate micrometer enabling a more accurate reading at the graduation of the rod as described by Deumlich & Staiger (2002, p. 247 f.). The rod itself had two adjacent and offset graduations made of Invar. Again a normal-orthometric correction was applied to the measured height differences, albeit gravity measurements were already available at that time for all first-order lines of the DHHN (Schulze, 1976, p. 14). The effect of gravity anomalies, which can be considered using surface gravity measurements, was investigated for levelling lines with large height differences in Baden-Württemberg by Ramsayer (1959). The influence of gravity anomalies on the mean error per km estimated within the adjustment of the data is small, 0.34 mm for the levelling network considered in Schulze (1976).

Between 1980 and 1985, a country-wide campaign for the remeasurement of all first-order levelling lines in Western Germany was performed, known as DHHN85. The instruments were now equipped with a compensator, which enables a better realisation of the horizontal sighting (Deumlich & Staiger, 2002, p. 248 ff.). In the beginning, mainly the Zeiss Ni 1 was used. As an error of the compensator with respect to the magnetic field was recognised at some of the instruments, most of the later measurements were carried out with the Zeiss Ni 2

(Weber, 1993a, p. 21 ff.), see Fig. 3.2(c). Concerning the Invar rods, graduation corrections have been determined in calibration laboratories (Weber, 1993a, p. 24 f.; Schellein, 1993) and added to the raw measurements on behalf of the data analysis. Accompanying to the levelling measurements, gravity measurements have been performed along the levelling lines between 1984 and 1989 (Weber, 1993a, p. 32 ff.). With typical distances between the measurements of 1, 2 and 4 km in mountainous, hilly and flat regions, respectively, representative gravity values for all levelling benchmarks of DHHN85 could be provided. After the German reunification, the height networks of the Federal Republic of Germany, i. e. DHHN85, and the German Democratic Republic, i. e. SNN76 (Staatliches Nivellementnetz 1976), have been merged to a unified height system for whole Germany which was implemented in 1992, i. e. DHHN92. Between 1990 and 1992 additional levelling and gravity measurements have been carried out in order to connect the two networks (AdV, 1995). The final heights were calculated as normal heights following the theory of Molodensky (1958) and refer to the mean sea level of the tide gauge in Amsterdam.

The latest measurement campaign of the DHHN was performed between 2006 and 2012. The calculation of heights is still going on and will be introduced as DHHN2016 (AdV, 2014). A major improvement of the levelling measurements was the use of digital levels with an automatic reading of a coded rod, firstly introduced with the Leica NA 2000, see Deumlich & Staiger (2002, p. 255 f.). For the measurements of the DHHN2016, only digital levels achieving an empirical standard deviation below 0.4 mm per km double levelling have been used, e. g. the Leica DNA03 shown in Fig. 3.2(d). The instruments have been checked on sensitivity w.r.t. the Earth's magnetic field. The coded rods had to be annually calibrated in a laboratory, so that corresponding correction values can be applied to the measured height differences (AdV, 2009, p. 7; Jahn et al., 2011).

Levelling measurements are susceptible to a range of errors which may occur at the levelling instrument, at the rod or because of external sources. Errors at the instrument are caused, e. g. by imperfect set-up of the instrument or residual errors of the compensator. Most of these errors are reduced (i) by using identical target distances for the forward and backward readings, (ii) by using a specific reading order and (iii) by calibration of the instrument and its components. Rod-specific errors like a scale factor or irregularities of the graduation of the rod are reduced by a calibration of the rod. External error sources like temperature differences or refraction are more difficult to handle. For the measurement campaign between 2006 and 2012 in Germany, temperature was observed simultaneously with the measurements in order to calculate a temperature correction for every height difference. For some of the measurements carried out in the 1980s, the compensator of the instrument has been influenced by the Earth's magnetic field resulting in systematic errors particularly at levelling lines with N–S direction (Beckers, 1983; Gessler, 1983; Leitz, 1983). A detailed list of different error sources, their impact on the measurements and strategies to reduce or omit the errors are given in AdV (2009, p. 9 ff).

Principally, the error budget of measured height differences splits into systematic and random errors. Systematic errors comprise, among others, a residual error of the compensator and scale or graduation errors of the rod. As they may effect the measurements in a unilateral way, small systematic errors can sum up to large values (several mm to cm) over large measurement distances. It is therefore crucial to reduce systematic influences on the measurements for country-wide levelling networks. Random errors may be caused by imperfect set-up of the instrument or the rod. Systematic and random errors are handled within the stochastic model of the levelling analysis described in Sect. 4.4.1.

3.1.2 Database

At the end of the 19th century, the countries of Europe started to set up country-wide levelling networks with the objective to provide a national geodetic reference frame of heights (Heck, 2003, 297 ff.). Since that time, the benchmarks of the country-wide height systems have been repeatedly measured as described in Sect. 3.1.1. The levelling measurements are carried out along lines forming closed loops of several 100 km length. Additional measurements within the loops are used to increase the spatial resolution of the levelling benchmarks. The network of available levelling data in the URG area provided by the surveying agencies from Germany, France and Switzerland is displayed in Fig. 3.3. The data was measured and made available by LGL[1], LVermGeo[2] and LVGL[3] for the German part, by IGN[4] for the French part and by swisstopo[5] for the Swiss part of the network.

The levelling lines are divided into different orders depicting the hierarchy of the measurements w.r.t. accuracy and repetition. In the German and the Swiss part of the network, a single first-order loop covers a smaller area than in the French part. The French part consists of one large first-order loop with a length of about 800 km. The first-order line between Nancy and Strasbourg is a traverse which was measured in 2001. It touches the formerly measured lines only at a few benchmarks. As only repeatedly measured benchmarks can be used for the calculation of displacements, the traverse contains few usable benchmarks (cf. straight lines in Fig. 3.3). This also applies for some connections at the French border using French third-order measurements as well as for parts of the historical data. The term historical data refers to data measured before the year 1900 and splits into

(i) data measured under the direction of Charles Lallemand in the years 1891 to 1896 on the western side of the French part (Lallemand & Prévot, 1927),
(ii) data measured by the Kingdom of Prussia in the years 1878, 1881 and 1891 on the eastern and northern side of the French part (belonging to the German Empire at this time), and in parts of Saarland and Rheinland-Pfalz, Germany (Prussia, 1883, 1894),
(iii) data measured by the Grand Duchy of Baden (*Großherzogtum Baden*), Germany, between 1875 and 1882 (Baden, 1885),
(iv) data measured by the Swiss Federal Geodetic Commission in 1867 and 1881 (Hirsch & Plantamour, 1891).

Fig. 3.4 shows the levelling lines measured before World War II with a political map of the German Empire (1871–1918) in the background. At that time, the northeastern part of France was part of the German Empire, the so-called *Reichsland Elsaß-Lothringen*. The levelling measurements in Alsace, Lorraine and adjacent regions have been organised and carried out by surveyors of the Prussian administration. The major part of the Prussian levellings was measured in 1878 and 1881 and is well documented in Prussia (1883). Some connection measurements to the French levelling lines have been added in 1891, documented in Prussia (1894). The connection measurements between Alsace-Lorraine and Baden have also been carried out by the Prussian surveyors, see black lines in Fig. 3.4 on the territory of the Grand Duchy of Baden. Some of the connection measurements have been performed in addition to measurements carried out by the surveyors of Baden for reasons of redundancy.

---

[1] LGL: Landesamt für Geoinformation und Landentwicklung Baden-Württemberg, Germany
[2] LVermGeo: Landesamt für Vermessung und Geobasisinformation Rheinland-Pfalz, Germany
[3] LVGL: Landesamt für Vermessung, Geoinformation und Landentwicklung Saarland, Germany
[4] IGN: Institut National de l'Information Géographique et Forestière, France
[5] swisstopo: Bundesamt für Landestopografie, Switzerland

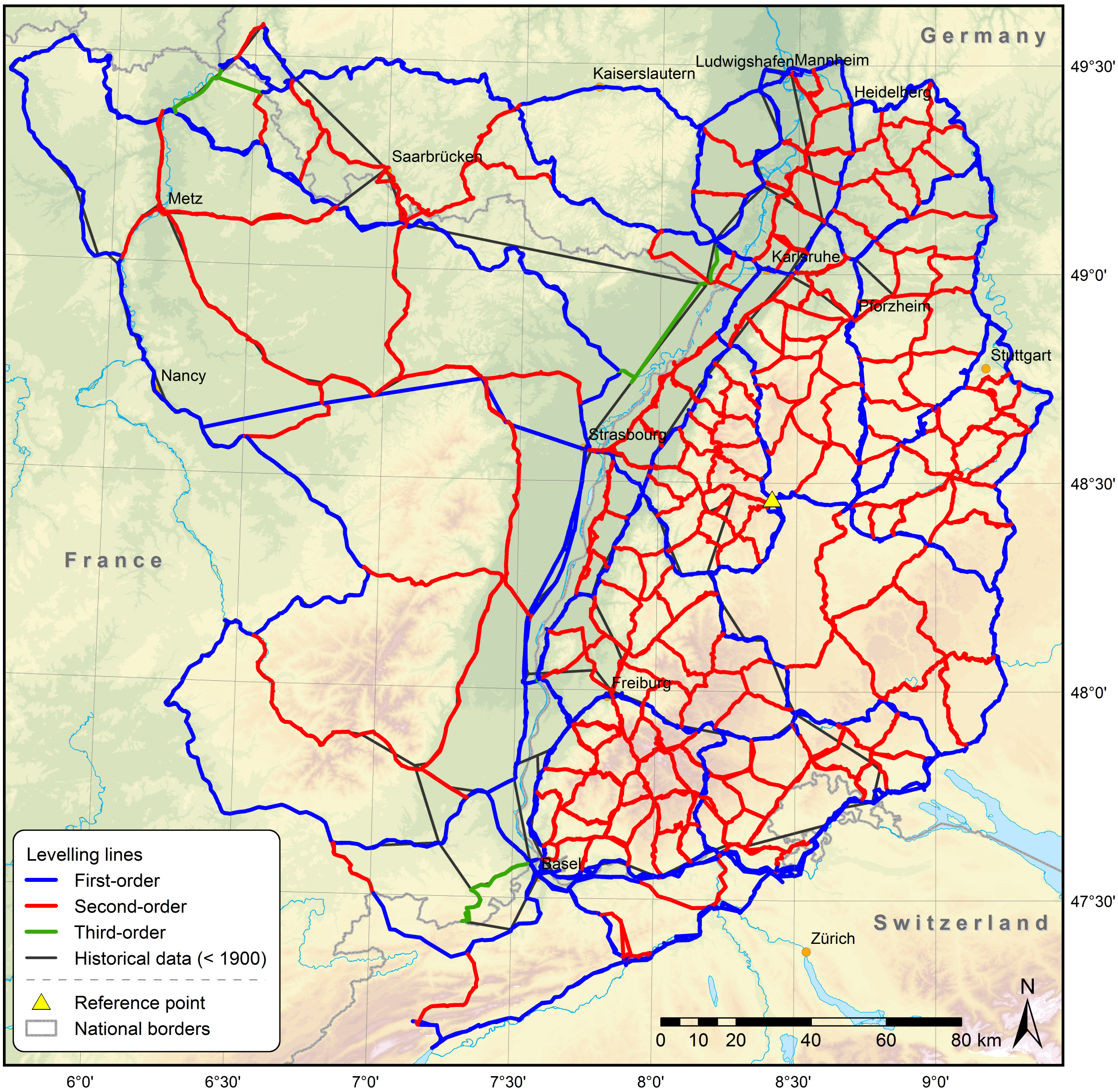

Figure 3.3: Levelling lines of French, German and Swiss surveying agencies. In the French part, the last complete first-order measurement was carried out in 1964. In 2001 a traverse from Strasbourg to Nancy was measured comprising only few of the former benchmarks. The historical data were measured before the year 1900. The course of the historical lines sometimes differs from later measurements, e. g. north of Strasbourg and west of Basel. The levelling benchmarks in these parts cannot be used for displacement estimation.

The levelling lines in Baden have been measured between 1875 and 1882 and are documented in Baden (1885). The lines mainly follow the course of railway tracks and most of the benchmarks are located at railway stations. The measurements of later epochs in Germany are mainly set-up along roads. Therefore, fewer benchmarks have been repeatedly measured in Baden compared to Alsace-Lorraine, where a large part of Prussian benchmarks were used in later epochs. However, the usage of the historical levelling data in Baden ensures that the connection measurements, particularly those crossing the river Rhine, are well integrated into the whole analysed network of repeatedly measured levelling data.

The French measurements (blue lines in Fig. 3.4) were carried out between 1891 and 1896, see Lallemand & Prévot (1927) and were, in contrast to the historical data from Germany, already provided by the French surveying agency (Institut National de l'Information Géographique et

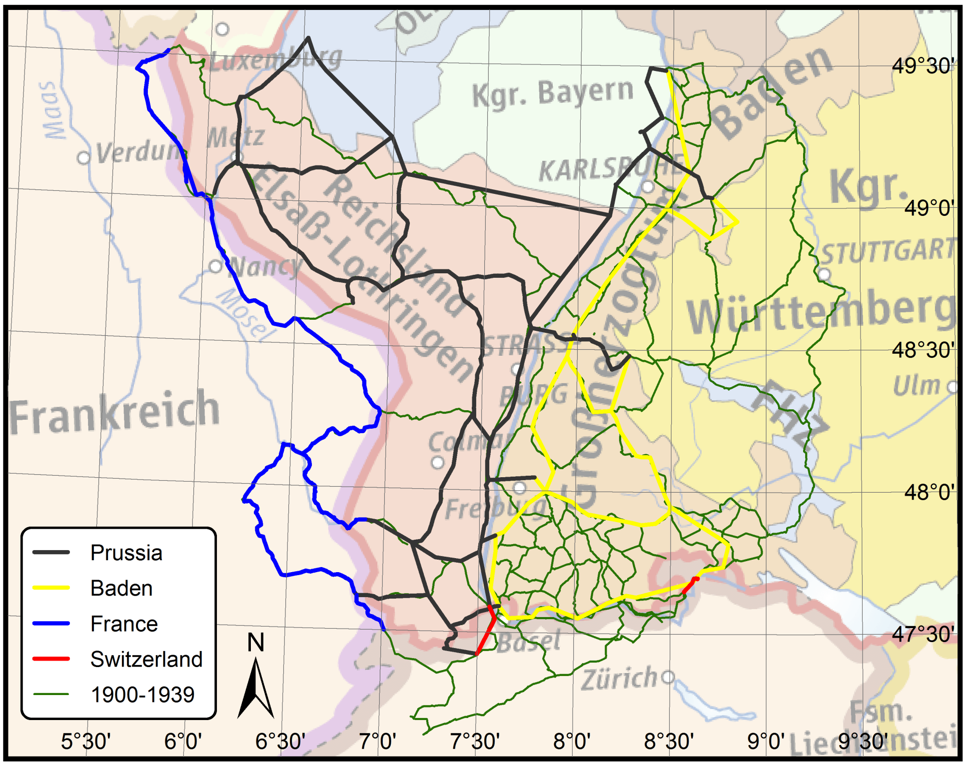

Figure 3.4: Levelling data measured before 1939 and used within the analysis of repeatedly measured benchmarks. Background: political map of the German Empire (1871–1918) provided by Ziegelbrenner (2006).

Forestière, IGN). One connection measurement between the French and the Prussian levellings in the southern VG was recovered using the records published by Ermery (1960).

The oldest measurement used within the whole URG analysis was measured in 1867 in the city of Basel, Switzerland, (Hirsch & Plantamour, 1891, originally published in book number 2 from 1868). Later historical measurements in Northwestern Switzerland were carried out in 1881 by the Swiss Geodetic Commission and are documented in Hirsch & Plantamour (1883). The first measurement epoch of whole Switzerland was finalised before World War II, while the major part was already measured before World War I. A detailed study on the evolution of the Swiss national height system and vertical movements estimated from the Swiss levellings is given by Schlatter (2007).

Although the precision of the historical data is worse than the precision of later measurements, see Tab. 4.2, the integration of this data provides two major advantages. First, the time span is increased yielding a higher accuracy for displacement rates, see Sect. 3.1.3. Second, the data sets contain many measurements at present-day borders to France, i. e. 12 transnational measurements to France before 1900. In later epochs, the measurements of the national surveying authorities often end near the border, without a connection to the levelling network of the neighbouring country measured at the same time. Only 13 transnational measurements to France with a time difference of the connection within seven years exist after 1900. As the transnational measurements are of special importance within the URG levelling analysis, the connections between French and German/Swiss levellings are listed in Tab. A.1 in Appendix A.

Measurements at the border between Germany and Switzerland have been performed more regularly compared to the French-German and French-Swiss border. The levelling lines 601 and 606 of the German height network are partly running through Swiss territory. The connection between the German and Swiss height systems is therefore much better determined. More than 300 levelling benchmarks at 14 border-crossing locations are recorded in both height systems. The mean difference between the Swiss and the German height values at the border benchmarks is 32 cm, with values increasing from the western part (Basel: 30 cm) to the eastern part (Schaffhausen/Thayngen: 34 cm). Differences between the French and the German benchmark heights vary between 54 cm in the northwestern part (Apach, Saarland) and 50 cm in the southern part (Breisach, Baden-Württemberg). The differences between the heights of the German, France and Swiss height systems result from the different datums defined within each system. They are in general agreement with the transformation parameters between the national height systems and the UELN published by Adam et al. (2000). For the transnational analysis of displacements presented within this work, the original datum-free data is used.

Before the levelling data are ready to be used for the derivation of vertical displacements, some preparation steps have to be performed. More than 50 % of the French raw data were provided not in digital form but on handwritten sheets, and had to be digitised. The same applies to the historical data and parts of the older data from Germany. The digital data sources differ in their format as they stem from different institutions and eras. The border benchmarks carry different indications in each country. In addition, the benchmarks set-up and measured within the historical database, have been renamed in later epochs. All identical points with ambiguous indications have to be detected and renamed for a proper use within a displacement analysis. After the data sets are incorporated into an homogeneous database, they have to be cleared up w.r.t. repeatedly measured benchmarks, see Sect. 4.2.3. The levelling lines displayed in Fig. 3.3 are already cleared up, which results in straight connections between distant benchmarks, when the levelling lines of different measurement epochs follow different paths. Fig. 3.5 shows the temporal distribution of height differences between repeatedly measured benchmarks for the German, French and Swiss part of the levelling network. Whereas most of the German data have been measured between 1960 and 2012, the French data show a clustering between 1920 and 1980. The Swiss data are equally distributed over time.

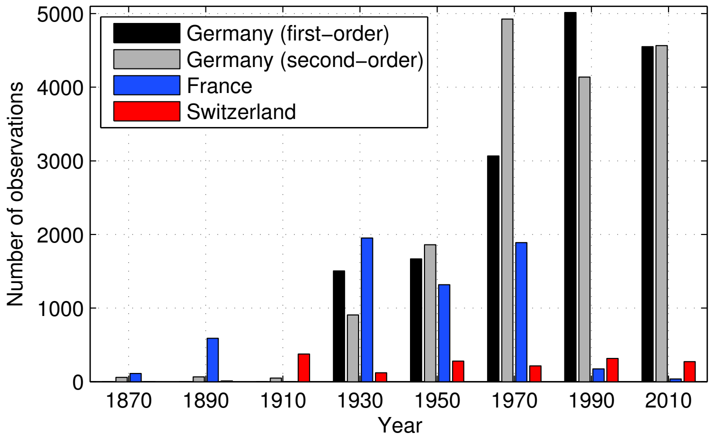

Figure 3.5: Temporal distribution of levelling observations at repeatedly measured benchmarks for different groups of data. Historical data were added to second-order measurements in the German part.

3.1.3 Analysis strategies

This section describes the analysis of levelling measurements particularly w.r.t. the derivation of vertical displacements. The height H_j of a levelling benchmark B_j is calculated by using the height H_0 of a start or reference point B_0 and consecutively adding the height differences of all intermediate measurement points between the start point and the point of interest, see Fig. 3.1:

$$H_j = H_0 + h_{0,1} + h_{1,2} + \ldots + h_{j-1,j} \quad . \tag{3.1}$$

Within a network of heights, redundant measurements are available from the network configuration enabling the application of a least-squares adjustment of heights. A Gauss-Markov model for height networks is given by

$$y = A \cdot \hat{x} + e \quad , \tag{3.2}$$

with a given set of observations y, the vector of adjusted parameters $\hat{x}$ and error vector e. For the example of one closed levelling loop, y and $\hat{x}$ take the form

$$y = \begin{pmatrix} h_{0,1} \\ h_{1,2} \\ \vdots \\ h_{j-1,j} \\ h_{j,0} \end{pmatrix} \quad , \quad \hat{x} = \begin{pmatrix} \hat{H}_0 \\ \hat{H}_1 \\ \hat{H}_2 \\ \vdots \\ \hat{H}_j \end{pmatrix} \quad . \tag{3.3}$$

The design matrix A describes the measurement relation between adjacent benchmarks and contains the values 0 (no relation) and 1 or -1 (measured height difference between the two corresponding heights), e. g. for one levelling loop:

$$A = \begin{pmatrix} -1 & 1 & 0 & \ldots & 0 & 0 \\ 0 & -1 & 1 & \ldots & 0 & 0 \\ \vdots & & & \ddots & & \vdots \\ 0 & 0 & 0 & \ldots & -1 & 1 \\ 1 & 0 & 0 & \ldots & 0 & -1 \end{pmatrix} \quad . \tag{3.4}$$

As the observations are relative quantities, i. e. height differences, only relative heights are estimable and the normal equation system has a rank deficiency. In order to solve Eq. (3.2), the datum of the height network has to be set by defining the height of at least one point.

One advantage of measuring levelling lines along a closed loop is the possibility to check and assess the quality of the measurements. The summation of all height differences in a closed loop, starting and ending at the same benchmark, should theoretically yield zero. Deviations from zero, so-called loop misclosures, are (among others) related to

(i) the non-parallelism of equipotential surfaces along the levelling loop, see Sect. 4.3,

(ii) a displacement of the start/end point of the loop during the measurement period, see Sect. 4.2.1,

(iii) residual measurement errors.

As (i) and (ii) are minimised by the application of gravity corrections and a proper choice of the start/end point of the loop, respectively, loop misclosures can serve as a measure for the quality of levelling data, see Sect. 4.2.1.

If height differences of at least two different measurement epochs are available, the determination of vertical displacements is possible. In contrast to space geodetic measurement techniques like GNSS and InSAR, levelling data is available over a large time span in the URG area. The large temporal baseline of the data offers the possibility to detect small secular movements with high accuracy. A displacement rate v_j of a leveling benchmark B_j is calculated in general from benchmark heights $H_{i,j}$ at different measurement epochs t_i, assuming a linear dependency on time:

$$v_j = \frac{H_{2,j} - H_{1,j}}{t_2 - t_1} = \frac{H_{2,j} - H_{1,j}}{\Delta t} \quad . \tag{3.5}$$

The precision of a displacement rate σ_v, calculated by error propagation and neglecting correlations between measurements of different epochs, yields

$$\begin{aligned} \sigma_v^2 &= \frac{1}{(\Delta t)^2}\sigma_{H_2}^2 + \frac{1}{(\Delta t)^2}\sigma_{H_1}^2 + \frac{(H_2 - H_1)^2}{(\Delta t)^4}\sigma_{\Delta t}^2 \\ &= \frac{2\sigma_H^2 + v^2\sigma_{\Delta t}^2}{(\Delta t)^2} \quad , \end{aligned} \tag{3.6}$$

under the assumption that the precision of H_1 and H_2 is identical. That means that $\sigma_v \sim \frac{1}{\Delta t}$, revealing an inversely proportional relation between time span and displacement rate. As usually the dates at which the measurements have been carried out are recorded, Δt is well-known and the second term of the numerator in Eq. (3.6) can be neglected. Even with a rather bad height precision σ_H of 5 mm, displacement rates are estimated with a precision better than 0.1 mm/a if there are 70 years or more between the two measurements.

The easiest way to determine displacements from levelling data is to calculate heights for each measurement epoch and subtract the height values of two or more epochs for each levelling benchmark (static approach). The calculation of heights can be either performed by consecutively adding the height differences between adjacent benchmarks to the height of a (presumably stable) starting point, see Eq. (3.1), or by least-squares adjustment of the height network for each epoch, see Eq. (3.2)–(3.4). The first option is suitable for local displacement analyses along a levelling line as presented in Sect. 4.6. The second option is, e. g. used to compare the height estimates of the epoch-wise measurements of the German height network (DHHN), see Wübbelmann (1993). Both options rely on the assumption that no deformation took place between the measurements within one epoch. For the measurements along a single levelling line of several tens of km length, this assumption is true in most cases as the survey is usually performed within a short time span (several weeks to months). For a country-wide height network, the assumption is hardly valid as the measurements take several years to decades. Ghitau (1970) therefore introduced a kinematic adjustment approach which allows for considering the dates of the observations within a single time-dependent adjustment model. The principal difference between a static and a kinematic adjustment approach for the derivation of displacements from levelling data of a height network is shown in Fig. 3.6.

The basic idea of the kinematic approach is to model a benchmark height $H_{i,j}$ using its height $H_{0,j}$ at a reference epoch t_0 plus a displacement rate $f_j(t)$ as a function of time:

$$H_{i,j} = H_{0,j} + \int_{t_0}^{t_i} f_j(t)dt \quad . \tag{3.7}$$

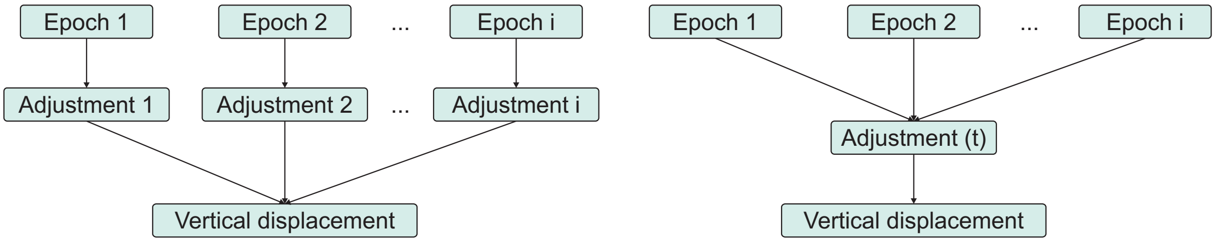

(a) Static approach (b) Kinematic approach

Figure 3.6: Adjustment approach for epoch-wise measured height differences of a levelling network.

Following Ghitau (1970), the integral of the movement is approximated using a Taylor expansion which yields

$$H_{i,j} \approx H_{0,j} + \frac{df}{dt}\Delta t_i + \frac{1}{2!}\frac{d^2 f}{dt^2}\Delta t_i^2 + \dots \quad \text{with } \Delta t_i = t_i - t_0 \quad . \tag{3.8}$$

From Eq. (3.8), two different models can be derived. The first one (surface model) approximates the vertical displacement as a function of horizontal position (Vanìček & Christodulidis, 1974; Holdahl & Hardy, 1979). In this case, the derivatives $\frac{df}{dt}$ and $\frac{d^2 f}{dt^2}$ are replaced by two-dimensional polynomial functions representing velocity and acceleration surfaces. The second model (point model) estimates displacement parameters directly at the levelling benchmarks and replaces the derivatives in Eq. (3.8) by constant velocity and acceleration parameters $v_{0,j}$ and $a_{0,j}$ (Holdahl, 1975; Mälzer et al., 1979):

$$H_{i,j} \approx H_{0,j} + v_{0,j}\Delta t_i + \frac{1}{2!}a_{0,j}\Delta t_i^2 + \dots \quad . \tag{3.9}$$

As only for a small part of the levelling benchmarks within the URG network three or more measurement epochs are available, Eq. (3.9) is cut after the accelerated term. To provide a higher redundancy and to estimate acceleration parameters only if they are significant, all benchmarks are assumed to follow a linear motion in time, expressed by the velocity $v_{0,j}$, in a first step. Second, accelerated motions are introduced at benchmarks which show a velocity change $a_{0,j}$ as proposed by Zippelt (1988, p. 28 f.). The decision, whether a second order term has to be introduced or not, is supplied by a statistical testing on model-related errors as described below. The adjustment uses the Gauss-Markov model of Eq. (3.2) with observations

$$y = h_{i,(j,k)} = H_{i,k} - H_{i,j} \quad , \tag{3.10}$$

where $h_{i,(j,k)}$ represents the measured height difference between benchmarks B_j and B_k at epoch t_i, and parameters

$$\hat{x} = \begin{pmatrix} \hat{H}_{0,j} \\ \hat{v}_{0,j} \\ \hat{a}_{0,j} \end{pmatrix} \quad . \tag{3.11}$$

A representative example for one line of the corresponding design matrix is given by

$$A_{i,(j,k)} = \begin{pmatrix} 0 & \dots & 0 & -1 & -\Delta t_i & [-\Delta t_i^2] & 0 & \dots & 0 & 1 & \Delta t_i & [\Delta t_i^2] & 0 & \dots & 0 \end{pmatrix} \quad , \tag{3.12}$$

where the terms in squared brackets are zero if the corresponding benchmark is modelled without an accelerated polynomial coefficient. The design matrix consists of n rows and

u columns, where n denotes the number of observations and u the number of unknown parameters. As one can see from Eq. (3.12), the design matrix A and thus the derived normal equation system contain many zeros for a large network of levelling data. For computational issues, it is hence reasonable to apply sparse memory techniques which use non-zero subsets of the matrices, see Schmitt (1973, p. 9 ff.).

The observations of the kinematic adjustment are relative quantities and the normal equation system suffers again from a rank deficiency, see Eq. (3.4). Zippelt (1988, p. 34 ff.) discusses different methods of datum definition in order to fix the rank deficiency of the kinematic adjustment model, e. g. (i) one (stable) reference point, (ii) stochastic reference points, and (iii) a minimum norm solution. For (i), all estimated parameters are relative to a specified, fixed reference point, whereas (ii) and (iii) relate to a subset or the total set of points. The use of (ii) and (iii) yields a more homogeneous distribution of the precision measures of $\hat{x}$, whereas (i) is easier considering the geophysical interpretation of the results because the estimated vertical velocities are relative to one single benchmark. As the geophysical interpretation of the displacements is of primary importance for a deformation analysis option (i) is chosen by setting

$$H = const., \quad v = const. = 0 \quad \text{and} \quad a = 0 \tag{3.13}$$

for a single specified reference point. As mentioned in Mälzer et al. (1983), the reference point has to be chosen carefully since the results of the adjustment are influenced by a potential individual movement of the reference point. Additional information on the geological setting of the investigated area is needed for a proper selection of the reference point. To ensure a robust integration into the network adjustment, the reference point should be measured at many epochs. As the uncertainty of the estimated parameters increases with the distance to the reference point, a central location within the network is preferable.

The functional model of the kinematic adjustment was described above, see Eq. (3.9)–(3.12). To solve the linear equation system, a stochastic model describing the precision and correlation of observations has to be defined. With a stochastic model of the form

$$C_{yy} = \sigma_0^2 \cdot Q_{yy} = \sigma_0^2 \cdot P^{-1} \quad , \tag{3.14}$$

where σ_0^2 represents the variance of unit weight and P the weight matrix, the least-squares solution for the parameter vector $\hat{x}$ results in

$$\hat{x} = (A^\top PA)^{-1} A^\top Py \quad . \tag{3.15}$$

In an optimum stochastic model, the elements of the covariance matrix Q_{yy} are known without errors. In practice, the covariance matrix is unknown. For the main diagonal elements of Q_{yy}, i. e. the precision of the measured height differences, accuracy measures from loop misclosures can be taken as an approximation. Attempts have been made to describe also the correlations between measurements along a levelling line (e. g. Lucht, 1983; Vaníček & Grafarend, 1980). However, it is hardly possible to make realistic assumptions on the correlations between observations for the tri-national, multi-temporal network of the URG area. Neglecting possibly existing correlations between the observations, leads to a covariance matrix of diagonal structure. The variances of Q_{yy} can be calculated from an overall model considering random and systematic errors (Sect. 4.4.1). In addition, variance component estimation can be used to account for inhomogeneous accuracy levels for data of different epochs, orders and countries (Sect. 4.4.2).

The large data set of height differences from different measurement epochs may contain gross errors or large outliers. In addition to the quality check using loop misclosures (Sect. 4.2), it is advisable to perform a statistical test of the observations using the parameter and precision estimates of the adjustment. Three different testing strategies are discussed in Zippelt (1988, p. 77 ff.):

(i) data snooping based on the redundancy components of observations (Baarda, 1968),

(ii) τ-test for the detection of gross errors using normalised residuals (Pope, 1976),

(iii) elimination of single observations and test of corresponding standard deviations using Student's t-distribution (Heck, 1981).

In addition to testing gross errors in the observations, an overall model test is often performed within a network adjustment, which tests the ratio of a posteriori and a priori variances against the Fisher distribution $\mathcal{F}$ with a certain significance level α, see e. g. Teunissen (2006, p. 61 f.). The null hypothesis, i. e. $\hat{\sigma}_0 = \sigma_0$, is rejected if

$$\frac{\hat{\sigma}_0^2}{\sigma_0^2} > \mathcal{F}_\alpha(n-u,\infty) \quad . \tag{3.16}$$

As described above, the functional model presupposes linear displacements in a first iteration step. To decide whether an additional accelerated parameter has to be introduced, a test of the motion model given in Eq. (3.9) is performed for every benchmark. Again a variance ratio test is used, see Eq. (3.16). The variance derived by elimination of the benchmark under investigation from the database is tested against the variance using all benchmarks (Zippelt, 1988, p. 82 ff.).

In general, apparent height variations from repeatedly measured levelling data are not identical to real crustal deformation as also the reference surface of the height system (Geoid, Quasigeoid) may change its shape. Heck & Mälzer (1983a,b) investigated the influence of temporal gravity changes on vertical displacements derived from levelling. Neglecting the influence of a changing gravity field in the calculation of height changes provokes a difference of 0.2 mm/a for displacement rates of 4 mm/a. For displacement rates at the sub-mm/a-level, the differences reduce to values below 0.1 mm/a. Measured gravity values are not available for the whole analysed levelling network and particularly not for the older measurement epochs. The influence of temporal changes of the gravity field therefore has to be neglected. Some considerations and investigations on the application of gravity corrections calculated from temporally constant gravity values are shown in Sect. 4.3.

3.2 GNSS

This section describes the methodology of Global Navigation Satellite Systems (GNSS) observations, focussing on GPS measurements at permanently operating sites (Sect. 3.2.1). The available GNSS sites and the corresponding data in the URG countries Germany, France and Switzerland are presented in Sect. 3.2.2, the analysis strategies for the derivation of displacements from these data sets in Sect. 3.2.3.

3.2.1 Methodology

GNSS have been developed for the purpose of timing and positioning, primarily for military applications. The first GNSS using one-way microwave measurements based on the ranging principle were developed in the 1970s, namely the U. S. Global Positioning System (GPS) and the Russian GLONASS (Torge & Müller, 2012, p. 135). Predecessor of GPS and GLONASS were the U. S. Navy Navigation Satellite System (NNSS) and the Russian Tsikada with first satellites launched in 1959 and 1974, respectively, see Hofmann-Wellenhof et al. (2008, p. 4 f.). Within the last years, satellites for the European GNSS Galileo and the Chinese Beidou have been launched. The number of globally usable GNSS satellites operating within the four systems on August 2015 is 30 for GPS, 24 for GLONASS, 4 for Galileo and 4 for Beidou (Langley, 2015). In addition, several regional satellite navigation systems are currently under development, such as the Japanese QZSS and the Indian INSS. The principal functionality of all GNSS is based on the emission of electromagnetic radio waves at several satellites (space segment), which are received by antennas on the Earth (user segment), see Fig. 3.7. In addition, a ground segment, also denoted as control segment, is responsible for maintaining the operation of the system, such as calculating and providing of the navigation data of the satellites (Torge & Müller, 2012, p. 138). GPS initially provided microwave signals on two frequencies at 1575.42 MHz and at 1227.60 MHz, called $L1$ and $L2$, respectively. Since 2010, the GPS satellites are able to emit signals at a third frequency at 1176.45 MHz, denoted as $L5$.

The analysis of GNSS signals makes use of two general measured quantities, i. e. code measurements and carrier phase measurements. Both rely on the calculation of the distance between satellite S and receiver R. The geometric distance d_R^S follows from the position vectors (X^S, Y^S, Z^S) and (X_R, Y_R, Z_R) of satellite and receiver antenna, respectively:

$$d_R^S = \sqrt{(X^S - X_R)^2 + (Y^S - Y_R)^2 + (Z^S - Z_R)^2} \quad . \tag{3.17}$$

Note that the position vectors of satellite and receiver antennas have to be referred to the same reference frame.

For code measurements, the principal observations, denoted as pseudoranges ρ_R^S, are given by

$$\begin{aligned} \rho_R^S &= c(t_R - t^S) + c\delta_R - c\delta^S + \epsilon_R^S \\ &= d_R^S + c\Delta\delta + \epsilon_R^S \quad , \end{aligned} \tag{3.18}$$

with the speed of light c, time measurements t_R and t^S as well as clock errors δ_R and δ^S of the receiver and satellite clocks, respectively, see Hofmann-Wellenhof et al. (2008, p. 105). The term ϵ represents noise as well as further influence factors affecting the travel time of the signal, such as ionospheric and tropospheric refraction or multipath effects. From multiple observations of different satellites S and corresponding pseudoranges ρ_R^S, the position of the

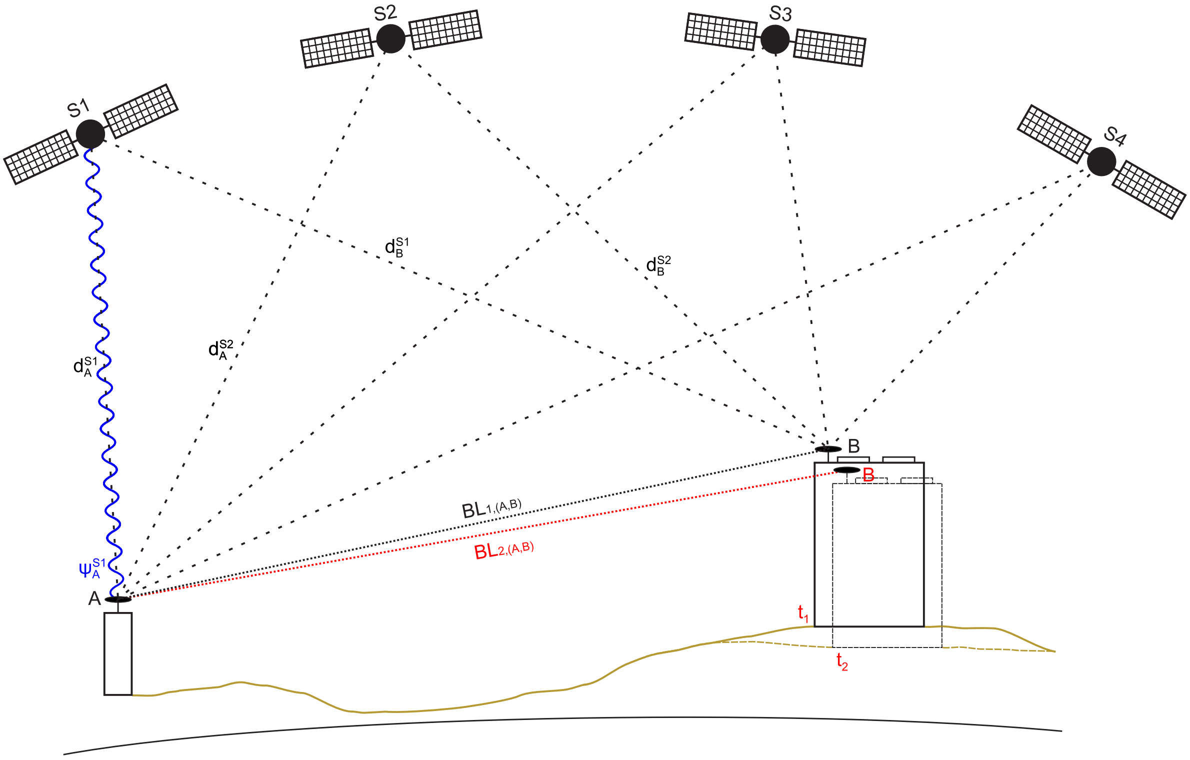

Figure 3.7: Principle of GNSS: carrier phase observations ψ at permanently operating GNSS antennas with a geometric distance d to the satellites $S1$, $S2$, ... By double differencing of observations, relative baselines BL are calculated between the antenna locations. A displacement at antenna B relative to antenna A between two measurement epochs t_1 and t_2 results in a difference of the baseline $BL_{A,B}$, and thus of the relative 3D coordinates of B.

receiver is estimable in a least-squares sense. At least four satellites have to be observed in order to solve Eq. (3.18) as there are four unknowns: three coordinate values (X_R, Y_R, Z_R) and the unknown clock difference $\Delta\delta$. Positioning estimates from these measurements achieve accuracies of several m under favourable conditions. For highly precise positioning applications on the mm- to cm-level, the carrier phases of the GNSS signals have to be exploited and analysed. The observation equation of carrier phase measurements ψ_R^S in units of cycles is given by Hofmann-Wellenhof et al. (2008, p. 106 f.):

$$\psi_R^S = \frac{F}{c} d_R^S - F\delta_R + F\delta^S + N + \epsilon_R^S \quad , \tag{3.19}$$

with the signal frequency F and the integer number N of cycles between S and R at the beginning of the measurement, also denoted as ambiguity.

According to Parkinson & Spilker (1996a, p. 478), the effects influencing the GNSS observations may be grouped into six classes listed in Tab. 3.1. Receiver-specific effects are split into influence factors of clock and antenna, here, as they are separately handled within the analysis of measurements at permanent sites. For a relative (or differential) analysis of GNSS carrier phase observations using double differences, see Sect. 3.2.3, some of the errors are eliminated or at least significantly reduced. In the following paragraphs, the error sources listed in Tab. 3.1 are further discussed w.r.t. carrier phase observations at permanently operating GNSS sites.

Table 3.1: Influence factors on GNSS observations and mitigation strategies. DD: double differences.

Influence factor	Mitigation
Ephemeris data (orbit error)	precise products, eliminated by DD
Satellite clock	precise products, eliminated by DD
Receiver clock	estimation, eliminated by DD
Ionosphere	model, ionosphere-free linear combination, reduced by DD
Troposphere	model and estimation, reduced by DD
Multipath	prevent reflections, antenna design, receiver architecture, data post-processing
Receiver antenna	model, calibration

Ephemeris data and satellite clock corrections are provided as input data for GNSS analyses. For near real-time applications, predictions for both data sets have to be used. For post-processing applications, it is reasonable to introduce more accurate orbit and clock data into the analysis. The final data products of the International GNSS Service (IGS, 2015) are available after 12–18 days and reach accuracy levels of 2.5 cm and 75 ps root mean square (20 ps standard deviation) for orbit and clock data, respectively. Receiver clock errors are eliminated when double differences are built from the GNSS phase observations. Otherwise, using non-differenced data, the clock bias of the GNSS receiver has to be estimated within the adjustment. Relativistic effects influence the time measurement at both satellites and receivers. General as well as special theory of relativity have to be considered as the difference in the gravitational potential between Earth and space as well as the velocity of the satellites on their orbit play a role. Because of time dilation, the satellites' clocks are ticking at a slower rate compared to clocks on Earth, which is why the frequency of satellite clocks is slightly adjusted during manufacturing of the satellites. Further corrections necessary to account for relativistic effects may be included to the clock polynomial broadcasted via the navigation message (Leick, 2004, p. 178).

Atmospheric effects strongly influence GNSS observations on their way from the satellites in approximately 20,000 km altitude above Earth to a receiving antenna located on the Earth's surface. In comparison to the signal propagation in vacuum, GNSS carrier phase signals are delayed, bended and dispersed in the atmosphere. The dominating atmospheric effect for positioning applications results from the delay in signal travel time and has to be considered within the analysis. In addition, absorption leads to transformation of parts of the signal energy into heat resulting in reduced signal quality and intensity (Mayer, 2006, p. 78). Concerning the electrical properties, the atmosphere is subdivided into an electrically neutral part, the neutrosphere, located up to a height of about 50 km above surface, and a part containing a significantly higher number of free electrons, the ionosphere, between 50 and 1000 km above surface (Hofmann-Wellenhof et al., 2008, p. 118). For electromagnetic waves, the ionosphere is a dispersive medium. Therefore, signal propagation is dependent on the frequency of the signals (Seeber, 2003, p, 54 f.). Ionospheric effects may cause range errors in the order of several meters up to 100 m (Torge & Müller, 2012, p. 142). Within the non-dispersive neutrosphere, electromagnetic signals with different frequencies are delayed in the same way. In GNSS literature, instead of *neutrosphere* usually the term *troposphere* is used, which corresponds to a classification w.r.t. atmospheric temperatures and represents the major part of the neutrosphere. The tropospheric delay is further divided into a dry component, which is hydrostatic and therefore slowly varying and easily describable by a model, and into a wet component mainly affected by the temporal and spatial variability of water vapour in the atmosphere (Leick, 2004, p. 189). The tropospheric delay varies depending on the latitude of the site location, the elevation angle of the observed satellite and the amount of water vapour. According to Parkinson & Spilker (1996a, p. 541), the total delay comprising dry and wet component varies between 2.3 and 2.6 m in zenith direction for latitudes between 30°N and 75°N. In slant direction, the total tropospheric delay is generally larger as the path length of the signal increases.

Multipath effects are caused by reflections in the near and far field of a GNSS antenna and represent a major error source for GNSS positioning applications, particularly as they are not reduced by differential positioning. For carrier phase measurements, multipath errors range up to a quarter of the wavelength, i. e. a few cm (Ray, 2006). As multipath is strongly site-specific, a generally valid and practicable analytical multipath model is still lacking. In order to reduce multipath effects, a suitable environment for the site location should be chosen. In addition, microwave-absorbing materials can be placed at the site location to prevent reflections, see Ning et al. (2011). A proper antenna design, such as choke ring or ground plane antennas, contributes to mitigate multipath at low elevation angles (Bedford et al., 2009). Receiver-based mitigation techniques are mainly applied to reduce code multipath as described by Parkinson & Spilker (1996a, p. 560). Many approaches have been developed in the last years to reduce multipath by means of data processing, such as in-situ calibration (Park et al., 2004), wavelet-based reduction (Zhong et al., 2008), SNR-based reduction (Bilich & Larson, 2007; Rost & Wanninger, 2009), adaptive filtering (Liu et al., 2011), electromagnetic modelling (Fan & Ding, 2006), sidereal stacking and filtering (Choi et al., 2004; Ragheb et al., 2006) as well as spatial stacking of phase residuals (Iwabuchi et al., 2004; Fuhrmann et al., 2010b, 2015d; Knöpfler, 2015).

Besides multipath, inaccuracies of the electrical phase centre position of the receiver antenna remain a main error source for high precision coordinate estimation at permanent GNSS sites. The electrical properties of a GNSS antenna are modelled using a constant offset between the mean electrical phase centre and the antenna reference point, denoted as phase centre offset (PCO). In addition, the phase centre of an individual measurement is described by azimuth- and elevation-dependent phase centre variations (PCV), see Hofmann-Wellenhof et al. (2008, p. 148 f.). Site-specific correction values for PCO and PCV can be introduced to a GNSS analysis in order to reduce antenna errors. For the calculation of the correction values, several calibration methods for GNSS antennas have been established, summarised by (Mayer, 2006, p. 47 ff.). Absolute, in-situ calibration for individual antennas is preferable compared to relative or laboratory calibration methods (Görres et al., 2006). If an individual calibration cannot be performed, antenna type-specific corrections provided by the U. S. National Geodetic Survey (NGS, 2015) and by IGS (2015) should be used. If a GNSS antenna at a permanent site is changed, the antenna gain and thus the interaction with the site environment may change resulting in an apparent coordinate change at the site (Krawinkel et al., 2014). Investigations on the gain pattern of receiver antennas and the influence on near-field multipath are presented by Smyrnaios et al. (2013, p. 102 ff.).

3.2.2 Database

The GNSS sites analysed within this thesis are part of the GNSS Upper Rhine Graben Network (GURN). The network was established in 2009 as a transnational cooperative project aiming at the fusion of GNSS data at permanently operating sites in the URG area (Knöpfler et al., 2010a). Most of the sites of GURN are operated by public or private institutions of the three participating countries, such as SA*POS*®[1] Baden-Württemberg and SA*POS*® Rheinland-Pfalz

---

[1] SA*POS*®: SAtellitenPOSitionierungsdienst der deutschen Landesvermessung

in Germany, Teria, Orpheon, RENAG[1] and RGP[2] in France and swisstopo in Switzerland. In addition, the sites of EPN[3] and IGS located in the URG area are used. Actually, GURN consists of more than 80 permanently operating GNSS sites with typical site distances of 30–40 km. Fig. 3.8 displays the location of 85 GURN sites, investigated within this work, considering the length of the individual coordinate time series.

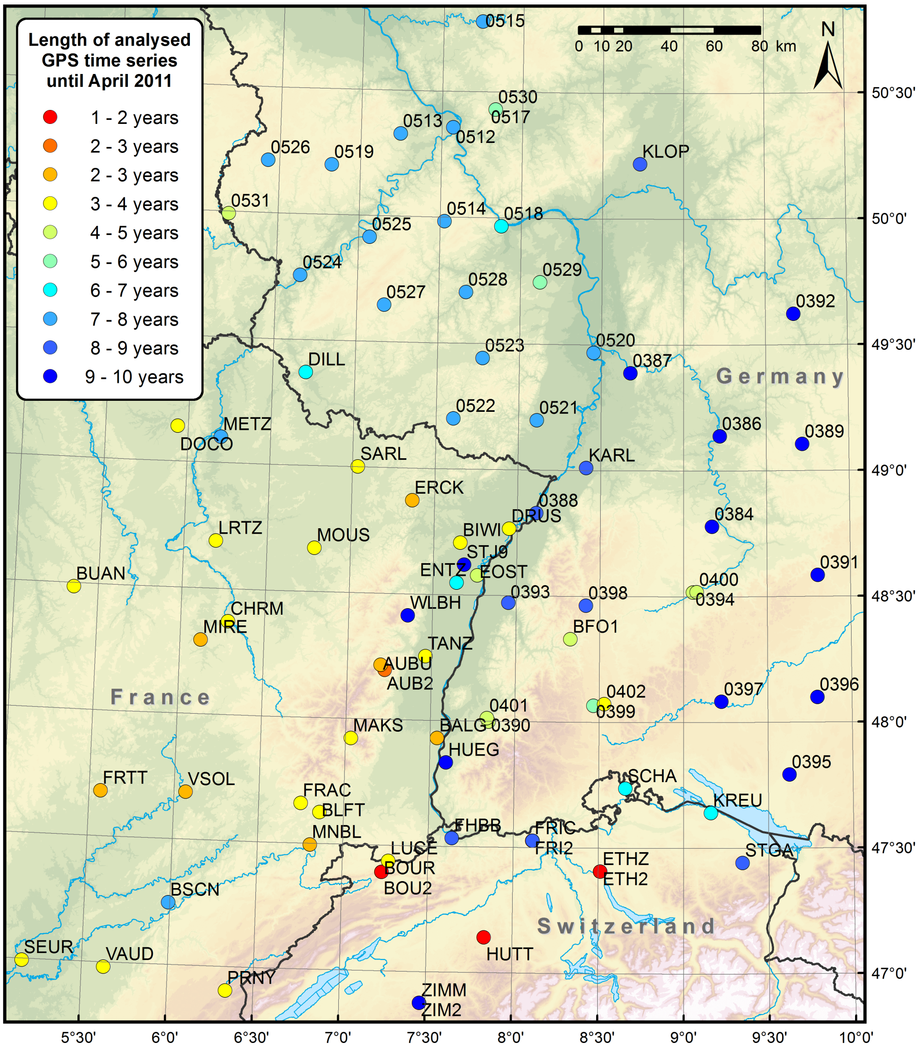

Figure 3.8: Sites of the GNSS Upper Rhine Graben Network (GURN). Colours indicate the length of the time series used for deformation analysis. The longest time series of sites located in Baden-Württemberg start in January 2002. The consistent reprocessing of the database currently ends in April 2011. Further information on the site locations of the corresponding four-digit site names is given in Tab. B.1 in Appendix B.

Most of the currently installed site equipment at the GURN sites enables the registration of both GPS and GLONASS signals. However, before 2008 less than 10 % of the sites were able to track GLONASS satellites. GLONASS data are therefore not used for the consistent processing of all GURN data available in the considered period between 2002 and 2011. The data record of the major part of the sites located in Baden-Württemberg starts in 2002. The sites located in Rheinland-Pfalz were established in 2004. Starting mainly in 2008, antennas and

---

[1] RENAG: RÉseau NAtional GPS permanent

[2] RGP: Réseau GNSS Permanent (IGN)

[3] EPN: EUREF (European reference frame) Permanent Network, see EPN (2015)

receivers of the sites located in Germany were changed to provide GLONASS capability. The documentation of hardware changes at permanently operating sites is important for displacement analyses as they may result in offsets in the coordinate time series, see Sect. 5.2.3. Most of the French time series start in 2007. For the Swiss part, more data is available at some sites, but was unfortunately not provided free of charge by swisstopo.

Most of the German sites were originally established for cadastral purposes serving as reference sites, particularly for real-time kinematic differential GNSS surveys. Therefore, the location of the sites was chosen to ensure long-term stability of the sites enabling high accuracy, availability and security of the differential GNSS service (Rosenthal, 2001). In addition, logistic aspects, like the accessibility to power supply and communication, as well as security for the site equipment are required. Because of these restrictions, many of the sites are located on public buildings and possibly affected by local movements, e. g. tilting of the monumentation or the building. At some sites, tiltmeter records and quality-related parameters, such as multipath, have been analysed by Knöpfler et al. (2010b) in order to gain insight into the GNSS data quality. In France most of the sites are operated by private companies offering GNSS data for real-time applications. Data quality and standards are comparable to the German sites as discussed above. In addition, EOST[1] set up pillar sites, especially dedicated to geodynamic purposes and properly founded on the ground. The sites located in Switzerland are operated with different types of monumentation. Some of them are mounted on buildings, others are well-founded in bedrock using steel masts or pillars. A special feature of the Swiss sites is the large number of collocated site locations, where two antennas are placed close to each other, but on different monumenations, such as the sites located at Bourrignon (BOUR and BOU2), Frick (FRIC and FRI2), ETH[2] Zürich (ETHZ and ETH2) and Zimmerwald (ZIMM and ZIM2), see Fig. 3.8. Fig. 3.9 displays three representative examples for site monumenatations within GURN. Site KARL is located on the rooftop of GIK[3], site STJ9, close to Strasbourg, is operated by EOST and mounted on a well-founded pillar, site ZIMM is attached to a high, robust steel mast.

(a) site KARL (EPN, 2015) (b) site STJ9 (EOST, 2015) (c) site ZIMM (EPN, 2015)

Figure 3.9: Monumenation at three GNSS sites of GURN, image sources are given in brackets.

---

[1] EOST: École et Observatoire des Sciences de la Terre, University of Strasbourg

[2] ETH: Eidgenössische Technische Hochschule (University of Zurich)

[3] GIK: Geodetic Institute, Karlsruhe Institute of Technology

In addtion to geodynamic investigations, GURN has also been used for studies of site-specific effects (Fuhrmann et al., 2010b, 2015d; Knöpfler, 2015) and for the derivation of water vapour maps (Fuhrmann et al., 2010a; Alshawaf et al., 2015b). For both investigations, the GNSS observations were analysed using the precise point positioning (PPP) method, see Sect. 3.2.3. In contrast to differential positioning approaches, PPP enables the derivation of independent parameter estimates and residuals at every site. Maps of stacked phase residuals for every site enable an assessment of site-specific effects, such as multipath at the GURN sites. Troposphere estimates at the GNSS sites are converted into water vapour, which is an important quantity for weather and climate research (Alshawaf et al., 2015b). In a second step, the water vapour resulting from GNSS analyses can be compared and combined with water vapour estimates from InSAR and numerical weather models (Alshawaf et al., 2015a,c).

Besides the GNSS code and phase measurements, several other data sets are required in order to estimate coordinates with high precision. Orbit data, clock data and Earth orientation parameters (EOP) are particularly important for PPP analyses. Corresponding products are provided by the analysis centres of IGS (2015). Approximate coordinates of the GNSS sites are introduced for the linearisation of the normal equations, see Eq. (3.19), within the adjustment procedure. Furthermore, the antenna model is defined for the correction of phase observations by PCO and PCV values. PCO values are given in three components (North, East, Up) by default. PCV values consist of corrections at different elevation angles, e. g. 5°, 10°, 15°, 20°, …, and if necessary, additional azimuth-dependent correction values for every elevation level. The antennas mounted at the German sites are individually and absolutely calibrated. Most of the French and Swiss sites are not individually calibrated, and thus type-specific calibration values have to be applied.

3.2.3 Analysis strategies

Two principle analysis strategies have been developed for the estimation of the position coordinates (X_R, Y_R, Z_R) of a receiver antenna from Eq. (3.19):

(i) relative (or differential) positioning, where most of the perturbation terms listed in Tab. 3.1 are eliminated or at least reduced by combining observations of different satellites and receivers at different measurement epochs,

(ii) precise point positioning (PPP), where most of the perturbation terms listed in Tab. 3.1 have to be determined by incorporating a priori information or by estimation within the data adjustment.

The basic principle of relative positioning is already implied in Fig. 3.7. Within a relative positioning, double differences between several satellites and receiving antennas can be formulated from Eq. (3.19), see Hofmann-Wellenhof et al. (2008, p. 174 ff.). The carrier phase of double differences $\psi_{i,(A,B)}^{S1,S2}$ between two antenna locations A, B and two satellites $S1$, $S2$ at a measurement epoch t_i results in

$$\psi_{i,(A,B)}^{S1,S2} = \frac{F}{c} d_{i,(A,B)}^{S1,S2} + N_{A,B}^{S1,S2} + \epsilon_{i,(A,B)}^{S1,S2} \quad . \tag{3.20}$$

Satellite and receiver clock errors are eliminated in this case. Depending on the length of the baseline $BL_{A,B}$ atmospheric effects are strongly reduced (Parkinson & Spilker, 1996b, p. 11 ff.). The integer number of double differenced ambiguities $N_{A,B}^{S1,S2}$ remains constant as long as the signal to the corresponding satellites is received at both antennas. Otherwise, the integer ambiguity counter has to be reinitialised causing a jump of the phase, denoted as cycle slip

(Hofmann-Wellenhof et al., 2008, p. 194 f.). Using several permanent GNSS sites, a network of independent baselines can be constructed resulting in mm-precision for coordinate estimates of long observation series, e. g. daily coordinate solutions (Torge & Müller, 2012, p. 323). Similar to height networks, the datum of the adjusted network solution has to be defined, which in case of regional GNSS networks is usually performed by a stochastic connection to surrounding reference sites, such as EPN or IGS sites. Care has to be taken on the selection of the reference sites as gross errors in the observations of reference sites affect the network adjustment.

PPP processing strategies enable an independent analysis of data recorded at one GNSS receiver. The advantage of a PPP analysis is that the resulting position estimates are absolute quantities and free of distortions imposed by erroneous fiducial constraints of other GNSS sites (Zumberge et al., 1997). The datum of the coordinate estimates at every site is introduced by the reference frame defined with the satellite orbits. PPP is therefore appropriate for the analysis of site-specific effects, such as multipath or the antenna model. In contrast to a differential analysis, many of the perturbation terms eliminated or reduced within a differential analysis have to be modelled or estimated (Witchayangkoon, 2000). Ionospheric effects are usually considered by applying the ionosphere-free linear combination $L3$, which eliminates the first-order ionospheric effects, see Seeber (2003, p. 331). Satellite clock errors are handled by introduction of satellite clock products, provided by the analysis centres of IGS. The receiver clock errors are estimated within the adjustment. As a consequence of the formation of $L3$ along with uncalibrated phase delays, simple integer ambiguity solution is prevented (Hinterberger et al., 2015). Ambiguities are commonly estimated within the adjustment, even if strategies to recover the integer nature of ambiguities have recently been developed, e. g. by Ge et al. (2008). However, PPP coordinate solutions depend on the quality of the introduced products and do currently not reach the same accuracy level as differential estimates.

The general procedure of post-processing GNSS observations is similar for relative positioning and PPP. The processing starts with reading and preparation of the relevant input data, i. e. code and carrier phase observations, satellite orbit and clock data, EOP, antenna corrections and approximate site coordinates. Based on both code and phase observations, outliers and cycle slips are detected. Finally, the adjustment of observations is performed in several iterative steps. Within each step, residuals are screened for outliers, which are excluded from the database in the next iteration. For baseline processing, integer-valued ambiguities are fixed using one of the strategies discussed by Hofmann-Wellenhof et al. (2008, p. 202 f.). For PPP, ambiguities have to be estimated as unknown parameters. The tropospheric delay in the line-of-sight towards a satellite is modelled using the delay in zenith direction along with a mapping function, e. g. the mapping functions separately defined for the dry and wet part of the delay by Niell (1996) or Böhm et al. (2006). The dry part of the delay is usually calculated from a model using meteorological parameters, such as the models described by Hopfield (1969) or Saastamoinen (1973). The wet part is estimated within the adjustment using the observations of a given period. In addition, the functional model can be extended by horizontal gradients modelling the azimuth-dependence of the troposphere (Meindl et al., 2004).

Finally, the major results of the adjustment of GNSS observations are site coordinates valid for a given period, e. g. daily solutions. The coordinate estimates are relative results w.r.t. a given reference frame, such as the International Terrestrial Reference Frame (ITRF). From the time series of daily coordinate estimates at one site, a velocity within the introduced reference frame is deduced. A special focus of this work is on the handling of jumps and periodic effects present in the coordinate time series, see Sect. 5.2.3.

3.3 InSAR

This section describes the methodology of satellite-based SAR interferometry (InSAR) for the derivation of surface displacements (Sect. 3.2.1). The analysed SAR data in the URG area are presented (Sect. 3.2.2) as well as the analysis strategies for the derivation of displacements from the data sets (Sect. 3.2.3).

3.3.1 Methodology

Spaceborne synthetic aperture radar (SAR) systems have been widely used since the launch of the first civilian SAR sensor on-board the Seasat mission in 1978 (Moreira et al., 2013). More than a dozen SAR systems have been launched in the meantime focussing on various applications such as DEM generation, land surface mapping, oceanography, glaciology, agricultural monitoring, biomass quantification, environmental monitoring including change detection, surface displacement measurement, military surveillance and moving target indication. SAR systems are active sensors using the radar (radio detection and ranging) technique. A radar instrument installed on a platform with a forward movement (airborne or spaceborne) transmits electromagnetic pulses with high power and receives the echoes of the backscattered signal. Most SAR sensors use frequency modulated, pulsed waveforms for transmission, so-called chirp signals, which means that the frequency of the signal is linearly varied over time. The varying frequency widens the bandwidth and thus enables a high ground resolution in the direction of the pulse (Doerry, 2006).

The principal measurement quantities are the range, i. e. the distance to the detected object, and the intensity of the backscattering. From the side-looking image geometry, SAR sensors are able to provide a 2D map of the Earth's surface in the coordinate system of the platform, which is made up by the satellites heading (along-track or azimuth direction) and a direction perpendicular to the flight path (across-track or range direction). While the ground resolution in range direction depends on the bandwith or pulse duration of the transmitted signal, the azimuth resolution δ_A depends on the size of the antenna L_a, the range R to the object and the wavelength λ of the radar sensor, see Curlander & McDonough (1992, p. 16):

$$\delta_A = \frac{R \cdot \lambda}{L_a} \quad . \tag{3.21}$$

However, for a spaceborne radar sensor at 800 km altitude, the antenna ought to have a length of several hundreds of m to achieve a resolution below 100 m for common radar wavelengths at the cm- to dm-level. Therefore, a synthetic aperture is used consisting of several antenna elements which are built from periodic transmitting and receiving of radar signals during the pass of a satellite. Typical ground resolutions of spaceborne SAR systems are in the range of 1 to 20 m.

SAR interferometry (InSAR) makes use of two SAR images acquired either by two different antennas (single-pass interferometry) or at different times (repeat-pass interferometry). Single-pass interferometric acquisitions are used to derive a high quality DEM, such as with the Shuttle Radar Topography Mission (SRTM, Rabus et al., 2003) or the TanDEM-X (TerraSAR-X add-on for Digital Elevation Measurement) mission (Moreira et al., 2004). Repeat-pass interferometry is less appropriate for DEM derivation as the quality of the measurements is reduced due to temporal decorrelation and atmospheric delay variations, see Hanssen (2001, p. 103 f. and p. 148 ff., respectively). The first measurement of surface displacements has been successfully performed by Gabriel et al. (1989) by application of repeat-pass interferometry to

SAR data acquired by Seasat. Many studies of surface displacements caused by earthquakes, volcanoes, landslides and extraction of groundwater or hydrocarbons have been performed since that time. A variety of analysis strategies working on different spatial and temporal scales has been developed. Fig. 3.10 shows the principal functionality of repeat-pass InSAR w.r.t. the derivation of heights and surface displacements.

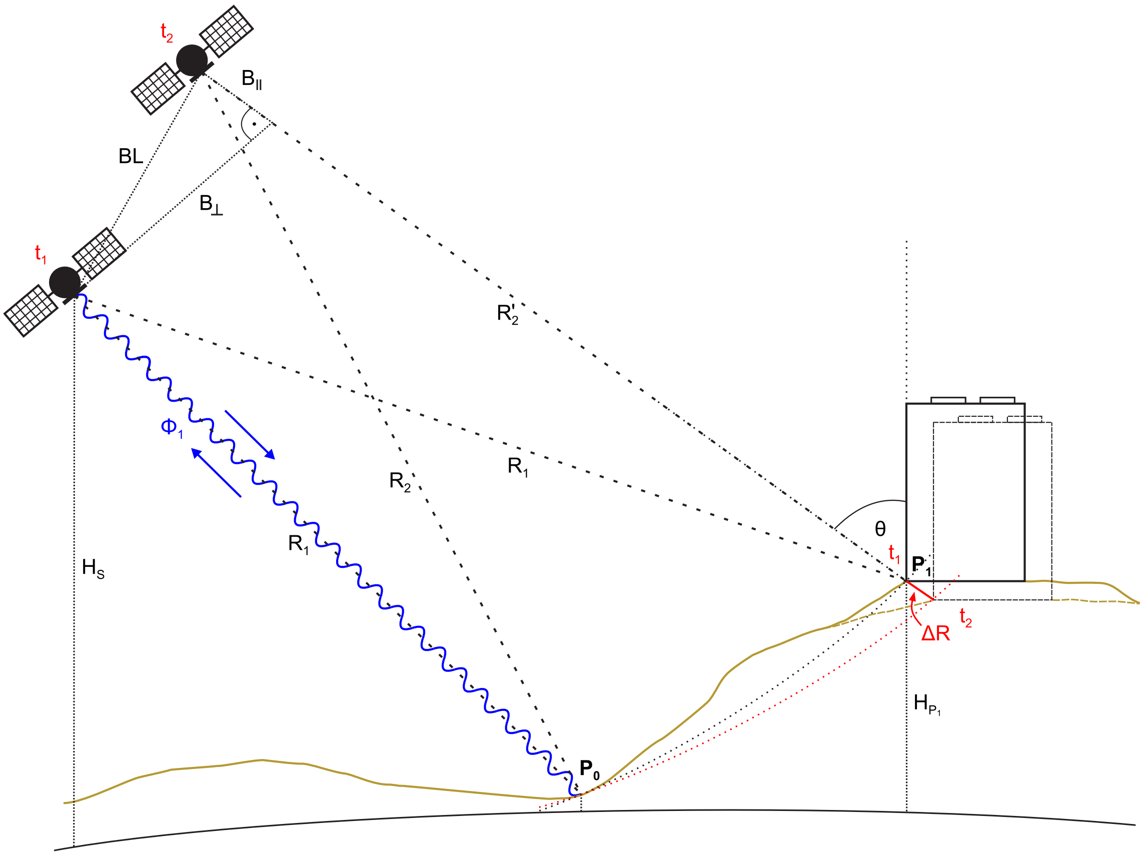

Figure 3.10: Principle of repeat-pass interferometry: the relative height H_{P_1} of point P_1 w.r.t. a reference point P_0 is resolvable from the complex measurements at different ranges R_1, R_2, R_2' and the satellite height H_S. Note that point P_0 and P_1 are at the same range R_1 in the example for the first acquisition. The second acquisition at t_2 is performed from a slightly different satellite position, differing from the acquisition position at t_1 by the baseline BL, which splits into the parallel baseline component $B_{\|}$ and the perpendicular baseline $B_{\perp}$. The change in incidence angle θ is determined from the interferometric phase $\Delta\phi = \phi_1 - \phi_2$. A displacement at point P_1 relative to point P_0 between the two acquisitions at t_1 and t_2 results in a change of range ΔR along the line of sight (LOS) towards the satellite.

The basic observations at the SAR antenna are the amplitude A of the received electromagnetic signal and the phase change ϕ between transmitted and received pulse. A complex representation of the SAR signal reflected at location P_1 is given by

$$y_1 = |y_1| \cdot \exp(j\phi_1) = A_1 \cdot \exp(j\phi_1) \quad , \tag{3.22}$$

where j denotes the imaginery unit. The phase change ϕ depends on the two-way path from the radar sensor to the target and the radar wavelength λ, see Curlander & McDonough (1992, p. 24) or Hanssen (2001, p. 36):

$$\phi_1 = -\frac{4\pi R_1}{\lambda} + \phi_{scat,1} \quad . \tag{3.23}$$

ϕ_{scat} represents the scattering phase resulting from the reflection characteristics of the target and is close to zero for metal objects and may largely differ from zero in case of absorption. From two acquisitions, an interferometric set of signals follows from complex conjugate multiplication of two SAR signals y_1 and y_2, denoted as interferogram:

$$y_1 y_2^* = A_1 A_2 \exp(j(\phi_1 - \phi_2)) = A_1 A_2 \exp(j\Delta\phi) \quad . \tag{3.24}$$

Assuming constant backscattering characteristic of the object, the interferometric phase $\Delta\phi$ between two acquisitions of the same target results from Eq. (3.23):

$$\Delta\phi = \phi_1 - \phi_2 = -\frac{4\pi\Delta R}{\lambda} \quad . \tag{3.25}$$

A displacement along the line of sight towards the satellite (LOS) is associated with a change in range $\Delta R = R_1 - R_2$ and is thus measurable with the interferometric phase. Besides the phase ϕ_{defo} related to a displacement, the interferometric phase consists of several other phase terms which have to be considered during an InSAR analysis, i. e. a phase term ϕ_{ref} related to a reference surface, e. g. an ellipsoid, see Fig. 3.10, a topographic phase ϕ_{topo}, a phase ϕ_{atmo} caused by different atmospheric states during the two acquisitions, a phase term ϕ_{orbit} due to inaccuracies of the orbit parameters used to calculate the satellite positions, residual noise ϕ_{noise} and a term representing the integer ambiguity N of the phase which is initially wrapped in the interval $[-\pi \dots \pi)$, see van Leijen (2014, p. 10):

$$\Delta\phi = \phi_{ref} + \phi_{topo} + \phi_{defo} + \phi_{atmo} + \phi_{orbit} + \phi_{noise} \pm 2\pi N \quad . \tag{3.26}$$

Strategies for the separation of the deformation phase ϕ_{defo} from Eq. (3.26) are discussed in Sect. 3.3.3.

The residual noise term introduced in Eq. (3.26) subsumes several effects, commonly denoted as decorrelation of the phase signal. A measure for the correlation of complex signals from two acquisitions is the complex correlation coefficient γ, denoted as interferometric coherence, given by Bamler & Just (1993); Goldstein & Werner (1998):

$$\gamma = \frac{E\{y_1 y_2^*\}}{\sqrt{E\{|y_1|^2\}E\{|y_2|^2\}}} \quad , \tag{3.27}$$

where $E\{\cdot\}$ denotes the expectation operator and * the complex conjugate. For practical calculations, $E\{\cdot\}$ is replaced by a spatial mean value, obtained over a limited area around the considered pixel. Sources of decorrelation, i. e. $1 - \gamma$, are discussed by Hanssen (2001, p. 98 ff.) and split into geometric decorrelation effects due to different incidence angles between the acquisitions, decorrelation due to different Doppler Centroid (DC) frequencies of the acquisitions, temporal decorrelation caused by changes of the surface characteristics, e. g. different vegetation, and thermal noise due to the characteristics of the SAR system. The DC frequency denotes the mean shift of the Doppler frequency of a scene resulting from the relative movement of the targets on Earth w.r.t. the moving platform (Curlander & McDonough, 1992, p. 17 ff.). Due to slightly different squint angles steering the antenna away from the normal to the flight direction of the satellite at different overflights, the DC frequency may adopt different values resulting in frequency differences F_{DC} and thus decorrelation. Zebker & Villasenor (1992) showed that the decorrelation effects, expressed by their correlations terms γ_{temp}, γ_{geom}, $\gamma_{F_{DC}}$, γ_{therm}, contribute multiplicatively to the overall coherence:

$$\gamma_{total} = \gamma_{temp} \cdot \gamma_{geom} \cdot \gamma_{F_{DC}} \cdot \gamma_{therm} \quad . \tag{3.28}$$

Eq. (3.28) is used for the selection of a master image within a stack of SAR data, see Sect. 6.1.1. Temporal decorrelation effects are connected to the revisit time of the satellite. The revisit time of current and past satellite missions ranges between 4 and 46 days, see Tab. 3.2. However, not every possible image is acquired due to the satellite-specific operation modes.

The backscattering properties of the emitted pulse, particularly the depth of penetration into the ground, depend on the wavelength of the electromagnetic signal (Curlander & McDonough, 1992, p. 46 ff.). In addition, atmospheric perturbations, the achievable spatial resolution and the sensitivity to ground motion differ for different wavelengths (Prati et al., 2010). Current SAR missions used for displacement measurement can be classified w.r.t. three major wavelengths, i. e. L-band, C-band and X-band, see Tab. 3.2. C-band SAR satellites provide a global coverage with regular acquisitions at a medium resolution and sensitivity level and therefore constitute a good compromise for spaceborne Earth observation missions. Since the first C-band acquisitions of ERS-1 in 1993, C-band data has almost continuously been acquired by ESA's satellite missions ERS-1, ERS-2, Envisat and Sentinel-1 (Salvi et al., 2012). In addition, C-Band missions cover the largest strips on the Earth's surface, denoted as swath, along the satellites' tracks and are therefore well-suited for large-scale InSAR applications. Tab. 3.2 gives an overview of past and current civilian SAR missions suitable for investigations on surface deformation.

Table 3.2: Past and current SAR missions and their properties w.r.t. interferometry, compiled from Hanssen (2001, p. 17), Moreira et al. (2013), van Leijen (2014, p. 34 f.) and the Earth observation portal of ESA (2015). The swath width and corresponding resolutions given in the table refer to a standard mode if several modes are available. The resolution relates to the spacing on the ground (average spacing for the range component). T_{min} denotes the revisit time of the satellite.

Mission	Institution, country	Period of operation	λ [cm]	Band	θ [°]	Swath [km]	T_{min} [days]	H_S [km]	Resolution [m]	
									azimuth	range
ERS-1	ESA, Europe	1991–2000[a]	5.6	C	23	100	35	785	4.0	20.0
ERS-2	ESA, Europe	1995–2011[b]	5.6	C	23	100	35	785	4.0	20.0
Radarsat-1	CSA, Canada	1995-2013	5.6	C	20–49	100	24	792	5.1	21.1
Envisat	ESA, Europe	2002–2012[c]	5.6	C	23	105	35	785	4.0	20.1
ALOS-1	JAXA, Japan	2006–2011	23.6	L	8–60	40–70	46	691	3.1	7.5
TerraSAR-X[d]	DLR Germany	2007–today	3.1	X	20–45	30	11	514	1.9	2.1
Radarsat-2	CSA, Canada	2007–today	5.5	C	20–49	100	24	798	4.9	21.1
COSMO-Skymed	ASI, Italy	2007–today	3.1	X	20–60	40	4[e]	620	2.3	2.2
Kompsat-5	KARI, Korea	2013–today	3.2	X	20–45	30	28	550	< 3	< 3
Sentinel-1	ESA, Europe	2014–today	5.5	C	29–46	250	6[f]	693	17.4	3.7
ALOS-2	JAXA, Japan	2014–today	22.9	L	8–70	55–70	14	628	< 5.3[g]	< 9.1[g]

[a] Usable for interferometry in the periods 1993–1994 and 1995–2000.
[b] Limited usability for interferometry after gyroscope failure in February 2000.
[c] Extended mission between 2010–2012 using different swaths.
[d] In formation with a second satellite denoted as TanDEM-X.
[e] Revisit time of the constellation comprising four satellites.
[f] Revisit time of the constellation comprising two satellites.
[g] Different resolution modes available in Stripmap mode, highest resolution is 3 m.

3.3.2 Database

For the investigations on surface displacements in the URG area, archived SAR data of ESA's satellites ERS-1/2 and Envisat acquired between 1992–2000 and 2002–2010, respectively, are ordered and analysed. The SAR sensors of ERS-1 and ERS-2 are identical in construction. Therefore, the acquired SAR data of both satellites is usable within the same data stack. Both missions, ERS and Envisat, have similar properties w.r.t. wavelength, swath width, revisit time, altitude and resolution, see Tab. 3.2. They operated on an almost polar orbit at approximately 98.5° inclination. The common SAR satellites pass every region on Earth in two different image geometries, heading from south to north (ascending track) and on the other side of the Earth from north to south (descending track). Fig. 3.11 displays the regions on the ground covered by acquisitions of two ascending and one descending track in the URG area. The track numbers are identical for ERS and Envisat, even if the ground track does not exactly cover the same area. The number of corresponding ERS and Envisat acquisitions within each track is shown in Tab. 3.3.

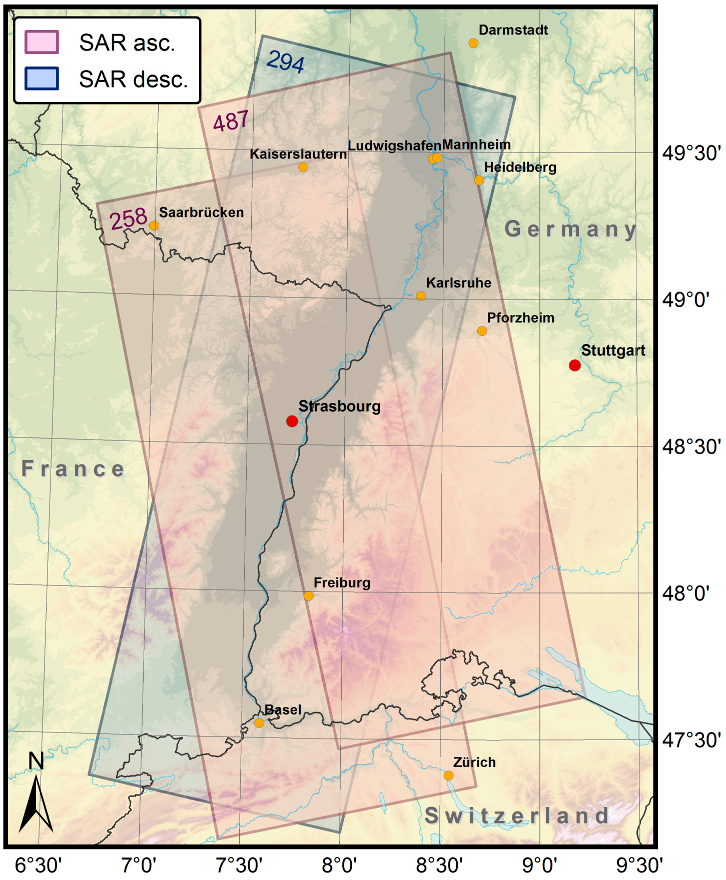

Figure 3.11: Ground tracks of SAR data acquired by ERS-1/2 and Envisat in the URG area. The region is covered by descending (desc.) track 294 and ascending (asc.) tracks 258 and 487.

ERS and Envisat data is available free of charge for scientific purposes. However, a project proposal has to be submitted including the intended objectives of the investigation and the number of SAR standard frames needed. The large amount of SAR data used within this study was kindly provided by ESA under the project ID 14193. Query, selection and ordering of the data is accomplished via ESA's Earth Observations Link client (EOLi, 2015). SAR data is generally available on two different processing levels: raw (unfocussed) data or single look complex (SLC) data. SLC data is only available for so-called standard frames covering an area of 100 km × 100 km. For the 300 km long stripes of data displayed in Fig. 3.11, raw data has to be ordered and focussed by oneself. The usage of ERS-2 data acquired after February 2000 is limited due to different yaw-steering modes, implemented because of gyroscope failure (Miranda et al., 2004). Fig. 3.12 shows the DC frequencies of an ERS-1/2 image stack at track 294 in Northern Germany from an InSAR analysis incorporating ERS-2 data after the gyroscope failure.

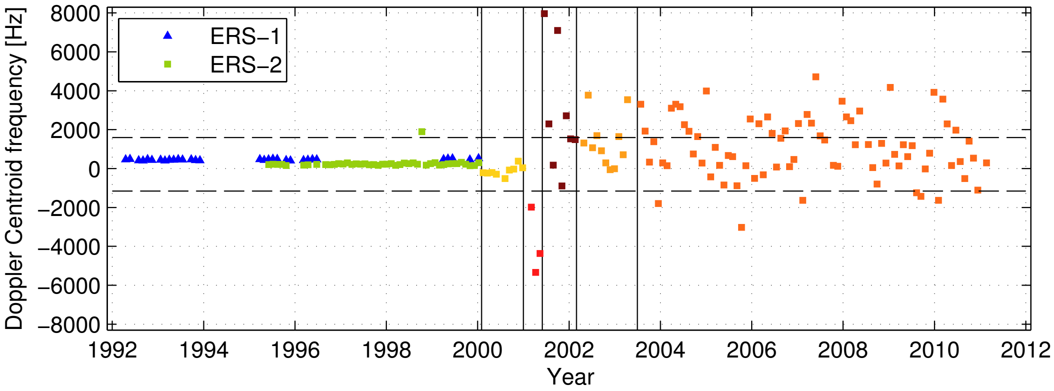

Figure 3.12: Doppler Centroid frequency F_{DC} of ERS-1 and ERS-2 data acquired between 1992 and 2011 in Northern Germany on descending track 294. Different colours for the ERS-2 data correspond to the piloting modes applied in order to account for gyroscope failures as presented by Miranda et al. (2004). The dashed lines mark critical F_{DC} values for the whole data stack if a ERS-2 scene acquired before 2000 is chosen as master scene.

As a difference in F_{DC} influences the coherence of an interferogram, see Eq. (3.28), only scenes within a given range of F_{DC} values can be considered within the analysis of a whole data stack. For an analysis of a whole image stack, a single master scene is chosen and interferograms of all other scenes (slaves) are calculated w.r.t. the master, see Sect. 6.1. Scenes with a larger F_{DC} difference have to be excluded from the image stack. Because of the large F_{DC} values of the year 2001 and later, ERS data is commonly used until the end of year 2000 only. However, within a project analysing ERS data in track 294 in Northern Germany, where no Envisat data is available, the author proved that ERS-2 data after 2001 is sensibly usable along with the reprocessed orbits provided by the Delft Institute of Earth Observation and Space Systems (DEOS, 2008). Note that only the scenes with an F_{DC} difference within the range of the critical F_{DC} values can be used, see dashed lines in Fig. 3.12.

For the analyses of SAR data in the URG area, a sufficient number of Envisat scenes is available in all three image stacks. Therefore, only ERS data acquired before 2001 was selected and ordered. Some of the ERS scenes selectable within EOLi could not be delivered by ESA because of bad data quality or missing azimuth lines in the raw SAR data. Other scenes had to be excluded from the stack analysis, because (i) no orbit data is available for a certain period, (ii) the scene does not cover the entire analysed area, (iii) decorrelation is high due to a large temporal baseline, perpendicular baseline or F_{DC} difference, (iv) coregistration failed for a specific master-slave combination or (v) strong weather conditions or snow coverage harm the separation of phase terms. The number of ordered, delivered and used scenes is given in Tab. 3.3 for each track and sensor. Particularly within the Envisat stacks, many scenes do not cover the entire tracks shown in Fig. 3.11. In order to provide the highest possible precision in the southern part of the URG area, where more Envisat scenes are available, the InSAR analyses in track 294 and track 487 are split into three, respectively two, overlapping subtracks. The remaining image stack in Envisat track 258 only covers the southern part of the track shown in Fig. 3.11, starting north of Freiburg. Because of the large amount of data available in ERS track 294, a selection of scenes with small perpendicular baselines and thus high coherence could be applied.

Table 3.3: Usable SAR acquisitions in the URG area in ascending tracks 258 and 487 and descending track 294. Significantly more Envisat scenes are available in the southern part of tracks 487 and 294.

Satellite	Track	Number of scenes			Period: date of		Date of the
		ordered	delivered	used	first scene	last scene	master image
ERS-1/2	258	34	31	24	1993-03-30	2000-05-26	1996-08-30
ERS-1/2	487	41	27	23	1993-04-15	2000-06-11	1997-06-22
ERS-1/2	294	83	79	51	1992-04-17	2000-02-14	1997-08-18
Envisat	258	27	27	19	2004-12-31	2008-08-22	2006-10-27
Envisat	487N[1]	40	40	19	2003-07-06	2010-08-08	2008-08-03
Envisat	487S[3]			37	2002-12-08	2010-08-08	2007-06-10
Envisat	294N[1]	46	46	18	2003-12-15	2008-12-08	2005-08-01
Envisat	294C[2]			33	2003-12-15	2008-12-08	2006-05-08
Envisat	294S[3]			43	2003-12-15	2010-10-04	2007-07-02

[1] Northern part of the URG
[2] Central part of the URG
[3] Southern part of the URG

In analogy to the GNSS analysis, additional data is needed for a proper analysis of SAR data. Precise orbits are necessary to calculate the perpendicular baselines $B_\perp$ and for the coarse coregistration, see Sect. 3.3.3. Orbit data for ERS and Envisat is provided by ESA. In addition, reprocessed orbits making use of the altimeter measurements of the ERS and Envisat missions are available at DEOS (Scharroo & Visser, 1998). In the case of Envisat, additional instrument files have to be used containing calibration parameters of the Envisat SAR sensor. Furthermore, an initial DEM is subtracted within the processing in order to reduce the major part of the topographic phase ϕ_{topo}. The freely available SRTM-3 data with a spatial resolution of three arcseconds, i. e. approximately 90 m, is used. Since the end of 2014, the U. S. Geological Survey (USGS, 2015) provides SRTM-1 data with one arcsecond resolution also for regions outside the USA. SRTM-1 data has already been successfully applied within the InSAR processing chain by the author. However, the differences in the resulting displacement estimates are negligible as a residual DEM error is estimated within the processing.

3.3.3 Analysis strategies

The processing of SAR data for displacement analyses is based on interferograms, which follow from Eq. (3.24). Having a whole stack of image data, the interferograms are calculated relative to one image, denoted as master. First of all, an appropriate master image has to be selected based on the expected decorrelation of all other images (slaves) resulting from Eq. (3.28). The selection of the master image and corresponding decorrelation models are discussed in detail in Sect. 6.1.1. As raw SAR data is used for the URG InSAR analysis, see Sect. 3.3.2, all images have to be focussed, first. Focussing describes the procedure necessary to convert a raw SAR image into an SLC image. The SLC results from a convolution of the raw data with a range reference function and a subsequent convolution with an azimuth reference function, see Moreira et al. (2013). The range reference function depends only on the transmitted chirp waveform, whereas the azimuth reference function is range-dependent. Fig. 3.13 presents the workflow for the computation of interferograms as it is performed by the Delft Object-oriented Radar Interferometric Software (DORIS, Kampes et al., 2003).

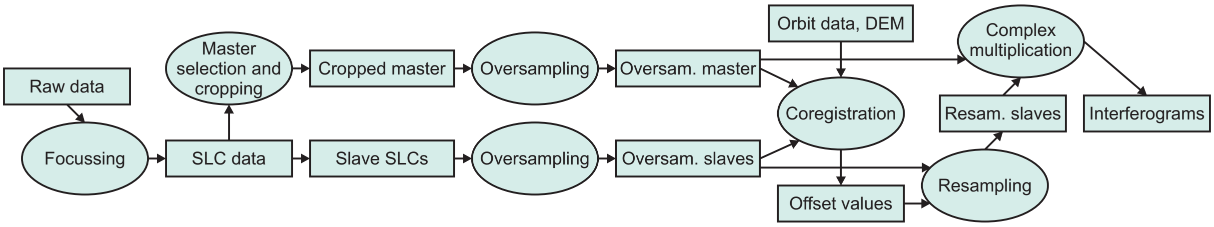

Figure 3.13: Workflow for the calculation of interferograms from a stack of raw SAR image data.

Before the interferograms are formed, the chosen master image has to be cropped to an area contained in all slave images. If only a subregion of the SAR images shall be processed, it is sensible w.r.t. runtime to crop all images at the very beginning of the processing. The complex multiplication of SAR signals acquired at different times corresponds to a convolution in the frequency domain resulting in spectral contributions above the Nyquist frequency (Hanssen, 2001, p. 52). To avoid aliasing effects the SLC data is oversampled in azimuth and range direction.

For the calculation of interferograms, the SAR images have to be aligned to a common grid. Coregistration enables the transformation of the observations of several images into a common spatial reference. Due to slightly different satellite positions and antenna orientations at different acquisition times, the original radar images are shifted, rotated, stretched and distorted w.r.t. each other (van Leijen, 2014, p. 36). Within the coregistration process, offset values are calculated for every pixel position in the target grid coordinate system defined by the master image. An external DEM is used as input in order to simulate an amplitude image and estimate the timing error of the master image (Eineder, 2003). Based on precise orbit data, the relative timing errors of each slave image w.r.t. the master are calculated and used as a rough estimate for the desired offsets (coarse coregistration). In a second step, the offsets between master and slave are estimated using a large number of matching windows and computing the correlation of the amplitude at the sub-pixel level (fine coregistration, DORIS, 2008, p. 44). Applying the estimated offsets to the slave pixels, all slave images are resampled to the geometry of the master image. In order to decrease the noise level of an interferogram, multilooking can be applied, which means that the complex data within a specified window is averaged (Goldstein et al., 1988). Multilooking applied with a certain range-azimuth ratio, e. g. 1:5, 2:10 or 4:20, is used to produce approximately square pixels for ERS and Envisat data, see Tab. 3.2, particularly for visualisation purposes.

The deformation signal present in the phase of an interferogram is generally superimposed by other phase terms due to atmospheric, orbital or topographic effects as shown in Eq. (3.26). Following Hanssen (2001, p. 52 f.), ϕ_{ref} is calculated and subtracted using the distances between the satellite orbit and the reference surface, e. g. WGS84 ellipsoid, for every resolution cell. The major part of ϕ_{topo} is subtracted by the introduction of a DEM. Furthermore, the orbital parameters and the DEM are used to transform the position of every pixel into a geocoded reference frame providing, e. g. geographic coordinates (geocoding). If ϕ_{defo} is clearly dominant in the remaining phase, orbital or atmospheric contributions may be neglected for the calculation of LOS displacements between two or more acquisitions. This assumption particularly holds for investigations on the deformation by large earthquakes (e. g. Massonnet et al., 1993; Fialko et al., 2005), or at volcanoes (e. g. Rosen et al., 1996; Amelung et al., 2000). Deformation models for seismic or volcanic activity have been largely enhanced within the last years using the information present in SAR interferograms, see also Jónsson (2002).

In the case of smaller deformation phenomena, ϕ_{defo} is often significantly superimposed by other phase terms. Particularly atmospheric effects related to temporal and spatial variations of the atmospheric delay of the signal may largely influence the phase of corresponding interferograms, see Sect. 6.3. The principal strategy to separate ϕ_{defo} from other phase terms is based on time series analysis considering correlation properties for individual phase terms. The remaining part $\phi_{topo,res}$ of ϕ_{topo} after subtraction of a radar-coded DEM is related to the residual height error δH and correlates with the perpendicular baseline $B_\perp$, see Hanssen (2001, p. 66):

$$\phi_{topo,res} = -\frac{4\pi}{\lambda}\frac{B_\perp}{R\sin\theta}\delta H \quad , \tag{3.29}$$

with slant range R and incidence angle θ at the analysed pixel position, see Fig. 3.10.

Orbital effects have been intensively studied by Bähr (2013). As they induce an almost linear error signal to the interferometric phase, a linear trend is estimated in every interferogram, commonly denoted as phase ramp, removing the major part of ϕ_{orbit}. Note that also large-scale deformation signals might be removed by subtraction of a phase ramp. Atmospheric effects and noise can be largely reduced if the stack of SAR data contains a large number of scenes, applying low- and high-pass filters in the spatial as well as in the temporal domain. Several approaches have been proposed within the last years to properly separate the phase terms either using a single master scene along with Persistent Scatterers (PS) or using a small baseline subset (SBAS) derived from different interferogram combinations along with Distributed Scatterers (DS). Both approaches are discussed in the following paragraphs. For the consistent processing of all available SAR data in the URG area, PS-InSAR is used. Sect. 6.4 presents results of an SBAS analysis applied to data of one image stack and discusses the advantages and disadvantages related to the conditions for InSAR in the URG area. Furthermore, attempts have been made to combine the partly complementary sets of PS and DS pixels[1] in order to extract a deformation signal at more points and with higher overall signal-to-noise ratio (Hooper, 2008). A new approach has recently been published by Ferretti et al. (2011), denoted as SqueeSAR, which jointly processes PS and DS based on statistical properties. This approach is not (yet) available to the research community, however, attempts are being made to include the stochastic modelling of SqueeSAR into other SAR processors (Even, 2015).

The concept of PS-InSAR was introduced by Ferretti et al. (2000, 2001), refined by Colesanti et al. (2003), as Permanent Scatterer Technique. The term *Permanent Scatterer* relates to the trademark of the original method protected by international patents. Several reimplementations have been developed in recent years falling back on the principal PS concept based on point scatterers with constant backscattering characteristics, but with different strategies for the selection of PS and for the separation of phase terms, see e. g. Hooper et al. (2004, 2007); Adam et al. (2003); Kampes (2005). The procedure of a PS analysis starting with a linearly independent set of interferometric combinations w.r.t. the same master scene, see Fig. 3.15(a), is discussed in the following related to the workflow within the Stanford Method for Persistent Scatterers (StaMPS, Hooper et al., 2007), see Fig. 3.14.

After the removal of ϕ_{ref} and the major part of ϕ_{topo} using the phase ϕ_{DEM} derived from a radar-coded DEM, the geocoded pixels are further investigated w.r.t. their phase stability. In order to reduce the amount of data, a threshold for the amplitude dispersion D_A is set, e. g. $D_A = 0.4$. Ferretti et al. (2001) show that D_A is a measure of phase stability, at least for pixels with a high signal-to-noise ratio. It follows from the mean value μ_A and standard deviation

---

[1] The terms PS pixel and DS pixel denote the pixels to which the signal of the corresponding persistent or distributed scatterers are attributed.

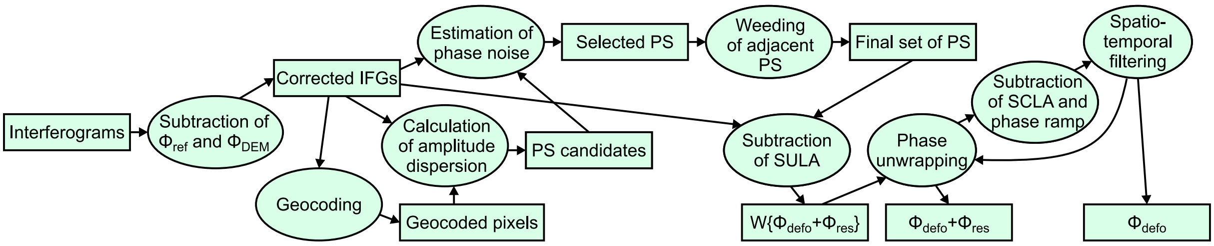

Figure 3.14: Workflow for the calculation of the LOS deformation phase ϕ_{defo} from interferograms within StaMPS. ϕ_{res} denotes residual phase terms and comprises particularly ϕ_{orbit}, ϕ_{atmo} and ϕ_{SCLA}. $W\{\cdot\}$ corresponds to the wrapping operator. SULA: spatially uncorrelated look angle error, SCLA: spatially correlated look angle error.

σ_A of amplitude values at a pixel in different interferograms:

$$D_A = \frac{\sigma_A}{\mu_A} \quad . \tag{3.30}$$

In a second step, the phase noise of each pixel is estimated by band-pass filtering of the wrapped phase in the frequency domain. Spatially correlated contributions present in the phase of the PS candidates are removed prior to the phase analysis. Hooper et al. (2007) define a measure of phase variation similar to coherence, see Eq. (3.27), but rather in time than in space domain and regardless of the amplitude of the pixel in different interferograms. A threshold for the phase stability is set based on statistics, and only the PS candidates with stable phases are kept (Selected PS). Furthermore, pixels are weeded w.r.t. their neighbourhood. Phase noise standard deviations of pixel pairs are calculated and noisy pixels are dropped resulting in the final set of PS. As the threshold standard deviation used within the weeding step is crucial for the further processing, this parameter is intensively tested within this work, see Sect. 6.2.2.

With the final set of PS, the separation of phase terms is initiated. The phase values are still wrapped in the interval $[-\pi \ldots \pi)$ at this stage of the processing. A difference between the real surface height measured with InSAR and the introduced DEM is related to the look angle θ, see Eq. 3.29, and denoted as look angle error. Although there is also a contribution from the phase centre sub-pixel position to the look angle error, it is commonly referred to as DEM error (Hooper et al., 2012). Following Hooper et al. (2007), the look angle error consists of a spatially uncorrelated part (SULA), which can be estimated from the wrapped phase, and a spatially correlated part (SCLA), which is separated and estimated after phase unwrapping. The wrapped phase values are unwrapped in order to provide a continuous phase signal for all PS pixels in the analysed image stack. Unwrapping is performed either spatially in two dimensions (Chen & Zebker, 2000) or using the additional dimension of time. Hooper et al. (2004) consider the 3D unwrapping as a series of 2D problems and use temporal phase differences at every PS (stepwise 3D unwrapping). Real 3D phase unwrapping algorithms have been proposed by Pepe & Lanari (2006); van Leijen et al. (2006); Hooper & Zebker (2007); Hooper (2010) and are available within StaMPS.

Finally, the remaining phase terms are separated by a sequence of different filters. First, the master contribution to atmosphere and orbit errors is separated by a low-pass filter in time. The remaining spatially correlated nuisance terms are supposed to be temporally uncorrelated and high-pass filtered in time followed by a spatial low-pass filter in order to exclude the signal of individual PS from the filtering (Hooper et al., 2007). The resulting phase should optimally exclusively contain the deformation signal. But however, residual orbital effects may still be present in the phase signal of several interferograms. Particularly large-scale effects are expected to remain in the resulting phase due to the high spatial wavelength of orbit errors, see Bähr (2013, p. 17). To account for residual orbit errors, phase ramps can be calculated and removed from the interferograms before the other spatially correlated terms are estimated. In addition, atmospheric effects mainly caused by variations of atmospheric water vapour are often visible in the remaining phase of the interferograms. Besides spatio-temporal filtering of the resulting time series for the separation of deformation and atmospheric signals, different methods for the calculation of the atmospheric phase screen (APS) are proposed by Hooper et al. (2012). Sect. 6.3 shows the results of different calculation methods of APS achieved with data available for the SAR scenes in the URG area.

PS approaches make use of the fact that the decorrelation phase is strongly reduced if one scatterer returns significantly more energy than other scatterers within a resolution cell. If a cell does not contain one dominant scatterer, the phase variation due to decorrelation is often large enough to obscure the signal. SBAS approaches only form interferograms between images with small temporal and perpendicular baselines in order to minimise decorrelation. Hence, the signal of cells with DS is still usable for interferometry. SBAS has been introduced by Berardino et al. (2002) and Schmidt & Bürgmann (2003) and has also been implemented within StaMPS in the meanwhile. In a first step, the interferogram combinations have to be selected based on a maximum permitted decorrelation and corresponding baseline lengths. Fig. 3.15 compares the baseline configuration of SBAS interferograms with single master interferograms of a PS analysis. Note that the baselines of the SBAS approach depend on various images, whereas the PS baselines are related to one single master image. After suitable small baseline interferograms are chosen and calculated from the complex SAR signals, a selection procedure of stable points similar to the PS selection is performed. In general, significantly more DS pixels are selected compared to PS, and w.r.t. runtime it may hence be reasonable to resample the set of selected DS to a coarser posting. Phase unwrapping and separation of phase terms can be handled in the same way as described for the PS processing. The results of an SBAS processing for one stack of SAR data in the URG area are presented in Sect. 6.4, focussing on the selection of small baseline interferograms and on differences compared to the results of a PS processing.

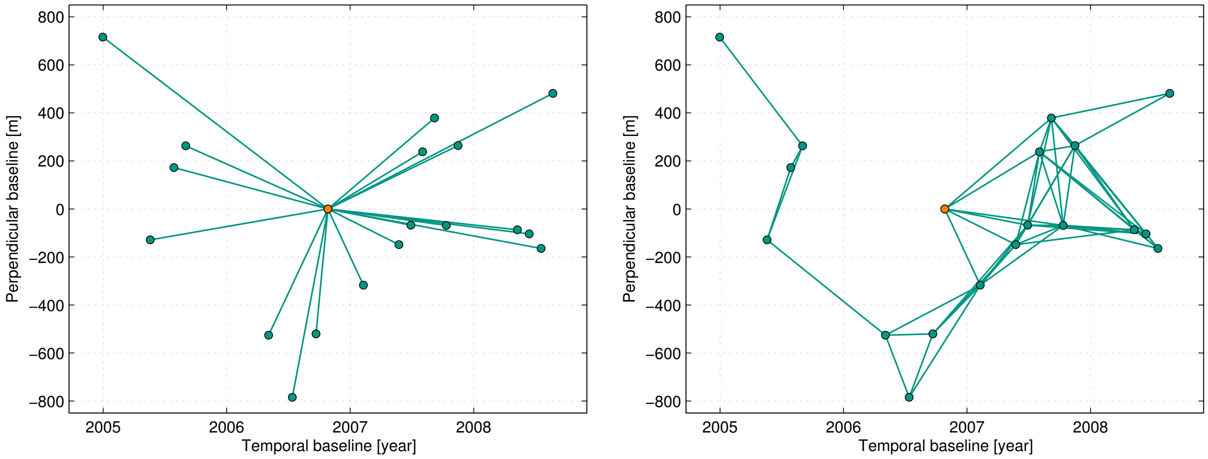

(a) Single master (PS approach) (b) Small baseline subset, $B_\perp < 500$ m, $T < 365$ days

Figure 3.15: Comparison of baseline configurations for a PS analysis using a single master scene and for an SBAS analysis using interferograms with small perpendicular baseline $B_\perp$ and temporal baseline T. SAR data acquired by Envisat on track 258 in the southern URG area.

3.4 Summary

- Three complementary geodetic techniques are used to estimate surface displacements in the whole URG area, i. e. levelling, GNSS and InSAR.

- Levelling data is available over a large time span and therefore enables an accurate estimation of vertical displacements.
- Measured height differences between levelling benchmarks in Germany, France and Switzerland have been collected and merged to a regional URG levelling network.
- A kinematic adjustment of the data directly yields vertical displacement rates at repeatedly measured benchmarks.
- A static analysis along selected levelling lines enables detailed investigations on the temporal behaviour of displacements, e. g. at faults.

- GNSS data at permanently operating sites are available in the URG area since 2002, earliest.
- Most of the sites are located on buildings. They differ in quality w.r.t. monumentation and environment (horizon-free, multipath effects).
- The GNSS observations are analysed either using differential processing strategies related to a network of baselines between the sites or using precise point positioning, where every site is analysed independently of the others.
- Displacements at GNSS sites are deduced in three dimensions from time series analysis of the GNSS coordinate estimates with the height component being worse than horizontal components.

- SAR data is acquired from active sensors mounted on a moving platform (satellite), transmitting and receiving radar pulses.
- The phase measurements of acquisitions of the same area at different times relate to a displacement along the line of sight towards a SAR satellite.
- The URG area is covered by SAR data of ESA's satellites ERS-1/2 and Envisat acquired on one descending and two ascending tracks between 1992 and 2010.
- Applying SAR interferometry at Persistent Scatterers (PS-InSAR) enables the separation of the deformation signal from other disturbing signal contributions, such as orbital and atmospheric effects.

Chapter 4

Levelling Analysis

This chapter presents the results of the levelling analyses performed in the URG area. First, the main conclusions of an assessment of the kinematic adjustment model using simulated measurements are presented (Sect. 4.1). Sect. 4.2 describes the necessary preparation steps applied to the levelling data, including a quality check based on loop misclosures as well as the clearing up of the database to repeatedly measured benchmarks. Possibilities for the detection and modelling of non-linear displacements are also discussed within this section. In addition, a case study at a levelling line with a strong systematic effect inherent in the height differences of the latest remeasurement in Germany is presented within this section. Gravity corrections for measured height differences and the influence of gravity on the kinematic adjustment are presented by means of a test loop in the southern BF (Sect. 4.3). Sect. 4.4 describes the stochastic model used within the adjustment process. The results of an iterative variance component estimation are presented within a subsection.

The analysis of the URG levelling network presented in Sect. 3.1.2 is performed using the software package KaGeMoV (Karlsruher Geschwindigkeitsmodelle zur Berechnung von Vertikalbewegungen) described in detail by Zippelt (1988). Further developments have been added to the software documented by Zippelt & Dierks (2007); Fuhrmann & Zippelt (2013); Fuhrmann et al. (2014a), particularly the integration of a database management system. KaGeMoV enables the application of a kinematic adjustment model to repeatedly measured height differences of large levelling networks. A former version of KaGeMoV has also been used for displacement estimation in the Netherlands (Lorenz et al., 1991); the results of this analysis including a geological interpretation were published by Kooi et al. (1998). Key parameters used within the adjustment of the URG levelling network and the final results for vertical displacement rates are shown in Sect. 4.5.

Besides the kinematic adjustment, static comparisons of height calculations along levelling lines measured in different epochs may also provide useful information on tectonic or anthropogenic deformation phenomena. The basic principle of the static approach was already discussed in Sect. 3.1.3. The results and main conclusions of two case studies are presented in Sect. 4.6.

Parts of this chapter have already been published by the author in the following papers: Fuhrmann et al. (2013a), Fuhrmann et al. (2013b), Fuhrmann et al. (2014a), Fuhrmann et al. (2014b). These publications are not explicitly cited within the text.

4.1 Kinematic adjustment of simulated data

In order to investigate the impact of several influence factors on the kinematic adjustment of levelling data, particularly on the precision of the estimated parameters (height and vertical displacement rate), simple model calculations are performed and applied on different network configurations shown in Fig. 4.1. The influence factors to be investigated are:

- network configuration and reference point selection,
- precision of observations, i. e. height differences,
- number and temporal distance of measurement epochs,
- number of observations at the points,
- deviation of the point movement from linearity,
- erroneous or inaccurate measurement date of the observations.

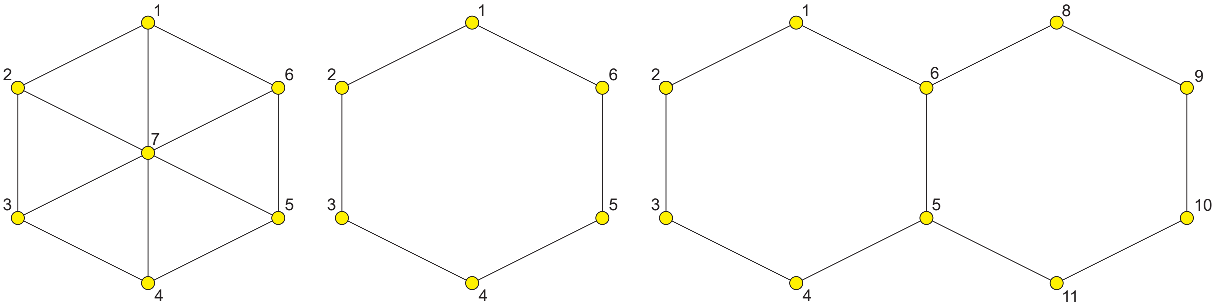

(a) Network 1 (b) Network 2 (c) Network 3

Figure 4.1: Network configurations used for the testing of different influence factors on a kinematic adjustment of levelling data. Network 1 is a rather optimal network, whereas networks 2 and 3 represent the situation of single and connected levelling loops, respectively.

For a thorough evaluation of the aforementioned influence factors, random observations according to a normal distribution $\mathcal{N}(\mu, \sigma)$ are created, whereas μ exactly fulfils a given motion behaviour. From 10,000 automated runs of the kinematic adjustment using random observations with a given precision σ, the mean value and dispersion of the standard deviations of the adjusted parameters (height and linear rate) are derived for each test. Fig. 4.2 shows by way of example the resulting standard deviations for the different network configurations introduced in Fig 4.1.

The influence factor *network configuration and reference point selection* has similar effects on both estimated heights and velocities. As one would intuitively expect, network 1 provides the best precision. Within this network, all points are connected by at least three observations to other benchmarks. With a reference point in the centre of the network (point 7), the precision of all the other benchmarks is equal. For network 2 and network 3, the standard deviations are higher and depend on the distance to the reference point. The results of network 3 nicely show that the standard deviation is lower for the loop, in which the reference point is located. Similar investigations have been performed for the other influence factors. The resulting effects on height and velocity estimation using reasonable numbers and scenarios for the influence factors are classified in Tab. 4.1.

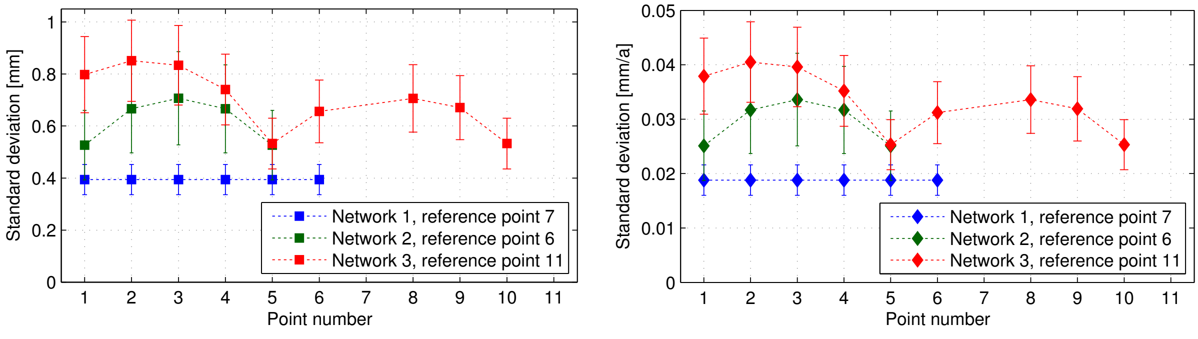

(a) Standard deviation of heights (b) Standard deviation of velocities

Figure 4.2: Mean value and dispersion of standard deviations of estimated parameters from 10,000 runs with normally distributed random observations with $\sigma = 1$ mm.

Table 4.1: Effect of different influence factors on the resulting parameters of a kinematic adjustment of simulated data.

Influence factor	Effect on the precision of height estimates	 velocity estimates
Network configuration	strong	strong
Reference point selection	strong	strong
Accuracy of observations	moderate	moderate
Number of measurement epochs	strong	moderate
Total time span covered	moderate	strong
Number of observations at the points	moderate	moderate
Unmodelled non-linear motions	strong	strong
Inaccurate measurement date	weak	weak

Also the influence of the selected reference epoch t_0, see Eq. (3.7)–(3.9), is investigated. Fig. 4.3 shows the standard deviations of heights and velocities as well as the condition number of the normal equation matrix $N = (A^\top PA)^{-1}$ for different reference epochs t_0. The simulated observations comprise three measurement epochs in the years 1950, 1975 and 2000 at network 1. Normally distributed observations are simulated using a standard deviation of 1 mm.

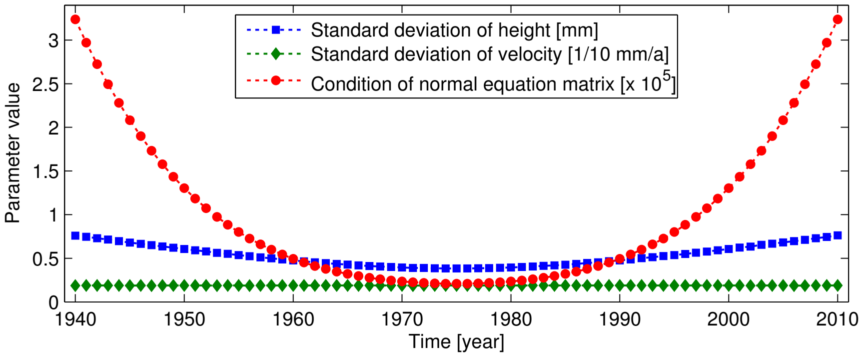

Figure 4.3: Effect of the assigned date of the reference epoch t_0 on the estimated height and velocity precision as well as on the condition of the normal equation matrix.

For the estimation of vertical rates, the assigned date of the reference epoch does not significantly change the precision of the estimates, even if t_0 is beyond the total covered measurement period between 1950 and 2000. A slight increase is observed for the height estimates and a strong increase for the condition of the normal equation matrix. Therefore, a central location within the analysed observation period is preferable for t_0, which does not coincide with an observation date ($\Delta t \neq 0$). For the analysis of levelling data in the URG area, the reference epoch is set to $t_0 = 1945.0$ (1945-01-01), which is more or less the middle of the total observation period and without measurements close to that date.

4.2 Data preparation

In a first step, the levelling data is homogenised and merged into a common database management system containing two major tables. One table lists the levelling benchmarks and contains the following information: benchmark number, position coordinates, height value, survey marker type, brief description of the support of the benchmark, order of the corresponding levelling line and gravity value, see Sect. 4.3. The second table lists the measurements and contains information on the following items: start point and end point of the measurement, date, path length, measured height difference, difference between forward and backward run, order of the corresponding line, line number, loop number and gravity correction value, see Sect. 4.3. More information on the structure of the database and the interaction with KaGeMoV and visualisation tools like ArcGIS are given by Zippelt & Dierks (2007, p. 8 ff.).

The database management system is used for the import of the data, for line- and point-related data queries, for editing line and point information, for clearing up of the database on repeatedly measured benchmarks, described in Sect. 4.2.3, and for the export to KaGeMoV or to ArcGIS. All position coordinates of the German, French and Swiss levelling benchmarks are transformed to a common UTM[1] zone, which is also used for the combination with GNSS and InSAR data. In a first step, the data is line-wise exported for different user-defined measurement epochs in order to calculate loop misclosures and check the quality of the measurements (Sect. 4.2.1). One line of the latest remeasurement of the DHHN (2006–2012) featured a large systematic behaviour discovered within the quality check. A comparison with former measurement epochs and with a remeasurement of the line as well as possible explanations for the systematic effect are discussed in Sect. 4.2.2. After the database is cleared up to repeatedly measured benchmarks, see Sect. 4.2.3, the kinematic network adjustment is applied, firstly assuming a linear displacement model at all benchmarks. For several reasons, some benchmarks do not behave linearly in time and therefore have to be treated in a special way, see Sect. 4.2.4. The modelling of point displacements is iteratively improved within subsequent adjustments and therefore considered as a preparation step to the final adjustment result.

4.2.1 Quality check

An assessment of the quality of the levelling measurements is crucial for the usage of the data within displacement analyses. Therefore, loop misclosures are calculated by summation of all height differences along lines, starting and ending at the same benchmark. The summation theoretically should yield zero at the start/end point neglecting measurement inaccuracies and the influence of gravity. For the German and Swiss measurements, the height differences are corrected for the influence of gravity using a normal correction, see Sect. 4.3. In the French height network, gravity measurements are only available along the large first-order loops. For the other French loops consisting of second-order lines, the influence of gravity still remains in the loop misclosures.

If a time difference exists between the measurements at a displacing benchmark, a kinematic loop misclosure is added to the sum of height differences along the loop, discussed by Schlatter (2007, p. 168 f.). As there are sometimes several years between the measurements at a tie point of adjacent levelling lines, a displacement of the tie point may result in a significant kinematic loop misclosure. This is observable at French levelling lines crossing a mining area shown in Fig 4.4. The loop misclosures in the adjacent loops are much larger than in other

---

[1] Universal Transverse Mercator

areas and depend on the chosen tie point. As the loop misclosures result, by convention, from a clockwise summation of all height differences along the levelling lines, they have an opposite sign for the northern and the southern loop in Fig. 4.4, but with similar magnitude. The height differences along the loop have been measured in 1964 (first-order lines) and 1973 (second-order lines). Benchmark *A* is located further inside the mining area, and therefore is more exposed to subsidence compared to benchmark *B* located at the edge of the mining area. The usage of benchmark *B* as junction point between the first- and second-order lines reduces the loop misclosure by 189 mm.

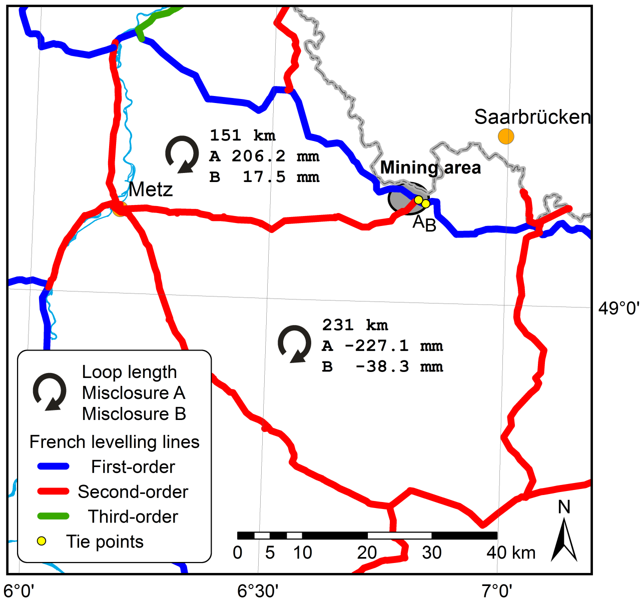

Figure 4.4: Example for a kinematic loop misclosure caused by a strong displacement at the tie point, i. e. subsidence in a French mining area.

Loop misclosures for every measurement epoch have been calculated within this work and are listed in several tables in Appendix A. Tab. A.2, A.3 and A.4 contain the loop misclosures of the German and Swiss first-order levelling lines used within the URG analysis. In Saarland also second-order levelling lines are used for the formation of loops and the calculation of misclosures. In Switzerland one second-order line is used for the formation of loops, i. e. the connection between Delémont and Sonceboz. The large, about 800 km long French first-order levelling loop shown in the western part of Fig. 3.3 has a gravity-corrected loop misclosure of +86.7 mm calculated from the measurements of 1964, see also Duquenne et al. (2007), which was the latest complete remeasurement of the whole loop. Before 1964, this loop has not been measured within a short time period, either because the eastern part of the loop was part of the German Empire or because the measurements had to be interrupted because of World War II. A loop misclosure mainly calculated from data of the measurement epoch between 1878 and 1895 therefore also contains data from 1922 until 1938 and sums up to −126.6 mm. The second measurement epoch between 1920 and 1957 was interrupted by World War II and needs to be connected at one 8 km long section with data measured in 1964. The corresponding loop misclosure sums up to −196.9 mm. For a further quality check of the French part of the network, the interior part of the large first-order loop is split into 10 loops comprising first- and second-order lines. These loops are of a similar size and path length to the German and Swiss first-order loops. The corresponding loop misclosures, see Tab. A.5, are hence better comparable. In addition, transnational loops are built from the connection measurements between the countries. The corresponding loop misclosures shown in Tab. A.6 have the same order of magnitude compared to the national loops.

Mean loop misclosures for levelling loops in the URG area are listed in Tab. 4.2 for different countries and measurement epochs. For the loops comprising data of a long time span, the kinematic loop misclosures are minimised by properly selecting the tie points if several connections are possible. Particularly in the German part of the network, an improvement of the data quality with time is visible. With a mean loop misclosure of less than 1 $\mathrm{mm}/\sqrt{\mathrm{km}}$, all measurements since 1922 are of high quality. In comparison to the other parts of the network, the measurements in the French part are of poorer quality, which is partly due to the lack of gravity corrections. For the calculation of transnational loops, measurements related to varying dates have to be used, see remarks [3, 4, 5] of Tab. 4.2. The mean loop misclosures of these loops comprising measurements from different countries indicate a good fit of the transnational connection measurements.

Table 4.2: Mean loop misclosures (absolute values) for German, French and Swiss levelling loops at different epochs.

Region	Measurement epoch (years)	Loop misclosure ($\mathrm{mm}/\sqrt{\mathrm{km}}$)	Number of loops
Germany[1]	1876–1882	1.57	5
	1922–1939	0.65	10
	1950–1970	0.58	19
	1981–1987[2]	0.55	16
	2003–2012	0.49	15
France	1878–1896	1.96	5
	1920–1957	1.46	8
	1964–1973	1.40	10
Switzerland	1906–1928	1.69	2
	1949–1997	0.08	2
	1978–2008	0.78	2
Transnational	1867-1922[3]	1.37	8
	1954-1973[4]	0.91	9
	1964-2012[5]	0.63	8

[1] Only first order measurements were used, except for the lines in Saarland.

[2] Including two loops from Saarland with measurements from 1978 to 1998.

[3] All measurements before 1900 except some Swiss lines.

[4] Using two observations from 1881 for a connection between France and Switzerland.

[5] 1964 (first-order lines) and 1973 (second-order lines) measurements from France combined with later measurements from Germany and Switzerland.

4.2.2 Systematic effects at line 638

Within the quality check of the levelling data, relatively large loop misclosures were detected in two adjacent levelling loops in the BF. As the clockwise calculated loop misclosures of these two loops carry reverse signs, it is reasonable to assume that the error is related to the levelling line shared by both loops. Fig. 4.5 shows the location and height profile of line 638, which is part of loops 611 and 612.

Line 638 was measured in 2007. The gravity-corrected loop misclosures are $+24$ mm and -25.9 mm, respectively for loop 611 and loop 612, or 1.4 $\mathrm{mm}/\sqrt{\mathrm{km}}$ (both loops), which is much higher compared to other loop misclosures in Germany calculated from the levelling data of the latest measurement epoch, see Tab. 4.2 and A.2. In order to detect possible measurement errors responsible for the large loop misclosures, a static comparison of the heights

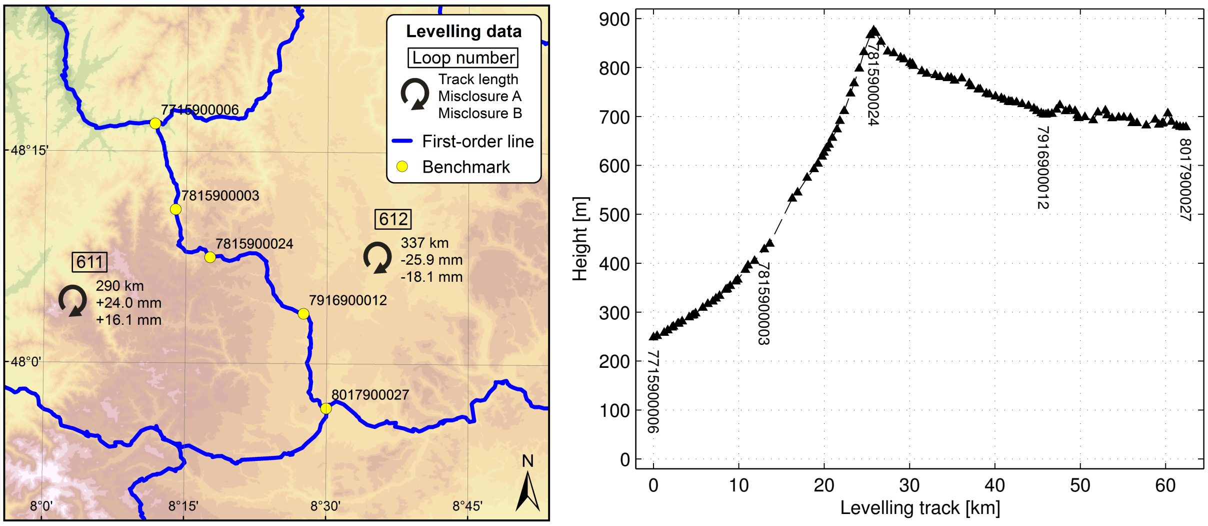

(a) Course of line 638 and loop misclosures using the measurements of 2007 (A) and 2012 (B).

(b) Height profile of the benchmarks along line 638.

Figure 4.5: Overview of levelling line 638 in the BF, passing from Hausach (benchmark 7715900006) to Donaueschingen (benchmark 8017900027).

along line 638 in different epochs is performed using height differences measured since the 1920s. Analogous to the calculation of loop misclosures, a normal correction is applied to the measured height differences to account for the influence of gravity. As explained in Sect. 3.1.3, the height of one benchmark has to be fixed within a static comparison of different measurement epochs. Afterwards, the heights of all other benchmarks are calculated by simply adding the measured height differences for each epoch. Fig. 4.6 shows the height changes starting at benchmark 7715900006 at Hausach. The height changes of the measurement epochs 1959, 1984 and 2007 are plotted relatively to the first measurement epoch (1927). Only small height changes are observed until benchmark 7815900024 (located between Triberg and St. Georgen, BF), which is the highest point along the line, see Fig. 4.5(b). In the further course, the height changes of the latest epoch systematically drift away from the height changes in proceeding epochs ending up at a difference of more than 2 cm.

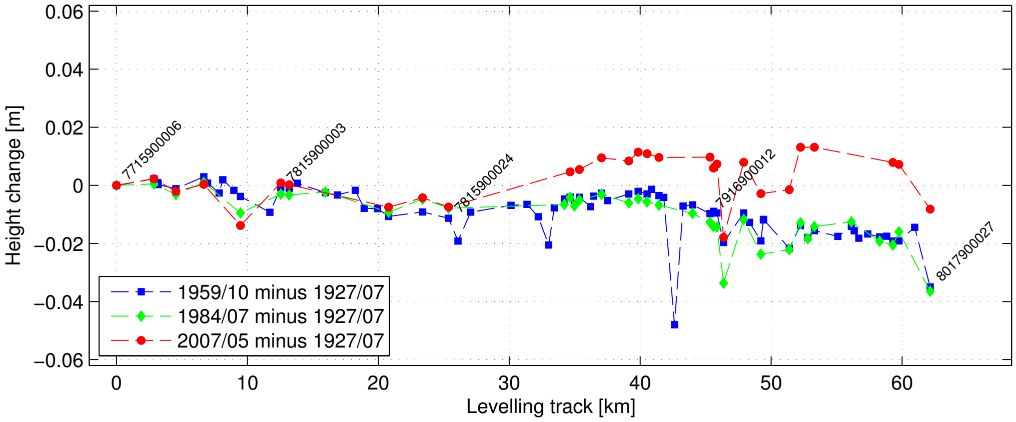

Figure 4.6: Height changes between the first and later measurement epochs along levelling line 638. Benchmark 7715900006 is kept fixed. Dates correspond to the average of observation times.

Based on this result, the southern part of line 638 has been remeasured in 2012. Incorporating the new measurements to the calculation of loop misclosures, reduces the misclosures of loop 611 and 612 by approximately 8 mm, see Fig. 4.5(a). A static comparison of heights calculated from the measurements of 2007 and 2012 to the measurement of 1984 is shown in Fig. 4.7. The remeasurement started approximately 6 km north of benchmark 7815900024. It reduces the total discrepancy, but still a systematic effect relative to the measurements of the 1980s is visible.

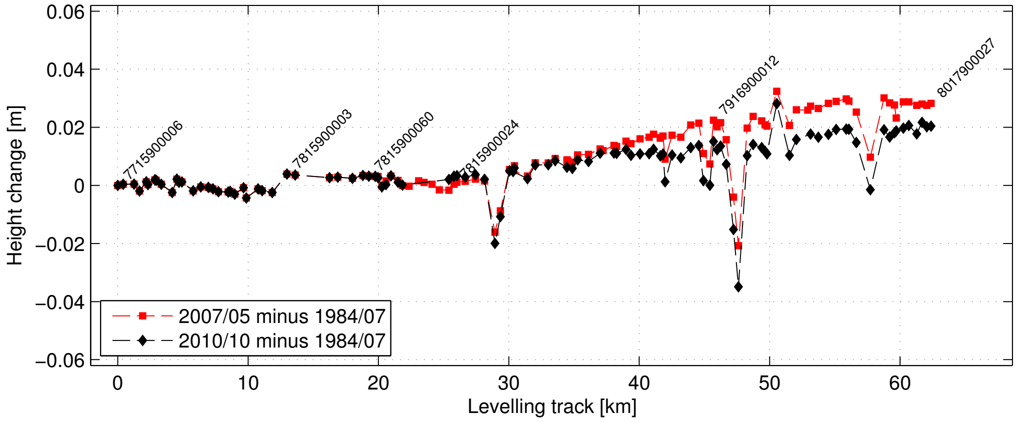

Figure 4.7: Height changes between the last two measurement epochs along levelling line 638. Benchmark 7715900006 is kept fixed. Dates correspond to the average of observation times. The black markers denote the remeasurement of the southern part of the line starting at benchmark 7815900060.

Possible sources of the systematic effect detected in the 2007 and 2012 measurements of line 638 are discussed in the following. From the raw data of line 638 provided by LGL, several analyses are performed to assess and pinpoint the error. One can state that (i) both forward and backward run are affected by erroneous measurements, (ii) the systematic effect was not observed in former epochs, at least not as strong, and (iii) the measurements from 2007 and 2012 are affected in a similar way, albeit the effect is smaller in the 2012 measurements. The following error sources are possible candidates for a systematic error occurring in both backward and forward run measurements:

(i) temperature differences and unilateral exposure to sunlight, see Pelzer (1983, p. 15 f.); Zippelt (1983, p. 165 ff.),

(ii) refraction, see Heer (1983, p. 251 ff.); Mozzhukhin (2010, p. 110 ff),

(iii) inclination of the touchdown surfaces of the rods and longitudinal and transverse inclination of the rods, see Deumlich & Staiger (2002, p. 273 f.),

(iv) erroneous scaling of the rod, see Deumlich & Staiger (2002, p. 273 and p. 291 f.),

(v) periodic graduation errors at the rod, see Pelzer (1983, p. 12 ff.); Woschitz (2005, p. 242 f.).

The measurements have been carried out between 2007-04-16 and 2007-06-28 and between 2012-03-26 and 2012-05-09. Temperature has been recorded at every set-up and largely varies between +4 and +34 °C for the 2007 measurements, but no significant differences are seen between the southern, erroneous part of the line and the northern part. In addition, a temperature correction is applied to the raw measurements. Also unilateral exposures to sunlight may be excluded as an error source as the measurements have been carried out at various times with varying positions of the sun. Item (ii) is difficult to handle but largely reduced by omitting readings at the bottom end of the rod. However, it is unlikely that refraction causes a systematic effect on the measurements of both forward and backward runs of the 2007 and 2012 measurements. Inclination (iii) and scaling (iv) errors of the rod are again unlikely as the same pair of rods has been used for the survey of the whole line, but the systematic effect starts not until benchmark 7815900024. At this benchmark the highest point of the profile is reached, after which the height of the benchmarks decreases with more or less constant slope, see Fig. 4.5(b). Periodic errors of the graduation of one or both rods are a candidate for the systematic effect as they may sum up to large numbers if the readings are performed at locations with opposite amplitude of the graduation error. In Fig. 4.8 the general measurement configuration at a levelling line with constant slope is visualised.

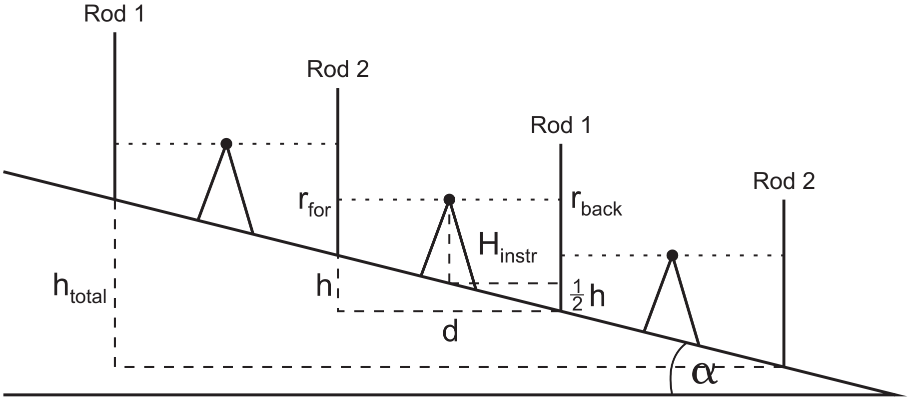

Figure 4.8: Measuring height differences along a line with constant slope.

The relation between slope angle α, height difference h between two rod set-ups and rod distance d, i. e. the double target distance for equal target distances, follows from Fig. 4.8:

$$\tan\alpha = \frac{h}{d} = \frac{\frac{1}{2}h}{\frac{1}{2}d} \quad . \tag{4.1}$$

With a constant slope of $\alpha = 0.45°$ and a target distance $d/2 = 25$ m, height differences of 0.4 m result from Eq. (4.1). Assuming a constant instrumental height H_{instr} of 1.6 m, the backsight readings r_{back} are always performed at $H_{instr} + \frac{1}{2}h = 1.8$ m and the forsight readings r_{for} at $H_{instr} - \frac{1}{2}h = 1.4$ m. A relative height error in the system of digital level and coded rod of only 40 μm between the reading sections 1.4 and 1.8 m at both rods would result in a systematic error of 0.12 mm for 1.2 m total height difference. In the example given in Fig. 4.8, the backward reading would be at 1.39998 m and the forward reading at 1.80002 m. With three instrumental set-ups, the true height differences would be at $3 \cdot 0.4$ m $= 1.2$ m, but the measured height differences yield $3 \cdot 0.40004$ m $= 1.20012$ m. An error of 0.1 mm per m height difference corresponds to the order of magnitude of the systematic error observed at line 638.

The levelling rods are calibrated every year according to DIN[1] 18717 (DIN, 1996). The mean scaling error is estimated using different positions on the rod, which also allows for detecting graduation inaccuracies (AdV, 2009, p. 42 ff.). The coded rods are calibrated without the digital levelling instrument. However, periodic graduation errors have been found to be related to the system comprising the digital level and the coded rods (Heister et al., 2005; Gassner & Ruland, 2006). The periodic error can thus only be detected by system calibration (Woschitz &

---

[1] DIN: Deutsches Institut für Normung e.V. (German Institute for Standardisation)

Brunner, 2003). Typical values of the maximum amplitude of graduation inaccuracies are between 50 and 200 μm as published for different level-rod combinations by Takalo et al. (2001); Takalo & Rouhiainen (2004).

For the Leica digital level DNA03, which was used for the survey of line 638, large periodic graduation errors occur at two, so-called, critical distances, related to the relative size of the rod's code elements and the pixels on the CCD array. The critical distances of the DNA03 at 13.25–13.50 m and 26.65–26.90 m are documented in Leica (2006, p. 16) and further investigated by Gassner et al. (2004); Gassner & Ruland (2006). Several measurements of the survey of line 638 have been performed within the critical sections, most of them in the erroneous, southern part of the line.

In the framework of a collaboration of LGL and Graz University of Technology (TU Graz), the digital level and the pair of rods used for the measurements were brought to the calibration facility at TU Graz (Woschitz & Brunner, 2003) which, in contrast to other facilities, allows for a vertical system calibration (Schauerte & Heister, 2005). The system calibration performed by H. Woschitz and his team revealed systematic effects of up to 200 μm at rod positions between 1.8 and 2.0 m, which might sum up to large numbers particularly at a levelling line with constant slope and increased number of readings in this section. Also the effects at critical distances are larger for the used digital level compared to other DNA03 systems.

For the kinematic adjustment of levelling data presented in Sect. 4.5, the measurements carried out in 2012 have been used for the southern part of the line. The remaining systematic effect will affect the results. But as there are at least three other epochs available, the influence is reduced for the vertical displacement rates which represent the mean movement of a benchmark throughout the whole period of measurements. As systematic effects over large distances may also be present in other levelling lines, it is thus worth mentioning that height changes between only two measurement epochs of country-wide levelling networks should not be used as an indicator for tectonic deformation.

4.2.3 Clearing up on repeatedly measured benchmarks

Only benchmarks which have been measured in at least two epochs are relevant for displacement analyses. Therefore, the height differences have to be cleared up to a set of repeatedly measured benchmarks before the adjustment is performed. A benchmark might not have been remeasured in the subsequent epoch, since the track of the line was changed or the benchmark got lost, e. g. because the support of the benchmark (building, bridge, ...) was demolished. According to Jahn et al. (2011), the continuous destruction rate of levelling benchmarks in the German height network is 3 to 5 % per year. If a benchmark along a line gets lost, it is usually replaced by a new one, since the major objective of national levelling networks is to provide heights for surveying tasks. For the analysis of displacements, benchmarks which have only been measured once have to be bridged by simply summing up the height differences of the adjacent measurements. However, more complex cases of benchmarks measured in only one epoch exist as shown in Fig. 4.9 and 4.10.

A connection to a polar point was measured in all three epochs displayed in Fig. 4.9. Benchmark A got lost between 1978 and 2003 and was renewed by benchmark B, resulting in the situation shown in Fig. 4.9(a), denoted as case I. In the first step of the clearing, benchmark B and the adjacent measurements remain in the data set. A displacement cannot be estimated at the benchmark, since it was only measured in one epoch and the polynomial degree of the displacement model is zero, see Eq. (3.9). As the date of the adjacent measurements might

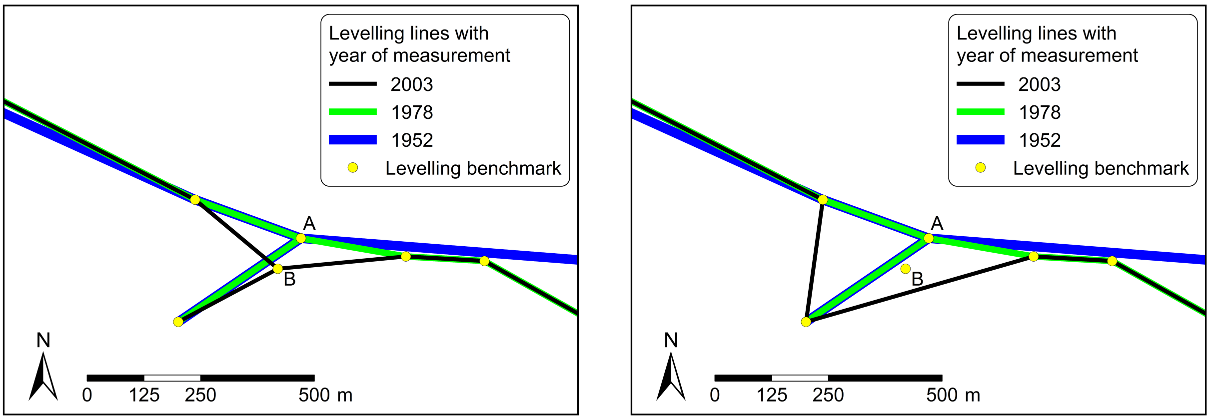

(a) Situation before automatic clearing of benchmarks with polynomial degree zero.

(b) Situation after automatic clearing of benchmarks with polynomial degree zero.

Figure 4.9: Representative example of a benchmark with polynomial degree zero, i. e. a benchmark observed in one epoch only, and automatic clearing of the situation (case I).

not be equal, a possible movement of benchmark *B* could affect the measured height differences. In this case, a point with polynomial degree zero has the same effect on the network adjustment as an additional reference point. Fuhrmann & Zippelt (2013, p. 23 ff.) studied the influence of benchmarks with polynomial degree zero in a network comprising levelling data in Southwest Germany and Switzerland. The differences of the resulting vertical rates between an adjustment with and without points with polynomial degree zero are small (98 % within ±0.1 mm/a). However, the linear rates are pushed towards zero as points with polynomial degree zero and a time difference at the adjacent measurements introduce additional constraints into the normal equation system. Fig. A.1 in Appendix A shows a comparison of the effect of points with polynomial degree zero present in the URG network on the resulting vertical rates when different maximum time differences of the adjacent measurements are tolerated. One can observe that the whole adjustment is heavily pushed towards zero if a maximum time difference of five years is tolerated, see Fig. A.1(a). For a maximum time difference of one year (Fig. A.1(b)), the solution is still slightly pushed towards zero. Applying a maximum time difference of nine months the effect on the vertical rates becomes negligible, see Fig. A.1(c). It is therefore advisable to either (i) exclude all benchmarks with polynomial degree zero and a time difference of more than nine months at the adjacent measurements from the database or (ii) set the polynomial degree manually to one and estimate a linear rate at these points.

The situation in Fig. 4.9(a) can be solved by temporarily duplicating the measurement to the polar point and bridging benchmark *B*, see Fig. 4.9(b). The dates of the original measurements, which are within nine months, are averaged. This procedure has been automated within a function of the database management system. Fig. 4.10 shows a more complex case, denoted as case II, where a new connection point (benchmark *C*) was introduced at the junction of three levelling lines. Again benchmark *C* is characterised by a polynomial degree of zero. In this case, the situation cannot be easily solved by duplicating one measurement. If no time difference exists between the adjacent measurements, the point with polynomial degree zero is kept in the database and only a height is estimated at the point as it does not negatively influence the normal equation system. If a time difference exists, the polynomial degree is set to one and a vertical rate is estimated at the benchmark.

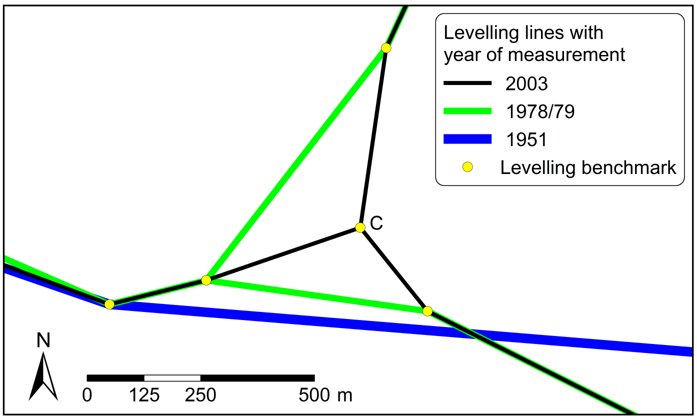

Figure 4.10: Representative example of a benchmark with polynomial degree zero (case II). A new connection benchmark *C* was introduced at the junction of three levelling lines.

The clearing of the database to repeatedly measured benchmarks, i. e. a polynomial model of degree one or more is applicable, reduces the database from 55,494 observations at 30,204 benchmarks to 40,049 observations at 15,816 benchmarks. From the remaining 15,816 benchmarks, 286 (1.8 %) have a polynomial degree of zero. At 63 of them the maximum tolerated time difference of nine months is exceeded and the polynomial degree is set to one.

4.2.4 Modelling of non-linear displacements

The functional model of the kinematic adjustment assumes a linear displacement in a first step, see Sect. 3.1.3. A variance ratio test, see Eq. (3.16), is used to check whether the model introduced at a certain benchmark fits to the observations. As most of the outliers detected in the testing of observations are due to an insufficient modelling of benchmark displacements, it is important to analyse model-related errors in detail. A misfit to the firstly assumed linear motion can originate from various deformation behaviours. Different displacement types and corresponding linear and accelerated displacement models are shown in Fig. 4.11.

All types of displacements simulated in Fig. 4.11 correspond to real movements present in the analysed data set. Most of the tectonic and natural movements measurable in the URG area within the last century behave linear in time. Accelerated displacements may occur in areas where groundwater is used, particularly when the amount of extracted water changes with time. Construction and drilling works carried out between two measurement epochs would cause an abrupt movement between the epochs. Some benchmarks are directly driven into the ground (driven piles). They tend to firstly subside relative to the ground before they move with the ground, resulting in a motion behaviour similar to the red dots in Fig. 4.11. In order to model non-linear displacements within a kinematic adjustment of the measured height differences, the following three options are applied at the corresponding benchmarks:

(i) bridge the point by a tie of adjacent observations in one or several epochs,

(ii) split the displacement into two partial displacements, e. g. if there is an abrupt movement between two measurement epochs,

(iii) increase the polynomial degree.

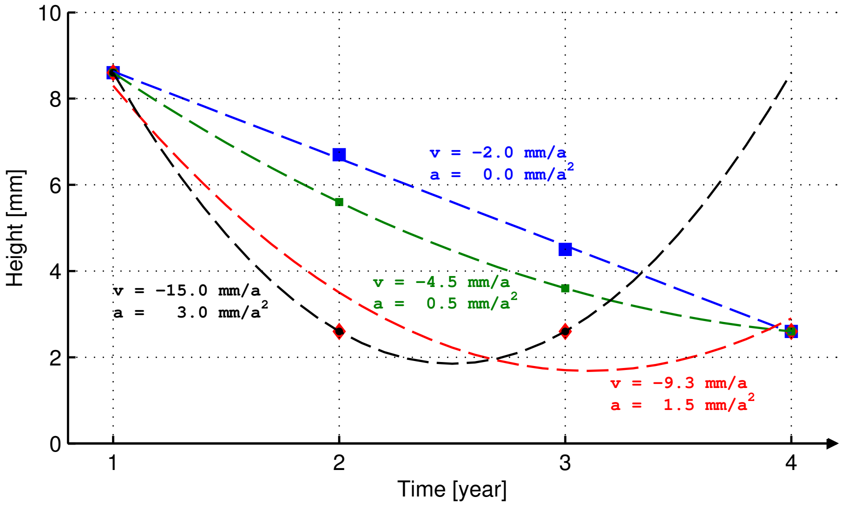

Figure 4.11: Modelling of displacement types in the kinematic adjustment of levelling data with polynomial functions of degree 2, blue: nearly perfect linear displacement (subsidence), green: accelerated displacement (decaying subsidence), black: abrupt displacement between first and second measurement, no displacement between second and third measurement, red: abrupt displacement between first and second measurement, no displacement between second, third and fourth measurement.

The decision which modelling option describes the displacement of a specific benchmark best strongly depends on the number and temporal distribution of the measurements. All three possibilities are applied to several benchmarks of the levelling database. The kinematic adjustment of the data is optimised step by step utilising the presented statistical tests. In every iteration, the observations related to the largest test statistics and the corresponding benchmark movements are investigated in detail. The data set is then manually optimised until the adjusted parameter solution converges. Finally, at 206 benchmarks at least one measurement has been bridged, at 61 benchmarks the displacement has been split into two partial displacements and at 65 benchmarks a polynomial degree of two was introduced.

4.3 Influence of gravity

Height estimation is closely coupled with the Earth's gravity field. Globally the gravitational potential is approximated using spherical harmonics (Heiskanen & Moritz, 1967, p. 20 ff.). Local or regional variations in the gravity field are observed by in situ measurements using absolute and relative gravimeters. As the equipotential surfaces of the Earth's gravity field are not parallel, levelling measurements between two benchmarks are dependent on the chosen path. For a levelling loop starting and ending at the same benchmark, the summation of height differences is theoretically always different from zero if the measurements cross equipotential surfaces. Gravity measurements have to be carried out at the benchmarks of a levelling line in order to consider the theoretical loop misclosure.

Different height systems may be deduced depending on the way how measured surface gravity values are applied to the levelled height differences. Heiskanen & Moritz (1967, p. 162 f.) present the derivation of four height representations, which follow from levelling and gravity measurements: Geopotential numbers, dynamic heights, orthometric heights and normal heights. While the latter is related to the Quasigeoid, which is not an equipotential surface and thus not physically interpretable, the other three relate to the Geoid, which represents the physical shape of the Earth. Leismann et al. (1992, p. 81 ff.) compare different height systems w.r.t. their characteristics for application as a national height system. In addition, normal-orthometric heights and ellipsoidal heights are discussed, which are both independent of measured gravity values. The authors conclude that normal heights H^N according to the theory of Molodensky (1958) are most appropriate for national height systems. If measured surface gravity values are not available, normal-orthometric heights H^{NO} may be used as a substitute for H^N, such as for the height systems of Western Germany before 1993 (Heck, 2003, p. 297 f.).

For reasons of economy, gravity measurements are not performed at every set-up of a levelling campaign. Torge & Müller (2012, p. 253) recommend station distances between 5 and 20 km for flat areas and between 1 and 2 km for mountainous regions. Gravity corrections for the height differences are then calculated from interpolated gravity values. The following steps are used for the calculation of gravity-corrected loop misclosures:

1. Calculation of Bouguer anomalies Δg_B at levelling benchmarks with measured gravity values, Eq. (4.2)
2. Interpolation of Δg_B at benchmarks without gravity values
3. Calculation of interpolated gravity values at levelling benchmarks without a measured gravity value, Eq. (4.3)
4. Calculation of the gravity correction between the starting and end point of a measurement, Eq. (4.4)

The interpolation of gravity values is performed using gravity anomalies which describe local differences of the Earth's gravity field w.r.t. a normal gravity field depending on height and latitude, only. Bouguer anomalies Δg_B are smooth in space and therefore commonly used to interpolate measured gravity values to other locations. Assuming an infinite plate with constant density for the topographic effect on a gravity value, Δg_B results from the measured surface gravity value g, the free-air reduction δg_F, the Bouguer plate reduction δg_P and the normal gravity value γ_0, see Torge & Müller (2012, p. 268):

$$\begin{aligned}\Delta g_B &= g + \delta g_F - \delta g_P - \gamma_0 \\ &= g + \left(-\frac{\partial\gamma}{\partial H^N} H^N\right) - 2\pi G\rho H^N - \gamma_0 \\ &= g + 3.086\cdot 10^{-6}\cdot H^N - 1.119\cdot 10^{-6}\cdot H^N - \gamma_0 \quad .\end{aligned} \tag{4.2}$$

The normal gravity γ_0 at a given latitude is obtained from the parameters of the reference ellipsoid, see Heiskanen & Moritz (1967, p. 69 f.). Applying a normal gradient of gravity $\partial\gamma/\partial H^N = -0.3086$ mgal/m, see Eq. (4.5) and Heiskanen & Moritz (1967, p. 131), the gravitational constant $G = 6.67248\cdot 10^{-11}\,\mathrm{m}^3\,\mathrm{kg}^{-1}\,\mathrm{s}^{-2}$ (Petit & Luzum, 2010, p. 18) and a conventional density ρ of $2,670\,\mathrm{kg\,m}^{-3}$ (Heiskanen & Moritz, 1967, p. 131), Δg_B is calculated for all in situ gravity measurements and afterwards interpolated to the location of levelling benchmarks without gravity observations. At these benchmarks a surface gravity value is obtained from the interpolated Bouguer anomaly $\Delta g_{B,int}$:

$$g = \gamma_0 - \delta g_F + \delta g_P + \Delta g_{B,int} \quad . \tag{4.3}$$

The gravity correction based on normal heights H^N for a measured height difference $h_{j,k}$ between two benchmarks B_j and B_k is given by Leismann et al. (1992, p. 42); Heiskanen & Moritz (1967, p. 171):

$$NC_{j,k} = \frac{g_{j,k} - G_0}{G_0}\cdot h_{j,k} + \frac{\bar{\gamma}_j - G_0}{G_0}\cdot\; H_j^N - \frac{\bar{\gamma}_k - G_0}{G_0}\cdot\; H_k^N \quad , \tag{4.4}$$

and denoted as normal correction (NC). $g_{j,k}$ is the mean gravity along the levelling section between B_j and B_k and approximated using the gravity values of the two benchmarks ($g_{j,k} = 0.5\cdot(g_j + g_k)$). G_0 is an arbitrary but constant gravity value and $\bar{\gamma}_j$ the mean normal gravity along the ellipsoidal normal between the benchmark and the quasigeoid.

The gravity value of a point at latitude φ and height H above the ellipsoid is given by Taylor series expansion in terms of H (Heiskanen & Moritz, 1967, p. 78 f.):

$$\begin{aligned}\gamma_H &= \gamma_0 + \frac{\partial\gamma_0}{\partial H}H + \frac{1}{2}\frac{\partial^2\gamma_0}{\partial H^2}H^2 + \ldots \\ &\approx \gamma_0 + \left(-2\frac{\gamma_0}{a}\left(1 + f + m - 2f\sin^2\varphi\right)\right)H + \left(3\frac{\gamma_0}{a^2}\right)H^2 \\ &\approx \gamma_0\left(1 - \frac{2}{a}\left(1 + f + m - 2f\sin^2\varphi\right)H + \frac{3}{a^2}H^2\right) \quad .\end{aligned} \tag{4.5}$$

Applying the parameters a and f, of an rotational ellipsoid and the parameter m describing the ratio between the centrifugal acceleration and the normal gravity at the equator (Torge & Müller, 2012, p. 103), γ_H can be calculated at a given latitude and height, e. g. using the geometric and physical constants given in the Geodetic Reference System 1980 (GRS80, Moritz, 1984). Torge & Müller (2012, p. 110 f.) provide numerical formulae for the latitude- and height-dependent calculation of Eq. (4.5) w.r.t. GRS80. $\bar{\gamma}_j$ results from integration of γ_H from zero height to H_j^N (Heiskanen & Moritz, 1967, p. 170 f.):

$$\begin{aligned}\bar{\gamma} &= \frac{1}{H^N}\int_0^{H^N}\gamma_H dH \\ &= \gamma_0\left(1 - \frac{1}{a}\left(1 + f + m - 2f\sin^2\varphi\right)H^N + \frac{1}{a^2}(H^N)^2\right) \quad .\end{aligned} \tag{4.6}$$

As measured gravity values are not available for the whole transnational network of levelling data, a gravity correction based on normal gravity values is used for the kinematic adjustment. Analogous to Eq. (4.4), a normal-orthometric correction (NOC) is obtained for normal-orthometric heights together with the mean value of normal gravity values γ_H at B_j and B_k (Leismann et al., 1992, p. 45; Heck, 2003, p. 294):

$$NOC_{j,k} = \frac{\gamma_{H,j,k} - G_0}{G_0} \cdot h_{j,k} + \frac{\bar{\gamma}_j - G_0}{G_0} \cdot \ H_j^{NO} - \frac{\bar{\gamma}_k - G_0}{G_0} \cdot \ H_k^{NO} \quad . \tag{4.7}$$

In this case, γ_H is calculated w.r.t. a normal gravity field, see Eq. (4.5) and no gravity measurements are needed to calculate the correction. Fig. 4.12 shows a comparison of normal gravity values γ_H calculated according to Eq. (4.5) and measured (or interpolated) gravity values g at a levelling loop in the southern BF. Gravity values of the normal gravity field are increasing with increasing latitude and decreasing with increasing height. In the southern and western part of the levelling loop, the observed gravity is close to the normal gravity, whereas the values largely differ in areas with significant topography. A general tendency to positive differences between γ_H and g is observable ($\gamma_H > g$, average value: +33 mgal), which may result from a reduction of the vertical gradient of gravity in the high mountains and from a higher density of the rocky underground of the BF compared to the "normal density" implicitly defined with the parameters of the normal gravity field. Maximum differences are in the order of +132 mgal at the Feldberg (1,493 m above sea level), the highest mountain of Baden-Württemberg.

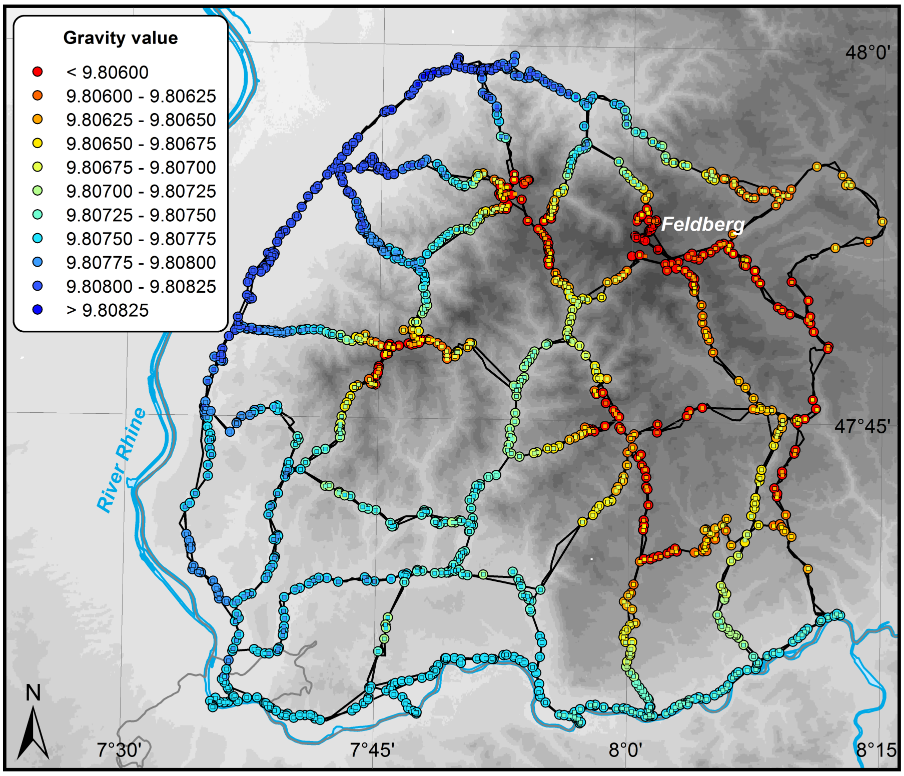

Figure 4.12: Comparison of normal gravity values (circles) and measured gravity values (squares) in levelling loop 601 (southern BF). Grey background: DEM using SRTM-3 data.

The loop misclosures calculated for the German and Swiss levelling loops listed in Tab. 4.2 and Tab. A.2–A.4 are corrected for the influence of gravity using measured gravity values along with the NC given in Eq. (4.4). Fig. 4.13 compares the differences between NC and

NOC along levelling loop 601 in the southern BF. It becomes obvious that the corrections have similar values in flat areas (line South and line West) and may largely differ in areas with significant topography (line North and line East). The overall theoretical loop misclosure is underestimated by about 13.5 mm when NOC is applied instead of NC. As long as the levelling measurements follow a similar path in each measurement epoch and gravity does not significantly change with time, the gravity corrections of different measurement epochs are almost identical, as shown with the standard deviations in Fig. 4.13. One can therefore assume that the influence of gravity on the vertical rates resulting from a kinematic adjustment of levelling data is small. As the vertical rates are differential results of data from several measurement epochs, the error caused by neglecting the influence of gravity should be significantly reduced. In order to investigate the influence of gravity corrections on the resulting vertical rates, the levelling observations of the lines shown in Fig. 4.12 are used within a kinematic adjustment in three different variants: (i) no gravity correction, (ii) NC and (iii) NOC. The mean value of absolute differences between vertical rates at 1,400 levelling benchmarks of levelling loop 601 are compared in Tab. 4.3.

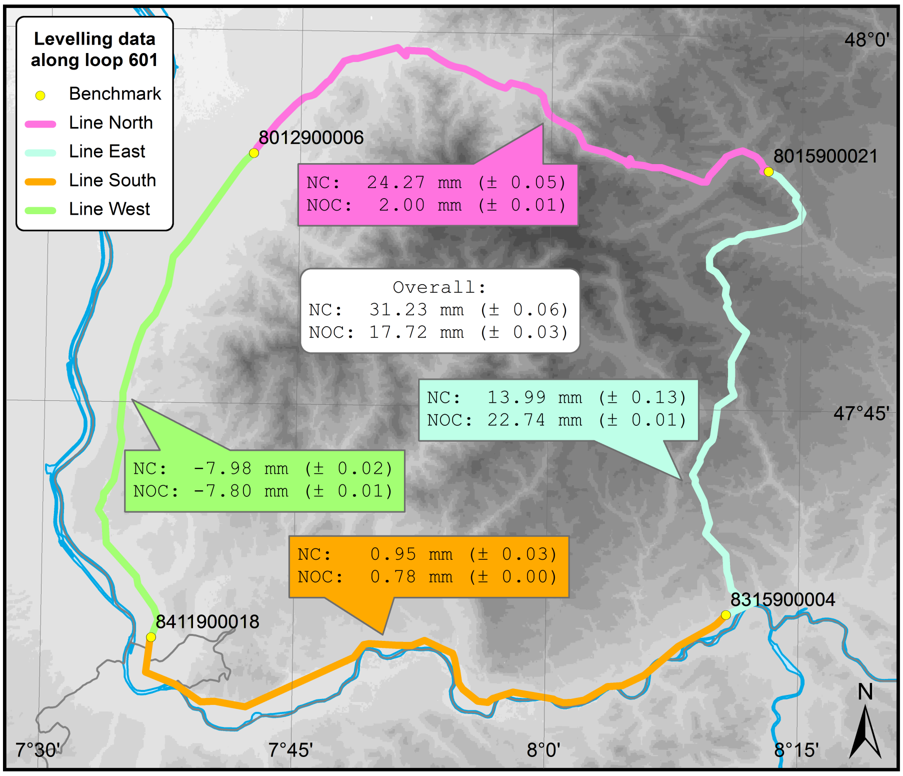

Figure 4.13: Comparison of normal correction (NC) and normal-orthometric correction (NOC) calculated along levelling lines of loop 601. The mean value (± standard deviation) results from the levelling measurements of four different epochs.

The differences between the variants are small compared to the accuracy level of the resulting vertical displacement rates of the order of 0.1 mm/a. For the kinematic adjustment of all data within the URG network, NOC was applied to the height differences. The mean absolute difference (MAD) of 0.039 mm/a of the vertical rates of variant (iii)–(i) is also small compared to the standard deviation of vertical rates (mean: 0.18 mm/a). However, at one benchmark a large difference of -0.291 mm/a is observed. Largest differences in the displacement rates are observed at benchmarks, which are poorly constrained by the adjacent measurements, i. e. few measurements with a small temporal difference. At these benchmarks the small differences in the observations results in relatively large differences in the estimated velocities. For the major part of the vertical rates (99.4 %), the differences are within ±0.1 mm/a and therefore not significant. The estimated standard deviations of (iii) are slightly better compared to (i) at all considered benchmarks. However, with a reduction in standard deviation of 0.1 to 0.2 % the increase in precision is small.

Table 4.3: Mean absolute differences (MAD), minimum (MIN) and maximum (MAX) differences between vertical rates resulting from kinematic adjustment of height differences using different gravity corrections.

Region	Number of benchmarks	Gravity corrections	MAD [mm/a]	MIN [mm/a]	MAX [mm/a]
Loop 601	1,400	(ii)–(i)	0.018	−0.017	+0.087
		(iii)–(i)	0.006	−0.012	+0.023
		(iii)–(ii)	0.013	−0.007	+0.064
All URG data*	14,098	(iii)–(i)	0.039	−0.291+	+0.139

* Only NOC was calculated and applied to the height differences due to the lack of gravity data in the French part of the network.

\+ Note that this is an extreme outlier. The second smallest value is −0.122 mm/a.

4.4 Stochastic model

The stochastic model of the kinematic adjustment was already introduced in Sect. 3.1.3. This section describes the possibilities to model random and systematic errors in KaGeMoV and the model parameters used within the analysis of levelling data in the URG area (Sect. 4.4.1). In order to account for inhomogeneities in the database comprising measurements from different countries, orders and epochs, a classification of the measurements into groups and iterative variance component estimation is applied. Sect. 4.4.2 presents the relevant formulae as well as results for a test network and for the whole URG network.

4.4.1 Modelling of random and systematic errors

In order to model random errors inherent to levelling measurements, generally a weighting proportional to the square root of the length of the levelling path is applied. This relation was already used for the calculation of heights within the arc measurement between Swinemünde (Baltic Sea) and Konstanz (Lake Constance), see Seibt (1882, p. 3) and within the first precise levelling of Switzerland (Hirsch & Plantamour, 1867). For a purely distance-depending weighting, the elements p_l of the weight matrix P result from the variance of a single observation σ_l (related to unit length) and the path length $d_l = d_{j,k}$ between the corresponding benchmarks B_j and B_k:

$$p_l = \frac{1}{\sigma_l^2 \cdot d_l} \quad . \tag{4.8}$$

If one assumes all measurements corresponding to the same path length to be of the same precision, σ_l^2 can be incorporated to the a priori variance factor σ_0^2 and Eq. (4.8) reduces to $p_l = 1/d_l$.

An additional random error at the starting and end points of a measurement section (σ_{AB}) is added to Eq. (4.8):

$$p_l = \frac{1}{\sigma_l^2 \cdot d_l + 2\sigma_{AB}^2} \quad . \tag{4.9}$$

σ_{AB} models the uncertainty of the set-ups at the starting/end points of a line, so-called unrest or noise of the benchmarks, and is independent of the path length. Following Zippelt (1988, p. 58 f.), an additional random error $\sigma_{\delta AB}$ at intermediate benchmarks may exist if the point unrest has different magnitudes at the intermediate benchmarks. This error scales with the number of intermediate set-ups n_B along the line and Eq. (4.9) extends to

$$p_l = \frac{1}{\sigma_l^2 \cdot d_l + 2\sigma_{AB}^2 + (n_B - 1) \cdot \sigma_{\delta AB}^2} \quad . \tag{4.10}$$

Systematic errors present in the levelling measurements are considered by adding further terms to the denominator of Eq. (4.10). Different types of systematic errors are discussed in detail in Zippelt (1988, p. 59 ff.) depending on path length d_l, height difference h_l and azimuth A_l of the observations. Tab. 4.4 lists possible systematic error sources and their dependencies. A full model accounting for all discussed random and systematic errors would describe the elements of P by

$$p_l = \frac{1}{\sigma_l^2 \cdot d_l + 2\sigma_{AB}^2 + (n_B - 1) \cdot \sigma_{\delta AB}^2 + (b_1^2 \cdot d_l + b_2^2 \cdot h_l) + b_3^2 \cdot h_l^2 + b_4^2 \cdot (d_l \cos A_l)^2} \quad . \tag{4.11}$$

Table 4.4: Systematic error sources for levelling measurements depending on the distance d_l, the height difference h_l and the azimuth A_l of corresponding observations.

Influence factor	depending on	Parameter in Eq. (4.11)
Graduation error of the rod	d_l, h_l	b_1, b_2
Irregular temperature influences	d_l, h_l	
Refraction	d_l, h_l	
Scaling error of the rod	h_l	b_3
Systematic temperature influences	h_l	
Systematic influences of the Earth's magnetic field	d_l, A_l	b_4

The magnitude of all introduced random and systematic error parameters in Eq. (4.11) is previously unknown and has to be assumed. In Fuhrmann & Zippelt (2013) the six random and systematic error parameters, i. e. σ_{AB}, $\sigma_{\delta AB}$, b_1, b_2, b_3, b_4, have been investigated using different combinations and quantities applied on data of a levelling network in Southern Germany and Northern Switzerland. In approximately 35,000 adjustments, different quantities and combinations of the six error types were tested w.r.t. the resulting standard deviations of the adjusted parameters, yielding only for σ_{AB} a value significantly different from zero. For the stochastic model of the URG network, σ_l is set to 1.0 mm/$\sqrt{\text{km}}$ according to the results of mean loop misclosures in Tab. 4.2. A suitable value for σ_{AB} is calculated from several iterations of the adjustment with different parameter values for σ_{AB}. The resulting a posteriori standard deviations and mean standard deviations for the estimated heights and velocities are compared in Fig. 4.14.

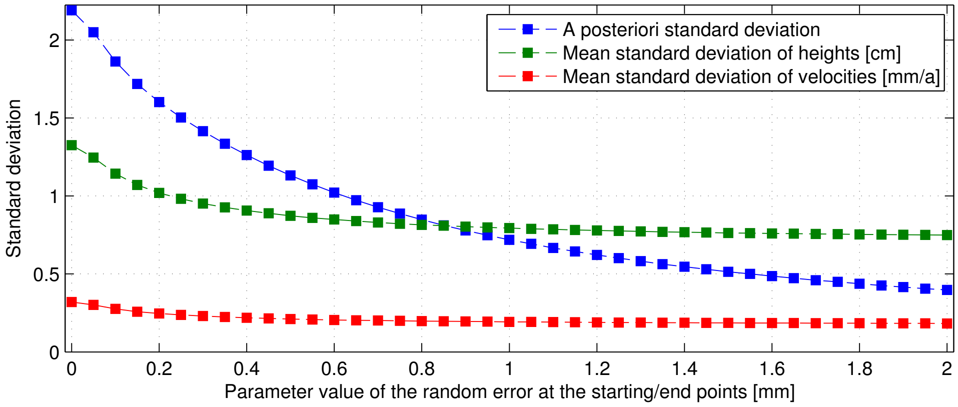

Figure 4.14: A posteriori standard deviation and mean standard deviations of estimated heights and velocities for different parameter values of σ_{AB}.

For $\sigma_{AB} = 0.65$ mm, the a posteriori standard deviation falls below the a priori standard deviation of 1.0 and the overall model test, see Eq. (3.16), is accepted. In addition, the mean standard deviations of heights and velocities are close to their saturation value at 0.8 cm and 0.2 mm/a for $\sigma_{AB} = 0.65$ mm. The basic stochastic model applied to the observations therefore results in

$$p_l = \frac{1}{1\ \text{mm}^2/\text{km} \cdot d_l + 2 \cdot (0.65\ \text{mm})^2} \quad . \tag{4.12}$$

4.4.2 Variance component estimation

To account for inhomogeneities in the accuracy of observations, variance component estimation (VCE) is an effective tool enabling the determination of different levels of variance for multiple groups of observations. VCE was introduced by Helmert (1907). A statistically rigorous formulation in matrix notation is given by Koch (1999, p. 230 f.); Teunissen & Amiri-Simkooei (2008). In general, iterative VCE is applicable to a set of observations in a sensible way if

- the observations carry significantly different accuracies,
- the accuracies are previously unknown,
- the observations are dividable into groups with different accuracy levels,
- each variance group contains a significant number of observations,
- the adjustment already yields robust results without VCE ($\hat{\sigma}_0 \approx \sigma_0$).

Neglecting correlations between different variance groups, the standard form of the covariance matrix of observations given in Eq. (3.14) is extended to

$$C_{yy} = \begin{pmatrix} \sigma_1^2 Q_1 & 0 & \dots & 0 \\ 0 & \sigma_2^2 Q_2 & \dots & 0 \\ \vdots & \vdots & \ddots & \vdots \\ 0 & 0 & \dots & \sigma_k^2 Q_k \end{pmatrix} \quad . \tag{4.13}$$

The matrices $Q_1 \dots Q_k$ are calculated based on the weighting model given in Eq. (4.12). Each group of observations has its own, unknown variance component $s = \sigma_i^2$ $(i = 1 \dots k)$. The estimates $\hat{s}$ then follow from the algorithm

$$\begin{aligned} & W = P - PA(A^\top PA)^{-1}A^\top P = P - PQ_{\hat{y}\hat{y}}P = PQ_{vv}P \quad , \\ & c_{ij} = tr(WD_iWD_j) \qquad i,j = 1 \dots k \quad , \\ & q_i = e^\top PD_iPe \qquad i = 1 \dots k \quad , \\ & \hat{s} = C^{-1}q \quad , \quad \text{with} \quad C = (c_{ij}) \quad , \quad q = (q_i) \quad \text{and} \end{aligned} \tag{4.14}$$

$Q_{\hat{y}\hat{y}}$: Covariance matrix of adjusted observations ($n \times n$)
Q_{vv} : Covariance matrix of residuals ($n \times n$)
D_i : Covariance matrix for ith variance group ($n \times n$), containing non-zero elements only at the position of Q_i
k : Number of variance groups .

The estimated variance components are then used as initial values in Eq. (4.13) and the adjustment procedure is repeated (iterative VCE). Besides the rigorous Helmert type estimator, which may be rather time-consuming, several simplifications have been proposed in literature, discussed in Bähr et al. (2007). A simplified estimator fulfilling the condition for asymptotic convergence to Helmert's estimator has been given by Förstner (1979, p. 450):

$$\hat{s} = \frac{e^\top PD_iPe}{tr(WD_i)} \quad . \tag{4.15}$$

For a covariance matrix of block-diagonal structure, Eq. (4.15) simplifies to

$$\begin{aligned}\hat{s} &= \frac{e_i^\top P_i e_i}{n_i - tr(N^{-1} A_i^\top P_i A_i)} \\ &= \frac{e_i^\top P_i e_i}{tr(q_{vv,i} \cdot p_i)} \\ &= \frac{e_i^\top P_i e_i}{r_i} \quad .\end{aligned} \tag{4.16}$$

This formulation is much easier than the statistically rigorous estimator of Helmert type in Eq. (4.14).

Further simplifications proposed in literature replace the redundancy number r_i by a simpler expression. Helmert's simple estimator (Helmert, 1907, p. 358) simply uses the number of observations within each variance group n_i. In Altamimi et al. (2007a) a so-called classical estimator is presented using

$$r_i = n_i - \frac{n_i}{n} u \quad . \tag{4.17}$$

The estimators proposed by Kubik (1967) and Persson (1980) both use differences between n_i and the total number of unknowns u or a subset of u, respectively. For the kinematic adjustment of levelling data available in the URG area, n_i is smaller than u, or the subset of u. Thus, the denominator in Eq. (4.16) would become negative. The different methods of VCE are summarised and compared w.r.t. their applicability for a kinematic adjustment of levelling data in Tab. 4.5.

Table 4.5: Comparison of different methods of VCE

VCE method	Solvability	Convergence
Helmert (rigorous)	yes	less than 10 iterations
Förstner	yes	more than 20 iterations
Classical estimator	yes	divergent
Helmert's simple estimator	yes	divergent
Kubik's estimator	no	–
Persson's estimator	no	–

A comparison of VCE based on three different methods is performed for an iterative adjustment of a sub-network with 2,521 observations and 10 groups, classified by date, i. e. five different epochs, and state, i. e. Baden-Württemberg and Rheinland-Pfalz. The behaviour of the variance components with 30 iteration steps is shown in Fig. A.2 in Appendix A. For the classical estimator, the iterative solution does not converge and some variance components increase with each iteration. The rigorous Helmert estimator (Eq. (4.14)) and Förstner's simplification (Eq. (4.16)) deliver nearly the same results for the variance components, but need a different number of iteration steps. Helmert's method converges faster (within 10 iterations), but needs much more computation time for a single evaluation as full matrices have to be used. Förstner's method needs more than 20 iterations for convergence but is much faster in every step as only the block-diagonal elements of the matrices are used. The difference in the estimated variance components by the two methods after 30 iteration steps is about 2 %. This leads to a mean value of absolute differences in velocity estimates between Helmert's and Förstner's method of 0.04 mm/a (90% within ±0.01 mm/a), which is much smaller than the precision of the estimated velocities in the sub-network (mean value 0.14 mm/a). As the computation time of the rigorous method of iterative VCE strongly increases with an increasing number of observations, only Förstner's method is applied to the data of the whole URG network.

For the application of VCE, an appropriate classification of the data set into groups with a sufficient number of observations per group is needed. Tab. 4.6 presents the classification of levelling data in the URG network resulting from the national responsibility and temporal distribution of the data. The levelling data is divided into four major measurement epochs. As most of the data of the network is located in Germany, two groups of German data were formed (first- and second-order lines), additionally to a group of data from the French and Swiss part, respectively. In total, the 40,049 measured height differences are divided into 16 groups. The number of observations assigned to each group is also listed in Tab. 4.6. The two German groups contain the major part of observations (over 80 %). The Swiss group is the smallest one, but well distributed over time. In contrast to the German and French national networks, where complete remeasurements of the first order loops are carried out within a specific period of several years, the Swiss national network is periodically remeasured in parts, see Schlatter (2007, p. 138). The French data set is not equally distributed over time as only few observations stem from the last period (about 3 % of the French data). This fact, together with the poorer data quality, leads to higher variance components for the French data.

Table 4.6: Groups used for VCE including the measurement period (years) and the number of observations n_i per group. D1: Germany first-order, D2: Germany second-order, F: France, CH: Switzerland

Class	Epoch 1		Epoch 2		Epoch 3		Epoch 4	
	Period	n_i	Period	n_i	Period	n_i	Period	n_i
D1	1922–1939	1504	1950–1978	4736	1980–1994	4875	1996–2012	4692
D2	1875–1942	1149	1949–1979	6720	1980–1994	3221	1995–2012	5484
F	1878–1897	701	1920–1939	1953	1947–1973	3207	1986–2012	212
CH	1867–1911	333	1917–1949	266	1953–1978	408	1980–2009	588

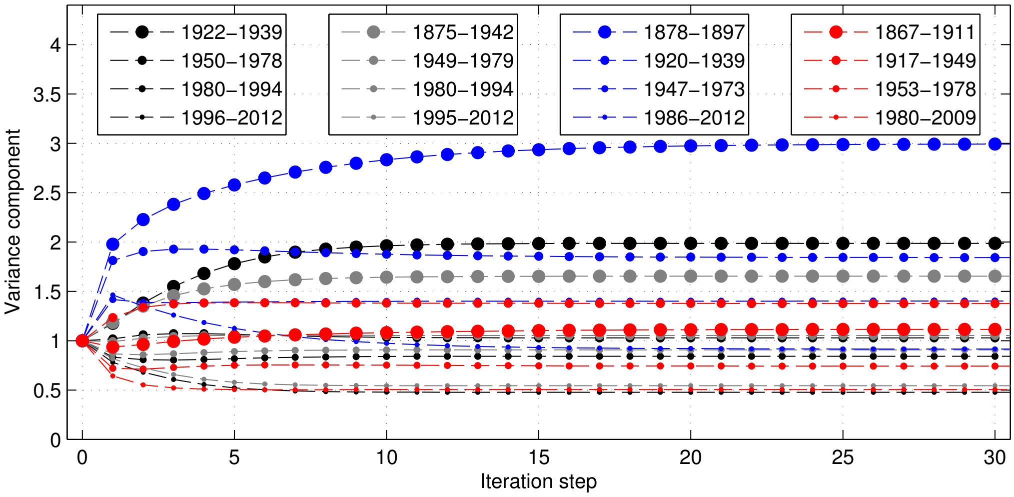

Figure 4.15: Variance components for iterative VCE of 40,049 observations of the URG levelling network containing data from Germany, France and Switzerland. The corresponding variance groups are defined in Tab. 4.6, black: D1, grey: D2, blue: F, red: CH.

The iteratively estimated variance components of the 16 groups displayed in Tab. 4.6 are shown in Fig. 4.15. The variance components of the French data group are significantly larger than the variance components of the other groups, whereas no significant difference between German measurements along first- and second-order lines is visible.

The influence of VCE on the estimated displacement rates and their accuracies is investigated in detail. Fig. 4.16 compares the standard deviations of displacement rates before and after iterative VCE is applied. Before VCE is applied, the standard deviation is mainly characterised by an increase with distance to the reference point resulting from the distance-depending weighting of observations. Some levelling lines with significantly higher standard deviations are visible in Fig. 4.16(a), mainly resulting from a low number of observations, i. e. benchmarks measured only in two epochs with a rather short time difference. After the application of VCE, poorer standard deviations in the French part of the network are observed. This result is reasonable as it reflects the data quality as well as the temporal and spatial distribution of the data in the French part. The influence of VCE leads to a mean change in displacement rates of 0.07 mm/a (mean of absolute differences) with about 15 % of the differences being less than −0.1 mm/a and 5 % larger than +0.1 mm/a. Particularly the regions adjacent to the French part show significant changes in the vertical rates.

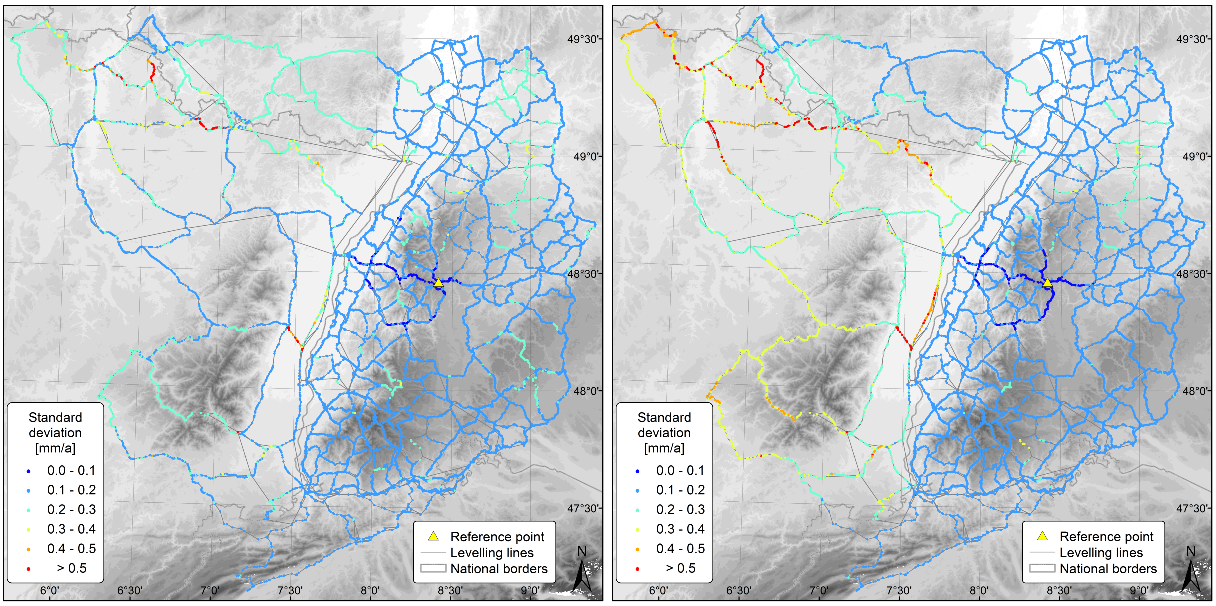

(a) without iterative VCE (b) after iterative VCE

Figure 4.16: Standard deviation of vertical displacement rates in the URG levelling network before and after application of iterative VCE

4.5 Resulting surface displacements

Within this section, the results of the kinematic adjustment of levelling data are shown. Sect. 4.5.1 presents the final set of levelling data focussing on the number and temporal coverage of measurements at the benchmarks. In Sect. 4.5.2 some remarks on the selection of the reference point defining the datum of the adjustment are given. The vertical rates resulting from the adjustment of 40,049 observations are filtered for outliers (Sect 4.5.3) and finally presented and discussed in Sect. 4.5.4.

4.5.1 Data set for the kinematic adjustment

After the pre-processing steps described in Sect. 4.2 have been performed, the database is reduced to a set of consistent observations at repeatedly measured benchmarks. The location of the remaining benchmarks and the number of measurement epochs of the corresponding height differences is shown in Fig. 4.17. The German first-order lines have been observed in four or more epochs, whereas only some second-order lines have been observed in more than two epochs. The French first-order levelling loop has only partly been observed in three or more epochs, the second-order lines have mainly been measured in two epochs. In Switzerland the junction points have been observed in three or more epochs, but some of the connecting lines only in two epochs.

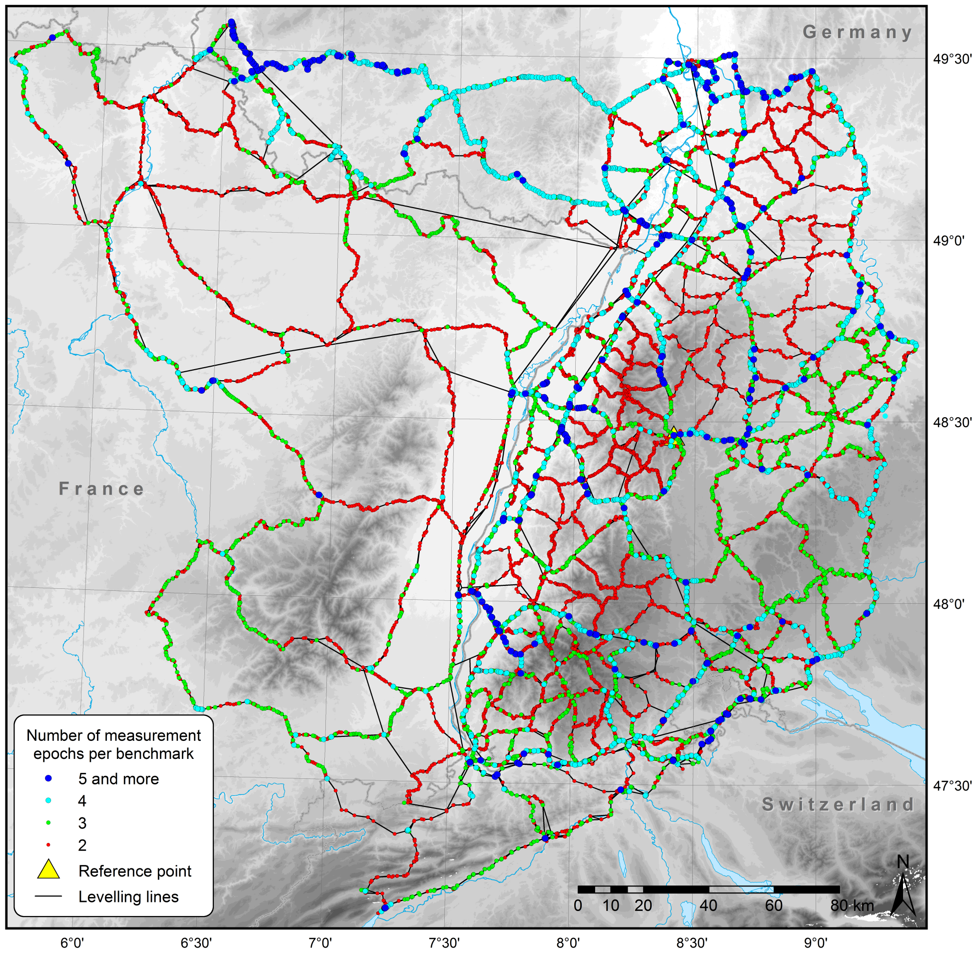

Figure 4.17: Number of measurement epochs at the levelling benchmarks. An additional measurement epoch is counted if a time difference of at least seven years between corresponding measurements at a benchmark exists.

If a benchmark has been measured in only two epochs with a short time difference, the accuracy of the corresponding vertical rates is lower compared to benchmarks which have been measured in several epochs and cover a longer time span, see Fig. 4.16. Tab. 4.7 shows point-wise redundancy numbers r_i and standard deviations for benchmarks covering a large overall time span T compared to the mean values for all benchmarks used in the kinematic adjustment. In general, benchmarks which exist over a long period are also observed more frequently. Thus, these benchmarks strongly contribute to the overall redundancy of the adjustment. The historical benchmarks and measurements therefore largely contribute to the accuracy of the vertical rates even if the precision of the measured height differences is lower compared to later measurements, see Tab. 4.2.

Table 4.7: Influence of the temporal coverage of measurements at levelling benchmarks on the kinematic adjustment. Benchmarks classified as outliers, see Sect. 4.5.3, are excluded. MPR: mean point-wise redundancy number, MSTD: mean standard deviation of vertical rate.

	Number	MPR	MSTD [mm/a]
Benchmarks with $T > 100$ years	178	2.86	0.140
Benchmarks with $T > 90$ years	450	2.77	0.151
Benchmarks with $T > 80$ years	978	2.65	0.144
Benchmarks with $T > 70$ years	2,276	2.52	0.169
Benchmarks with $T > 60$ years	4,103	2.42	0.168
Benchmarks with $T > 50$ years	7,270	2.33	0.168
All benchmarks with estimated rates	14,098	1.12	0.183

The kinematic adjustment is applied to the data set in many iterations as the displacement model of several benchmarks has to be adapted and the corresponding observations of different epochs have to be checked, see Sect. 4.2.4. Many of the benchmarks with a model misfit are for instance located in one of the mining areas of the investigation area, see Fig. 2.9 and Tab. 2.2. At more than 60 % of the benchmarks with a model misfit, it is sufficient to bridge the corresponding observations of at least one epoch at the benchmark. The final number of observations and parameters of the kinematic adjustment is given in Tab. 4.8.

Table 4.8: Key numbers of the kinematic adjustment.

Number of observations (n)	40,049
Number of benchmarks	15,816
Number of estimated heights	15,815
Number of linear coefficients	15,592
Number of accelerated coefficients	65
Total number of unknowns (u)	31,472
Degree of freedom ($n - u$)	8,577

4.5.2 Selection of the reference point

As the normal equation system of the kinematic adjustment has a rank deficiency, the datum of the levelling analysis has to be defined. Choosing the single reference point model described in Sect. 3.1.3, Eq. (3.13), the following requirements for the selection of the reference point are desirable:

(i) small (or well-known) displacement within the analysed period,

(ii) measured in several epochs over a long time span,

(iii) located in the centre of the network.

If the reference point is exposed to uplift or subsidence, all estimated vertical rates are shifted by the reference point displacement. A subsidence of e. g. 1 mm/a at the reference point would result in a relative uplift of 1 mm/a at all other benchmarks (additionally to their own movement) if the reference point is introduced with a vertical rate of zero. If the reference point is exposed to a non-linear movement, a model-related error is introduced to the network adjustment. It is therefore advisable to include additional information on the geological setting of the investigated area for a proper selection of the reference point. To ensure a robust integration into the network adjustment, the reference point should be measured at many epochs (ii). As the precision of the estimated parameters decreases with the distance to the reference point, a central location within the network is preferable (iii).

A reference point located in a presumably stable region at the east side of the BF is selected, see Fig. 3.3 or Fig. 4.18. The corresponding benchmark is mounted at a church in the city of Freudenstadt, founded on triassic rocks. As a junction point of three levelling lines, it was measured at the following dates: 1933, 1938, 1956, 1957, 1960, 1968, 1986, 1987 and 2007 and is therefore well-integrated in the levelling network. In a distance of approximately 4.5 km to the reference point, a group of five subsurface benchmarks was established in 1960 denoted as major levelling benchmarks of the Federal State of Baden-Württemberg (Landesnivellementhauptpunkte, LNH), see LVBW (1983, p. 10). Tab. 4.9 shows a height comparison between the five benchmarks relative to the reference point in Freudenstadt. The differences between heights of different measurement epochs are below 2 mm at all points, which means that the relative movement between the five LNH (benchmark number 7516900080, 7516900083, 7516900085, 7516900087, 7516900089) and benchmark 7516900006 is well below 0.1 mm/a.

Table 4.9: Height changes between different measurement epochs at the major levelling benchmarks of Baden-Württemberg w.r.t. the reference point 7516900006 located at Freudenstadt, BF. The heights are directly calculated from the measured height differences without prior adjustment or error calculation.

Year of measurement	Height [m] at benchmark 7516900006	7516900080	7516900083	7516900085	7516900087	7516900089
1960	730.6400	805.0604	807.2302	807.1410	804.2515	808.8991
1987	730.6400	805.0600	807.2298	807.1409	804.2516	808.8993
2007	730.6400	805.0592	807.2313	807.1423	804.2532	808.9006
	Height changes [mm]					
1987 − 1960	0.0	−0.3	−0.4	0.0	0.2	0.2
2007 − 1987	0.0	−0.9	1.6	1.3	1.5	1.3
2007 − 1960	0.0	−1.2	1.2	1.3	1.7	1.5
	Estimated vertical rate from kinematic adjustment [mm/a]					
	–	0.01	0.05	0.05	0.06	0.05

The estimates for the vertical rates from the kinematic adjustment (also given in Tab. 4.9) confirm that the chosen reference point is not exposed to a significant displacement relative to the group of subsurface benchmarks. However, as long as the results are regarded and interpreted as relative displacements w.r.t. the reference point and not as an absolute motion, also a reference point with a large displacement might be selected. The transition of one solution to another is easily feasible by means of an S-transformation (Baarda, 1968; Teunissen, 2006, p. 39 f.). In Appendix A the resulting vertical rates when using a different reference point are displayed. In Fig. A.3 a reference point which is directly mounted at the bedrock is chosen. Only small differences are visible w.r.t. the reference point located in Freudenstadt. In Fig. A.4 a reference point located within a subsidence area close to the city of Landau is used, see Sect. 4.6.2. The vertical rates of all other benchmarks are shifted by about +3 mm/a. Tab. 4.10 summarises the results of the kinematic adjustments using different reference points.

Table 4.10: Comparison of vertical rates from kinematic adjustment using different reference points. FDS: Freudenstadt, STD: Standard deviation.

Reference point location	Relative rate w.r.t. FDS [mm/a]	Mean rate [mm/a]	Mean STD of rates [mm/a]	Mean STD of differences in rates w.r.t. FDS [mm/a]
Freudenstadt	–	-0.092	0.183	–
Laufenburg	$+0.067$	-0.159	0.185	0.000
Ramonchamp	-0.050	-0.052	0.421	0.001
Landau	-7.872	$+2.964$	0.225	0.004

The mean vertical rates of the adjustment solutions using a reference point in Laufenburg and Ramonchamp are shifted by the relative vertical rate estimated in the adjustment using the reference point in Freudenstadt (Freudenstadt-solution). The reference point located in Landau is modelled by an accelerated displacement within the adjustment. The relative vertical rate given in Tab. 4.10 is therefore not representative for the linear movement of the benchmark as shown in Fig. 4.11. The vertical rates using the reference point located at Laufenburg are comparable to the Freudenstadt-solution regarding the mean standard deviation of rates and the low standard deviation of the differences, which means that the vertical rates of both solutions are purely shifted against each other. For a reference point located in Ramonchamp, the standard deviations of vertical rates are on a higher level, which may be explained by the poor integration of the reference point within the network along a levelling line with relatively high standard deviations w.r.t. the Freudenstadt-solution, see Fig. 4.16(b). Besides the large shift and the higher standard deviations of vertical rates for the solution using the subsiding benchmark in Landau, a higher dispersion in the differences to the vertical rates of the Freudenstadt-solution is observed. The non-linear behaviour of the selected reference point in Landau also contaminates the vertical rates of other points in the network and does not result in a pure shift.

4.5.3 Outlier handling

The linear displacement rates at 65 benchmarks, at which an additional accelerated coefficient is estimated, shall not be displayed in the final result for vertical rates as the linear coefficient in this case may not be representative for the movement, see Fig. 4.11. In addition, the vertical rates at benchmarks observed in one epoch only, but with a polynomial degree set to one because of a short time difference of adjacent measurements are excluded, see Sect. 4.2.3. The displacement of these benchmarks is not estimable with significance due to the short time difference ($\sigma_v \sim \frac{1}{\Delta t}$, see Sect. 3.1.3). This reduces the data set of vertical rates to 15,464.

Some of the remaining vertical rates are significantly larger than the rates of benchmarks in the neighbourhood. In most cases, the large displacement rates of these points have non-tectonic reasons. Large subsidence rates at single benchmarks are often caused by a movement of the support of the benchmark, e. g. building, bridge, driven pile, w.r.t. the ground. At 1 % of the benchmarks a vertical rate below −2 mm/a is observed. Large uplift rates occur more rarely (0.3 % of rates larger than +2 mm/a) and may be caused by construction works or a mismatch of benchmark identities. As this work is mainly interested in tectonic displacements, outliers are filtered out using a spatial filtering of the vertical rates described in Zippelt & Dierks (2007). The filter tests all rates within a 5 km × 5 km moving window for outliers. The residuals w.r.t. an adjusted "plane" calculated from the vertical rates are statistically analysed in every window position. In order to improve the performance of the spatial filter, the largest displacement rates are previously excluded from the dataset (101 vertical rates less than −5 mm/a or larger than +2.5 mm/a). The vertical rates at 1,265 benchmarks (8 %) are excluded within the spatial filtering of outliers.

For a better interpretation of subsidence and uplift rates, a geological assessment of the quality of a levelling benchmark is advisable, e. g. performed for benchmarks in Southern Germany and Northern Switzerland by Fuhrmann & Zippelt (2013). Within the assessment, the benchmarks are visited in situ and classified w.r.t. the geological setting and the stability of the support of the benchmark. Based on the classification, different visualisations of the resulting velocity field are possible displaying only high quality benchmarks or benchmarks mounted directly at bedrock. This kind of filtering may deliver a detailed insight into the tectonic displacement field of a region. Since the geological assessment is very time-consuming, such a filtering has not been performed for the total set of benchmarks of the URG levelling network.

4.5.4 Discussion of final results

The final result for the remaining 14,098 vertical rates from kinematic adjustment is displayed in Fig. 4.18. The standard deviations of the estimates are shown in Fig. 4.16(b). With a mean value of 0.18 mm/a (90 % < 0.3 mm/a), the standard deviations are small compared to standard deviations of the estimates from GNSS and InSAR, see Sect. 5.3 and 6.5, respectively. Most of the vertical rates (93 %) are in the range of −0.5 to +0.5 mm/a, which leads to the conclusion that the URG area is exposed to small deformations compared to other regions on Earth, e. g. close to plate boundaries or active volcanoes.

Particularly, east of the river Rhine, the spatial resolution is high enough for an interpretation of the vertical velocity field w.r.t. local and regional deformation processes. West of the river Rhine an interpretation is more difficult because of the sparse spatial resolution and the poorer accuracy, see Fig. 4.16(b). Most of the vertical rates in the French part of the network are larger than the rates in the other regions which is partly due to the data quality as well as temporal and spatial resolution of the measurements. In general, the estimated rates are smaller than results presented in previous investigations of levelling measurements in the URG area where less data were available (Mälzer et al., 1983, 1988; Zippelt, 1988; Demoulin et al., 1998).

Some non-tectonic features are still visible in the vertical rates, even if large outliers and strongly non-linear movements have already been filtered out. Most of these features are related to the underground activities presented in Sect. 2.4. The subsidence close to the city of Landau coincides with oil extraction since 1955 and is further investigated in a static height comparison (Sect. 4.6.2) and in combination with GNSS and InSAR data (Sect. 6.5.5). The large subsidences and uplifts at the border between France and Saarland, Germany (near the city of Saarbrücken), are caused by coal mining activities in northern Lorraine and southern Saarland, mainly between the beginning of the 19th century and the end of the 20th century. The levelling line crossing the VG in E–W direction follows the Silver Valley (Val d'Argent), where silver

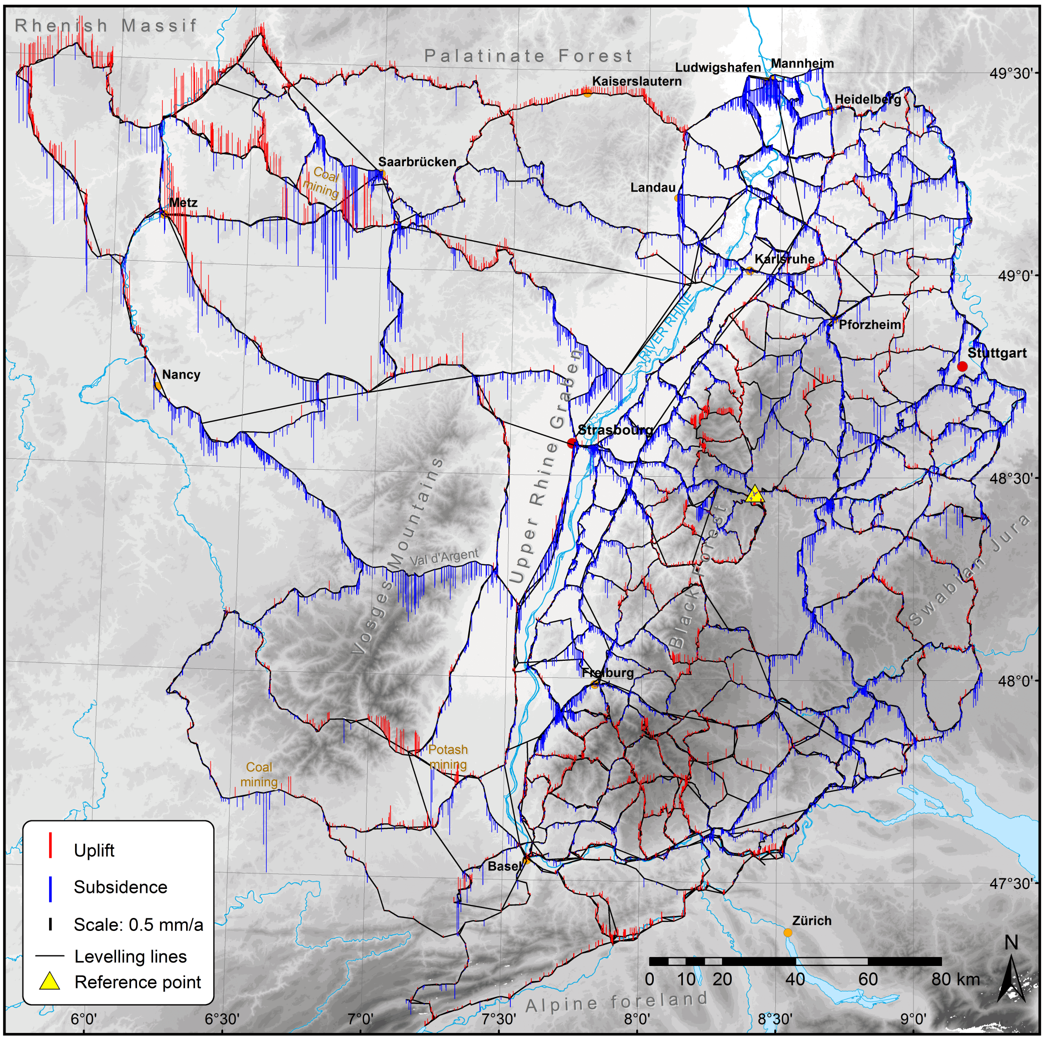

Figure 4.18: Vertical displacement rates in the URG area after spatial filtering of outliers. The displacement rates are calculated using levelling data covering a period from 1867 to 2012. The reference point is located at a church in Freudenstadt (8.411°E, 48.463°N).

was extensively extracted in the Middle Ages. The system of pits and underground tunnels still exists, possibly inducing the subsidence of the levelling benchmarks located in this area. The larger subsidences north of Strasbourg are possibly caused by mining of quartz sand and gravel in the vicinity of the levelling benchmarks. In the area of Mannheim/Ludwigshafen, the subsidences of about -0.5 to -1.0 mm/a are at least partly caused by groundwater extraction for industrial purposes. A strong correlation between the groundwater level and the subsidence is visible from static comparisons of levelling data, where a low groundwater level between the 1960s and 1980s correlates with velocities larger than 1 mm/a. From hydrogeological models and historical groundwater records, Wolf (2014, p. 50 ff.) found that these local subsidence processes in Mannheim/Ludwigshafen last over several decades causing a total subsidence up to 1 m.

A proper separation of anthropogenic surface deformations from tectonic movements is challenging and needs information from various geosciences. Nevertheless, the rates shown in Fig. 4.18 allow for the derivation of some general tectonic features, which fit well to the geological and tectonic context of the URG (Illies, 1979; Illies et al., 1981). The graben itself is mainly subsiding with velocities of about -0.2 to -0.5 mm/a, caused by a superposition of tectonic subsidence and sedimentary load, see Eisbacher (1996, p. 249 ff.). The shoulders of the graben, particularly the BF in the east, the Palatinate Forest and the VG in the west reveal slight uplifting tendencies up to 0.3 mm/a relative to the reference point located in Freudenstadt, see Sect. 4.5.2. The subsidence pattern in the region south of Stuttgart (-0.2 to -0.4 mm/a), studied based on the results of this work by Tschan (2013), may at least partly be caused by natural geochemical processes in the subsurface. The two levelling lines crossing the Swabian Jura reveal a slight uplift of about 0.1 mm/a, which is documented by Strasser et al. (2009) from a geological point of view and likely causing the karstification of the Swabian Jura. The uplift tendency towards the northwest Alpine foreland, particularly west of Zürich, was already observed in previous publications (Schlatter, 2013; Fuhrmann et al., 2013b) and is part of the Alpine uplift which increases to more than 1 mm/a in the Central Alps. Although the rates in the French part of the network seem to overestimate the real movements, the trend is mostly compatible with geological and tectonic settings. This holds particularly for the uplift in the northwestern part of the network, which might be a tail of the Plateau Uplift of the Rhenish Massif (Illies & Fuchs, 1983).

In order to investigate the movements of the graben w.r.t. the shoulder areas, four velocity profiles are derived from the estimated rates. Fig. 4.19(a) shows the location of the profiles crossing the graben in W–E and WNW–ESE directions. The profiles use all data perpendicular to the profile axis within a buffer of 1 km and display the vertical rates and the standard deviations along the axis from west to east.

Profile 1 in Fig. 4.19(b) nicely illustrates the relative uplift of the Palatinate Forest west of the URG w.r.t. the graben. The transition zone is well-documented by several groups of levelling benchmarks revealing a smooth gradient when crossing the western border fault (WBF). The relative subsidences are largest in the eastern part of the graben where the *Heidelberger Loch* is located, see Sect. 2.2. East of the graben the vertical rates are increasing, however, the rates do not reach the same vertical level of the part west of the graben. At profile 2 only few benchmarks are located within the graben. About 20 km before the WBF is reached a descending gradient can be observed, which may be connected to the Saverne depression zone. At the eastern border fault (EBF), an ascending gradient is present followed by stronger subsidence east of the graben, which is likely connected to the loose fluvial sediments present at the benchmark locations along a river valley towards the BF. Along profile 3, the observed displacement rates are small. However, one can observe an ascending gradient from the centre of the graben to the BF. Profile 4 again contains only few benchmarks in the western part. The relative uplift in the centre of the graben determined by only a few benchmarks is possibly superimposed by non-tectonic deformation. The largest subsidence is found in a tectonically active part, in which two branches of the Rhine river fault (RRF) are located, investigated in detail in Sect. 4.6.1. A large ascending gradient is then observed along the further course of the profile crossing the EBF towards the BF.

In general, it can be stated that the northern and the southern segment of the URG are exposed to larger tectonic movements compared to the central part, which reveals only small deformation gradients. From a scientific point of view, it would be desirable to have repeated levelling measurements along profiles similar to the ones shown in Fig. 4.19(a), in order to study the tectonic settings of active faulting in the URG and its border areas. However, the resulting vertical rates presented in Fig. 4.18 and 4.19 deliver important boundary conditions for numerical models of faulting mechanisms in the URG area.

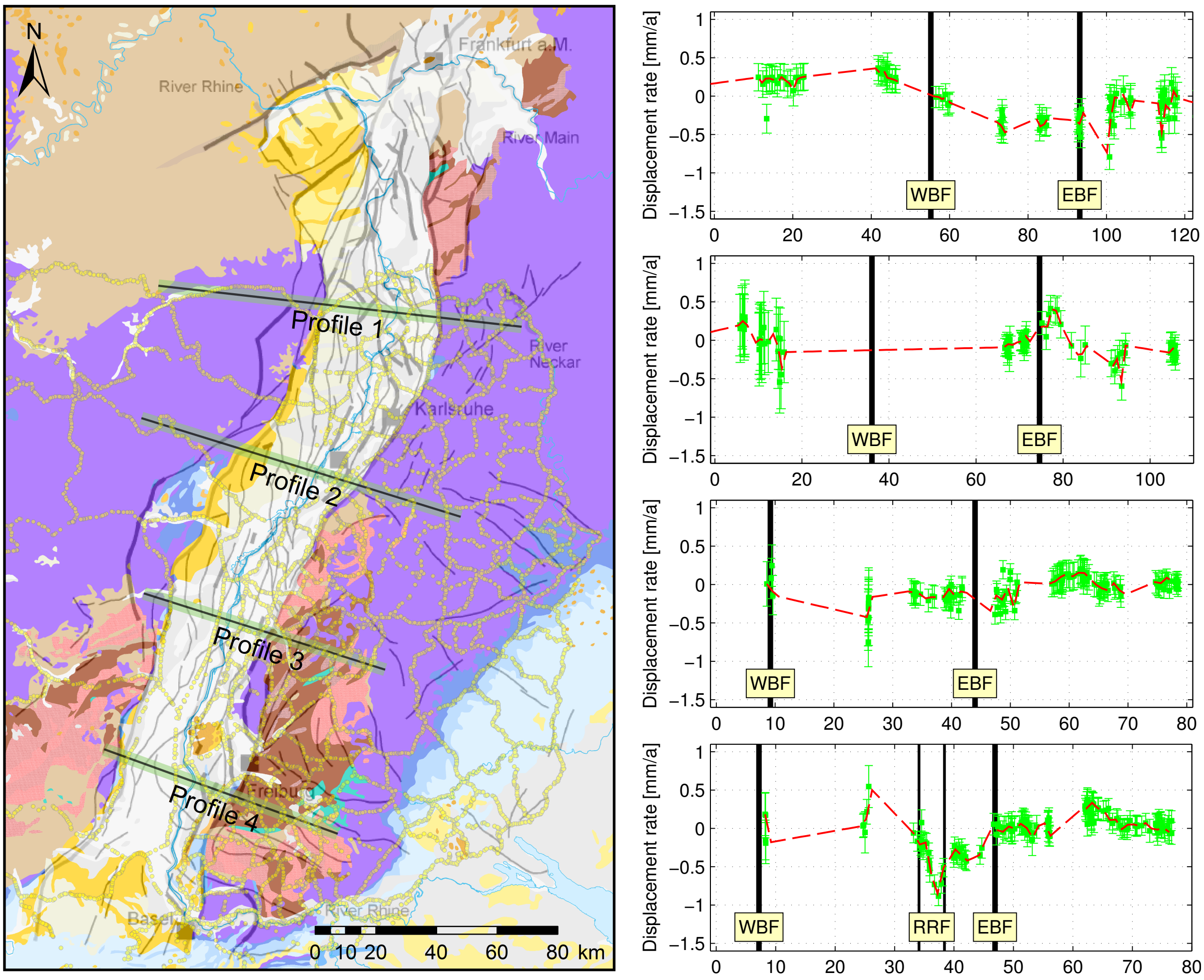

(a) Location of the profiles

(b) Vertical rates along the profiles 1–4 (from up to down). Red line: moving average of the rates.

Figure 4.19: Profiles of vertical rates crossing the URG from western to eastern directions. The locations of the profiles are given w.r.t. a geological map provided by OneGeology (BGS, 2015, legend given there as well and partly in Fig. 4.20(a)) and faults given by Peters (2007, p. 166). Yellow dots represent the location of levelling benchmarks of the analysed network. WBF: western border fault, EBF: eastern border fault, RRF: Rhine river fault. The green error bars in (b) represent the standard deviations of vertical rates resulting from the kinematic adjustment.

4.6 Static comparisons along levelling lines

The principle of a static comparison of levelled heights was already introduced in Sect. 3.1.3. Starting at a presumably stable point, heights are calculated by subsequently adding the measured height differences between levelling benchmarks. Height changes then follow from a comparison of the heights of different measurement epochs. A static comparison of heights along a levelling line crossing a fault enables detailed insight into surface movements related to tectonic activity of the fault. Resulting height changes along fault-crossing levelling lines in the southern URG are presented in Sect. 4.6.1. In addition, a static comparison is useful if the temporal characteristics of a (anthropogenic) deformation phenomenon shall be investigated. Sect. 4.6.2 presents a case study of strongly non-linear surface movements close to the city of Landau, where oil is extracted since 1955. Both analyses shown within this section use the static approach based on raw levelling measurements which have only been corrected for the influence of gravity using a normal correction along with measured surface gravity, see Sect. 4.3.

4.6.1 Levelling lines close to Freiburg

A static comparison of heights in different epochs is performed in the southern URG close to Freiburg, where a first-order levelling line crosses the eastern border fault (EBF). The tectonic situation in this area is complex with several faults and fault blocks located in the graben. The first-order levelling lines and the geological setting of the area are shown in Fig. 4.20(a). Starting at benchmark A (right-hand side in Fig. 4.20(a)), heights are calculated for the benchmarks along levelling lines 603 and 601 as well as along levelling lines 603 and 639. Different measurement dates within one epoch are neglected. Due to its small displacement rate from kinematic adjustment (-0.02 mm/a) and its geological situation, benchmark A is considered to be stable. Furthermore, benchmark A was measured in all four epochs and is therefore taken as a reference point for the static analysis. In Fig. 4.20(b) the height changes between the first and the subsequent measurement epochs are shown along both tracks between benchmark A and benchmark E and between benchmark A and benchmark Z, respectively.

Following benchmarks B–C–D–Y, the lines 601 and 639 cross several fault strands. Between benchmark B, located in front of the EBF near Freiburg, and benchmark C, located close to the western border fault of the Schönberg block (SBB), a significant subsidence is visible during all measurement epochs. Following line 601 towards south a strong anomaly caused by mining activities becomes obvious close to benchmark E. From 1928 to 1973 potash was extracted close to the village Buggingen located in the URG, see Röhr (2014). The mining activities lead to a subsidence of more than 6 cm between the first and the second measurement epoch at benchmark E. Between the second and the third measurement epoch the subsidence accumulates to about 10 cm. Finally, between the last two measurement epochs, and thus after potash mining was stopped, only a small additional subsidence is seen (Fig 4.20(b), top). This example shows that anthropogenic influences may significantly superimpose potentially existing tectonic deformation patterns in the URG. However, it is hard to believe that local mining effects are responsible also for the negative height changes near Freiburg (at benchmarks B–C), which is located at a distance of more than 20 km.

Along levelling line 639 shown in Fig 4.20(b), bottom, a sudden negative height change is visible at benchmark Y, which is close to a crossing point between the Weinstetten Fault (WSF) and the RRF. Towards benchmark Z the displacements are decreasing ending up close to zero. A mining effect is not known for this area. Fig. 4.21 shows a comparison of the last two campaigns, where a larger number of revisited benchmarks allows for a more detailed

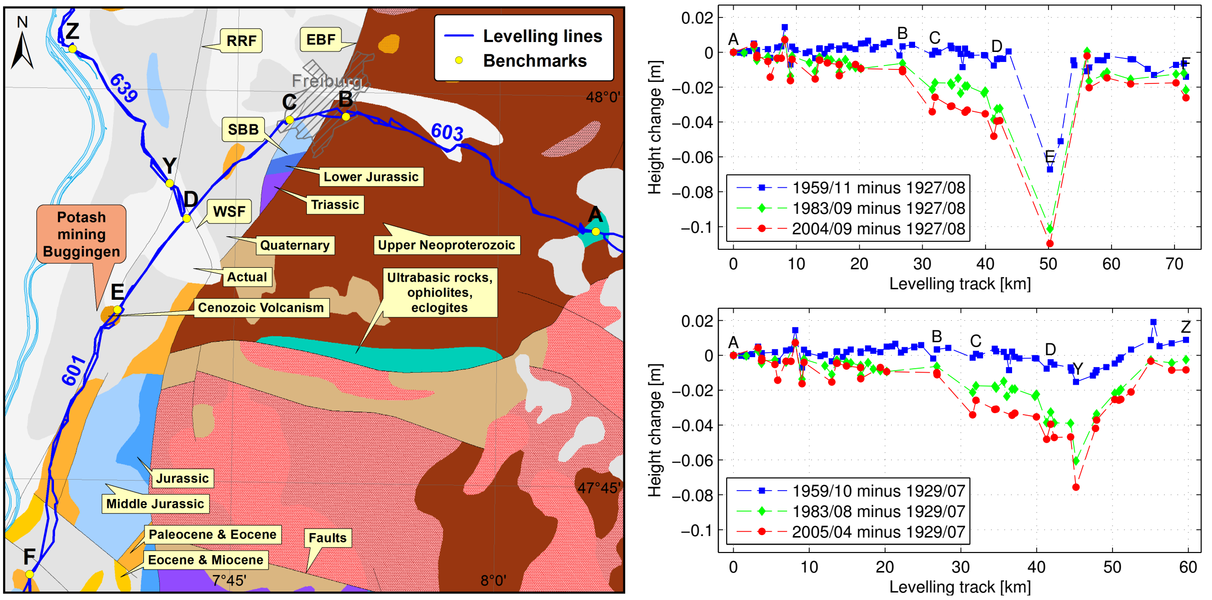

(a) Location of the levelling lines and benchmarks

(b) Height changes along levelling lines 603 and 601 (top) and along levelling lines 603 and 639 (bottom).

Figure 4.20: Height changes between the first epoch and later epochs along levelling lines close to Freiburg. Benchmark *A* is kept fixed. Dates correspond to the average of observation times. The location of the lines and benchmarks is given w.r.t. a geological map including faults provided by OneGeology (BGS, 2015). EBF: eastern border fault, RRF: rhine River fault, WSF: Weinstetten fault, SBB: Schönberg block.

study. It turns out that the already mentioned significant height change between benchmarks *B*–*C* coincides with the location of the EBF, see Fig. 4.20(a). The subsidence accumulates to 1.0–1.5 cm in 22 years and prevails until benchmark *Y*. Close to this benchmark, the levelling line crosses the RRF, which is marked by a sudden offset of about −0.7 cm. Afterwards, the subsidences are decreasing, reaching the zero level within three kilometres.

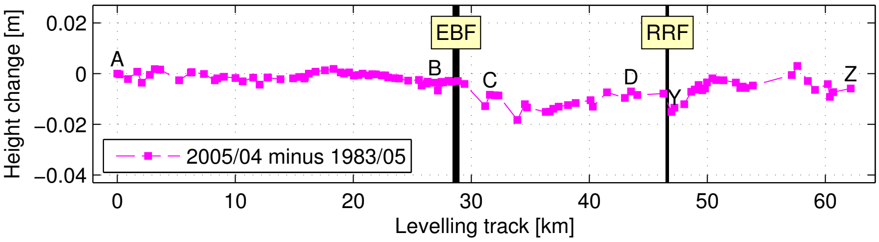

Figure 4.21: Height changes between the latest two measurement epochs along levelling lines 603 and 639. Benchmark *A* is kept fixed, dates correspond to the average of observation times. EBF: eastern border fault, RRF: Rhine river fault.

There are some arguments that the levelling results on lines 603 and 639 reflect ongoing tectonic processes. The subsiding area is situated in or at least close to a releasing bend regime caused by a trend change of the URG from N to NNE (Buchmann & Connolly, 2007). According to Behrmann et al. (2003), the levelling lines cross actively moving fault segments between *B*–*C* (EBF) and near *Y* (RRF). Fault activity is deduced from recent earthquake clusters, see

Fig. 2.8, their hypocentres fitting well to the downdip projections of the faults. Taking into account that the fault planes near the eastern border of the URG dip towards west or southwest, the observed subsidence is compatible with normal faulting or oblique strike slip in a transtensional regime. This fits to the conclusions of Lopes Cardozo & Behrmann (2006) who obtained a predominating normal faulting mechanism along the RRF south of 48°N from a compilation of fault plane striation measurements at geological outcrops of the URG main border faults. Thus, the levelling results may be interpreted as indicators for active faulting south of Freiburg.

Although the temporal resolution of the levelling campaigns is rather coarse, the sequence shown in Fig. 4.20(b), bottom, suggests that the observed subsidence is not due to episodic slip but rather reflects continuous motion. However, the rates seem to be larger between the second and third epoch (1959–1983), indicating that the deformation process is either nonlinear in time, or that systematic effects deteriorate the determination of height changes, see Sect. 4.2.2. Another important issue is whether the inferred slip occurs on creeping or locked faults. At an aseismically creeping fault segment, a relative offset between two benchmarks located on different sides of the fault would be observable in the heights of different measurement epochs, as for example near benchmark Y. In contrast, the gentle slopes of the displacement profile between km 28–33 and km 47–50 in Fig. 4.21 are more compatible with a fault model that is effectively locked in the upper part of the crust and stably sliding below. This conclusion is in contrast to the findings of Demoulin et al. (1998), who concluded that the faults in the southern URG are creeping aseismically.

The discussion demonstrates that the archived levelling data of the surveying authorities enables to deliver detailed information on fault movement and tectonic deformation in the URG area. However, a potential interference with non-tectonic processes has always to be kept in mind. Long-term hydrological trends result in changes of the pore pressure and likely influence the vertical motion measured at the surface. Provided that the faults create impermeable barriers for groundwater flow or pore pressure diffusion, a regional subsidence phenomenon delineated by faults as observed in Fig. 4.21 is conceivable. Additional information is necessary for a separation of effects and a proper interpretation of the resulting height changes at the surface.

4.6.2 Levelling lines close to Landau

The second example for a static analysis deals with an interesting surface deformation close to the city of Landau in the northern URG. The vertical rates from kinematic adjustment already show significant subsidences of 3 mm/a and more north of Landau, see Sect. 4.5.4, shown in detail in Fig. 4.22(a). Within the iterative adaption of the displacement model as described in Sect. 4.2.4, nine benchmarks close to Landau had to be handled in a special way to model their non-linear motion behaviour. As oil is extracted north of Landau since 1955, it seems reasonable that the observed subsidences are related to the anthropogenic activities and corresponding compaction of the ground. The levelling line crossing Landau and the oil field from south to north was measured in seven epochs, and is therefore optimally suited to investigate the temporal characteristics of the displacements in detail. A static comparison of the available levelling data measured between 1955 and 2009 was performed by Wampach (2012). Fig. 4.22 shows the location of analysed benchmarks along the levelling line running from Kandel to Neustadt via Landau, as well as the resulting height changes from the static comparison of levelling data.

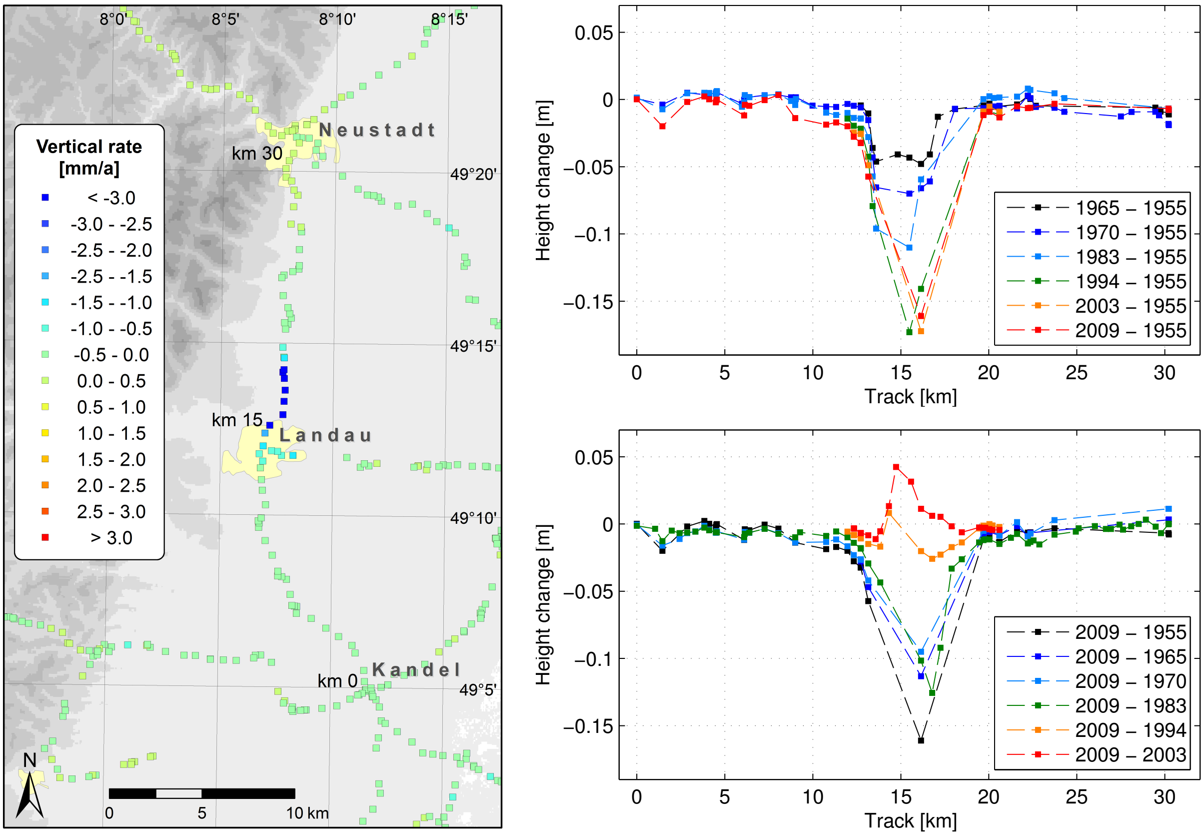

(a) Vertical rates at levelling benchmarks from kinematic adjustment

(b) Height changes at the levelling benchmarks w.r.t. the first epoch (1955, top) and w.r.t. the last epoch (2009, bottom).

Figure 4.22: Height changes at levelling benchmarks along the levelling line Kandel–Landau–Neustadt (northern URG). A benchmark in Kandel is kept fixed and used as starting point of the analysis. Dates correspond to the average of observation times.

In Fig. 4.22(b), top, the first measurement epoch (1955) is taken as a temporal reference and the heights of all other measurement epochs are subtracted from the heights calculated from the 1955 measurements. It becomes obvious that the total subsidence of the levelling benchmarks between km 13 and km 19 increases between the first five measurement epochs and sums up to about 17 cm in 1994. After 1994 no additional subsidence is observable. However, many benchmarks measured in the first epoch were lost over time in the area of interest, resulting in a sparse spatial resolution in the major subsidence area for the last two epochs (2003 and 2009). Hence Fig. 4.22(b), bottom, shows the reverse temporal differences using the 2009 measurements as a temporal reference and subtracting the height of all other epochs from the 2009 height calculations. From this figure, it becomes obvious that subsidence did not only stop after 1994, but turned around to an uplift of almost 5 cm. The uplift is likely related to local reinjections of the reservoir water which is removed from the oil within the production process. The deformation pattern close to Landau is further investigated using InSAR, which enables to observe the phenomenon with high spatial resolution, see Sect. 6.5.5.

4.7 Summary

- The vertical uplift/subsidence rates resulting from a kinematic adjustment of levelling data are mainly influenced by the network configuration, the selected reference point, the total time span of available data and the modelling of non-linear motions.
- A quality check of levelling data using loop misclosures is crucial, since levelling is susceptible to systematic errors which sum up over large distances.
- The influence of gravity on a kinematic adjustment is not significant as long as a similar measurement path is used in every epoch.
- Variance component estimation is an appropriate tool to handle levelling data of different epochs and countries, and thus different accuracy levels.
- The kinematic adjustment of 40,049 observations at 15,816 levelling benchmarks performed within this work resolves the vertical displacements of the URG area with unprecedented detail and accuracy.
- The major tectonic feature of the analysed region is a relative subsidence of the graben of 0.5–0.8 mm/a w.r.t. the shoulders.
- The velocity gradients observed at four profiles crossing the graben in W–E directions vary for different regions of the graben, while the northern and southern segments of the graben indicate larger tectonic-related displacements compared to the central segment.
- Anthropogenic displacements have been detected at several locations in the URG area and are related to groundwater usage, oil extraction and mining of minerals.
- Static comparisons of heights enable the possibility to pursue the spatio-temporal behaviour of displacements, which is particularly important for investigations of man-made deformations or at faults.

Chapter 5

GNSS Analysis

This chapter presents the results of the GNSS analyses performed in the URG area. The GPS observations acquired at 85 GNSS sites have been processed in differential mode applying state-of-the art strategies and parameters, see Sect. 3.2.3. The processing of the database was carried out by A. Knöpfler (GIK) using Bernese GPS Software (Dach et al., 2007). The key parameters of the processing as well as an overview of the results is given in Sect. 5.1. In Sect. 5.2 the resulting GPS coordinate time series are presented. In addition, the derivation of velocities from time series analysis is shown. Sect. 5.3 presents the resulting surface velocities and discusses the results for horizontal and vertical components w.r.t. the geological and geophysical setting of the URG area. For a proper tectonic interpretation of the results, strain rates are calculated from the horizontal velocity field. A case study on the 2004 Waldkirch earthquake demonstrates further possibilities of the interpretation of coordinate time series at permanent GNSS sites.

Parts of this chapter have already been published by the author in the following paper: Fuhrmann et al. (2015b). This publication is not explicitly cited within the text.

5.1 Differential GNSS analysis

A consistent post-processing of all available GPS observations acquired at GURN and surrounding EPN sites was performed by A. Knöpfler using Bernese GPS Software, Version 5.0 (BS5, Dach et al., 2007). The Bernese processing engine for double difference processing, denoted as RNX2SNX (Dach et al., 2007, p. 437 ff.), was applied to GPS observations with 30 s sampling rate. Reprocessed orbit, EOP and clock data were introduced, particularly in order to enhance the results of the code-based pre-processing. The elevation cut-off angle was set to 10° avoiding observations affected by strong atmospheric perturbations at low elevations. Phase ambiguity fixing is attempted for baselines up to 2000 km length based on the quasi-ionosphere-free resolution strategy (Dach et al., 2007, p. 443).

The troposphere model applied describes the total tropospheric path delay Δ_{slant} from a satellite to a receiving antenna. The model comprises a constant a priori value representing the dry part of the delay and three time-dependent parameters representing the wet part of the delay, induced by atmospheric water vapour:

$$\Delta_{slant} = \Delta_{apriori} \cdot MF_d(z) + \Delta_U \cdot MF_w(z) + \Delta_N \cdot \frac{\partial MF_w(z)}{\partial z} \cdot \cos A + \Delta_E \cdot \frac{\partial MF_w(z)}{\partial z} \cdot \sin A \quad . \tag{5.1}$$

Δ^U denotes the wet delay in zenith directions, whereas Δ^N and Δ^E correspond to horizontal troposphere gradient parameters as described by Meindl et al. (2004). The gradient parameters model a possible tilting of the tropospheric zenith and depend on the azimuth A of the GNSS observations. For the calculation of a slant delay, the site-specific, constant a priori value and the time-dependent parameters have to be mapped into the direction of the satellite by application of a zenith-dependent mapping function MF and the corresponding derivatives w.r.t. the zenith angle z. A first-order approximation of a MF is given by $MF(z) = \frac{1}{\cos z}$. Further refinements incorporate latitude- and height-dependent parameters derived from global weather observations (Marini, 1972; Herring, 1992; Niell, 1996). A concise description of the MF used for mapping of dry and wet zenith delays into slant directions is given by Fuhrmann et al. (2010a, p. 18 f.).

The total atmospheric delay Δ_{total} in metric scale is deduced from a model based on the ideal gas law, such as the model given by Saastamoinen (1973):

$$\Delta_{total} = \frac{0.002277}{\cos z} \left(p + \left(\frac{1255}{T} + 0.05 \right) e - B_{corr} \cdot tan^2 z \right) \quad , \tag{5.2}$$

with pressure p and partial pressure of water vapour e in millibar, temperature T in Kelvin given at the observation site and height-dependent, tabulated values for the correction factor B_{corr}. Note that this model implicitly contains a zenith-dependent MF, which has to be replaced if one of the aforementioned refined MF is used. Eq. (5.2) can be split into an a priori value $\Delta_{apriori}$, representing the major part of the total delay, and a wet part representing time-dependent variations. $\Delta_{apriori}$ is then calculated from meteorological parameters p, T and e. As the meteorological parameters are not available for most of the GURN sites, they are extrapolated for the altitude of each site using time-independent default values from the so-called standard atmosphere. Finally, the time-dependent parameters Δ^U, Δ^N, Δ^E are introduced as unknowns within the adjustment of GPS data. While for the zenith delay Δ^U a rather high sampling is appropriate, e. g. one parameter every two hours, for the horizontal gradients a lower sampling rate is sufficient, e. g. one parameter set per day.

The key parameters of the differential processing applied to GPS data observed at permanently operating sites are summarised in Tab. 5.1. The data processing is performed sequentially based on daily parameter estimates for all sites with valid GPS observations at the corresponding day. In addition to the GURN sites, surrounding EPN sites are included in the BS5 baseline processing in order to introduce a datum for the coordinate estimates. The baselines are selected based on site quality and continuity, in a way that a core network of baselines exists over the whole analysed period.

Table 5.1: Key parameters and settings of the differential GPS data processing.

Observations	$L1$, $L2$
Sample interval	180 s
Stochastic model	elevation-dependent weighting ($\cos^2 z$)
Minimum elevation angle	10°
Orbits	CODE[1] final product, sample interval: 15 min
EOP	CODE[1] final product, sample interval: 24 h
Satellite clock corrections	CODE[1] final product, sample interval: 30 s
Troposphere model	Saastamoinen (dry, wet) along with Niell-MF (dry, wet) and horizontal gradients
Temporal resolution of site-specific troposphere parameters	2 h for Δ_U, 24 h for Δ_N, Δ_E
Antenna correction	PCO, absolute PCV (individual or IGS type-specific)

[1] CODE: Center for Orbit Determination in Europe (University of Bern)

The database covers a maximum period between 2002-01-01 and 2011-06-27. The IGS changed the reference frame from IGS05 to IGS08 on 2011-04-17. A small shift is visible in the GURN coordinate time series at that date, which is mainly attributed to IGS antenna calibration updates (Rebischung et al., 2012). Therefore, only data until 2011-04-16 is used in the time series analysis, see Sect. 5.2.1. In addition, the ITRF solutions reveal slight inconsistencies w.r.t. IGS reference frames and the corresponding products. However, for the regional network analysed within this work, these differences are considered to be negligible, particularly as the major trend of the Eurasian plate is subtracted in order to resolve the relative movements of the URG area, see Sect. 5.2.2.

5.2 Displacement estimation from differential coordinate estimates

Within this section, strategies and results for the computation of displacements from differential GNSS coordinate estimates are presented. Sect. 5.2.1 introduces the coordinate time series resulting from the BS5 processing. In order to reveal the relative movements of the URG area, the trend of the Eurasian plate w.r.t. ITRF has to be subtracted, as discussed in Sect. 5.2.2. Finally, a sophisticated time series analysis using the CATS software (Williams, 2008) is presented in Sect. 5.2.3.

5.2.1 GPS coordinate time series

The basic subjects for the analysis of displacements from GNSS data are the coordinate estimates and their precision. Tab. B.2 in Appendix B shows the mean standard deviations of all coordinate estimates resulting from the BS5 parameter estimation, converted into North, East and Up components. In average, the mean standard deviations of all 85 GURN sites are 0.32, 0.43 and 1.42 mm for North, East and Up components, respectively. As commonly known from GNSS coordinate estimates, the standard deviation of the Up component is about a factor 3–4 worse compared to the horizontal components. Comparing individual sites, the coordinate estimates reveal a similar precision level. Some sites have significantly higher standard deviations, particularly in the Up component, such as BFO1 and WLBH. At these sites, GNSS observations at low elevation angles show a strong scattering due to shadowing by vegetation affecting the daily coordinate estimates, see also Knöpfler (2015, p. 88 ff.). The standard deviations of the daily coordinate estimates for the whole analysed period are exemplarily shown at site 0391 (Geislingen) in Fig. 5.1. Besides the higher standard deviation values for the Up component, a periodicity revealing higher standard deviations in the summer months is observed, also present at all other analysed GURN sites. The effect is larger for the standard deviations of the Up component compared to the horizontal components and likely caused by stronger tropospheric variations during summer. Following Beutler et al. (1988, p. 41), relative troposphere biases cause primarily biased estimates of the Up component. In the summer months, the highly variable wet component has a larger relative influence on the total delay compared to the winter months. From the results of ray tracing profiles, Janes et al. (1991) show that the wet delay in zenith direction at 45°N is about 2 % of the total delay in January and about 7 % in July.

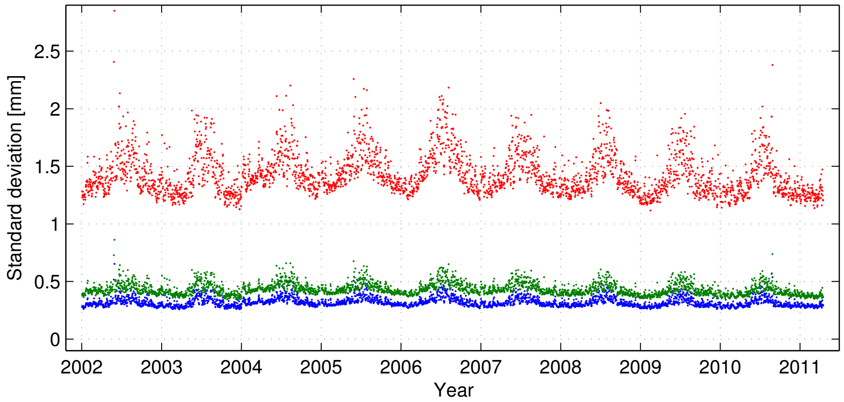

Figure 5.1: Standard deviations of daily coordinate estimates at site 0391 (Geislingen). East component: blue, North component: green, Up component: red.

In addition to the standard deviations, the mean velocities directly calculated from the coordinate estimates of BS5 are shown in Tab. B.2. If the time series of a site was split into several subsections because of documented antenna changes, the mean velocity of all subsections is given in the table. The datum of the network solution is attached to the movements of surrounding EPN sites w.r.t. ITRF2005. The general NE trend of the Eurasian plate is therefore visible as a main feature of the horizontal coordinate results, see Fig. 5.2 and Sect. 5.2.2. At site BIWI, large offsets of 20 to 70 cm are visible in the time series of the three coordinate components (North, East, Up), which largely influence the velocities at the site. After the date of the jump, i. e. 2010-07-05, the time series of the site reveals a significantly higher noise level. Data acquired after 2010-07-05 is therefore excluded from the time series of site BIWI. At the sites 0392, 0522, 0526 and PRNY, additional offset dates were introduced as a significant jump was visually detected within the time series. The mean values of the velocities of all GURN sites shown in Tab. B.2 are 19.49 and 15.80 mm/a for the East and North component, respectively, reflecting the NE trend of the Eurasian plate w.r.t. ITRF with a magnitude of approximately 2.5 cm. The initial horizontal coordinate time series are shown in Fig. 5.2 for site 0391, exemplarily for all other GURN sites.

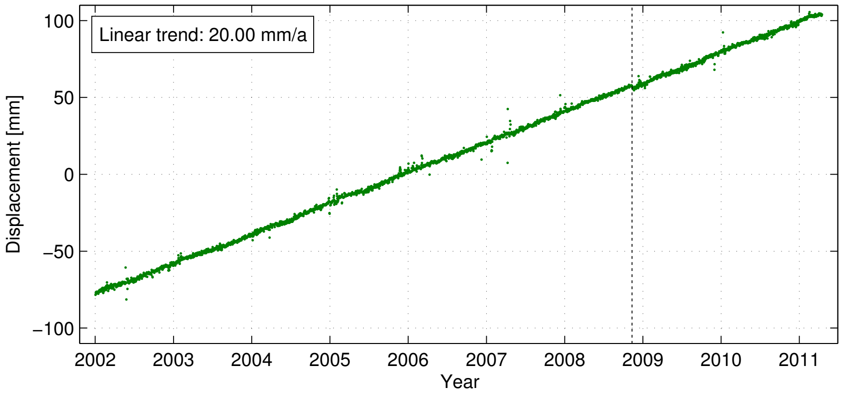

(a) East component

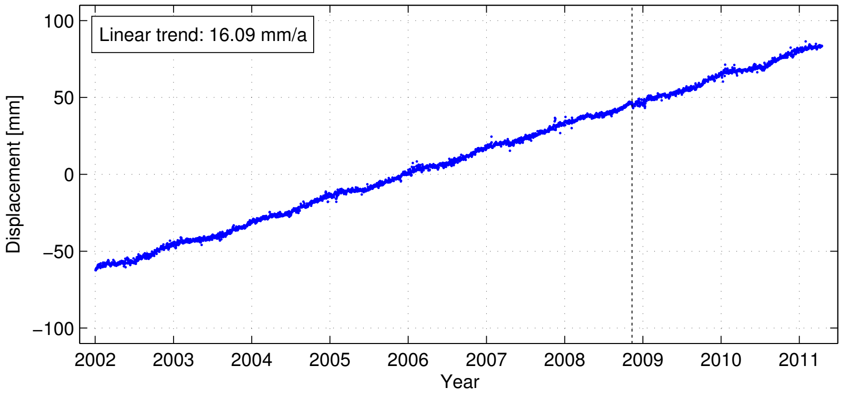

(b) North component

Figure 5.2: Coordinate time series at site 0391 (Geislingen) resulting from the analysis of GPS observations at GURN sites attached to surrounding EPN sites. The vertical dashed line marks the date of an antenna change at the site performed on 2008-11-12.

5.2.2 Euler pole estimation

As the coordinate estimates of the 85 analysed GURN sites are attached to the ITRF2005 coordinates of surrounding EPN sites, the main signal present in the coordinate time series reflects the movement of the Eurasian plate. In order to remove the Eurasian trend, the movement of the Eurasian plate at the location of every GURN site has to be calculated. Movements of tectonic plates are commonly modelled by a rotation of a spherical shell about a pole, the so-called Euler pole. The velocity vector $\vec{v}_j$ of an arbitrary location j on a tectonic plate is expressed by the cross product of the rotation vector $\vec{\omega}$, denoted as Euler vector, with the position vector $\vec{R}_j$, e. g. represented by Cartesian coordinates X_j, Y_j, Z_j (Lliboutry, 2000, p. 99 f.):

$$\vec{v}_j = \vec{\omega} \times \vec{R}_j = \begin{pmatrix} \omega_x \\ \omega_y \\ \omega_z \end{pmatrix} \times \begin{pmatrix} X_j \\ Y_j \\ Z_j \end{pmatrix} = \begin{pmatrix} 0 & Z_j & -X_j \\ -Z_j & 0 & X_j \\ Y_j & -X_j & 0 \end{pmatrix} \cdot \begin{pmatrix} \omega_X \\ \omega_Y \\ \omega_Z \end{pmatrix} \quad . \tag{5.3}$$

According to Aktuğ & Yıldırım (2013), $\vec{\omega}$ can be solved in a least-squares sense from several GNSS sites with known position coordinates and velocities:

$$\vec{v}_j = \begin{pmatrix} v_{X,j} \\ v_{Y,j} \\ v_{Z,j} \end{pmatrix} = A \cdot \hat{x} + e = \begin{pmatrix} 0 & Z_j & -Y_j \\ -Z_j & 0 & X_j \\ Y_j & -X_j & 0 \end{pmatrix} \cdot \begin{pmatrix} \omega_X \\ \omega_Y \\ \omega_Z \end{pmatrix} + e \quad . \tag{5.4}$$

Assuming an ideal network configuration with identical precision of the velocity estimates, the stochastic model is derived from the identity matrix I:

$$C_{yy} = \sigma_0^2 \cdot Q_{yy} = \sigma_0^2 \cdot I \quad . \tag{5.5}$$

The whole coefficient matrix A is formed by stacking of observations $v_{X,j}$, $v_{Y,j}$, $v_{Z,j}$ with corresponding position coordinates X_j, Y_j, Z_j in Eq. (5.4) for each site. The three components ω_X, ω_Y, ω_Z of the rotation vector $\vec{\omega}$, may be transformed to spherical coordinates, i. e. φ_P, λ_P, ω, by solving

$$\vec{\omega} = \begin{pmatrix} \omega_X \\ \omega_Y \\ \omega_Z \end{pmatrix} = \begin{pmatrix} \omega \cos\varphi_P \cos\lambda_P \\ \omega \cos\varphi_P \sin\lambda_P \\ \omega \sin\varphi_P \end{pmatrix} \quad , \tag{5.6}$$

where φ_P and λ_P represent the coordinates of the Euler pole and ω represents the rate of angular velocity.

Euler pole parameters of various tectonic plates for the ITRF solutions are published by Altamimi et al. (2007b, 2012) for ITRF2005 and ITRF2008, respectively. The Euler vectors have been calculated from a global combination of several space geodetic data sets, i. e. GNSS, Very Long Baseline Interferometry (VLBI), Satellite Laser Ranging (SLR) and Doppler Orbitography Radiopositioning Integrated by Satellite (DORIS). Using the published values of φ_P, λ_P, ω or w_X, w_Y, w_Z, the Eurasian trend of each GNSS site results from Eq. (5.3). On the other hand, applying the site velocity estimates at the GURN sites to Eq. (5.4), a local Euler pole can be estimated using least-squares adjustment of the observed site velocities. Within this work, the site velocities for the subtraction of the Eurasian trend are calculated from both the ITRF solutions and a local estimate of the Euler vector, and compared to each other, see Sect. 5.3.1.

After removal of the Eurasian trend the relative, intraplate velocities in the URG area become visible as displayed in Fig. 5.3 for site 0391. The horizontal displacements at the site are within a few mm. Particularly in the East component some large outliers are visible. In addition, it becomes obvious that the antenna change performed at 2008-11-12 provokes a significant jump in the time series attributed to differences in the antenna gain of the corresponding antennas. Periodic effects are particularly visible in the North component and likely caused by annual temperature changes affecting the building or the mount at which the antenna is attached to.

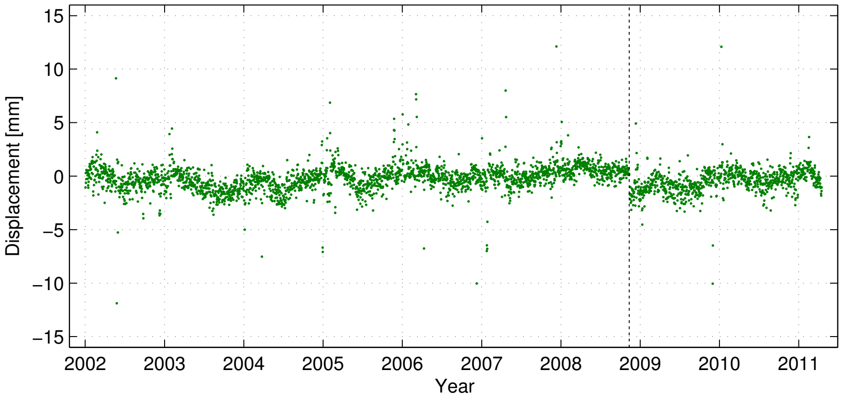

(a) East component

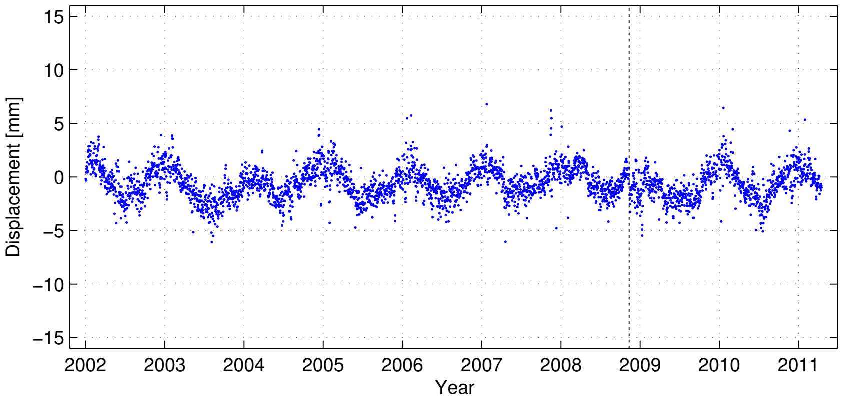

(b) North component

Figure 5.3: Coordinate time series at site 0391 (Geislingen) after removal of the Eurasian trend calculated from a local Euler pole estimate of the GURN sites. The vertical dashed line marks the date of an antenna change at the site performed on 2008-11-12.

5.2.3 Time series analysis using CATS

The representative example of a detrended time series shown in Fig. 5.3 illustrates several challenges for the determination of small movements at GNSS sites. The following issues deteriorate the estimation of a linear trend:

(i) periodic effects, particularly when the time series starts and ends in different seasons,

(ii) jumps in the time series, e. g. due to antenna changes,

(iii) unmodelled temporal correlations resulting in over-optimistic parameter estimates,

(iv) outliers in the daily coordinate estimates, e. g. caused by strong atmospheric effects, reduced amount of data at certain days or changes in the network geometry.

Items (i), (ii) and (iii) are handled within a GNSS time series analysis software provided by Williams (2008), called *Create and Analyze Time Series* (CATS). From the coordinate time series data at every GNSS site, the mean velocities in North, East and Up components and corresponding uncertainties are estimated. The coordinate time series of the three components (North, East, Up) are analysed independently at every site. The functional model of a sophisticated GNSS time series analysis considers a linear trend with constant velocity v together with the intercept b, time-dependent offsets $o(t)$ and periodic effects $p(t)$, see Gazeaux et al. (2013), resulting in

$$f(t) = vt + b + o(t) + p(t) + \epsilon(t) \quad . \tag{5.7}$$

Time-dependent noise $\epsilon(t)$ present in GNSS time series is handled within the stochastic model. Several noise models have been proposed by Williams (2003b); Williams et al. (2004); Langbein (2008), such as white noise, flicker noise, power law noise, band pass noise or first-order Gauss-Markov noise, see also Luo (2013), and are applicable within CATS. The influence of different noise models on the velocity estimates and their uncertainties was studied by Leinen et al. (2013); Saleh & Becker (2014). They found that the influence of the stochastic model on the horizontal velocity components is negligible, whereas the uncertainties are varying for different methods. Using a combination of white noise and flicker noise, however, results in realistic estimates for the standard deviations of the three velocity components, particularly for the ratio between horizontal and vertical components.

Offsets in the time series are modelled using the date t_{off} at which a jump occurs and an offset parameter x_{off} (Williams, 2003a):

$$o(t) = k \cdot x_{off} \ , \ \text{with} \ k = 1 \ \text{for} \ t > t_{off} \ \text{and} \ k = 0 \ \text{for} \ t < t_{off} \quad . \tag{5.8}$$

At every date of a reported antenna change, an offset is estimated. The number of antenna changes is given in Tab. B.1 in Appendix B. Some of the resulting pieces of time series are noisy or cover only a short period of several days to months and thus deteriorate the parameter estimation. They are therefore excluded from the data set. At some sites, also receiver changes are visible as a significant jump of the coordinate time series, and thus an offset is estimated at the corresponding dates. Furthermore, four significant jumps have been detected and estimated at dates, where no activity at the site is documented (sites 0392, 0522, 0526, PRNY).

Periodic effects in geodetic time series are modelled using sinusoidal harmonic functions as described by Davis et al. (2012). Two coefficients b_1 and b_2 are applied to model a sinusoidal effect with periodicity T:

$$p(t) = b_1 \sin(\frac{2\pi}{T}t) + b_2 \cos(\frac{2\pi}{T}t) \quad . \tag{5.9}$$

The coefficients b_1 and b_2 can also be transformed to amplitude A and phase ϕ of the signal:

$$A = \sqrt{b_1^2 + b_2^2} \quad , \tag{5.10}$$

$$\phi = \arctan \frac{b_1}{b_2} \quad . \tag{5.11}$$

Within CATS, different cycle durations T, and also combinations of several T, can be applied to the model. As the main periodic signal present in most of the coordinate time series at GURN sites reveals a yearly period, T is set to one year resulting in an annual sinusoidal function.

In addition to the parameter estimation within CATS, outliers present in the coordinate time series have to be filtered out (iv) in order to provide reliable estimates for the linear trend, the sinusoidal function and potential offsets. The outlier filtering is performed iteratively, in a way that the largest coordinate residuals w.r.t. the full model function given in Eq. (5.7) are eliminated before CATS is rerun. The threshold for the outlier detection is reduced in every iteration step, starting with 10 and 30 mm for the horizontal and vertical components, respectively, and ending with 4 and 12 mm. Fig. 5.4 shows the filtered coordinate time series of site 0391 along with the estimated model function (red curve). The major result of the GNSS analysis is the linear trend (black curve), further discussed and presented in Sect. 5.3.

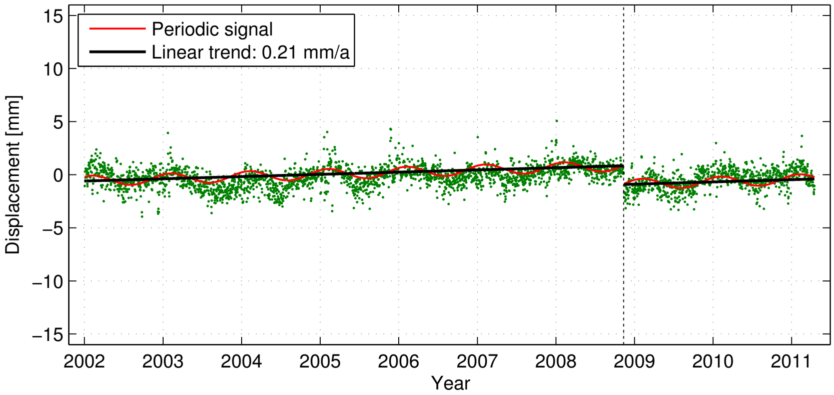

(a) East component

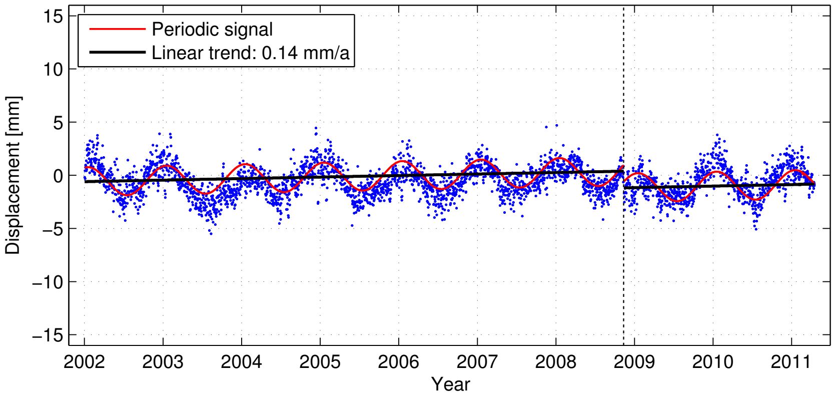

(b) North component

Figure 5.4: Coordinate time series at site 0391 (Geislingen) after removal of the Eurasian trend calculated from a local Euler pole estimate of the GURN sites and iterative outlier filtering. The linear trend is estimated together with an annual sinusoidal function and an offset using CATS. The vertical dashed line marks the date of an antenna change at the site performed on 2008-11-12.

5.3 Resulting surface displacements

The results of time series analyses at 85 GURN sites are mean velocities in East, North and Up components. Tab. B.3 compares the velocities resulting from a linear regression of each subsection of a time series with the velocity estimates of CATS including the modelling of jumps, periodic effects, temporal correlations and outliers present in the time series. It becomes obvious that the velocities resulting from linear regression of subsections at a site largely deviate. If the subsection covers a short time span, the estimated velocity may reach a large and thus unrealistic absolute value, e. g. at sites 0384 and PRNY, where the last subsections cover only 68 and 105 days, respectively. The mean absolute deviation of velocities is 0.42, 0.49 and 1.21 mm/a for the East, North and Up components, respectively, for the velocities resulting from linear regression and 0.34, 0.36 and 1.06 mm/a for the corresponding components resulting from the CATS analysis. Tab. B.3 also displays the uncertainties of the estimated velocities. From the estimates of linear regression, the standard deviations are unrealistically low if a large amount of data is available in the corresponding sections. The over-optimistic estimation of the parameter uncertainties is a consequence of the incorrect assumption that the observations, i. e. the daily coordinates, are stochastically independent. The standard deviations resulting from CATS are in the range of 0.05–0.49, 0.06–0.77 and 0.21–2.26 mm/a for East, North and Up components, respectively, with mean values at 0.18, 0.21 and 0.66 mm/a for the three components, see Tab. 5.2. Again, the ratio between vertical and horizontal uncertainties is about 3–4, see Sect. 5.2.1. The mean values of velocity uncertainties from CATS are three times larger than the mean values resulting from the linear regression of subsections (0.06, 0.06, 0.22 mm/a).

Table 5.2: Comparison of velocities and standard deviations for all investigated GURN sites and for a subset of 76 GURN sites with significant velocities: minimum (MIN), maximum (MAX) and mean absolute deviation (MAD) for each velocity component. Note that MAD for standard deviations is equal to the mean value.

	East [mm/a]			North [mm/a]			Up [mm/a]		
	MIN	MAX	MAD	MIN	MAX	MAD	MIN	MAX	MAD
Velocities									
all 85 GURN sites:	−0.52	1.50	0.34	−1.53	1.23	0.36	−2.29	2.50	1.06
subset of 76 GURN sites:	−0.52	1.04	0.33	−0.85	0.70	0.28	−1.99	2.11	0.98
Standard deviations									
all 85 GURN sites:	0.05	0.49	0.18	0.06	0.77	0.21	0.21	2.26	0.66
subset of 76 GURN sites:	0.05	0.49	0.17	0.06	0.51	0.18	0.21	2.17	0.56

It may be stated that the time series analysis using CATS provides more realistic estimates of linear rates and uncertainties at GNSS sites compared to a simple linear regression of subsections as the whole time span of observations is consistently analysed. Particularly, unmodelled periodic effects at the GNSS sites result in wrong estimates of linear rates if not a number of full cycles, starting and ending at the same season, is analysed. The velocity estimates resulting from the CATS analysis are presented and discussed in Sect. 5.3.1 and 5.3.2. Nine GURN sites are excluded from the visualisation of velocities, because the time span of observations is short (less than two years) or the observations are too noisy to estimate the CATS parameters given in Eq. (5.7) with significance, i. e. sites AUB2, BFO1, BIWI, BOU2, BOUR, ERCK, ETH2, FRI2, VSOL. Tab. 5.2 compares velocities and corresponding standard deviations for the full set of 85 GURN sites and for the remaining 76 sites. The velocities of the reduced subset of sites range within ±1.0 mm/a for the horizontal components and ±2.1 mm/a for the vertical component. Sect. 5.3.3 deals with the calculation of strain rates from the resulting horizontal velocity field. Sect. 5.3.4 presents an investigation of GPS coordinate time series at site 0390 (Freiburg) related to the 2004 Waldkirch earthquake, which was the largest seismic event in the last decades in Southwest Germany.

5.3.1 Horizontal surface displacements

In order to resolve the relative horizontal velocities present in the URG area, the general NE trend of the Eurasian plate, see Fig. 5.2, has to be subtracted as discussed in Sect. 5.2.2. First, the Eurasian trend is calculated using the Euler vector of ITRF2005, published by Altamimi et al. (2007b), as the GNSS analysis in BS5 is also based on ITRF2005 parameters, e. g. the EOP. Fig. 5.5(a) shows the horizontal velocities at 76 GURN sites relative to ITRF2005. A general ENE trend of site velocities is visible, also reflected by the mean values of site velocities of 0.60 and 0.17 mm/a for East and North component, respectively. In a second step, the velocities of eight time series at the sites 0384, 0386, 0389, 0391, 0394, 0396, 0397 and 0400 are averaged and subtracted from the velocity field in order to resolve the relative movements of the URG area w.r.t. a presumably stable block situated in the east of the network. Fig. 5.5(b) shows the resulting velocity field, which is now relative to the fixed block. The eight sites are selected as they represent a consistent velocity pattern w.r.t. ITRF2005. Furthermore, a location in the eastern part of the region was also chosen as reference point for the levelling analysis, see Sect. 4.5.2. However, this choice is arbitrary and a more sophisticated strategy of datum definition for regional GNSS networks is given with the estimation of a local Euler pole, presented in the following.

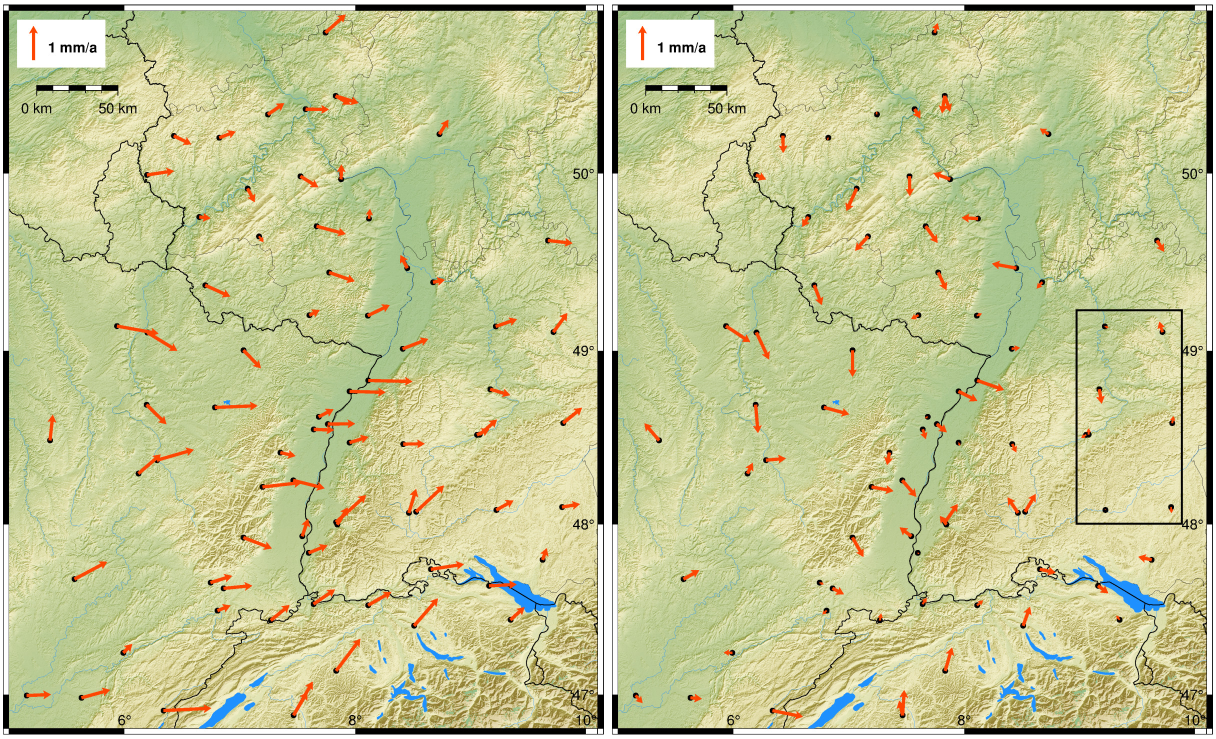

(a) Relative to ITRF2005

(b) Relative to a block in the east

Figure 5.5: Horizontal velocities at 76 GURN sites. The Eurasian trend calculated from the Euler vector parameters of ITRF2005 is subtracted (a). Furthermore, the average of eight velocity estimates in the eastern part of the network is subtracted, marked by a black rectangle (b).

Besides the velocity field solution relative to ITRF2005 along with the subtraction of a fixed block motion, a local Euler pole from the velocities at the 76 GNSS sites is calculated in order to obtain the relative movements of the URG region. Tab. 5.3 compares the parameters of the estimated local Euler pole with those valid for ITRF2005 and ITRF2008 (Altamimi et al., 2007b, 2012). The local Euler pole is located close to the ITRF Euler poles, northeast of the ITRF2005 Euler pole. The rate of angular velocity ω is slightly larger compared to the ITRF solutions. Fig. 5.6 displays the resulting velocities, using the estimated local Euler vector to calculate the main trend of the Eurasian plate. The corresponding site velocities are subtracted from the coordinate time series before the parameter estimation and outlier filtering is performed.

Table 5.3: Comparison of estimated Euler pole parameters for the URG region with ITRF Euler pole parameters.

	φ_P [°]	λ_P [°]	ω [°/Ma]
Local Euler pole	57.120	265.835	0.270
ITRF2005	56.330	264.021	0.261
ITRF2008	54.225	261.165	0.257

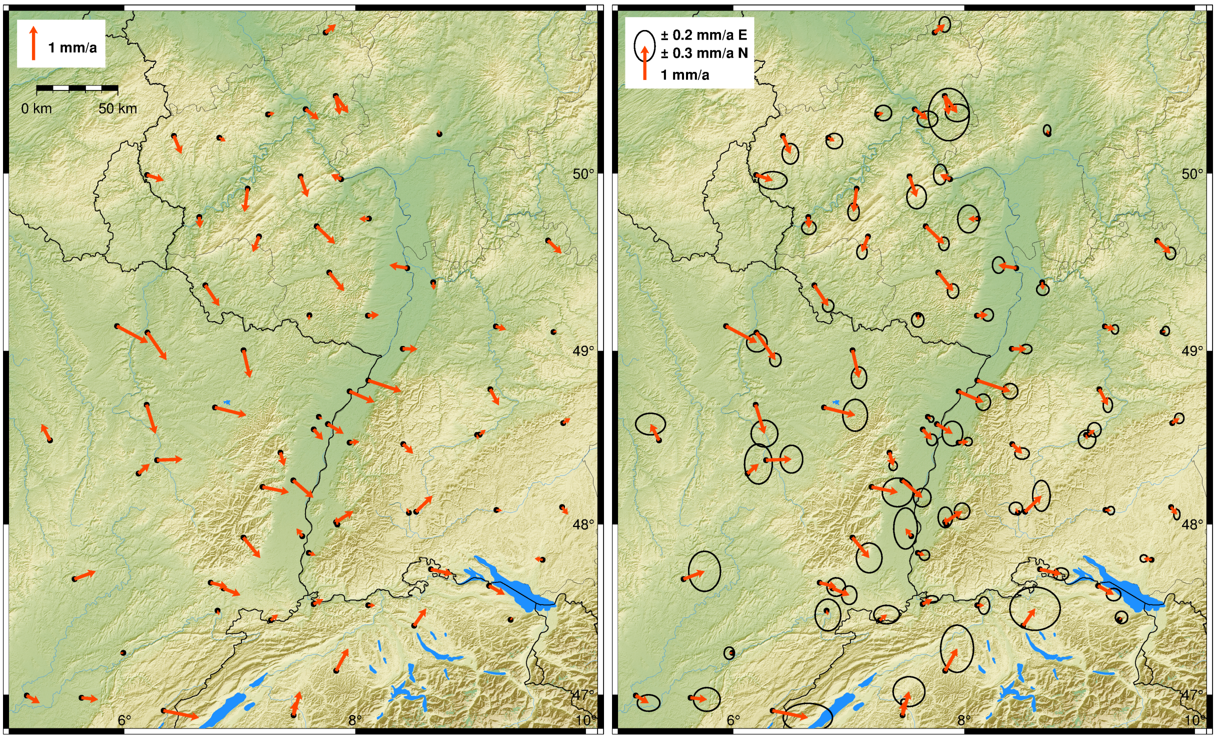

(a) Velocities

(b) Velocities and uncertainties

Figure 5.6: Horizontal velocities at 76 GURN sites. The Eurasian trend calculated from the parameters of the estimated local Euler pole is subtracted (a). In addition, confidence ellipses corresponding to the standard deviations of velocities are shown in (b).

Even if some of the velocities shown in Fig. 5.6 may be affected by local influences of the monumentation of the GNSS sites, some general trends are observable from the velocity field. The URG is clamped between SSE directed movements of the Rhenish Massif and NNE directed movements of the Alps, which is in general accordance with the kinematic model of the URG area published by Buchmann & Connolly (2007). The horizontal stress enforced by the Rhenish Massif and the Alps results in sinistral shearing at the graben shoulder areas as revealed from predominating strike-slip fault plane solutions of seismic records, particularly in the southern URG (Bonjer et al., 1984). Note that following the horizontal rates shown in Fig. 5.6, the southern URG is not subjected to extension, today, as reported from numerical models for earlier periods such as Chattian and Aquitanian (Schwarz & Henk, 2005). In the central and northern URG, an antithetic horizontal velocity field is observed in a region where the graben axis is bended. The restraining part of the bend is characterised by a progressive eastward velocity gradient at the sites 0521, KARL, 0381 and DRUS, while vanishing velocities with a slight west tendency are observed in the releasing part at sites 0387, 0520, 0529, 0518. The antithetic movements imply the existence of a sinistral shear zone between the two regimes in the northern and the central URG, which is compatible with the sense of shearing of the N–S to NNW–SSE striking Riedel faults crossing the graben in this area, see Fig. 2.6. As demonstrated by the $M_L = 2.8$ Speyer earthquake on 2005-02-10, most of the fault elements in this region are active, although the normal-faulting mechanism of this special event does not fit to sinistral shearing (Ritter et al., 2009). The existence of basin-crossing sinistral shear faults along with significant rotations of surface displacements is predicted from analogue as well as numerical models of transtensional, left-stepping strike-slip basins (Wu et al., 2009; Joshi & Hayashi, 2010).

The confidence ellipses given in Fig. 5.6(b) differ w.r.t. their magnitude and direction. Larger magnitudes generally correspond to shorter time series, e. g. at the Swiss sites, ETHZ and HUTT, where the time series cover less than two years. The confidence ellipses are smallest in Baden-Württemberg, where a total time span of more than nine years could be analysed at most of the GNSS sites. In most cases, the precision of the north component is slightly worse compared to the east component, which is attributed to effects of the satellite geometry in mid-northern latitudes. The horizontal uncertainties appropriately reflect the characteristics of individual time series w.r.t. the length of the time series, the general noise level, the number of jumps and the magnitude and consistency of periodic effects.

5.3.2 Vertical surface displacements

In contrast to the horizontal velocities, the vertical velocities estimated from the GPS time series do not show a significant pattern within the URG area. Fig. 5.7 compares the velocity estimates of the Up component resulting from CATS with the vertical rates estimated from levelling, see Fig. 4.18. Principally, the vertical velocities from GNSS estimates refer to the reference ellipsoid used, whereas the vertical velocities from levelling are related to the physical shape of the Earth. Due to the deflection of the vertical, the vertical rates from GNSS and levelling at the same location would be slightly tilted against each other. However, the deflection of the vertical reaches maximum values of some arcseconds, even in mountainous areas (Torge & Müller, 2012, p. 228 f.). The difference in the vertical rates caused by the deflection of the vertical is therefore negligible, even if the absolute displacements are in the order of several m. A more serious effect, which one should keep in mind when comparing the velocity estimates, is the different temporal baseline used for the calculation of velocities. While the vertical rates from levelling cover a time span of at least several decades at every location, the vertical rates from GNSS are obtained from time series of several years, only.

Consistent uplifting trends are visible in Fig. 5.7 for the Rhenish Massif and the Alpine foreland, albeit the magnitudes of 1.2 mm/a (mean value of 10 sites) and 1.4 mm/a (mean value of eight sites), respectively, considerably exceed geological estimates of the uplift in both regions. From the mean value of the vertical velocities of 0.6 mm/a, a general uplift trend of the investigation area is observed. The slight uplift tendency might eventually be related

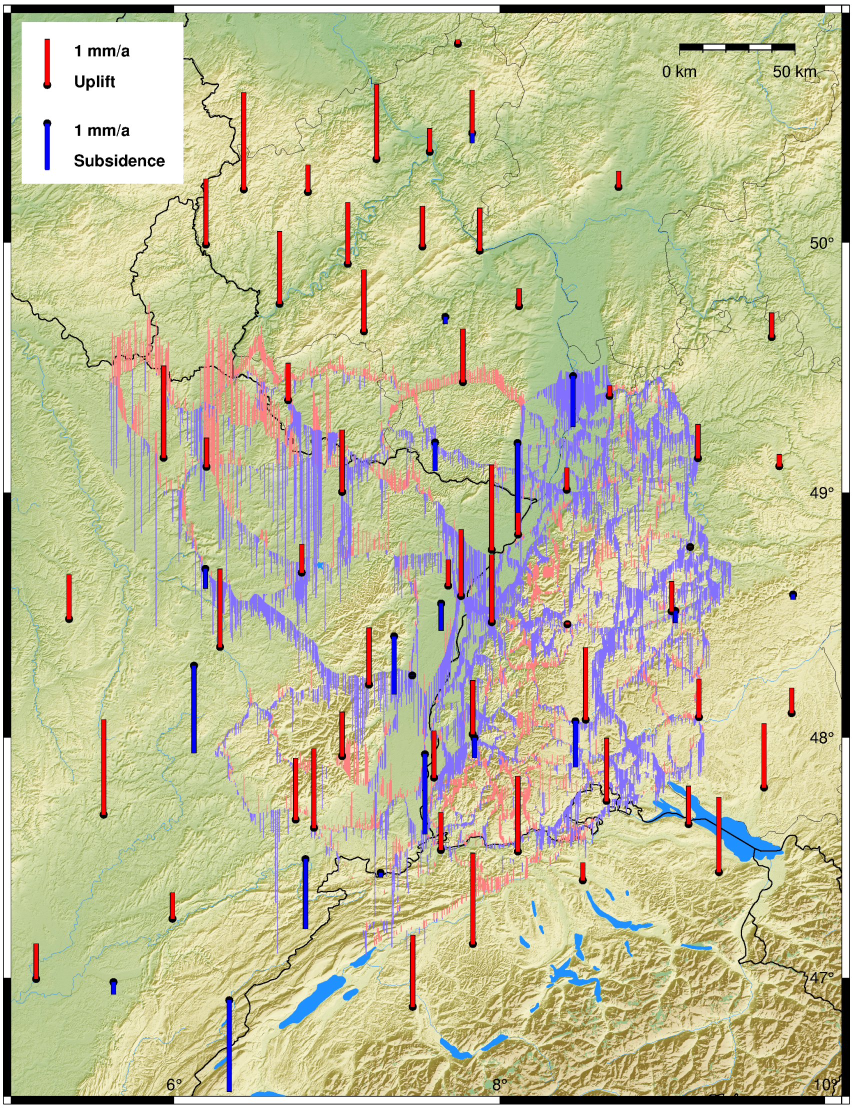

Figure 5.7: Vertical velocities at 76 GURN sites compared to the velocities at 14,098 levelling benchmarks (red and blue bars in the background), see Fig. 4.18. Note that the velocities of GPS and levelling are related to a different vertical datum.

to the solid Earth's viscous response to unloading of the late Pleistocene ice sheets (glacial isostatic adjustment, GIA). In contrast to the intraplate deformation of Central and Northern Europe, GIA has been unambiguously identified by space geodesy (Nocquet et al., 2005; Argus & Peltier, 2010; Lidberg et al., 2010; Peltier et al., 2015). However, the maximum uplift of more than 1 cm/a in Fennoscandia decreases toward zero in Central Europe. Predicted GIA-induced vertical rates in the URG are on the sub-mm/a level and depend on the used ice and earth models (Serpelloni et al., 2013; Peltier et al., 2015). As also the gradient of vertical and horizontal motion attributed to GIA is low in the URG area, GIA is regarded to have a small influence on the estimated velocity fields resulting from this work.

With values ranging between ±2 mm/a and a mean absolute deviation of 1 mm/a, see Tab. 5.2, the vertical velocities at the GNSS sites show larger magnitudes compared to the estimates at adjacent levelling benchmarks. In most areas, the velocities from GPS seem to overestimate the real movement. Only at locations with larger movements, a good fit between the vertical velocities is obtained, such as at sites 0520 (Ludwigshafen) and 0521 (Landau). A general pattern of similar velocities at nearby site locations as visible for the horizontal velocity components, see Fig. 5.5 and 5.6, is not observable for the vertical component. Previous investigations have shown that GNSS coordinate time series covering less than eight years are not able to resolve vertical movements below 0.5 mm/a with significance (Serpelloni et al., 2013). As the vertical rates from levelling are more accurate and available on a higher spatial resolution, the Up component of the velocities estimated from GPS is not used within the data assimilation in Chap. 7. In contrast to levelling, however, vertical coordinate estimates from GNSS provide a high precision over large distances. With increasing lengths of the coordinate time series, the Up component of GNSS velocity estimates will deliver useful information on vertical displacement rates in the investigation area in the future.

5.3.3 Calculation of tectonic strain

Strain is a measure of deformation and defined as a change in volume, surface, length or angle, see Eisbacher (1996, p. 37 ff.). Strain rates describe the change of strain w.r.t. time and can be inverted from a given velocity field, e. g. deduced from GNSS measurements. Although earthquakes cannot be predicted, they are preceded by the slow build up of tectonic strain. It is hence accepted that strain rates correlate to earthquake occurrences (Hagiwara, 1974; Shen et al., 2007). High strain rates correspond to a higher level of tectonic deformation (Crowley & Elliott, 2012). Thus, strong and devastating earthquakes almost exclusively occur in regions with high strain rates, mainly at the plate boundaries.

Tape et al. (2009) published a toolbox to calculate the strain rate tensor, which is deduced from the spatial velocity gradient, using spherical wavelets. The freely available strain rate calculation tool is applied to the horizontal GPS velocity field shown in Fig. 5.6. The spherical wavelets are based on different spatial supports represented by spherical grids of orders q. A minimum order q_{min} is selected w.r.t. the outer length scale of the GNSS network in a way that the support of the q_{min} wavelets exceeds the spatial extent of the network of about 450 km. For $q = 4$, the spatial support is 697 km and hence larger than the spatial extent of GURN. A maximum order q_{max} has to be chosen in order to stabilise the parameter estimation and to reduce the possibility of overfitting. q_{max} is strongly connected to the station density. In the case of GURN, typical site distances are between 20 and 40 km, which relates to grid orders of $q = 8$ or $q = 9$ and corresponding spatial supports of 43.6 or 21.8 km, respectively. Strain rate tensors are derived for the URG area from horizontal velocities at 74 GURN sites. The sites 0515 and BUAN in the very north and west of the network have been excluded as they are far away from the other sites and deteriorate the wavelet analysis. According to Leppäranta (2011, p. 69 f.), the magnitude of strain rates, denoted as total strain rate, follows from the Frobenius norm of the strain tensor, i. e. the square root of the sum of squares of all components of the strain rate tensor. The total strain rate contains hence both normal and shear strain, and is invariant to the direction of maximum strain axes. Fig. 5.8 displays the resulting total strain rates in the URG area for two different parameter settings of q_{max}.

The distribution of patterns with high total strain rates observed in Fig. 5.8 is similar for the two computation variants. Fig. 5.8(b) differs from Fig. 5.8(a) only in the central and southern part of the URG, where the site density is high. Maximum strain rates are in the order of $0.8 \cdot 10^{-8}$/a and $1.0 \cdot 10^{-8}$/a for the strain solution in Fig. 5.8(a) and Fig. 5.8(b), respectively. The strain rates are smaller by a factor of 30 compared to strain rates at plate boundaries, such as at the San Andreas fault ($3 \cdot 10^{-7}$/a, Tape et al., 2009), corresponding also to the ratio of surface displacements in both regions. It is remarkable that the strain rates calculated from the GURN velocity field correlate with major earthquake clusters in the URG, see Fig. 2.8(b). The largest signal is visible in the southern URG, which has a significantly higher number of

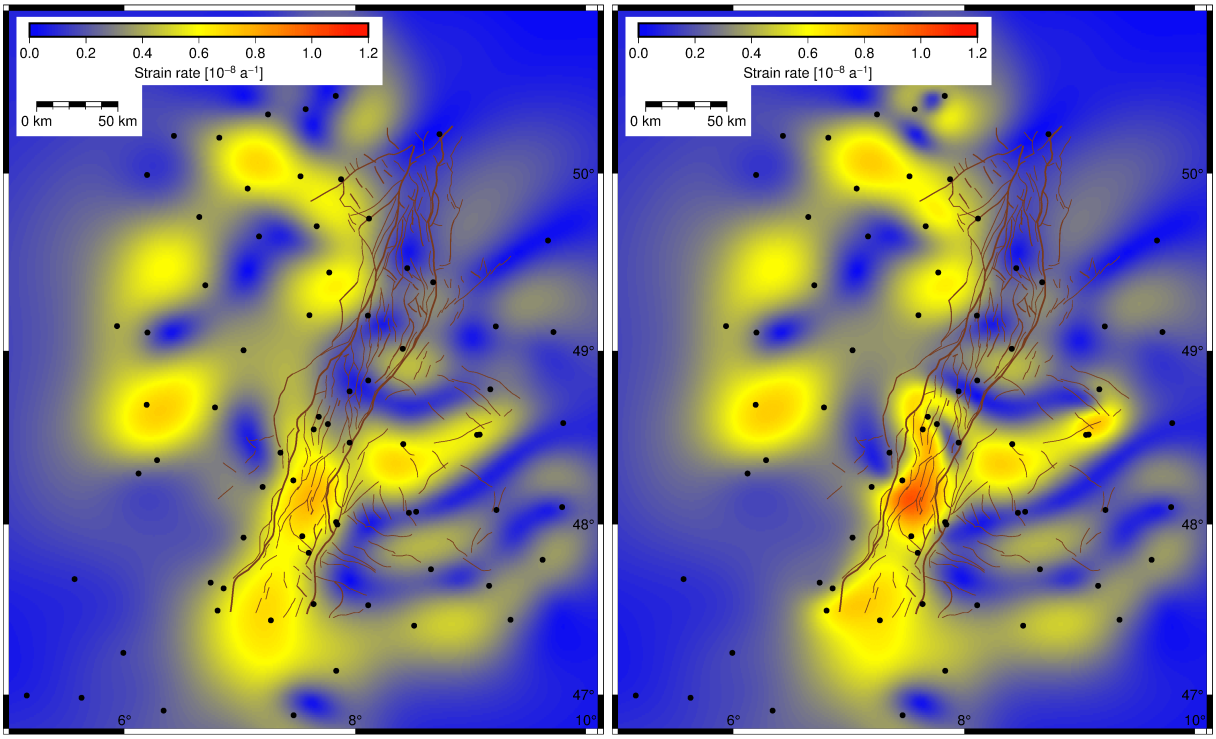

(a) $q_{min} = 4$, $q_{max} = 8$

(b) $q_{min} = 4$, $q_{max} = 9$

Figure 5.8: Magnitude of horizontal strain rates in the URG area estimated from horizontal velocities at 74 GURN sites (black dots) using the strain rate toolbox provided by Tape et al. (2009). Brown lines represent faults in the URG area after Peters (2007, p. 166), main border faults (thick), active faults (medium thick) and other faults (thin).

small earthquakes ($M_L < 2$) compared to other parts of the URG (Barth et al., 2015). Lower strain is visible in the central and northern URG, but also worse estimable due to the lack of sites in the northeastern part of the analysed region. The strain cluster in the northwest might be related to the continuation of the graben structure towards the Lower Rhine Graben. The strain rate patterns east of the URG are orientated in the direction of Variscan fault structures, see Fig. 2.2(b), and potentially related to seismic activity of the Swabian Jura and the Alps.

In any case, the strain rate calculation depends on the accuracy of introduced velocities as well as station distribution and density. Some of the patterns might be artefacts caused by inaccurate velocities or by lack of stations. It is however remarkable that the big picture of strain rate magnitude and distribution fits well to the present knowledge on seismicity in the URG area. Two main conclusions follow from the strain rate calculation: (i) a consistent reprocessing of all GPS data until present is advisable in order to increase the accuracy and, hence, also the number of usable time series. As mentioned in Sect. 5.3, the velocity estimates at nine GURN sites have been excluded from the visualisations due to the low significance of the estimates. (ii) The analysed network should be extended, particularly in the northern, western and southern part in order to minimise boundary effects. An extension of GURN to the north is currently under development by integration of the SA*POS*® stations located in Saarland, Hessen and Nordrhein-Westfalen. In addition, the presented strain analysis provides promising results and thus might be extended to other methods of strain calculation, such as Delauney triangulation.

5.3.4 GPS time series analysis for the 2004 Waldkirch earthquake

The temporal resolution of the GPS time series used for displacement estimation is high compared to levelling and InSAR, see Tab. 7.1. The daily coordinate estimates are therefore optimally suited for the analysis of interseismic, coseismic and postseismic deformations related to earthquakes. The strongest earthquake since the beginning of the GPS time series recording in the URG area happened on 2004-12-05 about 15 km northeast of Freiburg close to the city of Waldkirch, see LGRB (2015). The epicentre of the $M_L = 5.4$ event is located at a distance of 16.9 km to GNSS site 0390 (Freiburg). Häge & Joswig (2009) investigate the main event and several aftershocks and estimate the orientation of the fault plane to 99° ±12°, which is in accordance with the strike of 109° of one of the focal plane solutions for the main shock calculated by LGRB (2015). The GPS time series of the horizontal coordinate components at site 0390 are investigated w.r.t. tectonic deformation in the following. The linear trend and the sinusoid function estimated with CATS are subtracted from the coordinates. Fig. 5.9 displays the residual coordinate time series along with a moving average resulting from a convolution of the time series data with a 50 days rectangular window.

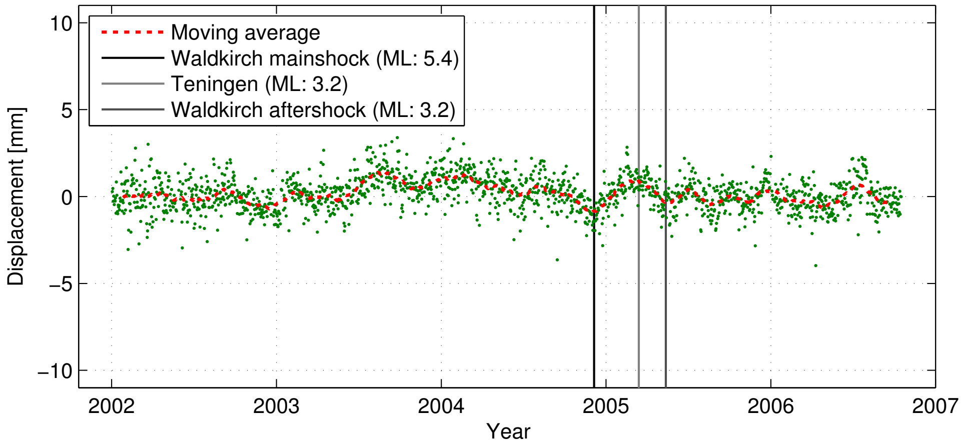

(a) East component

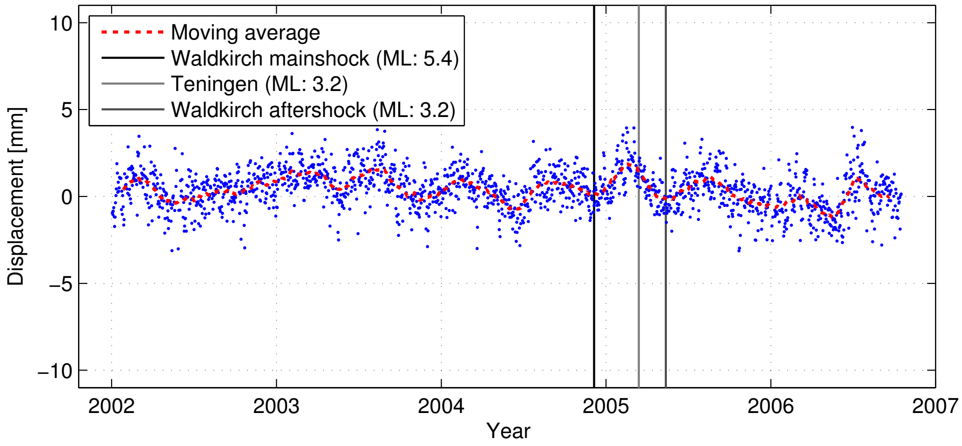

(b) North component

Figure 5.9: Residual coordinate time series at site 0390 (Freiburg) after removal of the Eurasian trend calculated from a local Euler pole estimate of the GURN sites, iterative outlier filtering and removal of a linear trend and sinusoidal function. The moving average is calculated by convolution of the time series with a rectangular window.

The time series shown in Fig. 5.9 are affected by various residual effects, such as noise and quasi-periodic movements likely not related to tectonics. However, an interesting behaviour becomes observable around the dates of the seismic events from the moving average. A sharp bend of the movement along with a change in the movement direction is visible for both components exactly correlating with the date of the Waldkirch main shock. No similar bend is found in time series of surrounding GNSS sites, which indicates that the effect is not introduced by the differential processing of baselines. Starting in the end of 2003, a continuous westward movement of 2–3 mm is observable in Fig. 5.9(a) and a smaller southward movement in Fig. 5.9(b), which could be related to interseismic strain accumulation. A WSW directed movement of the block located south of the epicentre fits to the dextral slip of the WNW–ESE striking fault zone evidenced by Häge & Joswig (2009). A coseismic effect is not visible from GPS data as from numerical computations a $M_L = 5.4$ event is evoking coseismic surface displacements below 1 mm, which is well below the precision of daily coordinate estimates. After the main shock, the directions of movement change, which could be interpreted as a postseismic relaxation. In addition, two major after shocks in the region, marked in Fig. 5.9, might have influenced the postseismic movements close to the fault. The discussion shows that the interpretation of GNSS coordinate time series affected by earthquakes with medium magnitude is difficult as the surface displacements are in the order of magnitude of the noise level and superimposed by non-tectonic effects. Although the time series reveals an exceptional behaviour around the date of the main shock, random effects cannot be fully ruled out as explanation of the effects.

5.4 Summary

- Differential processing of GNSS observations results in precise coordinate estimates, which can be used for displacement analysis of GNSS time series.
- The main feature of site movements present in all sites of GURN is the NE directed movement of the Eurasian plate.
- The Eurasian trend can be calculated from the ITRF solutions or from the GNSS sites themselves by estimation of a local Euler pole.
- For a robust estimation of velocities from coordinate time series, temporal correlations, jumps and periodic effects present in the time series have to be handled carefully.
- The resulting velocities at 76 GURN sites are in the range of ± 1 and ± 2 mm/a for the horizontal and vertical components, respectively.
- An ENE directed trend of the displacement rates in the URG area w.r.t. ITRF2005 is observed from the horizontal velocity field.
- Relative movements in the URG area evidence the sinistral shearing of the graben, which is controlled by SSE directed movements of the Rhenish Massif in the northwest and NNE directed movements of the Alps in the south east.
- The velocities of the Up component do not show a significant pattern and are supposed to overestimate the real displacement at most of the sites.
- Strain rate maps from a wavelet-based inversion of the horizontal velocity field indicate more strain accumulation in the southern URG and are in general agreement with earthquake distribution and seismic activity.
- Residual coordinate time series at a GNSS site located close to the Waldkirch 2004 epicentre shows an exceptional behaviour at the date of the event, which might be related to the activity at the fault.

Chapter 6

InSAR Analysis

This chapter presents the analysis of a large amount of SAR data available in the URG area, performed with the StaMPS software package (Hooper et al., 2007). First, the necessary preprocessing steps for a Persistent Scatterer (PS) analysis are explained in Sect. 6.1. For the selection of a suitable master scene, a new model for the temporal and geometric decorrelation is developed, which is suitable for InSAR analyses in the URG area and comparable non-arid regions. The second section within this chapter deals with the PS analyses applied to the investigated data stacks. Special investigations on the weeding of PS pixels and the modelling of error sources, such as the Envisat oscillator drift, are presented within this section. Options to separate or at least mitigate atmospheric effects from the deformation signal are discussed within a special section, i. e. Sect. 6.3. In addition to PS analyses, the SBAS approach, which was already introduced in Sect. 3.3.3, is applied to the data. A new strategy for the selection of the network of baselines is developed, and the resulting displacements are compared to the results of corresponding single master analyses in Sect. 6.4. Finally, the resulting surface displacements from StaMPS are further investigated w.r.t. the quality of the data in Sect. 6.5. A new filtering approach based on quality indicators and their statistical distribution is applied in order to keep only high quality PS and suppress the effects of side lobes. Resulting displacement rates are presented at the end of Sect. 6.5 for the whole URG area as well as for areas revealing significant deformation patterns related to anthropogenic activities.

Parts of this chapter have already been published by the author in the following papers: Fuhrmann et al. (2013b), Fuhrmann et al. (2015b), Fuhrmann et al. (2015c). These publications are not explicitly cited within the text.

6.1 Data preparation

Archived data of ESA's satellites ERS-1/2 and Envisat are used to calculate surface displacements in the tracks shown in Fig. 3.11. For a PS analysis, interferograms are formed w.r.t. a common master scene. Sect. 6.1.1 presents criteria for the selection of an appropriate master scene for a stack of SAR data including a decorrelation model suitable for non-arid regions. In addition, some remarks on the formation of interferograms from unfocussed SAR images acquired by ERS and Envisat within the three tracks in the URG area are given in Sect. 6.1.2.

6.1.1 Selection of a master image

The master image should be selected in a way that the total decorrelation of all interferograms is minimised. A detailed description of the sources of decorrelation and their characteristics is given by Hanssen (2001, p. 98 ff.). A rule of thumb for the total coherence γ based on linear models for the three components temporal decorrelation, geometric decorrelation and decorrelation caused by different DC frequencies follows from Kampes (2005, p. 6 f.); Hooper et al. (2007) and is shown in Eq. (6.1). The decorrelation due to thermal noise γ_{therm} is unknown and treated as a constant value (Zebker & Villasenor, 1992), see also Eq. (3.28):

$$\begin{aligned} \gamma \approx \left[1 - f\left(\frac{T}{T^c}\right)\right] \cdot \left[1 - f\left(\frac{B_\perp}{B_\perp^c}\right)\right] \cdot \left[1 - f\left(\frac{F_{DC}}{F_{DC}^c}\right)\right] \cdot \gamma_{therm} \quad , \\ \text{with} \quad f(x) = x \quad \text{for} \quad x \leq 1 \\ \text{and} \quad f(x) = 1 \quad \text{for} \quad x > 1 \quad . \end{aligned} \tag{6.1}$$

Fig. 6.1 displays the predicted coherence calculated from the decorrelation model given in Eq. (6.1) w.r.t. temporal and perpendicular baseline as well as DC frequencies for a large image stack of 62 ERS-1/2 scenes in Northern Germany. Note that the DC frequencies possess a different level for ERS-1 and ERS-2 with average values at 452 and 221 Hz, respectively. The gyroscope failure of ERS-2 in February 2000 is visible in the larger DC variation of the last two ERS-2 acquisitions. The critical value for DC frequency differences F_{DC}^c follows from the radar bandwidth in azimuth direction and is approximately 1378 Hz for ERS-1 and ERS-2 (Hanssen, 2001, p. 30 f.). The critical temporal baseline T^c is set to five years and the critical perpendicular baseline $B_\perp^c$ is set to 1100 m for the prediction shown in Fig. 6.1. In order to validate the decorrelation model, the mean coherence after coregistration of slave images w.r.t. a master acquired on 1996-06-24 is calculated and displayed in Fig. 6.2.

When comparing the numbers given in Fig. 6.1 and 6.2, it becomes obvious that a linear decorrelation model does not fit adequately to the real coherence of the interferograms. Therefore, an exponential model for the temporal decorrelation is introduced as proposed by Parizzi et al. (2010), in a first step. The temporal decorrelation is modelled with an exponential decay using the model parameters $\gamma_{a,temp}$, $\gamma_{b,temp}$ and τ, see also Rocca (2007):

$$\gamma_{temp} = f(T) = \left(\gamma_{a,temp} - \gamma_{b,temp}\right) \cdot \exp\left(-\frac{T}{\tau}\right) + \gamma_{b,temp} \quad . \tag{6.2}$$

In addition to temporal decorrelation, the geometric decorrelation is investigated based on the length of the perpendicular baselines between master and slave acquisitions. Again a linear decorrelation model does not fit the real coherence values of interferograms. Thus, an empirical model is developed by the author to better describe the total decorrelation. Therefore, a decaying exponential function is fitted to the data in order to model the geometric decorrelation using the model parameters $\gamma_{a,geom}$, $\gamma_{b,geom}$ and β:

$$\gamma_{geom} = f(B_{\perp}) = \left(\gamma_{a,geom} - \gamma_{b,geom}\right) \cdot \exp(\frac{B_{\perp}}{\beta}) + \gamma_{b,geom} \quad . \tag{6.3}$$

In extension of Eq. 6.1, the full decorrelation model is then given by

$$\begin{aligned} \gamma_{total} = & \left[\left(\gamma_{a,temp} - \gamma_{b,temp}\right) \cdot \exp(-\frac{T}{\tau}) + \gamma_{b,temp}\right] \cdot \\ & \left[\left(\gamma_{a,geom} - \gamma_{b,geom}\right) \cdot \exp(\frac{B_{\perp}}{\beta}) + \gamma_{b,geom}\right] \cdot \left[1 - f\left(\frac{F_{DC}}{F^{c}_{DC}}\right)\right] \cdot \gamma_{therm} \quad . \end{aligned} \tag{6.4}$$

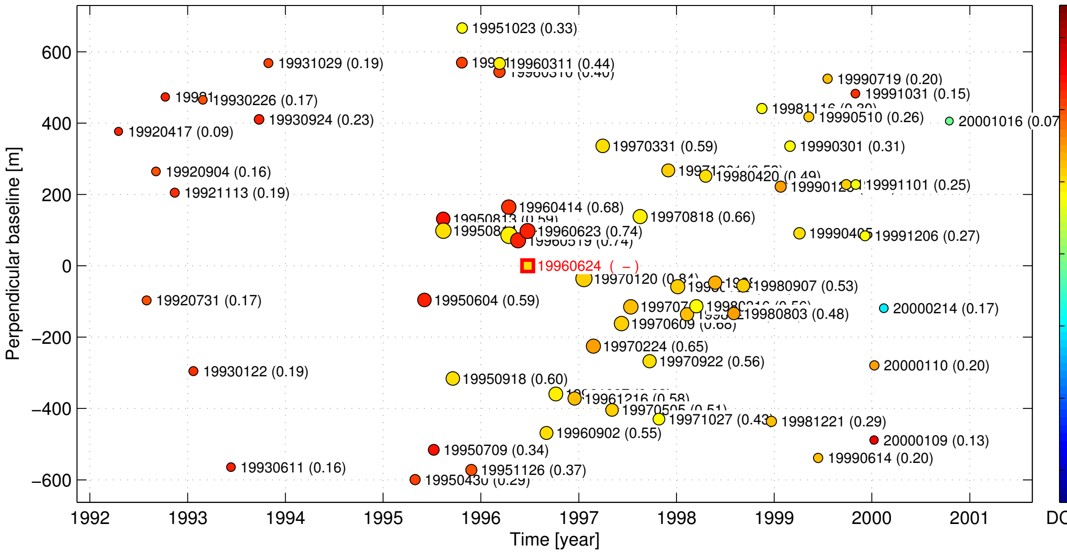

Figure 6.1: Mean predicted coherence (circle size and values in brackets) of slave images w.r.t. the master image (1996-06-24, red square) using the decorrelation model given in Eq. (6.1).

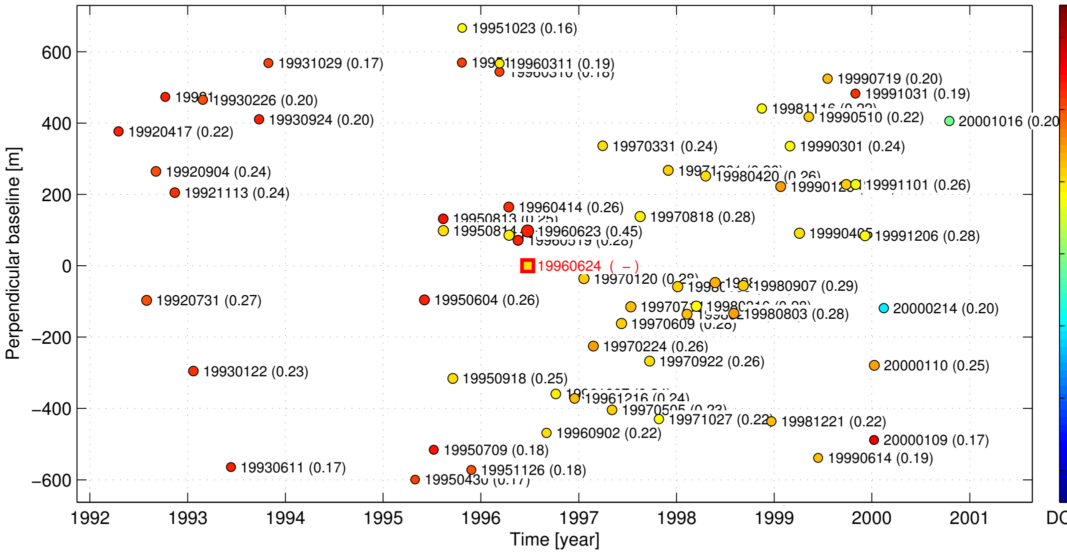

Figure 6.2: Mean estimated coherence (circle size and values in brackets) of slaves images w.r.t. the master image (1996-06-24, red square) after coregistration.

From the analysis of the ERS-1/2 data in Northern Germany, the decorrelation model displayed in Fig. 6.3 is derived. The database of 62 ERS-1/2 scenes is well suitable particularly for the estimation of a temporal decorrelation model as scenes with small temporal differences to the master scene are available within the image stack, see Fig. 6.3(a). The coherence of the ERS-1/2 tandem interferogram with a temporal difference of one day already dropped below 0.8. After 35 days, which is the revisit time of ERS-1, ERS-2 and Envisat, almost the same coherence level is found as for larger temporal differences. An exponential function is able to model the temporal decorrelation in an appropriate way. Using a linear decorrelation model with a total decorrelation after five years as proposed by Hooper et al. (2007) for arid regions, would result in completely different coherence values and is not suitable for the temporal decorrelation of this image stack. The main reason for this misfit is the fact that coherence is mainly found at man-made structures (buildings, bridges, railways) which are coherent over a large time span. In contrast, coherence is immediately lost in non-urban areas as the backscattering characteristics change rapidly. However, the decorrelation behaviour is different if another extent would be used, e. g. a purely urban area, or for SAR sensors with a different wavelength.

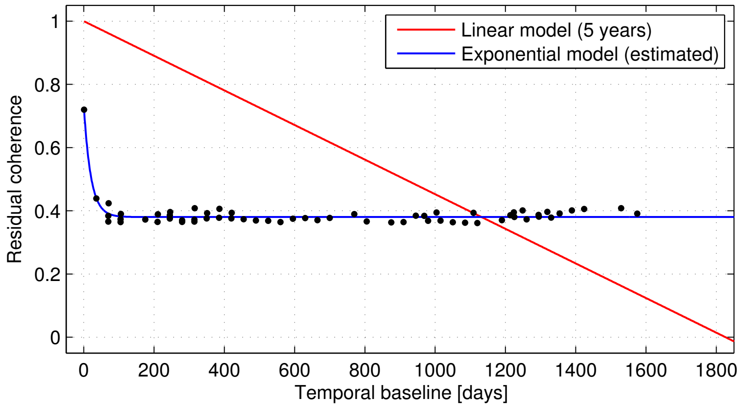

(a) Temporal decorrelation

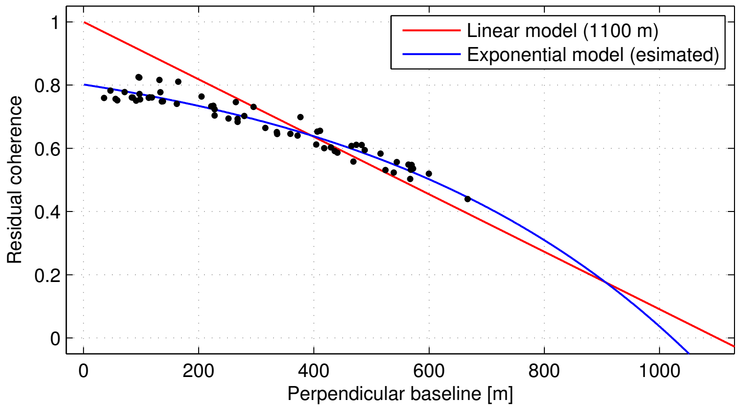

(b) Geometric decorrelation

Figure 6.3: Residual coherence of interferograms representing the temporal and geometric decorrelation (black dots) and estimated model functions of temporal and geometric decorrelation.

The model parameters of $f(T)$ and $f(B_\perp)$ are not separable in terms of their contribution to the total coherence level. Therefore, all six parameters of both models are estimated in one step by least-squares adjustment, resulting in the model parameters given in Tab. 6.1 and the corresponding exponential curves in Fig. 6.3. Note that a linear decorrelation model is used for $\gamma_{F_{DC}}$, and γ_{therm} is set to one, i.e. assuming no decorrelation related to thermal noise. The final exponential model for the decorrelation w.r.t. perpendicular baseline is shown in Fig. 6.3(b). The critical value of the exponential function, i.e. the intersection with a residual coherence of zero, is related to a baseline of about 1030 m, and fits well to the theoretical value of the critical perpendicular baselines calculated according to Hanssen (2001, p. 102).

Table 6.1: Parameters of exponential functions for the temporal and geometric decorrelation models, estimated using 62 ERS-1/2 scenes in Northern Germany.

	Temporal decorrelation			Geometric decorrelation		
Model parameters:	$\gamma_{a,temp}$	$\gamma_{b,temp}$	τ	$\gamma_{a,geom}$	$\gamma_{b,geom}$	β
Estimated values:	0.74	0.38	20 days	0.80	0.96	575 m

With the model parameters given in Tab. 6.1, the predicted coherence is calculated for all 61 ERS-1/2 interferograms in the image stack, see Fig 6.4. The coherence values fit much better to the real interferogram coherences shown in Fig 6.2, compared to the use of a linear model for both temporal and geometric decorrelation. The absolute differences between the coherence values calculated from the coregistered interferograms and the predicted coherences using different models are given in Tab. C.1 in Appendix C. The mean absolute differences for all 61 interferograms are listed in Tab. 6.2.

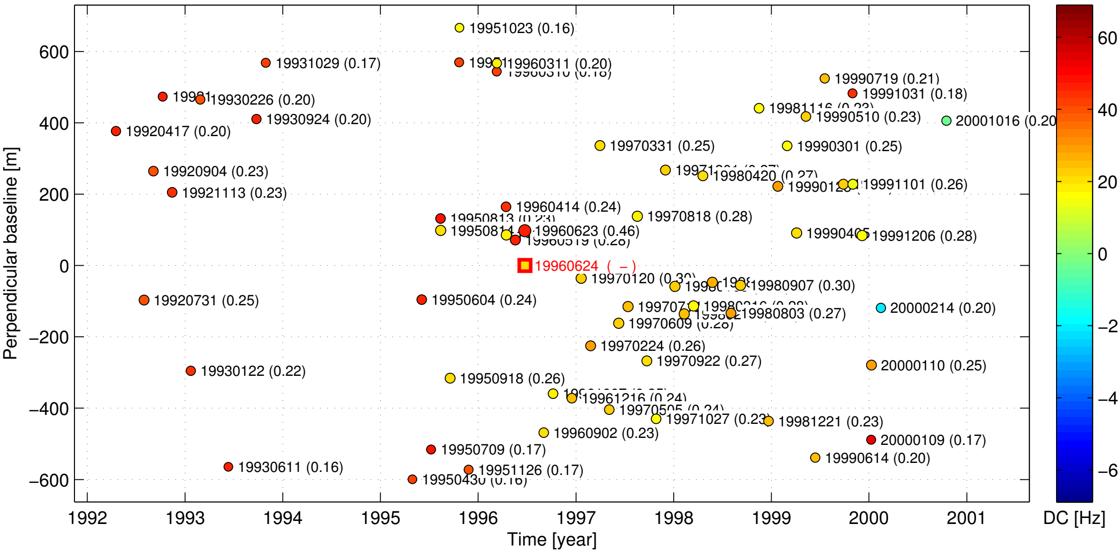

Figure 6.4: Mean predicted coherence (circle size and values in brackets) of slave images w.r.t. the master image (1996-06-24, red square) using the advanced decorrelation model given in Eq. (6.4) with the parameters given in Tab. 6.1. To be compared with Fig. 6.2.

Table 6.2: Mean absolute difference between interferogram coherence and predicted coherence calculated from linear and exponential decorrelation models.

Model function for geometric and temporal decorrelation	Mean absolute difference
γ_{geom} linear, γ_{temp} linear:	0.204
γ_{geom} linear, γ_{temp} exponential:	0.027
γ_{geom} exponential, γ_{temp} exponential:	0.007

The model parameters given in Tab. 6.1 have been used to predict coherence values for the SAR data in the URG area. Tab. 6.3 displays the deviation of the predicted coherences with the real interferogram coherences for the nine different image stacks of ERS and Envisat data for a linear model, see Eq. (6.1), and for an exponential model, see Eq. (6.4). The deviations between predicted and real coherences are much smaller for the exponential model compared to the linear model in all image stacks. For the Envisat image stacks, the mean absolute deviation is a bit larger than for the ERS stacks, which might be due to the fact that the model parameters have been calculated from ERS data.

Table 6.3: Difference between mean interferogram coherence and mean predicted coherence calculated from linear and exponential decorrelation models for both γ_{temp} and γ_{geom} for the image stacks in the URG area. Minimum (MIN), maximum (MAX) and mean absolute differences (MAD).

Satellite	Track	Linear model			Exponential model		
		MIN	MAX	MAD	MIN	MAX	MAD
ERS	294	−0.52	0.72	0.26	−0.08	0.01	0.03
ERS	258	−0.43	0.39	0.22	−0.05	0.02	0.03
ERS	487	−0.57	0.29	0.17	−0.05	0.04	0.03
Envisat	294N	−0.64	0.05	0.32	−0.07	0.10	0.05
Envisat	294C	−0.61	0.03	0.31	−0.08	0.04	0.05
Envisat	294S	−0.69	0.29	0.23	−0.10	0.04	0.05
Envisat	258	−0.49	0.02	0.26	−0.06	0.02	0.05
Envisat	487N	−0.60	0.21	0.25	−0.08	0.01	0.04
Envisat	487S	−0.65	0.75	0.25	−0.10	0.06	0.05

The optimum master is mathematically determined by calculating predicted coherences for all possible master-slave combinations. The combination with the lowest overall decorrelation is proposed as a master image. However, it should be denoted that the master selection for investigation areas in Central Europe may also depend on other influence factors like the season or atmospheric conditions. Master scenes in winter may be affected by snow, master scenes in spring by strong vegetation and therefore generally reduce the coherence level. Strong atmospheric effects mainly affect the InSAR processing if only a small number of scenes is available within the image stack and may result in a smaller number of detected PS pixels (Heublein et al., 2014, p. 33 f.). The master scenes chosen for the image stacks in the URG area are given in Tab. 3.3.

6.1.2 Interferogram formation

The formation of interferograms requires several pre-processing steps discussed in Sect. 3.3.3 and summarised in Fig 3.13. The pre-processing steps are embedded into the framework of StaMPS, even if other programs are called by the executed commands. Focussing and cropping of the data is performed using the Repeat Orbit Interferometry PACkage (ROI_PAC, Rosen et al., 2004). The SLC data has to be cropped in a way that all slave images completely contain the extent of the master image. The maximum overlapping area is used, enabling displacement estimates in an area as large as possible. Further processing steps for interferogram formation are performed using DORIS. Oversampling is applied to all SLC images with a factor of two in both azimuth and range direction in order to avoid aliasing of the complex interferometric signal. Sousa et al. (2011) and Arıkan et al. (2010) showed that a higher PS density is achieved especially in rural areas when oversampling is applied to the SLC data.

As discussed in Sect. 3.3.2, reprocessed orbit data from DEOS and the SRTM-3 DEM are used as input data for the coregistration of the slave images to the corresponding master. For a total of five ERS-2 scenes acquired between 1996-06-02 and 1996-07-10 in the three analysed tracks, coregistration failed. At that time, the satellite was in its commissioning phase and the failure may be associated with the premature status of the sensor.

After coregistration and resampling, the interferograms between master and slaves are formed by complex multiplication, see Eq. (3.24). Note that the number of interferograms corresponds to the number of scenes within the stack minus one. For the computation of ϕ_{ref}, WGS84 is applied as a reference surface, see DORIS (2008, p. 77). Again, SRTM-3 is used to calculate ϕ_{DEM} from a radar-coded DEM. Both phase terms, ϕ_{ref} and ϕ_{DEM}, are then subtracted from the interferometric phase resulting in the interferograms shown in Fig. 6.5. The three exemplary interferograms are built for master-slave combinations with different temporal and perpendicular baselines. All images show the same area with the river Rhine in the centre. Rivers and lakes appear black in the amplitude image as SAR signals striking a water body are reflected away. The dark spot visible in the centre of the image corresponds to a big water basin southeast of Strasbourg called *Plan d'Eau de Plobsheim*.

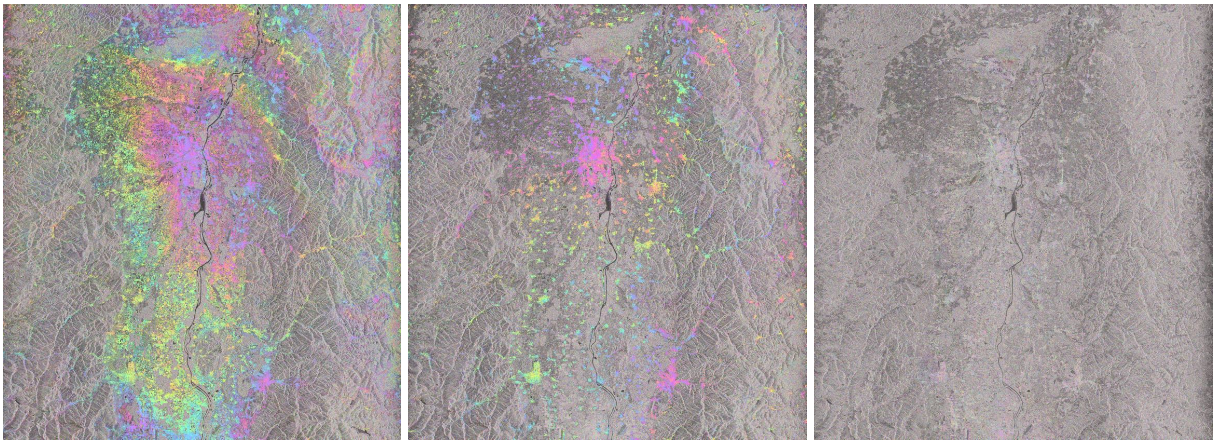

(a) 2006-06-12, BL: -122 m / 35 days (b) 2008-05-12, BL: -35 m / 735 days (c) 2006-07-17, BL: $+818$ m / 70 days

Figure 6.5: Comparison of three interferograms of Envisat track 294C in the central URG between approximately 47.8° and 49.0°N w.r.t. a master scene acquired on 2006-05-08. The amplitude is shown in grey scale, colors in the sequence magenta–blue–green–yellow–magenta represent phase values in the interval $[-\pi \ldots \pi)$. The caption gives the date of the corresponding slave image and the baselines BL: $B_\perp$ / T.

The interferogram in Fig. 6.5(a) results from a small temporal and perpendicular baseline between master and slave. Hence, many resolution cells provide usable phase values, particularly within the URG located in the centre of the image. Most pixels in the surrounding mountain areas are already decorrelated and the resulting phase is noisy. The interferogram shown in Fig. 6.5(b) is formed from a slave image with a large temporal baseline (more than two years), but a small perpendicular baseline. Resolution cells providing visible phase information are concentrated in the urban areas of the crop. Besides several smaller villages and towns, the agglomeration of the city of Strasbourg is nicely visible in the central part of the image. The third interferogram, shown in Fig. 6.5(c), is built from a slave with a large perpendicular baseline w.r.t. the master scene. Not much phase information is visible within the image. However, within a PS analysis the phase signal present in this interferogram is still usable.

In order to provide geographic coordinates for every resolution cell, the interferograms are geocoded using the orbital parameters and the DEM. The pixel coordinates could be improved by additional parameters estimated later within the PS processing, such as the estimates of the DEM error. However, for an analysis of large-scale deformation, a position accuracy of several m is sufficient (Hooper et al., 2007). Besides the interferograms, also the coherence can be calculated from the coregistered master and slave images according to Eq. (3.27). This is performed in order to enable a comparison with the predicted coherence calculated from decorrelation models, see Fig. 6.1, 6.2, 6.4 and comparisons given in Tab. C.1, 6.2, 6.3.

6.2 Persistent Scatterer analysis

Within this section, some remarks and special issues related to the PS processing with StaMPS are presented. First, the number of PS using different subsets of ERS interferograms available in the image stack with the largest number of scenes, i. e. track 294, is analysed (Sect. 6.2.1). Second, different parameter settings for a spatial filtering of PS pixels, the so-called weeding, are compared for the same database of Envisat scenes in track 294N (Sect. 6.2.2). Sect. 6.2.3 describes the iterative phase unwrapping and parameter estimation consistently applied to all image stacks, exemplarily for Envisat data in track 294N. Finally, in Sect. 6.2.4 the implemented correction of the Envisat oscillator drift is presented.

6.2.1 Selection of Persistent Scatterers

The procedure of selecting PS pixels has been discussed in Sect. 3.3.3. Three subsets of pixels are distinguished, see Fig. 3.14: PS candidates, selected PS and the final set of PS after weeding. Besides the threshold for the weed standard deviation, discussed in detail within Sect. 6.2.2, the default parameter settings given by Hooper et al. (2013) are used for the selection process. The number of PS is heavily reduced within each stage of the processing. Furthermore, it largely depends on the amount of data, the number of interferograms and the corresponding time span. Fig. 6.6 compares the number of PS at each processing stage using different subsets of the basic set of data for a crop of a 100 km × 100 km area of the large stack of ERS-1/2 data. The maximum usable subset contains 69 interferograms acquired between 1992-04-17 and 2000-08-07. It becomes obvious that the number of PS strongly depends on the time span and the corresponding number of interferograms.

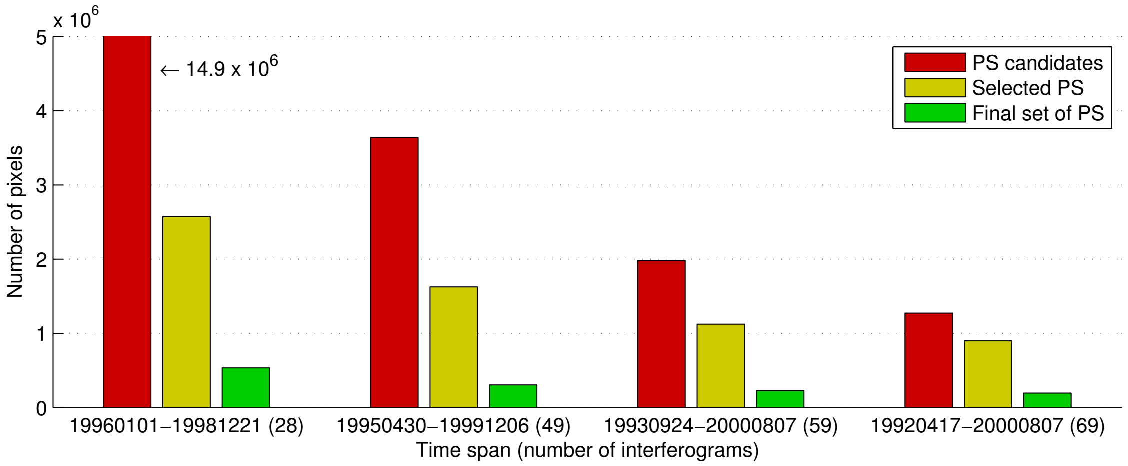

Figure 6.6: Number of PS at different processing stages of the selection and for different subsets of interferograms from the same image stack. Time is givein in yyyymmdd-format.

The PS selection is based on statistics with a certain probability that non-reliable pixels may pass through the selection process. A maximum acceptable spatial density of selected pixels with random phase is applied in the selection step in order to filter the subset of PS candidates. According to Hooper et al. (2013, p. 18), a high density can be accepted as pixels with a random phase are dropped in an additional filtering step, denoted as *PS weeding*. If only a small number of interferograms is analysed, more PS are selected and it is more likely that unreliable PS remain in the selection. Thus, the weed standard deviation threshold has to be adapted to a suitable value for each image stack as discussed in the next section.

6.2.2 Weeding

Depending on the number of interferograms, a certain amount of the selected PS are noisy and hence deteriorate the further phase analysis. Particularly for image stacks comprising only few interferograms, the phase unwrapping may fail if too many noisy pixels are included in the final subset of PS. In addition, the noisy PS will not contribute to the visual interpretation of the surface displacements as the resulting time series of displacement values will also be noisy. In a first step, the weeding algorithm analyses neighbouring pixel-pairs and keeps only those pixels with the highest coherence, see also Sect. 6.5.3. In a second step, the remaining set of pixels is filtered by applying a user-defined threshold for the phase noise standard deviation. This standard deviation threshold is one of the most crucial parameter settings within the StaMPS processing chain, and is further discussed in the following.

Fig. 6.7 shows the wrapped phase of remaining PS pixels when different weed standard deviation thresholds are applied to the same data set. Without a threshold, many noisy pixels are included in the wrapped phase values, see Fig. 6.7(a). Applying a strong threshold, i. e. a low phase noise standard deviation, few pixels are kept and the spatial extent of a deformation signal might not be resolvable any more. Regarding the noise characteristics of wrapped phase values, a threshold between 0.6 and 0.8 rad seems appropriate for the data set shown in Fig. 6.7. However, the choice of a suitable weed standard deviation threshold strongly depends on the analysed region, the number of scenes and the corresponding time span covered.

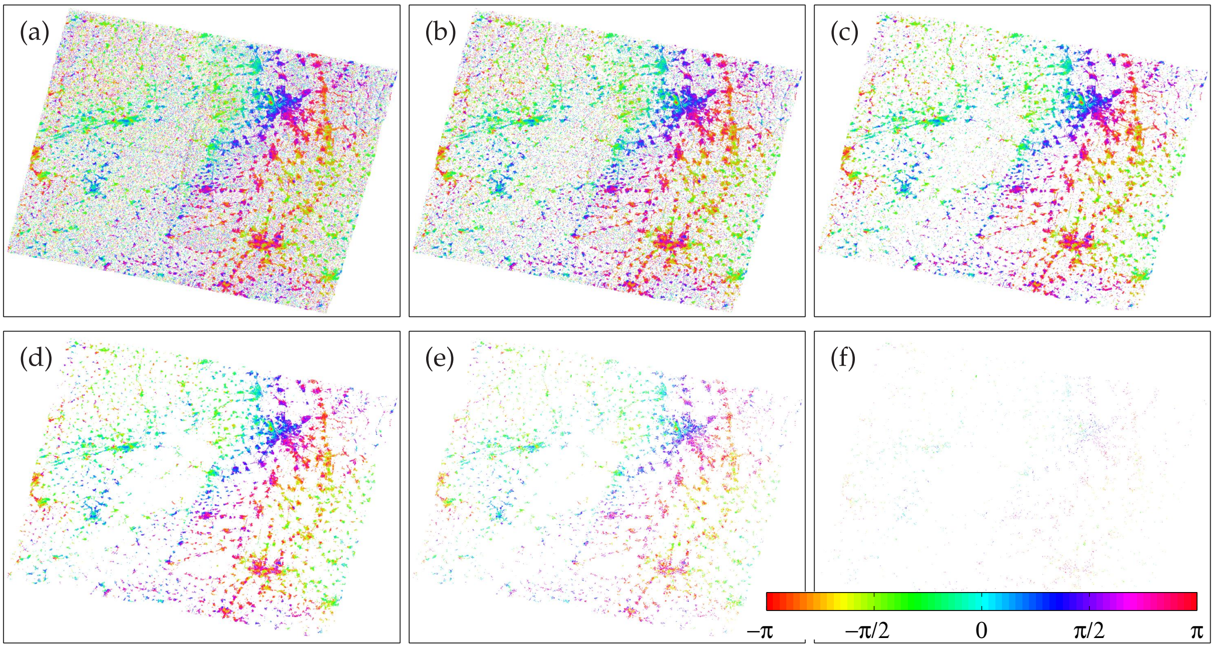

Figure 6.7: Wrapped phase $[-\pi \ldots \pi)$ [rad] for an interferogram of Envisat track 294N (master: 2005-08-01, slave: 2005-04-18) applying different weed standard deviation thresholds. The spatial extent of the figures is 7.188°–9.012°E, 48.748°–49.852°N. The thresholds / corresponding number of pixels are (a) ∞ / 1,074,573, (b) 1.0 rad / 992,463, (c) 0.8 rad / 718,762, (d) 0.6 rad / 352,890, (e) 0.4 rad / 104,113, (f) 0.2 rad / 7,292.

In order to provide a similar set of final PS for the analysis of the same region from different image stacks, a measure to define suitable thresholds for each stack is sought. In addition to the visual interpretation of the set of final PS, as shown in Fig. 6.7, the PS density within several test areas is used to approximate the desired value. The chosen threshold value for each data stack and the corresponding number of PS/km^2 within 12 test areas are shown in Tab. 6.4. Urban areas are chosen as test areas assuming that the PS density is similar in these areas. In fact, the number of PS/km^2 differs for the areas between about 200 and more than 600 PS/km^2. The mean value of PS densities may therefore be different for the image stacks as a different set of test areas is included in the region covered by each stack. However, the number of PS in each test area gives a first impression on how a suitable threshold should be chosen. Furthermore, the threshold is related to the statistical distribution of the quality indicators calculated from resulting unwrapped and corrected phase values, investigated in detail in Sect. 6.5.2.

Table 6.4: Weed standard deviation threshold $\sigma_{weed,\,thres}$ used for the analysed data stacks and number of PS/km^2 within the test areas. As the Envisat subtracks cover smallers parts of the investigation area, less test areas are included in the corresponding SAR images.

Satellite	ERS			Envisat					
Track	294	258	487	294N	294C	294S	258	487N	487S
$\sigma_{weed,\,thres}$ [rad]	1.00	0.75	0.70	0.65	0.80	0.85	0.65	0.65	0.8
Test areas:	Number of PS/km^2:								
Mannheim	399	–	441	390	–	–	–	475	–
Kaiserslautern	538	606	365	633	–	–	–	468	–
Pirmasens	503	471	266	547	–	–	–	334	–
Karlsruhe	361	–	292	340	–	–	–	350	–
Strasbourg	471	493	223	–	462	–	–	332	–
Offenburg	319	371	262	–	375	–	–	301	–
Lahr	191	289	190	–	344	–	255	230	–
Sélestat	340	199	–	–	393	–	406	–	–
Colmar	583	434	–	–	583	575	561	–	–
Freiburg	392	292	193	–	392	403	314	251	189
Mulhouse	655	415	–	–	–	608	517	–	–
Basel	357	372	–	–	–	334	469	–	–
Mean	426	394	279	477	425	480	420	343	189

6.2.3 Phase unwrapping and parameter estimation

After the final subset of PS is selected, unwrapping is applied to the phase values originally wrapped within one phase cycle in the interval $[-\pi \ldots \pi)$. Following Hooper et al. (2013), a 3D phase unwrapping approach considering space and time is applied to the interferometric phases including phase filtering by application of a Goldstein filter (Goldstein & Werner, 1998). The remaining nuisance terms, i. e. ϕ_{SCLA}, ϕ_{orbit} and ϕ_{atmo}, are estimated within the following two processing steps as shown in Fig. 3.14 and discussed in Sect. 3.3.3. From a comparison of different estimates of ϕ_{atmo} to atmospheric phase values calculated from measurements of the MEdium Resolution Imaging Spectrometer (MERIS) onboard Envisat, it could be seen that the major part of atmospheric influences present in the interferometric phase is pushed into the estimated phase ramps if they are estimated before the spatio-temporal filtering. Therefore, an iterative strategy of phase unwrapping and estimation of residual phase terms is applied which skips the estimation of phase ramps in the first iteration. At least four iterations are applied to the analysed interferogram stacks. If the final solutions for the estimated phase terms addressed to residual DEM, orbital and atmospheric errors have not converged within four iterations, additional iterations are performed.

However, if the PS phase values are noisy and interferograms with long perpendicular baselines are included in the stack, unwrapping errors may still occur after some iterations. In this case, the weed standard deviation threshold is reduced, see Sect. 6.2.2. The residual DEM error is estimated from Eq. (3.29). Orbital and atmospheric effects of the master image are present in all interferograms and would not affect linear rates calculated from displacement time series. They are however estimated and subtracted from the remaining phase in order to enable a proper separation of the other phase terms. Fig. 6.8 exemplarily shows the estimates of errors attributed to atmosphere and orbit errors and the remaining deformation phase after subtraction of all other phase terms. Particularly the atmospheric effects may largely vary within several phase cycles (fringes). Following a detailed investigation of atmospheric effcets present in ERS tandem interferograms (Hanssen, 1998, p. 127), extreme ranges of up to four fringes are observed in case of thunderstorms. From spatio-temporal filtering of the phase signal present in the analysed image stacks of the URG area, maximum variations of 27.7 rad, i. e. 4.4 phase cycles, are found. However, most of the phase variations in the filtered signals, which are attributed to atmospheric effects present at the slave acquisition date, are within $\pm 2\pi$, corresponding to two fringes, see Sect. 6.3.4.

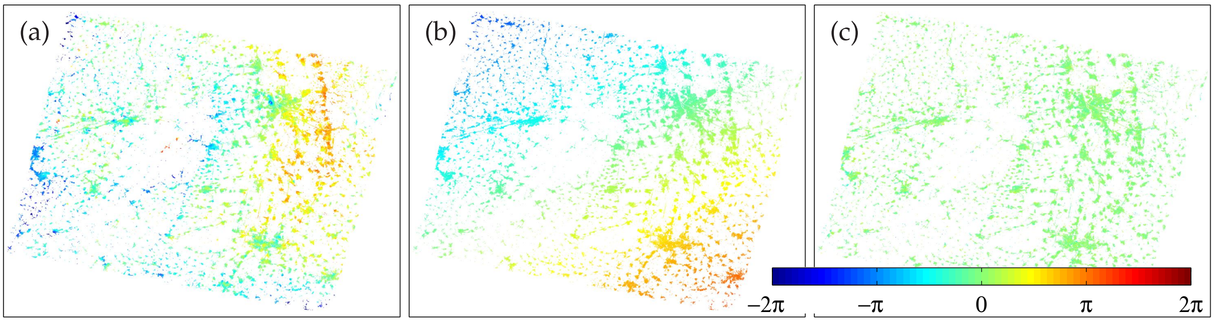

Figure 6.8: Unwrapped phase terms [rad] for the interferogram shown in Fig. 6.7. (a) atmospheric phase estimated from spatio-temporal filtering, (b) estimated phase ramp addressed to orbit errors, (c) remaining deformation phase after subtraction of (a), (b) and the estimate of the residual DEM error.

Orbit errors result in an error of the interferometric baseline between two acquisitions. According to Bähr & Hanssen (2012), the orbit accuracy of Envisat is in the range of 10 cm and somewhat worse for ERS. In a first approximation, the baseline errors induce linear fringes in azimuth and range direction in the order of several fringes. The estimated phase ramps reveal slightly higher linear trends for the ERS data, particularly for ERS-1, compared to the Envisat data. For Envisat track 294N, the phase ramp estimates are in the range of 5.8 to 10.1 rad and thus within two phase cycles. For the other analysed ERS and Envisat tracks, similar numbers are observed with a maximum linear trend of about three fringes. This is in accordance with the magnitude of 1.6 fringes in azimuth and 2.5 fringes in range for orbit error estimates from a network adjustment of Envisat data in Western Australia performed by Bähr & Hanssen (2012); Bähr (2013, p. 86). However, the estimated phase ramps may also contain parts of the atmospheric phase or long wavelength deformation signals. The influence of orbit inaccuracies on estimated velocities from InSAR are investigated by Fattahi & Amelung (2014). They find that the uncertainty of LOS velocities related to ERS or Envisat orbit errors are below 1.5 mm/a per 100 km in range and azimuth direction.

In addition to orbit errors, Bähr et al. (2012, p. 97 ff.) and Bähr (2013) discuss the effect of plate motion on large-scale InSAR analyses, denoted as effect of the reference frame. The tectonic plates perform a relative movement w.r.t. the satellite orbits between two SAR acquisitions inducing a phase trend in range due to different LOS vectors at near and far ranges. The phase bias in range can be estimated from a given plate velocity, e. g. measured at GNSS sites, the temporal baseline between the acquisitions and the look angle difference between near and far range. From the numbers given by Bähr (2013, p. 102) for the Eurasian plate, a maximum phase difference of 2.9 and 1.4 rad between near and far range is introduced for a time difference of five years between master and slave acquisitions in ascending and descending image geometry, respectively. The effect of the reference frame is small compared to the magnitude of orbit errors. As it results in a linear trend in range direction, it is subsumed in the estimated phase ramps.

In contrast to phase signals induced by atmospheric and orbital effects, the remaining deformation phase is small in most areas of the analysed image stacks. Larger phase variations are only visible in areas with significant displacements, particularly in interferograms with a large temporal baselines. However, small surface displacements of 1 mm/a or less are resolvable from time series analysis of all interferograms within one image stack.

6.2.4 Envisat oscillator drift

A significant spatial trend in PS velocities estimated from Envisat interferograms of about 15 mm/a over a distance of 100 km has been observed by Ketelaar (2009, p. 133 f.). The trend cannot be associated with the phase terms discussed in Sect. 6.2.3 as it is larger than the expected long wavelength deformation and plate motion signals, and correlated in time. Marinkovic & Larsen (2013) evidenced that the trend is associated with a frequency drift of the reference oscillator integrated in the Envisat SAR sensor. The drift is approximated with an empirical model presented by Marinkovic & Larsen (2013), published by Fattahi & Amelung (2014). The model describes a velocity v_{osc} attributed to the oscillator drift in range direction:

$$v_{osc} = \nu' \cdot k_r \cdot \frac{\Delta r_{slant}}{l_{ovs}} \quad , \tag{6.5}$$

with frequency decay ν' of $0.387 \cdot 10^{(-6)}$ per year, the pixel count k_r in range direction, the slant range pixel size $\Delta r_{slant} = 7.8$ m for Envisat and the oversampling factor l_{ovs}.

Between near and far range, which corresponds to a ground distance of about 100 km for Envisat, a velocity difference of 15 mm/a results from Eq. (6.5). In order to account for the Envisat oscillator drift, a correction is added to the StaMPS processing chain and performed before the parameter estimation of other phase terms. At every PS pixel, v_{osc} is transformed to a phase value $\phi_{corr,osc}$ accounting for the temporal baseline w.r.t. the master scene, such as:

$$\phi_{corr,osc} = -\frac{4\pi}{\lambda} \cdot v_{osc} \cdot T \quad . \tag{6.6}$$

The correction results in a linear phase ramp in range, which is applied to all analysed Envisat image stacks. Fig. 6.9 exemplarily shows the correction values for three interferograms in track 294N. As the drift depends on the time difference T between slave and master scene, larger correction values correspond to larger temporal baselines, and the sign of the correction in near and far range is reversed for scenes acquired before and after the master, respectively.

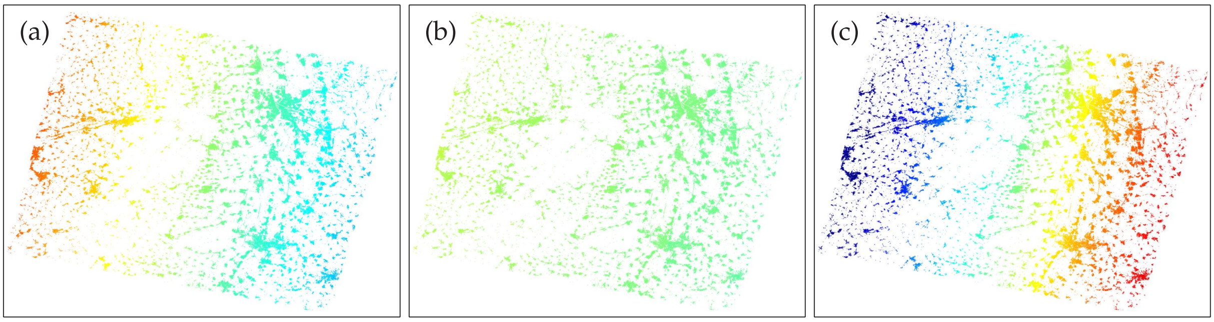

Figure 6.9: Correction values [rad] for the Envisat oscillator drift applied to different interferograms of Envisat track 294N formed with a master acquired on 2005-08-01. The spatial extent is the same as in Fig. 6.7 and 6.8. The color scale is the same as in Fig. 6.8. The dates of the slave images and the corresponding temporal baselines are (a) 2003-12-15, $T = 595$ days, (b) 2005-04-18, $T = 105$ days, (c) 2008-12-08, $T = 1225$ days.

6.3 Atmospheric influences and corrections

Atmospheric effects are a major error source for InSAR applications related to deformation measurement. The influence of ionospheric and tropospheric phase delays on the parameter estimation has already been discussed within this work w.r.t. GNSS observations in Sect. 3.2.1 and 5.1. In the case of InSAR, only changes of the atmospheric phase delay between two acquisition times have to be considered. The ionospheric phase delay depends on the frequency of the electromagnetic signal and is hence different for the SAR frequency bands. According to Meyer et al. (2006), the ionosphere is assumed to have considerable effects on SAR data acquired from L-band sensors, but only small impact on X- and C-band data. Furthermore, the dry part of the troposphere is less important for InSAR applications as it is almost constant over time and therefore largely reduced in the interferometric phase. However, the wet part of the troposphere is highly variable in space and time and is able to provoke a phase signal of several fringes in a 100 km × 100 km interferogram. Here, the atmospheric signal is treated as an unwanted phase term which deteriorates the estimation of surface displacements and has to be corrected. On the other hand, the signal can be treated as a valuable source of information to derive the content of water vapour in the atmosphere (Hanssen et al., 1999; Pichelli et al., 2010; Alshawaf, 2013). Within this section, the atmospheric signal present in Envisat interferograms of the southern URG is investigated in detail. Sect. 6.3.1 and 6.3.2 describe corrections calculated from external data sources such as optical spectrometer data and weather models, respectively. Based on a toolbox provided by D. Bekaert, University of Leeds, tropospheric phase delays are deduced from atmospheric quantities and transformed to interferometric phase values. A new tropospheric correction technique for InSAR data based on a power-law relationship was developed by Bekaert et al. (2015a) and kindly provided for the URG analysis, see Sect. 6.3.3. The spatio-temporal filtering approach of StaMPS is investigated in detail in Sect. 6.3.4. Finally, Sect. 6.3.5 compares the results of the four different correction methods for tropospheric phase delays.

6.3.1 Phase correction using MERIS data

MERIS is an optical sensor onboard Envisat primarily devoted to the measurement of ocean colour (ESA, 2006, p. 11). As a passive, nadir-looking spectrometer, MERIS performs spatial and spectral imaging of the Earth at daytime. From a comparison of the radiance ratio between two infrared frequency bands, the determination of vertically integrated water vapour (IWV) is possible under cloud-free conditions. Following Bevis et al. (1992, 1994), integrated water vapour can be deduced from the zenith wet delay (ZWD) of electromagnetic signals, such as the GPS signal by:

$$\mathrm{IWV} = \Pi \cdot \mathrm{ZWD} = \frac{10^6}{\rho_w R_w \left(\frac{k_3}{T_m} + k_2 - k_1 \frac{R_d}{R_w} \right)} \cdot \mathrm{ZWD} \quad , \tag{6.7}$$

with the density of water ρ_w, the specific gas constants R_d and R_w for dry air and water vapour, respectively, and empirical refractivity coefficients k_1, k_2, k_3 defined by Smith & Weintraub (1953). The mean atmospheric temperature T_m depends on the location and height of the observation site, as well as on the season and local weather conditions (Leick, 2004, p. 201). Bevis et al. (1992) give an empirical formula derived from radiosonde profiles in the USA to approximate T_m from surface temperature measurements and approximate Π with a value of 0.15. From empirical investigations on the magnitude of $Q = \Pi^{-1}$, a variation between 6.19 and 6.50 was found by Webley et al. (2002) for the region around Mount Etna, Italy, and between 6.04 and 6.63 by Alshawaf et al. (2015b) for the URG area. As surface temperatures significantly differ in winter and summer at mid-latitudes, Alshawaf et al. (2015b) recommend to deduce Π from surface temperature measurements, if available. The IWV estimates of MERIS are converted to a wet tropospheric delay according to Bekaert et al. (2015b):

$$\phi_{tropo,wet} = \frac{-4\pi}{\lambda} \frac{Q}{\cos\theta} \cdot \mathrm{IWV} \quad . \tag{6.8}$$

Neglecting seasonal variations of $\Pi = Q^{-1}$, balloon sounding data can be used to estimate an appropriate value of Π. The freely available sounding data provided by the Department of Atmospheric Science of the University of Wyoming (UWDAS, 2015) is downloaded at a site located close to the URG, i. e. at Idar-Oberstein, Rheinland-Pfalz. From data between 2003 and 2009, Q results in 6.41 at the chosen site.

MERIS data is available for registered users at ESA (2015) with a spatial resolution of approximately 1 km × 1 km. The advantage of using MERIS data for the correction of tropospheric phase delays present in Envisat data is the fact that the measurements have been performed at the same time. However, MERIS is an optical sensor and therefore strongly depending on the daily cloud cover of both master and slave images. Hence, a master scene with as less cloud coverage as possible, but still minimising decorrelation, see Sect. 6.1.1, is selected for the analysis of atmospheric phase delays from the stack of 43 usable SAR scenes in Envisat track 294S. The scene acquired on 2007-08-06 is almost cloud-free enabling the calculation of phase delays at 99.9 % of the PS locations. At 27 scenes of the images in the analysed stack, the percentage of PS locations with available IWV values from MERIS is below 30 %. Only for 12 scenes including the master, more than 70 % of the PS pixels could be used for the calculation of $\phi_{tropo,wet}$ from MERIS IWV estimates. The atmospheric phase screen (APS) of interferograms follows from subtraction of $\phi_{tropo,wet}$ of the slave acquisition date from $\phi_{tropo,wet}$ of the master date. Images of APS for all interferograms of the stack are shown in Fig. C.1(a) in Appendix C. The results indicate that the interferometric delays may contain large-scale effects as well as variations with a spatial scale of several km. Note that the analysis of phase delays under more or less cloud-free conditions may bias the assumptions on the magnitude of the delays as much larger variations are possible in case of extreme weather events along with thunderclouds.

6.3.2 Phase correction using weather model data

Following Jolivet et al. (2011), the ERA-Interim global meteorological model can be used to calculate phase delays at the acquisition dates. ERA-Interim is a global atmospheric reanalysis starting in 1979 provided by the European Centre for Medium-Range Weather Forecasts (ECMWF, 2015). ERA-Interim data is available free of charge and accessible via automated download scripts from the ECMWF server. Atmospheric and surface parameters are given on different vertical levels, but with a rather sparse spatial resolution of about 80 km (horizontal) and a temporal resolution of 6 h. The phase delay along the InSAR LOS results from the temperature T, air pressure p and partial pressure of water vapour e, deduced from relative humidity, at different height levels. The atmospheric parameters are integrated along the vertical profiles at the grid nodes of the weather model data between surface height H_0 up to the maximum height of the troposphere H_{max} (Bekaert et al., 2015b):

$$\phi_{tropo} = \frac{-4\pi}{\lambda} \frac{1}{10^6 \cos\theta} \int_{H=H_0}^{H_{max}} \left[k_1 \frac{p}{T} + \left(k_2 - R_d \cdot \frac{k_1}{R_w} \right) \frac{e}{T} + k_3 \frac{e}{T^2} \right] dH \quad . \tag{6.9}$$

Note that the dry component of the tropospheric delay is included in Eq. (6.9), in contrast to the phase delay shown in Eq. (6.8). The phase delays are calculated for each acquisition time and interpolated at the spatial sampling of the PS pixels.

The APS for the interferograms in the analysed image stack in Envisat track 294S follows from subtraction of ϕ_{tropo} between slave and master acquisition dates and is shown in Fig. C.1(b). It becomes obvious that the weak resolution of the ECMWF weather model is able to account only for the long-wavelength atmospheric variation. The high temporal and spatial variations of water vapour with spatial wavelengths of several km are not resolvable from the ERA-Interim data. Weather models with higher temporal and spatial resolution are needed in order to model the atmospheric phase delays present in InSAR data, such as atmospheric models calculated with the Weather Research and Forecasting Modelling System (WRF, see Alshawaf, 2013, p. 28 ff.). However, the phase delays are in a similar order of magnitude compared to the MERIS estimates, and some visible correlation to MERIS is found, particularly at dates revealing strong long-wavelength atmospheric signals, such as on 2005-08-01 or 2006-07-17.

6.3.3 Spatial phase filtering using the power-law method

The power-law method developed by Bekaert et al. (2015a) applies a spatial phase filter to the interferometric phase after best possible reduction of other phase terms. The proposed model describes the variation of phase delays with height H using a height H_{max} at which the tropospheric delays reduced to a value close to zero and a decay coefficient κ:

$$\phi_{tropo} = K_{\Delta\phi} \left(H_{max} - H\right)^{\kappa} \quad . \tag{6.10}$$

H_{max} and κ are estimated from balloon sounding data of a nearby site available at UWDAS (2015). Again site Idar-Oberstein is used resulting in $H_{max} = 13.5$ km and $\kappa = 2.0$. The coefficient $K_{\Delta\phi}$ relates the tropospheric phase to topography and varies for different acquisitions. According to Bekaert et al. (2015a), it can be estimated from filtering of phase values in different spatial bands selected in a way that the contribution from other signals is reduced. For the investigation of interferograms in Envisat track 294S, the spatial filter bands are selected based on empirical studies of correlation to the APS calculated from MERIS data. A high correlation is found for spatial filter bands between 2 and 18 km. Fig. C.2(a) displays the resulting APS estimated using the power-law technique. The general distribution of positive and negative phase values is mainly in accordance with the results derived from spatio-temporal filtering in Fig. C.2(b), see Sect. 6.3.4. The mean correlation between APS resulting from the power-law method and from the spatio-temporal filtering of StaMPS is 0.65, with 80 % of the interferograms revealing a correlation larger than 0.5. However, the power-law method seems to overestimate the magnitude of atmospheric delays for most of the interferograms. In addition, the resulting APS largely depends on the chosen filter bands for the analysed SAR data in the URG area. A proper validation with MERIS or weather model data is therefore advisable if the method shall be applied.

6.3.4 Spatio-temporal filtering of the phase

As noted in Sect. 6.2.3, a spatio-temporal filtering method can be applied to the residual interferometric phase ϕ_{res} of each interferogram in order to separate the atmospheric signal. In a first step, a temporal low-pass filter f of length T_{filt} is applied to the phase signal of all n interferograms using, e. g. a Gaussian exponential window function:

$$\phi_{low\text{-}pass,i} = \sum_{i'=1}^{n} \phi_{res}(i) \cdot f(T_{i,i'}, T_{filt}) = \sum_{i'=1}^{n} \phi_{res}(i) \cdot \exp(-0.5\frac{T_{i,i'}^2}{T_{filt}^2}) \quad , \tag{6.11}$$

where $T_{i,i'}$ represents the temporal differences between one slave acquisition i and all other slave acquisitions i' within the stack. The values of f are scaled, so that the sum of all weights in f equals one, resulting in a filter kernel of the form:

$$f(T_{1,i'}, T_{filt}) = \begin{pmatrix} 0.093 & 0.089 & 0.083 & 0.081 & 0.079 & \ldots & 0.023 & 0.004 \end{pmatrix} \quad , \tag{6.12}$$

exemplarily calculated for the first interferogram of Envisat track 294N with $T_{filt} = 730$ days. All phase values of every interferogram are then multiplied with the corresponding filter kernel. The filtered low-pass phase values result from summation of the weighted phase values. In a second step, $\phi_{low-pass}$ is subtracted from ϕ_{res}. The resulting phase values represent the desired atmospheric signal, which is subsequently smoothed in space. A spatial low-pass filter is applied in a similar way as for the temporal filtering using a given spatial filter wavelength S_{filt}. The filter lengths of the temporal and spatial filtering are previously unknown. Gong et al. (2015) propose to estimate temporal filter parameters from a cross-check with numerical weather prediction models. Within this work, a validation of the remaining deformation signal in areas with known displacement from levelling analyses is performed, such as in the area close to Landau, see Fig. 6.10. In addition, the resulting atmospheric signal is validated with the APS calculated from MERIS data.

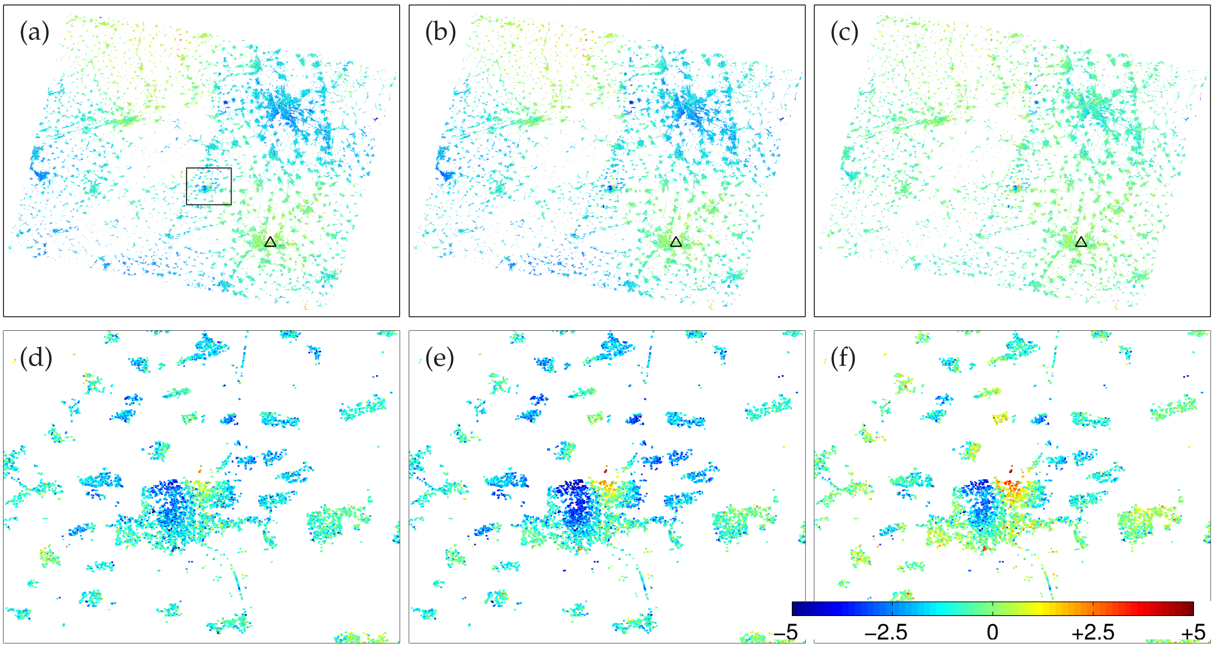

Figure 6.10: LOS displacement rates [mm/a] at PS of Envisat track 294N applying the spatio-temporal filtering with different parameters. The reference area, located in Karlsuhe, is marked by a black triangle and represents the mean of 235 PS within a 500 m radius. The spatial extent of figures (a)–(c) is the same as in Fig. 6.7, 6.8 and 6.9; (d)–(f) show a zoom on the area close to Landau with an extent of 8.030°–8.230°E, 49.150°–49.270°N, marked by a black frame in (a). The filter parameters are $T_{filt} = 365$ days, $S_{filt} = 100$ m for (a) and (d), $T_{filt} = 365$ days, $S_{filt} = 2,000$ m for (b) and (e), $T_{filt} = 730$ days, $S_{filt} = 2,000$ m for (c) and (f).

The example shows that besides the atmospheric signal also parts of the deformation signal may be filtered out by the spatio-temporal filtering. The default parameter settings of

$T_{filt} = 365$ days and $S_{filt} = 100$ m in StaMPS are not suitable for a separation of atmospheric effects from the anthropogenic deformation signal close to the city of Landau. A larger minimum wavelength prevents the Landau deformation from being filtered out, see Fig. 6.10(e), while a larger time window reduces the spatially correlated noise present in the whole analysed area, see Fig. 6.10(c). A time window of two years along with a minimum wavelength of 2,000 m turns out to provide a good solution for the filtering of spatially correlated nuisance terms without deteriorating the deformation signal, which is validated by a comparison with the results from levelling. Furthermore, a higher correlation of the estimated atmospheric signal with APS resulting from MERIS data, see Sect. 6.3.1, is achieved with the adapted filter parameters $T_{filt} = 730$ days and $S_{filt} = 2,000$ m. Note that some of the PS shown in Fig. 6.10 reveal a different displacement behaviour compared to their neighbourhood and are assumed to be noisy. Therefore, an additional filtering for high quality PS is performed, described in Sect. 6.5.2.

In addition to the filtering approach of StaMPS, a slightly different atmospheric filter method provided within the Delft PS-InSAR software (DePSI, van Leijen, 2014, p. 29 ff.) is applied to the image stack of Envisat track 294S. The temporal filtering of DePSI is similar to the StaMPS method shown in Eq. (6.11) and is performed with the same time window. In contrast to StaMPS, Kriging is used for spatial interpolation of atmospheric signals in DePSI. In general, the atmospheric filtering is performed at an earlier stage of the processing within DePSI and only applied to a subset of high quality PS pixels, the so-called first-order network. For the comparison of tropospheric correction methods within this work, the filter approach of DePSI is implemented within the StaMPS processing chain and compared to the other correction methods in Sect. 6.3.5.

6.3.5 Comparison of results

The APS estimated from the five different correction methods as described above is shown for one interferogram of Envisat track 294 in Fig. 6.11. APS for all interferograms of the stack are provided in Fig. C.1 and C.2. The atmospheric signal resulting from MERIS, shown in Fig. 6.11(a), varies within approximately three phase cycles over the 100 km × 100 km scene. From the MERIS estimate, the high spatial variability of the phase delays present on different spatial scales becomes obvious, which is hardly reconstructible by the other correction methods. As already discussed, only large-scale tropospheric effects are resolvable using the ERA-Interim weather model for the calculation of APS. The power-law technique is working fine for the interferogram shown in Fig. 6.11, but significantly deviates for others, see Fig. C.2(a). The spatio-temporal filtering approaches of StaMPS and DePSI yield similar results and a high correlation to the MERIS phase delays. Only some small-scale effects cannot be resolved, which is partly due to the spatial wavelength used with the filtering, discussed in Sect. 6.3.4.

In addition to the visual interpretation of different correction methods, a numerical comparison is performed using the MERIS estimates as validation for the other methods. Tab. 6.5 presents 2D correlation coefficients between APS of MERIS and the other methods for all interferograms with a MERIS pixel coverage of more than 70 %. Highest correlations are achieved for the spatio-temporal filtering of StaMPS and DePSI. A generally lower correlation level is observable for some interferograms, e. g. for 2005-09-05 or 2008-09-29, which may as well be attributed to inaccuracies of the MERIS water vapour estimation or the Π-factor used for transformation of water vapour into phase delay. For the reduction of atmospheric effects in the analysed URG data stacks the spatio-temporal filtering is used as it is applicable to all analysed scenes and shows the highest correlation with MERIS water vapour estimates.

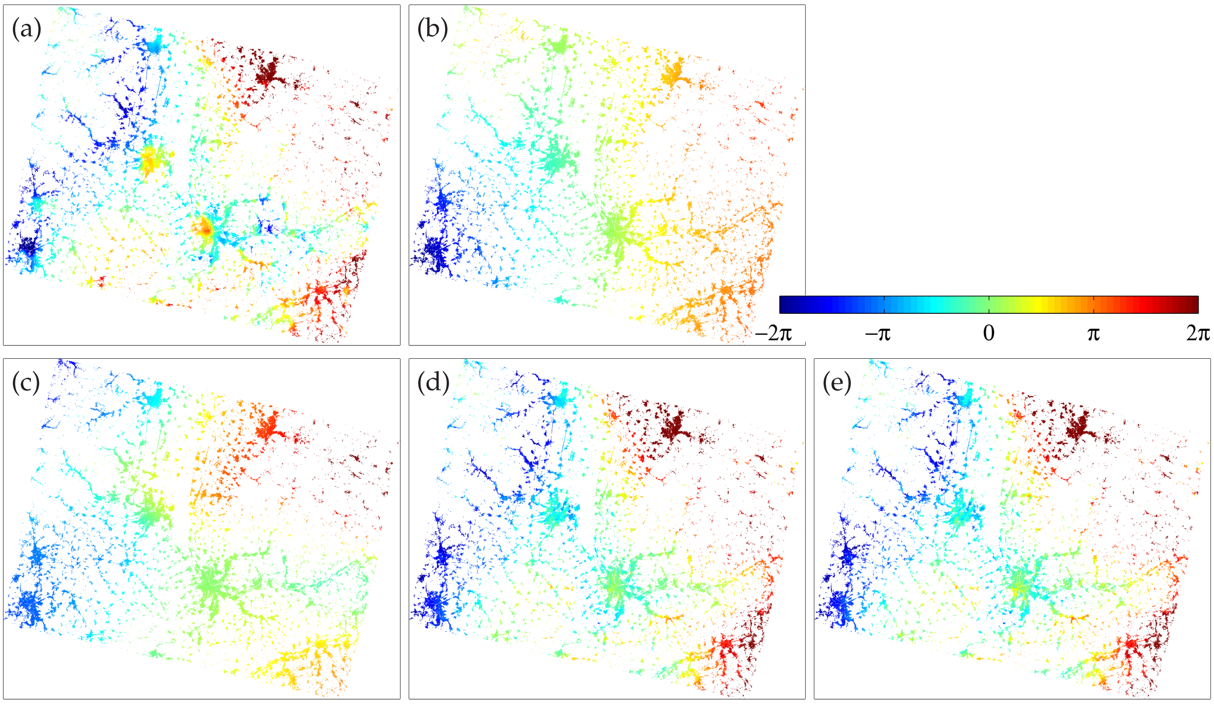

Figure 6.11: APS [rad] of a slave of Envisat track 294S acquired on 2006-07-17 w.r.t. the master acquired on 2007-08-06, calculated using different methods and data sources. The spatial extent of the figures is 6.709°–8.400°E, 47.237°–48.196°N. The correction data and methods are (a) MERIS data, (b) ERA-Interim data, (c) Power-law method, (d) Spatio-temporal filtering of StaMPS, (e) Spatio-temporal filtering of DePSI.

Table 6.5: 2D correlation coefficients of APS estimates using ERA-Interim data, Power-law method and spatio-temporal filtering of StaMPS and DePSI w.r.t. APS deduced from MERIS data

Slave date	ERA-Interim	Power-law	StaMPS	DePSI
2006-06-27	0.55	0.52	0.77	0.77
2005-08-01	0.46	0.44	0.60	0.59
2005-09-05	−0.03	0.25	0.49	0.48
2006-06-12	0.33	0.65	0.73	0.73
2006-07-17	0.60	0.73	0.89	0.89
2007-04-23	0.35	0.80	0.80	0.80
2007-09-10	0.50	0.62	0.70	0.70
2007-10-15	0.17	0.56	0.76	0.77
2008-05-12	−0.04	0.50	0.76	0.76
2008-08-25	0.45	0.65	0.77	0.76
2008-09-29	0.34	0.34	0.40	0.40
Mean	0.34	0.55	0.70	0.70

6.4 Small Baseline Subset analysis

The principal analysis strategy of Small Baseline Subset (SBAS) approaches was introduced in Sect. 3.3.3. This section presents the results of SBAS analyses with SAR data in the URG area. First, the developed strategy to select the small baseline interferograms is presented (Sect. 6.4.1). Second, a comparison of results from SBAS to those achieved with the single master PS approach is done (Sect. 6.4.2).

6.4.1 Interferogram selection

Different baseline configurations are conceivable for SBAS w.r.t. the temporal and spatial distribution of the data set as well as the analysis strategy as shown by van Leijen (2014, p. 23 f.). In Fig. 3.15(b) a baseline configuration depending on maximum values for $B_\perp$ and T is shown. The default baseline configuration in StaMPS follows from a threshold for the minimum coherence calculated based on maximum temporal and perpendicular baselines. However, a large number of interferograms may be built resulting in long runtime for the subsequent processing steps. On the other hand, some slave images are badly connected to the network of small baselines, e. g. first slave image in Fig. 6.12(a). Hence, a modified selection approach has been developed within this work. In addition to the predicted coherence values, a minimum and maximum number of connections per scene is considered in order to constrain the network of baselines. The resulting network configuration is shown in Fig. 6.12(b). The modified selection approach (i) ensures a proper integration of slave scenes in the SBAS network and (ii) reduces the total number of interferograms and thus also the runtime of the SBAS processing.

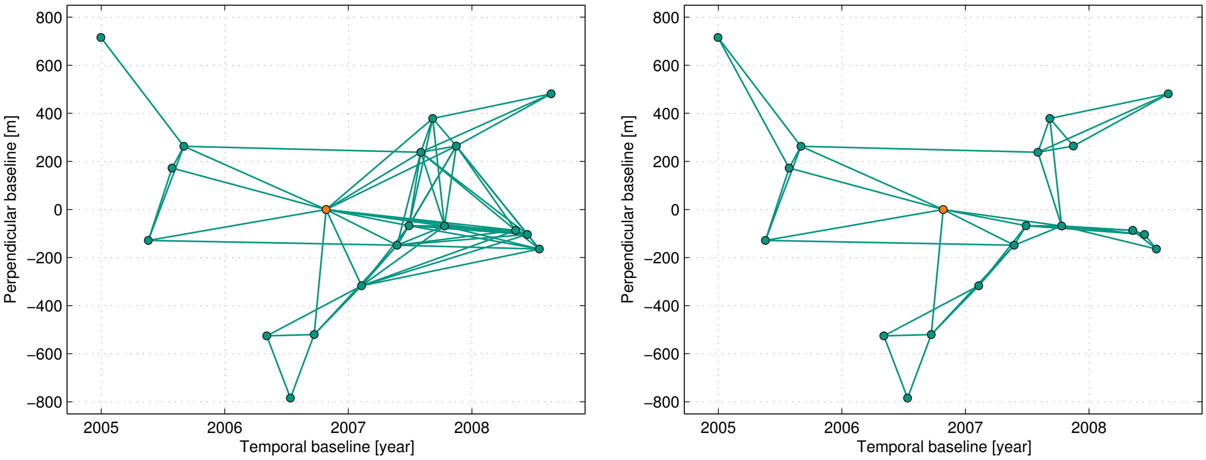

(a) Default baseline configuration of StaMPS based on minimum coherence, resulting in 65 interferograms.

(b) Modified baseline configuration accounting for a minimum and maximum number of connections, resulting in 41 interferograms.

Figure 6.12: Comparison of baseline configurations for SBAS analyses. SAR data acquired by Envisat on track 258 in the southern URG area. The orange point represents the master scene selected within a corresponding single master approach.

Note that in contrast to a single master approach, the interferograms built within an SBAS analysis are no more independent as more than $n-1$ connections are built between n SAR scenes. Thus, the same basic information is used several times.

6.4.2 Comparison to single master approach

The major difference of a single master PS-InSAR analysis and an SBAS analysis is the subset of final pixels at which the phase signal is analysed. While PS focusses on pixels with one major backscatterer, SBAS uses also pixels with distributed scattering properties and several contributors to the backscattered phase. Hence, the number of selected pixels is usually higher for an SBAS analysis resulting in a larger computation time. Within StaMPS, the subset of resolution cells is by default reduced to a coarser sampling for SBAS processing in order to keep computation time within an acceptable frame. Furthermore, the implemented SBAS approach applies a different phase unwrapping method compared to the PS analysis, denoted as *3D Quick*, see Hooper et al. (2013, p. 23 f.). The separation of phase terms is handled in a similar way as for a single master PS analysis. In order to enable the estimation of APS for every slave acquisition time, the phase values of the SBAS interferograms are transformed to values w.r.t. a single master by least-squares inversion (Hooper et al., 2013, p. 23). LOS velocities are computed from the remaining phase attributed to deformation either from the SBAS interferograms or from a weighted least-squares inversion of single master interferograms. The resulting velocities of PS and SBAS analyses using the same data set are compared to each other in Fig. 6.13. The total number of pixels is almost twice as large for the SBAS analysis. However, the number strongly depends on the weeding threshold applied to the respective data set, see Sect. 6.2.2.

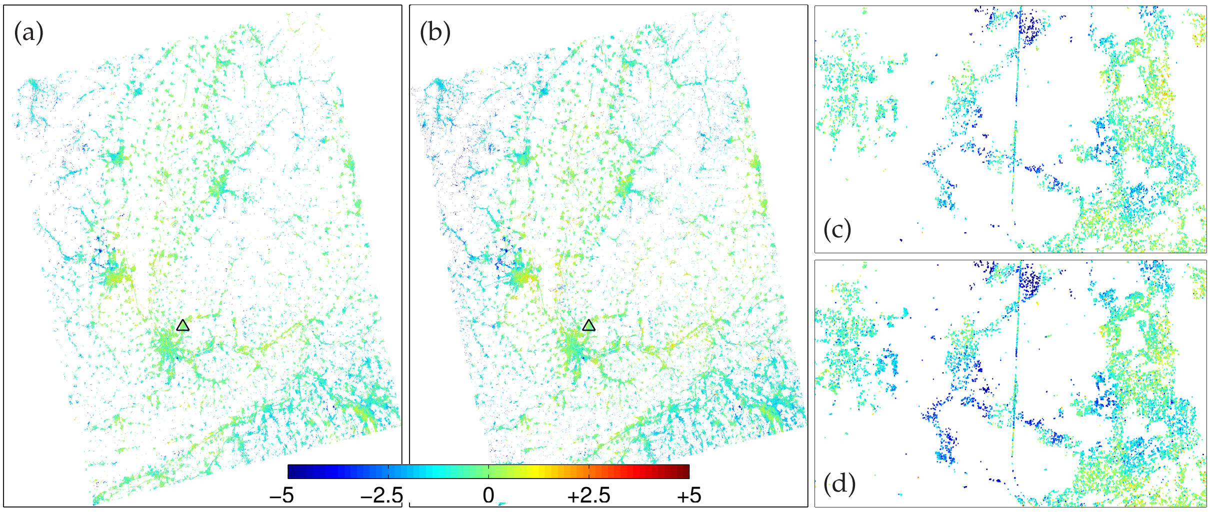

Figure 6.13: LOS displacement rates [mm/a] resulting from PS and SBAS analyses of Envisat track 258. The reference area, located in Lörrach, is marked by a black triangle and represents the mean of pixels within a 500 m radius. The spatial extent of figures (a) and (b) is 6.81°–8.70°E, 47.12°–48.50°N; (c) and (d) show a zoom on a potash mining area close to Wittelsheim in the central western part of the scene, see also Fig. C.9, with an extent of 7.16°–7.36°E, 47.76°–47.83°N. The displacements shown in (a) and (c) result from a PS analysis of 497,708 pixels, the displacement rates in (b) and (d) from an SBAS analysis of 920,925 pixels.

The resulting LOS velocities of PS and SBAS analyses are comparable in magnitude and in the spatial distribution of the pixels. Because of the large amount of SBAS pixels found within the selection, a resampling to a posting of 100 m is performed by default within StaMPS. As this reduces the spatial coverage especially in urban areas, a value of 20 m is set for the SBAS processing shown in Fig. 6.13(b) and (d). Processing without resampling results in a large amount of pixels, i. e. more than 5 million within the analysed frame (below 1 million for a 20 m posting) and could not be performed within an acceptable computation time.

However, the higher amount of measurement points resulting from the SBAS analysis does not provide significantly more information on the deformation field in the URG area compared to the PS analysis. Most of the additional SBAS pixels are located in the cities and villages, where the field of PS is already dense, see Fig. 6.13(c) and (d). A further comparison of LOS displacements from PS and SBAS analyses is shown in Fig. 6.20 w.r.t. side lobe effects.

The estimates of the nuisance terms ϕ_{SCLA}, ϕ_{orbit} and ϕ_{atmo} are similar compared to the PS analysis. As the spatio-temporal filtering is performed on basis of single master interferograms, the separation of phase terms does not significantly improve for an SBAS analysis. For the analysis of all available SAR data in the URG area, the PS approach is used as it delivers an adequate amount of information for the large-scale investigation of surface displacements in the whole URG area w.r.t. the runtime needed for the processing of this large database. However, for investigations on local surface displacements with an extent of several km, the SBAS approach is well-suited enabling the extraction of displacements at a high spatial resolution, see e. g. Schenk (2015).

6.5 Resulting surface displacements

After subtracting all perturbation terms from the phase values, the phase representing the surface displacement between the acquisition time of the master and the slave images, called deformation phase ϕ_{defo}, remains as the major result of the PS-InSAR analysis. Surface displacements along the LOS towards the satellite are converted from phase to metric scale using the relation:

$$\phi_{defo} = -\frac{4\pi \Delta R}{\lambda} \tag{6.13}$$

where positive ΔR values denote LOS displacements towards the satellite in m. The following sections present the results of the PS-InSAR analyses carried out in the URG area. In Sect. 6.5.2 an additional quality estimation of PS pixels is explained based on the frequency distribution, see Sect. 6.5.1, of two quality indicators. The calculation of quality indicators enables a filtering of high quality PS and is, inter alia, capable to minimise the effect of side lobes present in the SAR data, see Sect. 6.5.3. The resulting LOS velocities are presented in Sect. 6.5.4. Within the Envisat tracks in the URG area, significantly more SAR images are available in the southern part of the URG. In order to enhance accuracy, tracks 294 and 487 are split into subregions for the Envisat data, and the highest number of available scenes is analysed within each subtrack, see Tab. 3.3. The partly overlapping subtracks are stitched together for the data fusion, see Sect. 7.4.3. For investigations on local surface deformation related to anthropogenic activities, the results of the subtracks are considered. Sect. 6.5.5 presents a case study on temporally changing surface displacements at oil fields close to the city of Landau, observed by levelling, GNSS and InSAR. The results of two further investigations on surface deformation at mining areas are shown in Appendix C.

6.5.1 Frequency distribution of phase values

This section presents frequency distributions of PS phase values for data of an ERS track with two different parameter settings for the threshold standard deviation applied in the StaMPS weeding, see Sect. 6.2.2. A lower threshold results in less PS to be kept. The absolute numbers of remaining PS are 756,771 and 1,084,280 for a threshold standard deviation of 0.7 rad and 0.8 rad, respectively. In both cases, the distribution of deformation phase values is close to a normal distribution with zero mean, but with a higher peak and heavier tails, see Fig. 6.14. The probability density function (PDF) of a normal distribution $\mathcal{N}(\mu, \sigma) = f(x|\mu, \sigma)$ is fitted to the histogram of phase values using maximum likelihood estimation:

$$f(x|\mu,\sigma) = \frac{1}{\sigma\sqrt{2\pi}} \exp\left(\frac{-(x-\mu)^2}{2\sigma^2}\right) \tag{6.14}$$

The resulting mean value μ is -0.020 rad (corresponds to 0.089 mm) and the standard deviation σ is 0.876 rad (3.943 mm) for the weed standard deviation threshold of 0.7 rad, shown in Fig. 6.14(a). For a weed standard deviation threshold of 0.8 rad, shown in Fig. 6.14(b), the resulting standard deviation of the PDF is higher: $\sigma = 0.938$ rad (4.225 mm).

According to Rocca (2007), especially target decorrelation and noise due to residual atmospheric contributions make the PDF of phase observations non-Gaussian. Tison et al. (2004) discusses the application of other, non-Gaussian distributions in order to describe the scattering statistics of SAR amplitude images. As a Gaussian normal distribution does not ideally fit the histogram of ϕ_{defo}, see Fig. 6.14, different distributions are investigated. In contrast to a normal distribution, Student's t-distribution can be used to describe sample data drawn from

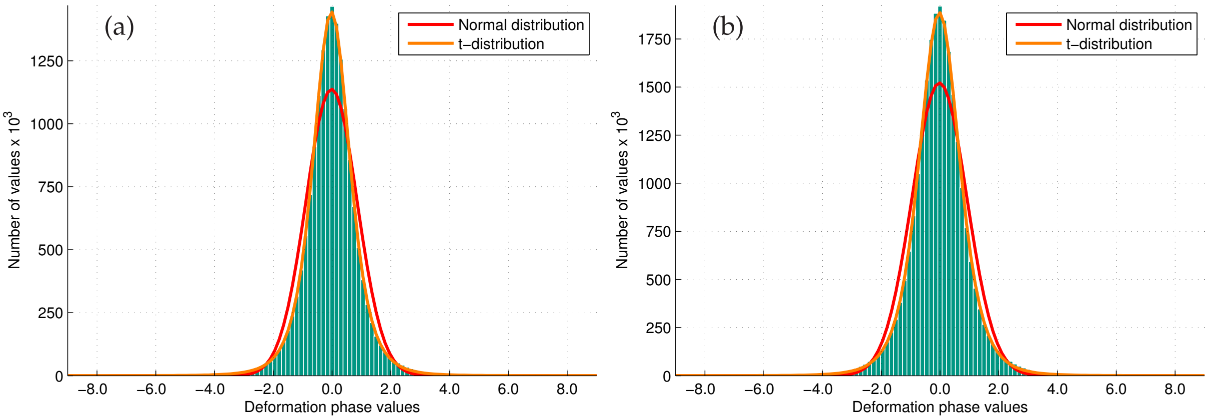

Figure 6.14: Histogram and fitted PDFs of a normal distribution and a t-distribution for the deformation phase values of all 22 interferograms at PS pixels of ERS, track 487. (a) weed standard deviation threshold: 0.7 rad, 756,771 PS, (b) weed standard deviation threshold: 0.8 rad, 1,084,280 PS.

a full population. The density of a non-standardised t-distribution with mean μ, standard deviation σ and degree of freedom ν is given by:

$$f(x|\mu,\sigma,\nu) = \frac{\Gamma(\frac{\nu+1}{2})}{\sigma\sqrt{\nu\pi}\Gamma(\frac{\nu}{2})}\left(1+\frac{1}{\nu}\left(\frac{x-\mu}{\sigma}\right)^2\right)^{-\left(\frac{\nu+1}{2}\right)} \tag{6.15}$$

using the Gamma function $\Gamma(n) = (n-1)!$. The t-distribution becomes a normal distribution for $\nu \to \infty$. From Fig. 6.14, one can see that the PDF of a t-distribution nicely fits the histogram of phase values. The corresponding parameters used in Fig. 6.14(a) are $\mu = -0.022$ rad (0.099 mm), $\sigma = 0.650$ rad (2.926 mm) and $\nu = 4.185$. Note that ν may adopt non-integer values for the best-fitting curve resulting from maximum likelihood estimation.

6.5.2 Quality estimation

The quality of the results of a PS-InSAR analysis is difficult to handle. As only one observation per measurement epoch is available, a classical geodetic description, e. g. using redundant observations, is not possible. Several quality indicators have been described by van Leijen (2014, p. 112 ff.). Two of them, i. e. the ensemble coherence (EC) and the spatio-temporal consistency (STC) are presented in the following. They are used in order to filter the PS resulting from the StaMPS analysis as the data set still contains some pixels with unrealistic deformation behaviour or at unrealistic places.

EC, also denoted as temporal coherence, was introduced by Ferretti et al. (2001), see van Leijen (2014, p. 113 f.):

$$\hat{\gamma}_{EC,k} = \left|\frac{1}{n}\sum_{i=1}^{n}\exp(j(\phi_k^i - \phi_{k,model}^i))\right| \quad . \tag{6.16}$$

Following Eq. (6.16), the EC value is estimated at every PS pixel k and describes the deviation between the displacement time series and the deformation model, e. g. a linear model as denoted in Eq. (6.17). The resulting EC values $\hat{\gamma}_{EC}$ range between 0 and 1, where 1 corresponds to a perfect match of the deformation time series to the model. The major disadvantage of a temporal coherence estimator is the fact that a (linear) model has to be subtracted in order to provide ergodicity of phase values. As the deformation in the URG is small at most places and the focus of the investigation is on linear movements, EC serves as a quality indicator for PS within this study. The modelled deformation phase $\phi^i_{k,model}$ is estimated from linear regression of the observations $y = \phi^i_k$ using the temporal differences of the slave acquisition dates t_i:

$$A = \begin{pmatrix} 1 & t_1 - t_1 \\ 1 & t_2 - t_1 \\ \vdots & \vdots \\ 1 & t_n - t_1 \end{pmatrix} \quad ; \quad \phi^i_{k,model} = \hat{y} = A \cdot \hat{x} \quad . \tag{6.17}$$

Fig. 6.15 displays the frequency distribution of resulting EC values of ERS track 487 in the URG area. The EC values do not follow a normal distribution (or t-distribution) as the exponential function is applied to the original deformation phase values. When x is a normally distributed random variable and $y = \exp(x)$, then y follows a log-normal distribution (Montgomery & Runger, 2011, p. 144). The PDF of a log-normal distribution is given by

$$f(x|\mu,\sigma) = \frac{1}{x\sigma\sqrt{2\pi}} \exp\left(\frac{-(\ln x - \mu)^2}{2\sigma^2}\right) \quad ; \quad x > 0 \quad . \tag{6.18}$$

A best fitting PDF is estimated for the histogram of EC values shown in Fig. 6.15 according to Eq. (6.18). The fitted curve of Fig. 6.15(a) nicely describes the distribution of EC values, even if a normal distribution of the full population is assumed instead of a better fitting t-distribution. However, some PS with low EC values (below 0.5) deviate from the fitted curve. In order to filter out the PS with low coherence, a threshold for the minimum EC value $\hat{\gamma}_{EC,min}$ is calculated using the fitted PDF along with a given percentile, e. g. 98 %. When the threshold standard deviation of the weeding is chosen too generously, the resulting frequency distribution does not resemble the theoretical PDF in a suitable way, see Fig. 6.15(b) for ERS track 487 as well as Fig. C.3 in Appendix C for Envisat track 487S. The ensemble coherence is therefore also an effective measure to find an appropriate value for one of the most important parameter settings within StaMPS, i. e. the weed standard deviation threshold discussed in Sect. 6.2.2.

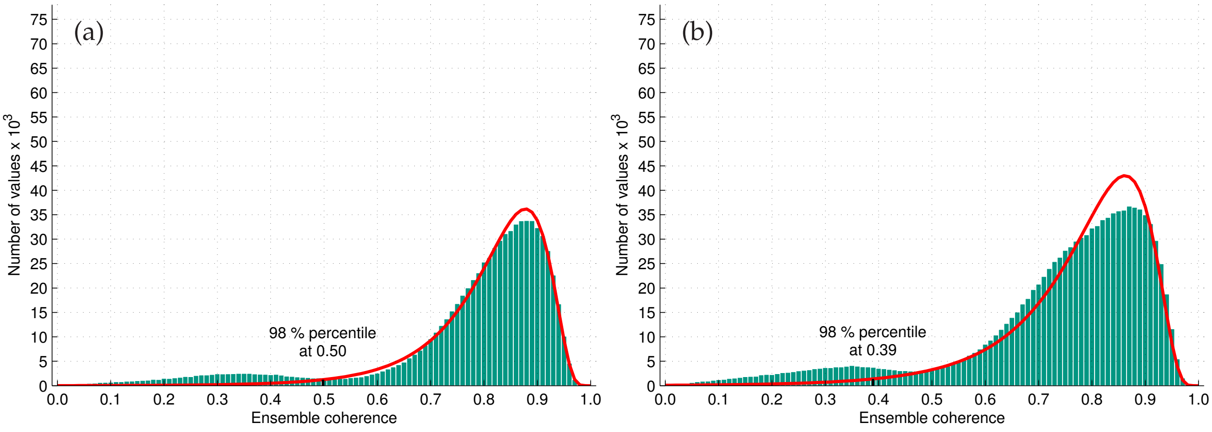

Figure 6.15: Histogram, fitted PDF of the log-normal distribution and filtering threshold for EC values calculated at PS locations of ERS track 487. (a) weed standard deviation threshold: 0.7 rad, 756,771 PS pixels, (b) weed standard deviation threshold: 0.8 rad, 1,084,280 PS pixels.

The second quality indicator, spatio-temporal consistency (STC), was introduced by Hanssen et al. (2008, p. 64 f.) as a measure which is independent of the temporal deformation behaviour. Taking into account the minimum root mean squared deviation of surrounding PS phase values, the influence of the spatial deformation pattern on STC values is minimised. The STC value is calculated for every PS pixel k using surrounding PS j within a specific minimum and maximum radius, see Hanssen et al. (2008, p. 64 f.) or van Leijen (2014, p. 118):

$$\rho_{STC,k} = \min_{\forall j} \frac{\lambda}{4\pi} \sqrt{\frac{1}{n-1} \sum_{i=1}^{n-1} ((\phi_j^i - \phi_k^i) - (\phi_j^{i+1} - \phi_k^{i+1}))^2} \quad . \tag{6.19}$$

The maximum radius defines the area in which the deformation behaviour is considered to mainly represent the measurement noise. The minimum radius is applied to reduce the influence of side lobes on the STC estimates. If no neighbouring PS pixels are found within the search radius, the STC value remains undetermined. Hanssen et al. (2008) and van Leijen (2014) propose a minimum and maximum radius of 50 m and 250 m, respectively, for ERS and Envisat data. Tab. 6.6 compares the number of PS pixels without STC estimate for a maximum radius of 250 and 500 m. Choosing a maximum radius of 250 m, many PS with undetermined STC value remain in the data set for the URG area. Furthermore, the low frequency deformation patterns in the URG are assumed to change within several km. Therefore, an increased maximum radius of 500 m seems more suitable for the calculation of STC values in the SAR tracks of the URG area.

Table 6.6: Number of PS pixels without STC values in ERS track 487, total number of PS pixels: 756,771

Maximum radius:	250 m		500 m	
PS without STC estimate:	8,303	(1.10 %)	2,832	(0.37 %)
Thereof sorted out by EC threshold:	1,448		544	
Rejected PS, not STC-checked	6,855	(0.91 %)	2,288	(0.30 %)

The frequency distribution of resulting STC values is shown in Fig. 6.16. As Eq. (6.19) uses the respective minimum of a sample of neighbouring pixels, the STC values ρ_{STC} are not normally or t-distributed. Block maxima or minima of a sample drawn from a very large collection of random observations from the same arbitrary distribution follow the so-called extreme value distribution (EV) developed by Gumbel (2004). For any well-behaved initial distribution, i. e. $f(x)$ is continuous and has an inverse, the EV distribution is the limiting distribution of the minimum of a large number of unbounded identically distributed random variables. The PDF of the EV distribution is given by

$$f(x|\mu,\sigma) = \frac{1}{\sigma} \exp(\frac{x-\mu}{\sigma}) \exp(-\exp(\frac{x-\mu}{\sigma})) \quad . \tag{6.20}$$

In order to estimate an appropriate threshold for the filtering of high quality PS pixels using STC values, a distribution is fitted to the histogram. The fitted PDF along with a given percentile, e. g. 98 %, is then used to determine the threshold $\rho_{STC,max}$ for the filtering. Again, the higher weed standard deviation threshold of 0.8 rad results in a worse fit of the PDF to the histogram compared to the lower weed standard deviation of 0.7 rad, particularly in the peak region of the histogram. A comparison of STC histograms for different weed standard deviation thresholds applied to Envisat track 487S is shown in Fig. C.4 in Appendix C. In

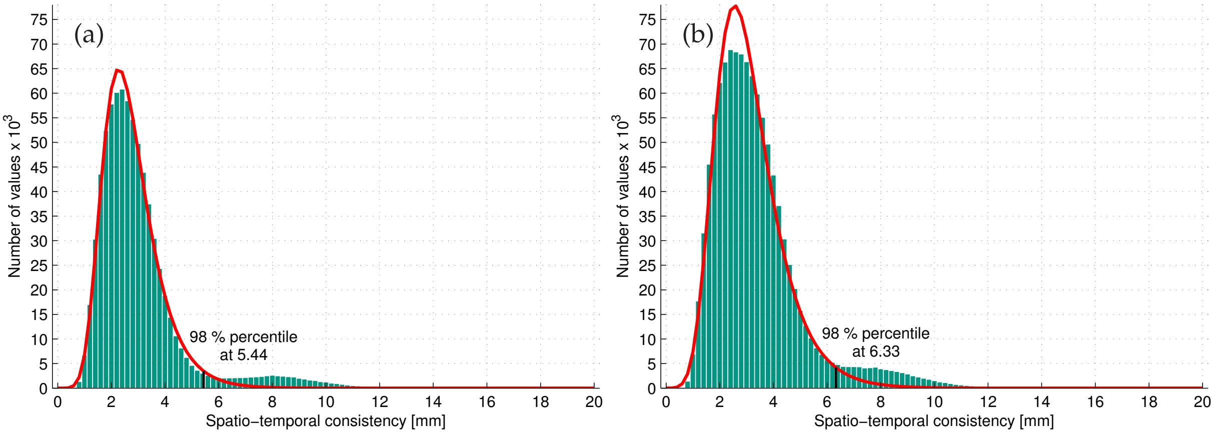

Figure 6.16: Histogram, fitted PDF of the EV distribution and filtering threshold for STC values calculated at PS locations of ERS track 487. (a) weed standard deviation threshold: 0.7 rad, 756,771 PS pixels, (b) weed standard deviation threshold: 0.8 rad, 1,084,280 PS pixels.

addition, Tab. C.2 compares the number of (filtered) PS pixels and corresponding EC and STC value thresholds for the corresponding analyses with different weed standard deviation thresholds.

Quality indicators have been calculated for all analysed SAR tracks in the URG area in order to filter the final subset of StaMPS PS pixels and provide high quality information for the combination with levelling and GNSS. The estimated filter thresholds and corresponding numbers of discarded and remaining PS pixels are summarised in Tab. 6.7. Between 7.7 % and 14.0 % of the PS pixels have been filtered out within the analysed image stacks.

Table 6.7: Comparison of the quality filtering thresholds in the analysed SAR tracks and number (No.) of discarded and remaining PS. The weed standard deviation thresholds used within the different data stacks are given in Tab. 6.4.

Satellite, track	$\hat{\gamma}_{EC,min}$ [–]	$\rho_{STC,max}$ [mm]	No. of all PS	No. of good PS	No. of bad PS	bad PS [%]	bad EC [%]	bad STC [%]
ERS, 294	0.45	7.03	702,348	628,998	73,350	10.4	9.4	7.7
ERS, 258	0.46	5.77	639,977	584,509	55,468	8.7	7.2	5.7
ERS, 487	0.50	5.44	756,771	669,464	87,307	11.5	10.0	7.8
Envisat, 294N	0.51	5.03	435,556	393,634	41,922	9.6	8.2	7.0
Envisat, 294C	0.48	6.09	297,065	255,543	41,522	14.0	12.4	8.6
Envisat, 294S	0.45	6.51	266,813	235,139	31,674	11.9	10.2	8.2
Envisat, 258	0.45	5.17	497,708	454,643	43,065	8.7	6.7	5.3
Envisat, 487N	0.57	4.54	870,006	803,418	66,588	7.7	6.0	5.2
Envisat, 487S	0.53	6.01	305,927	271,814	34,113	11.2	9.6	9.6

Spatial plots of EC and STC values in the northern URG area are shown in Fig. 6.17. PS pixels with low EC values, i. e. PS to be filtered out, are mainly found within isolated PS patterns. Some larger patterns with low EC values are close to the cities of Karlsruhe and Hockenheim and are both located in areas where the surface has changed due to construction works. The red EC values east of Hockenheim are located at a racetrack which was partly rebuilt starting in 2002. In addition, the EC values are low if side lobes remain in the data set, see the WNW–ESE oriented PS pattern west of Karlsruhe and Sect. 6.5.3. No significant dependence of EC values on the distance to the reference area could be found for the analysed data, even for the 300 km long stripes of ERS data. This indicates that trends and atmospheric effects present in the phase values have been largely reduced within the PS processing, see van Leijen (2014, p 113 f.). The deformation pattern close to the oil fields of the city of Landau does not provide significantly larger EC values, although the deformation is known to be non-linear. Within the analysed period (2003/12–2008/12), the deformation is still close enough to a linear movement to pass the EC threshold given in Tab. 6.7. PS pixels with high STC values, i. e. PS to be filtered out, are more homogeneously distributed over the whole area. As they represent PS pixels with phase values which do not fit to the phase values of surrounding PS, see Eq. (6.19), they are not appearing within large patterns.

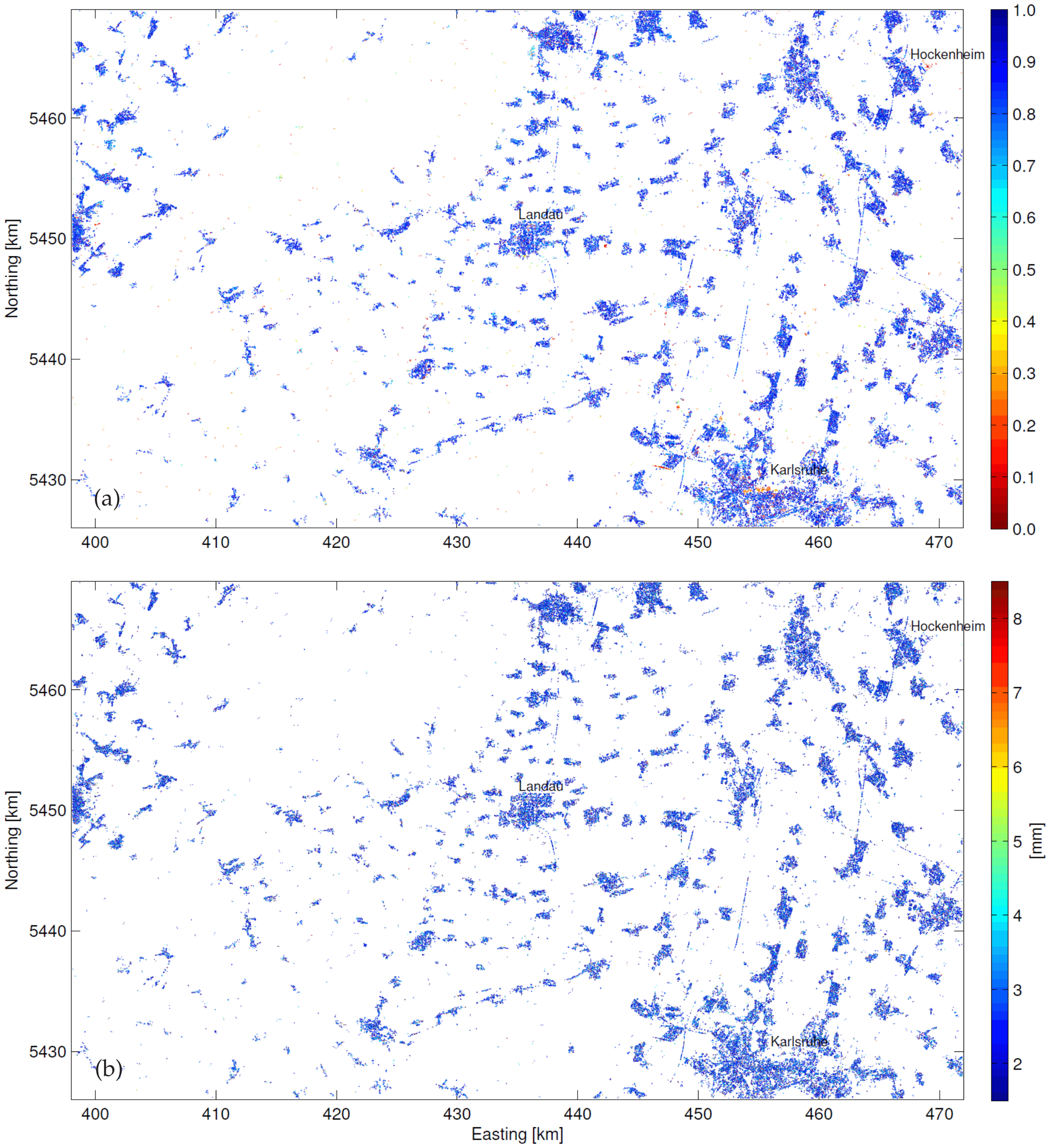

Figure 6.17: Quality indicators in the northern URG, crop of an Envisat analysis (track 294N). (a) Ensemble coherence (EC), (b) Spatio-temporal consistency (STC). The spatial extent of the figures is 7.601°–8.616°E, 48.984°–49.370°N. The reference area is located in Karlsruhe and the same as in Fig. 6.10.

The resulting PS deformation pattern after filtering is smoother because most of the pixels with unrealistic displacement values have been filtered out. Fig. 6.18 compares the original PS LOS displacements of a crop close to the city of Landau in the northern URG to the filtered PS LOS displacements. Different PS pixels are filtered out when applying the EC and STC thresholds, respectively, shown in Fig. C.5 in Appendix C. The application of both quality indicators for the filtering results in a smooth deformation pattern as shown in Fig. 6.18(b). The main subsidence and uplift signal in the area close to the Landau oilfields, which is also confirmed by levelling measurements, see Sect. 4.6.2, is still preserved and not filtered out.

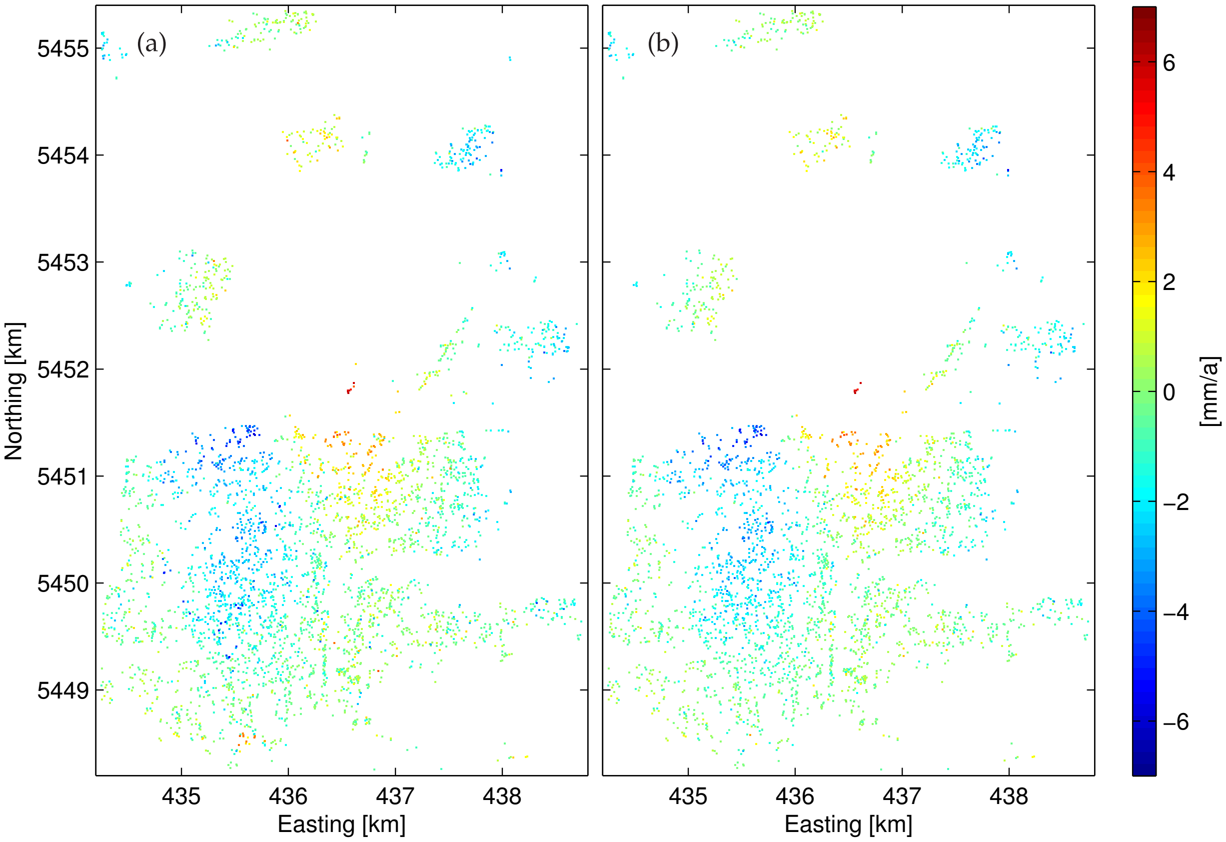

Figure 6.18: LOS velocities at PS locations, crop of a region in northern URG close to the city of Landau also shown in Fig. 6.22(b), Envisat track 294N. (a) all PS pixels selected within StaMPS, (b) high quality PS pixels: bad EC or STC values are filtered out. The spatial extent of the figures is 8.096°–8.160°E, 49.183°–49.248°N. The reference area is located in Karlsruhe and the same as in Fig. 6.10.

6.5.3 Side lobes

Strong point scatterers in a SAR image result in side lobes in azimuth and range directions as the spatial signature of a point scatterer is a *sinc* function (van Leijen, 2014, 45 ff.). The phase of the side lobes is shifted by π and hence does not add valuable information to the interferometric SAR signal. Because of their similar characteristics compared to the main lobe, side lobes have a significant probability to be selected as PS. Fig. 6.19(a) and (b) display some strong side lobes present in an amplitude image of Envisat track 258. The side lobe in the northern part of Fig. 6.19(b) can be attributed to the jagged shape of the roof of greenhouses shown in Fig. 6.19(d) resulting in a strong backscattering signal. As the phase values of a strong side lobe are located at completely different positions compared to the main lobe and the reference phase is not corrected for this offset, the resulting ϕ_{defo} is misleading for the further interpretation of surface displacements. In addition, an error signal in range direction is introduced due to the subtraction of ϕ_{ref} and ϕ_{DEM}, which are calculated for the location of every pixel. Such an error is nicely visible in the resulting LOS displacements shown in Fig. 6.19(c).

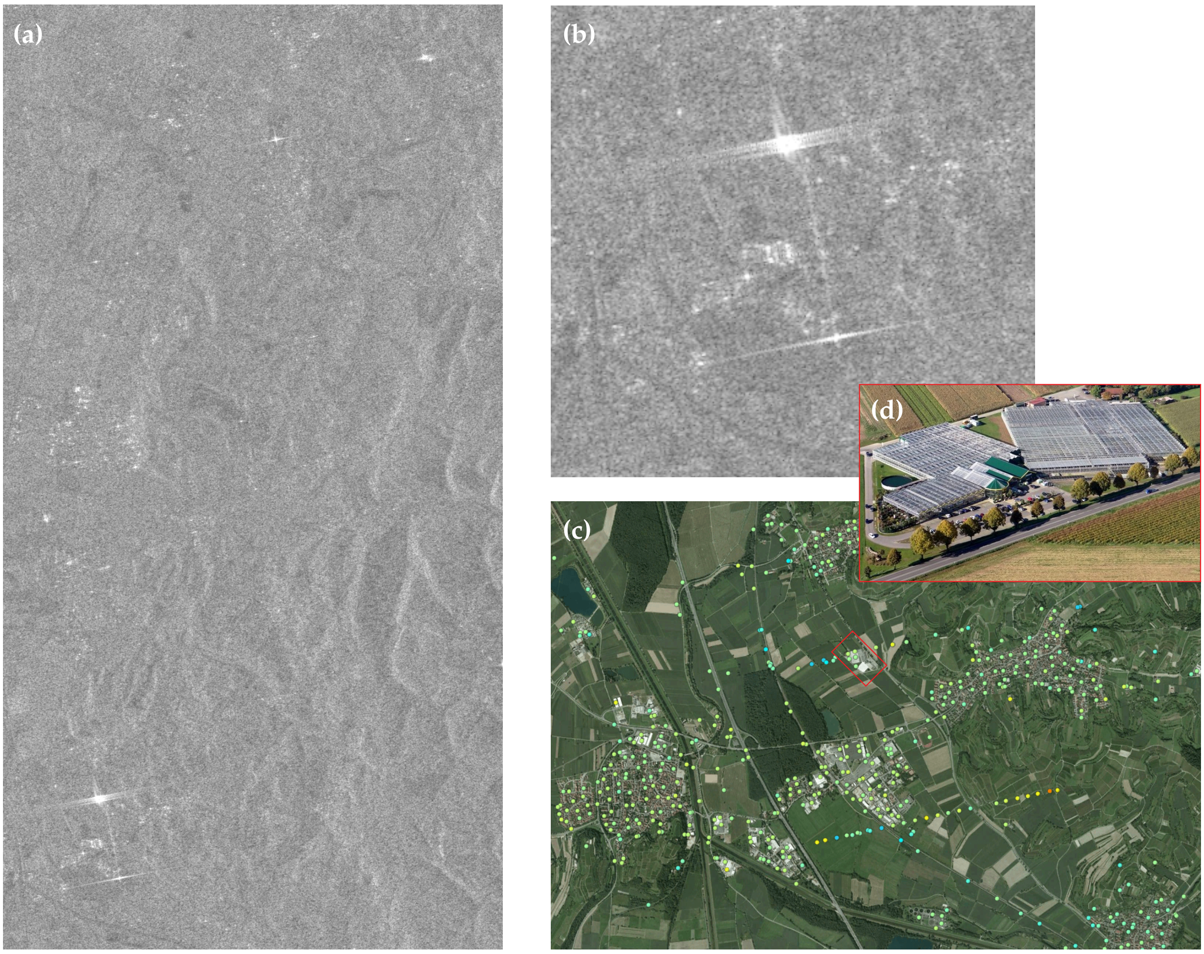

Figure 6.19: Side lobes and their influences on InSAR analyses. (a) amplitude image of the area displayed in Fig. 6.20 for an Envisat scene of track 258 acquired on 2008-08-22, including side lobes in the southwestern and in the northeastern parts of the crop. The spatial extent of the image is similar as in Fig. 6.20. (b) zoom on the side lobes in the southwestern part of (a). (c) resulting LOS velocities at DS locations of an SBAS analysis (weed standard deviation threshold 0.6 rad), similar crop as in (b) at 7.738°–7.813°E, 48.139°–48.173°N. (d) aerial image of the garden centre marked in (c) by a red rectangle (source: http://www.pflanzen-keller.de/unsere-gaertnerei). The jagged roofs of the greenhouses induce strong side lobes visible in (a) and (b).

Within StaMPS, adjacent pixels are assumed to be dominated by the same scatterer (Hooper, 2006, p. 24). In order to avoid the selection of pixels with systematic phase artefacts, the less coherent of adjacent pixels are considered to be affected by side lobes of the brighter pixel and discarded (Agram, 2010, p. 33 f.). However, for the large side lobe effects shown in Fig. 6.19, this procedure fails and PS affected by side lobes effects pass into the final subset of PS. In order to investigate the influence of the processing strategy on the number and significance of pixels affected by side lobes, the LOS velocities from SBAS and PS analyses for the same data set are compared to each other, see Fig. 6.20. Furthermore, the influence of the weed standard deviation threshold, see Sect. 6.2.2, along with the additional quality filtering, see Sect. 6.5.2, on the final set of pixels is investigated.

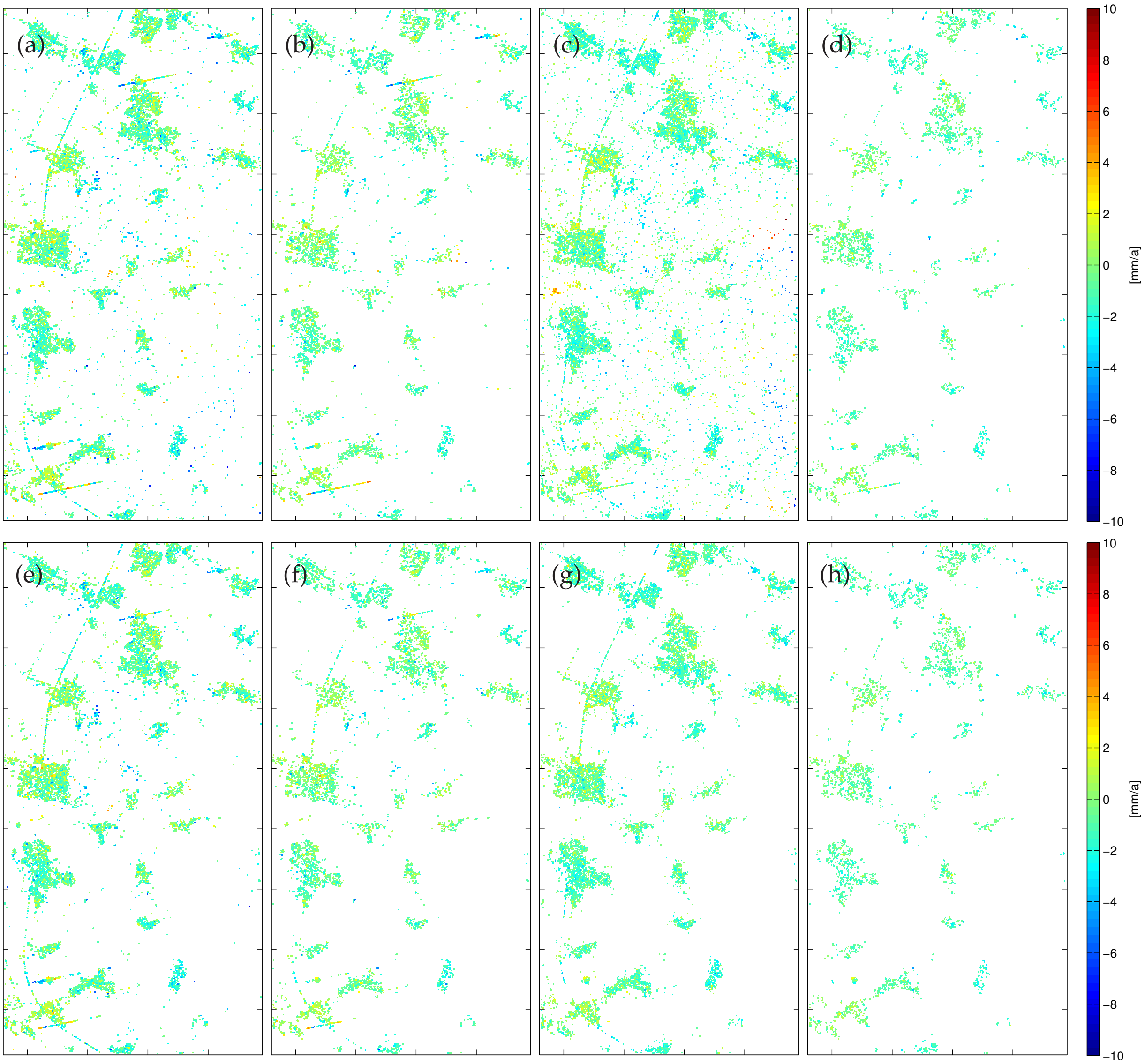

Figure 6.20: LOS velocities at PS/DS pixels in the region in the southern URG used in Fig. 6.19(a), Envisat track 258. (a)–(d) all PS/DS, (e)–(h) high quality PS/DS only. (a) and (e) SBAS analysis, weeding threshold: ∞, (b) and (f) SBAS analysis, weeding threshold: 0.6 rad, (c) and (g) PS analysis, weeding threshold: ∞, (d) and (h) PS analysis, weeding threshold: 0.6 rad. The spatial extent of the figures is 7.752°–7.868°E, 48.140°–48.293°N. Ticks mark 2 km distances in East and North direction.

When comparing the results in Fig. 6.20(f) (SBAS) and Fig. 6.20(h) (PS), it becomes obvious that both techniques provide significant surface displacement estimates almost exclusively in the cities and villages, even if the number of detected pixels is larger in the SBAS case, see Sect. 6.4.2. Side lobes effects are visible in all four variants before low quality pixels are filtered out, see Fig. 6.20(a)–(d), particularly in the SBAS results. After the filtering using thresholds for EC and STC, pixels affected by side lobes only remain partly in the DS LOS velocities and are completely filtered out for the PS LOS velocities. Weeding with an appropriate standard deviation threshold already reduces the number of side lobe pixels in the analysed crop before the quality filtering is applied. In addition to the lower computation time as discussed in Sect. 6.4, the PS approach is less susceptible for side lobe effects and therefore preferred for the analysis of SAR data in the whole URG area.

6.5.4 LOS displacement rates in the URG area

LOS displacement rates result from linear regression of displacement values at PS pixels in each interferogram. An approach to estimate displacement rates from a combination of ERS and Envisat on the level of time series is presented in the framework of the fusion of InSAR with levelling and GNSS in Sect. 7.4.4. The LOS velocities of ERS ascending track 258 and descending track 294 are exemplarily shown in Fig. 6.21. For visualisation purposes, the velocities are interpolated to a 200 m grid carrying values only close to the PS pixels by application of Kriging, described in detail in Sect. 7.3.

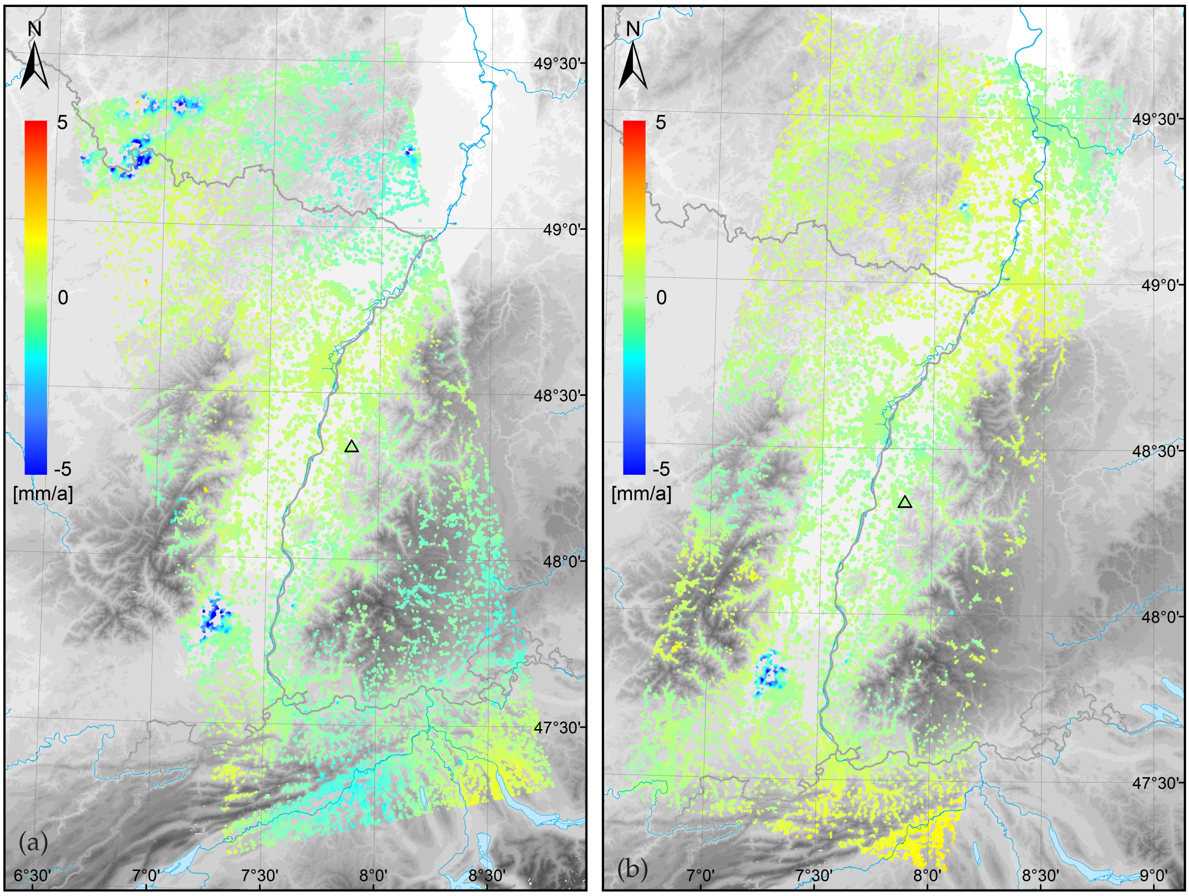

Figure 6.21: LOS velocities interpolated to a 200 m grid in the vicinity of PS locations. (a) ERS track 258 (ascending), (b) ERS track 294 (descending). The reference area of both tracks is located at the city of Lahr and contains a subset of PS pixels within a 500 m radius around 7.876°E, 48.342°N, marked by a black triangle.

Besides larger subsidences in regions with known anthropogenic activities, the velocity within the two analysed tracks is small. 98 % and 99 % of the LOS velocities are within ±2 mm/a for ERS track 258 and 294, respectively, 84 % and 86 % within ±1 mm/a. The LOS velocities are relative to the same reference area and show a similar deformation pattern in the URG area. However, larger differences between the velocity values area visible in some regions, which can be addressed to the different image geometries (ascending vs. descending), the different time span covered by the two analyses along with a different number of scenes, see Tab. 3.3, and remaining contributions of nuisance terms in the deformation phase. As the data stack acquired in ERS track 294 comprises a larger number of scenes, the resulting velocities are supposed to be more accurate compared to the velocities of ERS track 258. The velocity field shown in Fig. 6.21(a), seems to be affected by large-scale trends, particularly at the edges of the analysed area. The LOS velocities in the southern part of track 258 around the Jura Mountains, for example, might be affected by residual atmospheric effects. Within the data fusion approach presented in Sect. 7.4, the accuracy and validity of the velocity estimates is enhanced by combination of ERS and Envisat displacement time series. In addition, the InSAR results are incorporated into the reference frames of levelling and GNSS by estimating offsets and trends between the techniques as described in Sect. 7.4.5. The uncertainties of LOS velocity estimates from combined ERS/Envisat time series are at the level of 0.6 mm/a (2σ), see Tab. 7.3. Thus, displacement estimates at the sub-mm/a-level from single-sensor analysis are at the edge of significance. Particularly if only a small number of scenes is available within one image stack (< 20), a proper separation of the deformation phase from other nuisance terms is not possible and deteriorates the estimated LOS velocities.

Large displacements attributed to anthropogenic activities are observed in the LOS velocities displayed in Fig. 6.21 in three areas: (i) in the northwestern part of track 258 at the mining areas of Lorraine and Saarland, (ii) in the northern part of both tracks close to the city of Landau and (iii) in the southern part of both tracks close to Mulhouse. The deformation close to Landau is further investigated in Sect. 6.5.5 using ERS and Envisat LOS displacement rates along with displacement rates from levelling and GNSS. The other two deformation patterns are shown in detail in Appendix C. Fig. C.6 and C.7 show a zoom on the region of the mining areas at the French-German border, Fig. C.8 shows two displacement time series related to a strong subsidence and a smaller uplift. Subsidence results from compaction of the ground above the subsurface mines. In some parts of the deformation area, the total amount of the subsidence signal is not measurable with the available SAR database as the displacement between two subsequent slave acquisitions is larger than one phase cycle (28 mm). At the corresponding locations, most of the pixels are discarded as they do not fulfil the PS selection criteria. This is why some of the urban areas in Fig. C.7 are sparsely covered by PS, particularly at Freyming-Merlebach or Forbach. Mining was terminated in 2004 and 2012 in the French and German part of the area, respectively, see Tab. 2.2. At some former mines, the water level increases resulting in surface uplift, which might be the case at the location of the time series shown in Fig. C.8(b).

LOS velocities from ERS and Envisat analyses at the potash mining area northwest of Mulhouse are shown in Fig. C.9. Mining was terminated in 2002 in this area, see Tab. 2.2. Hence the velocity field resulting from Envisat track 294S shows smaller displacements in most parts compared to the ERS velocities. A small bias may be introduced as a different reference area has to be used for the Enivsat analysis, see Sect. 7.4.3. However, the bias is small as areas with a certain distance to the potash mining area carry velocities close to zero for both analysis. At Bollwiller, in the northern part of the crop, no PS are selected within the ERS analysis shown in Fig. C.9(a). As observed for the LOS velocities in Lorraine/Saarland, the displacement between subsequent acquisitions might exceed the phase cycle threshold of 28 mm here. A static comparison from two levelling campaigns in 1973 and 1994 revealed an absolute subsidence of almost 3 m, i. e. 140 mm/a, at levelling benchmarks in the southern part of the mining area. For the kinematic adjustment of levelling data presented in Sect. 4.5, these benchmarks had to be excluded from the data set because of strong non-linearities.

6.5.5 Deformation pattern close to Landau

The deformation pattern close the city of Landau in Rheinland-Pfalz has already been investigated from the levelling records, see Sect. 4.6.2. While subsidence is observed at the levelling benchmarks crossing the oil field in the measurement epochs between 1955 and 1994, some of the benchmarks are uplifting after 1994. The area close to Landau is selected as a test site for intercomparison and validation of levelling, GNSS and InSAR for the following reasons: (i) the observed displacement rates are significantly larger than in most other parts of the URG, (ii) the LOS velocities are expected to be mainly affected by vertical movements, assuming a point-like pressure source in the ground, and (iii) a large number of levelling campaigns has been carried out in the area. For a comparison of the levelling results with those obtained from GNSS and InSAR, two periods with temporally overlapping data sets are available covering the years 1992–2003 for levelling and SAR data of ERS and 2003–2009 for levelling, GPS and SAR data of Envisat. Resulting velocity values are shown in Fig. 6.22. The reference area of the velocity estimates in both tracks is set to the same area as for the local levelling analysis at the city of Kandel 15 km south of Landau, see Fig. 4.22. Note that the LOS velocities from InSAR are compared to vertical velocities from levelling and GNSS. Assuming no horizontal movements, LOS velocities can be converted into vertical velocities by multiplication with $1/cos(\theta) = 1/cos(20^\circ) = 1.06$ (e. g. 5 mm/a LOS velocity $\widehat{=}$ 5.3 mm/a vertical velocity). Vertical velocities from InSAR can be calculated using data from ascending and descending LOS directions as described in Sect. 7.2. However, the combination of ascending and descending data requires interpolation and approximation of the displacement rates as the location of PS and the covered time span are generally not identical for PS data of different image geometries. In addition, the separation of horizontal and vertical velocity components from SAR data of one ascending and one descending track is not possible without assumptions, e. g. assuming no horizontal movement in north directions.

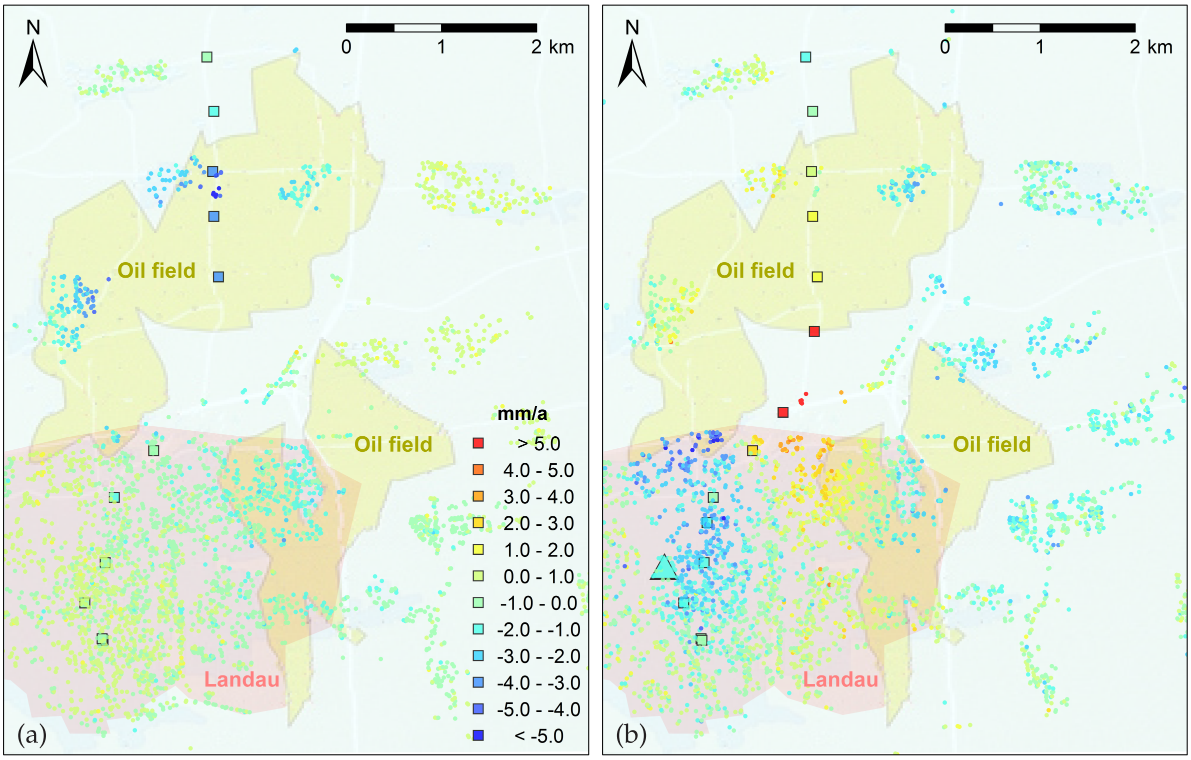

Figure 6.22: Oil fields close to Landau and deformation measured by InSAR, GPS and levelling. (a) LOS velocities at PS locations (circles) estimated from ERS-1/2 data between 1992 and 2000, (b) LOS velocities estimated from Envisat data between 2003 and 2008. Vertical displacement rates at levelling benchmarks (squares) from two epochs (a) 1994 and 2003, (b) 2003 and 2009. Linear trend of Up component for GNSS site Landau from 2004 to 2009 (triangle). The spatial extent of the figures is 8.101°–8.184°E, 49.183°–49.253°N.

The LOS velocities from ERS and Envisat and the vertical displacement rates calculated from levelling data of two epochs in each period fit well at places where both data sets coincide.

This indicates that the major part of the deformation is vertical. For the first period (before 2003), significant subsidence of 1 to 5 mm/a is visible within the oil fields north and east of Landau, whereas the surface at the city of Landau, marked by a pink shape in Fig. 6.22, behaves more or less stable. After 2003 the centre of subsidence is shifted southwards showing velocity magnitudes of -1 to -6 mm/a. In the area between the two oil fields, a reverse movement with velocities of up to $+7$ mm/a is visible, determined by both levelling and InSAR observations. The detected surface uplift corresponds to a Mogi point source at 800 m depth with a volume change of 20,000 m^3 (Mogi, 1958). Since 2000, water is reinjected into boreholes which have formerly been in use for oil production. The depth of the fitted Mogi model is in accordance with the depth of the boreholes of 700–1,400 m.

From the Up component of the coordinate time series at the GNSS site 0521 (Landau) from 2004 to 2009, a linear displacement rate of -1.9 mm/a is deduced. The value is in general accordance with levelling and InSAR, slightly overestimating the displacement rates at adjacent benchmarks and PS locations of about -1.5 mm/a for both techniques. The difference is in the range of the 2σ standard deviation of about 0.6 mm/a for the vertical GNSS component at site Landau. The case study illustrates that levelling, GNSS and InSAR are capable to resolve displacement rates at the mm/a-level consistently under the prevailing conditions of the URG area. Improved information is drawn from a combination of the three techniques as they have complementary properties, see Sect. 7.1.

6.6 Summary

- The temporal decorrelation of the SAR data analysed within this thesis behaves non-linear in time, due to rapidly changing backscatter characteristics of the non-urban areas. Exponential models for temporal as well as geometric decorrelation are proposed in order to predict an optimum master scene for a given image stack.
- The number of selected PS pixels strongly depends on the chosen parameter settings, especially for the standard deviation threshold used for the weeding of PS. Suitable parameter values are found from test areas and from statistical analysis of quality indicators.
- A separation of the desired phase signal attributed to surface displacements from other phase terms such as DEM uncertainties, orbital or atmospheric effects is challenging, but indispensable for displacement studies on the sub-mm/a-level.
- Atmospheric effects are a major influence factor for InSAR analyses. For large image stacks, they are appropriately handled by spatio-temporal filtering of phase values.
- An SBAS analysis does not provide significantly more information on LOS displacements in the whole, large-scale URG area. The gain in information is not compensating the additional computational effort.
- A new filtering technique based on statistical analysis of two quality indicators was implemented enabling to drop unrealistic and inaccurate displacement values from the set of PS pixels.
- The resulting LOS displacements in the URG area provide insight into surface deformation on a high spatial resolution, albeit on a lower accuracy level compared to the results from levelling.
- Large displacements (> 5 mm/a) are observed in three areas with known anthropogenic activities, i. e. at mining areas close to Mulhouse and Landau as well as in Lorraine/Saarland.
- InSAR is most suitable to measure local deformation phenomena with displacements in the order of several mm/a, for instance related to anthropogenic activities. In addition, insights into the temporal deformation behaviour can be drawn from the displacement time series at the PS locations.

Chapter 7

Fusion of Techniques

This chapter deals with the fusion of surface displacements resulting from levelling, GNSS[1] and InSAR. Chap. 4, 5 and 6 presented the separate analysis and results of the available data sources from levelling, GNSS and InSAR in the URG area. In order to exploit the advantages of each technique, the resulting displacement estimates shall be combined to a 3D velocity field with high spatial resolution and accuracy. Sect. 7.1 reviews the characteristics of the three complimentary techniques. Some theoretical aspects of the data fusion are discussed in Sect. 7.2 and validated using a simulated velocity field. As the measurement locations of the techniques do not coincide, spatial interpolation is needed for a suitable data fusion. The geostatistical interpolation method *Kriging* is used to predict values from a given set of sample data at the locations of a dense grid. The theoretical background on Kriging is given in Sect. 7.3. The developed approach for the fusion of levelling, GNSS and InSAR displacement data is explained in detail in Sect. 7.4 including a section on the combination of ERS and Envisat displacements at the time series level. Finally, 3D displacement rates resulting from the data fusion of levelling, GNSS and InSAR in the URG area are presented and discussed w.r.t. the tectonic setting of the region in Sect. 7.5.

Parts of this chapter have already been published by the author in the following papers: Fuhrmann et al. (2015a), Fuhrmann et al. (2015b). These publications are not explicitly cited within the text.

---

[1] In contrast to Chap. 5, the term GNSS is consequently used within this chapter, even though the GNSS velocities are calculated from GPS observations, only.

7.1 Characteristics of the techniques

This section aims at a comparative characterisation of levelling, GNSS and InSAR w.r.t. the measurement of surface displacements. The results of the three techniques have already been compared within the scope of the case study of the deformation pattern close to the city of Landau, see Sect. 6.5.5. The corresponding locations of levelling benchmarks, one GNSS site and PS pixels are displayed in Fig. 6.22. In Fig. 7.1 the spatial properties of the three techniques are shown for a larger area in the northern URG. It becomes obvious that the information derived from the levelling data is dense along the levelling lines with large gaps in between the loops, particularly in the French part, southwestern area in Fig. 7.1. The GNSS sites are sparsely distributed, but provide coordinate time series with a high temporal resolution. The PS pixels resulting from analyses of ERS and Envisat on one ascending and one descending track reside at more or less the same locations in the urban areas of the region with a typical density of about 400 PS/km^2. In rural and forest areas, coherence is lost resulting in larger spatial gaps. The ERS and Envisat tracks do not exactly cover the same region, but are shifted in range direction by approximately 6 km.

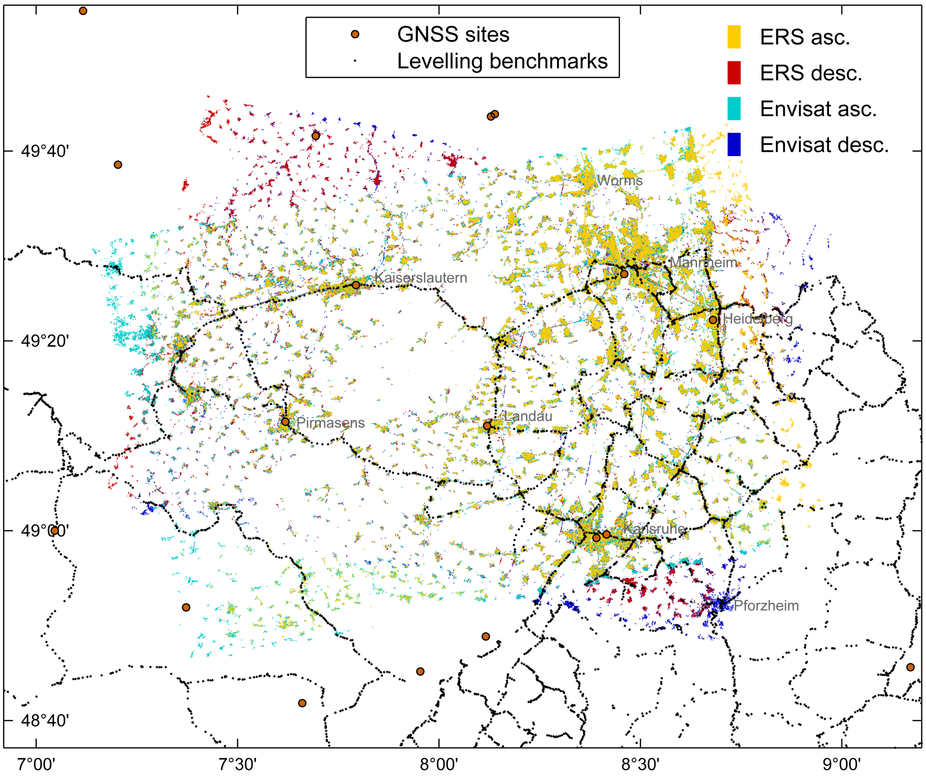

Figure 7.1: Spatial distribution of PS pixels, levelling benchmarks and GNSS sites in the northern URG. The four different stacks of SAR data (ERS 487, ERS 294, Envisat 487N, Envisat 294N) are displayed in different colours.

Further properties of the three techniques are compared in Tab. 7.1. It becomes obvious that the techniques have complementary properties w.r.t. the spatial and temporal resolution, accuracy and sensitivity to different displacement components. A combination of displacement estimates from levelling, GNSS and InSAR should be able to

- (i) fill spatial gaps in the levelling and GNSS point distribution,
- (ii) convert the InSAR LOS information into horizontal and vertical components,
- (iii) bring the InSAR results of different tracks into the same spatial reference frame.

Table 7.1: Characteristics of levelling, GNSS and InSAR data w.r.t. displacement estimation in the URG area.

	Levelling	GNSS	InSAR
Temporal coverage	long (20–130 a)	medium (max. 10 a)	medium (max. 20 a)
Temporal resolution	low (campaigns, >20 a)	high (daily)	medium (min. 35 days)
Spatial resolution	medium (high along lines)	low (30–40 km)	high (20 m in urban areas)
Precision[1]	high (0.2 mm/a)	medium (0.4/1.1 mm/a)	medium (0.6 mm/a)
Sensitivity[2]	East: x, North: x, Up: ++	East: +, North: +, Up: o	East: o, North: −, Up: +
Reference frame	single reference point	surrounding EPN sites	single reference area

[1] Values in brackets reflect mean standard deviations of levelling (vertical), GNSS (horizontal/vertical) and InSAR (LOS). 2σ is used for GNSS and InSAR as the precision estimates resulting from time series analysis are supposed to be too optimistic compared to the levelling results.

[2] Sensitivity to displacement components; x: not measurable, −: low, o: medium, +: high, ++: very high.

Regarding the fusion of techniques, one major issue results from the difference in the temporal coverage of the data. The levelling measurements started already at the end of the 19th century and cover more than 100 years at some benchmarks, whereas GNSS and InSAR data are available only within the last 10 and the last 20 years, respectively. The combination approach presented in Sect. 7.4 therefore focusses on constant linear velocities assuming no change in velocity for the tectonic movements. This is reasonable as no seismic event in the URG should have caused any coseismic or postseismic displacement larger than a few mm according to the seismic records of the last decades, see Fig. 2.8(b).

The precision of a linear velocity is inversely proportional to the time span covered by the measurements, see Eq. (3.6). This means that the displacement rates from levelling in the URG area achieve higher accuracies compared to InSAR and GNSS. On the other hand, the number of measurements at the same location is high using satellite techniques, particularly in the GNSS case. In addition, the variance of differential estimates from levelling, GNSS and InSAR depends on the spatial distance between the measurement points. Particularly in the levelling case, a strong dependence of the uncertainties on the location of the reference point is observed as discussed in Sect. 4.5.2. Moreover levelling measurements are susceptible for systematic inaccuracies and errors which may affect the velocity estimates in some areas. In contrast to levelling, GNSS data enables a high relative accuracy over large distances. The significance of estimated velocities depends on the length of the time series and a proper consideration of site-specific effects. The precision of linear displacement rates from InSAR largely depends on the number of analysed scenes as well as on the temporal and spatial baselines between the acquisitions. If acquisitions over a large time span are available, a linear rate can be estimated more precisely. Furthermore, the separation of temporally correlated and uncorrelated nuisance terms improves. On the other hand, temporal decorrelation becomes stronger for SAR data acquired over a long time span, see Hanssen (2001, p. 103 f.), and less PS pixels are found within the analysed area, see Fig. 6.6. In order to improve the estimate of linear rates, ERS and Envisat displacements are combined at the time series level, see Sect. 7.4.4. The InSAR precision given in Tab. 7.1 corresponds to the mean 2σ standard deviation of all linear rates estimated from the combined displacement time series.

7.2 Theoretical considerations based on simulated displacements

Within this section, a surface displacement is simulated using a Mogi point source model causing an uplift of about 6 mm/a (Mogi, 1958). In the model as in reality, every uplift is accompanied by horizontal movements as shown in Fig. 7.2. The modelled maximum vertical velocity of about 6 mm/a results in maximum horizontal velocities of 2.3 mm/a. Levelling and GNSS enable a measurement of the vertical and horizontal components, respectively, while InSAR measures along the LOS towards the satellite. The resulting LOS velocity has to be geometrically transformed to East, North and Up components for the combination with levelling and GNSS.

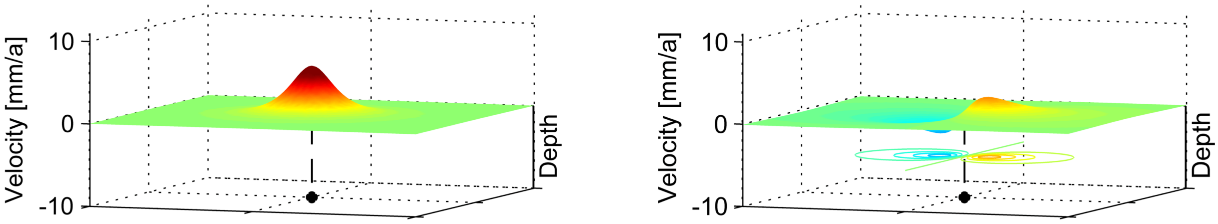

(a) Up component (b) East component

Figure 7.2: Simulated surface displacement using a Mogi model with a point source at 2 km depth and a corresponding volume change of 100,000 m^3.

The vertical velocity component v_U follows from the incidence angle. The LOS velocity vectors V_{asc} and V_{desc} are defined positive towards the satellite within StaMPS. Hence, the relationship between V_{asc} and v_U is given by

$$\cos\theta_{asc} = \frac{v_U}{V_{asc}} \quad \text{or} \quad V_{asc} = v_U \cdot \cos\theta_{asc} \quad , \tag{7.1}$$

and equivalent for V_{desc}, see Fig. 7.3(a). The projection of the LOS into the E–N-plane follows from

$$b = V_{asc} \cdot \sin\theta_{asc} \quad , \tag{7.2}$$

and equivalent for a descending geometry. As LOS displacements are defined positive towards the satellite, the azimuth for the calculation of the East and North components of V_{asc} results in $\alpha_{asc} - 90°$.

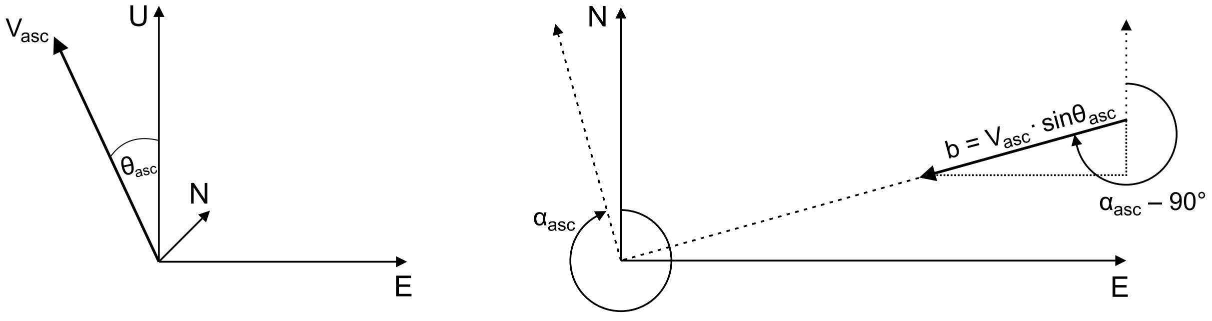

(a) View of the E–U-plane (b) Projection into the horizontal E–N-plane

Figure 7.3: Transformation of LOS displacements into East, North and Up components.

The horizontal components are then given by:

$$\begin{aligned} v_E &= b \cdot \sin(\alpha_{asc} - 90^\circ) = V_{asc} \sin\theta_{asc} \sin(\alpha_{asc} - 90^\circ) = -V_{asc} \sin\theta_{asc} \cos\alpha_{asc} \quad \text{and} \\ v_N &= b \cdot \cos(\alpha_{asc} - 90^\circ) = V_{asc} \sin\theta_{asc} \cos(\alpha_{asc} - 90^\circ) = V_{asc} \sin\theta_{asc} \sin\alpha_{asc} \quad . \end{aligned} \tag{7.3}$$

The full projection vectors S_{asc} and S_{desc} for the transformation of LOS velocities into East, North and Up components follow from Eq. (7.1) and (7.3):

$$S_{asc} = \begin{pmatrix} -\sin\theta_{asc}\cos\alpha_{asc} \\ \sin\theta_{asc}\sin\alpha_{asc} \\ \cos\theta_{asc} \end{pmatrix} \quad , \qquad S_{desc} = \begin{pmatrix} -\sin\theta_{desc}\cos\alpha_{desc} \\ \sin\theta_{desc}\sin\alpha_{desc} \\ \cos\theta_{desc} \end{pmatrix} \tag{7.4}$$

Fig. 7.4 shows the nominal values for velocities v_E, v_N and v_U and simulated observations for levelling and InSAR assuming that every grid point of the simulated velocity field could be measured. The simulated observations shown in Fig. 7.4(e) and (f) are transformed to the ascending and descending LOS using the projection vector given in Eq. (7.4) with a constant incidence angle of $\theta_{asc} = \theta_{desc} = 20^\circ$ and heading angles $\alpha_{asc} = 344.5^\circ$ and $\alpha_{desc} = 195.5^\circ$. One can nicely see that the largest LOS velocities are not centred, but slightly shifted towards west and east for ascending and descending data, respectively.

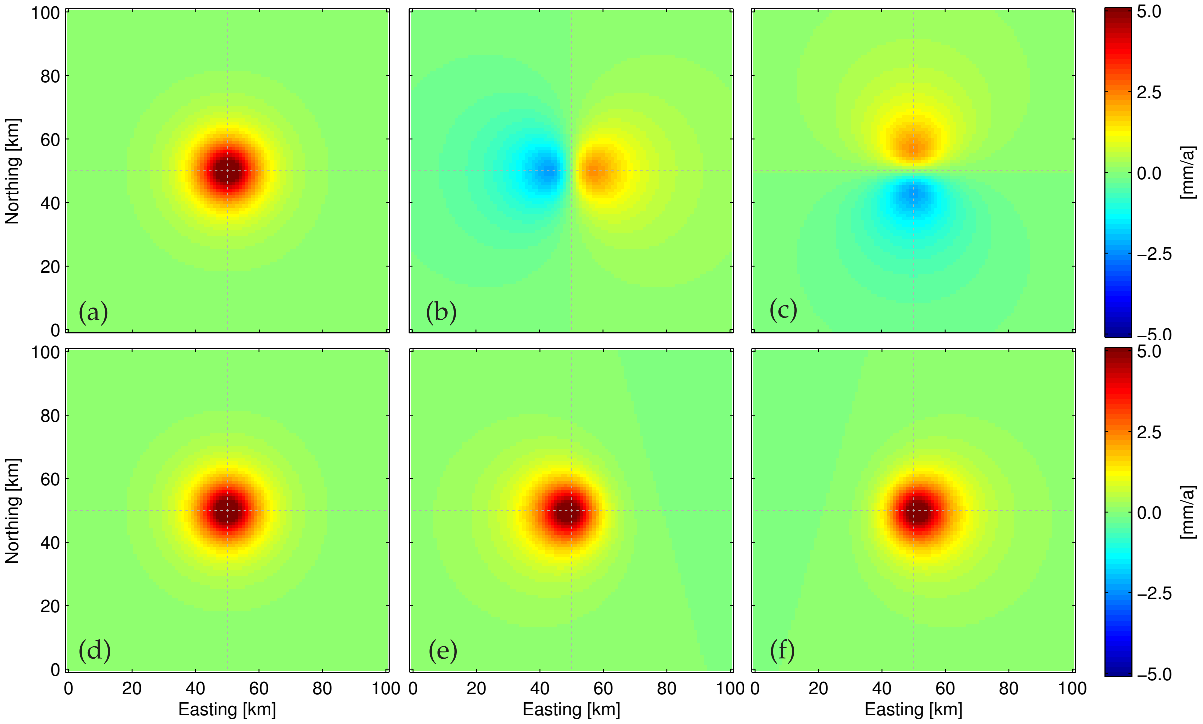

Figure 7.4: Nominal grid values of the simulation for the Up, East and North components (a), (b) and (c), respectively, and simulated observations μ for levelling (d), InSAR ascending (e) and descending (f). Grey dots mark cross sections through the centre coordinates of the simulation area.

Random observations according to a normal distribution $\mathcal{N}(\mu, \sigma)$ are created, with μ exactly fulfilling the given motion behaviour as shown in Fig. 7.4. According to Samsonov & Tiampo (2006) and Samsonov et al. (2008), a combination of InSAR velocities in ascending and descending image geometries with velocities V_{lev} from levelling and V_{GNSS} from GNSS is achieved in a least-squares sense by minimising the function f w.r.t. the three velocity components v_E, v_N and v_U at locations j of an interpolated grid:

$$\begin{aligned} f\left(v_E, v_N, v_U\right) = \sum_{j=1}^{n} \Bigg\{ & \frac{1}{2\left(\sigma_{j,Lev}\right)^2}\left(V_{j,Lev} - v_{j,U}\right)^2 + \\ & \frac{1}{2\left(\sigma_{j,GNSS,E}\right)^2}\left(V_{j,GNSS,E} - v_{j,E}\right)^2 + \frac{1}{2\left(\sigma_{j,GNSS,N}\right)^2}\left(V_{j,GNSS,N} - v_{j,N}\right)^2 + \\ & \frac{1}{2\left(\sigma_{j,asc}\right)^2}\left(V_{j,asc} - S_{j,E}v_{j,E} - S_{j,N}v_{j,N} - S_{j,U}v_{j,U}\right)^2 + \\ & \frac{1}{2\left(\sigma_{j,desc}\right)^2}\left(V_{j,desc} - S_{j,E}v_{j,E} - S_{j,N}v_{j,N} - S_{j,U}v_{j,U}\right)^2 \Bigg\} \quad . \end{aligned} \tag{7.5}$$

As each term of $f\left(v_E, v_N, v_U\right)$ is positive, a global minimum is reached when the subgroups corresponding to each j are minimal and hence

$$\nabla f = \begin{pmatrix} \frac{\partial f}{\partial v_{j,E}} \\ \frac{\partial f}{\partial v_{j,N}} \\ \frac{\partial f}{\partial v_{j,U}} \end{pmatrix} = 0 \quad . \tag{7.6}$$

The system of equations results in a standard inverse problem which may be solved by least-squares approaches. However, the resulting normal equation system may be ill-conditioned in the case of heterogeneously distributed GNSS sites or levelling benchmarks and large uncertainties σ. Hu et al. (2011) therefore propose to solve Eq. (7.5) and (7.6) by numerical optimisation using the BFGS method, named after the independent developers of the approach: Broyden (1970); Fletcher (1970); Goldfarb (1970); Shanno (1970). The BFGS algorithm is a practical and effective method to solve non-linear optimisation problems in an iterative way with fast convergence (Lewis & Overton, 2013).

Within the simulation, a classical least-squares adjustment is compared to the BFGS method using different combinations of input data, (i) all three techniques, (ii) InSAR and levelling and (iii) InSAR only. In addition, another numerical optimisation approach proposed by Lagarias et al. (1998) is tested denoted as Nelder-Mead Simplex method. For the combination of all three techniques, the resulting velocity estimates of least-squares adjustment and both numerical optimisation approaches are identical if the data is not too noisy and the standard deviations of the observations used within the stochastic model are at a comparable level. A comparison of the resulting velocities to the original simulated motion shows that errors are introduced to the combined solution if the standard deviations of the simulated random observations are high. It is hence advisable to avoid large extrapolations of the input data which result in higher standard deviations of observations at the corresponding grid locations.

The combination of InSAR with levelling observations is not redundant as there are only three observations for the estimation of three parameters. If only the East and Up components are estimated, the normal equation system is well-conditioned and reduces to:

$$\begin{pmatrix} V_{asc} \\ V_{desc} \\ V_{lev} \end{pmatrix} = \begin{pmatrix} -\sin\theta_{asc}\cos\alpha_{asc} & \cos\theta_{asc} \\ -\sin\theta_{desc}\cos\alpha_{desc} & \cos\theta_{desc} \\ 0 & 1 \end{pmatrix} \begin{pmatrix} v_E \\ v_U \end{pmatrix} + e \quad . \tag{7.7}$$

However, an error of about 10 % of the maximum horizontal deformation is introduced to the Up component at some grid points as the motion of the North component is neglected. If the Up component shall be estimated in an unbiased way, it is hence advisable to estimate one horizontal component perpendicular to the heading angle, denoted as azimuth look direction (ALD), see Ketelaar (2009, p. 110); Samieie-Esfahany et al. (2010). In this case, the horizontal motion component is completely subsumed by the ALD component.

In order to derive v_E, v_N and v_U from a combination of InSAR ascending and descending velocities (InSAR only), least-squares adjustment is not applicable as the design matrix A gets singular:

$$A = \begin{pmatrix} -\sin\theta_{asc}\cos\alpha_{asc} & \sin\theta_{asc}\sin\alpha_{asc} & \cos\theta_{asc} \\ -\sin\theta_{desc}\cos\alpha_{desc} & \sin\theta_{desc}\sin\alpha_{desc} & \cos\theta_{desc} \end{pmatrix} = \begin{pmatrix} 0.33 & -0.09 & 0.94 \\ -0.33 & -0.09 & 0.94 \end{pmatrix} \quad . \tag{7.8}$$

The numerical optimisation methods are still able to produce results from the underdetermined system of equations, albeit with large inaccuracies in the North component. Note that the numbers given in Eq. (7.8) represent a measure of the sensitivity of InSAR observations to the three components which is high for the Up component and low for the North component. However, it is again possible to calculate only the East and Up components, albeit without redundancy in this case:

$$\begin{pmatrix} V_{asc} \\ V_{desc} \end{pmatrix} = \begin{pmatrix} -\sin\theta_{asc}\cos\alpha_{asc} & \cos\theta_{asc} \\ -\sin\theta_{desc}\cos\alpha_{desc} & \cos\theta_{desc} \end{pmatrix} \begin{pmatrix} v_E \\ v_U \end{pmatrix} \quad . \tag{7.9}$$

From the theoretical considerations within this section and the results of the simulations, the following main conclusions are found:

(i) least-squares adjustment can be used for the combination approach if the system of equations is redundant,

(ii) an error is introduced to the other components if one component of a 3D displacement is omitted, e. g. the North component,

(iii) extrapolation of the observations over large distances along with increasing uncertainties should be avoided.

For the combination of displacement rates from levelling, GNSS and InSAR, an approach is developed which only combines the data at locations where information of at least one technique is available. The InSAR measurement locations are chosen for the combination as InSAR provides the best spatial resolution and coverage. The velocities of all techniques are interpolated to a common grid which carries valid values only close to the locations of the original PS pixels, denoted as PS grid. Hence, it is guaranteed that every valid grid point contains at least four redundant observations, i. e. two horizontal velocities from GNSS, one vertical velocity from levelling and at least one LOS velocity from InSAR, to solve for the three unknown velocity components v_E, v_N, v_U.

7.3 Interpolation of scattered data using Kriging

Spatial interpolation of heterogeneously distributed data is needed within several steps of the combination and for displacement estimates of all three techniques. This section presents the theoretical background on interpolation using Kriging. Conversely, Sect. 7.4.2 discusses specific characteristics of the interpolation of surface displacements from levelling, GNSS and InSAR. A spatial interpolation of data predicts values at specified locations from a limited number of sample data points. Besides Kriging, other interpolation techniques exist, such as inverse distance weighting (IDW), multiquadric interpolation (Hardy, 1971), bilinear, bicubic or spline interpolation. According to Shepard (1968), an easy-applicable, distance-dependent interpolation of n observations y, measured at the locations x_j, to a location x_0 results from IDW with a given distance weight k:

$$y(x_0) = \frac{\sum_{j=0}^{n} \frac{y(x_j)}{d^k(x_0,x_j)}}{\sum_{j=0}^{n} \frac{1}{d^k(x_0,x_j)}} \quad . \tag{7.10}$$

For a 2D spatial interpolation, x is a two-element vector containing the East and North components x_E and x_N. However, the simple formulation of equation (7.10) does not consider the uncertainties inherent to the observations $y(x_j)$. In contrast to other interpolation techniques, which are based only on mathematical models, Kriging techniques additionally consider the statistical properties of the input data. Kriging is similar to IDW as it predicts values at locations x_0 by weighting the surrounding observations. Furthermore, Kriging techniques also consider the accuracy level and spatial correlations of the input data. The following two sections present the basic equations used for the spatial interpolation with Kriging, particularly in Sect. 7.3.1. The derivation of covariance functions from semivariogram models is discussed in Sect. 7.3.2.

7.3.1 The Kriging system

According to Li & Heap (2008, p. 11), Kriging is a generic name for a family of generalised least-squares regression algorithms, named in recognition of the pioneering work of Krige (1951). The predicted values $\hat{y}_0$ at locations x_0 are computed as a weighted average of the sample data:

$$\hat{y}_0 = w^\top \cdot y \quad , \tag{7.11}$$

where the weights w follow from the covariance matrix C of observations, also denoted as signal noise, and a vector D containing the covariances at the prediction location:

$$w = C^{-1} \cdot D \quad . \tag{7.12}$$

Eq. (7.11) and (7.12) represent a linear estimator of least-squares collocation (LSC, Moritz, 1973), or least-squares prediction as denoted by Teunissen (2007). The major problem of the Kriging system of equations is that the covariance functions defining the elements of the matrices C and D are unknown in most cases. Egli et al. (2007) presented a modified LSC method to interpolate velocity estimates from levelling in the Swiss Alps using empirical covariance functions. The Kriging system is solved in a similar way using an empirical semivariogram function $\gamma(d)$ depending on the point distance d, see Gringarten & Deutsch (2001). The determination of the entries for the covariance matrices using empirical semivariograms is further discussed in Sect. 7.3.2. Several Kriging models are deduced from Eq. (7.12) which are presented in the following.

Simple Kriging (SK):

A mean value μ is known and subtracted before the estimation. The covariance matrices C and D are directly deduced from the semivariogram model:

$$w = \begin{pmatrix} w_1 \\ w_2 \\ \vdots \\ w_n \end{pmatrix} \quad C = \begin{pmatrix} C_{11} & C_{12} & \dots & C_{1n} \\ C_{21} & C_{22} & \dots & C_{2n} \\ \vdots & \vdots & \ddots & \vdots \\ C_{n1} & C_{n2} & \dots & C_{nn} \end{pmatrix} \quad D = \begin{pmatrix} C_{10} \\ C_{20} \\ \vdots \\ C_{n0} \end{pmatrix} \quad . \tag{7.13}$$

An estimate of the uncertainty at the prediction location is then given by:

$$\hat{\sigma}_0^2 = C(0) - w^\top \cdot D \quad , \tag{7.14}$$

where $C(0)$ denotes the variance of the signal and corresponds to the values of the main diagonal of C.

Ordinary Kriging (OK):

A constant unknown mean μ is considered within the Kriging system. Therefore, an additional constraint in the form $\sum_{j=0}^{n} w_j = 1$ is added to Eq. (7.12) representing LSC with a constant trend (Schaffrin, 2001). The constraint is added to the Kriging system using the Lagrange multiplier λ resulting in:

$$w_{OK} = \begin{pmatrix} w_1 \\ w_2 \\ \vdots \\ w_n \\ \lambda \end{pmatrix} \quad C_{OK} = \begin{pmatrix} C_{11} & C_{12} & \dots & C_{1n} & 1 \\ C_{21} & C_{22} & \dots & C_{2n} & 1 \\ \vdots & \vdots & \ddots & \vdots & \vdots \\ C_{n1} & C_{n2} & \dots & C_{nn} & 1 \\ 1 & 1 & \dots & 1 & 0 \end{pmatrix} \quad D_{OK} = \begin{pmatrix} C_{10} \\ C_{20} \\ \vdots \\ C_{n0} \\ 1 \end{pmatrix} \quad . \tag{7.15}$$

Eq. (D.1)–(D.6) in Appendix D present a mathematical proof that OK is a specific case of least-squares prediction or LSC.

Universal Kriging (UK):

Not a constant unknown mean value is considered, but e. g. a linear trend or a polynomial function. The Kriging system extends to:

$$w_{UK} = \begin{pmatrix} w_1 \\ w_2 \\ \vdots \\ w_n \\ \lambda_1 \\ \vdots \\ \lambda_k \end{pmatrix} \quad C_{UK} = \begin{pmatrix} C_{11} & C_{12} & \dots & C_{1n} & x_{11} & \dots & x_{1j} \\ C_{21} & C_{22} & \dots & C_{2n} & x_{21} & \dots & x_{2k} \\ \vdots & \vdots & \ddots & \vdots & \vdots & \ddots & \vdots \\ C_{n1} & C_{n2} & \dots & C_{nn} & x_{n1} & \dots & x_{nk} \\ x_{11} & x_{12} & \dots & x_{1n} & 0 & \dots & 0 \\ \vdots & \vdots & \ddots & \vdots & \vdots & \ddots & \vdots \\ x_{k1} & x_{k2} & \dots & x_{kn} & 0 & \dots & 0 \end{pmatrix} \quad D_{UK} = \begin{pmatrix} C_{10} \\ C_{20} \\ \vdots \\ C_{n0} \\ x_{10} \\ \vdots \\ x_{k0} \end{pmatrix} \quad , \tag{7.16}$$

with k denoting the number of elements of the polynomial function.

As a constant mean cannot generally be assumed for the spatial interpolation of displacement data, SK is not further considered within this work. In contrast to SK, OK replaces μ by a local mean $\mu(x_0)$, that is the mean of samples within the specified search window (Li & Heap, 2008, p. 15). In order to find an appropriate interpolation method for the displacements in the investigation area, both OK and UK with a linear trend are applied to the displacement observations. It could be visually observed that artefacts are introduced to the interpolated velocity fields when UK is used, which might result from the heterogeneous distribution of the input data. In addition, OK is faster in runtime by a factor of two and more. Runtime is an issue as a large amount of sample data shall be interpolated to a high resolution grid, i. e. 200 m, for a region with a spatial extent of more than 200 km × 300 km in E–W and N–S directions. Hence, OK is preferred over UK for the spatial interpolations described in Sect. 7.4.2.

7.3.2 Covariance modelling using semivariograms

The semivariance γ between two data points x_j and x_k with distance d is defined as

$$\gamma = \frac{1}{2} \cdot E\left\{ \left[y(x_j) - y(x_k) \right]^2 \right\} = \frac{1}{2} \cdot E\left\{ \left[y(x_j) - y(x_j + d) \right]^2 \right\} \quad . \tag{7.17}$$

A semivariogram displays (average) semivariances for different point distances. From a semivariogram, a distance-dependent function describing the process (and measurement) noise of the signal to be interpolated is deduced based on the assumption that the underlying process exhibits ergodicity, homogeneity and isotropy. The function is estimated from the data itself by calculating the empirical correlation between value pairs at different distances d, denoted as lags. The relationship between the covariance C and the semivariogram γ is expressed according to Gringarten & Deutsch (2001):

$$C(d) = C(0) - \gamma(d) \quad . \tag{7.18}$$

One of the following three models is commonly used to describe the distance-dependent correlation of a signal:

- Spherical: $\gamma(d) = c_0 + c_1(\frac{3}{2}\min(\frac{d}{r},1) - \frac{1}{2}\min(\frac{h}{r},1)^3) \quad ,$
- Exponential: $\gamma(d) = c_0 + c_1(1 - e^{-(\frac{d}{r'})}) \quad ,$
- Gaussian: $\gamma(d) = c_0 + c_1(1 - e^{-(\frac{d}{r''})^2}) \quad .$

$$\begin{aligned} C(0) &: \text{Sill = nugget + partial sill} \\ c_0 &: \text{Nugget} \\ c_1 &: \text{Partial sill} \\ r &: \text{Range} \\ r', r'' &: \text{Modified ranges} \end{aligned} \tag{7.19}$$

The range of the models is a measure of correlation length of the signal (Journel & Huijbregts, 1981, p. 36). The sill $C(0)$ describes the total a priori variance of the function and contains both the variance of signal and noise. A nugget effect represents a discontinuity at the origin caused by measurement errors, i. e. the observation variance, or residual influences of all variablities at short distances (Journel & Huijbregts, 1981, p. 39 and p. 152). Fig. 7.5 shows an example for an empirical semivariogram calculated from LOS velocities of InSAR. When the sill is reached, approximately at 0.55 mm^2/a^2 in Fig. 7.5, the correlation between two data point locations is equal to zero. For the spherical model, the sill is reached at range r, for the exponential and Gaussian models the sill is only reached for $d \to \infty$. As the range represents the correlation length of the signal, modified ranges r' and r'' are used for these models. For the Gaussian model, about 98 % of the sill is reached at $d = 2\,r''$.

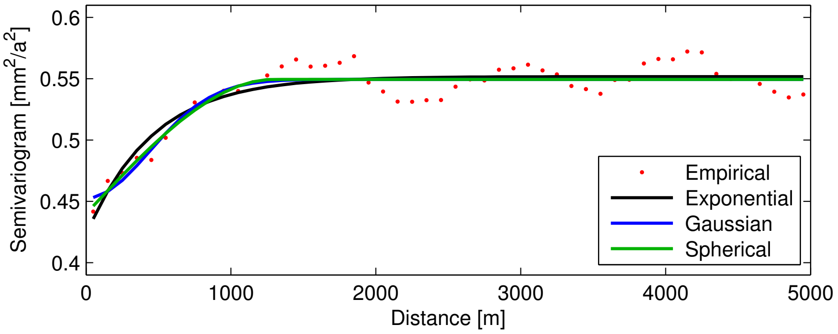

Figure 7.5: Example of an empirical semivariogram using 100 m lags and fitted models for LOS velocities from InSAR in a part of the northern URG. The nugget c_0 ranges from 0.42 to 0.45 mm^2/a^2 and the partial sill c_1 from 0.10 to 0.13 mm^2/a^2 for the three models, resulting in model functions with a similar behaviour.

The entries of matrix C are $c_0 + c_1$ for the main diagonal elements C_{jj} and $c_0 + c_1 - \gamma(d)$ for C_{jk} with $j \neq k$. By means of example, for the exponential model the non-main diagonal entries result in $c_1 \cdot e^{-(\frac{d}{r'})}$. The covariances D at the prediction location are calculated from the same semivariogram function applied to the distance w.r.t. the interpolation point. For a spatial interpolation of large data sets, the computational effort to solve the Kriging system is high. However, the correlation decreases with distance and observations of distant sample points have a minor contribution to the interpolated value as they obtain a low weight w_j. Therefore, only data points within a specified search distance to the prediction location are used to save runtime. The search radius is selected w.r.t. the empirical semivariogram. For the example shown in Fig. 7.5, a search radius of 2000 m would be sufficient as the empirical semivariogram models are saturated at this distance.

7.4 Fusion of surface displacements

The data sets from levelling, GNSS and InSAR differ in their spatial and temporal resolution. Therefore, the following hypotheses are implicitly assumed within the presented combination approach:

(i) levelling, GNSS and InSAR measure the same deformation signal,

(ii) the tectonic displacements behave linear in time (constant velocity),

(iii) the tectonic signal is smooth in space and does not abruptly change within short distances (< 200 m).

Hypothesis (i) is a strong assumption as the measurements of the three techniques actually do not represent the same location, even if they reside at nearby locations, e. g. ground vs. building, see Fig. 7.6. The levelling benchmarks are located close to the ground mounted at buildings, bridges, driven pillars or directly at the bedrock. In some cases, not the (tectonic) surface displacement is measured, but a movement of the support of the benchmark relative to the ground. The GNSS sites are mostly located on buildings in order to provide the best possible visibility to the satellites and for reasons related to sustainability, damage control and available infrastructure. The periodic signal visible in most of the coordinate time series is caused by movements of the building or the support of the GNSS antenna due to thermal expansion, and is filtered out within the time series analysis. However, tilt effects may still deteriorate the estimated velocity at the GNSS sites. In most cases, the location of the PS within the PS pixel is unknown. A superposition of multiple scatterers (often with one dominant scatterer) within the InSAR ground cell represents the measured signal. Attempts to characterise the dominating scatterer of a PS displacement signal have been made by Dheenathayalan & Hanssen (2011, 2013). As PS pixels may as well be allocated to a backscattering at rooftops, the tilting of buildings may influence the measured displacement signal, see Schenk (2015, p. 100 f.).

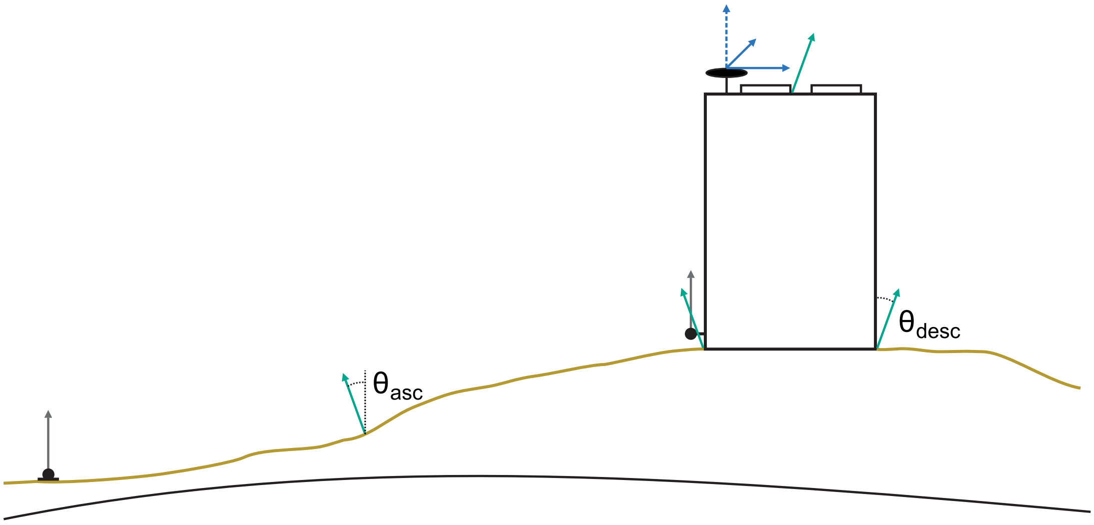

Figure 7.6: Schematic view of the principal measurement locations of levelling, GNSS and InSAR. The levelling benchmarks are located close to the ground, mainly attached to man-made objects and are sensitive to vertical displacements (grey). Most of the GNSS sites are located on buildings and are able to measure 3D displacements (blue), however, the Up component is not used here. The exact location of the InSAR backscattering points is unknown and may be situated close to the ground as well as on the top of a building. InSAR provides surface displacements in the slant LOS towards the satellite (green).

Hypothesis (ii) is an essential requirement as the dates of the measurements of levelling, GNSS and InSAR do not coincide and cover different time spans. On the other hand, the focus of the analysis is mainly dedicated to tectonic movements as most of the anthropogenic influences are characterised by a non-linear displacement signal. Nevertheless, some non-tectonic features still remain in the estimated velocities, either because they are more or less linear within decades (GNSS, InSAR) or the temporal sampling is not high enough to detect non-linearities (levelling).

Hypothesis (iii) becomes important for the interpolation which has to be applied to the data within the combination as the point locations of the three techniques do not coincide in most cases, see Fig. 7.6. The interpolation is performed at a common grid related to UTM coordinates (zone 32N) with a resolution of 200 m. Abrupt deformation changes are smoothed out in this case. The case study using levelling measurements at the EBF, presented in Sect. 4.6.1, indicates a stable sliding of the graben interior relative to the BF. In general, stable sliding at a certain depth results in seismic faulting and thus regional deformation of the surface. Deformation induced by seismic faulting appears on a large spatial scale (tens of km) and is therefore well resolved within the grid interpolation. In contrast, a sliding near the surface would result in aseimsic faulting and thus local deformation at the fault.

Fig. 7.7 presents the general workflow of the developed two-step combination approach. First, the PS displacement signal is interpolated to the location of levelling and GNSS measurements, respectively. At these locations, a vertical and an horizontal offset w.r.t. levelling and GNSS, respectively, is calculated considering the different reference frames of the InSAR stacks (Catalão et al., 2010). In addition, the InSAR displacement signal has to be checked for a trend caused by residual orbital or atmospheric effects or by the reference frame effect of plate motion inherent to InSAR as discussed in Sect. 6.2.3. The interpolation of PS displacements is performed separately for every sensor and interferogram, which enables the combination of ERS and Envisat time series within this step, described in detail in Sect. 7.4.4. The differences between the vertical velocities of levelling and InSAR and between the horizontal velocities of GNSS and InSAR also reflect the external accuracy of the measurements and serve as a validation of the single-technique results. In a second step, the displacement rate data of the three techniques is interpolated to a grid in the vicinity of the PS locations, denoted as PS grid. Again, the PS time series are used in order to determine a combined ERS/Envisat displacement rate if data of both sensors are available. Non-linear displacements in the ERS/Envisat time series are separated in this step. The mathematical combination at the PS grid points finally yields the 3D velocity solution.

In contrast to other combination approaches (Hu et al., 2011; Caro Cuenca et al., 2012; Wang & Wright, 2012; Walters et al., 2014), the mathematical fusion of the data is performed close to the PS locations only. This ensures that (i) large, local surface displacements, e. g. due to anthropogenic activities, are not extrapolated, (ii) the resulting velocity map displays values only close to locations where the information resides and (iii) the combination is numerically stable, see Sect. 7.2. In other words, the high spatial coverage of the PS data is exploited along with the accurate vertical and horizontal velocity information from levelling and GNSS. As the precision of the interpolated velocities from levelling and GNSS is high close to the measurement points and decreases with distance, see Fig. 7.10, the velocities from InSAR will predominate the combined solution in areas, where no information from levelling and GNSS is available. In contrast, the interpolation of PS data at large distances as performed in other approaches could possibly deteriorate the combined velocity field because of remaining orbit errors and unmodelled atmospheric signals.

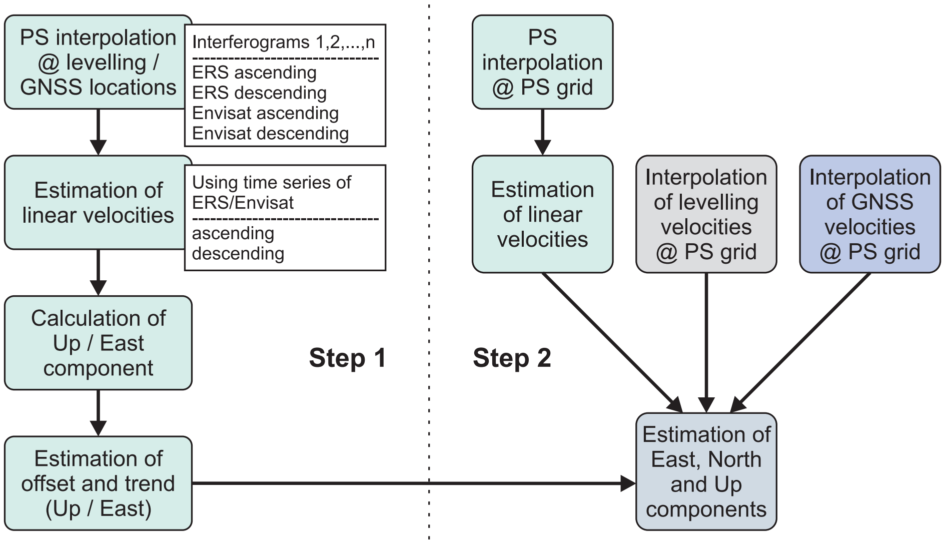

Figure 7.7: Workflow of the two-step combination approach. In step 1 the offset and trend between InSAR and levelling/GNSS are estimated. Step 2 mathematically combines the InSAR, levelling and GNSS velocity estimates at the PS grid. The offset and trend estimated in step 1 are considered in the final estimation of East, North and Up components.

7.4.1 Covariance models for the spatial interpolation

For the interpolation of scattered sample data from levelling, GNSS and InSAR, the covariance matrices C and D have to be determined. In the case of levelling and GNSS, the velocities resulting from kinematic adjustment and from CATS time series analyses are spatially interpolated. A priori information on the uncertainties of the levelling and GNSS velocities is already available. In the case of InSAR, the displacement values of each interferogram are interpolated in a first step. Velocities are subsequently estimated at every PS grid point from the corresponding displacement time series. The uncertainties of the InSAR displacements in each interferogram are previously unknown.

The covariance matrices for levelling and GNSS interpolation are determined equivalently. First, empirical semivariograms at certain lags are calculated from the velocity signal of both techniques. Then, an exponential function is fitted in a least-squares sense to the semivariogram describing the spatial correlation of the signal of interest, see Eq. (7.19). In order to account for the known uncertainties of each velocity estimate, the main diagonal elements of C are scaled individually at every prediction location using the formal errors of the velocities from the adjustment of the data. Therefore, the distance-weighted mean of the variances of all data points considered at a certain prediction location is calculated and divided by the overall mean variance. In order to provide an appropriate weight of the interpolated levelling and GNSS velocities for the final combination with InSAR, a regularisation parameter is added to the partial sill reflecting a decrease in accuracy with distance to the levelling lines and GNSS sites, respectively, see Fig. 7.10. The GNSS velocities are separately interpolated for the East and the North component. Correlations between the North and the East velocity components are considered in the final combination step discussed in Sect. 7.4.6.

For the spatial interpolation of displacement values from InSAR, empirical semivariograms are calculated from the LOS displacements in each interferogram. As the spatial resolution of the data is much denser compared to levelling and GNSS, not the whole area is used for the calculation of semivariograms. Because of computational issues, it is not reasonable to use input values at more than 20,000 data points. In addition, the semivariogram should as best as possible reflect the stochastic behaviour of the signal of interest, i. e. tectonic motion. As proposed by Caro Cuenca (2012, p. 73), a subset of PS pixels located in weakly and homogeneously deforming areas, denoted as test areas in the following, are used for fitting a semivariogram model function.

According to Snedecor & Cochran (1980), the minimum number of samples to calculate a mean value follows from

$$n_{min} = \frac{z^2_{(1-\alpha)} \cdot \sigma^2}{e^2} \tag{7.20}$$

where z_q denotes the q-quantile of the normal distribution, e is the absolute error and α is the significance level. With $\alpha = 10\%$ and $\sigma = 2e$, n_{min} results in 10.8. Hence, a number of 11 test areas seems to be a good trade-off between computation time and quality to calculate statistics of the semivariogram functions. The test areas are selected based on a minimum number of PS within a given search radius. Finally, the 11 test areas with the lowest standard deviation of estimated velocities and with a mean value of deformation below ±1 mm/a are chosen. The selected test areas in Envisat track 294C are displayed in Fig. 7.8. Only 26 of the 49 investigated areas provide a number of more than 2,500 PS, see Tab. 7.2. Most of them are located within the URG, where the PS density is much higher compared to the VG and the BF regions, west and east of the graben, respectively. The chosen areas with weak and homogeneous deformation are highlighted with different colours according to the mean standard deviation.

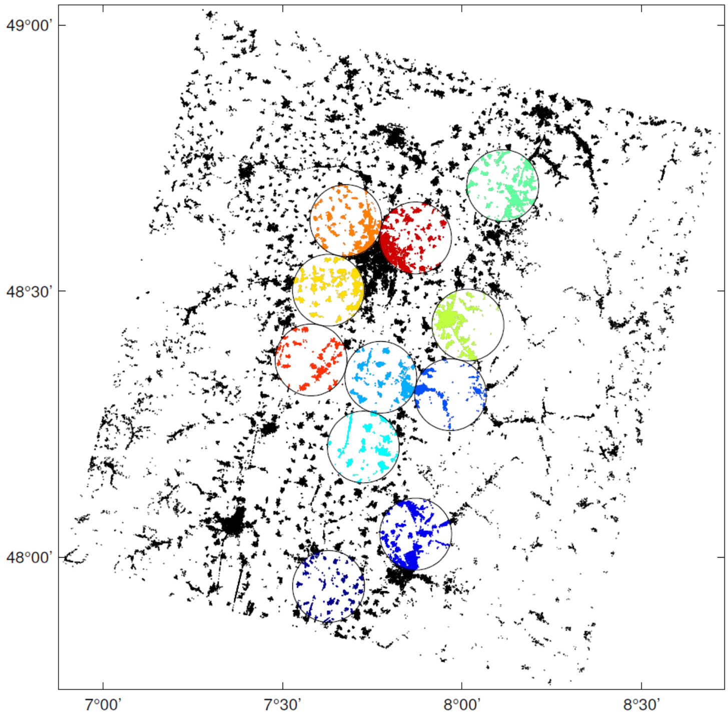

Figure 7.8: Areas selected for the estimation of empirical semivariograms in Envisat track 294C. The colours are sorted w.r.t. the standard deviation of the LOS displacements within each area from blue (low standard deviation) to red (high standard deviation) and correspond to the colours in Fig. 7.9.

Empirical semivariograms are calculated and an exponential model is fitted for each test area, shown in Fig. 7.9. Most of the fitted model functions of the 11 test areas reveal a similar behaviour. However, the three curves in yellow, orange and dark red reach a higher variance level corresponding to a higher value for the partial sill. Also the estimated range r' reaches larger values in these test areas. Interestingly, these test areas are located in the same region close to the city of Strasbourg, where anthropogenic movements likely influence the spatial displacement pattern. In order to suppress such outliers, the median values of the model function parameters nugget, partial sill and range are taken for the interpolation of PS displacements in each interferogram of the analysed image stack. Subsequently, the covariance matrices C and D are assembled according to Eq. (7.18) and (7.19) in order to solve the Kriging system.

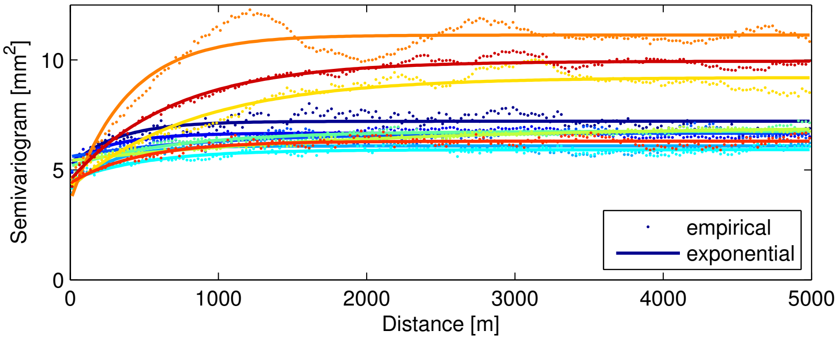

Figure 7.9: Empirical semivariograms and exponential models for LOS displacements in 11 weakly deforming areas of interferogram 8 in Envisat track 294C. The different colours of the semivariograms correspond to the colours of the areas in Fig. 7.8.

Tab. 7.2 summarises the covariance modelling for InSAR LOS displacements in the nine analysed image stacks. For the ERS scenes covering a large spatial extent, a high number of potential areas is available in contrast to the subtracks of the Envisat analyses, especially those in track 294. The nugget parameter is generally larger for interferograms with a large temporal baseline as generally higher absolute displacements are observed between master and slave for a longer time span. The exemplary function parameters, given for the respective first interferogram in each stack, demonstrate that the nugget effect reaches higher values compared to the partial sill. For the image stack of Envisat track 294C, the mean ratio between nugget and total sill resulting from 32 interferograms is 0.7 (and 0.3 between partial sill and total sill).

Table 7.2: Test areas and estimated covariance parameters for the nine analysed image stacks.

Sensor:		ERS				Envisat			
Track:	294	258	487	294N	294C	294S	258	487N	487S
Number of interferograms:	50	23	22	17	32	42	18	18	36
Number of areas:	119	112	119	42	49	35	56	119	49
Areas with $n_{PS} > 2,500$:	56	54	60	36	26	22	40	61	30
Parameters of the estimated exponential semivariogram model for the first interferogram:									
median(c_0) [mm]:	14.3	11.8	15.7	11.1	15.3	19.5	13.4	7.5	12.2
median(c_1) [mm]:	4.0	3.1	2.1	2.1	3.4	8.6	3.6	2.2	3.5
median(r') [m]:	1,145	350	716	673	793	1,324	1,504	980	1,070

7.4.2 Interpolation of levelling, GNSS and InSAR data

The spatial interpolation of the linear displacement rates from levelling and GNSS, and of the displacements in each interferogram of the InSAR stacks is performed using the Kriging system of OK defined in Eq. (7.15). The covariance models described in Sect. 7.4.1 are applied to solve Eq. (7.12) at each grid location. The computation time of the interpolation to a 200 m grid becomes large particularly in the case of InSAR, where the amount of sample data is high. As the influence of a certain sample value on the estimated value at the prediction location decreases with distance, not all sample data is used, but only a subset within a specific search radius (2 km). In any case, an interpolation is only performed at prediction locations where at least five sample data points are found within the given radius. For the interpolation of linear rates from levelling and GNSS, large radii are chosen (35 km and ∞ for levelling and GNSS, respectively) in order to provide interpolated values at almost all locations covered by the three SAR tracks. On the other hand, resulting extrapolated velocity estimates are down-weighted within the combination with InSAR as the standard deviation increases with distance to the location of the original measurements.

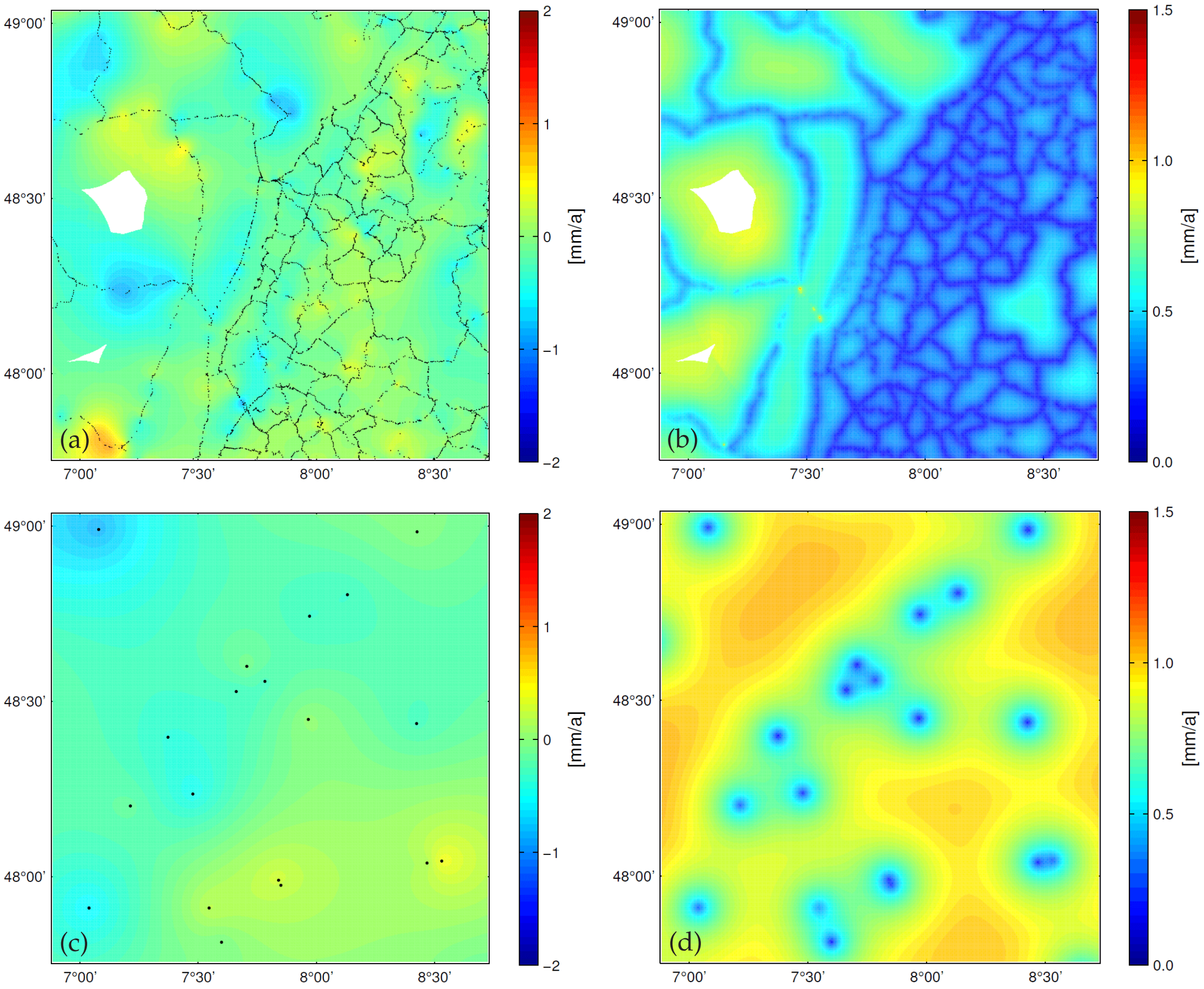

Figure 7.10: Interpolated displacement rates from levelling (a) and corresponding standard deviations (b), and interpolated displacement rates from GNSS North component (c) and corresponding standard deviations (d) in the central URG area. Black dots represent the locations of levelling benchmarks and GNSS sites.

Fig. 7.10 displays the interpolated velocity fields of levelling and GNSS along with corresponding standard deviations for the central URG area. In the western part of the crop shown in Fig. 7.10, the levelling lines are less dense resulting in extrapolation of the original measurements. A difference in the standard deviations in the western (French) part and the eastern (German) part is visible in Fig. 7.10(b) mainly due to the smaller number of repetitions inherent to the French measurements. Most of the French levelling lines were only measured in two or three epochs, see Fig. 4.17. In general, the standard deviations of the interpolated velocities of both levelling and GNSS are low close to the measurement points and increase with distance. The GNSS estimates are separately interpolated for the East and the North component and shown for the North component in Fig. 7.10(c). The spatial behaviour of the interpolated displacement rates and corresponding standard deviations is similar for the GNSS East component (not shown in Fig. 7.10). Correlations between the North and the East velocity components, which are determined from the same set of GNSS observations, are considered in the final combination step, see Sect. 7.4.6.

The displacement values at PS locations are interpolated to two different sets of prediction locations: (i) the location of levelling and GNSS points (step 1 in Fig. 7.7) and (ii) to a 200 m grid in the vicinity of the PS pixels (step 2 in Fig. 7.7). After the spatial interpolation of displacement values in each interferogram, linear velocities are estimated from combination of ERS and Envisat time series, see Sect. 7.4.4. As the final combination shall only be performed in the areas close to the PS locations, a maximum distance of the prediction location to the closest sample data point of 100 m is set. This means that the PS grid only contains valid numbers close to the original set of PS pixels. The resulting field of interpolated displacements is exemplarily shown in Fig. 7.11 for one interferogram of Envisat track 294C in the central URG area. Most of the displacement values shown in the crop are small. Particularly in the western part, some of the values reveal larger changes acting on a small spatial scale likely attributed to unmodelled atmospheric influences. However, these temporally uncorrelated influences will largely diminish in the estimates of linear rates from a large number of interferograms. The standard deviations resulting from the interpolation shown in Fig. 7.11(b) are on a similar level for each interferogram depending on the nugget and sill values of the corresponding semivariogram function, see Fig. 7.9. Slightly lower standard deviations are observable in the cities and villages located in the graben compared to other areas characterised by only few PS pixels, particularly in the sparsely populated areas of VG and BF.

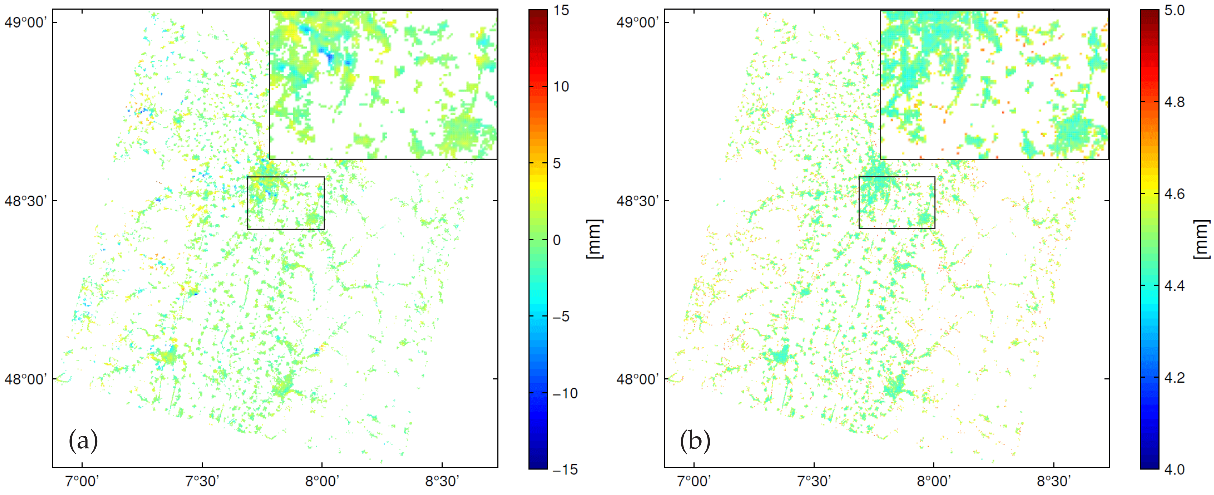

Figure 7.11: Interpolated displacements (a) and corresponding standard deviations (b) for interferogram 8 in Envisat track 294C. Black frames represent a zoom into a representative region.

7.4.3 Stitching of overlapping SAR image stacks

The analysis of Envisat data in tracks 487 and 294 has been split into subtracks in order to make use of the higher number of available scenes in the southern part of the URG area, see Tab. 3.3. After interpolation to a common grid, the subtracks shall be stitched together in a way that an homogeneous velocity field is obtained. Differences in the resulting LOS velocities of the subtracks may exist as a different spatial reference area is chosen within each subtrack resulting in an offset of the velocities of different subtracks. Further, non-constant velocity differences may occur, particularly due to a difference in the master selection and the total time span of available SAR data, but are neglected here. First, linear rates are estimated from the displacement time series of grid points in each subtrack applying least-squares adjustment along with the covariance model discussed in Sect. 7.4.4 to a single sensor time series. The offset between different subtracks follows from the resulting LOS velocities in the overlapping area of any two subtracks. The mean value of velocity offsets w.r.t. the subtrack which contains the defined reference area at the city of Lahr is finally used as overall offset for the whole subtrack. The estimated velocity offsets v_{off} are $+0.25$ mm/a for track 294S w.r.t. track 294C, $+0.76$ mm/a for track 294N w.r.t. track 294C and -0.08 mm/a for track 487S w.r.t. track 487N. The Envisat LOS velocitiy estimates within track 294 are shown in Fig. 7.12 before and after the veloity offset is applied to the velocities.

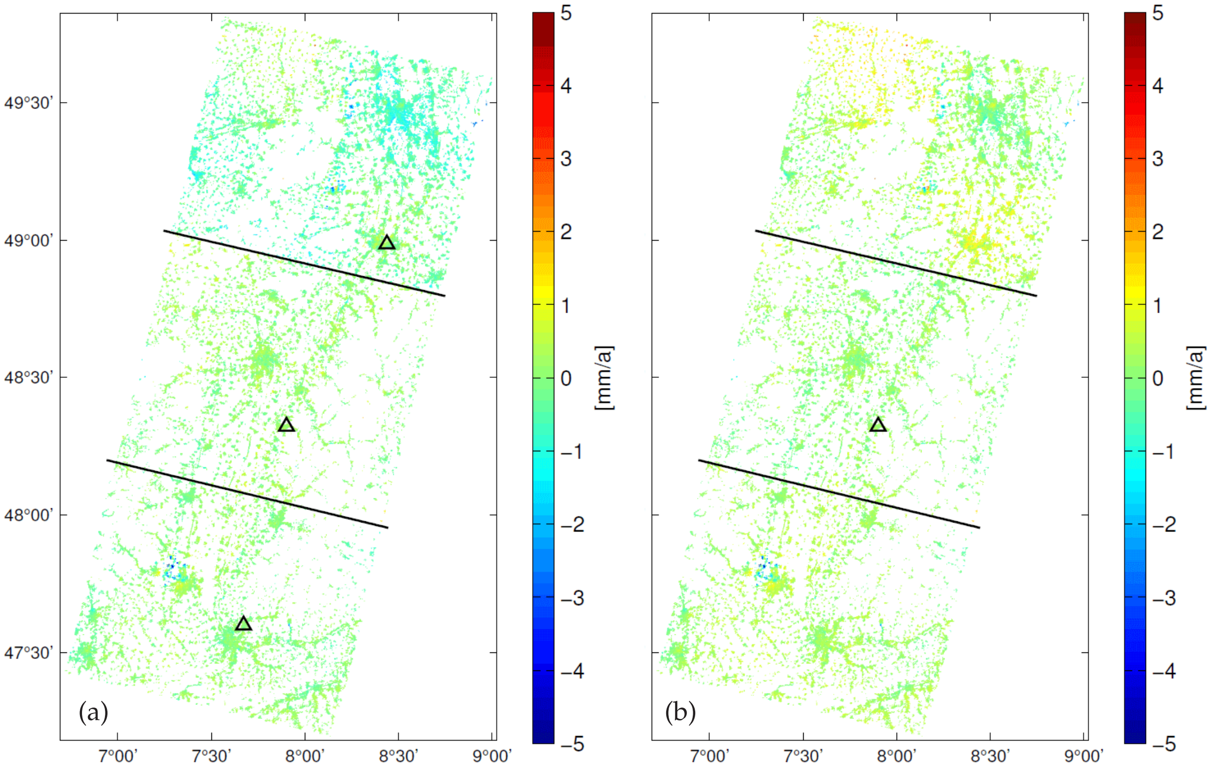

Figure 7.12: LOS velocities in track 294 calculated from Envisat displacement time series of three subtracks before (a) and after (b) stitching. Black triangles mark the location of the reference areas which is Karlsruhe for the northern subtrack, Lahr for the central subtrack and Lörrach (close to Basel) for the southern subtrack. Black lines separate the used extent of the subtracks.

As the displacement values of the stitched track shall be further used for the combination of ERS and Envisat, new, stitched displacement values have to be calculated for every valid grid point in all interferograms i of the subtracks 294S, 294N and 487S. A residual, detrended displacement $\Delta R_{i,res}$ follows from subtraction of the estimated linear trend with a velocity v_1, the time difference Δt w.r.t. a reference epoch, e. g. the date of the first acquisition, and the intercept b

$$\Delta R_{i,res} = \Delta R_i - v_1 \Delta t - b \quad . \tag{7.21}$$

The new, stitched displacement values $\Delta R_{i,new}$ result from the new velocity v_2 at the grid point with $v_2 = v_1 + v_{off}$, and can be reformulated as follows:

$$\begin{aligned} \Delta R_{i,new} &= \Delta R_{i,res} + v_2 \Delta t + b \\ &= \Delta R_i - v_1 \Delta t - b + v_2 \Delta t + b \\ &= \Delta R_i + (v_2 - v_1)\,\Delta t \\ &= \Delta R_i + v_{off} \Delta t \quad . \end{aligned} \tag{7.22}$$

The stitched displacement values are subsequently used for the combination of ERS and Envisat time series. Stitching is currently also an issue for InSAR analyses of Sentinel-1 data, where the SAR data is acquired and provided on three subswaths which have to be combined within the interferometric processing for the analysis of large areas.

7.4.4 Combination of ERS and Envisat time series

The analysed ERS and Envisat tracks in the URG area cover a similar region. In order to increase the length of the time series along with the resulting precision of estimated velocities, the displacement values of ERS and Envisat are combined on the basis of time series. When combining ERS and Envisat, linear rates are more precisely estimable as the temporal baseline covered by the InSAR displacement values is significantly increased. For a subregion in the northern URG, combined ERS/Envisat estimates of linear rates in ascending and descending image geometries are compared to linear rates estimated from separate ERS and Envisat time series. Differences of the Up and East components, calculated from ascending and descending linear rates, to linear rates obtained from levelling and GNSS are smaller and less dispersive for the combined ERS/Envisat solution. In addition, a separation of linear and non-linear movements is more effective with the combined time series, see Fig. 7.13. Caro Cuenca et al. (2010) presented a least-squares formulation for joint time series estimates by fitting a third order polynomial function to the ERS/Envisat displacement time series. The unknown offset x_{off} represents the total displacement between the ERS and Envisat acquisition period and is simultaneously considered within a least-squares adjustment:

$$\begin{pmatrix} \Delta R_{A,1} \\ \vdots \\ \Delta R_{A,n_A} \\ \Delta R_{B,1} \\ \vdots \\ \Delta R_{B,n_B} \end{pmatrix} = \begin{pmatrix} t_{A,1}^3 & t_{A,1}^2 & t_{A,1} & 1 & 0 \\ \vdots & \vdots & \vdots & \vdots & \vdots \\ t_{A,n_A}^3 & t_{A,n_A}^2 & t_{A,n_A} & 1 & 0 \\ t_{B,1}^3 & t_{B,1}^2 & t_{B,1} & 1 & 1 \\ \vdots & \vdots & \vdots & \vdots & \vdots \\ t_{B,n_B}^3 & t_{B,n_B}^2 & t_{B,n_B} & 1 & 1 \end{pmatrix} \begin{pmatrix} x_3 \\ x_2 \\ x_1 \\ x_0 \\ x_{off} \end{pmatrix} + e \quad . \tag{7.23}$$

$\Delta R_{A,i}$: Displacement in interferogram i, sensor A (ERS)
$\Delta R_{B,i}$: Displacement in interferogram i, sensor B (Envisat)
n_A : Number of interferograms of sensor A
n_B : Number of interferograms of sensor B
t_A : Acquisition time of sensor A
t_B : Acquisition time of sensor B

x_0, x_1, x_2, x_3 : Parameters of a polynomial function

x_{off} : Offset between sensor A and sensor B

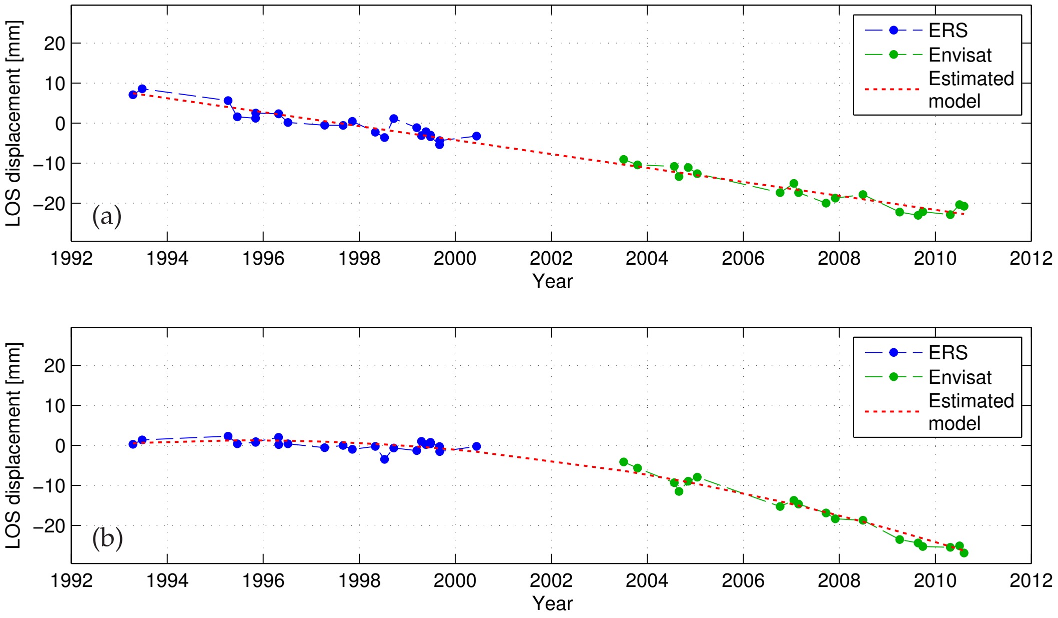

Figure 7.13: Example for ERS/Envisat time series combination using displacement values at two different locations of track 487. (a) Linear movement (subsidence), (b) Non-linear movement.

As the combination of InSAR velocities with GNSS and levelling velocities is based on linear movements, the results of Eq. (7.23) are used to separate linear and non-linear movements. At every interpolation point, the adjustment is performed with three different parameter sets on the time series data. First, the polynomial function contains all components displayed in Eq. (7.23). Second, the third-order monomial t^3 is omitted, and finally, also the second-order monomial t^2 is removed from the model, resulting in a purely linear velocity estimate. Afterwards, a test on significance of the second- and third-order polynomial coefficients against the null hypothesis of a linear movement is performed. The test value T_S for a significance test of the second-order polynomial follows a Fisher distribution with $(u_2 - u_1, n - u_2)$ degrees of freedom and is compared with a 1% quantile:

$$T_S = \frac{\frac{SSE_1 - SSE_2}{u_2 - u_1}}{\frac{SSE_2}{n - u_2}} \quad . \tag{7.24}$$

SSE_j : Sum of squared errors $\left(= e^\top C^{-1} e\right)$

u_j : Number of parameters with j=1: linear, j=2: quadratic

n : Number of observations

Note that SSE_j is distributed according to the chi-squared distribution. The ratio of two chi-squared variates follows a Fisher distribution if the two quotients are stochastically independent. As the parameter estimation is performed in separate least-squares adjustments with a different set of monomials, the quotients in Eq. (7.24) can be considered as independent even if the adjustments rely on the same observations. If T_S calculated from Eq. (7.24) is larger than the critical value of the Fisher distribution, the null hypothesis is rejected and the movement is considered to be non-linear. Two representative examples for a linear movement and for a non-linear movement with a significant second-order component are shown in Fig. 7.13. Both the ERS and Envisat time series data are related to the same reference area. From a separate estimation of linear rates of the time series data from ERS and Envisat shown in Fig. 7.13(b), both movements would be modelled with a linear function. In fact, the movement behaviour is completely different in the first and second period, such as for the deformation pattern close to the city of Landau presented in Sect. 6.5.5. A single-sensor approach to describe non-linear movements at PS pixels using polynomial functions was recently published by Busch & Linke (2014) and applied to Terra-SAR-X data in urban environments. However, in addition to the functional model, the stochastic model of the here developed joint time series adjustment is important and described in the following.

A realistic model for the accuracy of displacement values within the ERS and Envisat time series requires considering (i) the individual accuracy of the interpolation point, (ii) the accuracy level of the interferogram and (iii) temporal correlations between interferograms. The mean variance of the interpolated displacement values ΔR_i at different interferograms and grid points is used as variance or total sill $C(0)$ of the signal. The mean interpolated variances are smaller for the tracks containing fewer interferograms, see Fig. 7.14(a). It can be observed that already the StaMPS estimates of phase noise in the nine tracks depend on the number of interferograms within the stack, yielding a higher noise level for the stacks with a high number of images. Also the threshold values for the spatio-temporal consistency (STC), discussed in Sect. 6.5.2, have larger values for the stacks with a higher number of interferograms, see Fig. 7.14(b). However, from a stack analysis of InSAR data, it is reasonable that a lower standard deviation of resulting deformation values is achievable with a larger image stack as the phase terms shown in Eq. (3.26) are better separable.

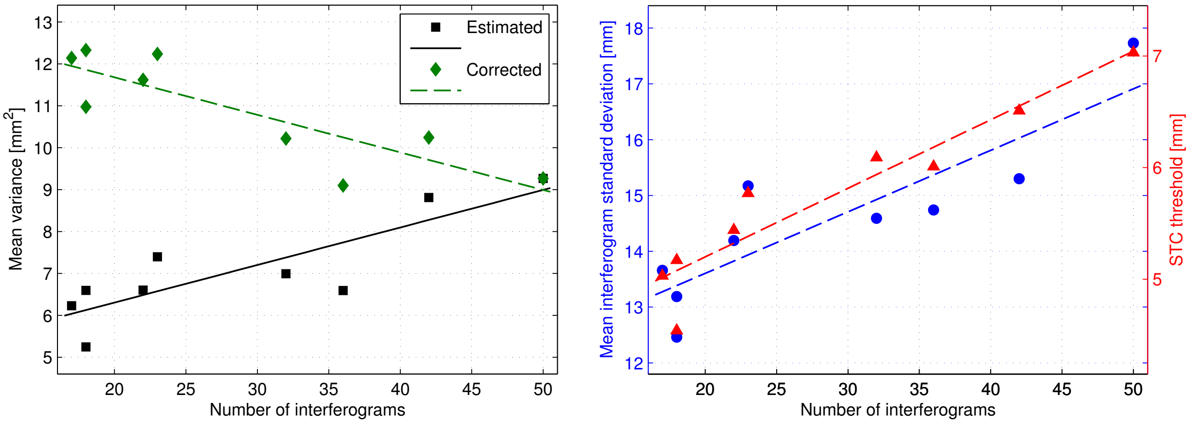

(a) Mean variances of interpolated displacement values and corrected values applied in the covariance model for time series combination.

(b) Interferogram standard deviation from phase noise and STC thresholds applied within the quality filtering, see Tab. 6.7.

Figure 7.14: Dependence of accuracy on the number of interferograms within each image stack. Mean variances of deformation values result from the spatial interpolation using Kriging. Phase noise standard deviations for each interferogram are calculated from the wrapped phases within StaMPS. Spatio-temporal consistency (STC) thresholds are calculated for each stack as described in Sect. 6.5.2. Linear regression of the dispersion measures is shown in order to illustrate the dependence on the number of interferograms within each stack.

Mahapatra et al. (2014) derive empirical precision values for InSAR displacements measured at active transponders at the level of 1.8–4.6 mm. From a comparison of two different Envisat stacks with GPS data observed at the same location, they find a significantly better precision for the image stack containing more images. In order to account for the fact that the precision of resulting deformation values in each interferogram is higher if the data stack comprises a large number of interferograms, an additional regularisation parameter is added to $C(0)$ depending on the number of interferograms in the corresponding image stack. A linear relationship is assumed to describe the decrease in precision for a smaller number of interferograms w.r.t. the stack containing the highest number of images, see green line in Fig. 7.14(a). The overall precision for the natural radar targets analysed within this study is assumed to be not better than the achievable precision at active transponders (Mahapatra et al., 2014) and is at the level of 3.0–3.5 mm for the different stacks. Only a slight decrease in precision for stacks with less images is used here as the real relationship between the number of interferograms and the precision of displacement values is unknown.

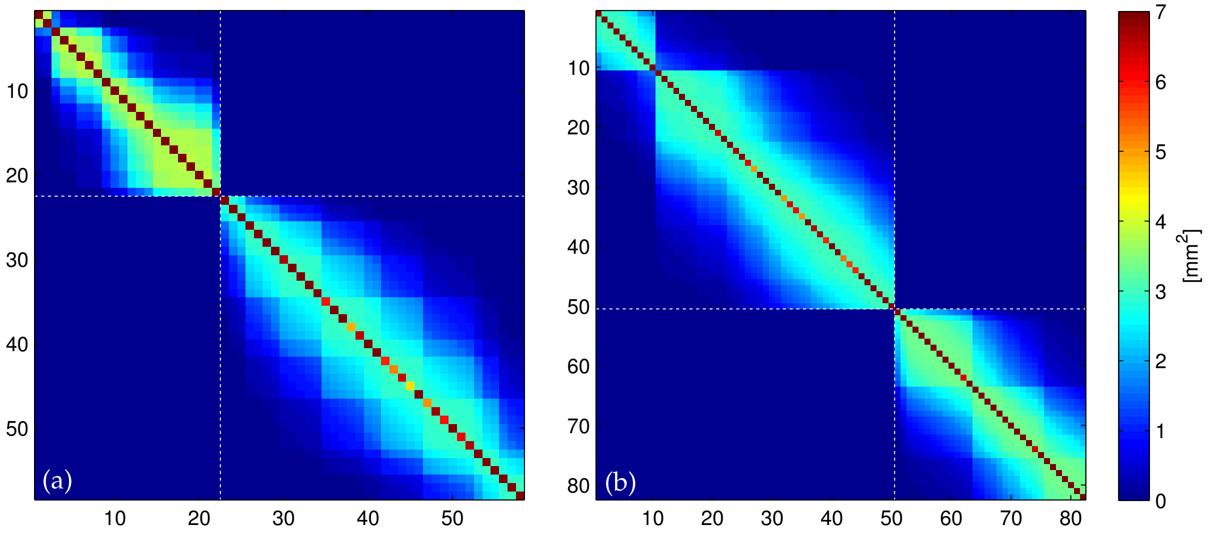

Figure 7.15: Covariance matrix of ERS/Envisat time series combination at grid points in track 487 (a) and track 294 (b). The left upper part represents the ERS interferograms, (a) number 1–22, (b) number 1–50, the part at the right bottom the Envisat interferograms, (a) number 23–58, (b) number 51–82. Note that no correlation between ERS and Envisat data is assumed. The two blocks in the ERS interferograms (interferogram 1–10 and interferogram 11–50 in (b)) result from a data gap between 1993-10-29 and 1995-06-04.

Temporal correlations between the displacement values are assumed to be present as the displacement values are related to the same master scene and temporal filters are applied within the stack analysis at several stages, particularly for the atmospheric filtering. A temporal variogram estimation is applied to the LOS displacements of each image stack using the time differences as distances d. However, the variogram parameters, i. e. sill, nugget and range are not detectable with high significance as only $n = 17$ to $n = 50$ data points are available for each PS location. At least, the estimated ratio between nugget and total sill and between partial sill and total sill can be constrained to values of $2/3$ and $1/3$, respectively. Note that similar ratios result from the variogram estimates for the spatial interpolation of interferograms, see Sect. 7.4.1. The temporal covariance model uses the corrected variance $C(0)$ at each interpolation point along with the aforementioned ratio to determine nugget and partial sill. A Gaussian model is applied to model the decrease of C with time, using a modified range $r'' = 730$ days, as Gaussian filters with a time window of 730 days are commonly used within the PS analysis of StaMPS. A 730 days smoothing window is used for the weeding and for the estimation of phase noise within the unwrapping (Hooper et al., 2013, p. 18 f.). In addition, the spatio-temporal filtering uses a Gaussian filter with a time window of 730 days, as discussed in Sect. 6.3.4. Finally, the main diagonal elements of the covariance matrix are scaled using the ratio between the variance of interpolated displacement values $C(0)_i$ per interferogram and the mean variance $C(0)$. Fig. 7.15 shows two representative examples of the final covariance matrix at grid points in tracks 487 and 294.

The importance of an appropriate covariance modelling in the times series combination becomes obvious from Tab. 7.3. If an identity matrix is used instead of the more sophisticated covariance matrix (Fig. 7.15), more than 20% of the movements are considered to be non-linear. When accounting for temporal correlations between displacements of different interferograms, the amount of displacements assigned to a non-linear motion model significantly decreases in all three tracks. The additional scaling of the main diagonal elements further reduces the amount of non-linear displacements to values between 0.9 and 5.9 %. The remaining non-linear displacements are mostly located in regions with man-induced deformations, see Fig 7.16. In track 487, a significant amount of non-linear movements is located in the northern part of the track, see Fig D.1(c) in Appendix D. These non-linear movements may be assigned to residual unmodelled phase contributions in the northern part of Envisat track 487N and a resulting misfit in the motion behaviour compared to the ERS time series data. For the combination of displacement results from PS-InSAR, levelling and GNSS, PS grid points with a non-linear displacement are omitted. Note that the standard deviations of the estimates increase when temporal correlations are considered and the main diagonal elements are scaled according to the individual interferogram accuracy, see Tab. 7.3. Values of 0.5 to 0.6 mm/a for the 2σ standard deviations of velocities are more realistic compared to values of 0.2 to 0.3 mm/a resulting from the case when an identity matrix is used within the stochastic model. Furthermore, the higher values are supported by several investigations on the precision of velocity estimates resulting from PS-InSAR analyses with C-band data (Rocca, 2007; Rucci et al., 2012; Rocca et al., 2013).

Table 7.3: Influence of the covariance model for the combination of ERS/Envisat time series on the amount of non-linear movements and on standard deviation (STD).

	Non-linear movements		Mean 2σ STD of LOS
	Number	Percentage	velocities [mm/a]
Track 258, 77,676 valid grid points			
Identity matrix:	17,678	22.8	0.30
Temporal correlations:	3,140	4.0	0.57
Temporal correlations and scaled main diagonal:	1,778	2.3	0.64
Track 487, 73,917 valid grid points			
Identity matrix:	25,509	34.5	0.25
Temporal correlations:	8,254	11.2	0.43
Temporal correlations and scaled main diagonal:	4,368	5.9	0.51
Track 294, 75,732 valid grid points			
Identity matrix:	19,538	25.8	0.23
Temporal correlations:	1,028	1.4	0.52
Temporal correlations and scaled main diagonal:	678	0.9	0.57

The resulting LOS velocities from joint time series estimation of ERS and Envisat data at grid points in the URG area are shown in Fig. 7.16 for track 294 along with the corresponding standard deviations of the estimates. 98 % of the LOS velocities in track 294 are within a range of ±1 mm/a. Larger subsidences of 5 mm/a and more are visible in the area of Landau in the northern part at 8°7′ E, 49°12′ N and close to Mulhouse in the southern part at 7°16′E, 47°47′N. A non-linear motion model is assigned to most of the movements in this areas, see black dots in Fig. 7.16(a). The non-linear displacements in the south eastern part of the track might be a result of residual unmodelled errors in this area due to strong atmospheric signals present in the Alpine foreland in some of the interferograms. The mean 2σ standard deviation is 0.57 mm/a with values ranging between 0.25 and 1.41 mm/a. Higher standard deviations are observed in the VG and in the BF, where the PS density is low and hence the separation of nuisance terms as well as the spatial interpolation is worse. However, higher uncertainties are as well observable in parts of the large cities, i. e. Mannheim, Karlsruhe, Strasbourg, Freiburg, Mulhouse and Basel, resulting from velocity estimates of noisy time series data. The standard deviations shown in Fig. 7.16(b) are used as input data for the stochastic model of the combination with levelling and GNSS velocities, see Eq. (7.26). At grid points with a high uncertainty of the LOS velocitiy, the weight applied within the data fusion will be low. The LOS velocities for the two ascending tracks and corresponding standard deviations are shown in Appendix D. Note that track 258 contains data of both sensors only in the southern part. The resulting LOS velocities cover different areas in the northern and southern parts as the overlapping area covered by both sensors is smaller in range direction, see Fig. D.1(a).

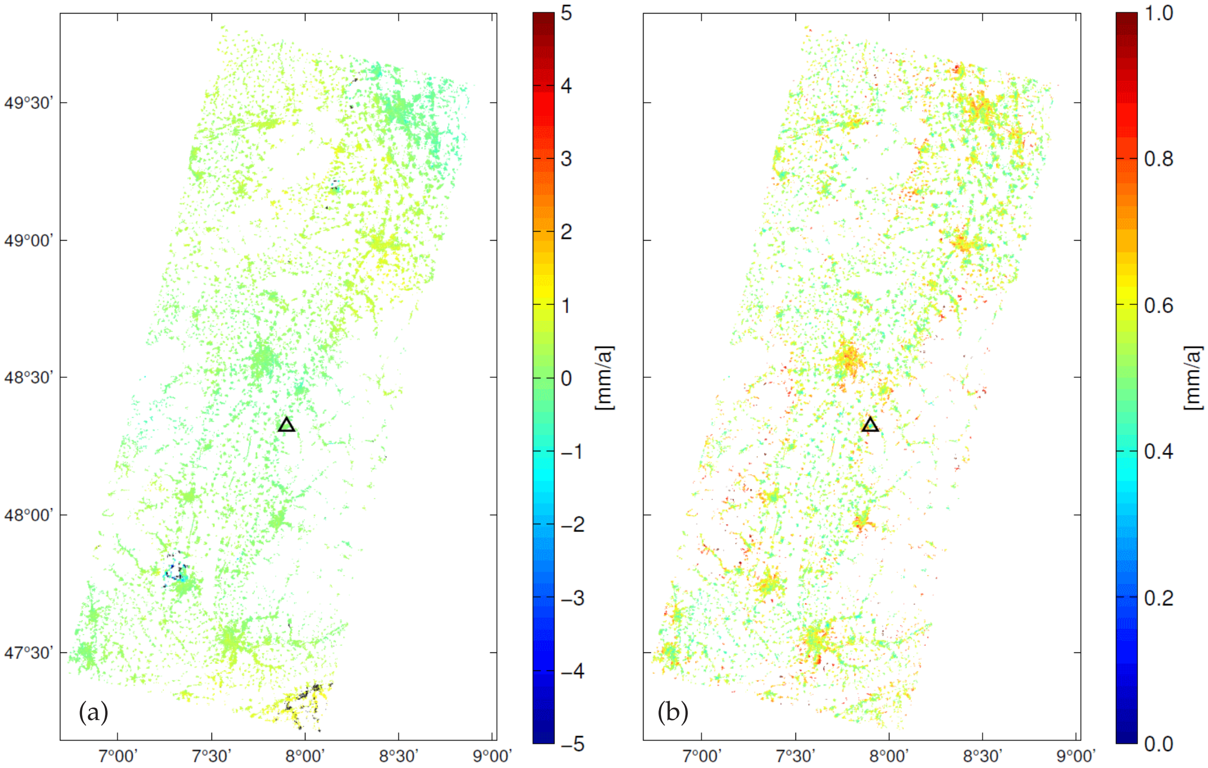

Figure 7.16: InSAR velocity estimates at grid locations in track 294 from ERS/Envisat combination. (a) LOS velocities, (b) Standard deviation (2σ) of LOS velocities. Grid points with a significant non-linear motion behaviour are marked as black dots in (a) and omitted in (b).

7.4.5 Reference frame integration

In the first step of the data fusion, the different reference frames of levelling, GNSS and InSAR are considered. Therefore, an offset and a linear trend, i. e. a velocity ramp, between levelling and InSAR (vertical component) and between GNSS and InSAR (horizontal component) are estimated. After stitching of subtracks, the PS analyses of the three tracks refer to the same reference area located at the city of Lahr (7.876°E, 48.342°N). Levelling benchmarks located within the selected reference radius of 500 m reveal a small subsidence tendency of the reference area w.r.t. the levelling reference point located in the eastern BF. The average linear displacement rate of six levelling benchmarks located within or close to the InSAR reference area is -0.16 mm/a. The horizontal displacement rates at surrounding GNSS sites are also small close to the InSAR reference area. The 15 km distant site at Offenburg (0393) has a velocity of $+0.28$ and $+0.03$ mm/a for the East and North component, respectively.

In order to integrate the InSAR velocities into the reference frame of levelling, offset and trend are estimated from LOS velocities interpolated at the locations of the levelling benchmarks, see Fig. 7.7. The ascending and descending velocity estimates are converted to Up and East components by application of Eq. (7.9). Note that the sensitivity of InSAR to the North component is low because of the near polar orbits and the side-looking geometry. The offset follows from the mean difference between the vertical velocities from levelling and the InSAR Up component, and is attributed to a bias of the InSAR reference frame w.r.t. the vertical datum of levelling (Catalão et al., 2010). Subsequently, a velocity trend is estimated from the residual differences after subtracting the offset. Offset and trend estimates for the two track combinations are shown in Tab. 7.4.

Table 7.4: Offset and trend between the vertical components of levelling and InSAR at the location of levelling benchmarks.

Track (asc., desc.)	Offset [mm/a]	Trend [mm/a per 100 km]
Track 258, 294	-0.13	0.17
Track 487, 294	-0.34	0.36

Both offsets reveal negative values, which means that the level of the InSAR Up component is higher compared to the level of the levelling results. This is in general agreement with the slight subsidences of the levelling benchmarks close to the InSAR reference area. As the InSAR reference area is slightly subsiding all other InSAR velocities are slightly shifted upwards and have to be reduced by application of a negative offset. However, both estimates of offset and trend are small indicating a good agreement between the vertical linear rates from InSAR and levelling. A trend between the vertical rates from levelling and InSAR reflects differences on a larger spatial scale and can be attributed to various factors, such as residual orbital or atmospheric effects. The application of a trend enables to fit the InSAR displacement rates into the large-scale velocity field defined by the levelling estimates, while exploiting the capability of InSAR to resolve the spatial pattern of a deformation.

Different data combination strategies are possible to calculate the horizontal offsets between GNSS and InSAR:

(i) calculation of East and Up components from ascending and descending velocities (InSAR-only, equivalent to the levelling case),

(ii) estimation of East and Up components from ascending and descending velocities and levelling velocities,

(iii) calculation of East, North and Up components from ascending and descending velocities and levelling velocities.

For (i), no additional data is required, but the resulting East and Up components are erroneous if a significant North velocity component exists. For (ii) and (iii), the levelling displacement rates have to be interpolated to the locations of GNSS sites. While (ii) is able to solve the two components in a least-squares sense, but again may be erroneous because of neglecting the North component, (iii) constrains the Up component with the levelling velocity, but may estimate a potentially existing North component. However, the differences between GNSS and InSAR in the North component are much larger compared to the East component as the sensitivity of InSAR to the North component is low. For a subregion in the northern URG, the differences between the three calculation strategies are below 0.1 mm/a for the East component at the analysed GNSS sites if the combined ERS/Envisat velocities are used. In order to calculate an offset and trend for the east component which is unconstrained from the levelling result, the InSAR-only solution is preferred. The resulting offset and trend estimates for the two track combinations are shown in Tab. 7.5. As for the levelling calculations, all values are well below 1 mm/a indicating a good fit of velocities from GNSS and InSAR. However, the estimated trends are larger for the East component compared to the Up component, which is at least partly due to the lower sensitivity of the horizontal components from InSAR. Furthermore, a trend could have been introduced to the horizontal components of InSAR LOS velocities by the reference frame effect of plate motion described within Sect. 6.2.3.

Table 7.5: Offset and trend between East components of GNSS and InSAR at the location of GNSS sites.

Track (asc., desc.)	Offset [mm/a]	Trend [mm/a per 100 km]
Track 258, 294	−0.23	0.76
Track 487, 294	−0.02	0.55

Within the mathematical data fusion, offset and trend values are added to the LOS velocities of each grid point. Following Eq. (7.9), the ascending and descending contribution of the correction value at the corresponding pixel is calculated. For the calculation of offset and trend values, only grid points with LOS velocities in both ascending and descending image geometry, are used. For the reference frame integration of LOS velocities, also the grid points containing only ascending or only descending LOS velocities are corrected with the corresponding offset and trend values. Tab. 7.6 compares the standard deviations of the resulting 3D velocities with and without reference frame integration for the grid points located in areas with both ascending and descending LOS velocities and for the whole analysed area including also velocities in one image geometry only. In both cases, the standard deviations of all three velocity components are reduced. For the grid points containing ascending and descending velocities, the standard deviation in all components reduces by about 18 %, when the velocities are integrated into the reference frames of levelling and GNSS.

Table 7.6: Mean standard deviations of 3D velocities resulting from the mathematical fusion of levelling, GNSS and InSAR with and without application of offset and trend.

	East [mm/a]	North [mm/a]	Up [mm/a]
Asc. and desc. velocities (55,536 grid points)			
without offset and trend correction:	0.40	0.50	0.17
with offset and trend correction:	0.33	0.41	0.14
Whole analysed area (134,431 grid points)			
without offset and trend correction:	0.43	0.51	0.19
with offset and trend correction:	0.38	0.45	0.18

7.4.6 Mathematical data fusion

Finally, the mathematical fusion of linear displacement rates of the three techniques is performed. At every PS grid point containing LOS velocities in ascending and descending image geometries, least-squares adjustment is applied and three velocity components in East, North and Up direction (v_E, v_N, v_U) are estimated from the set of five given observations (V_{asc}, V_{desc}, $V_{GNSS,E}$, $V_{GNSS,N}$, V_{lev}):

$$\begin{pmatrix} V_{asc} \\ V_{desc} \\ V_{GNSS,E} \\ V_{GNSS,N} \\ V_{lev} \end{pmatrix} = \begin{pmatrix} -\sin\theta_{asc}\cos\alpha_{asc} & \sin\theta_{asc}\sin\alpha_{asc} & \cos\theta_{asc} \\ -\sin\theta_{desc}\cos\alpha_{desc} & \sin\theta_{desc}\sin\alpha_{desc} & \cos\theta_{desc} \\ 1 & 0 & 0 \\ 0 & 1 & 0 \\ 0 & 0 & 1 \end{pmatrix} \begin{pmatrix} v_E \\ v_N \\ v_U \end{pmatrix} + e \quad . \tag{7.25}$$

The design matrix contains the projection of LOS velocities to East, North and Up components using the satellites' heading α and the incidence angle θ, see Eq. (7.4). A constant heading is assumed for each track, whereas the incidence angle is range-dependent and individual values are used at every grid point location. The covariance matrix of the least-squares adjustment is given by

$$C = \begin{pmatrix} \sigma^2_{V_{asc}} & 0 & 0 & 0 & 0 \\ 0 & \sigma^2_{V_{desc}} & 0 & 0 & 0 \\ 0 & 0 & \sigma^2_{V_{GNSS,E}} & \sigma_{V_{GNSS,E,N}} & 0 \\ 0 & 0 & \sigma_{V_{GNSS,E,N}} & \sigma^2_{V_{GNSS,N}} & 0 \\ 0 & 0 & 0 & 0 & \sigma^2_{V_{lev}} \end{pmatrix} \quad . \tag{7.26}$$

While the velocity estimates calculated from InSAR in ascending and descending image geometries are assumed to be uncorrelated, the GNSS velocities in North and East direction are correlated as they stem from the same set of observations. The E–N covariance inherent to the daily coordinate estimates propagates into the E–N covariance of the linear velocity estimates $\sigma_{V_{GNSS,E,N}}$ in a way that the ratio between covariances and variances remains the same. Hence, the mean E–N correlation from all daily coordinate solutions is used to estimate linear velocities along with the full covariance matrix at every GNSS site. Subsequently, the resulting correlations are spatially interpolated in order to provide the input for Eq. (7.26) at every grid point. Only at seven of the 76 analysed GNSS sites, the E–N correlation of velocities is larger than ±2 %. The difference in the resulting 3D velocity field when the covariance matrix given in Eq. (7.26) is used instead of a diagonal covariance matrix is thus not significant. Maximum velocity differences at the grid points are observed for the North component, but still below 0.02 mm/a (92 % below 0.001 mm/a).

At the overlapping part of the two ascending tracks 258 and 487 the functional and stochastic models given in Eq. (7.25) and (7.26) are extended by one row and two LOS observations in ascending image geometry $V_{asc,1}$ and $V_{asc,2}$ are used. Also grid points with only one ascending or descending LOS observation can be handled. In this case, the functional and stochastic models reduce to four rows. For the data fusion of the analysed velocities in the URG area, seven combination cases are distinguished, summarised in Tab. 7.7.

Table 7.7: Different observation cases used within the fusion of velocities and number of corresponding grid points.

Case No.	Case description (InSAR velocity components)	Total number of observations	Track number(s) of observations	Number of grid points
1	1 ascending, 1 descending	5	258, 294	20,602
2			487, 294	17,758
3	2 ascending, 1 descending	6	258, 487, 294	17,176
4	1 ascending	4	258	28,790
5			487	23,079
6	1 descending	4	294	17,979
7	2 ascending	5	258, 487	9,047

7.5 3D velocity field of the URG

The combination of levelling, GNSS and InSAR displacement data is performed as described in Sect 7.4 finally resulting in 3D velocities at the PS grid with a spatial resolution of 200 m. According to Tab. 7.7, the final result provides valid grid values at 134,431 grid points. For visualisation purposes the horizontal velocities are interpolated to a sparser grid and displayed as velocity arrows above the colour-coded vertical velocities in Fig. 7.17. The presented velocity field reveals the on-going surface motion of the URG area in unprecedented detail and accuracy. Corresponding standard deviations of the velocity estimates are shown in Fig. 7.18.

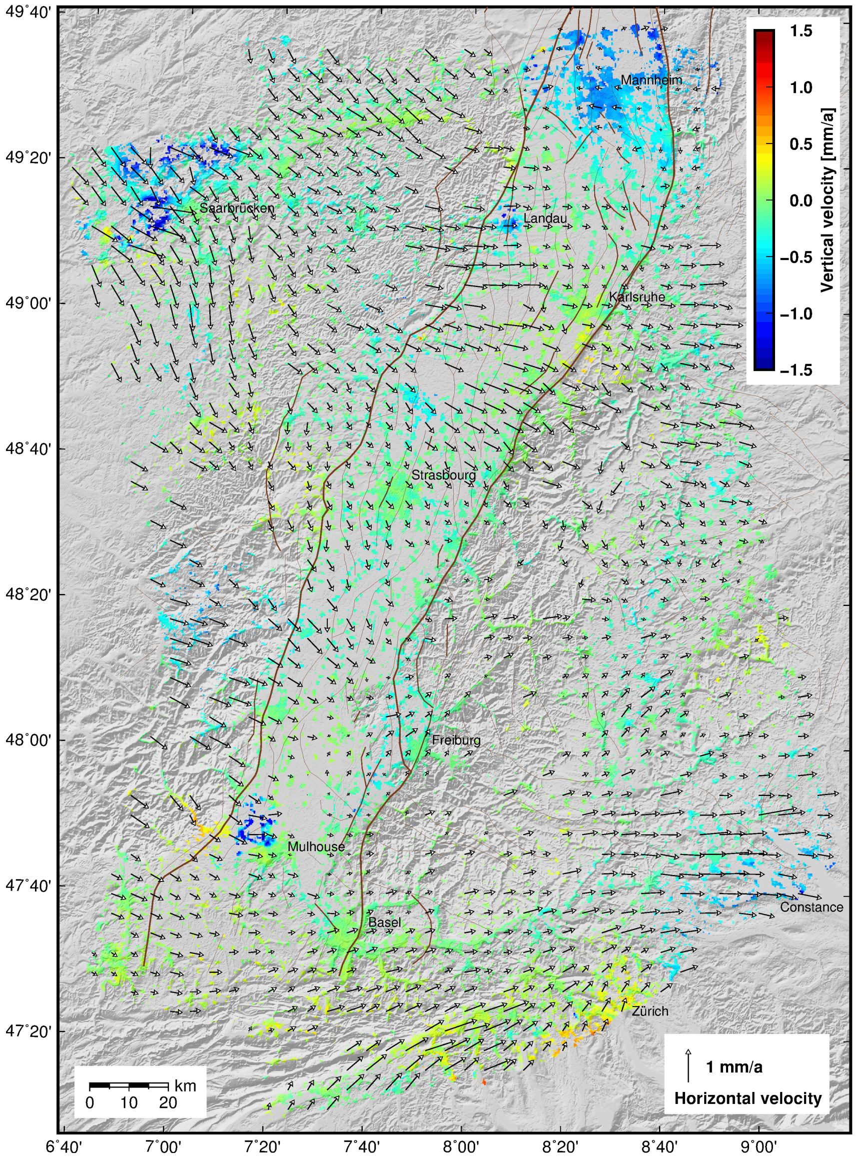

Figure 7.17: Final result of the combination of levelling, GNSS and InSAR: horizontal linear rates (arrows) and vertical linear rates (colour-coded). The horizontal velocity field is interpolated to a 5 km grid for visualisation purposes. The vertical movements are relative to a reference point in the eastern BF, the horizontal movements are relative to a local Euler pole estimated from all 76 GNSS sites in the URG area. Brown lines represent faults in the URG area after Peters (2007, p. 166), main border faults (thick), active faults (medium thick) and other faults (thin). Grey background: shaded DEM using SRTM-3 data.

7.5.1 Discussion of final results

In order to investigate the contribution of InSAR to the resulting velocity field, a comparison to a velocity field resulting from the levelling and GNSS observations is calculated, shown in Fig. D.2 in Appendix D. A velocity field with the same spatial extent and resolution related only to the levelling and GNSS velocities is easily obtained by setting the standard deviation of the InSAR observations to a high value ($\sigma_{V_{asc}},\ \sigma_{V_{desc}} \rightarrow \infty$). The horizontal velocity of the levelling-GNSS-only solution does not much differ from the result given in Fig. 7.17, see difference plot given in Fig. D.3. The general trends of the velocity arrows are similar, which is reasonable as InSAR is more sensitive to vertical deformations, see Eq. (7.8). However, some regional changes of horizontal trends are observable. The combined solution reveals stronger S directed movements at the WBF close to Strasbourg and stronger E directed movements at the EBF close to Karlsruhe as well as in the southeast at Lake Constance. The vertical velocity field shows major differences in areas with strong anthropogenic deformation, such as in the mining areas of Lorraine/Saarland and west of Mulhouse, see Fig. D.3. Besides these large changes, smaller differences are observed north of Strasbourg, where the magnitude of a local subsidence pattern present in the levelling results is significantly decreased. Furthermore, one can observe a slight increase of the uplift tendency close to Karlsruhe, a decrease of the uplift in the Palatinate Forest and increasing values for the subsidence at the *Heidelberger Loch*, particularly north of Heidelberg, as well as at Lake Constance. Larger differences at the borders of the InSAR tracks may be attributed to residual, unmodelled phase contributions in the InSAR analyses.

Table 7.8: Statistics on the East, North and Up components of the combined 3D velocities and their formal errors, i. e. standard deviation (STD) of least-squares adjustment. Minimum (MIN), maximum (MAX) and mean values are given in mm/a.

	Velocities			Velocities within		STD		STD within	
	MIN	MAX	Mean	±1 mm/a	±0.5 mm/a	MAX	Mean	1 mm/a	0.5 mm/a
East	−1.19	2.16	0.30	98.9 %	80.7 %	6.41	0.38	96.9 %	75.5 %
North	−0.81	0.77	−0.11	100.0 %	94.4 %	7.21	0.45	94.4 %	66.4 %
Up	−3.72	1.03	−0.13	99.1 %	90.8 %	2.99	0.18	99.2 %	96.5 %

In general, the estimated 3D velocities are small. Tab. 7.8 gives some statistical numbers on the three velocity components and their formal errors at the 134,431 grid points of the final solution. With more than 80 % of the velocity estimates in East, North and Up components being within ±0.5 mm/a, it can be stated that the URG is exposed to small crustal deformation. The mean standard deviations of velocities indicate a good fit of the three techniques in most parts of the investigation area. However, large standard deviations are observed in areas, where the displacement rates of the three techniques do not fit together. The spatial distribution of horizontal and vertical standard deviations are given in Fig. 7.18. Largest values are observed at the mining areas of Lorraine/Saarland and Wittelsheim. InSAR is the only technique covering the whole spatial extent of both mining areas. The interpolated velocity fields of levelling and GNSS are not able to capture the deformation in these areas and are thus delivering inaccurate information on the surface displacement. In addition to the significantly larger standard deviations compared to other regions, some unrealistic horizontal velocities are observed in these areas. A general increase in the standard deviations of horizontal velocities is observable with distance to the location of GNSS sites. The North component shows larger formal errors compared to the East component, which reflects the slightly larger standard deviations of the GNSS North components, see Tab. 5.2, and the low sensitivity of InSAR to the North component, see Eq. (7.8). The standard deviations of vertical velocities are smaller compared to the horizontal ones and more homogeneously distributed in the central part of the area as they are well constrained by the spatially dense levelling and InSAR data. At the border areas, increasing values are observed related to larger discrepancies of the InSAR results at the borders of the analysed tracks. In addition, the 3D velocities are calculated from ascending or descending data only at the borders of the investigation area and hence worse constrained by the InSAR data.

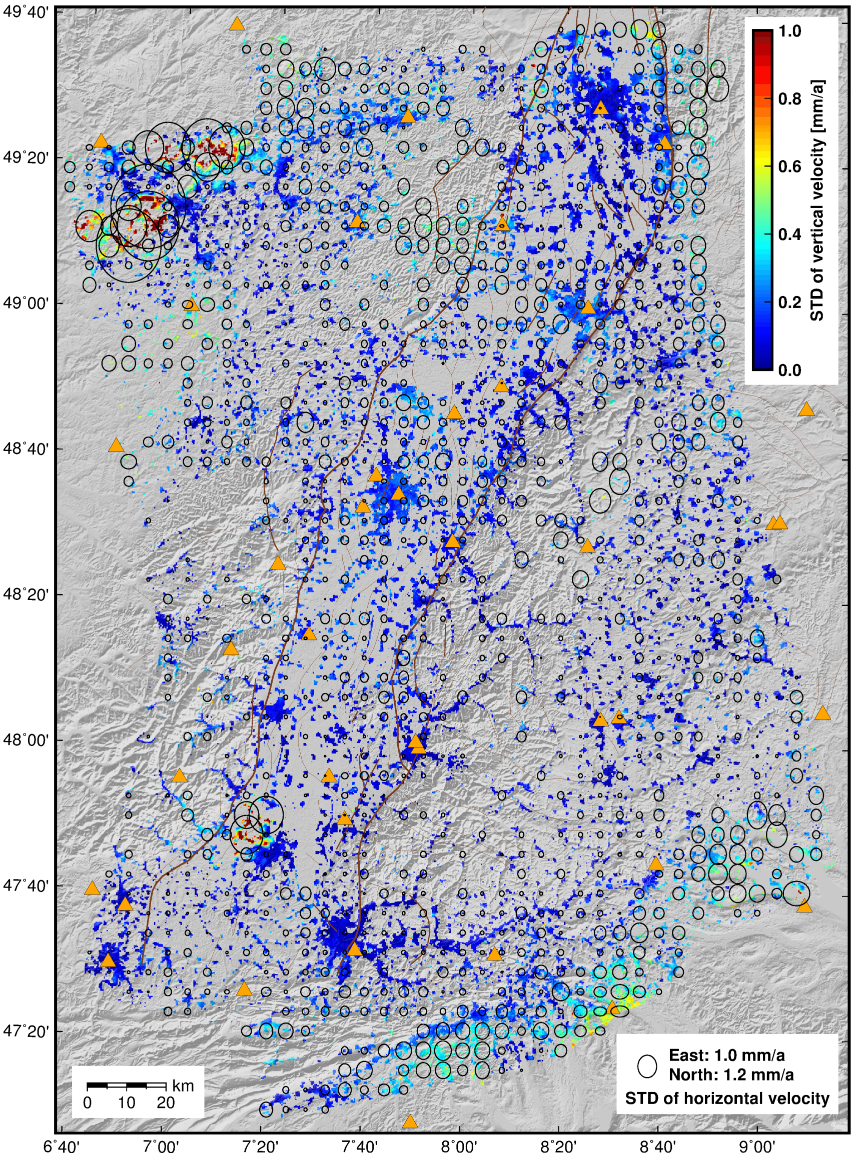

Figure 7.18: Standard deviation of linear rates: horizontal (ellipses) and vertical (colour-coded). Orange triangles mark the locations of GNSS sites. The horizontal standard deviations depend on the distance to the sites as the horizontal velocity field is mainly constrained by the GNSS velocities. Brown lines represent faults in the URG area after Peters (2007, p. 166), main border faults (thick), active faults (medium thick) and other faults (thin). Grey background: shaded DEM using SRTM-3 data.

The mean standard deviations of the velocities are 0.4 and 0.2 mm/a for horizontal and vertical components, respectively, and reflect the standard deviations of the input data given in Tab. 7.1. Compared to earlier geodetic studies on velocity fields in Central Europe (Zippelt & Mälzer, 1987; Nocquet & Calais, 2003, 2004; Vigny et al., 2002), the standard deviations are reduced while the spatial resolution is considerably improved. Furthermore, this is the first investigation of large-scale tectonic and anthropogenic deformation in the URG using InSAR, which particularly enables detailed insight into the spatial deformation behaviour related to anthropogenic activities in the region. The characteristics of the 3D velocity field along with the realistic formal errors evidence the high quality of the developed data fusion approach, which benefits from the advantages of the sensors taken into account. However, the deformation attributed to tectonics is found to be at a similar level as the uncertainties of the velocities, making a profound interpretation of the velocities difficult.

7.5.2 Geoscientific interpretation of the velocity field

For a proper interpretation of the results, the reader should keep in mind that all movements shown in Fig. 7.17 are of a relative nature. The vertical movements are relative to a levelling benchmark located in the eastern BF, the horizontal movements to a local Euler pole estimated from the velocities at 76 GURN sites. A detailed, quantitative interpretation of the velocity field w.r.t. tectonic deformation is beyond the scope of this work. Recent surface velocities measured by geodetic techniques are controlled by various factors and often not easily related to the dominant style of tectonic faulting, especially if the observed velocities are as small as in the URG area. In addition, tectonic deformation in the URG area is superimposed by non-tectonic effects resulting from anthropogenic activities. This particularly holds for areas with large vertical movements related to mining activities. Within this section, some conclusions attributed to the tectonic setting of the URG area are drawn, separately for the horizontal and vertical velocity fields. A major part of these conclusions has already been discussed within Sect. 4.5.4 and 5.3.1 for the vertical and horizontal velocities from levelling and GNSS, respectively.

Following fault plane solutions and 3D geomechanical models (Plenefisch & Bonjer, 1997; Buchmann & Connolly, 2007), the state of stress in the URG is transtensional with a dominating sinistral strike slip component. The maximum horizontal stress component in the URG is NW–SE orientated and trending obliquely to the graben axis (Illies et al., 1981; Buchmann & Connolly, 2007), see also Sect. 2.3.4. A relative southeastward motion at a level of about 0.6 mm/a is observed in the northwestern part of the investigated area in Fig. 7.17, which is in accordance with the maximum horizontal stress axis. The magnitude of velocities decreases along the western shoulder towards the VG, indicating about 0.3 mm/a of shortening across the WBF. The Tertiary and Quaternary sediments of the graben interior are pervaded by a variety of N–S to NNW–SSE striking, sinistral Riedel faults. According to Illies et al. (1981), shear strain is released along these faults by near-surface extensional faulting. A relation of these faults to the antithetic horizontal velocity field in the interior of the northern graben between Karlsruhe and Mannheim was already discussed on behalf of the GNSS results in Sect. 5.3.1. The observation of antithetic movements is nicely confirmed by the dense velocity grid shown in Fig. 7.17 along with the location of active fault segments in the northern URG. The change of velocity directions from eastward movements around Karlsruhe to westward movements around Mannheim coincides with a change in strike of the graben from about N30°E to N. Furthermore, the changing directions mark the transition from a restraining bend setting of the graben segment around Karlsruhe to a releasing bend setting in the northern part at Heidelberg and Mannheim (Buchmann & Connolly, 2007).

In the western part of the investigation area and west of Strasbourg, southward movements are observed, whereas N to N–E directed movements are visible in the southern part of the investigation area and close to Freiburg. This general movement pattern is in accordance with the general faulting mechanism of the URG dominated by sinistral shearing, see Sect. 2.3.3. In order to quantify the amount of strain resulting from the horizontal velocity field, the strain rate tool of Tape et al. (2009) is applied to the velocity data as described for the GNSS velocities in Sect. 5.3.3. The total strain rate, expressed as Frobenius norm of the strain rate tensor, is shown in Fig. 7.19. In accordance with the strain rates calculated from horizontal velocities at GNSS sites, the largest strain rates appear within the graben or at its borders. However, the magnitude of strain rate is larger compared to Fig. 5.8, which might be due to the smaller extent of the input data. In contrast to the strain rates from GNSS-only, two regions with larger strain rate values are observed in the central and northern URG. Even if the strain rates displayed in Fig. 7.19 are superimposed by artefacts caused by the uncertainties of the input data, it is remarkable that the results reveal ongoing strain accumulation within the graben.

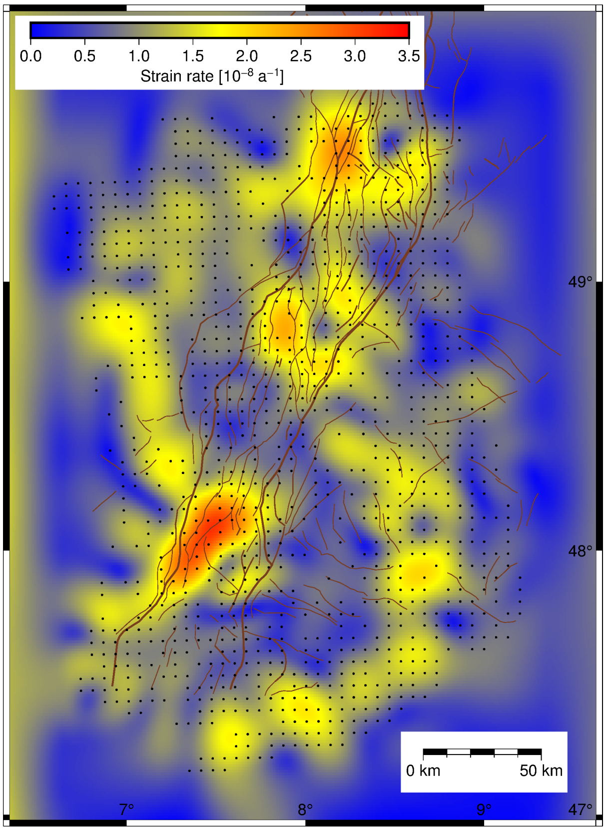

Figure 7.19: Magnitude of horizontal strain rates in the URG area estimated from horizontal velocities at the grid points (black dots) of the combined 3D displacement solution given in Fig. 7.17, calculated with the strain rate toolbox provided by Tape et al. (2009), see Sect. 5.3.3 (grid orders $q_{min} = 4, q_{max} = 9$). Brown lines represent faults in the URG area after Peters (2007, p. 166), main border faults (thick), active faults (medium thick) and other faults (thin).

Regarding the vertical velocity field, a separation of tectonic and anthropogenic deformation is challenging. However, areas with large anthropogenic deformation are well-determined by the InSAR results, see Sect. 6.5.4 and 6.5.5, not least due to non-linearities in the time series, see Sect. 7.4.4. The vertical velocities of Fig. 7.17 are shown again in Fig. 7.20 compared to Quaternary deposits in the interior of the URG. Ignoring the areas with large subsidence at Lorraine/Saarland, northwest of Mulhouse and close to Landau, the following conclusion on tectonic motion can be drawn. A general subsidence of the graben interior w.r.t. BF and VG is observed in the central and southern graben segments between north of Strasbourg and north of Basel. The subsidence in the central VG is poorly constrained by InSAR as there are only few PS in this mountainous region. The major part of the subsidence is thus addressed to the extrapolation of the levelling line crossing the former silver mining area of Val d'Argent, see Sect. 4.5.4. In the southeastern part of the investigation area, subsidences of the Molasse basin at Lake Constance, w.r.t. uplift tendencies at the alpine foreland around Zürich are observed. A slight uplift of the Swabian Jura is visible in the eastern part, which was already discussed in Sect. 4.5.4 and is now nicely traceable in its spatial behaviour.

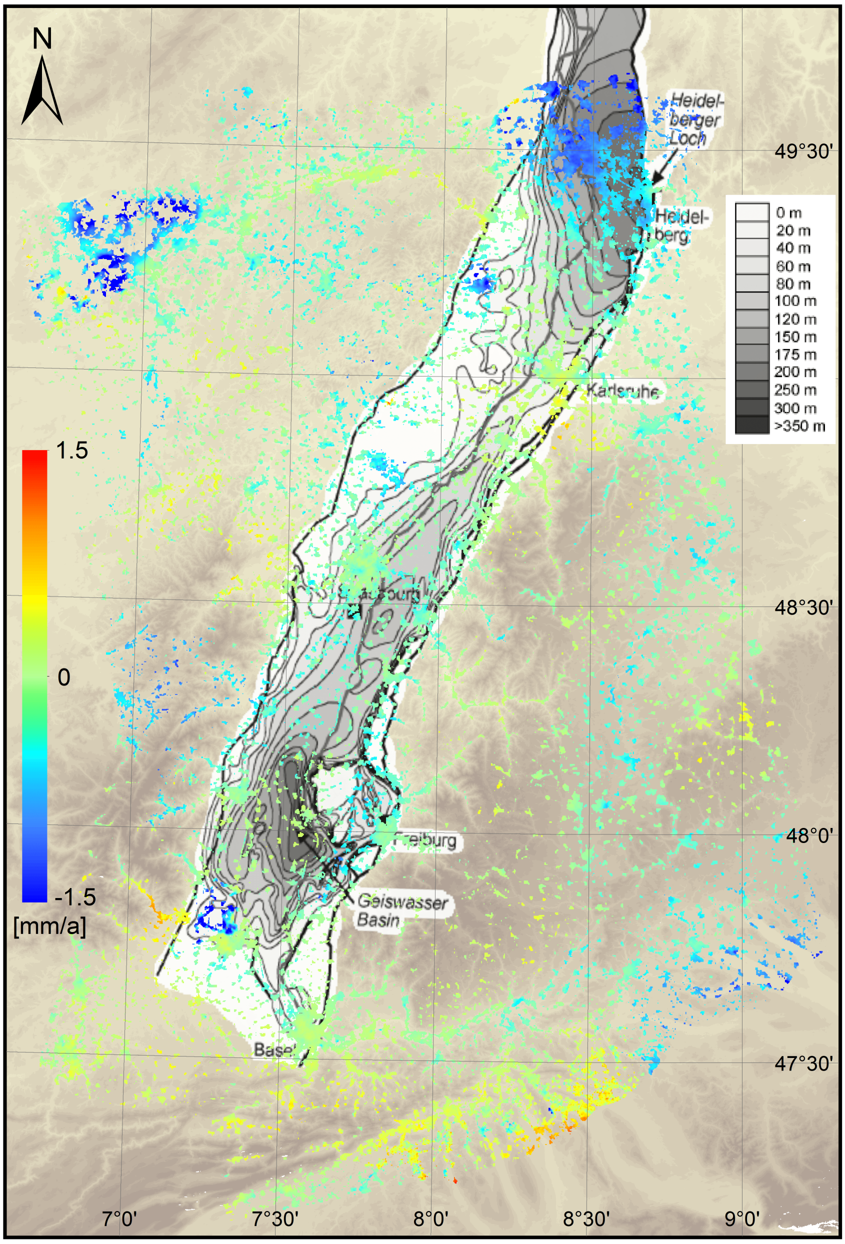

Figure 7.20: Vertical linear rates (colour-coded) in the URG area resulting from the data fusion compared to Quaternary deposits (gray scale) after Peters (2007, p. 9), original fault data sources from Bartz (1974); Haimberger et al. (2005).

The thickness distribution of Quaternary sediments in the interior of the graben was discussed in Sect. 2.3.2. Two known depocentres are the *Heidelberger Loch* and the *Geiswasser basin*, see Sect. 2.2. No relative subsidence is observed in the area of the deepest Quaternary base level of *Geiswasser basin*, but in the area east of the basin and west of Freiburg. The observed subsidence in this region is assumed to be related to the complex tectonic pattern between EBF and RRF as discussed in Sect. 4.6.1. In the northern part of the investigation area, uplift is observed in parts of the Palatinate forest w.r.t. a strong subsidence in the area of Mannheim. The subsidence in the urban area of Mannheim might be at least partly evoked by groundwater usage, see Sect. 4.5.4. However, subsidence is still observable at the *Heidelberger Loch*, which is the deepest Quaternary deposit of the URG with a thickness of about 350 m. The velocity gradient of -0.5 mm/a at Heidelberg to $+0.3$ mm/a at Karlsruhe fits well to the gradient of thickness distribution indicating continuation of the Quaternary deposition process. Furthermore, the vertical velocity field of the northern URG is in accordance with geomechanical models of restraining and releasing bends. Slight uplift tendencies are observed within the restraining part of the bend around Karlsruhe, whereas the releasing part is characterised by increased subsidence rates in the area of Heidelberg and Mannheim. Further conclusions may be drawn from the presented velocity fields in collaboration with other geoscientists, e.g. when using the velocity estimates within geomechanical models.

7.6 Summary

- Displacement estimates from levelling, GNSS and InSAR are complimentary w.r.t. their spatial resolution, accuracy and sensitivity to different displacement components.
- Because of differences in the location and the temporal coverage of the measurements, a suitable data fusion approach has to focus on linear movements at an interpolated surface grid.
- The 3D components of a displacement cannot be resolved from InSAR alone without assumptions on the displacement behaviour.
- The developed data fusion approach is based on two steps. First, offset and trend of InSAR velocities w.r.t. levelling and GNSS velocities are calculated, attributed to the different reference frames of the techniques. Second, 3D velocity components are estimated at a grid which carries values only in the vicinity of the PS locations.
- Covariance matrices for the Kriging interpolation of sample data from levelling, GNSS and InSAR are deduced from empirical semivariograms.
- A combination of ERS and Envisat time series enhances the precision of velocity estimates from InSAR and allows for separating non-linear movements.
- Offset and trend between InSAR and the other two techniques are small indicating a good agreement of the corresponding velocities and small differences between the chosen reference frames.
- The mathematical combination of surface velocities is performed at every valid grid point using least-squares adjustments of observations from levelling, GNSS and InSAR including realistic covariance information of the velocity estimates.
- The combined 3D velocity field enables a quantification of recent surface displacements in the whole URG area with high spatial resolution and accuracy.
- The major tectonic features deduced from the horizontal velocity components are NW–SE shortening of the central URG segment and sinistral shearing at the main border faults resulting in ongoing strain accumulation within the graben.
- From the vertical velocities, a subsidence coinciding with a known Quaternary depocentre is observed in the northern URG w.r.t. uplift tendencies at the area around Karlsuhe.
- The subsidence and uplift setting of the northern URG along with antithetic horizontal movements are in accordance with the restraining and releasing bend setting in this area.

Chapter 8

Conclusions and Outlook

The general research topic of this thesis was the detection of surface displacements in the URG area by using three complimentary geodetic techniques: levelling, GNSS and InSAR. This last chapter of the thesis summarises the major conclusions and discusses the contributions of the research (Sect. 8.1). Finally, recommendations for future investigations (Sect. 8.2) and an outlook on the further development of the available geodetic data sets (Sect. 8.3) are given.

8.1 Summary and Contributions

This research discussed the derivation of surface displacements in the URG area from levelling, GNSS and InSAR, and presented a new approach to combine the three techniques. A major contribution of this work was the analysis of a large amount of geodetic data in a region covering an area of approximately 300 km × 200 km in N–S and E–W directions. For the first time, both levelling and SAR data have been analysed for the whole URG area. The levelling database covers a period between 1867 and 2012. Linear rates have been estimated from a subset of 40,049 observations at 14,098 repeatedly measured benchmarks. The GNSS database contains daily coordinate estimates between 2002 and 2011 at a subset of 76 usable GNSS sites. SAR data has been analysed along one descending and two ascending tracks with a length of about 300 km. ERS-1/2 scenes acquired between 1992 and 2000 as well as Envisat scenes acquired between 2003 and 2010 were processed resulting in displacement estimates at the locations of Persistent Scatterers (PS).

One major research question was whether it is possible to measure the small tectonic deformation in the URG area with the available geodetic database. The formal errors of the velocity estimates resulting from levelling and GNSS analyses are at the magnitude level at which the tectonic deformation is presumed to act. The vertical rates from levelling achieve a mean precision of 0.15 mm/a for the German and Swiss part of the network and 0.34 mm/a for the French part. The horizontal velocities from GNSS time series analyses achieve a mean precision of 0.35 mm/a (2σ). Further indications that the resulting velocities are indeed related to large-scale tectonic deformation are the low magnitude of surface displacements and the smooth spatial distribution of the velocities. 93 % of the vertical rates from levelling are in the range of ±0.5 mm/a; more than 80 % of the East and North velocities at the GNSS sites are in the range of ±0.5 mm/a. The large-scale velocity field of both levelling and GNSS reveal similar deformation patterns for neighbouring locations. The general deformation trends of these large-scale patterns reflect the tectonic setting of the URG and its shoulder areas. Particularly for the vertical displacement rates, the tectonic deformation is however superimposed by effects related to sedimentation and anthropogenic activities. InSAR is well suited to study the spatial and temporal behaviour of surface deformation at the mm/a to cm/a scale, e. g. related to anthropogenic activities. For the measurement of tectonic deformation well below 1 mm/a, the resulting displacement estimates are at the edge of significance. However, from a combination of ERS and Envisat displacement time series a mean precision between 0.5 and 0.6 mm/a (2σ) was obtained for the three analysed tracks, with more than 70 % of the linear LOS displacement rates being in the range of ±0.5 mm/a. To summarise, the detected displacements resulting from the analyses of the three techniques can obviously be related to ongoing tectonic deformation at several parts of the investigation area. At other parts, the tectonic deformation might be below the detectability, or non-tectonic effects are stronger compared to the tectonic deformation.

Several investigations and developments of this work have been dedicated to an enhancement of the single-technique analyses in order to derive precise estimates of surface displacements from the database of each technique. For the analysis of levelling data, loop misclosures have been calculated for all measurement epochs in order to assess the quality of the database. Loop misclosures for transnational loops enabled an assessment of the levelling lines connecting the national data sets from Germany, France and Switzerland. Special efforts were made to investigations on the usability of historical levelling data measured at the end of the 19th century. A major investigation was dedicated to the influence of gravity and corresponding gravity corrections on the levelling measurements and the resulting displacement estimates. Furthermore, the stochastic model of the kinematic adjustment was enhanced by application of iterative variance component estimation, resulting in realistic accuracy levels for the observations. Static analyses along single levelling lines evidenced the capability to resolve the temporal behaviour of surface deformation related to anthropogenic activities or active faulting. The major contribution of this work performed in the framework of the GNSS analyses is the application of a sophisticated time series analysis on the daily site coordinates. The consideration of offsets at the dates of known hardware changes, periodic effects and a realistic stochastic model enabled the estimation of significant velocities at most of the GNSS sites. In addition, investigations on the reference frame of the resulting horizontal velocity field were carried out including the estimation of a local Euler pole for the URG area. For the analysis of SAR data in nine different image stacks, a new model for the selection of an optimum master scene was developed. In order to adapt the subset of PS pixels detected in the different stack analyses, the use of test areas has proven to be a helpful tool. The separation of atmospheric effects was investigated using filtering techniques as well as additional meteorological data. Finally, a filtering of high quality PS pixels was implemented based on two quality indicators and statistical frequency distributions.

The possibilities and limitations of the techniques have been discussed w.r.t. the combination of surface displacements resulting from single-technique analyses. The data fusion approach developed within this work aims at exploiting the advantages of each technique w.r.t. the derivation of linear displacement rates on the sub-mm/a-level. Spatial interpolation of the vertical displacement components from levelling, the horizontal components from GNSS and the slant LOS components from InSAR is applied using Kriging along with realistic covariance models. In a first step, the InSAR displacement estimates are interpolated to the location of levelling benchmarks and GNSS sites in order to integrate the LOS displacements into the vertical and horizontal reference frames of the levelling and GNSS analyses, respectively. In the second step, the mathematical combination of surface displacements is performed at a regular grid. The grid is restricted to values close to the location of PS pixels in order to minimise the effect of spatial extrapolation. In both steps, displacement rates from InSAR are derived from a least-squares combination of ERS and Envisat displacements at the time series level. The time series combination has proven to significantly enhance the precision of resulting velocities as the period covered by the data is increased. The result of the data fusion approach are 3D velocities and corresponding standard deviations at a dense surface grid. Mean formal errors are 0.38, 0.45 and 0.18 for East, North and Up velocity components, respectively. Compared to earlier studies of geodetically derived velocity fields in Central Europe (Zippelt & Mälzer, 1987; Vigny et al., 2002; Nocquet & Calais, 2003, 2004), the standard deviations are reduced while the spatial resolution is considerably enhanced. The combined velocity field benefits from the advantages of each technique and presents the ongoing deformation of a large area with unprecedented detail. However, the resulting velocities represent a mixture of tectonic and non-tectonic effects as deformation related to anthropogenic activities may still be included if it behaves linearly in time within the analysed period.

The resulting surface displacements of the data fusion as well as the single-technique analyses reveal several interesting deformation patterns which can be related to active tectonics in the investigation area. As expected, both the horizontal and vertical surface displacements attributed to tectonic deformation of the URG act on a small scale, mainly below 0.5 mm/a. The vertical velocities are relative to a levelling benchmark at Freudenstadt, Eastern BF, the horizontal velocities to a local Euler pole valid for the investigation area. The strongest subsidence attributed to tectonic deformation is observed in the northern part of the graben at the Quaternary deposit of the *Heidelberger Loch* with values at about 0.5 mm/a and more, relative to a slight uplift of the area close to Karlsruhe. The central and southern graben segments (south of Karlsruhe) are mainly subsiding relative to the graben shoulders. Uplift of maximum 0.3 mm/a is observed at the BF, parts of the VG and the Palatinate Forest as well as at the Swabian Jura. Subsidence in the central and southern segment is strongest in the area west of Freiburg with values reaching maximally 0.5 mm/a. The general motion trend, i. e. relative uplift in the area around Karlsruhe w.r.t. subsidence north and south of this area, is in general accordance with the deformation models published by Illies (1979); Illies et al. (1981); Zippelt & Mälzer (1987). The horizontal velocity field derived from the data fusion is mainly controlled by the GNSS results. The general setting of the URG between the Rhenish Massif in the northwest and the Alps in the southeast is observable from the horizontal velocity field by SE–S directed velocities in the northwestern part of the investigation area and N–NE directed velocities in the southern part of the investigation area, both at a magnitude of about 0.5 mm/a. This motion pattern results in sinistral shearing and is compatible with the generally accepted models of contemporary deformation of the graben. In contrast to numerical models and conclusions drawn from Moho depths, the horizontal velocities in the southern part of the investigation area indicate that the southern graben segment is not subjected to extension. Antithetic displacement directions in the northern part of the investigation area along with a significant clockwise rotation of the velocity vectors in the northwestern part can be attributed to the change in strike of the graben from N30°E to N. This observation fits to the releasing and restraining bend setting in this part of the graben discussed by Buchmann & Connolly (2007), and is also confirmed by the vertical velocity field in the region. The magnitude of strain rates derived from the horizontal velocity fields of both GNSS-only and the combined solution, indicate ongoing strain accumulation in the graben interior, particularly in the southern segment. Most of the discussed findings attributed to tectonic deformation of the URG area are in accordance with generally accepted deformation models. However, the spatial resolution and coverage of the obtained surface displacements allow for more detailed investigations when using the results of this work within geomechanical models. In addition, the magnitude of horizontal and vertical displacements resulting from this study can be assumed to be an upper bound for tectonic motion in the URG area. Calais & Stein (2009) showed that geodetic rates of small intraplate motion observed by GPS are commonly overestimated if the period covered by the data is short, but converge to smaller and more realistic magnitudes with increasing length of the database. In summary, the geodetic efforts performed within this work largely contribute to an improved understanding of intraplate deformation processes of the URG area and deliver important boundary conditions for geophysical models.

Particularly the resulting vertical velocities have to be carefully interpreted as they are superimposed by non-tectonic effects, natural as well as man-made. At several locations in the investigation area, surface displacements related to anthropogenic activities have been observed.

Strong subsidence of several mm/a to more than 1 dm/a was observed along levelling lines crossing the coal mining areas of Lorraine/Saarland and Ronchamp (southern VG). A large number of levelling benchmarks had to be excluded from the kinematic adjustment because of strong non-linearities. The spatial extent of the subsidence area in Lorraine/Saarland becomes visible from the InSAR analysis of ERS data in the region. At levelling benchmarks close to the potash mining areas at Wittelsheim (France) and Buggingen (Germany), subsidence at a similar level as for the coal mining areas is observed. Potash mining was stopped at Buggingen in 1973 and no significant displacement is found at adjacent levelling benchmarks after 1982. At Wittelsheim the extent of the mining area is larger and also the period of mining lasted longer (until 2002). The spatial extent and temporal behaviour of surface displacements can be nicely traced by the analysed ERS and Envisat data. The most interesting deformation behaviour observed in the URG area is the subsidence and uplift pattern close to the oil fields of Landau, not least as the surface displacements in the range of ±7 mm/a are well constrained by all three geodetic techniques. The subsidence in the area of Mannheim/Ludwigshafen of 1 mm/a and more is supposed to be affected by extensive groundwater usage, which becomes particularly obvious from increased subsidence rates resulting from levelling measurements of the 1970s compared to earlier and later measurements. However, a proper separation of tectonic and non-tectonic effects is challenging in this area. Local surface uplift related to geothermal activities, e. g. in the city of Staufen, was not investigated within this work as (i) the uplift phenomenon started at the end or after the period of the analysed database and (ii) the spatial extent of the deformation is small (250 m × 350 m in Staufen, Schenk, 2015, p. 99) and thus not compatible with the analyses performed within this work.

8.2 Recommendations

The results of this work deliver a complete picture of the recent surface displacements in the URG area. However, the extent of the investigated area does not include the very northern part of the URG around the cities of Mainz, Frankfurt and Darmstadt. An extension of the investigation area to the north is desirable using levelling data from Hessen and SAR data reaching to approximately 50°30'N. For the GNSS part, the SA*POS*® stations of Hessen, Saarland and Nordrhein-Westfalen could be included in a consistent reprocessing along with the sites used within this work. A cooperation with the authorities responsible for the available sites is already in progress. Particularly the calculation of strain rates will benefit from the extension. Furthermore, the analysis of permanently operating sites is somehow never finished. The coordinate time series used within this study end in April 2011. Since then, almost five years have past and a reprocessing of the whole database would significantly increase the length of the time series. Hence, linear rates can be determined more precisely, and more sites with significant displacement estimates can be included in the final velocity field solution. Potentially also the Up component resulting from the longer GNSS coordinate time series provides useful information on the tectonic deformation of the URG and surrounding areas. In addition to a differential GNSS analysis, the precise point positioning (PPP) technique could be applied to the GNSS database, which allows for an independent parameter estimation at each site, however, with reduced precision of the estimates.

Concerning the levelling database, it is not likely that a large amount of new levelling measurements will be available in the future, see Sect. 8.3. Hence, the vertical rates estimated within this work might represent a final result for displacement analyses from levelling in the study area. As levelling measurements over large distances are expensive and time-consuming, the focus will likely be on local to regional remeasurements of levelling benchmarks in the future. From a scientific point of view, it would be desirable to have traverse measurements crossing the URG at several profiles, such as calculated from the existing levelling lines in Fig. 4.19. Detailed insights on the recent deformation at faults could be deduced from such profile measurements, repeated at an interval of several years.

InSAR has proven to be a useful technique for the determination of surface displacements at a high spatial resolution. Within this work, three tracks have been used, but still more data is available. The investigation could be extended to adjacent tracks in the east and west, leading to redundant observations in the overlapping areas of the tracks. Furthermore, other spaceborne SAR sensors can be analysed such as Radarsat, ALOS and Sentinel-1. The application of ALOS is of special interest as information on surface displacements in non-urban areas can be obtained from SAR sensors operating with L-band. Regarding the processing strategies, atmospheric effects are regarded to be a major error source for displacement estimation within this work. Hence, better atmospheric input data, such as high resolution weather models, might improve the separation of surface displacements from atmospheric effects.

8.3 Outlook

The geodetic spatial reference in Germany is currently entering a new generation. Geodetic basic network benchmarks (Geodätische Grundnetzpunkte, GGP) integrate GNSS measurements with levelling and gravity information. Thereby, the separation of horizontal and vertical coordinates as well as the separation between geometric and physical heights is dissolved. Heckmann et al. (2015) state that benchmark coordinates, heights and gravity values are time-depending values in general. Also radar interferometry is mentioned as a development which will influence the future of geodetic spatial references. It is quite possible that the remeasurement of first-order levelling lines in Germany between 2006 and 2012 has been the last complete remeasurement for the whole country. In France the latest remeasurement performed between 2000 and 2006 did not follow the former levelling loops for economical reasons. Future investigations on surface displacements will hence mainly rely on GNSS and InSAR analyses. The GNSS sites will continue to observe GNSS data, including observations from GLONASS, Galileo and Beidou in the future. A combined processing of observations from several GNSS will enable a more robust coordinate estimation at the sites. However, the influence of a processing with single- as well as multi-GNSS-constellations on the coordinate time series and velocity estimation has to be investigated.

Following Moreira et al. (2013), SAR has entered a golden age since more than 20 spaceborne SAR sensors are operated today or will be launched within the next years. With the Corpenicus programme, formerly known as Global Monitoring for Environment and Security (GMES), ESA completely changed its data policy (Aschbacher & Milagro-Pérez, 2012). The data acquired by the five Sentinel missions will be provided free of charge for public, commercial and scientific users. The start of the first Copernicus satellite Sentinel-1A enables the continuity of globally and regularly acquired C-Band data. The data is operationally available since October 2014. With the start of the second Copernicus radar satellite Sentinel-1B scheduled for April 12, 2016 (SpaceflightNow, 2016), C-band data will be available over large areas within a short revisit time of only six days, see Tab. 3.2. Additional C-Band satellites, Sentinel-1C and Sentinel-1D, are already in the planning by ESA in order to ensure continuity. First results for surface displacements derived from Sentinel-1 data (Prats-Iraola et al., 2015; Wegmüller et al., 2015; González et al., 2015) are promising and evidence the high performance of the mission for the detection of natural as well as man-made surface displacements.

A Levelling Analysis

Table A.1: Transnational measurements from and to France. SL: Saarland, RP: Rheinland-Pfalz, BW: Baden-Württemberg. Information on the institutions is given below (next page).

Border crossed	Location	Year of measurement	Institution
French-German (SL)	Apach	1878	Prussia
		1956/1958	IGN/LVGL
		1973	IGN
		2011*	LVGL
	Waldwisse	1954/1955/1956	IGN/LVGL
		1965	IGN/LVGL
		1996*	LVGL
		1998*	LVGL
		2006/2007*	LVGL
	Creutzwald	2010*	LVGL
	Saarbrücken	1878	Prussia
	Sarreguemines	1878	Prussia
		1964/1965	IGN/LVGL
		2010*	LVGL
	Frauenberg	1964	IGN/LVGL
		2010*	LVGL
French-German (RP)	Lauterbourg	1878/1881	Prussia
		1973	IGN
French-German (BW)	Strasbourg	1881	Prussia
		1955	IGN/LGL
		1964	IGN/LGL
		1973*	LGL
		2001	IGN
		2012*	BfG
	Breisach	1881	Prussia
		1973	IGN
		2012*	BfG
	Bantzenheim	1881	Prussia
	Huningue	1881	Preusen
French-Swiss	Basel	1867	swisstopo
		1881	Prussia
		1911*	swisstopo
		1956*	swisstopo
		1964	IGN/swisstopo
		2001*	swisstopo
	Kiffis	1881	Prussia
		1939*	IGN
		1973*	IGN
	Boncourt	1891	IGN
		1973*	IGN
		1986	IGN

* Connections to the major levelling lines of both countries not measured within 7 years.

Institutions:
Prussia: Trigonometrische Abteilung der Landesaufnahme des Königreichs Preußen
IGN: Institut National de l’Information Géographique et Forestière (France)
LVGL: Landesamt für Vermessung, Geoinformation und Landentwicklung Saarland (Germany)
LGL: Landesamt für Geoinformation und Landentwicklung Baden-Württemberg (Germany)
BfG: Bundesanstalt für Gewässerkunde (Germany)
swisstopo: Bundesamt für Landestopografie (Switzerland)

Table A.2: Loop misclosures for levelling loops in Baden-Württemberg, Germany, in different measurement epochs.

Loop number	Track course (cities along the track)	Measurement epoch (years)	Track length [km]	Loop misclosure [mm] measured	theoretical	corrected
601	Basel – Bad Krozingen – Neustadt – Waldshut	1880–1882[1]	289.5	5.4	24.7	30.1
		1922–1935	218.5	−36.1	31.3	−4.8
		1959–1961	231.9	−24.7	31.3	6.5
		1982–1984	229.3	−30.2	30.9	0.7
		2004–2011	235.5	−18.9	30.9	12.1
602	Waldshut – Neustadt – Donaueschingen – Stockach	1922–1935	244.7	−0.1	−2.7	−2.8
		1959–1962	249.6	13.8	−2.7	11.1
		1982–1984	247.3	11.7	−2.2	9.5
		2004–2011	263.2	6.6	−2.2	4.3
611	Bad Krozingen – Offenburg – Hausach – Donaueschingen – Neustadt	1876–1882	226.7	−28.4	−7.2	−35.6
		1923–1939	277.0	−8.0	4.3	−3.7
		1959–1962	295.0	−19.0	4.3	−14.7
		1982–1984	283.0	−3.0	4.3	1.3
		2004–2012	293.0	11.9	4.3	16.1
612	Donaueschingen – Hausach – Freudenstadt – Horb – Gammertingen – Stockach	1923–1938	320.9	15.5	2.0	17.6
		1959–1969	340.5	9.3	1.7	10.9
		1981–1987	330.1	4.1	1.9	6.0
		2006–2012	341.8	−20.0	1.9	−18.1
610	Offenburg – Kuppenheim – Freudenstadt – Hausach	1876–1882[2]	138.4	−35.1	18.9	−16.3
		1924–1939	193.7	−19.5	13.1	−6.4
		1956–1960	203.2	−18.4	13.6	−4.8
		1982–1987	197.1	−2.2	13.6	11.4
		2005–2008	201.1	−23.5	13.6	−9.9
609	Freudenstadt – Kuppenheim – Karlsruhe – Bruchsal – Bretten – Horb	1878–1881[3]	91.0	−23.5	2.4	−21.1
		1924–1939	247.7	3.3	7.5	10.9
		1952–1968	262.1	12.4	7.6	20.0
		1980–1987	256.2	−3.8	7.4	3.5
		2005–2010	267.1	−3.9	7.4	3.5
613	Horb – Ludwigsburg – Fellbach – Honau – Gammertingen	1937–1939	258.0	11.6	−3.5	8.0
		1957–1969	272.0	14.3	−3.4	11.4
		1981–1986	271.3	−7.9	−3.2	−11.2
		2005–2008	284.5	−6.7	−3.2	−9.9
614	Horb – Bretten – Gundelsheim – Ludwigsburg	1924–1939	287.3	13.7	−3.5	10.2
		1952–1969	303.1	7.9	−3.6	4.3
		1981–1985	306.0	−1.2	−3.4	−4.6
		2007–2010	314.3	0.5	−3.5	−3.0
608	Bruchsal – Heidelberg – Eberbach – Gundelsheim – Bretten	1924–1937	178.1	−0.6	1.3	0.7
		1954–1968	186.9	1.8	1.3	3.1
		1981–1984	180.1	21.9	1.3	23.2
		2005–2009	193.9	−4.1	1.3	−2.8

[1] Different track: Basel – Bad Krozingen – Neustadt – Donaueschingen – Singen

[2] Different track: Offenburg – Appenweier – Freudenstadt – Hausach

[3] Different track: Karlsruhe – Bruchsal – Bretten – Pforzheim

Table A.3: Loop misclosures for levelling loops in Rheinland-Pfalz and Saarland, Germany, in different measurement epochs.

Loop number	Track course (cities along the track)	Measurement epoch (years)	Track length [km]	Loop misclosure [mm]		
				measured	theoretical	corrected
633	Kandel – Ludwigshafen – Mannheim – Heidelberg – Bruchsal – Karlsruhe	1880–1881[1]	126.3	−1.7	0.1	−1.6
		1928–1951	191.9	−34.5	0.5	−34.0
		1950–1957	190.1	−14.2	0.4	−13.8
		1980–1984	196.0	−15.0	0.4	−14.7
		2005–2011	208.2	−0.6	0.3	−0.3
633N*	Mutterstadt – Oggersheim – Ludwigshafen	1956	20.6	0.1	0.0	0.1
		1965–1966	20.6	0.7	0.0	0.6
		1983	21.2	4.3	0.0	4.3
		2010	27.7	1.0	0.0	1.0
501*	Kandel – Neustadt – Mutterstadt – Germersheim	1950–1955	117.4	11.1	−1.5	9.6
		1970–1970	117.2	−3.3	−1.5	−4.7
		1983–1985	127.5	14.0	−2.3	11.7
		2009–2011	132.4	−10.0	−2.3	−12.3
502*	Pirmasens – Bruchmühlbach – Kaiserslautern – Neustadt – Kandel	1950–1955	192.5	3.3	−4.0	−0.7
		1968–1970	191.2	9.2	−3.9	5.3
		1983–1985	199.9	2.0	−3.0	−1.1
		2009–2011	209.8	10.5	−3.0	7.5
502W*	Homburg-Einöd – Bruchmühlbach – Pirmasens	1954–1965	82.2	−7.4	−0.1	−7.4
		1983–1991	86.4	6.7	−0.1	6.6
503*	Saarbrücken – Saarlouis – Merzig – Bruchmühlbach – Homburg-Einöd	1954–1958	214.8	5.7	2.7	8.5
		1978–1998	219.1	−2.4	2.8	0.5
		2006–2011	247.8	5.2	2.7	7.9
504*	Borg – Trassem – Merzig – Silwingen	1954–1958	61.6	−8.8	−1.5	−10.3
		1971–1987	62.3	−7.1	−1.2	−8.3
		1978–1989	64.7	3.0	−1.5	1.5
		2003–2011	64.9	3.7	−1.6	2.1

* Internal, non-official loop number.

[1] Different track: Germersheim – Oggersheim – Mannheim – Schwetzingen – Graben

Table A.4: Loop misclosures for levelling loops in Switzerland in different measurement epochs.

Loop number	Track course (cities along the track)	Measurement epoch (years)	Track length [km]	Loop misclosure [mm]		
				measured	theoretical	corrected
III*	Biel – Delémont – Basel – Olten	1906–1928	203.4	−19.3	−0.3	−19.6
		1949–1997	196.8	0.3	−1.1	−0.8
		1988–2007	200.0	−2.1	−0.4	−2.5
IV	Olten – Pratteln – Kaiserstuhl – Brugg	1908–1911	164.6	28.4	−2.5	25.9
		1953–1978	166.7	3.0	−1.7	1.2
		1978–2008	166.1	−15.3	−2.5	−17.8

* Not the whole loop is used here, see Schlatter (2007, p. 135).

Table A.5: Loop misclosures for levelling loops in France in different measurement epochs.

Loop number	Track course (cities along the track)	Measurement epoch (years)	Track length [km]	Loop misclosure [mm] measured	theoretical	corrected
A.d	Belfort – Épinal – Cernay – Altkirch	1881–1896	249.9	−59.2	x	−59.2
		1922–1957[1]	254.2	−220.7	x	−220.7
		1964–1973	253.4	21.9	x	21.9
A.i	Cernay – Sélestat – Marckolsheim – Mulhouse	1881	150.1	7.5	x	7.5
		1922–1957	155.0	19.4	x	19.4
		1964–1973	150.5	10.9	x	10.9
A.j	Cernay – Pouxeux – Saint-Dié – Sélestat	1922–1955[1]	245.3	175.4	x	175.4
		1964–1973	231.2	6.9	x	6.9
A.c	Saint-Dié – Lunéville – Saverne – Sélestat	1922–1938	252.9	4.4	x	4.4
		1964–1973	246.9	12.2	x	12.2
A.h	Sélestat – Saverne – Vendenheim – Marckolsheim	1878–1881	171.5	−35.5	x	−35.5
		1920–1937	177.3	14.7	x	14.7
		1964–1973	180.3	35.0	x	35.0
A.b	Lunéville – Arnaville – Metz – Maizières-lès-Vic	1925–1953	198.7	−13.1	x	−13.1
		1964–1973	199.1	24.7	x	24.7
A.f	Maizières-lès-Vic – Metz – Sarreguemines – Sarrebourg	1878	235.5	−8.5	x	−8.5
		1920–1953[2]	226.7	−52.6	x	−52.6
		1964–1973[2]	231.1	−38.3	x	−38.3
A.g	Sarrebourg – Sarreguemines – Bischwiller – Vendenheim	1878–1881[3]	276.4	36.5	x	36.5
		1920–1939	218.9	−19.6	x	−19.6
		1964–1973	220.8	−9.6	x	−9.6
A.a	Arnaville – Longuyon – Thionville – Metz	1920–1939	188.9	−11.7	x	−11.7
		1964–1973	187.3	21.9	x	21.9
A.e	Metz – Thionville – Freyming-Merlebach	1878–1920[4]	210.3	−24.6	x	−24.6
		1920–1938[2]	150.6	26.2	x	26.2
		1964–1973[2]	154.1	17.4	x	17.4

[x] A theoretical loop misclosure could not be calculated for the French loops due to the lack of measured surface gravity data.

[1] Including some measurements from 1896. The 1922 measurements are erroneous causing a large loop misclosure. They are therefore partly excluded from the database of the kinematic adjustment.

[2] The loop misclosure is affected by the displacement of the tie point (mining area), see Fig. 4.4.

[3] Different track: Sarrebourg – Sarreguemines – Lauterbourg – Vendenheim

[4] Different track: Metz – Thionville – Saarbrücken – Sarreguemines – Freyming-Merlebach

Table A.6: Loop misclosures for transnational levelling loops in different measurement epochs.

Track course (cities along the track)	Measurement epoch (years)	Track length [km]	Loop misclosure [mm]
French-German border (Saarland):			
Thionville – Trassem – Saarbrücken – Metz	1878	201.3	50.5
Thionville – Borg – Silwingen – Bouzonville	1955-1956	101.2	−16.4
Thionville – Borg – Silwingen – Bouzonville	1978-1989	102.1	0.4
Bouzonville – Silwingen – Saarlouis – Sarreguemines	1955-1965[1]	154.9	15.1
Bouzonville – Silwingen – Saarlouis – Sarreguemines	1955-1971[2]	153.5	8.8
Bouzonville – Silwingen – Saarlouis – Creutzwald	1964-2010[3]	102.2	4.7
Creutzwald – Saarlouis – Sarrguemines	1964-2010[3]	123.4	−12.0
Sarreguem. – Kleinblittersdorf – Frauenberg	1964-2010[3]	29.8	−0.3
French-German border (Saarland and Rheinland-Pfalz):			
Sarreguem. – Homburg-Einöd – Kandel – Lauterbourg[4]	1957-1973	286.8	7.0
Sarreguem. – Homburg-Einöd – Kandel – Lauterbourg[5]	1957-1973	272.5	−5.1
French-German border (Rheinland-Pfalz and Baden-Württemberg):			
Strasbourg – Germersheim – Bruchsal – Appenweier	1878-1881	226.8	−49.2
Strasbourg – Kandel – Karlsruhe – Appenweier	1954-1973	193.5	−26.5
Strasbourg – Lauterbourg – Rheinstetten – Offenburg	1964-1992	180.6	−20.1
French-German border (Baden-Württemberg):			
Biesheim – Strasbourg – Appenweier – Freiburg	1875-1881	187.7	−5.7
Neuf-Brisach – Strasbourg – Appenweier – Breisach	1959-1973	189.1	2.4
Neuf-Brisach – Strasbourg – Offenburg – Breisach	1964-2012[3]	185.4	−12.1
Bantzenheim – Biesheim – Freiburg – Mülheim	1875-1882	89.3	7.1
French-German-Swiss border:			
Basel – Bantzenheim – Mülheim	1880-1882	72.1	11.9
Basel – Neuf-Brisach – Breisach – Mulhouse	1961-1973	138.2	−11.7
Basel – Neuf-Brisach – Breisach – Mulhouse	1964-2012[3]	151.9	4.0
French-Swiss border:			
Delémont – Belfort – Mulhouse – Basel	1881-1920[6]	215.7	−2.4
Delémont – Belfort – Mulhouse – Basel	1891-1922[7]	183.5	−3.0
Delémont – Belfort – Mulhouse – Basel	1964-1993	183.9	−9.0
Kiffis – St. Louis – Basel – Laufen	1867-1881	83.7	−10.7
Kiffis – St. Louis – Basel – Laufen	1881-1964[7]	84.2	−7.9

[1] French first-order measurements from 1956, border at Waldwisse measured in 1955.
[2] French first-order measurements from 1964, border at Waldwisse measured in 1971.
[3] French measurements from 1964 combined with the latest German measurements (2003–2012)
[4] Crossing the French-German border at Kleinblittersdorf.
[5] Crossing the French-German border at Frauenberg.
[6] Belfort – Mulhouse – St. Louis measured in 1891, St. Louis – Basel measured in 1881.
[7] Belfort – Mulhouse – St. Louis measured in 1922, St. Louis – Basel measured in 1911.
[8] Laufen – Kiffis (Swiss-French border) measured in 1881, all other lines between 1917 and 1964.

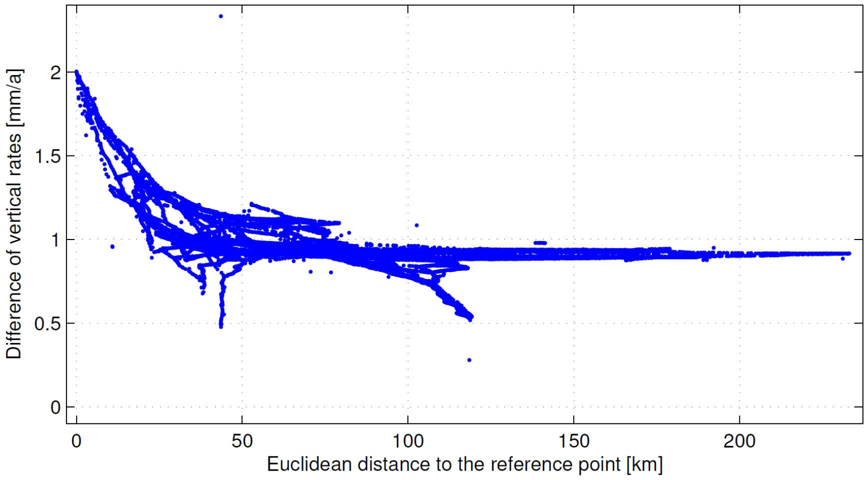

(a) Maximum time difference: five years

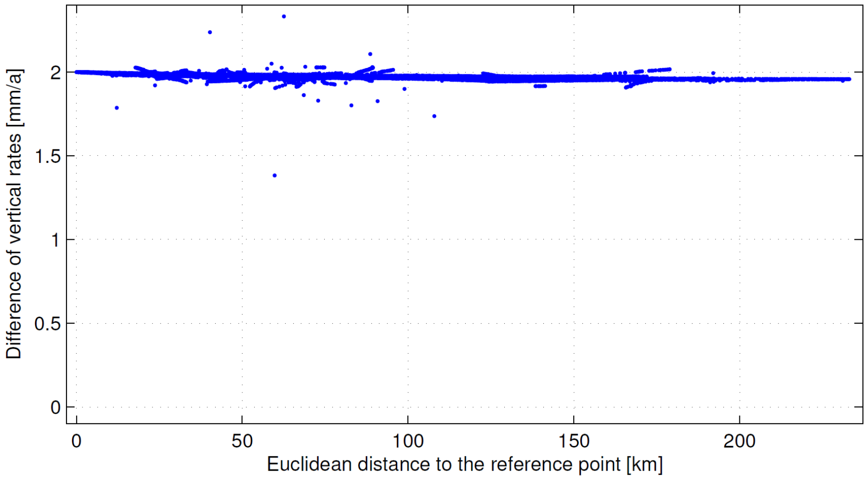

(b) Maximum time difference: one year

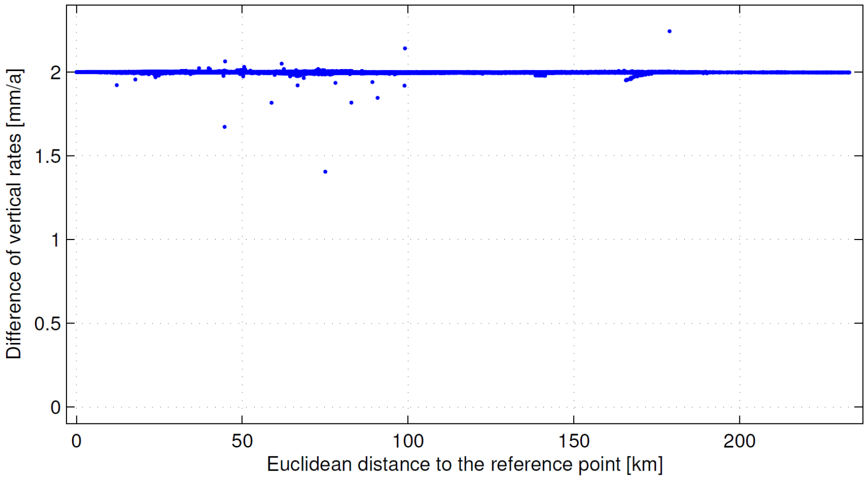

(c) Maximum time difference: nine months

Figure A.1: Difference in the vertical rates between an adjustment with a reference point velocity of 2 mm/a and an adjustment with a stable reference point (velocity: 0 mm/a). The polynomial degree is set to one at benchmarks with initial degree zero and a time difference at the adjacent measurements larger than the user-defined maximum value.

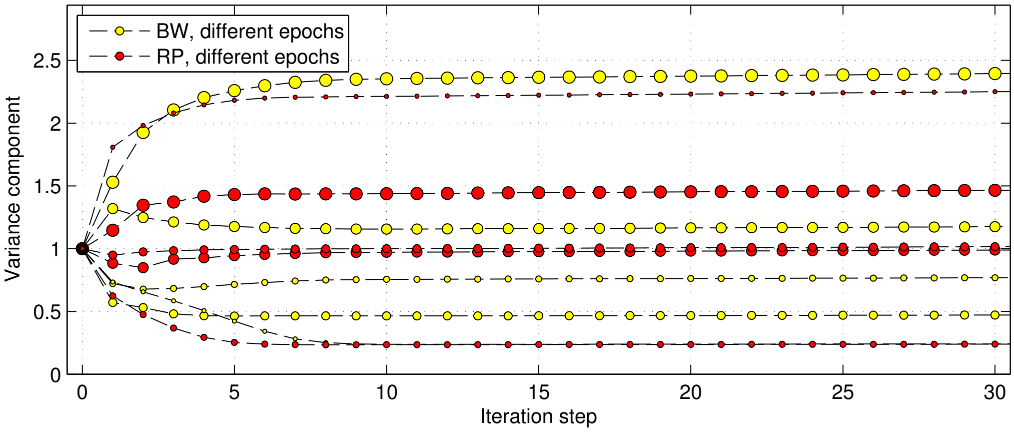

(a) Variance components using Helmert's rigorous estimator, see Eq. 4.14

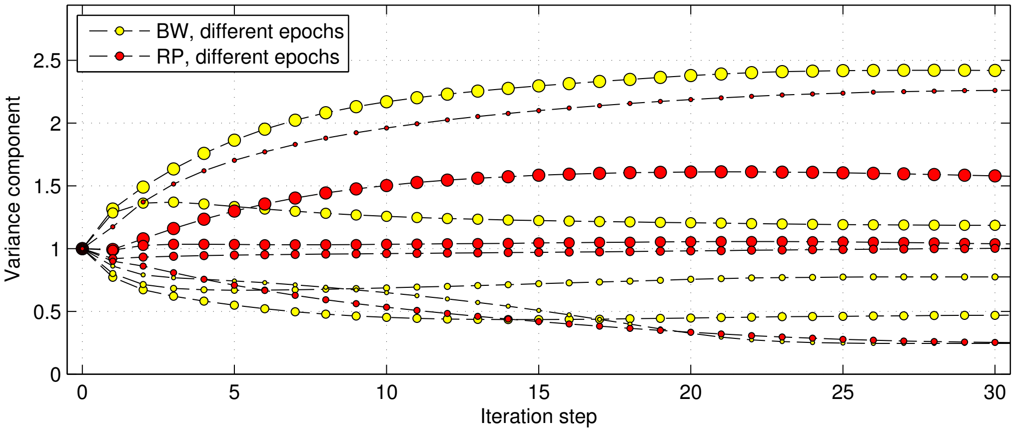

(b) Variance components using Förstner's estimator, see Eq. 4.16

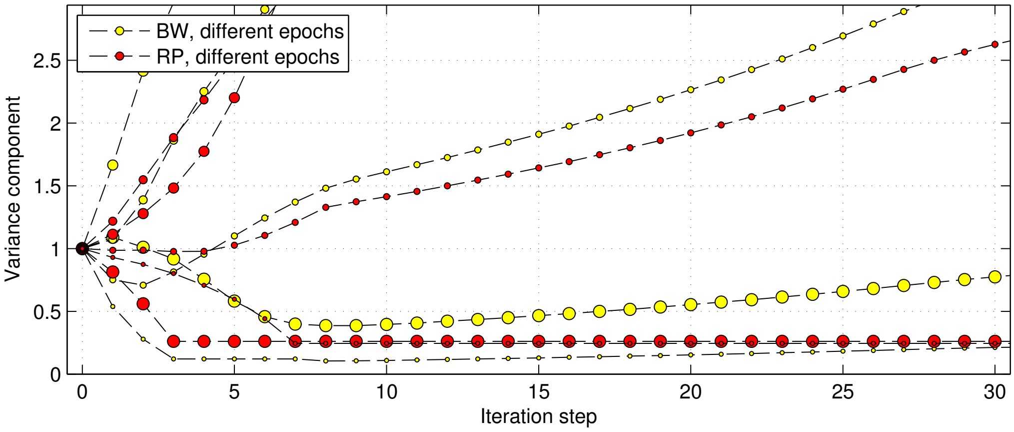

(c) Variance components using the Classical estimator, see Eq. 4.17

Figure A.2: Variance components using different estimators for iterative VCE of 2,521 observations from a sub-network in the northern URG containing data from Baden-Württemberg (BW) and Rheinland-Pfalz (RP). Different point sizes denote the measurement epochs from large (first epoch) to small (latest epoch).

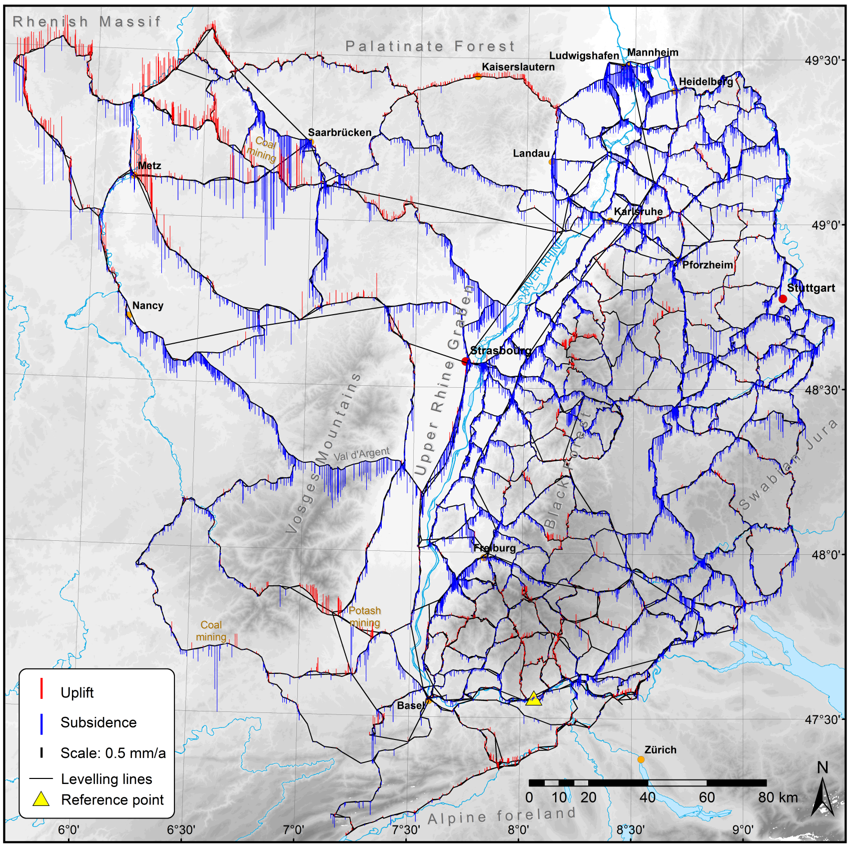

(a) Reference point at Laufenburg (8.061°E, 47.562°N), Switzerland

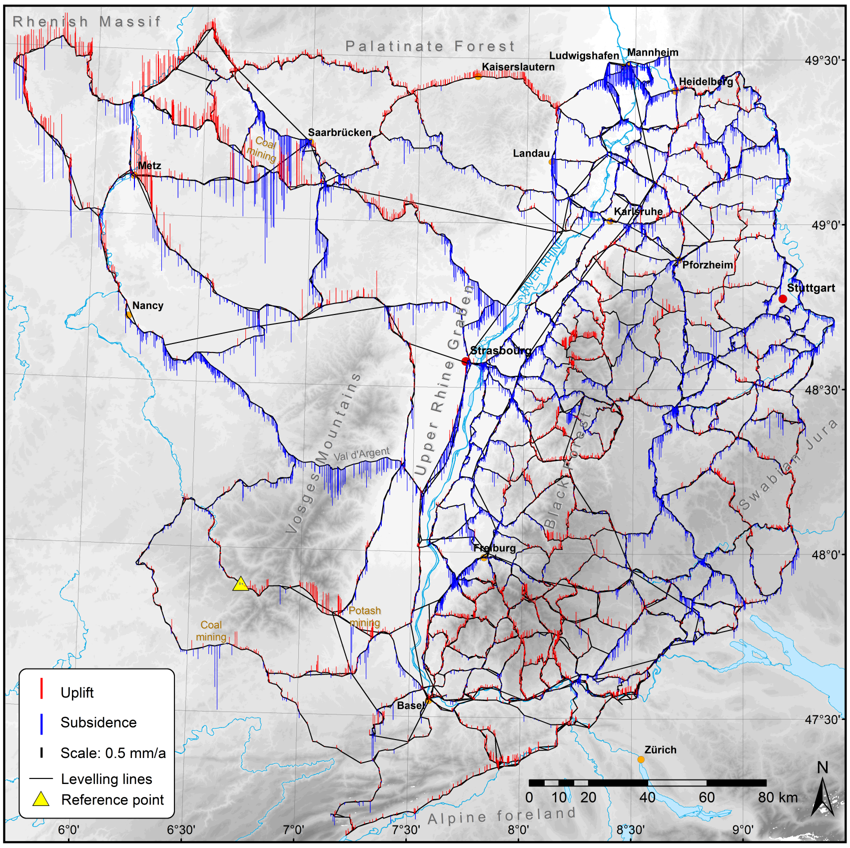

(b) Reference point at Ramonchamp (6.732°E, 47.891°N), France

Figure A.3: Vertical displacement rates in the URG area. Benchmark serving as reference point directly mounted at the bedrock.

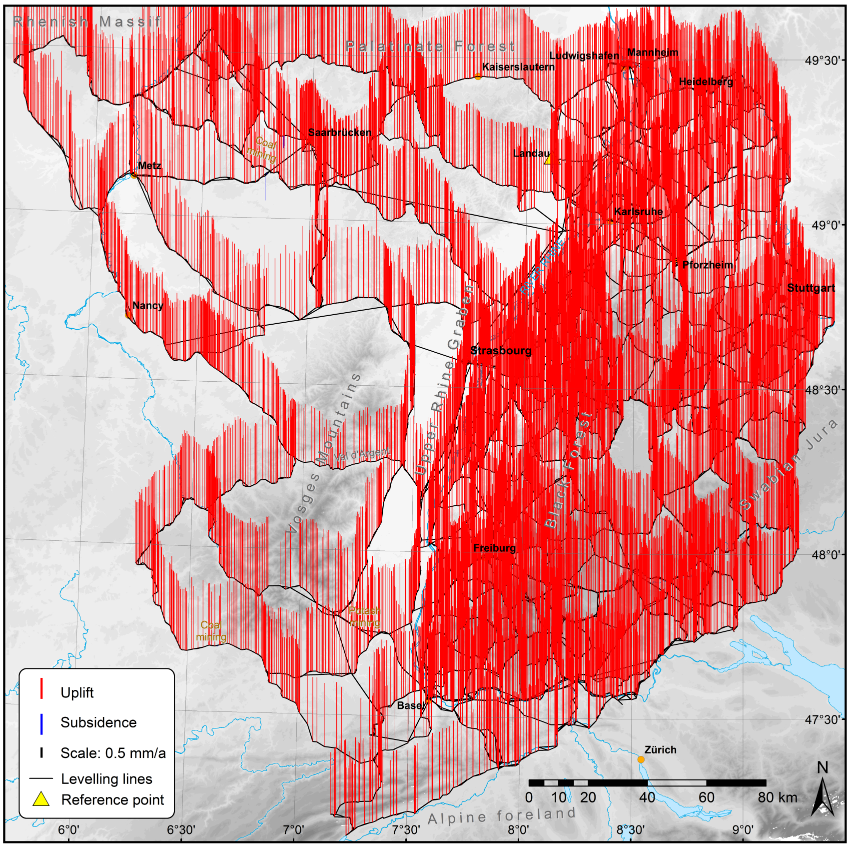

Figure A.4: Vertical displacement rates in the URG area. Reference point located within a subsidence area at Landau (8.115°E, 49.204°N), Rheinland-Pfalz, Germany

B GNSS Analysis

Table B.1: Analysed sites of the GNSS Upper Rhine Graben Network (GURN).

Four-digit site name	Full site name (Site location)	Site coordinates		Period[1]		Antenna changes[2]
		Lon. [°]	Lat. [°]	Start date	End date	
0384	Stuttgart	9.1709	48.7795	2002-01-02	2011-04-16	2
0386	Heilbronn	9.2183	49.1385	2002-01-02	2011-04-16	1
0387	Heidelberg	8.6753	49.3889	2002-04-04	2011-04-16	5
0388	Iffezheim	8.1126	48.8301	2003-03-12	2011-04-16	2
0389	Schwäbisch Hall	9.7176	49.1064	2002-01-02	2011-04-16	1
0390	Freiburg	7.8444	47.9990	2002-01-02	2006-10-16	1
0391	Geislingen	9.8024	48.5857	2002-01-02	2011-04-16	1
0392	Tauberbischofsheim	9.6708	49.6243	2002-01-02	2011-04-16	2
0393	Offenburg	7.9510	48.4730	2002-06-11	2010-11-08	3
0394	Tübingen	9.0559	48.5177	2002-01-02	2006-04-26	0
0395	Ravensburg	9.6242	47.7931	2002-02-15	2011-04-16	1
0396	Biberach	9.7932	48.1001	2002-03-21	2011-04-16	1
0397	Sigmaringen	9.2239	48.0836	2002-03-12	2011-04-16	1
0398	Freudenstadt	8.4158	48.4645	2002-12-02	2011-04-16	1
0399	Villingen-Schwenningen	8.4648	48.0669	2002-12-01	2008-01-23	0
0400	Tübingen 2	9.0784	48.5195	2006-04-28	2011-04-16	1
0401	Freiburg 2	7.8340	48.0132	2006-10-18	2011-04-16	1
0402	Villingen-Schwenningen 2	8.5276	48.0731	2008-01-25	2011-04-16	1
0512	Koblenz	7.5697	50.3583	2004-01-01	2011-04-16	1
0513	Mayen	7.2431	50.3293	2004-01-01	2011-04-16	1
0514	Simmern	7.5250	49.9845	2004-01-01	2011-04-16	2
0515	Wissen	7.7426	50.7809	2004-01-01	2011-04-16	1
0517	Montabaur	7.8305	50.4317	2004-01-01	2005-04-27	0
0518	Bingen	7.8769	49.9682	2004-09-28	2011-03-06	1
0519	Daun	6.8212	50.1999	2004-01-01	2011-04-16	2
0520	Ludwigshafen	8.4506	49.4687	2004-01-01	2011-04-16	1
0521	Landau	8.1094	49.1998	2004-01-01	2011-04-16	1
0522	Pirmasens	7.6025	49.2021	2004-01-01	2011-04-16	1
0523	Kaiserslautern	7.7740	49.4441	2004-01-01	2011-04-16	1
0524	Trier	6.6474	49.7569	2004-01-01	2011-04-16	1
0525	Bernkastel	7.0665	49.9161	2004-01-01	2011-04-16	1
0526	Prüm	6.4275	50.2101	2004-01-01	2011-04-16	1
0527	Birkenfeld	7.1658	49.6475	2004-01-01	2011-04-16	1
0528	Meisenheim	7.6653	49.7049	2004-01-01	2011-04-16	1
0529	Alzey 2	8.1187	49.7474	2005-05-09	2011-04-16	1
0530	Montabaur 2	7.8306	50.4316	2005-07-05	2011-04-16	1
0531	Rodershausen	6.1949	49.9921	2006-04-20	2011-04-16	1
AUB2	Aubure 2	7.2213	48.1975	2009-01-31	2010-11-10	0
AUBU	Aubure	7.1967	48.2169	2008-07-05	2011-04-16	1
BALG	Balgau	7.5407	47.9306	2009-04-14	2011-04-16	0
BFO1	Black Forest Observatory	8.3249	48.3305	2006-11-12	2011-04-16	0
BIWI	Biwisheim	7.6582	48.7088	2007-07-13	2011-04-02	0
BLFT	Belfort	6.8585	47.6259	2007-05-14	2011-04-16	1
BOU2	Bourrignon 2	7.2304	47.3941	2009-07-15	2011-04-16	0
BOUR	Bourrignon	7.2306	47.3941	2009-07-15	2011-04-16	0
BSCN	Besancon	5.9894	47.2469	2002-01-02	2009-01-13	1
BUAN	Bure-Andra	5.3536	48.4862	2007-11-14	2011-04-16	0
CHRM	Charmes	6.2812	48.3718	2007-10-31	2011-04-16	1
DILL	Dillingen	6.6997	49.3716	2004-12-06	2011-04-16	0

DOCO	Doncourt-les-Conflans	5.9345	49.1402	2007-08-22	2011-04-16	1
DRUS	Drusenheim	7.9506	48.7674	2007-05-13	2011-04-16	1
ENTZ	Entzheim	7.6399	48.5494	2004-12-01	2011-04-16	1
EOST	EOST Strasbourg	7.7625	48.5798	2007-04-12	2011-04-16	0
ERCK	Erckartswiller	7.3642	48.8730	2009-03-19	2011-04-16	0
ETH2	ETH Zürich 2	8.5106	47.4072	2009-07-15	2011-04-16	0
ETHZ	ETH Zürich	8.5105	47.4071	2009-07-15	2011-04-16	0
FHBB	FHNWMuttenz	7.6386	47.5339	2003-02-05	2011-04-16	1
FRAC	Frahier-et-Chatebier	6.7456	47.6597	2007-07-13	2011-04-02	0
FRI2	Frick 2	8.1116	47.5274	2008-09-21	2011-04-16	2
FRIC	Frick	8.1119	47.5274	2003-02-05	2011-04-16	0
FRTT	Frette	5.5663	47.6803	2008-08-13	2011-04-16	1
HUEG	Hügelheim	7.5962	47.8339	2002-01-02	2011-04-16	2
HUTT	Huttwil	7.8349	47.1411	2009-07-15	2011-04-16	0
KARL	Karlsruhe	8.4113	49.0112	2002-07-04	2011-04-16	1
KLOP	Kloppenheim	8.7299	50.2198	2002-07-03	2011-04-16	2
KREU	Kreuzlingen	9.1600	47.6413	2003-02-05	2009-03-25	1
LRTZ	Lycée Loritz, Nancy	6.1915	48.6905	2007-11-05	2011-04-16	0
LUCE	Lucelle	7.2682	47.4384	2007-11-01	2011-04-16	1
MAKS	Markstein	7.0315	47.9230	2007-05-09	2011-04-16	0
METZ	Metz	6.1979	49.1036	2004-02-13	2011-04-16	0
MIRE	Mirecourt	6.1213	48.2949	2009-04-14	2011-04-16	0
MNBL	Montbeliard	6.8061	47.4958	2009-04-15	2011-04-16	0
MOUS	Moussey	6.7838	48.6752	2007-07-13	2011-03-20	0
PRNY	Pontarlier	6.3383	46.9049	2007-10-31	2011-04-16	1
SARL	Sarralbe	7.0313	49.0025	2007-08-22	2010-09-28	1
SCHA	Schaffhausen	8.6558	47.7376	2003-02-05	2009-12-21	1
SEUR	Seurre	5.1515	46.9943	2006-09-17	2009-12-31	0
STGA	St. Gallen	9.3460	47.4418	2003-02-05	2011-04-16	2
STJ9	Strasbourg	7.6838	48.6217	2002-01-02	2011-04-16	0
TANZ	Selestat	7.4626	48.2549	2007-03-22	2010-09-27	1
VAUD	Vaudrey	5.6269	46.9812	2008-02-20	2011-04-16	0
VSOL	Vesoul	6.0666	47.6894	2009-04-15	2011-04-16	0
WLBH	Welsbruch	7.3513	48.4152	2002-01-02	2011-04-16	0
ZIM2	Zimmerwald 2	7.4650	46.8771	2007-11-22	2011-04-16	1
ZIMM	Zimmerwald	7.4653	46.8771	2002-01-02	2011-04-16	0

[1] Period of valid coordinate estimates from the adjustment of observations.

[2] Number of documented antenna changes within the analysed period.

Table B.2: Mean standard deviations of daily coordinate estimates at all 85 analysed GURN sites, and site velocities deduced from daily coordinate estimates. The mean velocity of all subsections is given in the table if the time series is separated by documented antenna changes.

Four-digit	Standard deviation [mm]			Velocity [mm/a]		
site name	East	North	Up	East	North	Up
0384	0.32	0.43	1.40	19.48	15.39	0.31
0386	0.32	0.43	1.41	19.88	15.74	0.38
0387	0.32	0.44	1.42	19.34	15.94	1.16
0388	0.32	0.43	1.41	19.92	15.30	0.59
0389	0.32	0.43	1.42	19.70	16.00	0.17
0390	0.32	0.44	1.45	19.47	16.04	−0.27
0391	0.32	0.43	1.43	20.00	16.09	0.09
0392	0.32	0.44	1.42	19.64	15.85	0.76
0393	0.32	0.43	1.43	19.79	15.82	1.79
0394	0.32	0.43	1.42	19.51	15.79	0.38
0395	0.32	0.43	1.43	19.83	16.15	1.20
0396	0.32	0.43	1.43	20.03	15.65	0.63
0397	0.32	0.43	1.42	20.04	16.08	0.95
0398	0.32	0.43	1.41	19.78	15.98	0.83
0399	0.33	0.45	1.47	19.42	16.16	−0.75
0400	0.32	0.43	1.42	19.54	16.00	−0.52
0401	0.31	0.42	1.39	19.85	16.48	0.01
0402	0.31	0.41	1.36	20.12	16.48	0.78
0512	0.31	0.43	1.38	19.01	15.62	0.98
0513	0.31	0.43	1.38	18.89	15.68	0.97
0514	0.32	0.44	1.42	18.91	15.26	1.14
0515	0.33	0.49	1.54	18.91	15.81	0.31
0517	0.32	0.45	1.42	19.01	15.02	−0.13
0518	0.33	0.45	1.47	18.61	16.06	1.03
0519	0.32	0.43	1.39	18.82	15.72	0.18
0520	0.31	0.43	1.37	18.73	16.23	−1.91
0521	0.32	0.43	1.40	19.03	15.63	−1.54
0522	0.34	0.45	1.55	18.92	15.68	−0.59
0523	0.31	0.43	1.38	19.29	15.39	1.11
0524	0.32	0.43	1.40	18.87	15.63	0.92
0525	0.32	0.44	1.43	18.44	15.65	−0.13
0526	0.34	0.47	1.54	18.80	15.34	2.16
0527	0.32	0.44	1.43	18.65	15.27	0.92
0528	0.32	0.43	1.39	19.22	15.10	−0.65
0529	0.31	0.43	1.38	19.48	16.74	−0.17
0530	0.31	0.43	1.38	18.84	15.39	0.67
0531	0.31	0.42	1.35	19.93	15.85	1.46
AUB2	0.32	0.42	1.40	20.96	15.16	0.96
AUBU	0.37	0.48	1.76	19.97	16.00	2.25
BALG	0.31	0.41	1.37	19.18	15.60	0.22
BFO1	0.42	0.46	2.15	19.18	15.05	3.34
BIWI	0.31	0.42	1.37	20.14	14.82	2.17
BLFT	0.31	0.41	1.35	19.80	15.64	1.48
BOU2	0.31	0.40	1.37	18.93	16.73	−1.53
BOUR	0.31	0.41	1.38	19.48	16.71	−2.38
BSCN	0.34	0.45	1.53	19.18	15.98	0.51
BUAN	0.30	0.41	1.34	18.83	16.42	1.26
CHRM	0.31	0.41	1.35	19.73	15.77	1.20
DILL	0.31	0.43	1.38	19.20	15.33	0.68
DOCO	0.31	0.42	1.36	19.52	15.49	1.70
DRUS	0.31	0.41	1.35	19.83	15.53	1.58

ENTZ	0.31	0.42	1.37	19.34	15.37	−2.54
EOST	0.31	0.42	1.38	19.80	15.72	1.68
ERCK	0.31	0.43	1.40	19.07	16.22	−0.80
ETH2	0.30	0.40	1.34	19.04	16.69	0.87
ETHZ	0.30	0.40	1.34	19.50	16.48	−0.19
FHBB	0.33	0.45	1.49	19.99	16.00	0.92
FRAC	0.31	0.42	1.37	19.52	15.75	1.54
FRI2	0.33	0.45	1.59	20.09	15.99	3.35
FRIC	0.35	0.47	1.58	20.01	16.05	1.26
FRTT	0.32	0.45	1.49	19.65	16.19	2.14
HUEG	0.32	0.44	1.45	19.74	16.07	0.78
HUTT	0.30	0.40	1.30	19.56	16.73	1.96
KARL	0.31	0.43	1.39	19.59	15.76	0.40
KLOP	0.29	0.39	1.27	18.94	15.98	0.49
KREU	0.32	0.44	1.45	20.53	15.26	1.08
LRTZ	0.31	0.42	1.36	19.25	15.18	0.21
LUCE	0.31	0.41	1.38	19.66	16.32	1.36
MAKS	0.31	0.42	1.38	19.80	15.49	1.33
METZ	0.33	0.46	1.51	19.40	15.23	0.61
MIRE	0.31	0.41	1.37	19.41	16.14	−0.62
MNBL	0.31	0.41	1.37	19.40	15.62	−0.62
MOUS	0.31	0.43	1.39	20.02	15.80	1.17
PRNY	0.31	0.40	1.34	19.95	15.89	0.40
SARL	0.31	0.42	1.37	19.24	15.17	1.73
SCHA	0.32	0.43	1.43	20.02	15.78	1.28
SEUR	0.32	0.42	1.41	19.49	15.77	0.68
STGA	0.32	0.43	1.42	19.88	16.02	1.19
STJ9	0.32	0.43	1.42	19.33	15.83	0.52
TANZ	0.31	0.42	1.37	19.91	15.46	0.35
VAUD	0.32	0.41	1.38	19.68	16.02	0.21
VSOL	0.32	0.41	1.39	19.50	15.27	−1.10
WLBH	0.39	0.51	1.79	19.35	15.44	−1.45
ZIM2	0.30	0.39	1.27	19.64	15.97	0.54
ZIMM	0.31	0.42	1.39	19.71	16.40	1.56

Table B.3: Velocity estimates and corresponding standard deviations (STD) resulting from linear regression (lin. reg.) and from CATS analysis. Site velocities calculated from a local Euler pole are already subtracted. Velocities from linear regression are estimated for every subsection of a time series.

Four-digit	Velocity from lin. reg. ± STD [mm/a]			CATS velocity ± STD [mm/a]		
site name	East	North	Up	East	North	Up
0384	0.11 ±0.02	−0.69 ±0.03	−1.17 ±0.06	0.25 ±0.09	−0.47 ±0.14	0.01 ±0.27
	0.82 ±0.03	−0.11 ±0.04	1.53 ±0.08			
	−12.72 ±1.59	−3.53 ±2.10	−5.13 ±5.27			
0386	0.24 ±0.01	−0.11 ±0.01	0.12 ±0.04	0.30 ±0.07	−0.09 ±0.09	0.74 ±0.25
	0.81 ±0.05	−0.04 ±0.05	0.53 ±0.14			
0387	0.39 ±0.10	0.32 ±0.11	1.89 ±0.31	0.02 ±0.12	−0.22 ±0.11	0.23 ±0.40
	−0.12 ±0.03	−0.29 ±0.02	−1.04 ±0.09			
	0.45 ±0.06	−0.16 ±0.05	0.49 ±0.15			
0388	0.81 ±0.03	−0.23 ±0.03	0.01 ±0.05	0.97 ±0.15	−0.32 ±0.15	0.48 ±0.38
	0.60 ±0.11	−0.94 ±0.11	1.07 ±0.21			
0389	−0.06 ±0.01	0.10 ±0.01	−0.28 ±0.03	0.10 ±0.07	0.03 ±0.09	0.26 ±0.27
	0.54 ±0.05	0.32 ±0.06	0.50 ±0.16			
0390	0.07 ±0.03	0.13 ±0.02	−0.32 ±0.06	−0.03 ±0.14	0.21 ±0.20	−0.44 ±0.42
0391	0.17 ±0.01	0.05 ±0.02	−0.38 ±0.04	0.21 ±0.09	0.14 ±0.10	−0.11 ±0.35
	0.56 ±0.05	0.59 ±0.07	0.44 ±0.19			
0392$^+$	0.28 ±0.31	0.71 ±0.17	1.63 ±0.57	0.40 ±0.10	−0.38 ±0.12	0.53 ±0.33
	1.33 ±0.29	−1.59 ±0.22	0.23 ±0.61			
	0.25 ±0.03	−0.38 ±0.02	−0.03 ±0.06			
	0.48 ±0.08	−0.10 ±0.05	0.53 ±0.15			
0393	0.33 ±0.01	0.11 ±0.01	1.64 ±0.04	0.28 ±0.08	0.03 ±0.08	1.47 ±0.28
	0.74 ±0.06	−0.19 ±0.06	1.87 ±0.20			
0394	0.00 ±0.03	−0.05 ±0.03	0.32 ±0.07	0.03 ±0.17	−0.13 ±0.18	0.65 ±0.45
0395	−0.28 ±0.01	0.11 ±0.01	1.31 ±0.03	−0.23 ±0.07	0.04 ±0.07	1.39 ±0.21
	0.31 ±0.05	0.62 ±0.05	0.98 ±0.16			
0396	0.15 ±0.01	−0.30 ±0.02	0.41 ±0.03	0.17 ±0.06	−0.22 ±0.10	0.55 ±0.23
	0.37 ±0.04	0.06 ±0.07	0.75 ±0.14			
0397	0.19 ±0.01	−0.05 ±0.01	0.65 ±0.03	0.16 ±0.07	−0.02 ±0.08	0.83 ±0.24
	0.58 ±0.05	0.59 ±0.06	1.14 ±0.18			
0398	0.17 ±0.03	−0.31 ±0.02	0.42 ±0.05	0.29 ±0.14	−0.28 ±0.11	0.05 ±0.34
	0.63 ±0.08	0.54 ±0.06	1.13 ±0.18			
0399	−0.10 ±0.02	0.27 ±0.02	−0.78 ±0.05	−0.06 ±0.13	0.13 ±0.12	−1.00 ±0.37
0400	−0.29 ±0.07	0.25 ±0.05	−2.08 ±0.19	0.17 ±0.13	0.14 ±0.14	−0.26 ±0.56
	0.37 ±0.04	0.10 ±0.04	0.95 ±0.14			
0401	0.39 ±0.13	0.73 ±0.09	−0.77 ±0.30	0.50 ±0.15	0.32 ±0.16	1.17 ±0.58
	0.35 ±0.04	0.15 ±0.04	1.97 ±0.14			
0402	−0.92 ±0.21	3.31 ±0.28	0.08 ±0.89	0.48 ±0.17	0.47 ±0.30	1.57 ±0.77
	0.61 ±0.05	0.63 ±0.06	0.72 ±0.16			
0512	0.32 ±0.04	−0.28 ±0.04	0.41 ±0.09	0.38 ±0.20	−0.30 ±0.16	0.51 ±0.41
	0.41 ±0.05	−0.31 ±0.04	1.44 ±0.12			
0513	0.11 ±0.02	−0.29 ±0.02	1.34 ±0.05	0.19 ±0.16	0.04 ±0.15	1.63 ±0.38
	0.51 ±0.11	−0.21 ±0.11	0.50 ±0.24			
0514	−0.00 ±0.04	−0.97 ±0.06	1.56 ±0.10	0.21 ±0.19	−0.61 ±0.23	0.88 ±0.41
	0.33 ±0.09	−0.35 ±0.25	0.63 ±0.19			
0515	0.11 ±0.03	0.13 ±0.03	0.17 ±0.08	0.30 ±0.11	0.24 ±0.15	0.09 ±0.44
	0.60 ±0.07	−0.31 ±0.07	0.33 ±0.19			
0517	0.03 ±0.11	−0.89 ±0.14	−0.18 ±0.33	0.12 ±0.40	−0.55 ±0.51	−0.22 ±1.07
0518	−0.22 ±0.02	0.16 ±0.02	0.97 ±0.05	−0.29 ±0.13	0.14 ±0.20	0.93 ±0.47
0519	−0.45 ±0.13	0.24 ±0.23	−1.31 ±0.39	0.18 ±0.16	−0.10 ±0.15	0.59 ±0.52
	0.88 ±0.07	−0.93 ±0.06	−0.48 ±0.19			
	0.40 ±0.04	−0.05 ±0.04	2.18 ±0.10			

0520	−0.73 ±0.03	−0.18 ±0.02	−1.90 ±0.06	−0.52 ±0.12	0.09 ±0.16	−1.10 ±0.40
	−0.00 ±0.08	0.91 ±0.06	−2.03 ±0.17			
0521	0.28 ±0.02	0.02 ±0.02	−2.55 ±0.05	0.32 ±0.11	0.02 ±0.12	−1.89 ±0.32
	−0.42 ±0.11	−0.52 ±0.12	−0.64 ±0.29			
0522$^+$	−0.44 ±0.09	−0.68 ±0.13	0.36 ±0.27	−0.02 ±0.12	−0.14 ±0.14	−0.62 ±0.39
	−0.18 ±0.04	−0.50 ±0.04	−1.45 ±0.10			
	0.36 ±0.06	0.45 ±0.07	−0.84 ±0.16			
0523	−0.04 ±0.03	−0.63 ±0.03	0.46 ±0.07	0.44 ±0.11	−0.55 ±0.14	1.16 ±0.41
	0.69 ±0.04	−0.39 ±0.05	1.65 ±0.11			
0524	0.07 ±0.03	−0.39 ±0.02	1.14 ±0.07	0.02 ±0.14	−0.32 ±0.13	1.58 ±0.39
	0.43 ±0.07	−0.28 ±0.06	0.59 ±0.17			
0525	−0.19 ±0.02	−0.98 ±0.03	1.38 ±0.05	−0.09 ±0.11	−0.69 ±0.17	1.34 ±0.37
	−0.28 ±0.17	0.39 ±0.27	−1.74 ±0.33			
0526$^+$	4.13 ±0.59	4.51 ±0.50	−3.04 ±1.92	0.22 ±0.16	−0.53 ±0.20	2.11 ±0.54
	0.20 ±0.10	−1.20 ±0.14	4.50 ±0.36			
	−0.13 ±0.04	−1.18 ±0.04	1.55 ±0.10			
	1.01 ±0.11	0.48 ±0.16	0.26 ±0.26			
0527	−0.30 ±0.02	−0.83 ±0.02	1.46 ±0.06	−0.18 ±0.10	−0.46 ±0.14	1.34 ±0.41
	0.06 ±0.13	−0.52 ±0.14	0.28 ±0.31			
0528	0.45 ±0.02	−0.82 ±0.02	0.51 ±0.05	0.54 ±0.10	−0.52 ±0.13	−0.15 ±0.39
	0.28 ±0.09	−0.79 ±0.10	−1.91 ±0.31			
0529	0.53 ±0.06	0.86 ±0.07	−0.22 ±0.17	−0.28 ±0.21	−0.01 ±0.27	0.39 ±0.59
	2.50 ±0.24	2.23 ±0.25	−2.37 ±0.67			
0530	0.40 ±0.04	−0.64 ±0.02	1.12 ±0.09	0.37 ±0.23	−0.50 ±0.17	0.94 ±0.57
	−0.08 ±0.20	−0.39 ±0.15	0.13 ±0.40			
0531	1.46 ±0.09	−0.15 ±0.03	1.40 ±0.08	0.49 ±0.28	−0.16 ±0.17	1.43 ±0.52
	9.77 ±0.53	1.78 ±0.28	−2.24 ±0.58			
AUB2*	1.76 ±0.15	−0.76 ±0.18	0.91 ±0.41	1.50 ±0.22	−1.53 ±0.77	2.50 ±1.86
AUBU	0.77 ±0.10	0.06 ±0.12	2.17 ±0.85	0.77 ±0.30	−0.16 ±0.28	1.24 ±1.09
BALG	−0.16 ±0.07	−0.31 ±0.07	0.17 ±0.32	−0.17 ±0.23	0.23 ±0.40	−1.74 ±1.20
BFO1*	−0.23 ±0.04	−0.83 ±0.03	3.29 ±0.12	−0.25 ±0.19	−0.62 ±0.20	2.33 ±0.74
BIWI*	0.98 ±0.04	−1.11 ±0.04	2.12 ±0.13	1.11 ±0.22	−0.94 ±0.20	1.89 ±0.73
BLFT	0.49 ±0.03	−0.33 ±0.04	1.43 ±0.09	0.49 ±0.15	−0.20 ±0.18	1.72 ±0.62
	0.17 ±0.34	−0.57 ±0.50	13.74 ±1.83			
BOU2*	−0.51 ±0.17	0.80 ±0.13	−1.58 ±0.59	0.18 ±0.37	1.23 ±0.46	−1.51 ±1.46
BOUR*	0.05 ±0.14	0.78 ±0.13	−2.43 ±0.60	−0.19 ±0.34	0.91 ±0.43	−1.58 ±2.05
BSCN	−0.06 ±0.01	−0.03 ±0.01	0.45 ±0.03	−0.09 ±0.10	−0.01 ±0.12	0.57 ±0.28
BUAN	0.08 ±0.04	0.39 ±0.03	1.21 ±0.09	−0.25 ±0.29	0.48 ±0.21	0.97 ±0.59
CHRM	0.76 ±0.04	−0.22 ±0.04	1.15 ±0.12	0.75 ±0.22	0.03 ±0.27	1.70 ±0.76
	−2.44 ±0.39	−1.19 ±0.45	13.65 ±2.00			
DILL	0.44 ±0.01	−0.63 ±0.01	0.62 ±0.04	0.41 ±0.11	−0.61 ±0.12	0.81 ±0.30
DOCO	0.84 ±0.05	−0.52 ±0.04	1.65 ±0.14	0.91 ±0.20	−0.49 ±0.18	2.00 ±0.76
	−6.14 ±0.37	−3.43 ±0.48	22.34 ±2.02			
DRUS	0.62 ±0.03	−0.37 ±0.03	1.53 ±0.11	0.73 ±0.14	−0.32 ±0.16	1.85 ±0.62
	−0.49 ±0.35	−2.83 ±0.42	12.34 ±1.74			
ENTZ	0.24 ±0.02	−0.38 ±0.02	0.04 ±0.06	0.27 ±0.10	−0.31 ±0.11	−0.59 ±0.48
	0.06 ±0.10	−0.70 ±0.09	−5.22 ±0.42			
EOST	0.58 ±0.03	−0.19 ±0.03	1.62 ±0.10	0.46 ±0.20	−0.28 ±0.24	1.45 ±0.57
ERCK*	0.04 ±0.07	0.21 ±0.07	−1.05 ±0.22	−0.04 ±0.24	0.36 ±0.36	−1.67 ±1.19
ETH2*	−0.65 ±0.11	0.83 ±0.10	0.82 ±0.96	−0.33 ±0.43	1.22 ±0.51	0.38 ±1.27
ETHZ	−0.19 ±0.15	0.63 ±0.13	−0.24 ±0.25	0.35 ±0.49	0.50 ±0.42	0.39 ±1.49
FHBB	0.15 ±0.03	0.33 ±0.02	0.74 ±0.06	0.28 ±0.12	0.14 ±0.07	0.82 ±0.29
	0.85 ±0.03	−0.16 ±0.03	0.98 ±0.10			
FRAC	0.32 ±0.04	−0.23 ±0.04	1.66 ±0.16	0.49 ±0.18	−0.13 ±0.18	1.34 ±1.04
FRI2*	0.71 ±0.13	0.61 ±0.18	3.48 ±0.75	0.55 ±0.34	1.18 ±0.47	−1.66 ±2.26
	0.32 ±0.15	−0.40 ±0.21	3.11 ±1.03			
FRIC	0.19 ±0.03	0.20 ±0.03	2.07 ±0.68	0.20 ±0.11	−0.01 ±0.17	1.64 ±0.52

FRTT	0.63 ±0.08	0.17 ±0.07	2.08 ±0.26	0.62 ±0.31	0.23 ±0.39	2.07 ±1.26
	−6.34 ±0.56	−0.84 ±0.73	−6.47 ±2.60			
HUEG	−0.11 ±0.03	−0.05 ±0.03	1.47 ±0.10	0.20 ±0.10	−0.07 ±0.10	1.02 ±0.28
	0.52 ±0.09	0.18 ±0.06	−0.62 ±0.27			
	0.64 ±0.03	0.33 ±0.04	1.32 ±0.10			
HUTT	−0.07 ±0.10	0.84 ±0.08	1.91 ±0.50	0.35 ±0.32	0.65 ±0.46	1.98 ±2.17
KARL	0.37 ±0.01	−0.11 ±0.01	0.35 ±0.02	0.43 ±0.11	−0.01 ±0.09	0.48 ±0.27
KLOP	−0.20 ±0.02	0.24 ±0.02	−0.16 ±0.06	−0.04 ±0.07	0.12 ±0.10	0.35 ±0.33
	0.21 ±0.03	0.03 ±0.03	1.05 ±0.10			
KREU	0.59 ±0.03	−0.16 ±0.02	1.14 ±0.09	0.46 ±0.14	−0.26 ±0.12	0.83 ±0.49
	0.89 ±0.12	−0.99 ±0.10	0.91 ±0.60			
LRTZ	0.40 ±0.04	−0.82 ±0.03	0.16 ±0.12	0.26 ±0.26	−0.85 ±0.26	−0.43 ±0.73
LUCE	−0.51 ±0.17	−0.33 ±0.20	−11.89 ±0.84	0.20 ±0.25	0.17 ±0.18	−0.10 ±0.87
	0.23 ±0.05	0.39 ±0.05	1.30 ±0.17			
MAKS	0.54 ±0.04	−0.46 ±0.04	1.27 ±0.09	0.49 ±0.25	−0.60 ±0.29	0.96 ±0.57
METZ	0.67 ±0.02	−0.77 ±0.02	0.56 ±0.04	0.56 ±0.11	−0.81 ±0.13	0.63 ±0.28
MIRE	0.47 ±0.08	0.16 ±0.09	−0.68 ±0.41	0.32 ±0.27	0.28 ±0.39	−1.90 ±1.05
MNBL	0.09 ±0.08	−0.33 ±0.07	−0.67 ±0.33	0.04 ±0.25	−0.13 ±0.31	−1.52 ±1.19
MOUS	1.03 ±0.05	−0.17 ±0.07	1.12 ±0.17	0.92 ±0.24	−0.23 ±0.31	0.62 ±0.79
PRNY[+]	1.27 ±0.16	−0.32 ±0.09	0.35 ±0.30	1.04 ±0.48	−0.21 ±0.28	−1.99 ±1.09
	−0.21 ±0.26	0.11 ±0.12	0.34 ±0.45			
	15.95 ±1.41	4.52 ±1.09	−9.71 ±3.04			
SARL	0.29 ±0.04	−0.78 ±0.03	1.67 ±0.11	0.19 ±0.15	−0.81 ±0.21	1.35 ±0.73
SCHA	0.31 ±0.04	0.12 ±0.03	0.91 ±0.07	0.62 ±0.15	−0.14 ±0.12	1.37 ±0.42
	0.43 ±0.07	−0.29 ±0.06	1.54 ±0.22			
SEUR	0.34 ±0.04	−0.28 ±0.03	0.63 ±0.12	0.38 ±0.22	−0.22 ±0.16	0.77 ±0.69
STGA	−0.00 ±0.04	0.18 ±0.03	0.65 ±0.33	0.06 ±0.12	0.07 ±0.12	1.63 ±0.39
	0.03 ±0.04	0.23 ±0.03	1.61 ±0.29			
STJ9	0.14 ±0.01	−0.09 ±0.01	0.47 ±0.02	0.10 ±0.05	−0.07 ±0.06	0.57 ±0.24
TANZ	0.65 ±0.04	−0.47 ±0.03	0.30 ±0.11	0.59 ±0.17	−0.51 ±0.18	−0.02 ±0.59
VAUD	0.44 ±0.04	0.00 ±0.04	0.15 ±0.12	0.48 ±0.26	−0.05 ±0.23	−0.27 ±0.65
VSOL[*]	0.39 ±0.07	−0.73 ±0.10	−1.15 ±0.34	0.02 ±0.31	−0.86 ±0.59	−2.29 ±1.35
WLBH	0.17 ±0.01	−0.49 ±0.02	−1.50 ±0.04	0.11 ±0.08	−0.39 ±0.09	−1.26 ±0.31
ZIM2	−0.10 ±0.12	−0.51 ±0.12	2.05 ±0.56	0.19 ±0.31	0.70 ±0.29	1.40 ±1.01
	0.08 ±0.12	0.59 ±0.14	−1.08 ±0.22			
ZIMM	0.07 ±0.01	0.47 ±0.01	1.51 ±0.02	0.04 ±0.06	0.39 ±0.06	1.56 ±0.22

[+] At this site an additional jump was detected and introduced for velocity estimation.

[*] The velocity of this site is not shown in the arrow plots (Fig. 5.5 and 5.6), as the time series is too short to estimate a sub-mm/a deformation with significance.

C InSAR Analysis

Table C.1: Difference between mean interferogram coherence and predicted coherence calculated from linear and exponential decorrelation models for the temproal / spatial decorrelation at 61 interferograms of an image stack in Northern Germany.

Acquisition date	linear / linear	exponential / linear	exponential / exponential
19920417	0.129	0.013	0.015
19920731	0.096	-0.028	0.017
19920904	0.087	-0.004	0.013
19921009	0.069	0.013	0.005
19921113	0.054	-0.016	0.010
19930122	0.039	0.000	0.012
19930226	0.032	0.010	0.002
19930611	0.014	0.019	0.005
19930924	-0.027	0.009	0.007
19931029	-0.021	0.016	0.001
19950430	-0.128	0.021	0.004
19950604	-0.331	-0.027	0.017
19950709	-0.164	0.016	0.005
19950813	-0.336	-0.019	0.018
19950814	-0.465	-0.059	-0.006
19950918	-0.351	-0.018	-0.007
19951022	-0.177	0.021	0.006
19951023	-0.167	0.017	-0.004
19951126	-0.190	0.018	0.003
19960310	-0.224	0.017	0.003
19960311	-0.257	0.007	-0.010
19960414	-0.414	-0.013	0.021
19960415	-0.581	-0.062	-0.005
19960519	-0.465	-0.055	0.000
19960623	-0.290	-0.084	-0.001
19960902	-0.331	-0.006	-0.015
19961007	-0.382	-0.010	-0.006
19961216	-0.344	-0.008	-0.005
19970120	-0.558	-0.078	-0.011
19970224	-0.386	-0.022	0.004
19970331	-0.342	-0.018	-0.010
19970505	-0.286	-0.008	-0.009
19970609	-0.404	-0.042	-0.003
19970714	-0.408	-0.050	-0.001
19970818	-0.384	-0.047	-0.003
19970922	-0.303	-0.024	-0.004
19971027	-0.209	-0.002	-0.007
19971201	-0.277	-0.027	-0.008
19980105	-0.368	-0.073	-0.012
19980209	-0.298	-0.047	-0.003
19980316	-0.287	-0.050	-0.002
19980420	-0.224	-0.029	-0.007
19980525	-0.279	-0.063	-0.001
19980803	-0.200	-0.036	0.007
19980907	-0.242	-0.073	-0.010
19981116	-0.086	-0.005	-0.011
19981221	-0.076	-0.004	-0.010
19990125	-0.100	-0.023	0.003
19990301	-0.072	-0.016	-0.008

19990405	-0.121	-0.062	-0.008
19990510	-0.035	-0.007	-0.011
19990614	-0.008	0.005	-0.010
19990719	0.000	0.003	-0.011
19990927	-0.009	-0.034	-0.007
19991031	0.039	0.016	0.007
19991101	0.013	-0.025	0.001
19991206	0.003	-0.059	-0.005
20000109	0.049	0.011	0.003
20000110	0.047	-0.016	0.001
20000214	0.032	-0.034	-0.001
20001016	0.133	0.007	0.005
MAD:	0.204	0.027	0.007

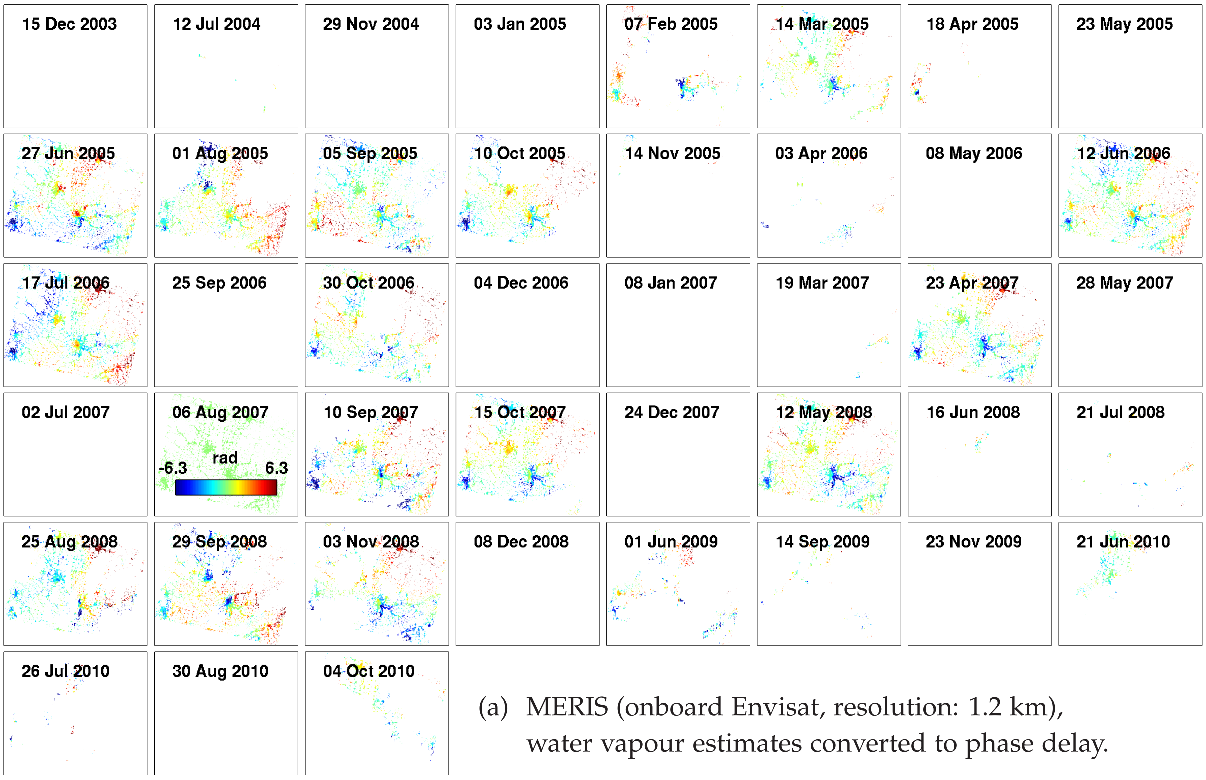

(a) MERIS (onboard Envisat, resolution: 1.2 km), water vapour estimates converted to phase delay.

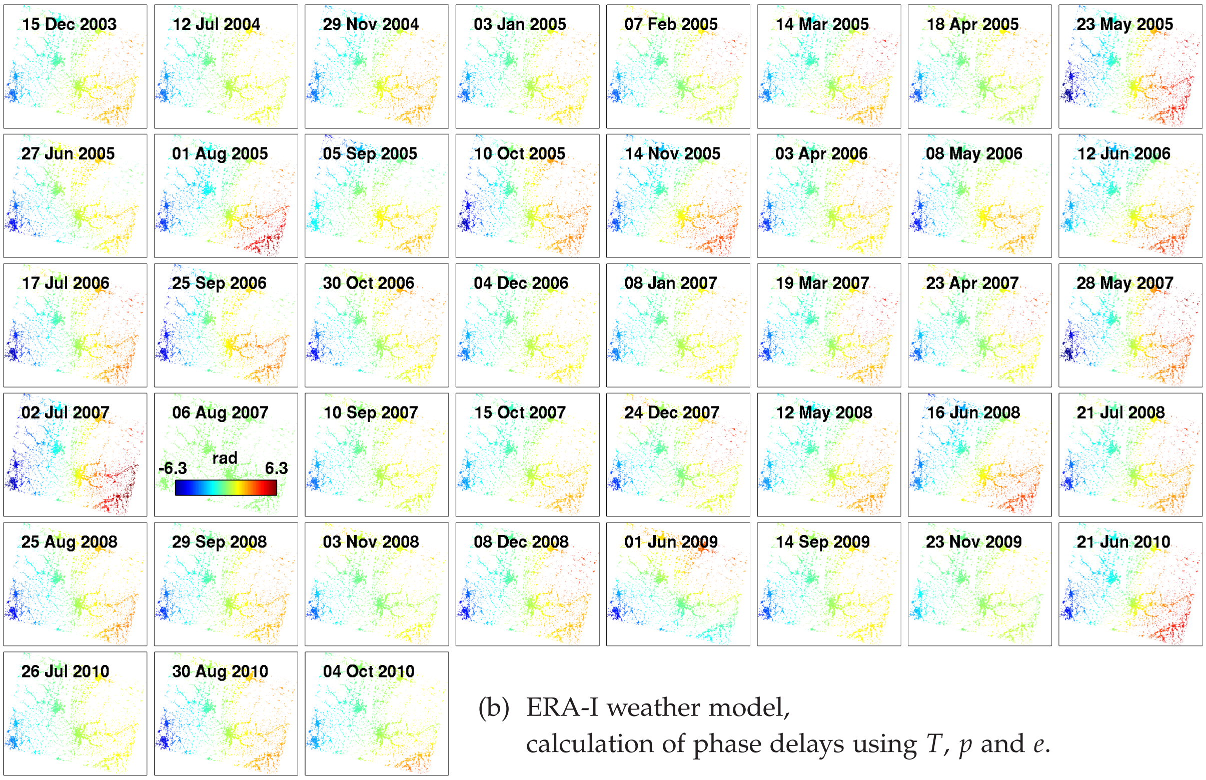

(b) ERA-I weather model, calculation of phase delays using T, p and e.

Figure C.1: Atmospheric phase screen for Envisat track 294S calculated from external data sources w.r.t. a master acquired on 2007-08-06. The spatial extent of the figures is 6.709°–8.400°E, 47.237°–48.196°N.

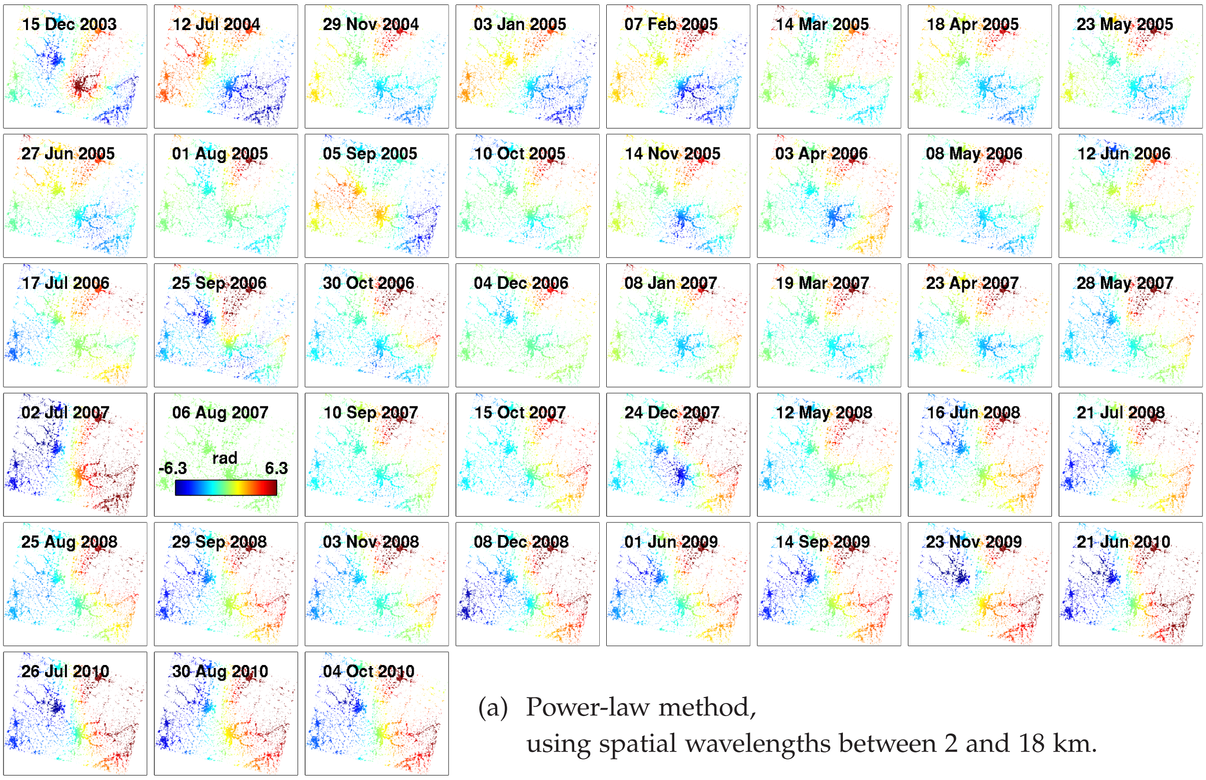

(a) Power-law method,
using spatial wavelengths between 2 and 18 km.

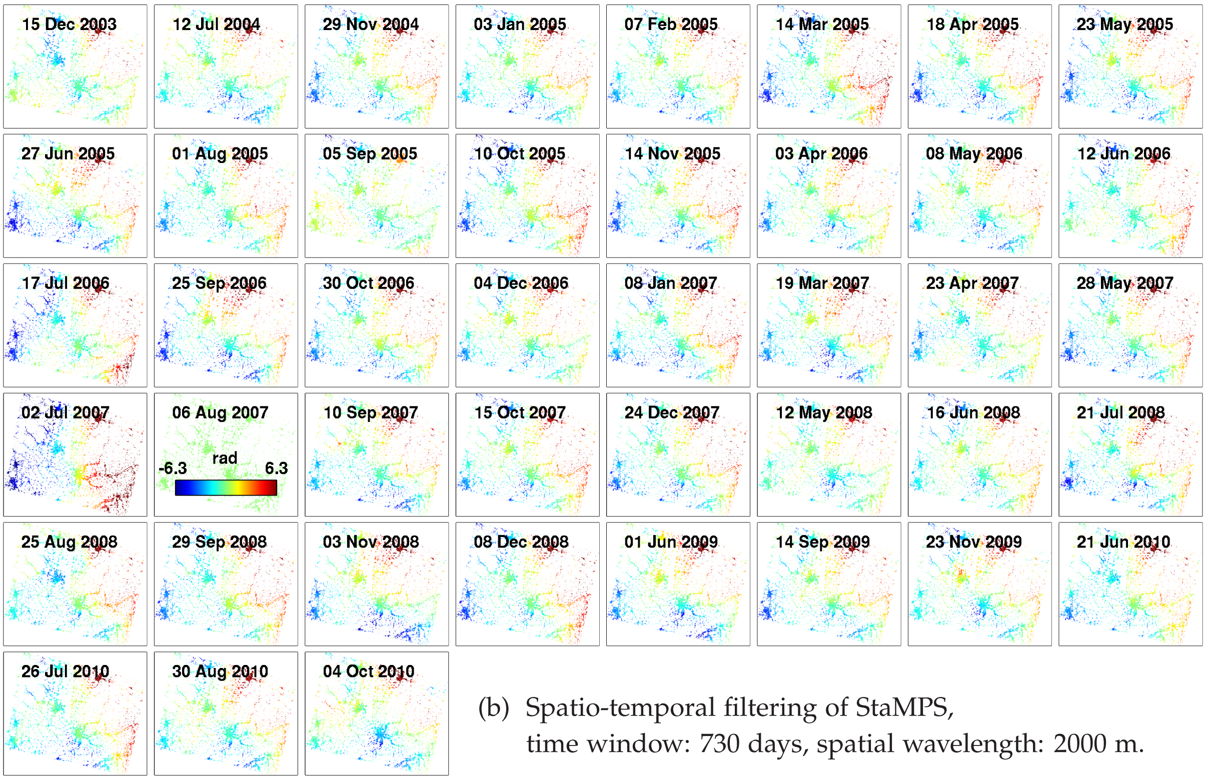

(b) Spatio-temporal filtering of StaMPS,
time window: 730 days, spatial wavelength: 2000 m.

Figure C.2: Atmospheric phase screen for Envisat track 294S calculated from the interferometric phase w.r.t. a master acquired on 2007-08-06. The spatial extent of the figures is 6.709°–8.400°E, 47.237°–48.196°N.

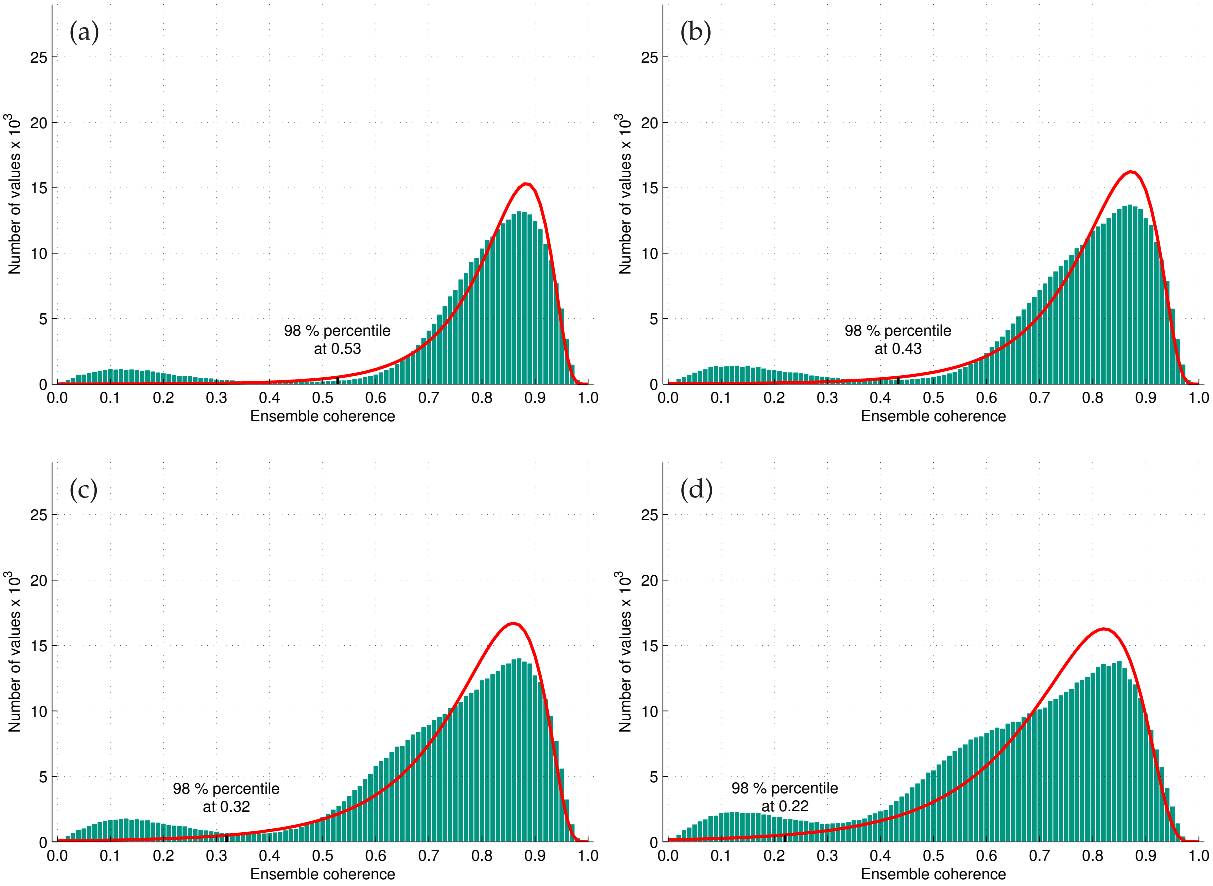

Figure C.3: Histogram, fitted PDF of the log-normal distribution and filtering threshold for EC values calculated at PS locations of Envisat track 487S for different weed standard deviation thresholds: (a) 0.8 rad, (b) 0.9 rad, (c) 1.0 rad, (d) 1.1 rad.

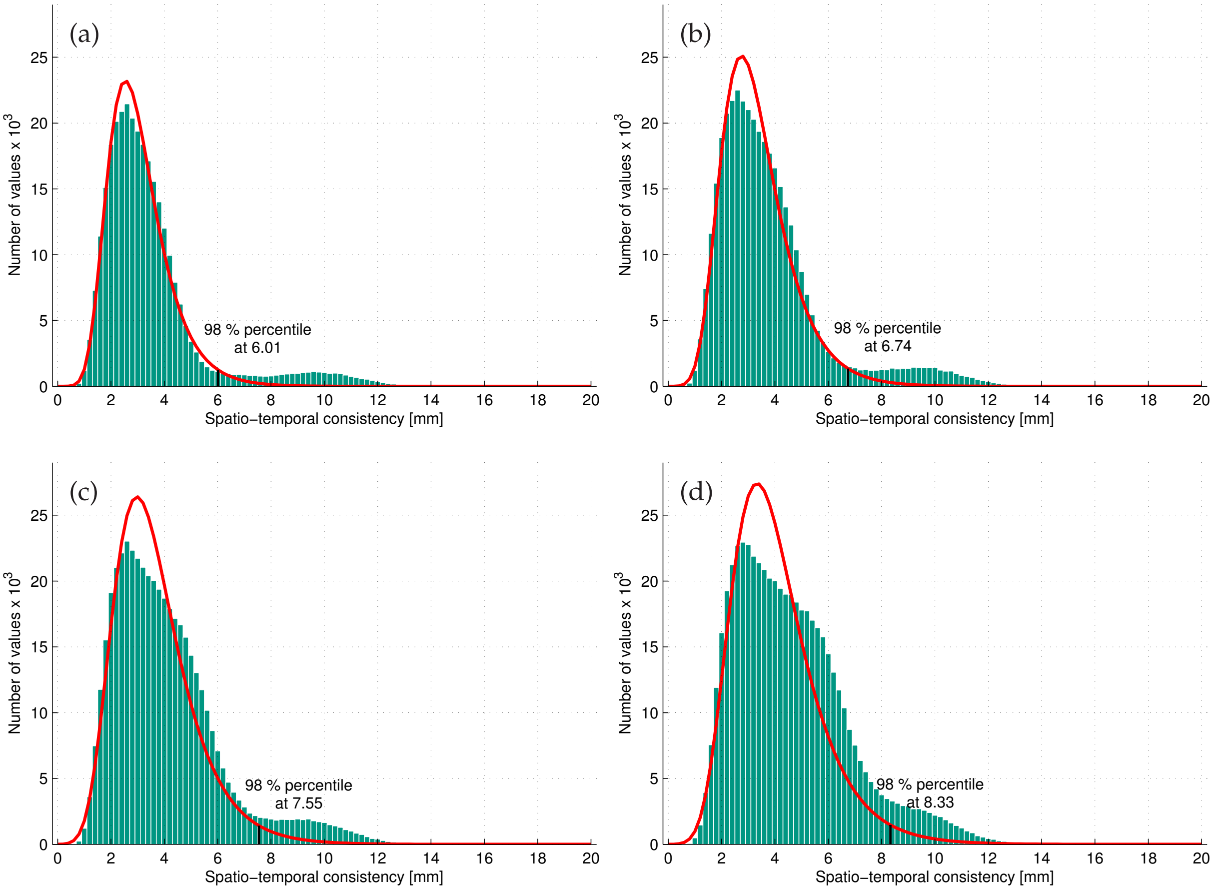

Figure C.4: Histogram, fitted PDF of the EV distribution and filtering threshold for STC values calculated at PS locations of Envisat track 487S for different weed standard deviation thresholds: (a) 0.8 rad, (b) 0.9 rad, (c) 1.0 rad, (d) 1.1 rad.

Table C.2: Comparison of the number of PS pixels and quality filtering results for different weed standard deviation thresholds, Envisat track 487S.

Threshold [rad]	γ_{min} [–]	ρ_{max} [mm]	No. of all PS	No. of good PS	No. of bad PS	bad PS [%]	bad EC [%]	bad STC [%]
0.8	0.53	6.01	305,927	271,814	34,113	11.2	9.6	9.6
0.9	0.43	6.74	381,013	340,546	40,467	10.6	9.3	8.8
1.0	0.32	7.55	463,233	417,524	45,709	9.9	8.4	7.8
1.1	0.22	8.33	549,209	498,139	51,070	9.3	7.1	7.2

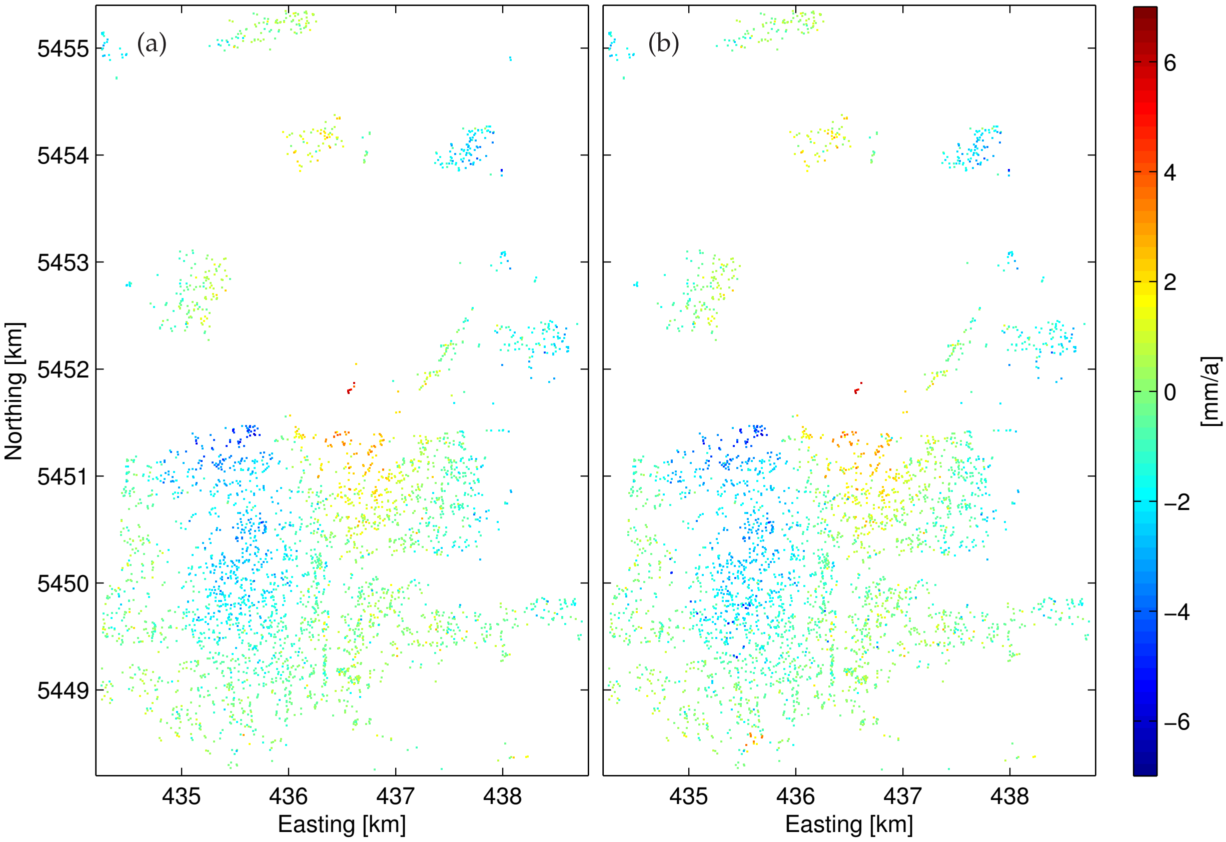

Figure C.5: LOS velocities at PS locations, crop of a region in the northern URG close to the city of Landau also shown in Fig. 6.22(b), Envisat track 294N. (a) filtered PS pixels: bad EC, (b) filtered PS pixels: bad STC. The spatial extent of the figures is 8.096°–8.160°E, 49.183°–49.248°N. The reference area is located in Karlsruhe and the same as in Fig. 6.10.

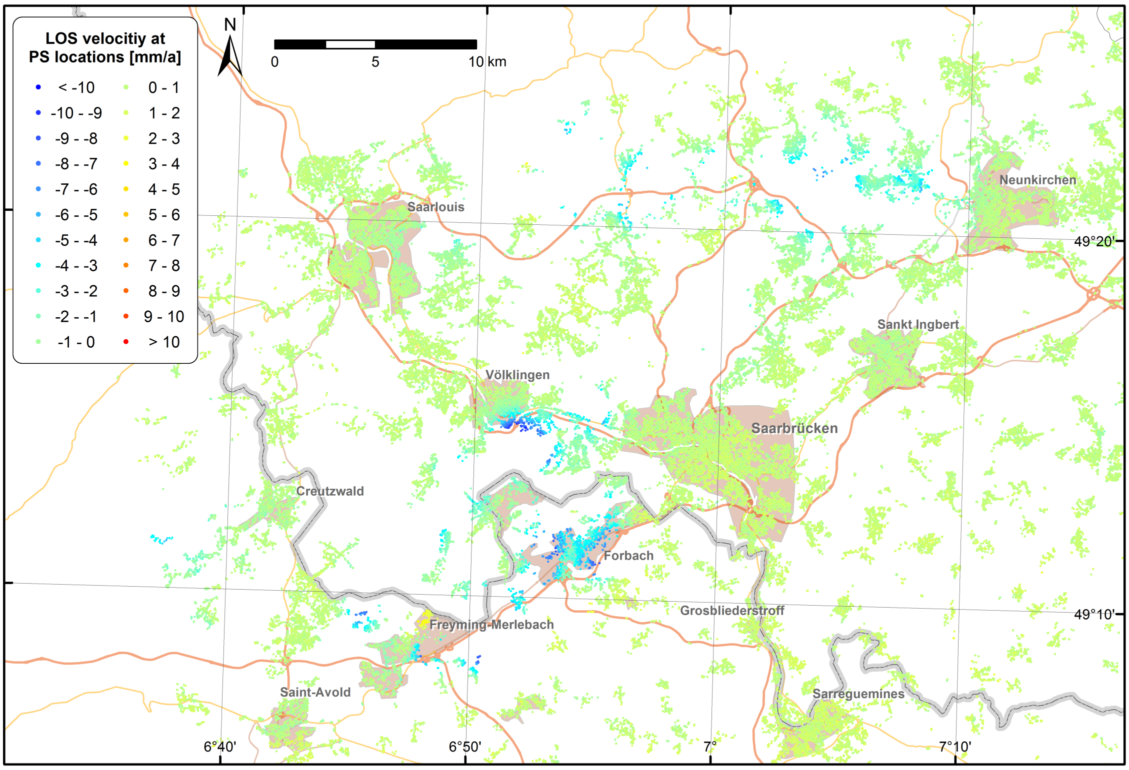

Figure C.6: LOS velocities at PS locations, crop of Lorraine/Saarland region at the northern French-German border, ERS track 258. The reference area is located in Lahr at 7.876°E, 48.342°N.

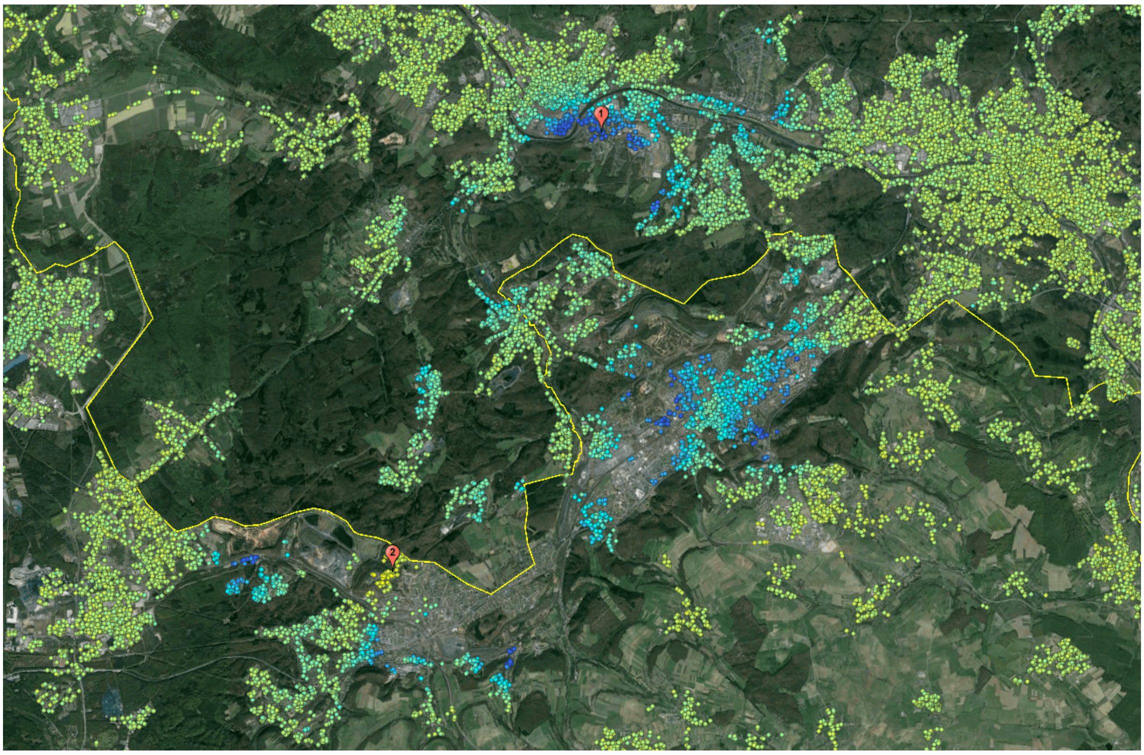

Figure C.7: LOS velocities at PS locations, crop of Lorraine/Saarland region at the northern French-German border between Creutzwald and Saarbrücken, ERS track 258. The colour scale and the reference area are the same as in Fig. C.6. The spatial extent of the figure is 6.684°–7.033°E, 49.120°–49.267°N. Background: Google Earth.

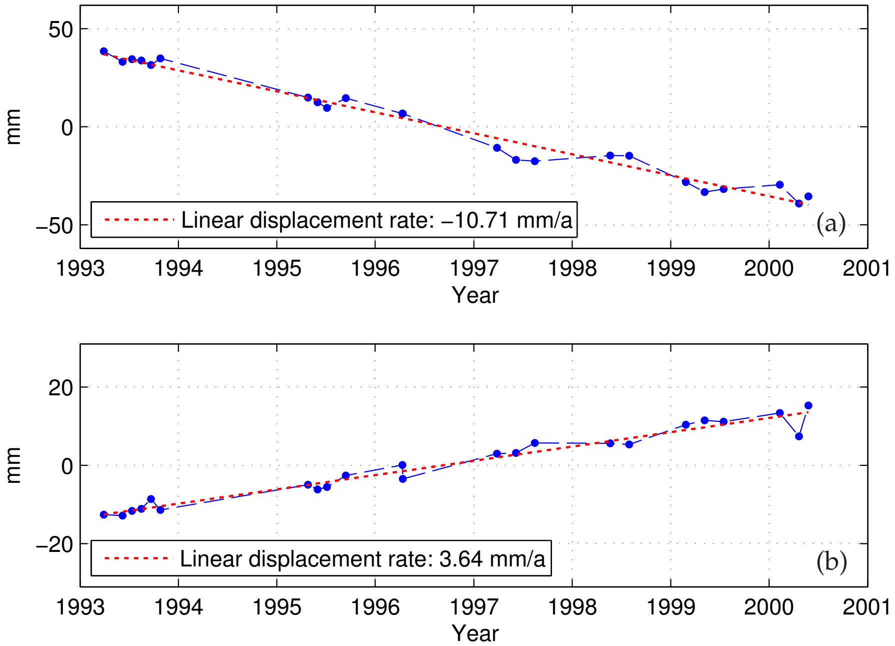

Figure C.8: Displacement time series at two different PS locations, (a) PS at Völklingen, location 1 in Fig. C.7, (b) PS at Freyming-Merlebach, location 2 in Fig. C.7.

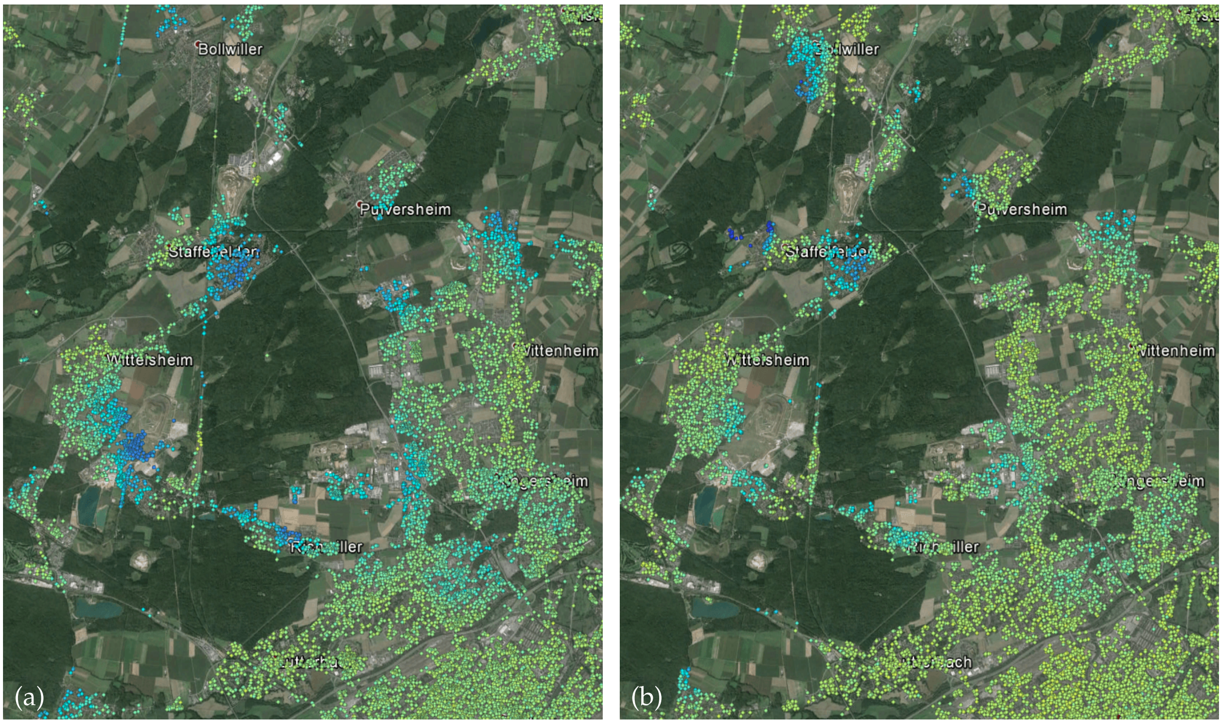

Figure C.9: LOS velocities at PS locations, crop of a region in the southern URG northwest of the city of Mulhouse, (a) ERS track 294, reference area located in Lahr at 7.876°E, 48.342°N, (b) Envisat track 294S, reference area located in Lörrach at 7.661°E, 47.616°N. The colour scale is the same as in Fig. C.6. The spatial extent of the figures is 7.216°–7.356°E, 47.751°–47.867°N. Background: Google Earth.

D Fusion of Techniques

Statement: Ordinary Kriging (OK) is a specific case of least-squares prediction.

The linear system of equations for least-squares prediction is given by Teunissen (2007):

$$\begin{pmatrix} y \\ y_0 \end{pmatrix} = \begin{pmatrix} A \\ A_0 \end{pmatrix} x + \begin{pmatrix} e \\ e_0 \end{pmatrix} \tag{D.1}$$

$$D\begin{pmatrix} e \\ e_0 \end{pmatrix} = D\begin{pmatrix} y \\ y_0 \end{pmatrix} = \begin{pmatrix} Q_{yy} & Q_{yy_0} \\ Q_{y_0y} & Q_{y_0y_0} \end{pmatrix} \quad . \tag{D.2}$$

The Best Linear Unbiased Predictor (BLUP) of y_0 is

$$\begin{aligned} \hat{y}_0 &= A_0\hat{x} + Q_{y_0y}Q_{yy}^{-1}\left(y - A\hat{x}\right) \\ &= A_0\left[\left(A^\top Q_{yy}^{-1}A\right)^{-1}A^\top Q_{yy}^{-1}y\right] + Q_{y_0y}Q_{yy}^{-1}\left(y - A\left[\left(A^\top Q_{yy}^{-1}A\right)^{-1}A^\top Q_{yy}^{-1}y\right]\right) \quad . \end{aligned} \tag{D.3}$$

Setting $A_0 = 1$ and $A = l = \begin{pmatrix} 1 \\ \vdots \\ 1 \end{pmatrix}$, we obtain

$$\hat{y}_0 = \left(l^\top Q_{yy}^{-1}l\right)^{-1}l^\top Q_{yy}^{-1}y + Q_{y_0y}Q_{yy}^{-1}\left(y - l\left(l^\top Q_{yy}^{-1}l\right)^{-1}l^\top Q_{yy}^{-1}y\right) \quad . \tag{D.4}$$

Following Eq. (7.12) and (7.15), the system of equations of OK can be written in the form:

$$\begin{aligned} w_{OK} = \begin{pmatrix} w \\ \lambda \end{pmatrix} &= \begin{pmatrix} Q_{yy} & l \\ l^\top & 0 \end{pmatrix}^{-1}\begin{pmatrix} Q_{yy_0} \\ 1 \end{pmatrix} \\ &= \begin{pmatrix} Q_{yy}^{-1} - Q_{yy}^{-1}l\left(l^\top Q_{yy}^{-1}l\right)^{-1}l^\top Q_{yy}^{-1} & Q_{yy}^{-1}l\left(l^\top Q_{yy}^{-1}l\right)^{-1} \\ \left(l^\top Q_{yy}^{-1}l\right)^{-1}l^\top Q_{yy}^{-1} & -\left(l^\top Q_{yy}^{-1}l\right)^{-1} \end{pmatrix}\begin{pmatrix} Q_{yy_0} \\ 1 \end{pmatrix} \\ &= \begin{pmatrix} Q_{yy}^{-1}Q_{yy_0} - Q_{yy}^{-1}l\left(l^\top Q_{yy}^{-1}l\right)^{-1}l^\top Q_{yy}^{-1}Q_{yy_0} + Q_{yy}^{-1}l\left(l^\top Q_{yy}^{-1}l\right)^{-1} \\ \left(l^\top Q_{yy}^{-1}l\right)^{-1}l^\top Q_{yy}^{-1}Q_{yy_0} - \left(l^\top Q_{yy}^{-1}l\right)^{-1} \end{pmatrix} \quad , \end{aligned} \tag{D.5}$$

where Q_{yy} represents the covariance matrix C of observations and Q_{yy_0} the vector of covariances D at the prediction location. We obtain the transposed vector $w^\top$ from Eq. (D.5):

$$\begin{aligned} w^\top &= Q_{y_0y}Q_{yy}^{-1} - Q_{y_0y}Q_{yy}^{-1}l\left(l^\top Q_{yy}^{-1}l\right)^{-1}l^\top Q_{yy}^{-1} + \left(l^\top Q_{yy}^{-1}l\right)^{-1}l^\top Q_{yy}^{-1} \\ &= \left(l^\top Q_{yy}^{-1}l\right)^{-1}l^\top Q_{yy}^{-1} + Q_{y_0y}Q_{yy}^{-1}\left(1 - l\left(l^\top Q_{yy}^{-1}l\right)^{-1}l^\top Q_{yy}^{-1}\right) \quad . \end{aligned} \tag{D.6}$$

Multiplication of Eq. (D.6) with the observation vector y, see Eq. (7.11), yields exactly the formulation of Eq. (D.4), proving that OK is a specific case of BLUP.

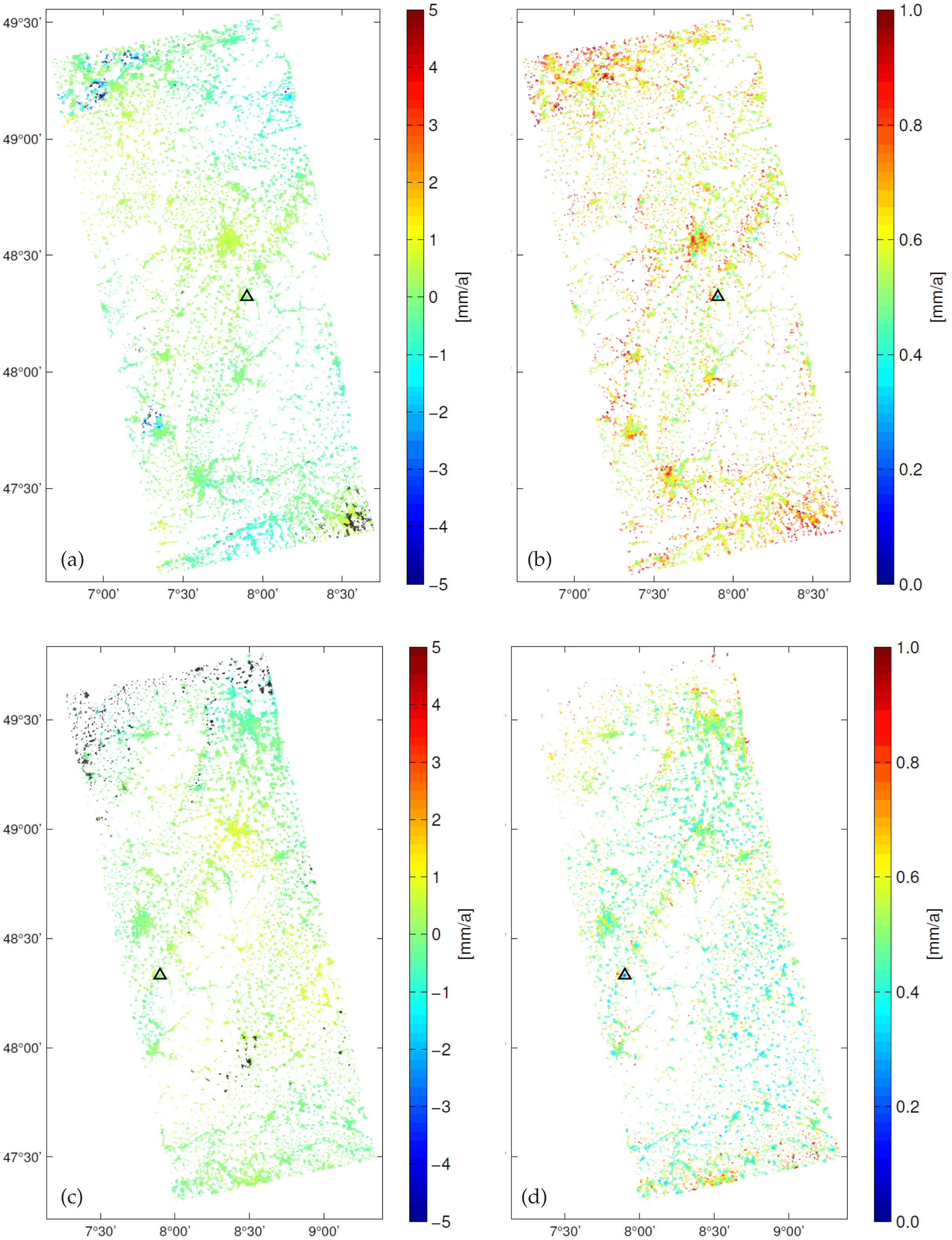

Figure D.1: InSAR velocity estimates at grid locations in track 258 (a), (b) and in track 487 (c), (d) from ERS and Envisat combination and from ERS only in the northern part of track 258. (a), (c) LOS velocities, (b), (d) standard deviation (2σ) of LOS velocities. Grid points with a significant non-linear motion behaviour are shown as black dots in (a), (c) and omitted in (b), (d).

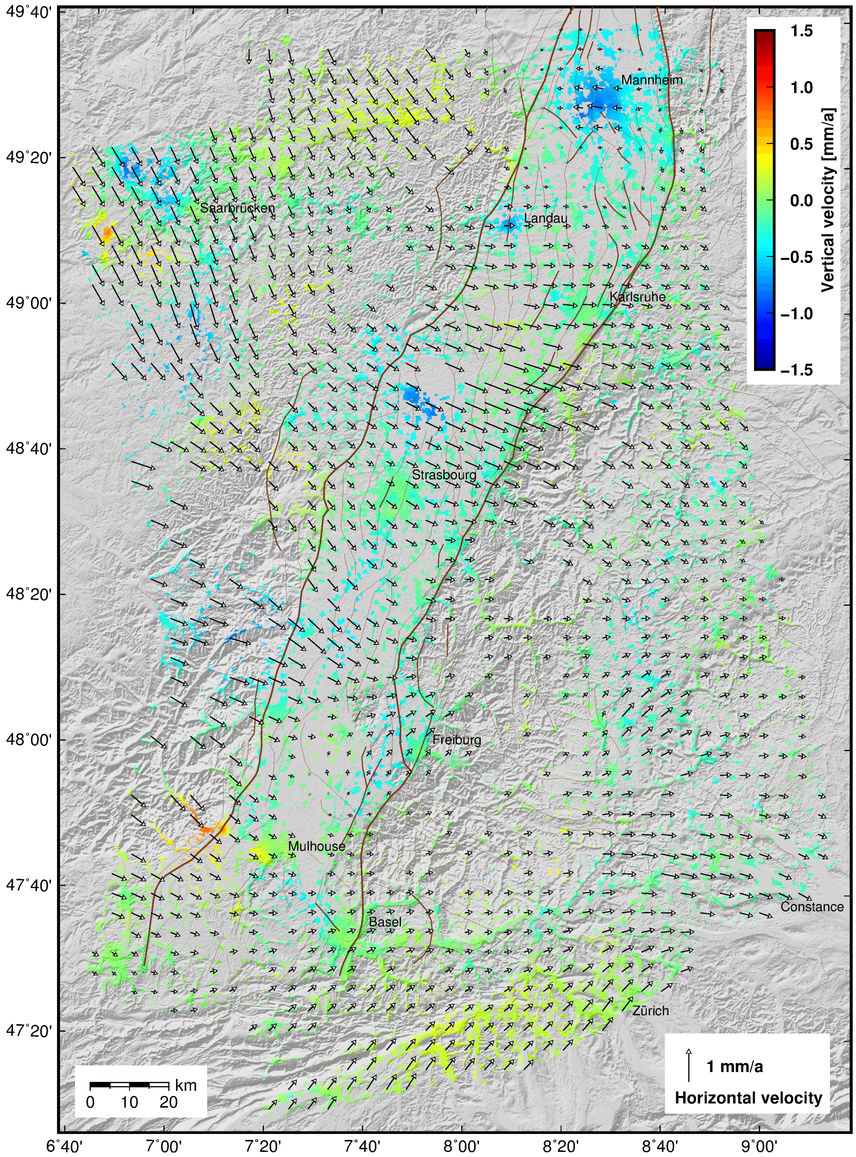

Figure D.2: Resulting velocity field from levelling and GNSS, only: horizontal linear rates (arrows) and vertical linear rates (colour-coded). The horizontal velocity field is interpolated to a 5 km grid for visualisation purposes. The vertical movements are relative to a reference point in the Eastern Black Forest, the horizontal movements are relative to a local Euler pole estimated from all 76 GNSS sites in the URG area. Brown lines represent faults in the URG area after Peters (2007), main border faults (thick), active faults (medium thick) and other faults (thin). Grey background: shaded DEM using SRTM-3 data.

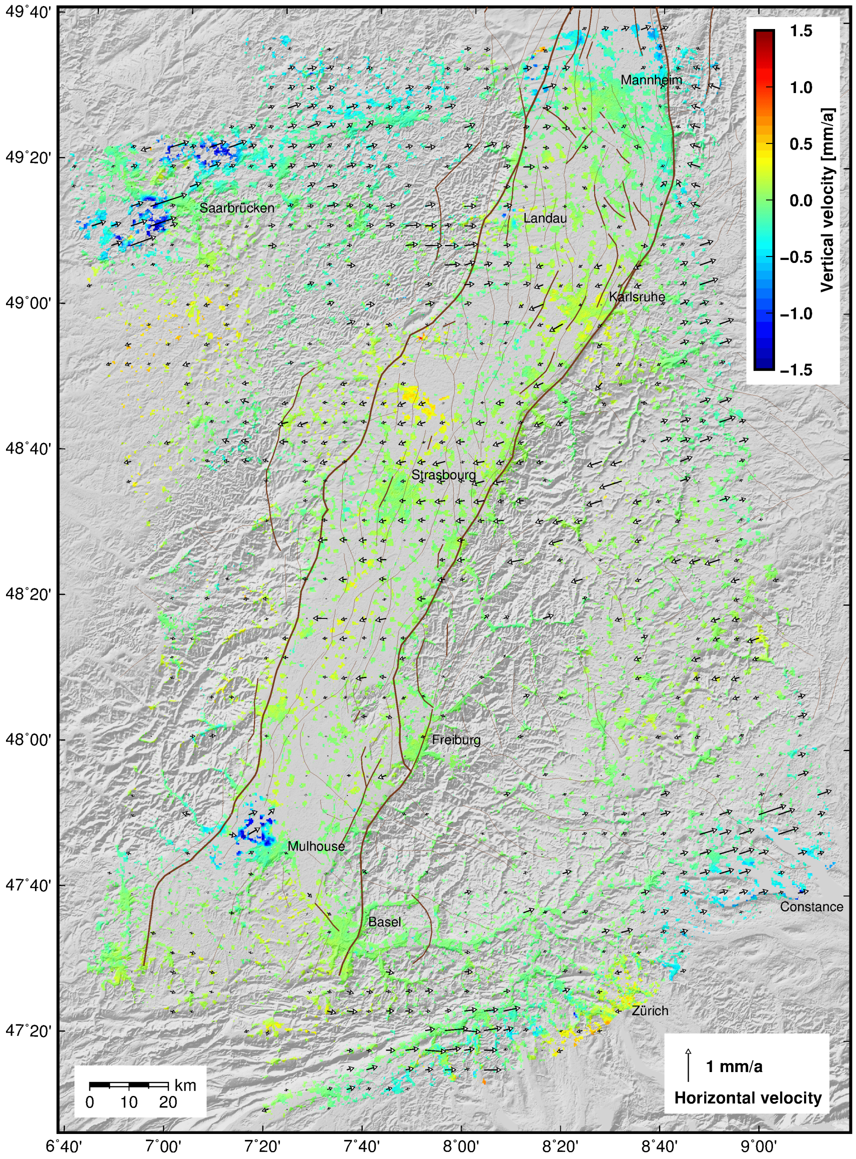

Figure D.3: Difference of the combined velocity field (Fig. 7.17) to the velocity field from levelling and GNSS, only (Fig. D.2): horizontal linear rates (arrows) and vertical linear rates (colour-coded). The horizontal velocity field is interpolated to a 5 km grid for visualisation purposes. Brown lines represent faults in the URG area after Peters (2007), main border faults (thick), active faults (medium thick) and other faults (thin). Grey background: shaded DEM using SRTM-3 data.

Bibliography

Adam, J., Augath, W., Brouwer, F., Engelhardt, G., Gurtner, W., Harsson, B. G., Ihde, J., Ineichen, D., Lang, H., Luthardt, J., Sacher, M., Schlüter, W., Springer, T., & Wöppelmann, G. (2000). Status and development of the European height systems. In Schwarz, K.-P., editor, *Geodesy Beyond 2000*, volume 121 of *International Association of Geodesy Symposia*, pages 55–60. Springer, Berlin Heidelberg, Germany.

Adam, N., Kampes, B. M., Eineder, M., Worawattanamateekul, J., & Kircher, M. (2003). The Development of a Scientific Permanent Scatterer System. In Schroeder, M., Jacobsen, K., & Heipke, C., editors, *Proceedings of the Joint ISPRS/EARSeL Workshop "High Resolution Mapping from Space 2003", Hannover, Germany, 6–8 Oct 2003*, pages 1–6.

AdV (1995). *Deutsches Haupthöhennetz 1992 (DHHN 92)*. Arbeitsgemeinschaft der Vermessungsverwaltungen der Länder der Bundesrepublik Deutschland (AdV), Bayerisches Landesvermessungsamt, Munich, Germany.

AdV (2009). *Feldanweisung für die Präzisionsnivellements zur Erneuerung und Wiederholung des Deutschen Haupthöhennetzes (DHHN) im Zeitraum 2006 bis 2011*. Arbeitsgemeinschaft der Vermessungsverwaltungen der Länder der Bundesrepublik Deutschland (AdV), Germany.

AdV (2014). Richtlinie für den einheitlichen integrierten geodätischen Raumbezug des amtlichen Vermessungswesens in der Bundesrepublik Deutschland. PDF file, available online at `http://www.adv-online.de/AdV-Produkte/Festpunkte`, Germany. Last checked on 2015-10-16.

Agram, P. S. (2010). *Persistent scatterer interferometry in natural terrain*. PhD thesis, Stanford University, California, USA.

Ahorner, L. (1975). Present-day stress field and seismotectonic block movements along major fault zones in Central Europe. *Tectonophysics*, 29(1-4):233–249.

Ahorner, L., Baier, B., & Bonjer, K.-P. (1983). General pattern of seismotectonic dislocation and the earthquake – Generating stress field in central Europe between the Alps and the North Sea. In Fuchs, K., von Gehlen, K., Mälzer, H., Murawski, H., & Semmel, A., editors, *Plateau Uplift: The Rhenish Shield – A Case History*, pages 187–197. Springer, Berlin, Germany.

Aktuğ, B. & Yıldırım, O. (2013). Regularized estimation of Euler pole parameters. *Earth, Planets and Space*, 65(7):699–705.

Alshawaf, F. (2013). *Constructing water vapor maps by fusing InSAR, GNSS and WRF data*. PhD thesis, Karlsruhe Institute of Technology.

Alshawaf, F., Fersch, B., Hinz, S., Kunstmann, H., Mayer, M., & Meyer, F. J. (2015a). Water vapor mapping by fusing InSAR and GNSS remote sensing data and atmospheric simulations. *Hydrology and Earth System Sciences Discussions*, 12(1):363–404.

Alshawaf, F., Fuhrmann, T., Knöpfler, A., Luo, X., Mayer, M., Hinz, S., & Heck, B. (2015b). Accurate Estimation of Atmospheric Water Vapor Using GNSS Observations and Surface Meteorological Data. *IEEE Transactions on Geoscience and Remote Sensing*, 53(7):3764–3771.

Alshawaf, F., Hinz, S., Mayer, M., & Meyer, F. J. (2015c). Constructing accurate maps of atmospheric water vapor by combining interferometric synthetic aperture radar and GNSS observations. *Journal of Geophysical Research: Atmospheres*, 120(4):1391–1403.

Altamimi, Z., Boucher, C., & Sillard, P. (2007a). CATREF Software – Combination and Analysis of Terrestrial Reference Frames. Technical manual, available online at `http://grgs.obs-mip.fr`, Institut National de l'Information Géographique et Forestière (IGN), Paris, France. Last checked on 2015-11-09.

Altamimi, Z., Collilieux, X., Legrand, J., Garayt, B., & Boucher, C. (2007b). ITRF2005: A new release of the International Terrestrial Reference Frame based on time series of station positions and Earth Orientation Parameters. *Journal of Geophysical Research: Solid Earth*, 112(B9):1–19.

Altamimi, Z., Métivier, L., & Collilieux, X. (2012). ITRF2008 plate motion model. *Journal of Geophysical Research: Solid Earth*, 117(B7):1–14.

Amelung, F., Jónsson, S., Zebker, H. A., & Segall, P. (2000). Widespread uplift and 'trapdoor' faulting on Galápagos volcanoes observed with radar interferometry. *Nature*, 407:993–996.

Argus, D. F. & Peltier, W. R. (2010). Constraining models of postglacial rebound using space geodesy: a detailed assessment of model ICE-5G (VM2) and its relatives. *Geophysical Journal International*, 181(2):697–723.

Arıkan, M., Hooper, A., & Hanssen, R. F. (2010). Radar Time Series Analysis over West Anatolia. In Lacoste, H., editor, *Proceedings of Fringe 2009 Workshop, Frascati, Italy, 30 November – 4 December 2009*, ESA Publications SP-677, pages 1–6.

Aschbacher, J. & Milagro-Pérez, M. P. (2012). The European Earth monitoring (GMES) programme: Status and perspectives. *Remote Sensing of Environment*, 120:3–8.

Aufranc, A. (2000). Mesure de la déformation crustale dans le fossé rhénan par comparaison de mesures GPS/triangulation. Master's thesis, University of Strasbourg, France.

Baarda, W. (1968). *A Testing Procedure for Use in Geodetic Networks*. Publications on Geodesy, volume 2(5). Netherlands Geodetic Commission, Delft, The Netherlands.

Baden (1885). *Die Grossh. Badischen Haupt-Nivellements mit den Anschlüssen an die Nachbarstaaten*. Oberdirektion des Wasser- und Straßenbaues, Braun, Karlsruhe, Germany.

Bähr, H. (2013). *Orbital Effects in Spaceborne Synthetic Aperture Radar Interferometry*. German Geodetic Commission (Deutsche Geodätische Kommission, DGK), series C 719. Bavarian Academy of Sciences and Humanities, Munich, Germany.

Bähr, H., Altamimi, Z., & Heck, B. (2007). *Variance Component Estimation for Combination of Terrestrial Reference Frames*. Schriftenreihe des Studiengangs Geodäsie und Geoinformatik, 2007-6. University of Karlsruhe, Germany.

Bähr, H. & Hanssen, R. F. (2012). Reliable estimation of orbit errors in spaceborne SAR interferometry. *Journal of Geodesy*, 86(12):1147–1164.

Bähr, H., Samiei-Esfahany, S., & Hanssen, R. F. (2012). On the effect of reference frame motion on InSAR deformation estimates. In Ouwehand, L., editor, *Proceedings of Fringe 2011 Workshop, Frascati, Italy, 19–23 September 2011*, ESA Publications SP-697, pages 1–8.

Baillieux, P., Schill, E., Edel, J.-B., & Mauri, G. (2013). Localization of temperature anomalies in the Upper Rhine Graben: insights from geophysics and neotectonic activity. *International Geology Review*, 55(14):1744–1762.

Bamler, R. & Just, D. (1993). Phase statistics and decorrelation in SAR interferograms. In *Geoscience and Remote Sensing Symposium, 1993. IGARSS '93. Better Understanding of Earth Environment., International*, volume 3, pages 980–984.

Banach, A. (2009). Le bassin houiller de Ronchamp. Website, available online at `http://lorraine.charbon.free.fr`, France. Last checked on 2015-07-22.

Barth, A. & Ritter, J. (2010). Seismicity pattern and magnitude frequencies of the Upper Rhinegraben. In *Proceedings of the 95th Journées Luxembourgeoises de Géodynamique, Echternach, Grand Duchy of Luxembourg, 9–11 November 2009*, pages 1–5.

Barth, A., Ritter, J., & Wenzel, F. (2015). Spatial variations of earthquake occurrence and coseismic deformation in the Upper Rhine Graben, Central Europe. *Tectonophysics*, 651-652(0):172–185.

Bartz, J. (1974). Die Mächtigkeit des Quartärs im Oberrheingraben. In Illies, J. H. & Fuchs, K., editors, *Approaches to Taphrogenesis, Proceedings of an International Rift Symposium held in Karlsruhe April 13–15, 1972*, pages 78–87. Schweizerbart, Stuttgart, Germany.

Baumann, H. (1981). Regional stress field and rifting in Western Europe. *Tectonophysics*, 73(1-3):105–111.

Beckers, H. (1983). Influence of Magnetism on Precise Levelling – Shown in the RhinRhine-Palatinate Part of the German First Order Levelling network. In Pelzer, H. & Niemeier, W., editors, *Precise Levelling – Contributions to the Workshop on Precise Levelling*, pages 67–83. Dümmler, Bonn, Germany.

Bedford, L., Brown, N., & Walford, J. (2009). New 3D four constellation high performance wideband choke ring antenna. In *Proceedings of ION GNSS 2009, Anaheim, USA, 26–28 Jan 2009*, pages 829–835.

Behrmann, J. H., Hermann, O., Horstmann, M., Tanner, D. C., & Bertrand, G. (2003). Anatomy and kinematics of oblique continental rifting revealed: A three-dimensional case study of the southeast Upper Rhine graben (Germany). *AAPG Bulletin*, 87(7):1105–1121.

Behrmann, J. H., Ziegler, P. A., Schmid, S. M., Heck, B., & Granet, M. (2005). The EUCOR-URGENT Project. *International Journal of Earth Sciences*, 94(4):505–506.

Bekaert, D., Hooper, A., & Wright, T. J. (2015a). A spatially variable power law tropospheric correction technique for InSAR data. *Journal of Geophysical Research: Solid Earth*, 120(2):1345–1356.

Bekaert, D., Walters, R. J., Wright, T. J., Hooper, A., & Parker, D. J. (2015b). Statistical comparison of InSAR tropospheric correction techniques. *Remote Sensing of Environment*, 170:40–47.

Benoît, P. & Bailly-Maître, M.-C. (1997). Les mines d'argent de la France médiévale. In *Actes des congrès de la Société des historiens médiévistes de l'enseignement supérieur public. 28e congrès, Clermont-Ferrand, France 1997. L'argent au Moyen Âge*, volume 28(1), pages 17–45. Société des Historiens Médiévistes de l'Enseignement Supérieur Public.

Berardino, P., Fornaro, G., Lanari, R., & Sansosti, E. (2002). A new algorithm for surface deformation monitoring based on small baseline differential SAR interferograms. *IEEE Transactions on Geoscience and Remote Sensing*, 40(11):2375–2383.

Berndt (1930). *Ergebnisse der Feineinwägungen – Vorheft*. Reichsamt für Landesaufnahme, Berlin, Germany.

Beutler, G., Bauersima, I., Gurtner, W., Rothacher, M., Schildknecht, T., & Geiger, A. (1988). Atmospheric refraction and other important biases in GPS carrier phase observations. In Brunner, F., editor, *Monograph 12, "Atmospheric Effects on Geodetic Space Measurements"*, volume 22, pages 15–44. School of Geomatic Engineering (formerly Surveying) , The University of New South Wales, Australia.

Bevis, M., Businger, S., Chiswell, S., Herring, T. A., Anthes, R. A., Rocken, C., & Ware, R. H. (1994). GPS Meteorology: Mapping Zenith Wet Delays onto Precipitable Water. *Journal of Applied Meteorology*, 3:379–386.

Bevis, M., Businger, S., Herring, T. A., Rocken, C., Anthes, R. A., & Ware, R. H. (1992). GPS meteorology: Remote sensing of atmospheric water vapor using the global positioning system. *Journal of Geophysical Research: Atmospheres*, 97(D14):15787–15801.

BGS (2015). OneGeology. Website, available online at `http://portal.onegeology.org`, British Geological Survey (BGS), Nottingham, United Kingdom. Last checked on 2015-11-13.

Bilich, A. & Larson, K. M. (2007). Mapping the GPS multipath environment using the signal-to-noise ratio (SNR). *Radio Science*, 42(6):1–16.

Billiris, H., Paradissis, D., Veis, G., England, P., Featherstone, W., Parsons, B., Cross, P., Rands, P., Rayson, M., Sellers, P., Ashkenazi, V., Davison, M., Jackson, J., & Ambraseys, N. (1991). Geodetic determination of tectonic deformation in central Greece from 1900 to 1988. *Nature*, 350:124–129.

Bogdanova, S., Bingen, B., Gorbatschev, R., Kheraskova, T. N., Kozlov, V. I., Puchkov, V. N., & Volozh, Y. A. (2008). The East European Craton (Baltica) before and during the assembly of Rodinia. *Precambrian Research*, 160(1-2):23–45.

Böhm, J., Werl, B., & Schuh, H. (2006). Troposphere mapping functions for GPS and very long baseline interferometry from European Centre for Medium-Range Weather Forecasts operational analysis data. *Journal of Geophysical Research: Solid Earth*, 111(B2):1–9.

Böhme, M., Aiglstorfer, M., Uhl, D., & Kullmer, O. (2012). The Antiquity of the Rhine River: Stratigraphic Coverage of the Dinotheriensande (Eppelsheim Formation) of the Mainz Basin (Germany). *Plos One*, 7(e36817):1–15.

Bonjer, K.-P. (1997). Seismicity pattern and style of seismic faulting at the eastern borderfault of the southern Rhine Graben. *Tectonophysics*, 275(1-3):41–69.

Bonjer, K.-P., Gelbke, C., Gilg, B., Rouland, D., Mayer-Rosa, D., , & Massinon, B. (1984). Seismicity and Dynamics of the Upper Rhinegraben. *Journal of Geophysics*, 55:1–12.

Bonnet, C., Malavieille, J., & Mosar, J. (2007). Interactions between tectonics, erosion, and sedimentation during the recent evolution of the Alpine orogen: Analogue modeling insights. *Tectonics*, 26(6):1–15.

Boucher, C., Altamimi, Z., & Duhem, L. (1993). ITRF 92 and its associated velocity field. IERS Technical Note 15, Central Bureau of IERS – Observatoire de Paris, France.

Bozorgzadeh, G. & Kuntz, E. (1974). Geodätische Messungen im Rheingraben. In Illies, J. H. & Fuchs, K., editors, *Approaches to Taphrogenesis, Proceedings of an International Rift Symposium held in Karlsruhe April 13–15, 1972*, pages 95–99. Schweizerbart, Stuttgart, Germany.

Brinkhoff, T. (2015). citypopulation. Website, available online at `http://www.citypopulation.de`, Oldenburg, Germany. Last checked on 2015-06-24.

Broyden, C. G. (1970). The Convergence of a Class of Double-rank Minimization Algorithms 1. General Considerations. *IMA Journal of Applied Mathematics*, 6(1):76–90.

Brüstle, W. & Stange, S. (2005). Seismic bulletin of Baden-Württemberg, 2004. Technical report, Landesamt für Geologie, Rohstoffe und Bergbau, Baden-Württemberg, Freiburg, Germany.

Buchmann, T. J. & Connolly, P. T. (2007). Contemporary kinematics of the Upper Rhine Graben: A 3D finite element approach. *Global and Planetary Change*, 58(1-4):287–309.

Busch, W. & Linke, J. (2014). Räumliche Höhenänderungsanalyse auf Grundlage einer automatisierten Ausgleichung massenhaft vorliegender PSI-Zeitreihen mittels orthogonaler Polynome. *Allgemeine Vermessungsnachrichten*, 121(8-9):298–310.

Calais, E. & Stein, S. (2009). Time-Variable Deformation in the New Madrid Seismic Zone. *Science*, 323(5920):1442–1442.

Caro Cuenca, M. (2012). *Improving radar interferometry for monitoring fault-related surface deformation*. PhD thesis, Delft University of Technology, The Netherlands.

Caro Cuenca, M., Hanssen, R. F., Hooper, A., & Arikan, M. (2012). Surface Deformation of the Whole Netherlands After PSI Analysis. In Ouwehand, L., editor, *Proceedings of Fringe 2011 Workshop, Frascati, Italy, 19–23 September 2011*, ESA Publications SP-697, pages 1–8.

Caro Cuenca, M., Samiei-Esfahany, S., & Hanssen, R. F. (2010). A least squares approach for joining Persistent Scatterer InSAR time series acquired by different satellites. In Lacoste-Francis, H., editor, *Proc. of ESA Living Planet Symposium, Bergen, Norway, 28 June – 2 July 2010*, ESA Publications SP-686, pages 1–8.

Catalão, J., Nico, G., Hanssen, R. F., & Catita, C. (2010). Integration of InSAR and GPS for Vertical Deformation Monitoring: A Case Study in Faial and Pico Islands. In Lacoste, H., editor, *Proceedings of Fringe 2009 Workshop, Frascati, Italy, 30 November – 4 December 2009*, ESA Publications SP-677, pages 1–6.

Chen, C. W. & Zebker, H. A. (2000). Network approaches to two-dimensional phase unwrapping: intractability and two new algorithms. *Journal of the Optical Society of America A*, 17(3):401–414.

Choi, K., Bilich, A., Larson, K. M., & Axelrad, P. (2004). Modified sidereal filtering: Implications for high-rate GPS positioning. *Geophysical Research Letters*, 31(22):1–4. L22608.

Cohen, K. M., Finney, S. M., Gibbard, P., & Fan, J.-X. (2013). The ICS International Chronostratigraphic Chart. *Episodes*, 36(3):199–204.

Colesanti, C., Ferretti, A., Novali, F., Prati, C., & Rocca, F. (2003). SAR monitoring of progressive and seasonal ground deformation using the permanent scatterers technique. *IEEE Transactions on Geoscience and Remote Sensing*, 41(7):1685–1701.

Crowley, K. & Elliott, J. R. (2012). Earthquake disasters and resilience in the global North: lessons from New Zealand and Japan. *The Geographical Journal*, 178(3):208–215.

Curlander, J. C. & McDonough, R. N. (1992). *Synthetic Aperture Radar: Systems and Signal Processing*. John Wiley & Sons, New Jersey, USA.

Dach, R., Hugentobler, U., Fridez, P., & Meindl, M. (2007). *User manual of the Bernese GPS Software Version 5.0*. Astronomical Institute, University of Bern, Switzerland.

Davis, J. L., Wernicke, B. P., & Tamisiea, M. E. (2012). On seasonal signals in geodetic time series. *Journal of Geophysical Research: Solid Earth*, 117(B1):1–10.

Demoulin, A., Launoy, T., & Zippelt, K. (1998). Recent crustal movements in the southern Black Forest (western Germany). *Geologische Rundschau*, 87:43–52.

DEOS (2008). Delft Institute for Earth-oriented Space Research. Website, available online at `http://www.deos.tudelft.nl/ers/precorbs/orbits`, Delft, The Netherlands. Last checked on 2015-12-07.

Deumlich, F. & Staiger, R. (2002). *Instrumentenkunde der Vermessungstechnik*. Wichmann, Heidelberg, Germany, 9th edition.

Dèzes, P., Schmid, S. M., & Ziegler, P. A. (2004). Evolution of the European Cenozoic Rift System: interaction of the Alpine and Pyrenean orogens with their foreland lithosphere. *Tectonophysics*, 389(1-2):1–33.

Dheenathayalan, P. & Hanssen, R. F. (2011). Target Characterization and Interpretation of Deformation using Persistent Scatterer Interferometry and Polarimetry. In Lacoste-Francis, H., editor, *Proceedings of the 5th International Workshop on Science and Applications of SAR Polarimetry and Polarimetric Interferometry, Frascati, Italy, 24–28 January 2011*, ESA Publications SP-695, pages 1–8.

Dheenathayalan, P. & Hanssen, R. F. (2013). Radar target type classification and validation. In *Geoscience and Remote Sensing Symposium (IGARSS), 2013 IEEE International*, pages 923–926.

DIN (1996). DIN 18717: Präzisions-Nivellierlatten. Technical report, Deutsches Institut für Normung (German Institute for Standardisation), Beuth GmbH, Berlin, Germany.

Doebl, F. & Olbrecht, W. (1974). An Isobath Map of the Tertiary Base in the Rhinegraben. In Illies, J. H. & Fuchs, K., editors, *Approaches to Taphrogenesis, Proceedings of an International Rift Symposium held in Karlsruhe April 13–15, 1972*, pages 71–72. Schweizerbart, Stuttgart, Germany.

Doerry, A. W. (2006). SAR processing with stepped chirps and phased array antennas. Technical Report SAND2006-5855, Sandia National Laboratories, Albuquerque and Livermore, USA.

DORIS (2008). *Delft Object-oriented Radar Interferometric Software – User's manual and technical documentation*. Delft Institute of Earth Observation and Space Systems, Delft University of Technology, The Netherlands.

Duquenne, H., Duquenne, F., Harmel, A., Rebischung, P., & Coulomb, A. (2007). Status of the zero-order levelling network of France and consequences for UELN. Presentation at EUREF Symposium 2007, London, UK, available online at `http://www.euref.eu/symposia/2007London/02-02-duquenne.pdf`. Last checked on 2015-10-16.

ECMWF (2015). European Centre for Medium-Range Weather Forecasts. Website, available online at `http://www.ecmwf.int`, Reading, United Kingdom. Last checked on 2015-12-17.

Egelkraut, U. (2014). Egelkraut Vermessungsartikel. Website, available online at `http://www.vermessungsartikel.de/Praezisions-Nivellier-Zeiss-NI-3`, Saara, Germany. Last checked on 2015-09-17.

Egli, R., Geiger, A., Wiget, A., & Kahle, H.-G. (2007). A modified least-squares collocation method for the determination of crustal deformation: first results in the Swiss Alps. *Geophysical Journal International*, 168(1):1–12.

Eineder, M. (2003). Efficient simulation of SAR interferograms of large areas and of rugged terrain. *IEEE Transactions on Geoscience and Remote Sensing*, 41(6):1415–1427.

Eisbacher, G. H. (1996). *Einführung in die Tektonik*. Enke, Stuttgart, Germany, 2nd edition.

Eisbacher, G. H. & Fielitz, W. (2010). *Karlsruhe und seine Region: Nordschwarzwald, Kraichgau, Neckartal, Oberrhein-Graben, Pfälzerwald und westliche Schwäbische Alb*. Sammlung geologischer Führer, number 103. Borntraeger, Stuttgart, Germany, 6th edition.

Engesser, W., Ruch, C., & Wirsing, G. (2010). Geologische Untersuchungen von Baugrundhebungen im Bereich des Erdwärmesondenfeldes beim Rathaus in der historischen Altstadt von Staufen i. Br. Technical report, Landesamt für Geologie, Rohstoffe und Bergbau, Baden-Württemberg, Freiburg, Germany.

EOLi (2015). Earth Observation Link, ESA's client for Earth Observation Catalogue and Ordering Services. Website, available online at `https://earth.esa.int/web/guest/eoli`, European Space Agency (ESA), Frascati, Italy. Last checked on 2015-12-07.

EOST (2015). École et observatoire des sciences de la Terre, University of Strasbourg. Website, available online at `https://eost.unistra.fr/observatoires/geodesie-et-gravimetrie/renag-eost`, Strasbourg, France. Last checked on 2015-11-19.

EPN (2015). EUREF Permanent Network. Website, available online at `http://www.epncb.oma.be`, Royal Observatory of Belgium, Brussels, Belgium. Last checked on 2015-11-19.

Ermery, H. (1960). *Correspondance entre les nivellements de base français et prussian en Alsace et en Lorraine et son interpretation géologique*. PhD thesis, University of Strasbourg.

ESA (2006). *European Space Agency – MERIS Product Handbook*. Frascati, Italy.

ESA (2015). ESA eoPortal. Website, available online at `https://directory.eoportal.org`, Frascati, Italy. Last checked on 2015-12-04.

Even, M. (2015). Advanced InSAR Processing in the Footsteps of SqueeSAR. In Ouwehand, L., editor, *Proceedings of Fringe 2015 Workshop, Frascati, Italy, 23–27 March 2015*, ESA Publications SP-731, pages 1–6.

Fäh, D., Gisler, M., Jaggi, B., Kästli, P., Lutz, T., Masciadri, V., Matt, C., Mayer-Rosa, D., Rippmann, D., Schwarz-Zanetti, G., Tauber, J., & Wenk, T. (2009). The 1356 Basel earthquake: an interdisciplinary revision. *Geophysical Journal International*, 178(1):351–374.

Fan, K. & Ding, X. (2006). Estimation of GPS Carrier Phase Multipath Signals Based on Site Environment. *Journal of Global Positioning Systems*, 5(1-2):22–28.

Fattahi, H. & Amelung, F. (2014). InSAR uncertainty due to orbital errors. *Geophysical Journal International*, 199(1):549–560.

Ferhat, G., Meghraoui, M., Masson, F., Henrion, E., & Ulrich, P. (2015). Combined leveling, triangulation and survey-mode GPS data in the southern Upper Rhine Graben: a review of centennial-old data to estimate crustal deformation. Presented at International Colloquium on Major Historical Earthquakes of the Rhine Graben Interplate – Intraplate Continental Deformation, May 11–13, 2015, Strasbourg, France.

Ferretti, A., Fumagalli, A., Novali, F., Prati, C., Rocca, F., & Rucci, A. (2011). A New Algorithm for Processing Interferometric Data-Stacks: SqueeSAR. *IEEE Transactions on Geoscience and Remote Sensing*, 49(9):3460–3470.

Ferretti, A., Prati, C., & Rocca, F. (2000). Nonlinear subsidence rate estimation using permanent scatterers in differential SAR interferometry. *IEEE Transactions on Geoscience and Remote Sensing*, 38(5):2202–2212.

Ferretti, A., Prati, C., & Rocca, F. (2001). Permanent scatterers in SAR interferometry. *IEEE Transactions on Geoscience and Remote Sensing*, 39(1):8–20.

Fialko, Y., Sandwell, D., Simons, M., & Rosen, P. (2005). Three-dimensional deformation caused by the Bam, Iran, earthquake and the origin of shallow slip deficit. *Nature*, 435:295–299.

Fletcher, R. (1970). A new approach to variable metric algorithms. *The Computer Journal*, 13(3):317–322.

Förstner, W. (1979). Ein Verfahren zur Schätzung von Varianz- und Kovarianzkomponenten. *Allgemeine Vermessungsnachrichten*, 86(11-12):446–453.

Frietsch, M., Groos, J. C., & Ritter, J. (2015). Detection and Delineation of a Fracture Zone with Observation of Seismic Shear Wave Anisotropy in the Upper Rhine Graben, SW Germany. *Pure and Applied Geophysics*, 172(2):267–282.

Frisch, W., Meschede, M., & Blakey, R. (2011). *Plate tectonics – continental drift and mountain building*. Springer, Berlin Heidelberg, Germany.

Fuhrmann, T., Caro Cuenca, M., Knöpfler, A., van Leijen, F. J., Mayer, M., Westerhaus, M., Hanssen, R. F., & Heck, B. (2015a). Combining InSAR, Levelling and GNSS for the Estimation of 3D Surface Displacements. In Ouwehand, L., editor, *Proceedings of Fringe 2015 Workshop, Frascati, Italy, 23–27 March 2015*, ESA Publications SP-731, pages 1–8.

Fuhrmann, T., Caro Cuenca, M., Knöpfler, A., van Leijen, F. J., Mayer, M., Westerhaus, M., Hanssen, R. F., & Heck, B. (2015b). Estimation of small surface displacements in the Upper Rhine Graben area from a combined analysis of PS-InSAR, levelling and GNSS data. *Geophysical Journal International*, 203(1):614–631.

Fuhrmann, T., Heck, B., Knöpfler, A., Masson, F., Mayer, M., Ulrich, P., Westerhaus, M., & Zippelt, K. (2013a). Recent surface displacements in the Upper Rhine Graben – Preliminary results from geodetic networks. *Tectonophysics*, 602(0):300–315.

Fuhrmann, T., Knöpfler, A., Luo, X., Mayer, M., & Heck, B. (2010a). *Zur GNSS-basierten Bestimmung des atmosphärischen Wasserdampfgehalts mittels Precise Point Positioning*. Schriftenreihe des Studiengangs Geodäsie und Geoinformatik, 2010-2. KIT Scientific Publishing, Karlsruhe, Germany.

Fuhrmann, T., Knöpfler, A., Mayer, M., Schenk, A., Westerhaus, M., Zippelt, K., & Heck, B. (2013b). Towards a Fusion of SAR-Interferometry, GNSS and Precise Levelling in the Upper Rhine Graben Area, Southwest Germany. In Ouwehand, L., editor, *Proceedings of ESA Living Planet Symposium, Edinburgh, United Kingdom, 9–13 September 2013*, ESA Publications SP-722, pages 1–8.

Fuhrmann, T., Knöpfler, A., Mayer, M., Schenk, A., Westerhaus, M., Zippelt, K., & Heck, B. (2015c). An Inventory of Surface Movements in the Upper Rhine Graben area, Southwest Germany, from SAR-Interferometry, GNSS and Precise Levelling. In *International Association of Geodesy Symposia*, pages 1–7. Springer, Berlin Heidelberg, Germany.

Fuhrmann, T., Knöpfler, A., Luo, X., & Mayer, M. (2010b). Zum Stacking von Phasenresiduen aus GNSS-Auswertungen mittels Precise Point Positioning. In Zippelt, K., editor, *Vernetzt und ausgeglichen: Festschrift zur Verabschiedung von Prof. Dr.-Ing. habil. Dr.-Ing. E.h. Günter Schmitt*, Schriftenreihe des Studiengangs Geodäsie und Geoinformatik, 2010-3, pages 77–87. KIT Scientific Publishing, Karlsruhe, Germany.

Fuhrmann, T., Luo, X., Knöpfler, A., & Mayer, M. (2015d). Generating statistically robust multipath stacking maps using congruent cells. *GPS Solutions*, 19(1):83–92.

Fuhrmann, T., Westerhaus, M., Zippelt, K., & Heck, B. (2014a). Vertical displacement rates in the Upper Rhine Graben area derived from precise leveling. *Journal of Geodesy*, 88(8):773–787.

Fuhrmann, T. & Zippelt, K. (2013). Berechnung und Beurteilung rezenter vertikaler Oberflächenbewegungen abgeleitet aus wiederholten Präzisionsnivellements in den Regionen Nordschweiz und Südwestdeutschland. Work report NAB 12-33, National Cooperative for the Disposal of Radioactive Waste (Nagra), Wettingen, Switzerland.

Fuhrmann, T., Zippelt, K., & Heck, B. (2014b). Historische Nivellements aus Preußen und Baden und ihre Bedeutung für die Bestimmung von Vertikalbewegungen im Oberrheingrabengebiet. *Zeitschrift für Vermessungswesen*, 6:389–397.

Gabriel, A. K., Goldstein, R. M., & Zebker, H. A. (1989). Mapping small elevation changes over large areas: Differential radar interferometry. *Journal of Geophysical Research: Solid Earth*, 94(B7):9183–9191.

Gassner, G. L. & Ruland, R. E. (2006). The SLAC Comparator for the Calibration of Digital Leveling Equipment. In Fuss, B., editor, *Proceedings of 9th International Workshop on Accelerator Alignment, 25–29 September 2006, Menlo Park, USA*, pages 1–11.

Gassner, G. L., Ruland, R. E., & Dix, B. (2004). Investigations of Digital Levels at the SLAC Vertical Comparator. In *8th International Workshop on Accelerator Alignment, CERN, Geneva, 4–7 October 2004*, pages 1–10.

Gaßner, L., Groos, J. C., & Ritter, J. (2014). Herdflächenanalyse induzierter Erdbeben in der Südpfalz. *Mainzer geowissenschaftliche Mitteilungen*, 42:195–214.

Gazeaux, J., Williams, S., King, M., Bos, M., Dach, R., Deo, M., Moore, A. W., Ostini, L., Petrie, E., Roggero, M., Teferle, F. N., Olivares, G., & Webb, F. H. (2013). Detecting offsets in GPS time series: First results from the detection of offsets in GPS experiment. *Journal of Geophysical Research: Solid Earth*, 118(5):2397–2407.

Ge, M., Gendt, G., Rothacher, M., Shi, C., & Liu, J. (2008). Resolution of GPS carrier-phase ambiguities in Precise Point Positioning (PPP) with daily observations. *Journal of Geodesy*, 82(7):389–399.

GeORG (2013). Geopotenziale des tieferen Untergrundes im Oberrheingraben – Fachlich-Technischer Abschlussbericht. Technical report, Landesamt für Geologie, Rohstoffe und Bergbau, Baden-Württemberg (Freiburg, Germany), Landesamt für Geologie und Bergbau, Rheinland-Pfalz (Mainz, Germany), Bureau de Recherches Géologiques et Minières (Orléans et Strasbourg, France), Abteilung Angewandte & Umweltgeologie (University of Basel, Switzerland).

Gessler, J. (1983). Some Results of the Determination of the Geomagnetic Influence on Automatic Level Instruments. In Pelzer, H. & Niemeier, W., editors, *Precise Levelling – Contributions to the Workshop on Precise Levelling*, pages 109–118. Dümmler, Bonn, Germany.

Geyer, O., Nitsch, E., & Simon, T. (2011). *Geologie von Baden-Württemberg*. Schweizerbart, Stuttgart, Germany, 5th edition.

GFSC (2012). Rhin supérieur faits et chiffres – Oberrhein Zahlen und Fakten. Technical report, Statistical offices in the framework of the working group "economic policy" of the German-French-Swiss Conference (GFSC) of the Upper Rhine, Kehl, Germany.

Ghitau, D. (1970). *Modellbildung und Rechenpraxis bei der nivellitischen Bestimmung säkularer Landhebungen*. PhD thesis, University of Bonn, Germany.

Goldfarb, D. (1970). A family of variable-metric methods derived by variational means. *Mathematics of Computation*, 24:23–26.

Goldstein, R. M. & Werner, C. L. (1998). Radar interferogram filtering for geophysical applications. *Geophysical Research Letters*, 25(21):4035–4038.

Goldstein, R. M., Zebker, H. A., & Werner, C. L. (1988). Satellite radar interferometry: Two-dimensional phase unwrapping. *Radio Science*, 23(4):713–720.

Gong, W., Meyer, F. J., Liu, S., & Hanssen, R. F. (2015). Temporal Filtering of InSAR Data Using Statistical Parameters From NWP Models. *IEEE Transactions on Geoscience and Remote Sensing*, 53(7):4033–4044.

González, P. J., Bagnardi, M., Hooper, A., Larsen, Y., Marinkovic, P., Samsonov, S. V., & Wright, T. J. (2015). The 2014-2015 eruption of Fogo volcano: Geodetic modeling of Sentinel-1 TOPS interferometry. *Geophysical Research Letters*, 42(21):9239–9246.

Görres, B., Campbell, J., Becker, M., & Siemes, M. (2006). Absolute calibration of GPS antennas: laboratory results and comparison with field and robot techniques. *GPS Solutions*, 10(2):136–145.

Gringarten, E. & Deutsch, C. V. (2001). Teacher's Aide Variogram Interpretation and Modeling. *Mathematical Geology*, 33(4):507–534.

Groos, J. C., Fritschen, R., & Ritter, J. (2013). Untersuchung induzierter Erdbeben hinsichtlich ihrer Spürbarkeit und eventueller Schadenswirkung anhand der DIN 4150. *Bauingenieur*, 88:374–384.

Grünthal, G., Stromeyer, D., & Wahlström, R. (2009a). Harmonization check of Mw within the central, northern, and northwestern European earthquake catalogue (CENEC). *Journal of Seismology*, 13(4):613–632.

Grünthal, G. & Wahlström, R. (2012). The European-Mediterranean Earthquake Catalogue (EMEC) for the last millennium. *Journal of Seismology*, 16(3):535–570.

Grünthal, G., Wahlström, R., & Stromeyer, D. (2009b). The unified catalogue of earthquakes in central, northern, and northwestern Europe (CENEC) – updated and expanded to the last millennium. *Journal of Seismology*, 13(4):517–541.

Gumbel, E. J. (2004). *Statistics of extremes*. Dover books on mathematics. Dover, New York, USA. Originally published: Columbia University Press, New York (1958).

Häge, M. & Joswig, M. (2009). Spatiotemporal distribution of aftershocks of the 2004 December 5 ML = 5.4 Waldkirch (Germany) earthquake. *Geophysical Journal International*, 178(3):1523–1532.

Hagiwara, Y. (1974). Focal processes and the prediction of earthquakes Probability of earthquake occurrence as obtained from a Weibull distribution analysis of crustal strain. *Tectonophysics*, 23(3):313–318.

Haimberger, R., Hoppe, A., & Schäfer, A. (2005). High-resolution seismic survey on the Rhine River in the northern Upper Rhine Graben. *International Journal of Earth Sciences*, 94(4):657–668.

Hamm, M. (2012). Bergmannsverein Buggingen. Website, available online at `http://www.bergmannsverein-buggingen.de`, Germany. Last checked on 2015-09-17.

Hanssen, R. F. (1998). *Atmospheric Heterogeneities in ERS Tandem SAR Interferometry*. Delft Univ. Press, Delft, The Netherlands.

Hanssen, R. F. (2001). *Radar Interferometry: Data Interpretation and Error Analysis*. Remote Sensing and Digital Image Processing. Kluwer Academic Publishers, Dordrecht, The Netherlands.

Hanssen, R. F., van Leijen, F. J., van Zwieten, G. J., Bremmer, C., Dortland, S., & Kleuskens, M. (2008). Validation of existing processing chains in TerraFirma stage 2; Product validation: Validation in the Amsterdam and Alkmaar area. GMES TerraFirma report, ESRIN/contract No. 19366/05/I-E, Delft University of Technology, The Netherlands, TNO, The Netherlands.

Hanssen, R. F., Weckwerth, T. M., Zebker, H. A., & Klees, R. (1999). High-Resolution Water Vapor Mapping from Interferometric Radar Measurements. *Science*, 283(5406):1297–1299.

Hardy, R. L. (1971). Multiquadric equations of topography and other irregular surfaces. *Journal of Geophysical Research*, 76(8):1905–1915.

Häring, M. O., Schanz, U., Ladner, F., & Dyer, B. C. (2008). Characterisation of the Basel 1 enhanced geothermal system. *Geothermics*, 37(5):469–495.

Hayford, J. & Baldwin, A. (1908). *The earth movements in the California earthquake of 1906*. Government Printing Office, USA.

Heck, B. (1981). Der Einfluß einzelner Beobachtungen auf das Ergebnis einer Ausgleichung und die Suche nach Ausreißern in den Beobachtungen. *Allgemeine Vermessungsnachrichten*, 88(1):17–34.

Heck, B. (1986). Sensitivitätsanalyse geodätischer Deformationsnetze. *Allgemeine Vermessungsnachrichten*, 93(5):169–181.

Heck, B. (2003). *Rechenverfahren und Auswertemodelle der Landesvermessung*. Wichmann, Heidelberg, Germany, 3rd edition.

Heck, B., Illner, M., & Jäger, R. (1995). Deformationsanalyse zum Testnetz Karlsruhe auf der Basis der terrestrischen Nullmessung und aktueller GPS-Kampagnen. In *Festschrift für Heinz Draheim zum 80. Geburtstag, Eugen Kuntz zum 70. Geburtstag, Hermann Mälzer zum 70. Geburtstag*, pages 75–91. Geodetic Institute, University of Karlsruhe, Germany.

Heck, B. & Mälzer, H. (1983a). Determination of Vertical Recent Crustal Movements by Levelling and Gravity Data. In Pelzer, H. & Niemeier, W., editors, *Precise Levelling – Contributions to the Workshop on Precise Levelling*, pages 435–448. Dümmler, Bonn, Germany.

Heck, B. & Mälzer, H. (1983b). Determination of vertical recent crustal movements by levelling and gravity data. *Tectonophysics*, 97(1-4):251–264.

Heckmann, B., Berg, G., Heitmann, S., Jahn, C.-H., Klauser, B., Liebsch, G., & Liebscher, R. (2015). Der bundeseinheitliche geodätische Raumbezug – integriert und qualitätsgesichert. *Zeitschrift für Vermessungswesen*, 3/2015:180–184.

Heer, R. (1983). Application of different refraction models on measuring results of the levelling test loop Koblenz. In Pelzer, H. & Niemeier, W., editors, *Precise Levelling – Contributions to the Workshop on Precise Levelling*, pages 251–281. Dümmler, Bonn, Germany.

Heidbach, O., Tingay, M., Barth, A., Reinecker, J., Kurfeß, D., & Müller, B. (2008). The World Stress Map database release 2008. Website, available online at `http://dc-app3-14.gfz-potsdam.de`, GFZ German Research Centre for Geosciences, Potsdam, Germany. Last checked on 2015-06-26.

Heinz, J. (2012). Geschichte des Bergbaus an der Saar. In Kurtz, H. P. & Backes, H., editors, *Der Bergbau an der Saar*, Arbeitnehmer – Zeitschrift der Arbeitskammer des Saarlandes, pages 3–10. Arbeitskammer des Saarlandes, Germany.

Heiskanen, W. A. & Moritz, H. (1967). *Physical geodesy*. Freeman, San Francisco, USA.

Heister, H., Woschitz, H., & Brunner, F. K. (2005). Präzisionsnivellierlatten, Komponenten- oder Systemkalibrierung? *Allgemeine Vermessungsnachrichten*, 6:233–238.

Heller, E. & Wernthaler, R. (1955). *Entwicklung und Genauigkeit des neuen deutschen Haupthöhennetzes*. German Geodetic Commission (Deutsche Geodätische Kommission, DGK), series B 17. Bavarian Academy of Sciences and Humanities, Munich, Germany.

Helmert, F. R. (1907). *Die Ausgleichsrechnung nach der Methode der kleinsten Quadrate mit Anwendung auf die Geodäsie, die Physik und die Theorie der Meßinstrumente*. Teubner, Leipzig, Germany.

Herring, T. A. (1992). Modeling atmospheric delays in the analysis of space geodetic data. In DeMunck, J. & Spoelstra, T., editors, *Refraction of Transatmospheric Signals in Geodesy*, pages 157–164, Netherlands Geodetic Commision, Delft, The Netherlands.

Heublein, M., Alshawaf, F., Mayer, M., Hinz, S., & Heck, B. (2014). *Towards a rigorous fusion of GNSS and InSAR observations for the purpose of water vapor retrieval*. Schriftenreihe des Studiengangs Geodäsie und Geoinformatik, 2014-1. KIT Scientific Publishing, Karlsruhe, Germany.

Hinterberger, F., Weber, R., Huber, K., & Lesjak, R. (2015). Ambiguity fixing in real-time PPP – Determination of uncalibrated phase delays using a regional network. *Vermessung & Geoinformation*, 2+3:130–137.

Hirsch, A. & Plantamour, E. (1867). *Nivellement de précision de la Suisse*, volume 1(1). H. Georg, Libraire-éditeur, Genève Bale Lyon, Switzerland.

Hirsch, A. & Plantamour, E. (1883). *Nivellement de précision de la Suisse*, volume 1(8). H. Georg, Libraire-éditeur, Genève Bale Lyon, Switzerland.

Hirsch, A. & Plantamour, E. (1891). *Nivellement de précision de la Suisse*, volume 1(9). H. Georg, Libraire-éditeur, Genève Bale Lyon, Switzerland.

Hofmann-Wellenhof, B., Lichtenberger, H., & Wasle, E. (2008). *GNSS – Global Navigation Satellite Systems*. Springer, Vienna, Austria.

Holdahl, S. R. (1975). Models and strategies for computing vertical crustal movements in the United States. Presented at International Symposium on Recent Crustal Movements, Grenoble, France.

Holdahl, S. R. (1983). Recomputation of Vertical Crustal Motions near Palmdale, California, 1959-1975. *Tectonophysics*, 97:21–38.

Holdahl, S. R. & Hardy, R. L. (1979). Solvability and Multiquadric Analysis as Apllied to Investigations of Vertical Crustal Movements. *Tectonophysics*, 52:139–155.

Hooper, A. (2006). *Persistent scatterer radar interferometry for crustal deformation studies and modeling of volcano deformation*. PhD thesis, Stanford University, USA.

Hooper, A. (2008). A multi-temporal InSAR method incorporating both persistent scatterer and small baseline approaches. *Geophysical Research Letters*, 35(16):1–5.

Hooper, A. (2010). A Statistical-Cost Approach to Unwrapping the Phase of InSAR Time Series. In Lacoste-Francis, H., editor, *Proceedings of Fringe 2009 Workshop, Frascati, Italy, 30 November – 4 December 2009*, ESA Publications SP-677, pages 1–5.

Hooper, A., Bekaert, D., & Spaans, K. (2013). *StaMPS/MTI Manual Version 3.3b1*. School of Earth and Environment, University of Leeds, United Kingdom.

Hooper, A., Bekaert, D., Spaans, K., & Arıkan, M. (2012). Recent advances in SAR interferometry time series analysis for measuring crustal deformation. *Tectonophysics*, 514-517:1–13.

Hooper, A., Segall, P., & Zebker, H. A. (2007). Persistent scatterer interferometric synthetic aperture radar for crustal deformation analysis, with application to Volcán Alcedo, Galápagos. *Journal of Geophysical Research: Solid Earth*, 112(B7):1–21.

Hooper, A. & Zebker, H. A. (2007). Phase unwrapping in three dimensions with application to InSAR time series. *Journal of the Optical Society of America A*, 24(9):2737–2747.

Hooper, A., Zebker, H. A., Segall, P., & Kampes, B. M. (2004). A new method for measuring deformation on volcanoes and other natural terrains using InSAR persistent scatterers. *Geophysical Research Letters*, 31(23):1–5.

Hopfield, H. (1969). Two-quartic tropospheric refractivity profile for correcting satellite data. *Journal of Geophysical Research*, 74:4487–4499.

Hu, J., Zhu, J. J., Li, Z. W., Ding, X. L., Wang, C. C., & Sun, Q. (2011). Robust Estimating Three-Dimensional Ground Motions from Fusion of InSAR and GPS Measurements. In *International Symposium on Image and Data Fusion (ISIDF), 2011*, pages 1–4.

HVA (1952). *Das deutsche Haupthöhennetz: Höhen über Normal Null im neuen System des ehemaligen Reichsamts für Landesaufnahme*, volume 6. Hauptvermessungsabteilung Reutlingen, Germany.

IGS (2015). International GNSS Service. Website, available online at `http://igscb.jpl.nasa.gov`, IGS Central Bureau, Pasadena, USA. Last checked on 2015-11-17.

IKGB (2013). Internationale Gewässerschutzkommission für den Bodensee. Website, available online at `www.igkb.org`, Bayerisches Landesamt für Umwelt, Augsburg, Germany. Last checked on 2015-07-02.

Illies, J. H. (1977). Ancient and Recent Rifting in the Rhinegraben. *Geologie en Mijnbouw*, 56(4):329–350.

Illies, J. H. (1979). Rhinegraben: Shear controlled vertical motions of the Graben Floor. *Allgemeine Vermessungsnachrichten*, 86(10):364–367.

Illies, J. H., Baumann, H., & Hoffers, B. (1981). Stress pattern and strain release in the Alpine foreland. *Tectonophysics*, 71:157–172.

Illies, J. H. & Fuchs, K. (1983). Plateau Uplift of the Rhenish Massif – Introductory Remarks. In Fuchs, K., von Gehlen, K., Mälzer, H., Murawski, H., & Semmel, A., editors, *Plateau Uplift: The Rhenish Shield – A Case History*, pages 1–8. Springer, Berlin, Germany.

Insee (2015). Institut national de la statistique et des études économiques. Website, available online at `http://www.insee.fr`, Paris, France. Last checked on 2015-06-24.

ISONG (2015). Informationssystem Oberflächennahe Geothermie für Baden-Württemberg. Website, available online at `http://isong.lgrb-bw.de`, Landesamt für Geologie, Rohstoffe und Bergbau, Baden-Württemberg, Freiburg, Germany. Last checked on 2015-07-03.

Iwabuchi, T., Shoji, Y., Shimada, S., & Nakamura, H. (2004). Tsukuba GPS Dense Net Campaign Observation: Comparison of Stacking Maps of Post-fit Phase Residuals from Three Software Packages. *Journal of the Meteorological Society of Japan*, 82(1B):315–330.

Jahn, C. H., Feldmann-Westendorff, U., Grüner, D., Kulle, U., & Lembrecht, P. (2011). Die Erneuerung des Deutschen Haupthöhennetzes in Niedersachsen (als Teil des bundeseinheitlichen, homogenen und integrierten Festpunktfeldes). *Nachrichten der Niedersächsischen Vermessungs- und Katasterverwaltung (NaVKV)*, 4:3–26.

Janes, H. W., Langley, R. B., & Newby, S. P. (1991). Analysis of tropospheric delay prediction models: comparisons with ray-tracing and implications for GPS relative positioning. *Bulletin géodésique*, 65(3):151–161.

Jolivet, R., Grandin, R., Lasserre, C., Doin, M.-P., & Peltzer, G. (2011). Systematic InSAR tropospheric phase delay corrections from global meteorological reanalysis data. *Geophysical Research Letters*, 38(17):1–6.

Jónsson, S. (2002). *Modelling volcano and earthquake deformation from satellite radar Interferometric observations*. PhD thesis, Stanford University, USA.

Joshi, G. & Hayashi, D. (2010). Finite element modelling of the pull-apart formation: implication for tectonics of Bengo Co pull-apart basin, southern Tibet. *Natural Science*, 2:654–666.

Journel, A. G. & Huijbregts, C. J. (1981). *Mining Geostatistics. Repr. with corrections*. Academic Press, London New York San Francisco, USA.

Kampes, B. M. (2005). *Displacement parameter estimation using permanent scatterer interferometry*. PhD thesis, Delft University of Technology, Delft, The Netherlands.

Kampes, B. M., Hanssen, R. F., & Perski, Z. (2003). Radar interferometry with public domain tools. In Lacoste, H., editor, *Proceedings of Fringe 2003 Workshop, 1–5 December 2003, Frascati, Italy*, ESA Publications SP-550, pages 1–10.

Ketelaar (2009). *Satellite radar interferometry – subsidence monitoring techniques*. Springer, Berlin, Germany.

Knöpfler, A. (2015). *Korrektur stationsabhängiger Fehler bei GNSS*. German Geodetic Commission (Deutsche Geodätische Kommission, DGK), series C 744. Bavarian Academy of Sciences and Humanities, Munich, Germany.

Knöpfler, A., Masson, F., Mayer, M., Ulrich, P., & Heck, B. (2010a). GURN (GNSS Upper Rhine Graben Network) Status and First Results. In *Proceedings of the 95th Journées Luxembourgeoises de Géodynamique, Echternach, Grand Duchy of Luxembourg, 9–11 November 2009*, pages 1–6. European Center for Geodynamics and Seismology.

Knöpfler, A., Mayer, M., Heck, B., Masson, F., & Ulrich, P. (2010b). GURN (GNSS Upper Rhine Graben Network) – status and first results. In *FIG Congress 2010 – Facing the Challenges – Building the Capacity, April 11–16, 2010, Sydney, Australia*, pages 1–14.

Koch, K. (1999). *Parameter Estimation and Hypothesis Testing in Linear Models*. Springer, Berlin, Germany.

Kooi, H., Johnston, P., Lambeck, K., Smither, C., & Molendijk, R. (1998). Geological causes of recent (~100 yr) vertical land movement in the Netherlands. *Tectonophysics*, 299(4):297–316.

Krawinkel, T., Lindenthal, N., & Schön, S. (2014). Scheinbare Koordinatenänderungen von GPS-Referenzstationen: Einfluss von Auswertestrategien und Antennenwechseln. *Zeitschrift für Vermessungswesen*, 4:252–263.

Krige, D. G. (1951). A Statistical Approach to Some Mine Valuation and Allied Problems on the Witwatersrand. *Journal of the Chemical, Metallurgical and Mining Society of South Africa*, 52(6):119–193.

Kubik, K. (1967). Schätzung der Gewichte der Fehlergleichungen beim Ausgleichsproblem nach vermittelnden Beobachtungen. *Zeitschrift für Vermessungswesen*, 92:173–178.

Kuntz, E., Lichte, H., & Mälzer, H. (1975). Ein geodätischer Beitrag zur Geodynamik des Oberrheingrabens. *Vermessung, Photogrammetrie, Kulturtechnik, Fachblatt III/IV*, 75:179–184.

Kutscher, F. (1952). Der geologische Aufbau Hessens. In *Das deutsche Haupthöhennetz: Höhen über Normal Null im neuen System des ehemaligen Reichsamts für Landesaufnahme*, volume 6, pages 49–62. Hauptvermessungsabteilung Reutlingen, Germany.

Lagarias, J. C., Reeds, J. A., Wright, M. H., & Wright, P. E. (1998). Convergence Properties of the Nelder-Mead Simplex Method in Low Dimensions. *SIAM Journal of Optimization*, 9(1):112–147.

Lallemand, C. & Prévot, E. (1927). *Le nivellement général de la France de 1878 à 1927*. Ministère des Travaux publics, Imprimerie nationale, France.

Langbein, J. (2008). Noise in GPS displacement measurements from Southern California and Southern Nevada. *Journal of Geophysical Research: Solid Earth*, 113(B5):1–12.

Langley, R. (2015). The Almanac – Orbit Data and Resources on Active GNSS Satellites. *GPS World*, 25(8):46–49.

Leica (2006). *DNA03/DNA10 Gebrauchsanweisung, Version 2.0, Deutsch*. Leica Geosystems AG, Heerbrugg, Switzerland.

Leick, A. (2004). *GPS satellite surveying*. Wiley & Sons, New Jersey, USA.

Leinen, S., Becker, M., & Läufer, G. (2013). Effect of stochastic model fitting on the significance of CORS coordinate time series parameters. *Journal of Applied Geodesy*, 7:21–37.

Leismann, M., Klees, R., & Beckers, H. (1992). *Untersuchungen verschiedener Höhensysteme, dargestellt an einer Testschleife in Rheinland-Pfalz*. German Geodetic Commission (Deutsche Geodätische Kommission, DGK), series B 296. Bavarian Academy of Sciences and Humanities, Munich, Germany.

Leitz, H. (1983). The Influence of the Geomagnetic Field on the Zeiss Ni 1 Precision Level. In Pelzer, H. & Niemeier, W., editors, *Precise Levelling – Contributions to the Workshop on Precise Levelling*, pages 97–108. Dümmler, Bonn, Germany.

Lemeille, F., Cushing, M. E., Cotton, F., Grellet, B., Audru, F. M. J.-C., & Flehoc, F. R. C. (1999). Evidence for Middle to Late Pleistocene faulting within the northern Upper Rhine Graben (Alsace Plain, France). *Comptes Rendus de l'Academie des Sciences Series IIA Earth and Planetary Science*, 328(12):839–846.

Leppäranta, M. (2011). *The Drift of Sea Ice*. Springer, Berlin Heidelberg, Germany.

Lewis, A. S. & Overton, M. L. (2013). Nonsmooth optimization via quasi-Newton methods. *Mathematical Programming*, 141(1):135–163.

Leydecker, G. (2011). *Erdbebenkatalog für Deutschland mit Randgebieten für die Jahre 800–2008*. Geologisches Jahrbuch E 59. Schweizerbart, Stuttgart, Germany.

LGRB (2015). Landesamt für Geologie, Rohstoffe und Bergbau, Baden-Württemberg, Erdbebendienst. Website, available online at `http://www.lgrb-bw.de/erdbeben`, Freiburg, Germany. Last checked on 2015-12-02.

Li, J. & Heap, A. D. (2008). *A Review of Spatial Interpolation Methods for Environmental Scientists*. Record 2008/23. Geoscience Australia, Canberra, Australia.

Lidberg, M., Johansson, J. M., Scherneck, H.-G., & Milne, G. A. (2010). Recent results based on continuous GPS observations of the GIA process in Fennoscandia from BIFROST. *Journal of Geodynamics*, 50(1):8–18.

Liu, H., Li, X., Ge, L., Rizos, C., & Wang, F. (2011). Variable length LMS adaptive filter for carrier phase multipath mitigation. *GPS Solutions*, 15(1):29–38.

Lliboutry, L. (2000). *Quantitative Geophysics and Geology*. Springer Praxis Books. Springer, London, United Kingdom.

Lopes Cardozo, G. & Behrmann, J. H. (2006). Kinematic analysis of the Upper Rhine Graben boundary fault system. *Journal of Structural Geology*, 28(6):1028–1039.

Lorenz, G. K., Groenewoud, W., & Schokking, F. (1991). *Heden en verleden, Nederland naar beneden??? Interim-rapport over het onderzoek naar bodembeweging in Nederland*. Rijkswaterstaat, Rijks Geologische Dienst, The Netherlands.

Louis, A., Hadadou, R., Franck, C., & Kimmel, M. (2014). Avis sur l'origine des désordres survenus sur la commune de Lochwiller (67). Technical report, Géodéris, Metz, France.

Lubitz, C., Motagh, M., Wetzel, H.-U., & Kaufmann, H. (2013). Remarkable Urban Uplift in Staufen im Breisgau, Germany: Observations from TerraSAR-X InSAR and Leveling from 2008 to 2011. *Remote Sensing*, 5(6):3082–3100.

Lucht, H. (1983). Neighbourhood – Correlations among Observations in Levelling Networks. In Pelzer, H. & Niemeier, W., editors, *Precise Levelling – Contributions to the Workshop on Precise Levelling*, pages 315–326. Dümmler, Bonn, Germany.

Luo, X. (2013). *GPS stochastic modelling – signal quality measures and ARMA processes*. Springer theses: recognizing outstanding Ph.D. research. Springer, Berlin, Germany.

LVBW (1983). Verwaltungsvorschrift des Innenministeriums über das Nivellementpunktfeld. Technical report, Landesvermessungsamt Baden-Württemberg (LVBW), Stuttgart, Germany.

Mahapatra, P. S., Samiei-Esfahany, S., van der Marel, H., & Hanssen, R. F. (2014). On the Use of Transponders as Coherent Radar Targets for SAR Interferometry. *IEEE Transactions on Geoscience and Remote Sensing*, 52(3):1869–1878.

Mälzer, H. (1967). *Untersuchungen von Präzisionsnivellements im Oberrheingraben von Rastatt bis Basel im Hinblick auf relative Erdkrustenbewegungen*. German Geodetic Commission (Deutsche Geodätische Kommission, DGK), series B 138. Bavarian Academy of Sciences and Humanities, Munich, Germany.

Mälzer, H., Hein, G., & Zippelt, K. (1983). Height changes in the Rhenish Massif: determination and analysis. In Fuchs, K., von Gehlen, K., Mälzer, H., Murawski, H., & Semmel, A., editors, *Plateau Uplift: The Rhenish Shield – A Case History*, pages 164–176. Springer, Berlin, Germany.

Mälzer, H., Rösch, H., Misselwitz, I., Ebert, M., & Moosmann, D. (1988). Höhenänderungen in der Nordschweiz und im Südschwarzwald bis zum Bodensee. Technical report NTB 88-05, National Cooperative for the Disposal of Radioactive Waste (Nagra), Baden, Switzerland.

Mälzer, H., Schmitt, G., & Zippelt, K. (1979). Recent vertical movements and their determination in the Rhenish Massif. *Tectonophysics*, 52(1-4):167–176.

Marini, J. (1972). Correction of satellite tracking data for an arbitrary atmospheric profile. *Radio Science*, 7(2):223–231.

Marinkovic, P. S. & Larsen, Y. (2013). Consequences of Long-Term ASAR Local Oscillator Frequency Decay – an Empirical Study of 10 Years of Data. Presented at ESA Living Planet Symposium, Edinburgh, United Kingdom, 9–13 September 2013.

Massonnet, D., Rossi, M., Carmona, C., Adragna, F., Peltzer, G., Feigl, K., & Rabaute, T. (1993). The displacement field of the Landers earthquake mapped by radar interferometry. *Nature*, 364:138–142.

Mayer, M. (2006). *Modellbildung für die Auswertung von GPS-Messungen im Bereich der Antarktischen Halbinsel*. German Geodetic Commission (Deutsche Geodätische Kommission, DGK), series C 597. Bavarian Academy of Sciences and Humanities, Munich, Germany.

Mayer-Rosa, D. & Cadiot, B. (1979). A review of the 1356 Basel earthquake: Basic data. *Tectonophysics*, 53(3-4):325–333.

Meghraoui, M., Delouis, B., Ferry, M., Giardini, D., Huggenberger, P., Spottke, I., & Granet, M. (2001). Active Normal Faulting in the Upper Rhine Graben and Paleoseismic Identification of the 1356 Basel Earthquake. *Science*, 293(5537):2070–2073.

Meidow, H. (1998). Rekonstruktion und Reinterpretation ausgewählter schadensverursachender Erdbeben im Bereich des Oberrheingrabens und seiner Randgebiete. Technical report, Seismo Geologisches Büro Dr. Meidow, Cologne, Germany.

Meindl, M., Schaer, S., Hugentobler, U., & Beutler, G. (2004). Tropospheric Gradient Estimation at CODE: Results from Global Solutions. *Journal of the Meteorological Society of Japan. Ser. II*, 82(1B):331–338.

Meyer, F. J., Bamler, R., Jakowski, N., & Fritz, T. (2006). The Potential of Low-Frequency SAR Systems for Mapping Ionospheric TEC Distributions. *Geoscience and Remote Sensing Letters, IEEE*, 3(4):560–564.

Milanovsky, E. E. (1972). Continental Rift zones: Their arrangement and development . *Tectonophysics*, 15(1-2):65–70.

Miranda, N., Rosich, B., Santella, C., & Grion, M. (2004). Review of the impact of ERS-2 piloting modes on the SAR Dopper stability. In Lacoste, H., editor, *Proceedings of Fringe 2003 Workshop, Frascati, Italy, 1–5 December 2003*, ESA Publications SP-550, pages 1–11.

Mogi, K. (1958). Relations between the eruptions of various volcanoes and the deformations of the ground surfaces around them. *Bulletin of the Earthquake Research Institute*, 36:99–134.

Molodensky, M. S. (1958). New methods of studying the figure of the earth. *Bulletin géodésique (1946-1975)*, 50(1):17–21.

Montgomery, D. C. & Runger, G. C. (2011). *Applied statistics and probability for engineers*. Wiley & Sons, New Jersey, USA, 5th edition.

Moreira, A., Krieger, G., Hajnsek, I., Hounam, D., Werner, M., Riegger, S., & Settelmeyer, E. (2004). TanDEM-X: A TerraSAR-X Ad on Satellite for Single Pass SAR Interferometry. In *Proceedings IGARSS'05, Anchorage, Alaska*, volume II, pages 1000–1003.

Moreira, A., Prats-Iraola, P., Younis, M., Krieger, G., Hajnsek, I., & Papathanassiou, K. P. (2013). A tutorial on synthetic aperture radar. *Geoscience and Remote Sensing Magazine, IEEE*, 1(1):6–43.

Moritz, H. (1973). *Least-Squares Collocation*. German Geodetic Commission (Deutsche Geodätische Kommission, DGK), series A 75. Bavarian Academy of Sciences and Humanities, Munich, Germany.

Moritz, H. (1984). Geodetic reference system 1980. *Bulletin géodésique*, 58(3):388–398.

Mozzhukhin, O. A. (2010). Zur Analyse von Nivellementergebnissen. *Allgemeine Vermessungsnachrichten*, 3:110–112.

Murawski, H., Albers, H. J., Bender, P., Berners, H.-P., Dürr, S., Huckriede, R., Kauffmann, G., Kowalczyk, G., Meiburg, P., Müller, R., Muller, A., Ritzkowski, S., Schwab, K., Semmel, A., Stapf, K., Walter, R., Winter, K.-P., & Zankl, H. (1983). Regional Tectonic Setting and Geological Structure of the Rhenish Massif. In Fuchs, K., von Gehlen, K., Mälzer, H., Murawski, H., & Semmel, A., editors, *Plateau Uplift*, pages 9–38. Springer, Berlin Heidelberg, Germany.

Murawski, H. & Meyer, W. (2010). *Geologisches Wörterbuch*. Spektrum Akademischer Verlag, Heidelberg, Germany, 12th edition.

NFI (2015). Naturefriends International. Website, available online at `http://www.nfi.at`, Naturfreunde Internationale, Vienna, Austria. Last checked on 2015-11-18.

NGS (2015). GPS Antenna Calibration. Website, available online at `http://www.ngs.noaa.gov/ANTCAL/`, National Geodetic Survey, Silver Spring, USA. Last checked on 2015-11-18.

Niell, A. (1996). Global Mapping Functions for the Atmospheric Delay at Radio Wavelengths. *Journal of Geophysical Research*, 101(B2):3227–3246.

Ning, T., Elgered, G., & Johansson, J. (2011). The impact of microwave absorber and radome geometries on GNSS measurements of station coordinates and atmospheric water vapour. *Advances in Space Research*, 47(2):186–196.

Nocquet, J.-M. (2012). Present-day kinematics of the Mediterranean: A comprehensive overview of GPS results. *Tectonophysics*, 579(0):220–242.

Nocquet, J.-M. & Calais, E. (2003). Crustal velocity field of western Europe from permanent GPS array solutions, 1996-2001. *Geophysical Journal International*, 154(1):72–88.

Nocquet, J.-M. & Calais, E. (2004). Geodetic Measurements of Crustal Deformation in the Western Mediterranean and Europe. *Pure and Applied Geophysics*, 161(3):661–681.

Nocquet, J.-M., Calais, E., & Parsons, B. (2005). Geodetic constraints on glacial isostatic adjustment in Europe. *Geophysical Research Letters*, 32(6):1–5.

Oczlon, M. S. (2006). Terrane Map of Europe. *Gaea Heidelbergensis*, 15:1–1.

Parizzi, A., Cong, X. Y., & Eineder, M. (2010). First Results from Multifrequency Interferometry. A Comparison of Different Decorrelation Time Constatns at L, C and X Band. In Lacoste-Francis, H., editor, *Proceedings Fringe 2009 Workshop, Frascati, Italy, 30–4 December 2009*, ESA Publications SP-677, pages 1–5.

Park, K.-D., Elósegui, P., Davis, J. L., Jarlemark, P. O. J., Corey, B. E., Niell, A. E., Normandeau, J. E., Meertens, C. E., & Andreatta, V. A. (2004). Development of an antenna and multipath calibration system for Global Positioning System sites. *Radio Science*, 39(5):1–13.

Parkin, E. J. (1948). Vertical movement in the Los Angeles Region, 1906-1946. *Eos Transactions, American Geophysical Union*, 29(1):17–26.

Parkinson, B. W. & Spilker, J. J. (1996a). *Global Positioning System: Theory and ApplicationsGlobal Positioning System: Theory and Applications, Band 1*. Progress in astronautics and aeronautics, volume 163. American Institute of Aeronautics & Astronautics, USA.

Parkinson, B. W. & Spilker, J. J. (1996b). *Global Positioning System: Theory and ApplicationsGlobal Positioning System: Theory and Applications, Band 1*. Progress in astronautics and aeronautics, volume 164. American Institute of Aeronautics & Astronautics, USA.

Peltier, W. R., Argus, D. F., & Drummond, R. (2015). Space geodesy constrains ice age terminal deglaciation: The global ICE-6G_C (VM5a) model. *Journal of Geophysical Research: Solid Earth*, 120(1):450–487.

Pelzer, H. (1983). Systematic instrumental errors in precise levelling. In Pelzer, H. & Niemeier, W., editors, *Precise Levelling – Contributions to the Workshop on Precise Levelling*, pages 3–17. Dümmler, Bonn, Germany.

Pepe, A. & Lanari, R. (2006). On the Extension of the Minimum Cost Flow Algorithm for Phase Unwrapping of Multitemporal Differential SAR Interferograms. *IEEE Transactions on Geoscience and Remote Sensing*, 44(9):2374–2383.

Persson, C. (1980). *Minque and Related Estimators for Variance Components in Linear Models*. Royal Institute of Technology, Stockholm, Sweden.

Peters, G. (2007). *Active tectonics in the Upper Rhine Graben – Integration of paleoseismology, geomorphology and geomechanical modeling*. PhD thesis, University Amsterdam, The Netherlands.

Peters, G. & van Balen, R. T. (2007a). Pleistocene tectonics inferred from fluvial terraces of the northern Upper Rhine Graben, Germany. *Tectonophysics*, 430(1-4):41–65.

Peters, G. & van Balen, R. T. (2007b). Tectonic geomorphology of the northern Upper Rhine Graben, Germany. *Global and Planetary Change*, 58(1-4):310–334.

Petit, G. & Luzum, B. (2010). IERS Conventions. IERS Technical Note 36, International Earth Rotation and Reference Systems Service (IERS), Federal Agency for Cartography and Geodesy, Frankfurt, Germany.

Pflug, R. (1982). *Bau und Entwicklung des Oberrheingrabens*. Erträge der Forschung, volume 184. Wissenschaftliche Buchgesellschaft Darmstadt, Germany.

Pichelli, E., Ferretti, R., Cimini, D., Perissin, D., Montopoli, M., Marzano, F. S., & Pierdicca, N. (2010). Water vapour distribution at urban scale using high-resolution numerical weather model and spaceborne SAR interferometric data. *Natural Hazards and Earth System Science*, 10(1):121–132.

Plant, J., Whittaker, A., Demetriades, A., Marsina, K., & De Vivo, B. (2005). The Geological and Tectonic framework of Europe. In Salminen, R., editor, *Geochemical Atlas of Europe: Part 1 Background Information, Methodology and Maps*, pages 1–20. Geological Survey, Espoo, Finland.

Plenefisch, T. & Bonjer, K.-P. (1997). The stress field in the Rhine Graben area inferred from earthquake focal mechanisms and estimation of frictional parameters. *Tectonophysics*, 275(1-3):71–97.

Pope, A. J. (1976). *The statistics of residuals and the detection of outliers*. NOAA technical report NOS 65 NGS 1. Department of Commerce, National Oceanic and Atmospheric Administration (NOAA), USA.

Popp, M. (2009). Virtuelles Museum Vermessungsinstrumente. Website, available online at `http://www.bau-popp.de/pages/carl-zeiss-jena/nivelliergeraete/ni-a.php`, Germany. Last checked on 2015-09-17.

Prati, C., Ferretti, A., & Perissin, D. (2010). Recent advances on surface ground deformation measurement by means of repeated space-borne SAR observations. *Journal of Geodynamics*, 49(3-4):161–170.

Prats-Iraola, P., Nannini, M., Scheiber, R., Zan, F. D., Wollstadt, S., Minati, F., Vecchioli, F., Costantini, M., Bucarelli, A., Borgstrom, S., Walter, T., Foumelis, M., & Desnos, Y.-L. (2015). Investigations with the Sentinel-1 Interferometric Wide Swath Mode. Presented at Fringe 2015 Workshop, Frascati, Italy, 23–27 March 2015. Available only at `http://seom.esa.int/fringe2015/files/presentation17.pdf`. Last checked on 2016-02-01.

Prodehl, C., Mueller, S., Glahn, A., Gutscher, M., & Haak, V. (1992). Lithospheric cross sections of the European Cenozoic rift system. *Tectonophysics*, 208(1-3):113–138.

Prussia (1883). *Nivellement im südwestlichen Theile des preußischen Staates und im Reichsland Elsaß-Lothringen*. Nivellements der Trigonometrischen Abtheilung der Landesaufnahme, volume 5. Königliche Hof-Buchhandlung von E. S. Mittler & Sohn, Berlin, Germany.

Prussia (1894). *Ost- und Westpreußen*. Nivellements der Trigonometrischen Abtheilung der Landesaufnahme, volume 8. Königliche Hof-Buchhandlung von E. S. Mittler & Sohn, Berlin, Germany.

Rabus, B., Eineder, M., Roth, A., & Bamler, R. (2003). The shuttle radar topography mission – a new class of digital elevation models acquired by spaceborne radar. *ISPRS Journal of Photogrammetry and Remote Sensing*, 57(4):241–262.

Ragheb, A. E., Clarke, P. J., & Edwards, S. J. (2006). GPS sidereal filtering: coordinate- and carrier-phase-level strategies. *Journal of Geodesy*, 81(5):325–335.

Ramsayer, K. (1959). *Genauigkeitsuntersuchungen der Schwerereduktion von Nivellements*. German Geodetic Commission (Deutsche Geodätische Kommission, DGK), series A 31. Bavarian Academy of Sciences and Humanities, Munich, Germany.

Ray, J. K. (2006). What receiver technologies exist for mitigating GNSS pseudorange and carrier phase multipath? *Inside GNSS*, 1(6):25–27.

Rebischung, P., Griffiths, J., Ray, J., Schmid, R., Collilieux, X., & Garayt, B. (2012). IGS08: the IGS realization of ITRF2008. *GPS Solutions*, 16(4):483–494.

Ringenbach, R. (2013). Kalivie – Le site du patrimoine du Bassin potassique alsacien. Website, available online at `http://kalivie.free.fr`, France. Last checked on 2015-07-23.

Ritter, J., Wagner, M., Bonjer, K.-P., & Schmidt, B. (2009). The 2005 Heidelberg and Speyer earthquakes and their relationship to active tectonics in the central Upper Rhine Graben. *International Journal of Earth Sciences*, 98(3):697–705.

Rocca, F. (2007). Modeling Interferogram Stacks. *IEEE Transactions on Geoscience and Remote Sensing*, 45(10):3289–3299.

Rocca, F., Rucci, A., Ferretti, A., & Bohane, A. (2013). Advanced InSAR interferometry for reservoir monitoring. *First Break*, 31(5):77–85.

Röhr, C. (2014). Der Oberrheingraben. Website, available online at `http://www.oberrheingraben.de`, Friedberg, Germany. Last checked on 2015-06-30.

Roll, A. (1979). *Versuch einer Volumenbilanz des Oberrheingrabens und seiner Schultern*. Geologisches Jahrbuch A 52. Schweizerbart, Stuttgart, Germany.

Rosen, P. A., Hensley, S., Peltzer, G., & Simons, M. (2004). Updated repeat orbit interferometry package released. *Eos Transactions, American Geophysical Union*, 85(5):47.

Rosen, P. A., Hensley, S., Zebker, H. A., Webb, F. H., & Fielding, E. J. (1996). Surface deformation and coherence measurements of Kilauea Volcano, Hawaii, from SIR-C radar interferometry. *Journal of Geophysical Research: Planets*, 101(E10):23109–23125.

Rosenthal, G. (2001). SAPOS – The German National Satellite Positioning Service. In Kaminskis, J. & Jäger, R., editors, *1st Common Baltic Symposium, Riga, June 11, 2001, GPS-Heighting based on the Concept of a Digital Height Reference Surface (DFHRS) and Related Topics*, pages 1–10.

Rost, C. & Wanninger, L. (2009). Carrier phase multipath mitigation based on GNSS signal quality measurements. *Journal of Applied Geodesy*, 3:81–87.

Rouchy, J.-M. (1997). Paleogene Continental Rift System of Western Europe: Locations of Basins, Paleogeographic and Structural Framework, and the Distribution of Evaporites. In Busson, G. & Schreiber, B. C., editors, *Sedimentary deposition in rift and foreland basins in France and Spain (Paleogene and lower Neogene)*, pages 45–94. Columbia University Press, New York, USA.

Rózsa, S., Heck, B., Mayer, M., Seitz, K., Westerhaus, M., & Zippelt, K. (2005a). Determination of displacements in the upper Rhine graben Area from GPS and leveling data. *International Journal of Earth Sciences*, 94(4):538–549.

Rózsa, S., Mayer, M., Westerhaus, M., Seitz, K., & Heck, B. (2005b). Towards the determination of displacements in the Upper Rhine Graben area using GPS measurements and precise antenna modelling. *Quaternary Science Reviews*, 24(3-4):425–438.

Rucci, A., Ferretti, A., Guarnieri, A. M., & Rocca, F. (2012). Sentinel 1 SAR interferometry applications: The outlook for sub millimeter measurements. *Remote Sensing of Environment*, 120:156–163.

Saastamoinen, J. (1973). Contributions to the theory of atmospheric refraction. *Bulletin géodésique*, 107:13–34.

Saleh, M. & Becker, M. (2014). A new velocity field from the analysis of the Egyptian Permanent GPS Network (EPGN). *Arabian Journal of Geosciences*, 7(11):4665–4682.

Salvi, S., Stramondo, S., Funning, G. J., Ferretti, A., Sarti, F., & Mouratidis, A. (2012). The Sentinel-1 mission for the improvement of the scientific understanding and the operational monitoring of the seismic cycle. *Remote Sensing of Environment*, 120:164–174.

Samieie-Esfahany, S., Hanssen, R. F., van Thienen-Visser, K., & Muntendam-Bos, A. (2010). On the effect of horizontal deformation on InSAR subsidence estimates. In Lacoste, H., editor, *Proceedings of Fringe 2009 Workshop, Frascati, Italy, 30 November – 4 December 2009*, ESA Publications SP-677, pages 1–7.

Samsonov, S. V. & Tiampo, K. F. (2006). Analytical optimization of a DInSAR and GPS dataset for derivation of three-dimensional surface motion. *Geoscience and Remote Sensing Letters, IEEE*, 3(1):107–111.

Samsonov, S. V., Tiampo, K. F., & Rundle, J. B. (2008). Application of DInSAR-GPS optimization for derivation of three-dimensional surface motion of the southern California region along the San Andreas fault. *Computers & Geosciences*, 34(5):503–514.

SCCS Survey (2013). Leica DNA03 Digital Level. Website, available online at `http://www.sccssurvey.co.uk/leica-dna03-digital-level.html`, Eaton Socon, United Kingdom. Last checked on 2015-09-17.

Schaffrin, B. (2001). Equivalent Systems for Various Forms of Kriging, Including Least-squares Collocation. *Zeitschrift für Vermessungswesen*, 2:87–94.

Scharroo, R. & Visser, P. (1998). Precise orbit determination and gravity field improvement for the ERS satellites. *Journal of Geophysical Research: Oceans*, 103(C4):8113–8127.

Schauerte, W. & Heister, H. (2005). Der Ringversuch 2003/2004 zur Kalibrierung von Präzisionsnivellierlatten. *Allgemeine Vermessungsnachrichten*, 6:221–228.

Schellein, H. (1993). Kalibrierung und Bestimmung der thermischen Ausdehnungskoeffizienten der Invarlatten. In *Die Wiederholungsmessungen 1980 bis 1985 im deutschen Haupthöhennetz und das Haupthöhennetz 1985 der Bundesrepublik Deutschland*, pages 71–86. Bayerisches Landesvermessungsamt, Munich, Germany.

Schenk, A. (2015). *PS-Interferometrie in urbanen Räumen – Optimierte Schätzung von Oberflächenbewegungen mittels Multi-SBAS-Verfahren*. PhD thesis, Karlsruhe Institute of Technology, Germany.

Schlatter, A. (2007). *Das neue Landeshöhennetz der Schweiz LHN95*. Geodätisch-geophysikalische Arbeiten in der Schweiz, volume 72. Swiss Geodetic Commission, Zurich, Switzerland.

Schlatter, A. (2013). Rezente vertikale Oberflächenbewegungen in der Nordschweiz und in Südwestdeutschland – Kinematische Ausgleichung der Landesnivellementslinien CH/D. Work report NAB 12-34, National Cooperative for the Disposal of Radioactive Waste (Nagra), Wettingen, Switzerland.

Schlatter, A., Schneider, D., Geiger, A., & Kahle, H.-G. (2005). Recent vertical movements from precise levelling in the vicinity of the city of Basel, Switzerland. *International Journal of Earth Sciences*, 94(4):507–514.

Schlunegger, F. & Mosar, J. (2011). The last erosional stage of the Molasse Basin and the Alps. *International Journal of Earth Sciences*, 100(5):1147–1162.

Schmidt, D. A. & Bürgmann, R. (2003). Time-dependent land uplift and subsidence in the Santa Clara valley, California, from a large interferometric synthetic aperture radar data set. *Journal of Geophysical Research: Solid Earth*, 108(B9):1–13.

Schmitt, G. (1973). *Speichertechnische und numerische Probleme bei der Auflösung großer geodätischer Normalgleichungssysteme*. German Geodetic Commission (Deutsche Geodätische Kommission, DGK), series C 195. Bavarian Academy of Sciences and Humanities, Munich, Germany.

Schottler, W. (1959). Der geologische Aufbau von Rheinland-Pfalz. In *Das deutsche Haupthöhennetz: Höhen über Normal Null im neuen System des ehemaligen Reichsamts für Landesaufnahme*, volume 8, pages 29–42. P. Steffgen KG, Koblenz, Germany.

Schulze, P. (1976). *Das deutsche Haupthöhennetz: Höhen über Normal-Null im neuen System des ehemaligen Reichsamts für Landesaufnahme*. Landesvermessungsamt Baden Württemberg, Stuttgart, Germany.

Schumacher, M. E. (2002). Upper Rhine Graben: Role of preexisting structures during rift evolution. *Tectonics*, 21(1):1–17.

Schwarz, M. & Henk, A. (2005). Evolution and structure of the Upper Rhine Graben: insights from three-dimensional thermomechanical modelling. *International Journal of Earth Sciences*, 94(4):732–750.

Schweizer, R. (1992). *Höhenänderungen von Nivellementpunkten im südlichen Oberrheingraben*. Schriftenreihe Angewandte Geologie Karlsruhe, volume 16. University of Karlsruhe, Germany.

Sedlacek (2002). Untertage-Erdgasspeicherung in Deutschland – Underground Gas Storage in Germany. *Erdöl, Erdgas, Kohle*, 118(11):498–504.

Seeber, G. (2003). *Satellite Geodesy*. de Gruyter, Berlin, Germany.

Seibt, W. (1882). *Gradmessungs-Nivellement zwischen Swinemünde und Konstanz*. Publikationen des Königlich Preussischen Geodätischen Instituts. Stankiewicz, Berlin, Germany.

Serpelloni, E., Faccenna, C., Spada, G., Dong, D., & Williams, S. D. P. (2013). Vertical GPS ground motion rates in the Euro-Mediterranean region: New evidence of velocity gradients at different spatial scales along the Nubia-Eurasia plate boundary. *Journal of Geophysical Research: Solid Earth*, 118(11):6003–6024.

Shanno, D. (1970). Conditioning of quasi-Newton methods for function minimization. *Mathematics of Computation*, 24:647–656.

Shen, Z.-K., Jackson, D. D., & Kagan, Y. Y. (2007). Implications of Geodetic Strain Rate for Future Earthquakes, with a Five-Year Forecast of M5 Earthquakes in Southern California. *Seismological Research Letters*, 78(1):116–120.

Shepard, D. (1968). A two-dimensional interpolation function for irregularly-spaced data. In *Proceedings of the 1968 ACM National Conference*, pages 517–524.

Smith, E. K. & Weintraub, S. (1953). The Constants in the Equation for Atmospheric Refractive Index at Radio Frequencies. *Proceedings of the IRE*, 41(8):1035–1037.

Smyrnaios, M., Schön, S., & Nicolás, M. L. (2013). Multipath Propagation, Characterization and Modeling in GNSS. In Jin, S., editor, *Earth and Planetary Sciences: Geodetic Sciences – Observations, Modeling and Applications*, pages 99–125. InTech, Rijeka, Croatia.

Snedecor, G. W. & Cochran, W. G. (1980). *Statistical methods*. Iowa State University Press, Ames, USA, 7th edition.

Sousa, J. J., Hooper, A., Hanssen, R. F., Bastos, L. C., & Ruiz, A. M. (2011). Persistent Scatterer InSAR: A comparison of methodologies based on a model of temporal deformation vs. spatial correlation selection criteria. *Remote Sensing of Environment*, 115(10):2652–2663.

SpaceflightNow (2016). Spaceflight Now – Launch schedule. Website, available online at `http://spaceflightnow.com/launch-schedule`. Last checked on 2016-01-27.

Stadtmuseum Aarau (2015). Studiensammlung Kern. Website, available online at `http://www.kern-aarau.ch/kern/rundgang/geodaesievermessung.html`, Aarau, Switzerland. Last checked on 2015-09-17.

Statistisches Amt (2015). Wohnbevölkerung nach Geschlecht, Heimat und Gemeinde. XLS file, available online at `http://www.statistik-bs.ch`, Basel, Switzerland. Last checked on 2015-06-24.

Statistisches Bundesamt (2014). Gemeinden in Deutschland mit Bevölkerung am 31. Dezember 2013 (Fortgeschriebene amtliche Einwohnerzahlen auf Grundlage des Zensus 2011). XLS file, available online at `https://www.destatis.de`, Wiesbaden, Germany. Last checked on 2015-06-24.

Strasser, M., Strasser, A., Pelz, K., & Seyfried, H. (2009). A mid Miocene to early Pleistocene multi-level cave as a gauge for tectonic uplift of the Swabian Alb (Southwest Germany). *Geomorphology*, 106:130–141.

Takalo, M. & Rouhiainen, P. (2004). On System Calibration of Digital Level. In *International Conference on Engineering Surveying, 15–19 March 2004, Zurich, Switzerland*, pages 1–10.

Takalo, M., Rouhiainen, P., Lehmuskoski, P., & Saaranen, V. (2001). On Calibration of Zeiss DiNi12. In *Technical Conference during the FIG Working Week, 8–10 May 2001, Seoul, Korea*, pages 1–10.

Tape, C., Musé, P., Simons, M., Dong, D., & Webb, F. (2009). Multiscale estimation of GPS velocity fields. *Geophysical Journal International*, 179(2):945–971.

Tesauro, M., Hollenstein, C., Egli, R., Geiger, A., & Kahle, H.-G. (2005). Continuous GPS and broad-scale deformation across the Rhine Graben and the Alps. *International Journal of Earth Sciences*, 94(4):525–537.

Tesauro, M., Hollenstein, C., Egli, R., Geiger, A., & Kahle, H.-G. (2006). Analysis of central western Europe deformation using GPS and seismic data. *Journal of Geodynamics*, 42(4-5):194–209.

Teunissen, P. J. G. (2006). *Network Quality Control*. Series on mathematical geodesy and positioning. Delft University of Technology, VSSD, The Netherlands.

Teunissen, P. J. G. (2007). Least-squares prediction in linear models with integer unknowns. *Journal of Geodesy*, 81(9):565–579.

Teunissen, P. J. G. & Amiri-Simkooei, A. R. (2008). Least-squares variance component estimation. *Journal of Geodesy*, 82(2):65–82.

Tison, C., Nicolas, J.-M., Tupin, F., & Maitre, H. (2004). A new statistical model for Markovian classification of urban areas in high-resolution SAR images. *IEEE Transactions on Geoscience and Remote Sensing*, 42(10):2046–2057.

Torge, W. & Müller, J. (2012). *Geodesy*. de Gruyter, Berlin, Germany, 4th edition.

Tschan, S. (2013). Geodetic and hydrochemical evidence for regional land subsidence by sulfate rock dissolution in South West Germany. Master's thesis, Karlsruhe Institute of Technology, Germany.

Urek, J. & Jegentowicz, P. (2003). Les puits miniers du bassin houiller lorrain. Website, available online at `http://lorraine.charbon.free.fr`, France. Last checked on 2015-07-22.

USGS (2015). U. S. Geological Survey. Website, available online at `http://www.usgs.gov`, USGS National Center, Reston, USA. Last checked on 2015-12-07.

UWDAS (2015). University of Wyoming, Department of Atmospheric Science. Website, available online at `http://weather.uwyo.edu/upperair/sounding.html`, Laramie, USA. Last checked on 2015-12-17.

van Balen, R. T., Houtgast, R. F., van der Wateren, F. M., Vandenberghe, J., & Bogaart, P. W. (2000). Sediment budget and tectonic evolution of the Meuse catchment in the Ardennes and the Roer Valley Rift System. *Global and Planetary Change*, 27(1-4):113–129.

van Leijen, F. J. (2014). *Persistent Scatterer Interferometry based on geodetic estimation theory*. PhD thesis, Delft University of Technology, The Netherlands.

van Leijen, F. J., Hanssen, R. F., Marinkovic, P. S., & Kampes, B. M. (2006). Spatio-temporal Phase Unwrapping using Integer Least-Squares. In Lacoste, H., editor, *Proceedings of Fringe 2005 Workshop, Frascati, Italy, 28 November – 2 December 2005*, ESA Publications SP-610, pages 1–6.

Vanìček, P. & Christodulidis, D. (1974). A Method for the Evaluation of Vertical Crustal Movement from Scattered Geodetic Relevellings. *Canadian Journal of Earth Sciences*, 11(5):605–610.

Vanìček, P. & Grafarend, E. W. (1980). *On the Weight Estimation in Leveling*. NOAA technical report NOS 86 NGS 17. Department of Commerce, National Oceanic and Atmospheric Administration (NOAA), USA.

Vigny, C., Chéry, J., Duquesnoy, T., Jouanne, F., Ammann, J., Anzidei, M., Avouac, J.-P., Barlier, F., Bayer, R., Briole, P., Calais, E., Cotton, F., Duquenne, F., Feigl, K. L., Ferhat, G., Flouzat, M., Gamond, J.-F., Geiger, A., Harmel, A., Kasser, M., Laplanche, M., Le Pape, M., Martinod, J., Ménard, G., Meyer, B., Ruegg, J.-C., Scheubel, J.-M., Scotti, O., & Vidal, G. (2002). GPS network monitors the Western Alps' deformation over a five-year period: 1993-1998. *Journal of Geodesy*, 76(2):63–76.

Villemin, T. & Bergerat, F. (1987). L'evolution structurale du fossée rhénan au cours du cénozoique: un bilan de la déformation et des effets thermiques de l'extension. *Bulletin de la Société Géologique de France*, 2:245–255.

von Raumer, J. F., Stampfli, G. M., & Bussy, F. (2003). Gondwana-derived microcontinents – the constituents of the Variscan and Alpine collisional orogens. *Tectonophysics*, 365(1-4):7–22.

Wagner, G. (1952). Die Bewegungen des Untergrunds in Südwestdeutschland. In *Das deutsche Haupthöhennetz: Höhen über Normal Null im neuen System des ehemaligen Reichsamts für Landesaufnahme*, volume 6, pages 39–47. Hauptvermessungsabteilung Reutlingen, Germany.

Walters, R. J., Parsons, B., & Wright, T. J. (2014). Constraining crustal velocity fields with InSAR for Eastern Turkey: Limits to the block-like behavior of Eastern Anatolia. *Journal of Geophysical Research: Solid Earth*, 119(6):5215–5234.

Wampach, M. (2012). Untersuchungen zu lokalen Vertikalbewegungen im Erdölfeld Landau unter Verwendung geodätischer Daten. Bachelor's thesis, Karlsruhe Institute of Technology, Germany.

Wang, H. & Wright, T. J. (2012). Satellite geodetic imaging reveals internal deformation of western Tibet. *Geophysical Research Letters*, 39(7):1–5.

Weber, D. (1993a). Arbeiten für die Wiederholungsmessungen 1980 bis 1985 im Deutschen Haupthöhennetz. In *Die Wiederholungsmessungen 1980 bis 1985 im deutschen Haupthöhennetz und das Haupthöhennetz 1985 der Bundesrepublik Deutschland*, pages 7–16. Bayerisches Landesvermessungsamt, Munich, Germany.

Weber, D. (1993b). Die Entwicklung des Deutschen Haupthöhennetzes. In *Die Wiederholungsmessungen 1980 bis 1985 im deutschen Haupthöhennetz und das Haupthöhennetz 1985 der Bundesrepublik Deutschland*, pages 7–16. Bayerisches Landesvermessungsamt, Munich, Germany.

Webley, P. W., Bingley, R. M., Dodson, A. H., Wadge, G., Waugh, S. J., & James, I. N. (2002). Atmospheric water vapour correction to InSAR surface motion measurements on mountains: results from a dense GPS network on Mount Etna. *Physics and Chemistry of the Earth*, 27:363–370.

Wegener, A. (1929). *Die Entstehung der Kontinente und Ozeane*. F. Vieweg & Sohn Akt.-Ges., Brunswick, Germany, 4th edition.

Wegmüller, U., Werner, C., Strozzi, T., Wiesmann, A., Frey, O., & Santoro, M. (2015). Sentinel-1 support in the GAMMA software. In Ouwehand, L., editor, *Proceedings of Fringe 2015 Workshop, Frascati, Italy, 23–27 March 2015*, ESA Publications SP-731, pages 1–4.

Weinberger, H. (2015). Hessisches Landesamt für Umwelt und Geologie. Website, available online at `http://www.hlug.de`, Wiesbaden, Germany. Last checked on 2015-07-23.

Wernthaler, R. (1939). Das Studium tektonischer Bewegungen und das Europäische Hauptnivellementsnetz (R.E.U.N.). *Bulletin géodésique (1922–1941)*, 62:303–310.

Wessel, P., Smith, W. H. F., Scharroo, R., Luis, J., & Wobbe, F. (2013). Generic Mapping Tools: Improved Version Released. *Eos, Transactions American Geophysical Union*, 94(45):409–410.

Williams, S. D. P. (2003a). Offsets in Global Positioning System time series. *Journal of Geophysical Research: Solid Earth*, 108(B6):1–13.

Williams, S. D. P. (2003b). The effect of coloured noise on the uncertainties of rates estimated from geodetic time series. *Journal of Geodesy*, 76(9-10):483–494.

Williams, S. D. P. (2008). CATS: GPS coordinate time series analysis software. *GPS Solutions*, 12(2):147–153.

Williams, S. D. P., Bock, Y., Fang, P., Jamason, P., Nikolaidis, R. M., Prawirodirdjo, L., Miller, M., & Johnson, D. J. (2004). Error analysis of continuous GPS position time series. *Journal of Geophysical Research: Solid Earth*, 109(B3):1–19.

Wilson, J. (1963). Evidence from Islands on the Spreading of Ocean Floors. *Nature*, 197:536–538.

Wilson, J. (1965). A New Class of Faults and their Bearing on Continental Drift. *Nature*, 207:343–347.

Wirsing, G. & Luz, A. (2007). Hydrogeologischer Bau und Aquifereigenschaften der Lockergesteine im Oberrheingraben (Baden-Württemberg). Informationen 19, Landesamt für Geologie, Rohstoffe und Bergbau, Baden-Württemberg, Freiburg, Germany.

Witchayangkoon, B. (2000). *Elements of GPS Precise Point Positioning*. PhD thesis, University of Maine.

Wolf, S. (2014). Untersuchung hydrogeologischer Ursachen von Landsenkungen im Rhein-Neckar-Raum. Master's thesis, Karlsruhe Institute of Technology, Germany.

Woschitz, H. (2005). Systemkalibrierung: Effekte von digitalen Nivelliersystemen. *Allgemeine Vermessungsnachrichten*, 6:239–244.

Woschitz, H. & Brunner, F. K. (2003). Development of a Vertical Comparator for System Calibration of Digital Levels. *VGI – Österreichische Zeitschrift für Vermessung und Geoinformation*, 91(1):68–76.

Wu, J. E., McClay, K., Whitehouse, P., & Dooley, T. (2009). 4D analogue modelling of transtensional pull-apart basins. *Marine and Petroleum Geology*, 26(8):1608–1623.

Wübbelmann, H. (1993). Vergleich zwischen Höhen im DHHN 85 und im Nivellementnetz 1960. In *Die Wiederholungsmessungen 1980 bis 1985 im deutschen Haupthöhennetz und das Haupthöhennetz 1985 der Bundesrepublik Deutschland*, pages 155–163. Bayerisches Landesvermessungsamt, Munich, Germany.

Zebker, H. A. & Villasenor, J. (1992). Decorrelation in interferometric radar echoes. *IEEE Transactions on Geoscience and Remote Sensing*, 30(5):950–959.

Zhong, P., Ding, X. L., Zheng, D. W., Chen, W., & Huang, D. F. (2008). Adaptive wavelet transform based on cross-validation method and its application to GPS multipath mitigation. *GPS Solutions*, 12(2):109–117.

Ziegelbrenner (2006). Map of German Reich 1871–1918. PNG file, available online at `http://commons.wikimedia.org/wiki/File:Deutsches_Reich1.png`. Last checked on 2015-10-16.

Ziegler, P. A. (1992). European Cenozoic rift system. *Tectonophysics*, 208:91–111.

Ziegler, P. A. & Dèzes, P. (2006). Crustal evolution of Western and Central Europe. *Geological Society, London, Memoirs*, 32(1):43–56.

Zippelt, K. (1983). Measurement of level rod's temperature and effects on precise levelling. In Pelzer, H. & Niemeier, W., editors, *Precise Levelling – Contributions to the Workshop on Precise Levelling*, pages 165–177. Dümmler, Bonn, Germany.

Zippelt, K. (1988). *Modellbildung, Berechnungsstrategie und Beurteilung von Vertikalbewegungen unter Verwendung von Präzisionsnivellements*. German Geodetic Commission (Deutsche Geodätische Kommission, DGK), series C 343. Bavarian Academy of Sciences and Humanities, Munich, Germany.

Zippelt, K. & Dierks, O. (2007). Auswertung von wiederholten Präzisionsnivellements im südlichen Schwarzwald, Bodenseeraum sowie in angrenzenden schweizerischen Landesteilen. Work report NAB 07-27, National Cooperative for the Disposal of Radioactive Waste (Nagra), Wettingen, Switzerland.

Zippelt, K. & Mälzer, H. (1987). Results of new geodetic investigations in SW-Germany. *Journal of Geodynamics*, 8(2-4):179–191.

Zumberge, J. F., Heflin, M. B., Jefferson, D. C., Watkins, M. M., & Webb, F. H. (1997). Precise point positioning for the efficient and robust analysis of GPS data from large networks. *Journal of Geophysical Research: Solid Earth*, 102(B3):5005–5017.

Acronyms and Symbols

List of acronyms

3D	Three-dimensional
APS	Atmospheric Phase Screen
BF	Black Forest
BS5	Bernese GPS Software, Version 5.0
CATS	Create and Analyze Time Series
DC	Doppler Centroid
DEM	Digital Elevation Model
DEOS	Delft Institute of Earth Observation and Space Systems
DePSI	Delft PS-InSAR software
DHHN	Deutsches Haupthöhennetz (German primary height network)
DORIS	Delft Object-oriented Radar Interferometric Software
DS	Distributed Scatterer
EBF	Eastern Border Fault
EC	Ensemble Coherence
ECMWF	European Centre for Medium-Range Weather Forecasts
EDM	Electronic Distance Measurement
Envisat	Environmental Satellite
EOLi	ESA's Earth Observations Link client
EOP	Earth Orientation Parameters
EOST	École et Observatoire des Sciences de la Terre, Université de Strasbourg
EPN	EUREF Permanent Network
ERS	European Remote Sensing Satellites
ESA	European Space Agency
EUCOR	EUropean COnfederation of Upper Rhine universities
EUREF	European Reference Frame
EV	Extreme Value
GIA	Glacial Isostatic Adjustment
GIK	Geodetic Insitute, Karlsruhe Institute of Technology
GPS	Global Positioning System
GNSS	Global Navigation Satellite Systems
GURN	GNSS Upper Rhine Graben Network
IGN	Institut National de l'Information Géographique et Forestière
IGS	International GNSS Service
InSAR	Interferometric SAR or SAR Interferometry
ITRF	International Terrestrial Reference Frame
IWV	Integrated Water Vapour
KaGeMoV	Karlsruher Geschwindigkeitsmodelle zur Berechnung von Vertikalbewegungen
LGL	Landesamt für Geoinformation und Landentwicklung Baden-Württemberg
LGRB	Landesamt für Geologie, Rohstoffe und Bergbau, Baden-Württemberg
LOS	Line Of Sight
LVermGeo	Landesamt für Vermessung und Geobasisinformation Rheinland-Pfalz
LVGL	Landesamt für Vermessung, Geoinformation und Landentwicklung Saarland
MAD	Mean Absolute Difference/Deviation
MAX	Maximum value
MERIS	MEdium Resolution Imaging Spectrometer
MIN	Minimum value
NC	Normal Correction
NOC	Normal-Orthometric Correction
PCO	Phase Centre Offset

PCV	Phase Centre Variations
PDF	Probability Density Function
PPP	Precise Point Positioning
PS	Persistent Scatterer
RRF	Rhine River Fault
SA*POS*®	Satellitenpositionierungsdienst der deutschen Landesvermessung
SAR	Synthetic Aperture Radar
SBAS	Small Baseline Subset
SCLA	Spatially Correlated Look Angle error
SLC	Single Look Complex
SRTM	Shuttle Radar Topography Mission
StaMPS	Stanford Method for Persistent Scatterers
STC	Spatio-temporal consistency
STD	Standard deviation
SULA	Spatially Uncorrelated Look Angle error
swisstopo	Bundesamt für Landestopografie (Swiss surveying authority)
UELN	United European Levelling Network
URG	Upper Rhine Graben
URGENT	Upper Rhine Graben: Evolution and NeoTectonics
VCE	Variance Component Estimation
VG	Vosges Mountains
WBF	Western Border Fault

List of latin symbols

a	Acceleration / Semi-major axis (in Sect. 4.3)
A	Design matrix / Azimuth (in Sect. 4.4.1 and 5.1) / Amplitude (in Sect. 3.3 and 5.2.3)
b	Intercept / Projection of LOS into the E–N-plane (in Sect. 7.2)
b_1, b_2, b_3, b_4	Model parameter or coefficient
B	Benchmark or measurement point (also used together with point A, point C, ...)
B_{corr}	Correction factor
BL	Baseline
$B_{\parallel}$	Parallel baseline
$B_{\perp}$	Perpendicular baseline
c	Velocity of light / Elements of covariance matrix C (in Sect. 4.4.2)
c_0	Nugget value
c_1	Partial sill
C	Covariance matrix
d	Distance
D	Covariance matrix
D_A	Amplitude dispersion
E	East (component)
e	Vector of errors or error term / Partial pressure (in Sect. 5.1 and 6.3)
f	Function / Flattening (in Sect. 4.3)
F	Signal frequency of GNSS
F_{DC}	Doppler Centroid frequency
$\mathcal{F}$	Fisher distribution
$g, \tilde{g}$	Measured or calculated gravity value
G	Gravitational constant
G_0	Constant gravity value
h	Measured height difference
H	Height
H^N	Normal height
H^{NO}	Normal-orthometric height

i	Index of time or index of interferograms
I	Identity matrix
j	Index of benchmark, point, pixel / Imaginery unit (in Sect. 3.3 and Eq. (6.16))
k	Index of benchmark, point, pixel
k_1, k_2, k_3	Refractivity coefficients
$K_{\Delta\phi}$	Coefficient relating tropospheric phase to topography
l	Index of height differences between benchmarks
l_{ovs}	Oversampling factor
L_a	Antenna length
$L1, L2$	GPS carrier frequencies
$L3$	Ionosphere-free linear combination
m	Ratio between centrifugal acceleration and normal gravity at the equator
MF	Mapping Function
M_L	Local magnitude
M_W	Moment magnitude
n	Number of benchmarks, points, pixels, interferograms, observations, parameters
N	North (component) / Ambiguity (in Chap. 3) / Normal equation matrix (in Chap. 4)
$\mathcal{N}$	Normal distribution
$o(t)$	Offset at a certain time t
p	Elements of the weight matrix P / Pressure (in Sect. 5.1 and 6.3)
$p(t)$	Periodic function
P	Weight matrix
P_0, P_1	SAR backscattering locations
q	Elements of a covariance matrix Q / Grid order (in Sect. 5.3.3)
Q	Covariance matrix / Constant of proportionality (in Sect. 6.3)
r	Redundancy / Range (in Sect. 7.3.2)
r', r''	Modified range
r_{back}, r_{for}	Backward reading, forward reading
R	Receiver / Range measurement (in Sect. 3.3)
$\vec{R}$	Position vector
R_d, R_w	Specific gas constants (dry, wet)
s	Unknown variance component
S	Satellite
S_{asc}, S_{desc}	Projection vector for LOS displacements
S_{filt}	Length (wavelength) of spatial filter
t	Time
t_0	Reference time
T	Period or temporal baseline / Temperature (in Sect. 5.1 and 6.3)
T_{filt}	Length (time span) of temporal filter
T_S	Test value of a significance test
u	Number of unknowns
U	Up (component)
v, V	Velocity
$\vec{v}$	Velocity vector
w	Weight or weight vector
W	Weight matrix
x	Vector of unknowns or unknown parameter
X, Y, Z	Cartesian coordinates
y	Vector of observations or observed parameter
z	Zenith angle
z_q	Quantile of the normal distribution

List of greek symbols

α	Heading / Significance level (in Sect. 3.1.3 and 7.4.1) / Slope angle (in Sect. 4.2.2)
β	Parameter of spatial decorrelation model
δ	Clock error
δ_A	Azimuth resolution
δg	Gravity reduction
δH	Residual height error
Δ	Tropospheric path delay
Δg	Bouguer anomaly
Δt	Time difference
$\Delta\phi$	Phase difference
Δr	Pixel size in range direction
ΔR	LOS displacement
ϵ	Residual errors or noise
γ	Coherence / Semivariance (in Sect. 7.3)
γ_a, γ_b	Parameters of decorrelation models
$\hat{\gamma}_{EC}$	Ensemble coherence
γ_0, γ_H	Normal gravity value, normal gravity value at height H
$\bar{\gamma}$	Mean normal gravity along the ellipsoidal normal
Γ	Gamma function
κ	Decay coefficient
λ	Wavelength / Lagrange multiplier (in Sect. 7.3.1)
λ_P	Longitude of an Euler pole
μ	Mean value
ν	Degree of freedom
ν'	Frequency decay
ω	Angular rate of rotation
$\vec{\omega}$	Rotation vector
φ	Geodetic latitude
φ_P	Latitude of an Euler pole
ϕ	Phase, particularly phase measurement of InSAR
Π	Constant of proportionality
ψ	GNSS phase observation
ρ	GNSS pseudorange
ρ_{STC}	Spatio-temporal consistency
ρ_w	Density of water
σ	Standard deviation
σ^2, σ_0^2	Variance, Variance of unit weight
τ	Parameter of temporal decorrelation model
θ	Incidence angle

List of operators

$\lvert x\rvert$	Absolute value of x
$\hat{x}$	Estimate of x from least-squares adjustment
x^*	Complex conjugate of x
$\exp(x)$	Exponential function of x
$\sum_{j=0}^{n} x_j$	Summation of values $x_0 \ldots x_n$
$\min_{\forall j} x_j$	Minimum value of all x_j
$\frac{df}{dx}$, $\frac{\partial f}{\partial x}$	Derivative of f w.r.t. x, partial derivative of f w.r.t. x
$E\{x\}$	Expectation value of x
$W\{x\}$	Wrapped value of x
$tr(X)$	Trace of matrix X

Acknowledgements

Although this dissertation represents an individual work, it would not have been written without the sincere help and support of many people. First, I would like to express my deep thanks to my principal supervisor, Prof. Bernhard Heck, for his guidance and support, and particularly for enabling me to have a full position for the whole period of my research activities at GIK. His positive attitude and feedback encouraged me at any time to advance the geodetic investigations in the URG area. I would like to thank Prof. Stefan Hinz for serving as a second reviewer. As the speaker of the GRAduate School for Climate and Environment (GRACE) at KIT, he was also in charge of the funding of my research stay at TU Delft. I would like to thank Prof. Ramon Hanssen for his warm welcome at TU Delft and for serving as an international referee of this work. My thanks go to all further members of the doctoral committee for their interest in this dissertation.

Further, I would like to extend my sincere thanks to all my colleagues at GIK and the Institute of Photogrammetry and Remote Sensing (KIT) for the good collaboration, their support and contribution to a pleasant work environment. In particular, I would like to thank Dr. Karl Zippelt, Dr. Michael Mayer and Dr. Malte Westerhaus for the fruitful discussions and advices during the development of this work. A special thanks goes to Malte, who accompanied the project through all phases and particularly supported the geoscientific interpretation of the results. I am grateful to the members of the radar group at TU Delft for many inspiring discussions, and to all other PhD students in the "grote kamer" at the Department of Geoscience and Remote Sensing for their warm welcome and the leisure activities we experienced together in and around Delft. Last but not least, I would like to thank the various scientific and non-scientific proofreaders who read parts of the thesis and contributed to a uniform appearance.

This work would not have been possible without the large amount of geodetic data provided by a variety of institutions. I want to thank all data providers for supplying GNSS and levelling data free of charge: Landesamt für Geoinformation und Landentwicklung Baden-Württemberg (LGL, Germany), Landesamt für Vermessung und Geobasisinformation Rheinland-Pfalz (LVermGeo, Germany), Landesamt für Vermessung, Geoinformation und Landentwicklung Saarland (LVGL, Germany), Institut National de l'Information Géographique et Forestière (IGN, France), REseau NAtional GPS permanent (RENAG, France), Teria (France), Orpheon (France), Bundesamt für Landestopografie swisstopo (Switzerland), EUREF Permanent Network (EPN), International GNSS Service (IGS). The ERS and Envisat SAR data were kindly provided by the European Space Agency (ESA). The whole research project was funded through the German Science Foundation (DFG) under grants HE 1433/17-1 and HE 1433/17-2.

I owe my deepest gratitude to my parents for their support in all situations, enabling me to continue my path and perform all the professional and private projects of the last decades. I want to thank my friends for spending leisure time together, particularly with sports and music. Finally, I would like to express my warmest thanks to my wife Claudia for her understanding and support. I am looking forward to our common future.